LAWRENCE
LIVERMORE
NATIONAL
LABORATORY

LLNL-TH-727717

Benchmarking transition energies and emission strengths for X-ray astrophysics with measurements at the Livermore EBITs

N. Hell

March 24, 2017

Disclaimer

This work performed under the auspices of the U.S. Department of Energy by Lawrence Livermore National Laboratory under Contract DE-AC52-07NA27344.

Benchmarking transition energies and emission strengths for X-ray astrophysics with measurements at the Livermore EBITs

Bewertung von Übergangsenergien und Emissionsstärken für die Röntgenastronomie mit Messungen an den Livermore EBITs

Der Naturwissenschaftlichen Fakultät
der Friedrich-Alexander-Universität
Erlangen-Nürnberg

zur

Erlangung des Doktorgrades Dr. rer. nat.

vorgelegt von

Natalie Hell
aus Freising

Als Dissertation genehmigt
von der Naturwissenschaftlichen Fakultät
der Friedrich-Alexander-Universität Erlangen-Nürnberg

Tag der mündlichen Prüfung:	3.3.2017
Vorsitzender des Promotionsorgans:	Prof. Dr. Georg Kreimer
Gutachter:	Prof. Dr. Jörn Wilms
Gutachter:	Dr. Gregory V. Brown

Zusammenfassung

Die charakteristischen Spektrallinien sowohl von Übergängen in die K-Schale von astrophysikalisch häufig vorkommenden Metallen als auch von Übergängen in die L-Schale von Elementen der Fe-Gruppe liegen im weichen Röntgenbereich mit Photonenenergien zwischen 0.1 und 10 keV. Diese Signaturen stellen eine wichtige Diagnostik dar für Plasmaparameter wie zum Beispiel die Temperatur und Dichte der im Plasma enthaltenen Elektronen und Ionen. Damit bilden diese eine wichtige Grundlage, um jene Physik zu verstehen, die energetischen Prozessen in astrophysikalischen Quellen zugrunde liegt. Mit den Fortschritten, die bei der spektralen Auflösung und der effektiven Fläche der für Beobachtungen im Röntgenbereich verwendeten, satellitenbasierten Instrumente und Teleskope erzielt werden, wächst die Zahl und Qualität der diagnostischen Möglichkeiten dieser Spektralllinien. Um jedoch vollen Nutzen aus diesen Diagnostiken ziehen zu können – sei es durch globales Modellieren der ganzen Bandbreite eines beobachteten Spektrums oder durch lokale Modellierung, bei der einzelne Linien als Diagnostik herangezogen werden –, ist es wichtig, dass die zugrunde liegende Atomphysik vollständig und sehr genau bekannt ist. Die nächste Generation von Röntgensatelliten für Spektroskopie im weichen Röntgenbereich wird Mikrokalorimeter benutzen wie z.B. das SXS auf *Astro-H/Hitomi* oder das X-IFU auf *Athena*. Diese Satelliten werden im Laufe des nächsten Jahrzehnts hochaufgelöste Spektroskopie mit großer effektiver Fläche über den gesamten weichen Röntgenbereich hinweg allgemeiner zugänglich machen. Dadurch werden die Plasmaparameter durch die Analyse der von diesen Satelliten aufgenommenen Spektren mit einer Genauigkeit ermittelt werden können, die mehr durch die Ungenauigkeit der atomphysikalischen Referenzdaten begrenzt ist als durch instrumentale Einschränkungen. Für Beobachtungen mit hochauflösenden Beugungsgittern wie dem *Chandra*-HETG und dem *XMM-Newton*-RGS ist die Ungenauigkeit der atomphysikalischen Referenzdaten schon jetzt manchmal problematisch. Daher ist es besonders wichtig, die Genauigkeit der atomphysikalischen Daten festzustellen und diese gegebenenfalls zu verbessern.

Dedizierte Messungen im Labor sind essentiell für die Bewertung von theoretischen Berechnungen, welche den Großteil der in der Astrophysik verwendeten Referenzdaten ausmachen. Experimente mit den Elektronenstrahl-Ionenfallen (EBIT-I und SuperEBIT) am Lawrence Livermore National Laboratory stellen eine etablierte Methode für solche Messungen dar. In dieser Arbeit präsentiere ich neue Messungen mit EBIT für Linienenergien und für absolute Wirkungsquerschnitte für Anregung durch Elektronenstöße, welche an aktuell offenem Bedarf an speziellen Referenzdaten ausgerichtet sind.

Zunächst wurden die Energien von Kα-Übergängen in jenen Ionen von Si und S gemessen, welche eine offene L-Schale haben. Dazu wurde das EBIT Calorimeter Spectrometer (ECS) mit einer spektralen Auflösung von 4.5–5.0 eV verwendet, also mit einer Auflösung ähnlich des *Astro-H/Hitomi*-SXS. Während diese Kα-Linien bisher am deutlichsten von Si und S Ionen in den Spektren einer Reihe von astrophysikalischen Quellen beobachtet wurden, wird erwartet, diese in Zukunft auch von den Ionen anderer astrophysikalisch relevanter Elemente zu detektieren. Die bei EBIT gemessenen Linienzentren haben eine

Unischerheit von $\lesssim 0.5\,\mathrm{eV}$ im Falle der stärkeren Spektrallinien und von $\lesssim 1\,\mathrm{eV}$ im Falle der schwächeren Linien. Diese Unsicherheit entspricht einer Dopplerverschiebung von weniger als $90\,\mathrm{km\,s^{-1}}$ und ist damit besser als die Unsicherheit der Wellenlängenkalibration des *Chandra*-HETG. Die gemessenen Linienzentren wurden mit Hilfe von Berechnungen mit dem Flexible Atomic Code (FAC) identifiziert und ausserdem mit diesen und Berechnungen von Palmeri et al. (2008) verglichen. Die Auswirkung unserer Messungen auf die Interpretation astrophysikalischer Spektren wurde anhand von Neuberechnungen der Dopplerverschiebungen in den Spektren der massiven Röntgendoppelsternsysteme Vela X-1 und Cyg X-1 gezeigt. Des Weiteren wurden die mit dem ECS erzielten Messergebnisse mit Hilfe des hochauflösenden, abbildenden und fokussierenden Kristallspektrometers EBHiX anhand der Kα-Linien in N- bis Li-artigen S Ionen verifiziert. Die Messung mit dem Kristallspektrometer hat eine spektrale Auflösung von bis $\sim 0.52\,\mathrm{eV}$ und eine Unischerheit von $\lesssim 0.2\,\mathrm{eV}$. Dies entspricht einer Dopplerverschiebung von $< 30\,\mathrm{km\,s^{-1}}$ und erfüllt damit die Anforderungen des geplanten *Athena* Röntgensatelliten.

Als zweites wurde das EBHiX Kristallspektrometer verwendet, um die Kα-Übergänge von Fe Ionen mit offener M-Schale zu messen, welche in einem engen Energiebereich um 6.4 keV stark üeberlappen. Der Beitrag dieser Ionen zum 6.4 keV Linienkomplex ist interessant für transiente Plasmen wie jenen in Supernovaüberresten. Eine einfache Berechnung der Linien in Cl- bis F-artigem Fe mit FAC deutete darauf hin, dass eine spektrale Auflösung von 2 eV ausreichend sein könnte, um zumindest die Hauptkomponenten jedes Ions aufzulösen. Dies konnte jedoch bisher nicht bestätigt werden, obwohl die Auflösung dieser Messung diejenige von vorherigen Messungen übertraf.

Als drittes wurden die absoluten Wirkungsquerschnitte für die Anregung der Linie w in He-artigem Fe und der Linien Lyα_1 und Lyα_2 in H-artigem Fe durch Elektronenstöße für verschiedene Elektronenenergien und Ladungsgleichgewichte gemessen. Diese Wirkungsquerschnitte werden auf eine absolute Skala gebracht, indem der gemessene Fluss der stoßangeregten Linien auf den gemessenen Fluss des Spektrums von radiativer Rekombination (RR) im gleichen Ion normalisiert wird. Dabei wurde das Spektrum der stoßangeregten Linien mit den ECS-Pixeln für niederenergetische Photonen aufgenommen und das der RR mit den dickeren ECS-Pixeln für hochenergetische Photonen mit einer Auflösung von etwa 30 eV. Letztere haben es zum ersten Mal ermöglicht, die spektralen Signaturen der RR in die $n = 2$ Schale von Fe Ionen mit offener L-Schale für Elektronenenergien zu messen, die ausreichend hoch sind für die direkte Anregung von Elektronen aus der K-Schalen von Fe Ionen. Die gemessenen Wirkungsquerschnitte haben eine Unisicherheit auf dem 10% Niveau und erfüllen damit die Anforderungen, die von der astrophyiskalischen Gemeinschaft gestellt wurden. Die Bewertung von theoretischen Wirkungsquerschnitten auf diesem Niveau verbessert die Genauigkeit wichtiger Diagnostiken, wie zum Beispiel die Messung von Elementhäufigkeiten oder resonanter Streuung in den hochaufgelösten Spektren des Galaxienclusters Perseus, welche mit dem *Hitomi*-SXS aufgenommen wurden.

Zuletzt wurde noch das EBHiX Kristallspektrometer unter der Verwendung verschiedener Quartzkristalle evaluiert und die Temperatur der in EBIT gefangen Ionen aus der mit dem EBHiX gemessenen thermischen Linienverbreiterung abgeleitet. Die Möglichkeit, EBHiX für Messungen des Polarisationsgrades der in EBIT erzeugten Strahlung zu verwenden, wurde anhand der Polarisation der Lyα_1 Linie in H-artigem Mn gezeigt.

Abstract

K-shell transitions in astrophysically abundant metals and L-shell transitions in Fe group elements show characteristic signatures in the soft X-ray spectrum in the energy range 0.1–10 keV. These signatures have great diagnostic value for plasma parameters such as electron and ion temperatures and densities, and can thus help understand the physics controlling the energetic processes in astrophysical sources. This diagnostic power increases with advances in spectral resolution and effective area of the employed X-ray observatories. However, to make optimal use of the diagnostic potential – whether through global spectral modeling or through diagnostics from local modeling of individual lines – the underlying atomic physics has to be complete and well known. With the next generation of soft X-ray observatories featuring micro-calorimeters such as the SXS on *Astro-H/Hitomi* and the X-IFU on *Athena*, broadband high-resolution spectroscopy with large effective area will become more commonly available in the next decade. With these spectrometers, the accuracy of the plasma parameters derived from spectral modeling will be limited by the uncertainty of the reference atomic data rather than by instrumental factors, as is sometimes already the case for the high-resolution grating observations with *Chandra*-HETG and *XMM-Newton*-RGS. To take full advantage of the measured spectra, assessment of the accuracy of and improvements to the available atomic reference data are therefore important.

Dedicated measurements in the laboratory are essential to benchmark the theoretical calculations providing the bulk of the reference data used in astrophysics. Experiments at the Lawrence Livermore National Laboratory electron beam ion traps (EBIT-I and SuperEBIT) have a long history of providing this service. In this work, I present new measurements of transition energies and absolute electron impact excitation cross sections geared towards currently open atomic physics data needs.

First, I measured the energies of Kα transitions in L-shell ions of Si and S at EBIT using the EBIT calorimeter spectrometer (ECS) with 4.5–5.0 eV resolution, i.e., a similar resolution to the *Astro-H/Hitomi* SXS soft X-ray spectrometer. While these lines will become interesting also for L-shell ions of other astrophysically abundant elements, they have been observed most prominently from L-shell ions of Si and S in the X-ray spectra of a variety of astrophysical sources. The measured line centers have an accuracy of $\lesssim 0.5$ eV for the strong transitions and $\lesssim 1$ eV for the weaker ones. This accuracy translates to Doppler shifts of less than 90 km s^{-1}, i.e., less than the calibration uncertainty of the *Chandra* high-energy transmission gratings. The measured line centers are identified with my own calculations with the Flexible Atomic Code (FAC) and compared to these and calculations by Palmeri et al. (2008). I demonstrate the impact of these measurements by re-evaluating Doppler shifts for the high-mass X-ray binaries Vela X-1 and Cyg X-1 with the new reference data. Using the high-resolution, imaging focusing spherical crystal spectrometer EBHiX with a quartz 101 crystal, I verified the results from the ECS measurements on Kα transitions in N- through Li-like S. The measurement has a spectral resolution of better

than 0.52 eV. The derived transition energies have an accuracy of $\lesssim 0.2$ eV, corresponding to Doppler shifts of $< 30\,\mathrm{km\,s^{-1}}$, i.e., within the requirements set by the planned *Athena* X-ray observatory.

Secondly, I used the EBHiX crystal spectrometer with a quartz 110 crystal in second order to measure the strongly blended Kα spectra of M-shell Fe ions around 6.4 keV. Contributions to the 6.4 keV line complex from these ions are important for transient plasmas such as those in supernova remnants. While a simple FAC model of Cl- through F-like Fe suggested it should be possible to resolve major contributions from different charge states to this complex at a 2 eV resolution, the data did not allow us to identify any new lines, although the spectral resolution of this measurement was higher than in previous experiments.

Thirdly, I measured absolute electron impact excitation (EIE) cross sections for He-like Fe line w and H-like Fe Lyα_1 and Lyα_2 at different electron energies and charge balances. The cross sections of the direct excitation lines are brought to an absolute scale by normalizing to the radiative recombination (RR) spectrum of the same ion. The direct excitation spectrum was measured with the low-energy pixels of the ECS with a spectral resolution of about 6 eV, while the RR spectrum was recorded with the ECS's thicker high-energy pixels with instrumental resolution of about 30 eV. The high-energy pixels thus allowed us, for the first time, to resolve the RR into the $n = 2$ shell of L-shell Fe ions at electron impact energies high enough to excite a K-shell electron in Fe ions. These measurements of absolute EIE cross sections using the ECS microcalorimeter at EBIT have accuracies on the 10% level, and therefore fulfill the requirements on atomic reference data identified by the astrophysics community. Benchmarking theoretical cross sections on this level tightens the constraints on important diagnostics for, e.g., elemental abundance measurements and resonance scattering in the high-resolution X-ray spectra of the Perseus galaxy cluster observed with *Hitomi*-SXS.

Finally, the performance of the EBHiX crystal spectrometer at EBIT was evaluated for various quartz crystals and the ion temperatures of the ions trapped in EBIT were derived from thermal line broadening measured with EBHiX. The EBHiX's capability to measure the degree of linear polarization for X-ray transitions excited in EBIT was demonstrated for the H-like Mn Lyα line.

Contents

It has been shown that each element has its own characteristic fluorescent line spectrum in X-rays. This is very conveniently represented as is a spectrum of ordinary light, except that without a knowledge of the wave-length we are obliged to define the radiations by their absorption in some standard substance.

Barkla (1911)

1 Introduction

X-RAYS, or Röntgen rays, were discovered in late 1895 by Wilhelm Conrad Röntgen (1895). Röntgen was studying cathode rays – a stream of electrons traveling between two electrodes in a vacuum tube, but only identified as a new subatomic particle by Thomson (1897). To block visible light from fluorescence in the cathode ray tube during his experiments, Röntgen wrapped the vacuum tube with black cardboard. Although he had verified that no visible light could escape from the covered tube, a nearby fluorescent screen shimmered during each discharge of the tube. While similar effects had been observed before in experiments with these cathode ray tubes, Röntgen was the first to conclude that an unknown kind of radiation – he dubbed it X-radiation – might be causing the fluorescence. He immediately set out to study these rays in more detail. By holding materials of various thicknesses and densities between the cathode ray tube and the screen, he found that, like cardboard, most of the tested materials are transparent to these X-rays to some degree. In accordance with these findings, he even took an X-ray image of a hand, where the soft and calcified (bone) tissues cast shadows of different intensity. The ability to take images of the skeleton inside a living human would soon revolutionize medicine, but in Röntgen's first report (Röntgen, 1895) it was merely an item in a long list of tested materials.

Soon, X-rays were the new hot topic in physics research. Similar to visible light, at first it was unclear if X-rays consist of electromagnetic waves or particles (called corpuscles; Compton & Allison, 1935). If they were a form of electromagnetic radiation, it was expected that they can be diffracted similar to visible light. Early experiments on X-ray diffraction with a slit by Haga & Wind (1899) and Haga & Wind (1903) concluded that the X-ray wavelengths would have to be on the order of 10^{-8} cm (~ 1 Å). These findings were dismissed by Walter & Pohl (1908), who argued based on their own experience that Haga & Wind (1899)'s results were due to non-uniformities in the photographic plates used rather than actual diffraction. In their own slit experiments they did not find clear evidence for diffraction and concluded from the slit width used that $\lambda < 0.1\,\mu$m (< 1000 Å; Walter & Pohl, 1908) and, after refining their slits, $\lambda < 1.2 \cdot 10^{-9}$ cm (< 0.12 Å;

Walter & Pohl, 1909), if X-rays were indeed diffracted. This order of magnitude is close to estimates by Wien (1907) and Stark (1907), who used Planck's law (Planck, 1900a,b) to derive $\lambda \approx 6\text{–}20 \cdot 10^{-9}$ cm ($\approx 0.6\text{–}2$ Å). Both Haga & Wind and Walter & Pohl analyzed their photographic plates visually with the aid of a microscope. Koch (1912) developed a photometric method to analyze the intensities of photographic plates. Using this method, Sommerfeld (1912) re-examined the very plates from Walter & Pohl (1909) and found clear evidence for diffraction, leading to $\lambda \approx 4 \cdot 10^{-9}$ cm, in better agreement with the predictions from Planck's law. A common material for the target in cathode ray tubes was platinum. The characteristic X-rays of Pt fall into the range of 9–13 keV or 0.9–1.4 Å (Thompson et al., 2009), confirming these early measurements. Barkla (1911), in a culmination of his work from previous years, showed that each material emits X-rays characteristic for its elements as a result of X-rays of higher energy scattering in gases.

Around the same time, based on crystal density, Max von Laue estimated the spacing of atoms in the crystal lattice to be on the order of 10^{-8} cm. With X-ray wavelengths around 10^{-9} cm he therefore expected to use X-ray diffraction as a new tool to do crystallography, which was confirmed experimentally by his colleagues Friedrich & Kipping (Friedrich et al., 1913). Bragg & Bragg (1913) picked up on this discovery and built the first X-ray spectrometer (see also Chapter 5). The question of the wave versus particle nature of light was finally settled when Einstein (1905) suggested the wave-particle duality of light where waves of frequency ν are associated with photons of energy $E_\gamma = h\nu$, with h Planck's constant, to explain that some experiments were evidence for a particle nature of light, while other experiments showed wave characteristics. His idea, however, was not widely accepted until measurements of scattering of X-rays by Compton (1923), long after detailed experiments on the photoelectric effect by Millikan (1914) had confirmed Einstein's equation (much to Millikan's dismay).

1.1 Outline

The remainder of Chapter 1 introduces X-ray astronomy and the development of spectral resolution of space-borne X-ray observatories. The field of laboratory astrophysics, specifically pertaining to atomic physics, is introduced, which provides astronomers with the tools and reference data to analyze and interpret their observations. Atomic data needs, i.e., missing reference data and open questions about the accuracy of available data, are outlined in general and specifically on the examples of astrophysical objects relevant to measurements presented in this work: the high-mass X-ray binaries Cyg X-1 and Vela X-1 for reference energies of K-shell transitions in L-shell ions of Si and S, and other astrophysically abundant elements; the transient plasmas of supernova remnants for the energies for the heavily blended K-shell transitions in M-shell Fe ions; and the Perseus galaxy cluster for collisional excitation cross sections of K-shell transitions in highly charged Fe. Chapter 2 summarizes atomic physics theory relevant for this work, including the nomenclature used in the description of spectral lines, the framework for atomic structure calculations and the various available relativistic and non-relativistic approximations in calculations, thermal Doppler broadening, and the correction terms for

the spatial distribution for emission of linearly polarized radiation. Chapter 3 explains the working principle of electron beam ion traps and lists injection methods and spectrometers available at the LLNL EBITs. In Chapters 4 and 5 two of these spectrometers used for this work are discussed in detail. Chapter 4 describes the operating principle and pulse height analysis of microcalorimeters, the specifications of the EBIT Calorimeter Spectrometer, ECS, and the effective area, gain calibration, and spectral resolution of the ECS. The high-resolution imaging spherical crystal spectrometer EBHiX is explained in Chapter 5, detailing the geometry of Bragg's law and of the reflection characteristics of spherical mirrors and the von Hámos and Johann geometries. This is followed by a description of the EBHiX spectrometer specifications and its performance at EBIT, including a proof of concept for the use of EBHiX for polarization measurements at EBIT based on the example of H-like Mn Lyα_1. Chapter 6 presents ECS measurements of the energies of Kα transitions in L-shell ions of Si and S and the direct application of these new reference energies to calculate Doppler shifts for these lines in X-ray spectra of Vela X-1 and Cyg X-1. A repeat measurement of the S spectrum with EBHiX at higher resolution confirms the ECS measurement. Upcoming new high-accuracy wavelength calculations with the MRMP code, similar measurements for Kβ transitions of the same ions, and measurements for additional elements are discussed as next steps of this project. Chapter 7 gives an overview of existing wavelength measurements of Kα transitions in Fe ions, followed by a renewed effort to resolve the heavily blended transitions in M-shell Fe ions using EBHiX. Chapter 8 introduces the theory behind cross sections, explains the measurement approach and spectrometer requirements for normalizing the direct excitation cross sections to the well known radiative recombination cross sections, and summarizes the available theoretical reference data relevant for the experiment. An overview of the experimental setup and measured datasets is given and preliminary results for measured electron impact excitation cross sections of He-like Fe line w and H-like Fe Lyα_1 and Lyα_2 at several electron impact energies are presented. Again, next steps for this project are discussed at the end of the chapter. Finally, Chapter 9 summarizes the results and outlooks of the previous chapters.

1.2 X-ray Astronomy

While X-rays played a big role in fields like medicine and crystallography, X-ray astronomy had to wait for the advent of space programs. The Earth's atmosphere is opaque to X-rays, prohibiting useful observations with ground-based X-ray observatories. Nevertheless, celestial X-ray sources have been predicted about a decade before the first space missions[1]. Around 1938, Hulburt (1938) and, more strongly, Vegard (1938) proposed X-rays originating from the sun as the source of ionization in the Earth's ionosphere, the upper region of our atmosphere. While the X-ray flux of a black body with 6000 K surface temperature is not strong enough to support this theory, around the same time it became evident that the solor corona is orders of magnitude hotter than the solar surface – hot enough

[1] for a timeline of milestones in high-energy astrophysics see, e.g., `https://heasarc.gsfc.nasa.gov/docs/heasarc/headates/heahistory.html`

to be an abundant source of X-radiation. Grotrian (1931) proposed that the observed smearing of Fraunhofer lines in solar spectra is due to scattering off of free electrons in the corona and that certain emission lines can be attributed to forbidden transitions in highly charged ions. Both effects require high plasma temperatures, but Grotrian did not yet draw this conclusion (Peter & Dwivedi, 2014). Similarly, Edlén (1943) identified forbidden lines from highly charged ions and derived a coronal temperature of 0.25 MK from their intensity. But Alfvén (1941) was the first who realized the full impact of the solar corona being hot (Peter & Dwivedi, 2014), summarizing six arguments supporting the conclusion and deriving a temperature of 1 MK, which falls well into the range of currently derived values (e.g., De Pontieu et al., 2011).

1.2.1 X-ray Observatories

The first direct observation of celestial X-rays was by a photographic plate mounted behind a Be window to block light at longer wavelengths than X-rays, flown on a V-2 rocket by the US Naval Research Laboratory (NRL) in 1948 (Burnight, 1949). A second V-2 flight using thermoluminescent phosphor also shielded by a Be window confirmed the observation (Tousey et al., 1951). Although neither mission had spatial resolution to confirm the theory, the Sun was believed to be the source of the observed signal. This was confirmed with another V-2 rocket flight that carried a photon counter tube and was capable of rolling the rocket around its axis in flight: the observed modulation of signal intensity clearly correlated with the Sun's position in the sky (Friedman et al., 1951). The first two X-ray satellites Vanguard 3 and Explorer 7, both launched in 1959, suffered from large background signal due to the van Allen belts and did not detect X-rays. The spatial resolution and sensitivity of X-ray detectors on subsequent rocket flights, however, improved such that in 1962 an Aerobee 150 rocket discovered the first cosmic (extra solar) X-ray source, the low mass X-ray binary Sco X-1[2] and the diffuse X-ray background (Giacconi et al., 1962). A few more sources were discovered by rocket flights until the first successful X-ray observatory, *Uhuru*, was launched in 1970 (Giacconi et al., 1971), adding another 339 objects to the growing list of X-ray sources (Forman et al., 1978). Subsequent missions set out to discover even mores sources: e.g., *HEAO-1*, launched in 1977, found more than 1000 sources (Levine et al., 1984; Wood et al., 1984; Nugent et al., 1983) and *ROSAT*, launched in 1990 (Trümper, 1982; Trümper et al., 1991), cataloged more than 200 000 sources (Voges et al., 1999). These all-sky surveys were usually equipped with some form of proportional counters with very low intrinsic energy resolution of $E/\Delta E < 10$, as cosmic X-ray sources are typically faint with fluxes of $\sim 10^{-3}$ photons cm^{-2} s^{-1} or less (Paerels & Kahn, 2003).

These observations only allowed qualitative analysis of the overall continuum shape but not discrete spectral features (Paerels & Kahn, 2003, see Fig. 1.1 for minimum spectral resolution required for some of these features). But in parallel, instead of simply searching for more X-ray sources, the focus shifted to spectroscopy (Beiersdorfer, 2003). While the first X-ray telescope was mounted on the US space station Skylab in 1973 (Vaiana et al., 1977; Underwood et al., 1977), the *HEAO-2/Einstein* observatory (Giacconi et al.,

[2] the first X-ray source detected in the constellation Scorpius

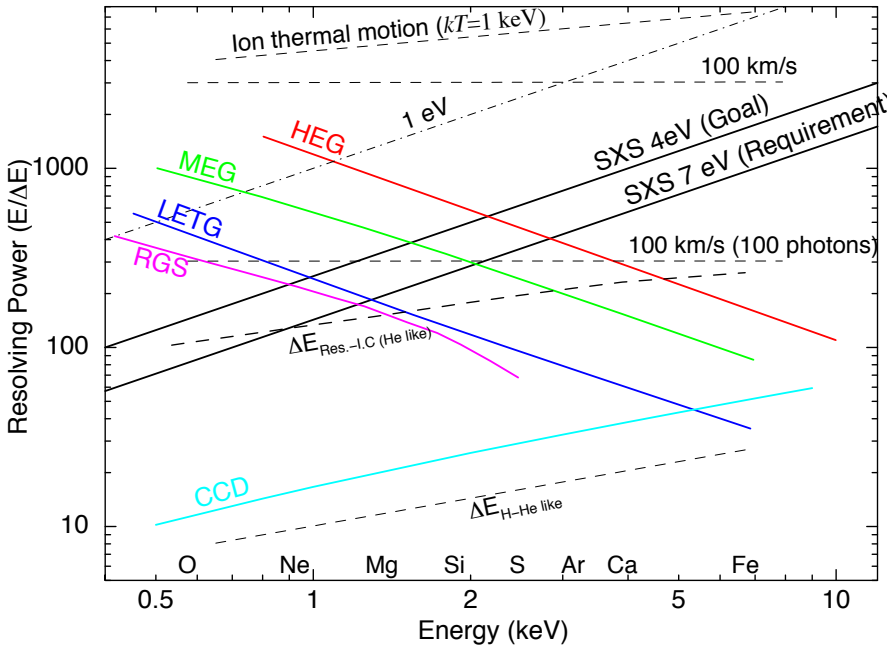

Figure 1.1: Resolving power of various satellites, taken from Mitsuda et al. (2010), Fig. 2.

1979), launched in 1978, was the first fully imaging orbiting X-ray telescope. It was also the first X-ray observatory featuring instrumentation for high-resolution spectroscopy, in the form of a crystal spectrometer with $E/\Delta E \approx 50$–1000 in the 0.42–2.6 keV energy band and a grating spectrometer with $E/\Delta E \sim 50$ below 3 keV, but with very small effective area. The US/Japanese mission *ASCA* (Tanaka et al., 1994), launched in 1993, was the first observatory to use a Charged Coupled Device (CCD) detector in X-ray astronomy and demonstrated the power of line spectroscopy (Paerels & Kahn, 2003). Despite a still moderate resolution of $E/\Delta E \approx 20$–50 (as for observatories equipped with CCD cameras that followed), the CCD resolving power was an order of magnitude better than that of the previously used proportional counters (Paerels & Kahn, 2003). While spectral features could clearly be identified with regions of line emission, their analysis was only possible with comprehensive plasma models (Paerels & Kahn, 2003).

XMM-Newton (Jansen et al., 2001) with its low-energy reflection gratings RGS (0.35–2.5 keV, $E/\Delta E \sim 200$–800; den Herder et al., 2001) and *Chandra* (Weisskopf et al., 2002) with the low- and high-energy transmission gratings (LETG: 0.08–6 keV, $E/\Delta E \sim$ 30–2000; HETG: 0.5–10 keV, $E/\Delta E \sim 60$–1000; Brinkman et al., 1987; Canizares et al., 1987, 2005; Markert et al., 1994) have provided the first high-resolution spectroscopy with sizable effective area. Both satellites also have CCD detectors for imaging on board (the Advanced Imaging Spectrometer ACIS on *Chandra*, Garmire et al., 2003, and the European Photon Imaging Cameras EPIC on *XMM-Newton*, Strüder et al., 2001, Turner et al., 2001), providing $E/\Delta E \sim 20$–50 resolving power[3]. While both satellites are still

[3]Other satellites with resolving powers on this level are *Suzaku* and *NuSTAR*. Both of these extend the observable energy range far beyond 10 keV. *Suzaku* (Mitsuda et al., 2007) features four CCD cameras

operational and expected to continue operations upwards of another decade, the grating spectrometers are impractical for very faint and for extended sources. The next generation of X-ray observatories will overcome these restrictions with even larger effective areas, i.e., higher sensitivity, and high-resolution energy-dispersive spectrometers (microcalorimeters, see also Chapter 4), for example the *Astro-H/Hitomi* observatory[4] in 2016 (Takahashi et al., 2010; Takahashi et al., 2016) and the *Athena* observatory with a planned launch in 2028 (Nandra et al., 2014; Ravera et al., 2014). Figure 1.1 shows a comparison of the energy-dependent resolving powers of current and future space-born X-ray spectrometers. Below ~ 2 keV, microcalorimeters with ~ 4 eV resolution will not constitute a leap in resolution. But for the Fe K region around 6 keV they bring unprecedented resolving powers, as currently the HETG on-board *Chandra* has barely twice the resolving power of a CCD detector at the price of much lower effective area. Moreover, for the first time high-resolution spectroscopy will be possible for extended sources like supernova remnants and clusters of galaxies.

Overall, the sensitivity and spatial resolution of current space-borne X-ray observatories are comparable to those of ground-based instruments in the visible part of the spectrum (Kallman & Palmeri, 2007). The highest spectral resolutions achieved to date are the gratings below 2 keV and of the few microcalorimeter spectra taken by *Hitomi* in the Fe region (Fig. 1.1).

1.2.2 X-ray Emitting Plasmas in Space

Classical physics can grossly be classified in two categories: theories describing and experiments testing our understanding of the Universe. In astronomy, however, the experimentalist's role is reduced to that of an observer. We cannot influence the physical parameters of celestial objects and it is not possible to isolate individual physical processes for examination. To test a new theory, sources have to be found which are either consistent or contradictory to the predictions of theory. Observing photons originating in distant cosmic sources is (almost) our only access to studying and understanding the universe. It is therefore of paramount importance to understand the physical processes underlying the production of these photons in order to interpret the physical environment of the cosmic sources (Beiersdorfer, 2003; Savin et al., 2012). Photons carry a wealth of information: the number of photons (intensity), changes in intensity over time (lightcurves), and the number of photons as a function of photon energy (spectral distribution), combined or individually, make it possible to paint amazingly accurate pictures of the evolution of the universe and its constituents.

We observe the universe in every wavelength band of the electromagnetic spectrum,

(X-ray Imaging Spectrometers XIS; Koyama et al., 2007) covering the 0.2–12.0 keV band and a collimated Hard X-ray Detector (HXD; Takahashi et al., 2007) covering 10–600 keV. The X-ray Spectrometer (XRS) microcalorimeter on-board unfortunately was lost at the very beginning of the mission (Kelley et al., 2007). *NuSTAR* uses CdZnTe semiconductor detectors ($E/\Delta E \sim 25$–75) covering the 3–79 keV band (Harrison et al., 2013).

[4] This mission was unfortunately very short-lived and could observe only a handful of objects, but the stunning quality of these few spectra (Hitomi Collaboration et al., 2016) gives an exciting new glimpse into the future of X-ray astronomy.

where each band has its own diagnostic utility. Many cosmic sources exhibit very energetic processes (e.g., supernovae, shocks, accretion of matter onto compact objects) leading to the presence of highly ionized material in their environment. Characteristic spectral signatures of highly charged ions of astrophysically abundant elements (up to $Z \approx 30$) fall into the energy band of 0.1–10 keV, often referred to as the soft X-ray band. Soft X-ray spectroscopy is therefore ideally suited for plasma diagnostics.

Most astrophysical plasmas can be classified either as coronal or as photoionized plasmas. Both types of plasmas have their own characteristics. In **coronal plasmas**, where electron densities typically are in the range $n_e \approx 10^{8...13}\,\mathrm{cm}^{-3}$ (Beiersdorfer, 2003), collisional equilibrium is dominated by collisions of the ions with electrons, i.e., the charge balance is determined by these electron-ion collisions (Paerels & Kahn, 2003; Kallman & Palmeri, 2007; Smith & Brickhouse, 2014). The electrons typically have a thermal (Maxwellian) energy distribution and the temperature of the most abundant ionic species is comparable to the electron temperature. Spectra of coronal plasmas are characterized by emission lines such as from resonance transitions, electric-dipole forbidden transitions, and dielectronic recombination satellite lines (Kallman & Palmeri, 2007). This is due to the low density in the coronal limit, where the radiative decay and Auger rates are faster than the collision rates (Beiersdorfer, 2003; Kallman & Palmeri, 2007; Smith & Brickhouse, 2014). At these low densities, the plasma is also optically thin to its own radiation (Mewe, 1999) such that photon scattering and re-absorption is negligible. The ionization and steady-state level populations are then a unique function of the plasma temperature and the X-ray luminosity is proportional to the emission measure $\epsilon_M = \int n_e^2 \mathrm{d}V$, i.e., the product of plasma density n_e squared and volume V (Paerels & Kahn, 2003). In case of a temperature gradient in the plasma, the differential emission measure $\partial \epsilon_M / \partial T$ is needed. Coronal plasmas are commonly found in stellar coronae, supernova remnants, clusters of galaxies, galaxies, stellar winds, and the hot interstellar medium (Kallman & Palmeri, 2007; Smith & Brickhouse, 2014; Paerels & Kahn, 2003; Brickhouse et al., 2006).

In contrast, in **photoionized plasmas** photons from a strong continuum radiation source are responsible for ionizing the gas and determine the charge balance (Kallman & Palmeri, 2007; Smith & Brickhouse, 2014). Since here the electron energy does not have to exceed the ionization potential of the ions, the electron temperature usually is much lower than for the same charge balance in a collisional plasma, around 5–10% of the ionization potential of the dominant ion species (Kallman & Palmeri, 2007). Electron-ion collisions are only important for recombination processes, especially radiative recombination, and gas cooling (Kallman & Palmeri, 2007; Smith & Brickhouse, 2014). Correspondingly, line emission is dominated by inner-shell fluorescence and collisions in low-lying levels and its equivalent widths, i.e., the line strength relative to the continuum, is smaller than in coronal plasmas (Kallman & Palmeri, 2007). Photoionization plasmas are often characterized via the ionization parameter $\xi = L/(n_e R^2)$ or similar, where L is the luminosity of the continuum source, n_e the electron density and R the distance of the plasma to the radiation source (Tarter et al., 1969; Davidson, 1972; Krolik et al., 1981; Paerels & Kahn, 2003). Examples for objects exhibiting photoionization plasmas are accretion powered sources such as active galactic nuclei (AGN) and X-ray binaries, planetary nebulae, HII regions, the intergalactic medium (IGM), Wolf-Rayet nebulae, and luminous blue variable

Table 1.1: List of atomic physics databases commonly used in X-ray astrophysics

Database	Reference	Usage	Url
NIST ASD	Kramida et al. (2016)	lists of wavelengths and transition rates	`https://www.nist.gov/pml/atomic-spectra-database`
AtomDB (APED)	Foster et al. (2012)	collisional plasma models (e.g., APEC), including models for non-equilibrium ionization	`http://atomdb.org/`
CHIANTI	Dere et al. (1997), Landi et al. (2013)	coronal plasmas, mostly solar physics	`http://chiantidatabase.org/`
uaDB (XSTAR)	Bautista & Kallman (2001)	photoionized plasma models	`http://heasarc.gsfc.nasa.gov/uadb/`
Cloudy	Ferland et al. (2013)	photoionized plasma modeling with collisions taken into account	`http://www.nublado.org/`
SPEX	Kaastra et al. (1996)	collisional ionization equilibrium model, based on MEKAL	`https://www.sron.nl/astrophysics-spex`

nebulae (Kallman & Palmeri, 2007; Smith & Brickhouse, 2014; Paerels & Kahn, 2003; Brickhouse et al., 2006).

From the description of the characteristics of these plasmas it becomes obvious that high-resolution spectroscopy greatly helps in distinguishing spectral features of the respective types of plasmas. The step from the CCD resolution of *ASCA* to the gratings on *Chandra* and *XMM-Newton* supports this point: in some cases, follow-up grating observations confirmed the previous astrophysical models for a source, in other cases the prevalent basic understanding of the source was challenged (Paerels & Kahn, 2003). For example, grating spectra discovered line features in spectra that had been thought featureless (Kallman & Palmeri, 2007). Suddenly, a requirement arose for significantly more comprehensive and accurate atomic databases than available and in use at that time (Kallman & Palmeri, 2007, for an overview of current databases see Table 1.1). Similar surprises are to be expected from the next generation X-ray observatories with their increased sensitivity and resolution in the Fe region for point sources and in general for extended sources (see, e.g., the *Astro-H* white papers, in particular Smith et al., 2014a, for a detailed overview of expected new spectral features). Where *Chandra* and *XMM-Newton* have revealed the shortcomings of existing atomic databases, *Hitomi* and *Athena* will push the limits even further. But as the example of *ASCA* shows, accurate and comprehensive atomic databases are equally important at low spectral resolution, since the measured spectra are incapable of announcing issues with the atomic data. Spectral modeling at CCD resolution can compensate for transitions of lines missing in the database by incorrectly filling the gaps through other processes (Brickhouse et al., 2000; Smith & Brickhouse, 2014).

A very important first step is a comprehensive line list to be able to identify transitions and ions involved. Once spectral features are clearly identified, their line fluxes can be used to determine a number of parameters, such as the number of ions, plasma temperatures

and densities. However, to do so, excitation rates have to be known, but currently the accuracy of the analysis is limited by the accuracy of the atomic data, not by the statistics of the observation (Kallman & Palmeri, 2007). In other words, we are currently not able to take full advantage of the diagnostic potential even in existing observations. The field of laboratory astrophysics was created as a response to solve these shortcomings (Beiersdorfer, 2003). Like detector and instrument development, laboratory astrophysics is necessary for astrophysics research (Brickhouse et al., 2006). Consequently, this need has been recognized, e.g., by the US National Research Council (NRC)'s 2010 decadal survey (Savin et al., 2010). The American Astrophysical Society (AAS) has a dedicated laboratory astrophysics division, and regular meetings are held to review recent progress and itemize the most critical needs (Salama et al., 2002; Brickhouse et al., 2006; Savin et al., 2010).

1.3 Laboratory Astrophysics

Laboratory astrophysics is the general area of research that collects and provides reference data relevant for the analysis and interpretation of astrophysical observations. As such, laboratory astrophysics is a broad field encompassing almost the full field of physics research: it covers atomic, molecular, plasma, particle, and nuclear physics, and even chemistry; it studies neutral gases and plasmas of various temperatures and densities, but also dust, ices, and solids; and it spans the entire electromagnetic spectrum from sub-mm to γ-rays. Atomic, molecular, and condensed matter physics are related to the generation of photons, while nuclear and particle physics are responsible for the evolution of matter, and plasma physics accounts for dynamic processes (Savin et al., 2012). This work will concentrate on atomic physics in the soft X-ray regime. Reviews about the physics, progress in the availability of data, specific problems solved by advances in laboratory astrophysics, and open data needs can be found in, e.g., Paerels & Kahn (2003), Beiersdorfer (2003), Brickhouse et al. (2006), Kallman & Palmeri (2007), Savin et al. (2010), Savin et al. (2012), and Smith & Brickhouse (2014).

Despite the word *laboratory*, laboratory astrophysics is often considered to include both measurements and theoretical work as means to collect the needed reference data (e.g., Brickhouse et al., 2006; Savin et al., 2010). For optimal results, it is crucial that theorists and experimentalists work together, as their work complements each other. For instance, laboratory measurements have repeatedly shown that theory is missing pieces, be it neglected transitions or relevant physical processes (Beiersdorfer, 2003). Especially for multi-electron systems, the atomic physics equations cannot be solved analytically and theory has to rely on approximations like perturbation theory. See, e.g., Kallman & Palmeri (2007) for a concise review of the various non-relativistic, semi-relativistic, and fully relativistic approximations and corrections commonly used in atomic physics theory, including a summary of commonly used codes and which of these approximations they rely on. For estimating uncertainties of the calculation and quantifying the effect of certain included processes, theory can often only compare calculations from different codes, using different gauges (Smith & Brickhouse, 2014). It is therefore important for

experiments to benchmark the accuracy of these calculations. On the other hand, it is very impractical – and sometimes nearly impossible – to measure each and every single transition wavelength or rate in the laboratory (Kallman & Palmeri, 2007). In these cases, benchmarked calculations are necessary to complete the atomic data. Also, often laboratory measurements rely on theory to identify transitions (see Chapter 6) or well known benchmarked calculations to correct for influences of the experimental setup such as detector effects (e.g., quantum efficiency, optical blocking filter transmission, crystal reflectivity, etc) and polarization and to bring the measurement to an absolute scale (see Chapters 4 and 8 and Section 5.6).

1.3.1 Data Needs

Although Smith & Brickhouse (2014) see "great strides in both accuracy and completeness, driven primarily by improvements in computational capability and the confrontation of atomic theoretical calculations with experimental benchmark studies and astrophysical observations", there are still open issues that need to be addressed (Paerels & Kahn, 2003; Beiersdorfer, 2003; Brickhouse et al., 2006; Kallman & Palmeri, 2007; Savin et al., 2010, 2012; Smith & Brickhouse, 2014). In the following some of these issues are summarized in general. Later in this chapter we outline more detailed the motivation relevant for the measurements presented in this work.

Atomic physics data needs can roughly be sorted into two categories: radiation, i.e., transitions connecting two levels within the same ion, and ionization/recombination, i.e., transitions connecting two levels in neighboring charge states, which are critical to determine the charge state distribution (Beiersdorfer, 2003; Smith & Brickhouse, 2014). This work focuses on needs in the radiation category.

Line Lists

The most fundamental – and simplest – atomic physics data needs are line lists (Kallman & Palmeri, 2007). As mentioned earlier, the identification of lines alone already gives hints to the present plasma conditions (Kallman & Palmeri, 2007): e.g., the presence of certain lines indicates elemental abundances; the type of observed transitions distinguishes collisional from photoionized plasmas; the range of ionization states hints at probable temperature or photon distributions depending on the type of plasma. If a line is missing from line lists, most likely other atomic physics like transition and excitation rates and branching ratios are not available for this line either, which can potentially influence the calculated rates and branching ratios for other transitions in the same and neighboring ions.

While comprehensive and complete line lists are essential, at the same time these lists should be critically evaluated and as accurate as possible (Brickhouse et al., 2006). But due to the vast number of lines in all astrophysically abundant ions, critically evaluated and complete can sometimes preclude each other. In a compromise to attempt both, the AtomDB database (Foster et al., 2012) aims at being comprehensive, but also sorts the

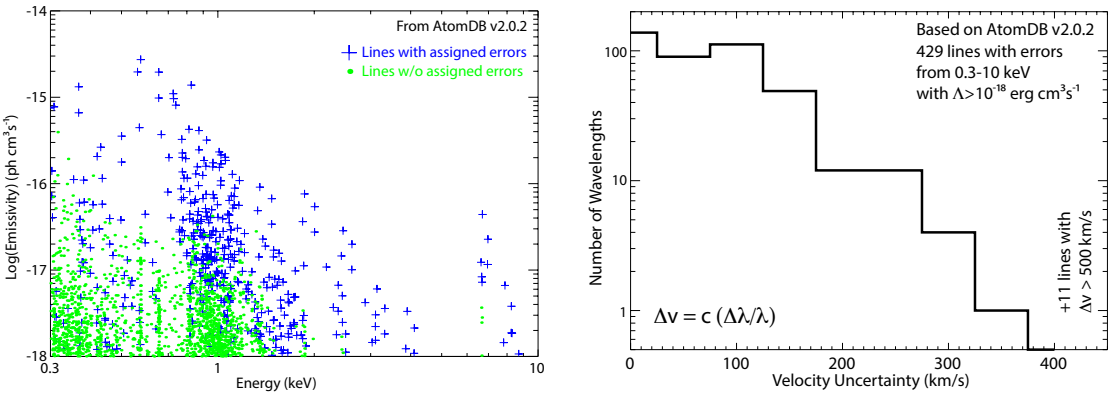

Figure 1.2: *Left*: lines with uncertainties in atomdb; *right*: uncertainties in wavelength translated to Doppler shifts. — From Smith & Brickhouse (2014, Figs. 5 & 6).

wavelengths of the listed lines into two categories, namely *observed* and *theory* values: the *observed* values are critically evaluated and can originate from either measurements or calculations, while the *theory* values stem from large atomic physics data production runs of less well known quality. AtomDB also includes uncertainty estimates for the wavelengths of the better known transitions. As shown in Fig. 1.2, so far only a fairly small number of lines in this database has reliable uncertainty estimates and some of these uncertainties are fairly large (Smith & Brickhouse, 2014).

Before the advent of high-resolution spectroscopy with gratings on *Chandra* and *XMM-Newton*, the content of line lists was largely driven by solar observations (Kallman & Palmeri, 2007). Laboratory measurements, especially with EBIT, made important contributions to add missing lines, but a lot of astrophysically relevant lines have not yet been studied in the laboratory (Beiersdorfer, 2003). Examples for lines typically still missing from the lists are L-shell transitions for low-Z ions and K-shell transitions in ions of charge below the He-like iso-electronic sequence (Beiersdorfer, 2003). For more details on K-shell transitions see Section 1.4.1 and Hitomi Collaboration et al. (2016). But even high-resolution spectrometers may not be able to resolve blends of very closely spaced line blends. For example, an L-shell transition in Na-like Fe has almost exactly the same wavelength (within 5 mÅ) as the Ne-like transition 3C such that the charge balance can strongly influence the measured line ratio of the Ne-like Fe lines 3C and 3D (Brown et al., 2001). A large number of weak unresolved lines can form a pseudo-continuum affecting the shape of the 'real' radiation continuum underlying the source spectrum (Fabian et al., 1994; Brown et al., 1998; Beiersdorfer, 2003; Foster et al., 2016). It is therefore important to reliably account for even weak and seemingly unimportant lines.

Wavelengths

Accurate reference wavelengths are particularly important to measure Doppler shifts. As a rule of thumb, the centroids of lines in the *Chandra* and *XMM-Newton* gratings spectra can be determined with an accuracy of about 10% of the instrumental resolution (Smith

& Brickhouse, 2014). This corresponds to 1–2 mÅ for HETG and a little larger for LETGS and RGS, which exceeds the precision of most *ab initio* calculations (Kallman & Palmeri, 2007). With the next generation of X-ray observatories, the required accuracy of reference wavelengths will be determined by the range of velocities (Doppler shifts) to be measured (Smith & Brickhouse, 2014). For the *Athena* X-ray observatory, the targeted velocities are about $30\,\mathrm{km\,s^{-1}}$ (Nandra et al., 2013), which corresponds to required accuracies of transition wavelengths of 0.01% or 1 mÅ at 10 Å (~ 0.1 eV at 1 keV; Smith & Brickhouse, 2014). Theoretical transition wavelengths listed in databases are usually derived from energy levels. The best calculations of energy levels are good to only $\sim 1\%$ (Smith & Brickhouse, 2014). Although the energy differences between levels connected by strong radiative transitions tend to be more accurate than the energy levels themselves, separate line lists in addition to the level lists are usually included in databases for plasma codes (Smith & Brickhouse, 2014). The accuracy of transitions in He- and H-like ions usually is considered very high (within about 40 ppm for both He-like, Beiersdorfer & Brown, 2015, and H-like ions, Beiersdorfer, 2009, and references therein) and these lines are often even used for calibration of the wavelength scale. Other strong lines have a good chance to have been measured in the laboratory. Here, transitions to the K- or L-shell do not suffer from the same uncertainties as M-shell ions, which are so closely spaced that uncertainties can even lead to an inversion of the ordering of energy levels (Smith & Brickhouse, 2014). Additionally, energy levels often enter rate calculations (Smith & Brickhouse, 2014) and any large uncertainties in level energy therefore propagate through to the rate coefficients.

Collisional Excitation Rates

Since a large number of X-ray emitting plasmas are in the coronal limit, collisional excitation rates constitute a very important contribution to the observed line ratios. Line ratios are the base to the determination of many plasma condition parameters: e.g., electron temperature and density, optical depth, and elemental abundances. As these parameters typically do not scale linearly with theoretical line ratios, small improvements in collisional excitation rates can make a large difference in the accuracy of the plasma parameter estimates (Smith & Brickhouse, 2014; Kallman & Palmeri, 2007). Brickhouse et al. (2006) state the need on the accuracy of excitation rates to at least 10%. Distorted wave calculations for H-like ions are expected to be good to 10–20%, but have not sufficiently been tested. R-Matrix calculations for Fe group elements (Kisielius et al., 1996; Ballance et al., 2002; Malespin et al., 2011) show that inclusion of relativistic effects and radiation damping at low temperatures are important if a 10% accuracy is to be reached (Smith & Brickhouse, 2014).

He-like ions – especially the four Kα transitions line w ($1s_{1/2}2p_{1/2}\,{}^1P_1^o \rightarrow 1s^2\,{}^1S_0$), line x ($1s_{1/2}2p_{1/2}\,{}^3P_2^o \rightarrow 1s^2\,{}^1S_0$), line y ($1s_{1/2}2p_{1/2}\,{}^3P_1^o \rightarrow 1s^2\,{}^1S_0$), and line z ($1s_{1/2}2s_{1/2}\,{}^3S_1 \rightarrow 1s^2\,{}^1S_0$; after the denotation of Gabriel, 1972) – are the most important diagnostic for plasma temperature and density (e.g., Gabriel & Jordan, 1969; Gabriel, 1972; Mewe & Schrijver, 1978a,b; Porquet & Dubau, 2000; Porquet et al., 2001a,b, and references therein), and for testing ionization equilibrium (Smith & Brickhouse, 2014). While there

is a consistent set of collisional excitation rates for transitions in He-like ions in AtomDB, their uncertainties still need to be benchmarked, especially for Fe (Smith & Brickhouse, 2014). It is crucial to know the uncertainty on rates and use appropriate error propagation on models based on these data. Otherwise the end user may overestimate the accuracy of their spectral models (Smith & Brickhouse, 2014).

1.3.2 Measurements

From the discussion in Section 1.3.1 it is clear that it is important to benchmark available theoretical calculations of atomic data experimentally through laboratory measurements. There are a variety of experimental facilities that have provided measurements relevant to astrophysics, such as magnetic fusion, inertial confinement fusion plasma devices, laser-produced plasmas, and heavy ion storage rings (Beiersdorfer, 2003). The first dedicated laboratory astrophysics program began at the electron beam ion trap (EBIT) facility at the Lawrence Livermore National Laboratory (Beiersdorfer et al., 1992a; Kahn et al., 1998). It was followed by similar efforts (Beiersdorfer, 2003) at the TSR heavy-ion storage ring (Savin et al., 1997), the National Spherical Tokamak Experiment (NSTX; Beiersdorfer et al., 2003b), and the electron cyclotron source (ECR; Greenwood et al., 2000). Common to all of these efforts is that the resolution of the employed spectrometers needs to at least match, but better exceed the resolving power of space instrumentation (Beiersdorfer, 2003).

EBIT (see Chapter 3), which operates in the coronal density limit with its typical electron densities of 10^{10}–10^{12}cm^{-3}, is the closest in density to the common astrophysical densities, making its results directly applicable to astrophysics (Beiersdorfer, 2003). Compared to older spark and laser devices, where a large portion of the experimental time had to be spent on understanding the source itself, newer generation atomic physics devices such as EBIT act as “analog computers” (Beiersdorfer, 2003) that can produce relatively large quantities of data in a short amount of time.

Among other things, EBIT measures electron impact excitation cross sections, high-energy dielectronic recombination, and spectral line and emission patterns (Beiersdorfer, 2003). With an EBIT, atomic physics can be benchmarked at a single electron energy, i.e., it can test fundamental calculations before they are convolved with an electron distribution. Similarly, atomic physics can be measured one element at a time, avoiding contamination and line blends from other elements. Within some limits it is even possible to choose specific ions as the dominant charge state in the trap. A portable EBIT has been combined with X-ray light sources such as synchrotrons, linear accelerators, and free electron lasers, where EBIT is used to breed and trap the charge states whose interactions with photons from the light source are to be studied (Epp et al., 2007, 2010; Bernitt et al., 2012; Rudolph et al., 2013). All relevant processes such as relativistic corrections and all levels influencing the branching ratios are automatically included in the measurement unlike in calculations (Beiersdorfer, 2003). Additionally, experiments automatically produce reliable uncertainty limits to the measured rates and wavelengths. However, measurements still depend on an appropriate and careful experimental setup (Beiersdorfer, 2003).

1.4 Specific Astrophysics Questions

Specific examples of astrophysical observations that suffer from lack of appropriate reference data illustrate the need for laboratory astrophysics better than generalized "wish-lists". This section highlights some of these observations that benefit directly from the measurements discussed in this work.

1.4.1 Kα Transitions in L-shell Ions

The spread of calculated transition energies for K-shell transitions in L-shell ions, where available, can amount to a few eV between different codes (see below in the Section *Available data*). While this is an issue for all astrophysically abundant metals, better reference data for these transition energies is most pressing in L-shell ions of Si and S. Therefore, the case for the need to measure the K-shell transition energies for L-shell ions is made on the example of Si and S. As stated in Hell et al. (2016b), X-ray features of these have already been observed in absorption and emission in many sources, including solar flares (Neupert, 1971), other stellar coronae (e.g., Kastner et al., 2002; Huenemoerder et al., 2013), various types of Active Galactic Nuclei (e.g., Lee et al., 2001; Kaspi et al., 2002; Kinkhabwala et al., 2002; Holczer et al., 2007; Holczer & Behar, 2012; Reeves et al., 2013), high-mass X-ray binaries (HMXB; e.g., Sako et al., 2002; Boroson et al., 2003; Watanabe et al., 2006; Chang & Cui, 2007; Hanke et al., 2008; Miškovičová et al., 2016), and cataclysmic variables (Girish et al., 2007). For all of these objects, the X-ray line diagnostic associated with the L-shell ions of Si and S is limited and often precluded by the relatively poor accuracy of the atomic reference data. Calculating the atomic structure for these multi-electron ions accurately is challenging as the calculations have to take into account the correlation effects between all of the involved electrons.

This section discusses the diagnostic value of these lines for the high mass X-ray binaries Cyg X-1 and Vela X-1 (Hanke et al., 2008; Sako et al., 2002), where these lines are observed most prominently. A list of available reference data is given as well as arguments why these lines will become important also for ions of elements other than Si and S.

The Clumpy Wind of Cyg X-1: Si and S

High-mass X-ray binaries (HMXB) consist of a supermassive, hot O- or B-type star and an evolved compact object such as a neutron star or a black hole. These OB stars exhibit strong stellar winds through radiation pressure onto spectral UV lines, i.e., the photons of the star's strong UV radiation transfer their momentum through photoabsorption to the material in the stellar atmosphere, thus driving this material away (Castor et al., 1975). In isolated O-stars, it has been shown with hydrodynamic simulations that this so-called line-driven wind is unstable such that small perturbations can grow into large density, velocity, and temperature variations that ultimately compress the gas into *clumps* (Lucy & Solomon, 1970; Owocki & Rybicki, 1984; Feldmeier et al., 1997; Dessart & Owocki, 2003; Oskinova et al., 2012; Sundqvist & Owocki, 2013). The stellar wind is therefore

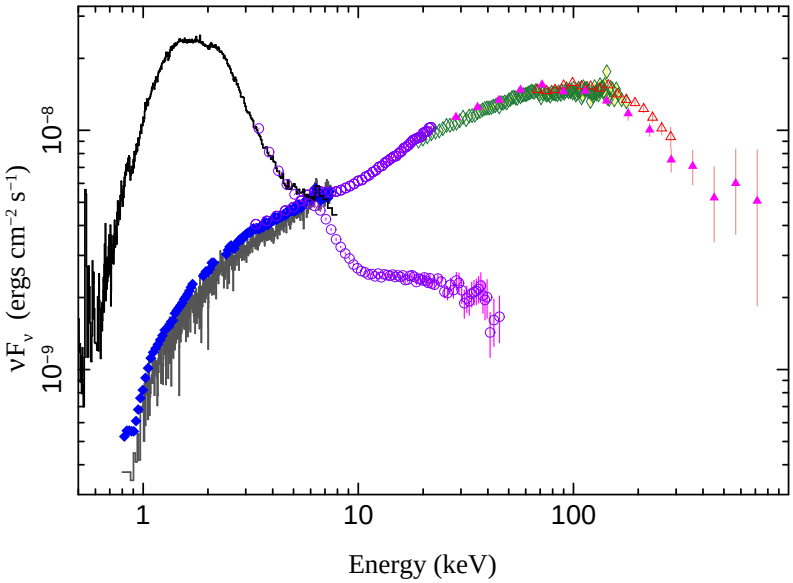

Figure 1.3: Characteristic spectra of the black hole HMXB Cyg X-1 in its two spectral states: The high/soft state spectrum is dominated by a thermal spectrum peaking between 1–2 keV and has a weak hard tail. The low/hard state spectrum is an exponentially cutoff broken powerlaw extending to hard X-rays with energies > 100 keV. The powerlaw describing the spectra below 10 keV typically have photon indices $\Gamma > 2.1$ in the soft state and $\Gamma < 2.1$ in the hard state. — From Nowak et al. (2012, Fig. 1).

often described as a two-component medium, where clumps of cool, dense material are embedded in the remaining hot, tenuous gas (e.g., Hanke, 2011, and references therein). Observational evidence for clumpy wind models is found, e.g., by Eversberg et al. (1998), Markova et al. (2005), and Oskinova et al. (2006). If such an OB star is a constituent of a HMXB, strong X-radiation ($10^{36} \ldots 10^{38}$ erg s^{-1}) is emitted from the HMXB when the stellar wind is accreted onto the compact object. Since the companion star typically almost fills its Roche lobe, i.e., the equipotential surface within which material is gravitationally bound to the star, the stellar wind of the companion is effectively focused onto the compact object. The X-rays emitted from the accretion ionize the wind material, thus removing the charge states whose strong UV resonance transitions are driving the outflow. While this ionization of the wind material can affect and even suppress the mass-loss rate of the companion in bright sources, in HMXBs with low X-ray luminosities the wind structure stays largely intact (Sako et al., 2002). It is important to understand the properties of the stellar wind in order to understand how the interplay between stellar wind, accretion flow, and ionizing radiation affects the changes between states of high and low luminosity in the binary. The X-radiation from the accretion process can be used to probe the stellar wind and its structure. Since similar wind models apply to both isolated stars and those in HMXBs, studies of HMXBs can be used to advance the understanding of the wind also for isolated stars. For more detailed overviews on stellar winds in isolated stars see, e.g., Leutenegger (2006) and in HMXBs, see, e.g., Hanke (2011), Fürst (2011), Hell (2012), and references therein.

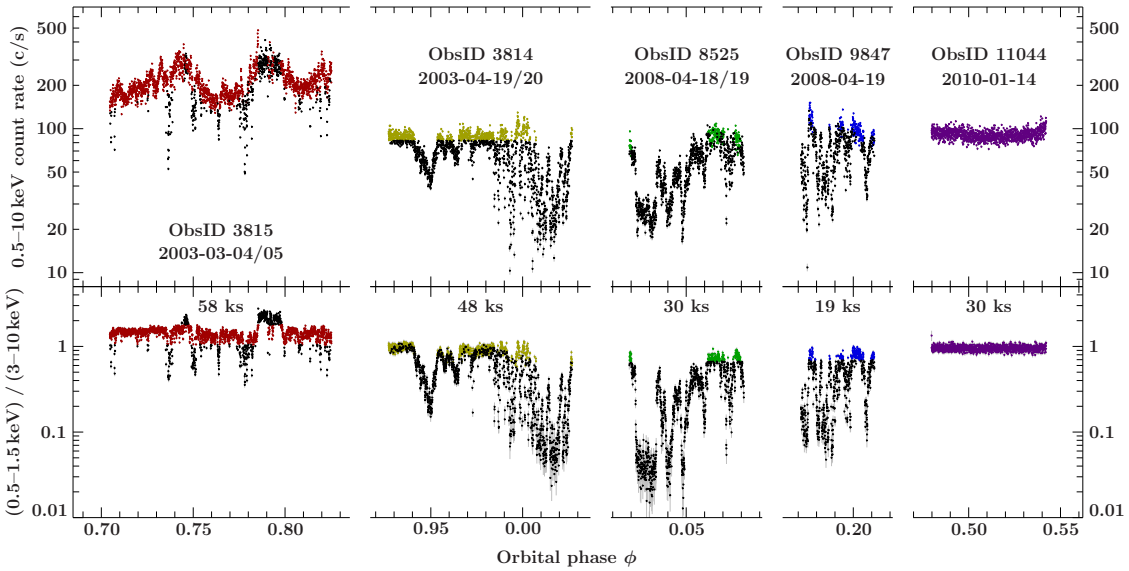

Figure 1.4: Lightcurves of *Chandra*-HETG observations of Cyg X-1 in the low/hard state show severe absorption dips that are also apparent in the hardness ratio. — From Miškovičová et al. (2016).

The overall wind structure in terms of number and size of clumps can be examined by long-term monitoring of variations in the neutral broadband continuum absorption as a function of orbital phase (Grinberg et al., 2015). The morphology and velocity of the wind and the clumps, on the other hand, are studied through the signature of the wind material in form of spectral line features caused by the X-rays re-processed by the wind material (e.g., Sako et al., 2002; Miller et al., 2005; Watanabe et al., 2006; Liedahl & Brown, 2008; Hanke et al., 2009; Miškovičová et al., 2016).

The black hole HMXB Cygnus X-1 is one of the best known persistent bright X-ray sources and with its companion's mass loss rate of $\sim 10^{-6}\,M_\odot\,\mathrm{year}^{-1}$ (Herrero et al., 1995) a prime target for stellar wind studies. Cyg X-1 has a O9.7 Iab type companion star HDE 226868 (Walborn, 1973) in a 5.6 d orbit (Webster & Murdin, 1972; Brocksopp et al., 1999; Gies et al., 2003) with an inclination of $i \approx 27°$ (Orosz et al., 2011) and is located at a distance of $d = 1.86$ kpc from the Sun (Xiang et al., 2011; Reid et al., 2011). Cyg X-1 switches between two spectral states (Fig. 1.3), the high/soft and the low/hard state (see Grinberg et al., 2013, for a classification using all-sky monitors). In the high/soft state of Cyg X-1 the soft X-ray luminosity is so high that the wind material is almost completely ionized, making this state unsuitable for examining the wind through spectral line features. We, therefore, concentrate efforts on wind studies on low/hard state observation (Hanke et al., 2009; Miškovičová et al., 2016).

There are five high quality *Chandra*-HETG observations of Cyg X-1 in the low/hard state, covering the prominent orbital phases $\phi_{\mathrm{orb}} \approx 0$ (where the line of sight passes above the companion and the wind is most dense), $\phi_{\mathrm{orb}} \approx 0.2$, $\phi_{\mathrm{orb}} \approx 0.5$ (opposite of the companion star and outside of the wind), and $\phi_{\mathrm{orb}} \approx 0.75$ (Hanke, 2011; Miškovičová et al., 2016). The lightcurves of these observations (Fig 1.4) show heavy drops in the

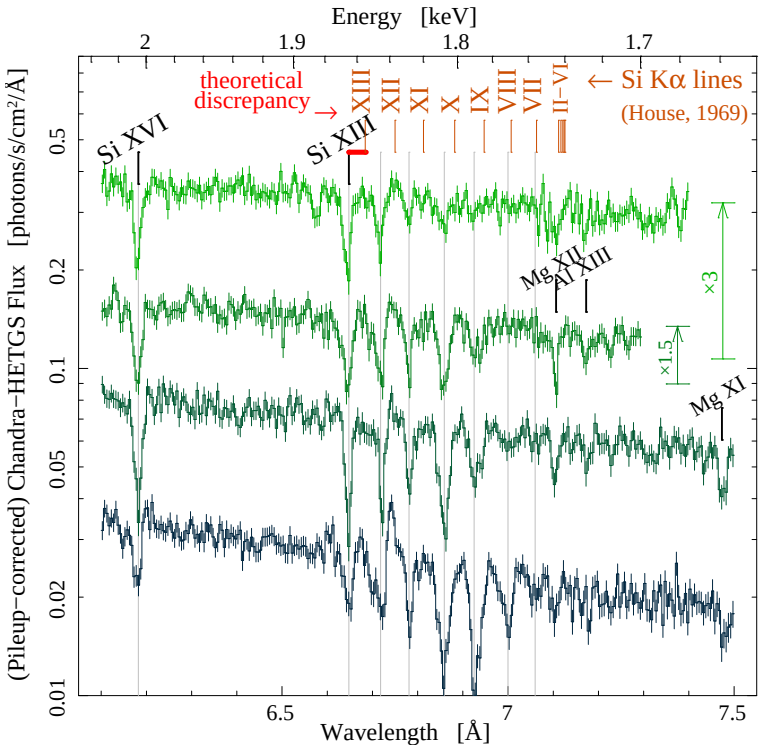

Figure 1.5: Spectra of the Si region in Cyg X-1 for ObsID 8525 ($\phi_{\rm orb} \approx 0$) for various stages of dipping (non-dip, weak dip, dip, and strong dip from top to bottom). The spectra are extracted based on cuts in hardness ratio A/C. — From Miškovičová et al. (2010).

observed X-ray flux. These dips are most severe at phase $\phi_{\rm orb} \approx 0$ closest to the star, while virtually no dipping occurs at $\phi_{\rm orb} \approx 0.5$. During these dips, the hardness ratio[5] of the energy bands A (0.5–1.5 keV) and C (3–10 keV) drops as well, i.e., the softer X-rays are affected more heavily, indicating that the dips are caused by excess absorption due to increased column densities. Therefore, the absorption dips are signatures of clumps crossing our line of sight.

Studying how spectral features change with dipping provides insights into the clump morphology. For example, during non-dip phases (indicated in color in Fig. 1.4) the X-ray spectrum is dominated by absorption lines in He- and H-like ions (Miller et al., 2005; Hanke et al., 2009; Hanke, 2011; Miškovičová et al., 2016). These lines are clearly signatures of the hot phase of the wind. The deeper into the dipping phases the spectra are taken, the lower the continuum flux becomes and absorption lines from K-shell transitions of L-shell Si and S ions appear (Fig. 1.5). The measured line centers do not vary between different dipping stages. This suggests that the bulk motion of each ionic species is constant between the center and the edge of the clump. To compare the motion between different ions and determine the velocity of the bulk motion, which are indicators

[5]The hardness ratio is defined as the number of counts integrated in one energy band divided by the number of counts in another, harder energy band. While this definition is a well established convention in X-ray astrophysics (Park et al., 2006), it can be confusing as in this definition of the hardness ratio a larger ratio corresponds to a softer spectrum.

for the morphology of the clump, reliable and accurate reference energies are necessary for these line blends. Otherwise it is unclear if the differences in shifts are caused by actual differences in ion velocities or by lack of atomic data. The accuracy of the reference energies should, therefore, be better than the $\sim 100\,\mathrm{km\,s^{-1}}$ calibration uncertainty of *Chandra* HETG (Marshall et al., 2004; Canizares et al., 2005; Chandra X-ray Center, 2015).

The Clumpy Wind of Vela X-1: Si

Vela X-1 is a neutron star HMXB with the B0.5 Ib supergiant companion HD 77581 (Brucato & Kristian, 1972; Hiltner et al., 1972) with a mass-loss rate of $(1\text{–}7 \cdot 10^{-6}\,M_\odot\,\mathrm{year}^{-1}$ (Hutchings, 1976; Dupree et al., 1980; Kallman & White, 1982; Sadakane et al., 1985; Sato et al., 1986). It is an eclipsing system (inclination $i \approx 0$) with an orbital period of 8.964 d (Forman et al., 1973; Kreykenbohm et al., 2008) at a distance of 1.9 kpc from the Sun (Sadakane et al., 1985). The pulsar has a pulse period of ~ 283 s (McClintock et al., 1976; Kreykenbohm et al., 2008). Similar to Cyg X-1, Vela X-1 is among the best studied objects in its class.

There are three *Chandra*-HETG observations, covering orbital phases $\phi_{\mathrm{orb}} \approx 0$ (eclipse), $\phi_{\mathrm{orb}} \approx 0.25$, and $\phi_{\mathrm{orb}} \approx 0.5$, that are extensively discussed in the literature (e.g., Sako et al., 2002; Schulz et al., 2002; Goldstein et al., 2004; Watanabe et al., 2006), and a newer observation to add $\phi_{\mathrm{orb}} \approx 0.75$. During the eclipse observation, the companion star blocks the line of sight to the continuum X-radiation from accretion onto the neutron star such that the spectrum is dominated by fluorescence emission lines and scattered components from regions extending beyond the shadow of the companion (Schulz et al., 2002; Watanabe et al., 2006). The observation at $\phi_{\mathrm{orb}} \approx 0.25$ has very bright continuum radiation and very few spectral lines. The observation at $\phi_{\mathrm{orb}} \approx 0.5$ is highly absorbed, indicating the presence of an absorber behind the neutron star. The strong absorption reduces the continuum radiation enough to allow observation of the fluorescence emission lines originating in other regions of the system also at this phase (Watanabe et al., 2006). Since the emission lines are stronger in this phase than during eclipse, a significant fraction of the line emission has to be produced between the neutron star and its companion (Watanabe et al., 2006).

The region between the neutron star and its companion is within the wind acceleration zone, where wind velocities ranging from zero to the terminal wind velocity of $\sim 1000\text{–}2000\,\mathrm{km\,s^{-1}}$ are expected (Liedahl & Brown, 2008). An ionization gradient is expected to accompany the velocity gradient (Liedahl & Brown, 2008). In photoionized plasmas, the charge state distribution depends on the available ionizing X-ray flux and, therefore, varies as a function of the ionization parameter ξ (Kallman & McCray, 1982). For example, in Si the charge state distribution is dominated by He-like, H-like, and bare ions for values of $\log \xi \gtrsim 2$ (Liedahl & Brown, 2008). Figure 1.6 shows a sketch of the Vela X-1 system, indicating regions of different $\log \xi$.

By analyzing the Doppler shifts and line profiles of the observed emission lines and comparing them to the predicted velocity and ionization gradients, the simulations of the

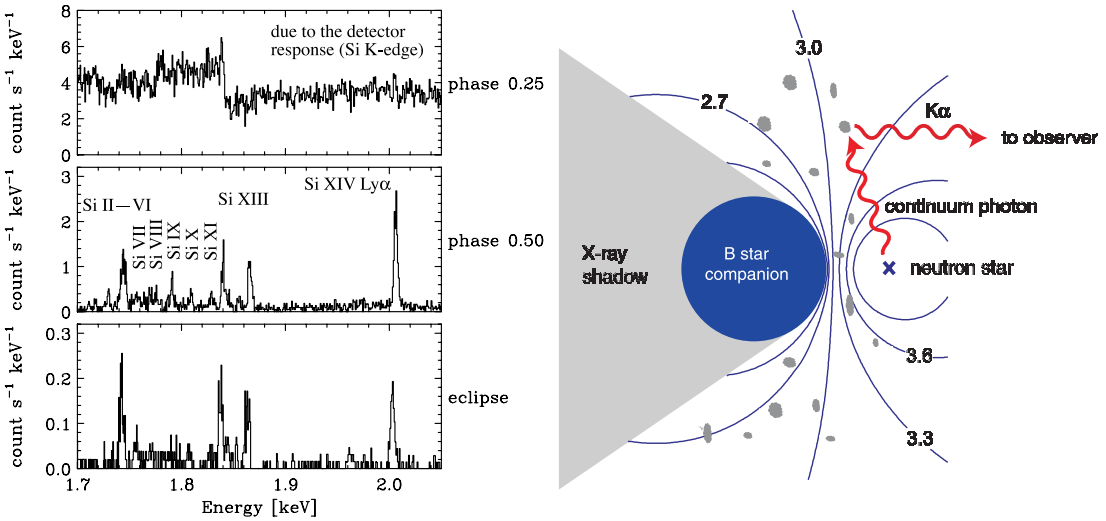

Figure 1.6: *Left:* Spectra of the Si region in Vela X-1 observed with *Chandra*-HETG at three different orbital phases, $\phi_{\rm orb} \approx 0$ (eclipse), $\phi_{\rm orb} \approx 0.25$, and $\phi_{\rm orb} \approx 0.5$ (From Watanabe et al., 2006, Fig. 5). *Right:* Sketch of the Vela X-1 system by Liedahl & Brown (2008, Fig. 2) using a Castor et al. (1975) law for the wind velocities, a mass loss rate of $3 \cdot 10^{-7}\,M_\odot\,\mathrm{year}^{-1}$, and an X-ray luminosity of $4 \cdot 10^{36}\,\mathrm{erg\,s}^{-1}$. The neutron star is treated as a point source denoted by x. The contours correspond to values of the ionization parameter $\log \xi$ and translate to variations in charge state distribution with lower $\log \xi$ corresponding to lower charge states. The K-shell transitions of L-shell Si ions (*left*) originate either from regions with low $\log \xi$ or from the dense clumps of the wind material.

wind structure in these systems can be tested. This is mostly done using transitions in He- and H-like ions. However, emission lines of L-shell ions of Si have also been observed in the *Chandra*-HETG spectra (Fig. 1.6 *left*; Sako et al., 2002; Schulz et al., 2002; Goldstein et al., 2004; Watanabe et al., 2006), offering unique diagnostic capability. These line features either probe the ionization gradient shown in Fig. 1.6 (*right*) or are signatures of localized density variations of a clumpy wind (Liedahl et al., 2002), where the dense material in the clumps has a lower charge balance. The accuracy of available wavelength calculations for these lines is only on the order of the expected Doppler shifts, i.e., ~ 5 eV, (Liedahl & Brown, 2008), precluding their use as a diagnostic for either of these two possibilities.

Previous analyses of Vela X-1 have used spectra added over the full range of the observation. Since Vela X-1 shows similar variability as Cyg X-1 with periods of highly variable high hardness and periods of stable low hardness (Grinberg et al., 2017). Recently, Grinberg et al. (2017) have been analyzing Vela X-1 grating spectra subdivided into these hardness periods and find significant differences between the two periods with lines changing their relative line strengths and even going from absorption into emission. They also find new spectral features previously absent in, e.g., the Goldstein et al. (2004) analysis. Most strikingly, Grinberg et al. (2017) have discovered absorption lines from K-shell transitions in low charge states of Mg (Mg V–Mg X) in the low hardness spectra. Again, the interpretation of the Doppler shifts in these ions is limited by the accuracy of the available reference data.

Available Data

Hell et al. (2016b) gives a census of the reference data available for these ions of Si and S, and the following paragraphs in this subsection are taken in verbatim from that publication. Historically, Hartree-Fock calculations of House (1969) were used to interpret high resolution solar spectra (Fritz et al., 1967), and more recently have been used to analyze data from both Vela X-1 (Schulz et al., 2002; Goldstein et al., 2004) and Cygnus X-1 (Hanke, 2011). However, House (1969) only provide simplified data listing only a single transition for each ion. To provide a more complete and accurate data set, more sophisticated calculations have been completed using more advanced atomic models. For example, Behar & Netzer (2002) used the Hebrew University Lawrence Livermore Atomic Code (HULLAC; Klapisch, 1971; Busquet et al., 2006, and references therein) to calculate transition energies and line strengths for the strongest K-shell transitions in He- through F-like silicon and sulfur ions. At present, the most complete calculation is provided by Palmeri et al. (2008a, P08), who use a semi-relativistic Hartree-Fock code to calculate level energies, transition wavelengths, and radiative decay rates for ∼1400 K-shell transitions in silicon and sulfur ions. The variation among the inner-shell transition energies calculated with various codes is ∼2–5 eV, i.e., on the order of several 100 km s^{-1} for the diagnostically important L-shell silicon Kα lines. This variation is comparable to the expected Doppler shift of the L-shell silicon Kα lines (Watanabe et al., 2006; Liedahl & Brown, 2008; Miller et al., 2005, 2012; Miškovičová et al., 2016), and significantly larger than the systematic wavelength error of *Chandra*'s High Energy Transition Grating Spectrometer (HETGS), which is on the order of 100 km s^{-1} (Marshall et al., 2004; Canizares et al., 2005; Chandra X-ray Center, 2015). Hence, the main systematic uncertainty in the determination of Doppler shifts from X-ray lines is our knowledge of atomic physics. This has been pointed out before in studies of the K-shell lines in L-shell oxygen ions (Schmidt et al., 2004; Gu et al., 2005).

When comparing atomic databases commonly used to interpret both Solar and extra-Solar X-ray spectra, the data from P08 are found in the Universal Atomic DataBase (uaDB) accompanying XSTAR (Bautista & Kallman, 2001); however, they are not included in either the atomic physics for astrophysics database, AtomDB v2 (Foster et al., 2012) or the CHIANTI atomic physics database (Dere et al., 1997; Landi et al., 2013). AtomDB v2 only includes K-shell transitions in helium-like and hydrogen-like ions; CHIANTI only includes H-like, He-like, and Li-like transitions.

There is one previous measurement available for L-shell transitions in Be- through F-like Si and S ions. Faenov et al. (1994) measured transitions produced in a CO_2 laser-produced plasma. They also provided a comparison to their own theoretical calculations. The density of this plasma ($n_e \sim 10^{19}$ cm^{-3}; Boiko et al., 1978) is significantly higher than typical densities in an astrophysical environment. The spectra reported by Faenov et al. (1994) therefore comprise mainly dielectronic satellites (see their Tables I and II) and are only of limited applicability for the photoionized plasmas in, e.g., Cyg X-1 and Vela X-1.

The first part of Chapter 6 presents our measurements of K-shell transitions in the L-shell ions of Si and S using the ECS microcalorimeter at the LLNL EBIT as published by Hell et al. (2016b). The results include follow-up measurements to Hell (2012) to

better assess the systematic uncertainties of the setup. It includes an expanded review of the utility of these new reference data for the analysis and interpretation of the Cyg X-1 and Vela X-1 spectra. An additional benchmark for the new reference data using a high-resolution spherical crystal spectrometer is discussed in Section 6.2.

Beyond Si and S

Kallman & Palmeri (2007) claim that up to their writing only the 15 or so most abundant elements (including C, N, O, Ne, Na, Mg, Al, Si, S, Ar, Ca, Fe, and Ni) had been observed in X-ray spectra from celestial sources. In the meantime, Cr and Mn have been identified in multiple source types (Smith & Brickhouse, 2014) such as the galactic center region (Nobukawa et al., 2010), galaxy clusters (Tamura et al., 2009; Hitomi Collaboration et al., 2016, see Fig. 1.8), HMXBs (only Cr; Fürst et al., 2011), micro-quasars (Kallman et al., 2009), and, most prominently, supernova remnants (Hwang et al., 2000; Miceli et al., 2006; Tamagawa et al., 2009; Yang et al., 2009; Yamaguchi & Koyama, 2010; Tamagawa, 2010; Park et al., 2013; Yang et al., 2013). With the exception of Kallman et al. (2009) and Hitomi Collaboration et al. (2016), all of these observations have been made with a CCD and hence at relatively low resolution.

The lower odd-Z elements Al, Na, Cl, P, and K (decreasing order of abundance) have higher or similar cosmic abundances than Cr and Mn (Asplund et al., 2009) and should therefore, in principle, be observable (Hughes et al., 2014). In fact, Na and Al are regularly detected in *Chandra*-HETG observations (e.g., Hanke et al., 2009). However, the K-shell transitions in elements below Ca are so tightly spaced that the weaker signatures of the odd-Z elements suffer from confusion with the stronger lines of the more abundant even-Z species at the low spectral resolution of CCD observations (Hughes et al., 2014). X-ray signatures from some of the less abundant elements such as Cl, Sc, Ti, Co, Cu, and Zn have been marginally detected in the source spectrum of the micro-quasar GRO J1655−40 (Kallman et al., 2009), the only grating observation in the above list of Cr and Mn detections. The Fe peak elements, including odd-Z, are also expected to be detected in other sources (Smith & Brickhouse, 2014). The next generation of X-ray observatories (e.g., *Athena*) will bring large improvement in effective area compared to the currently available grating spectrometers on *XMM-Newton* and *Chandra*, thus making high-resolution spectroscopy more commonly available and extending its application to faint and extended sources. This advance will allow to detect and disentangle X-ray signatures from these low-abundance elements as well as new spectral features (Smith et al., 2014a).

Assuming that the elements are mixed in the observed plasma rather than spatially separated – which at least for Cyg X-1 seems to be the case (Miškovičová et al., 2016) –, it is expected to find signatures of lower charge states in the other astrophysically abundant elements beyond Si and S. For K-shell transitions in these ions, good candidates are photoionized and transient collisional plasmas. For example, L-shell transitions ($n = 3 \rightarrow 2$) prove the presence of L-shell Fe ions in Cyg X-1 (e.g., Hanke et al., 2009). In case of the Tycho supernova remnant, Yamaguchi et al. (2014) assume that the strongest contribution to the Fe Kα line is attributed to ions around F-like Fe XVIII and Ne-like Fe XVII.

The Cr Kα emission peaks at a larger radius in the supernova remnant than the Fe Kα emission and should therefore be more highly ionized (Hughes et al., 2014), suggesting the presence of L-shell ions of Cr.

Some calculations for K-shell transitions in L-shell ions of these other elements are available from the same sources as the Si and S lines. For example, Behar & Netzer (2002) calculated transition energies for Ne, Mg, Al, Ar, Ca, and Fe in addition to Si and S. Palmeri et al. (2008a) additionally included Ne, Mg, Ar, and Ca, after already calculating Fe extensively (Palmeri et al., 2003a; Bautista et al., 2004), and then followed on with calculations of Ni (Palmeri et al., 2008b), Al (Palmeri et al., 2011), and F, Na, P, Cl, K, Sc, Ti, V, Cr, Mn, Co, Cu, and Zn (Palmeri et al., 2012).

Once these signatures are detected, it is crucial to have benchmarked reference wavelengths available. The recent discovery of the K-shell transition of Mg L-shell ions in the X-ray spectra of Vela X-1 by Grinberg et al. (2017) demonstrates this point. We are, therefore, extending our efforts of measuring the K-shell transition energies with the ECS microcalorimeter at EBIT also for other elements in the range Na through Ni (Section 6.3.3; Hell et al., 2015), but this is beyond the scope of this thesis.

1.4.2 Transient Plasmas: K-shell Transitions of M-shell Fe Ions

Iron is the most abundant of the astrophysically relevant high-Z elements (Asplund et al., 2009). Its $n = 2 \rightarrow 1$ K-shell transitions fall into the 6–7 keV energy region, where even CCD observations have somewhat decent energy resolution, and are relatively isolated from K-shell transitions of neighboring elements (Paerels & Kahn, 2003). For these reasons, Fe was the first line feature to be unambiguously identified in X-ray spectra (Serlemitsos et al., 1975; Sanford et al., 1975; Paerels & Kahn, 2003).

Sometimes this feature is just referred to as *the Fe line*, but often it is distinguished between the *neutral* Fe line at 6.4 keV, the *He-like* Fe line at 6.7 keV, and the isolated H-like Lyα line blend at 7.0 keV, because they are easily resolved by an X-ray CCD (see also Girish et al., 2007, for an example of all three of these features observed with *Chandra*-HETG). While the He-like Fe line consists of the four transitions w, x, y, and z (Gabriel, 1972) and may be accompanied by, e.g., Li-like and Be-like transitions (Fig. 1.9), the 6.4 keV line is a region of highly blended transitions that can come from any charge state between neutral and up to F-like Fe XVI (Decaux et al., 1995).

Because it is very abundant and covers nearly the entire range of possible plasma conditions encountered in astrophysics, Fe is particularly important as a diagnostic tool (Smith & Brickhouse, 2014). Currently, the diagnostic potential of its K-shell transitions is somewhat limited by the resolution available for the 7 keV X-ray region, but the next generation of X-ray observatories featuring microcalorimeters will change this (Hitomi Collaboration et al., 2016). The diagnostics cover at least three prominent types of plasmas: photoionized plasmas, collisionally ionized plasmas in equilibrium, and collisional transient plasmas with nonequilibrium ionization conditions. General properties of photoionized and coronal plasmas have been discussed above. Transient plasmas are found in the shock-front heated regions of young supernova remnants and in solar flares. In

these transient plasmas, a sudden increase in electron temperature causes the ionization balance to be much lower than would be expected for a plasma at equilibrium at this temperature.

The collision energy required to excite Kα lines in Fe ions (6.4–7 kev) is much higher than the ionization potential required to ionize through to He-like Fe (2.05 keV; Cowan, 1981). Additionally, collisional ionization of an M- or L-shell electron has cross sections on the order of $(0.44\text{–}1.1) \cdot 10^{-18}\,\mathrm{cm}^2$ and $5 \cdot 10^{-20}\,\mathrm{cm}^2$, respectively, while excitation of a K-shell electron is less likely with cross sections of a few $\cdot 10^{-22}\,\mathrm{cm}^2$ (Decaux et al., 1997). Therefore, for emitting plasmas in collisional ionization equilibrium K-shell transitions tend to be dominated by transitions in highly-charged He-like – or at higher electron temperatures – H-like Fe ions. Emission from the low charge states is only visible in transient plasmas outside of collisional ionization equilibrium (Decaux et al., 1995). Alternatively, cold photoionized plasmas in the vicinity of an X-ray continuum source show fluorescence Kα transitions from radiative decay after inner-shell photoionization (Paerels & Kahn, 2003). In this section we motivate transition energy measurements in these low charge states of M-shell Fe ions; for excitation cross sections of highly-charged Fe see the next Section.

A good example for Fe K lines in photoionized plasmas is the black-hole HMXB Cyg X-3. It has a plasma temperature of $kT \approx 50\,\mathrm{eV}$ as derived from the width of radiative recombination continua (Paerels et al., 2000). A *Chandra*-HETG observation resolved three groups of Fe Kα transitions, H-like (Fe Lyα), He-like (Fe Heα), and "neutral" (Fe Kα), of which the Fe Kα line is the most interesting. It has an apparent line center of 6394±3 eV and a width of $\sim 73\,\mathrm{eV}$ FWHM. From other spectral lines Paerels et al. (2000) derive a velocity (turbulence) broadening of $\Delta v \approx 1500\,\mathrm{km\,s^{-1}}$. Assuming that the low charge states of Fe responsible for the 6.4 keV emission have the same velocity distribution as the He- and H-like ions, still leaves an excess width of $\Delta E \approx 60\,\mathrm{eV}$. The energy spacing of the neutral Fe K transitions accounts only for $\Delta E \approx 13\,\mathrm{eV}$, but the measured width of 60 eV is consistent with the full spread of transitions from neutral up to Ne-like Fe seen in an EBIT measurement by Decaux et al. (1995). This indicates the presence of a range of charge states in this line (Paerels et al., 2000). There is a possibility that the near-neutral and the highly-charged ions originate from different parts of the wind, which can cause the fluorescence from either group of lines to show different broadening (Paerels et al., 2000). While the Fe Kα line width as a sum of broadening and ionization balance puts strong constraints on the wind parameters (Paerels et al., 2000), good knowledge of the line distribution of the charge states contributing to this blend are important and could help to disentangle the broadening from the ionization balance in higher-resolution observations, leading to new insights into the wind morphology.

Transient collisional plasmas can generally be observed in young supernova remnants. For example, Yamaguchi et al. (2014) analyze a deep *Suzaku* observation of the Tycho supernova remnant. They find that the Kα and Kβ emission peak in different locations of the supernova remnant, with the Kβ emission being located at smaller radii. Using theoretical calculations of the line centroids at CCD resolution as a function of charge state, they also find that the fitted line centers in the spectrum averaged over the whole remnant indicate a lower charge state for the Kβ emission ($\mathrm{Fe}^{8+\ldots10+}$) than for the K$\alpha$

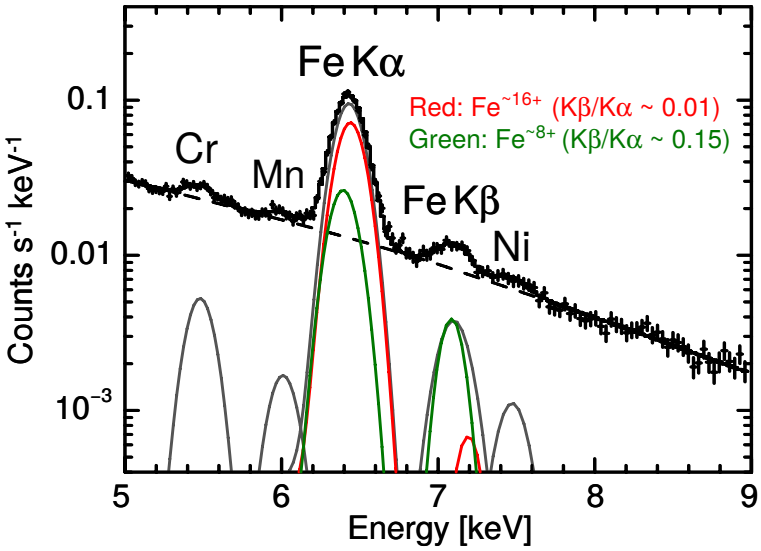

Figure 1.7: Deep *Suzaku* observation of the Tycho supernova remnant. The Fe Kα to Kβ line ratio and centroids suggest a complex ionization structure across the remnant. A two-component model self-consistently describes emission from two plasmas of different ionization age $n_e\tau$: one located at larger radii of the supernova remnant with the charge balance peaking around Ne-like Fe XVII; the other one at smaller radii and Ar-like Fe IX. — From Yamaguchi et al. (2014).

emission ($Fe^{15+\cdots17+}$). This is consistent with Kβ being emitted at smaller distances from the center, where the radiating plasma is expected to have a lower ionization age (Yamaguchi et al., 2014). Since the inconsistent line centers and flux ratio suggest the presence of a range of plasma conditions across the remnant, (Yamaguchi et al., 2014) fit the Fe lines with a two-component model (Fig. 1.7), where the Kα to Kβ flux ratios of the two components are fixed to the calculated values for the respective expected charge states. The best fit of this two-component model is able to describe the data self-consistently.

This analysis heavily relies on atomic data in terms of transition energies and emission cross sections. Each of the Fe ions up to Ne-like Fe XVII has a complex structure of transitions that roughly splits into two groups of lines (see Chapter 7). Since the detector broadening of the CCD spectrum is much larger than the spread in transition energies for each of the low charge states, determining a single Kα centroid for each ionization state is a working approach for estimating the peak charge state. However, at calorimeter resolution of a few eV, the line blend shows more structure than the CCD observation and is more sensitive to the exact charge balance, although charge states below F-like Fe are still not resolved. Since ionic systems with this many electrons are notoriously hard to calculate, the main features of blended transitions in M-shell Fe ions have been measured as part of this work, using a new very high-resolution crystal spectrometer (Chapter 7).

1.4.3 Perseus Galaxy Cluster

The Perseus cluster is one of the brightest and therefore best studied galaxy clusters, the largest gravitationally bound objects in the universe (see, e.g., Gursky et al., 1971;

Forman et al., 1972; Fabian et al., 1981; Boehringer et al., 1993; McNamara et al., 1996; Fabian et al., 2000; Churazov et al., 2004; Tamura et al., 2009; Simionescu et al., 2012; Tamura et al., 2014). Because of their large structure and mass, and since they are still forming, they are excellent tracers for cosmology and other astrophysical processes (Allen et al., 2011; Hitomi Collaboration et al., 2016). The intracluster medium consists of hot gas whose mass exceeds that of all the stars in the cluster combined. The dynamics of this gas are still not well understood (Hitomi Collaboration et al., 2016). To a large extent this lack of understanding is due to the quality of previous observations. Since galaxy clusters are spatially very extended and faint objects, gratings observations of them are not feasible. Existing observations are therefore done at CCD resolution, whose detector broadening is much larger than the thermal and turbulence broadening of the observed source. At CCD resolution it is also difficult to judge the exact charge balance of the emitting gas.

The recent first-light observation of the *Hitomi* microcalorimeter SXS (5 eV resolution; Hitomi Collaboration et al., 2016) of the Perseus cluster made a large step forward on this issue. Figure 1.8 compares the Fe region of the Perseus cluster as observed with *Suzaku* and *Hitomi*. Although the *Hitomi* spectrum suffers from some difficulties in gain scale calibration owing to the fact that it was measured during the "turn-on phase" of the mission, it was possible to constrain the turbulence velocity of the gas from line broadening to $164 \pm 10\,\mathrm{km\,s^{-1}}$ in the central region, revealing a remarkably quiescent atmosphere (Hitomi Collaboration et al., 2016).

A detailed analysis of the Fe spectrum reveals issues with existing atomic physics models. Figure 1.9 shows an empirical fit to the data using Gaussian lines centered at laboratory transition energies of Beiersdorfer et al. (1993). Line lists of the plasma modeling codes APEC and SPEX (see Table 1.1) were updated and then fitted to the spectrum (Hitomi Collaboration et al., 2016). The He-like resonance line w has been excluded from the fit because its line strength can be affected by resonant scattering. In resonant scattering, a photon from the line of sight is absorbed by an ion, photoexciting the ion to a higher energy level in the process. The excited ion subsequently decays back into its original state and emits a photon of the same energy into a random direction. Thus the photon is effectively scattered out of the line of sight. Resonant scattering is, therefore, a measure of the mean free path of a photon of this energy and a diagnostic for the ion density in the plasma. To gauge the amount of resonant scattering, accurate optically thin values of the excitation cross sections are required. *Hitomi*'s SXS has pushed the required accuracy to a new regime.

For a collisional plasma in the coronal density limit like the intracluster medium, the dominant line formation processes is from collisional excitation. Consequently, accurate emission cross sections for excitation through electron impact are especially crucial for spectral modeling (Beiersdorfer, 2003). Overall, calculations for collisional excitation rates have a larger practical importance because of the large number of ions and energy levels involved (Kallman & Palmeri, 2007). But the accuracy of these calculations needs to be benchmarked by dedicated laboratory measurements. Specifically, the accuracy of rate coefficients for collisional excitation needs to approach the 10% level in order to derive tight constraints for the electron temperature and density, the optical depth, and

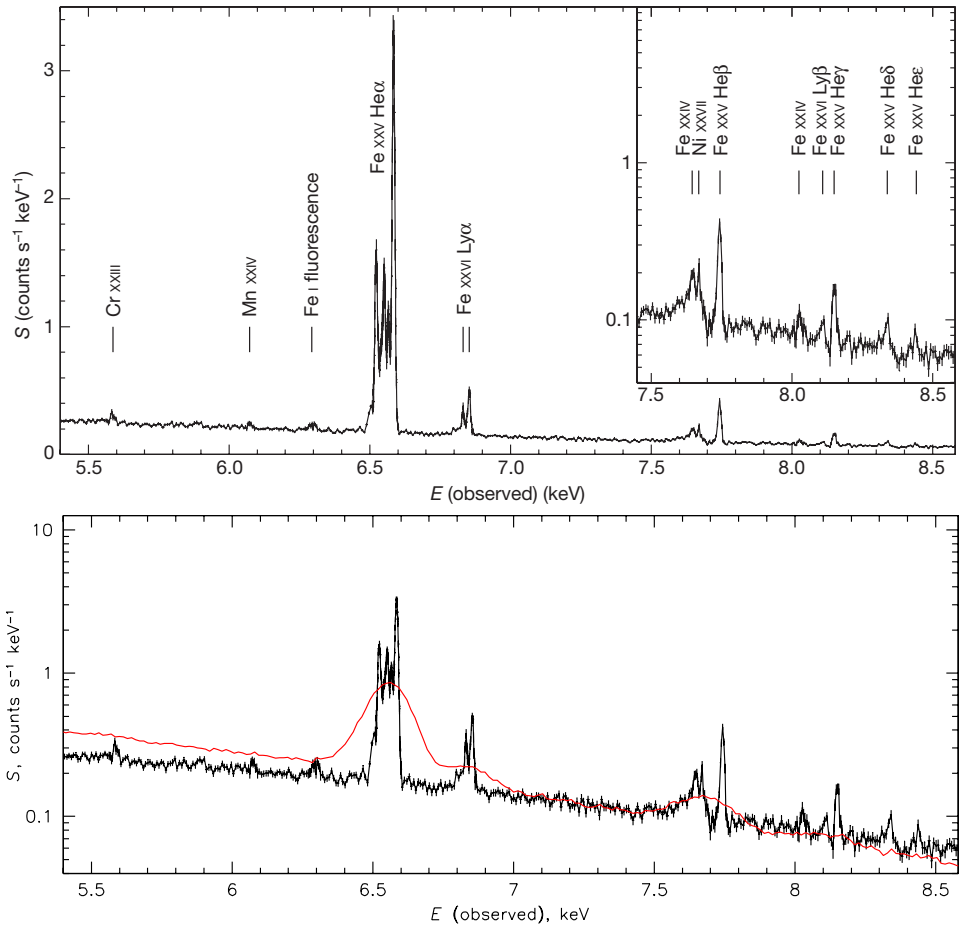

Figure 1.8: High-resolution *Hitomi* SXS spectrum of the Perseus galaxy cluster in comparison to a previous *Suzaku* observation at CCD resolution. The change in slope of the continuum is due to differences in effective area. — From Hitomi Collaboration et al. (2016, Fig. 1).

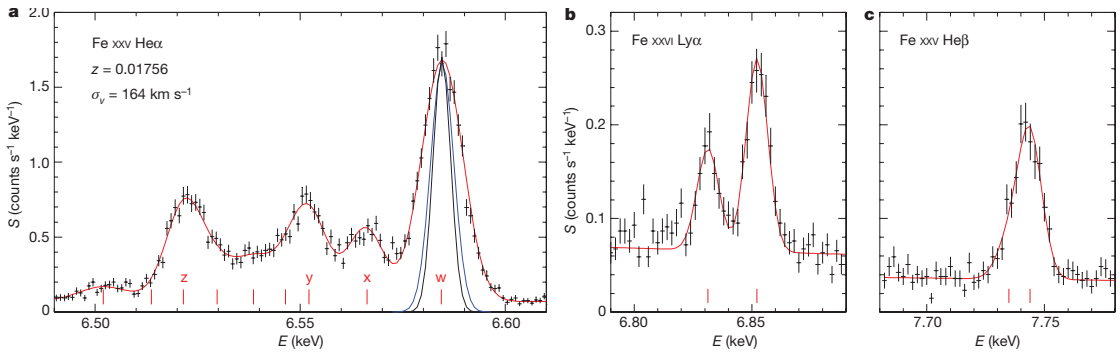

Figure 1.9: Zoom into the Fe lines of the *Hitomi*-SXS spectrum of the Perseus cluster. The lines have been modeled with individual Gaussians. In addition to the He-like Kα lines, transitions in Li-like and Be-like Fe are clearly visible. (From Hitomi Collaboration et al., 2016, Fig. 2).

abundances from line ratios (Brickhouse et al., 2006). On a 10% level the accuracies are better or on the order of the uncertainties of the flux calibration for X-ray observatories. For example, the absolute flux calibration of *Chandra*-HETG and of *Hitomi*-SXS is estimated to be around 10% (Madsen et al., 2017; Eckart et al., 2016), but the the cross calibration between X-ray spectrometers on various satellites can differ by 20% (Madsen et al., 2017).

The first measurement of collisional excitation cross sections for highly charged ions ($q > +6$) was made with EBIT-I (Marrs et al., 1988, Ne-like Ba;) and at least until 2008 remained the only device measuring these cross sections in highly charged ions for X-ray astrophysics (Beiersdorfer, 2003; Chen & Beiersdorfer, 2008); see Chen & Beiersdorfer (2008), e.g., Chantrenne et al. (1992), Wong et al. (1995), Gu et al. (1999a), Widmann et al. (2000), Gu et al. (2001), Chen et al. (2002), Chen et al. (2005), May et al. (2005), Chen et al. (2006), and Brown et al. (2006). Currently, we are working on benchmark measurements for the Fe K-shell transitions to help understand and improve the limitations of the plasma models (Chapter 8).

It is seen that the radiations fall into two distinct series, here denoted by the letter K and L [...], previously denoted by letters B and A. The letter K and L are, however, preferable as it is highly probable that series of radiations both more absorbable and more penetrating exist.

Charles Barkla (1911)

2 Atomic Physics in X-ray Spectroscopy

BEFORE going into details about the laboratory measurements and instruments involved, this chapter presents a quick overview of the relevant atomic physics processes. For a slightly more expanded summary of atomic physics refer to Hell (2012) and references therein.

2.1 Spectral Lines

The following gives a brief introduction on the notations used in the remainder of the thesis, based on the Bohr shell model of the atom (Bohr, 1913a,b,c). According to the Bohr model, electrons are distributed in "shells" around the nucleus. In this model, the different possible electron distributions through these shells give rise to the energy levels of the atom or ion. While the Bohr model (also dubbed planetary model) correctly predicts the quantization of the atomic energy, it is overly simplified. A better, more thorough description of the atomic structure is provided by quantum mechanics as developed by Erwin Schrödinger, Werner Heisenberg, and others, based on the ideas of Louis de Brogli (Bransden & Joachain, 2003, see also Section 2.2).

The energy levels are often depicted in a so-called Grotrian diagram (Fig. 2.1; Grotrian, 1928). The ground state has the energetically most favorable electron distribution without violating Pauli's exclusion principle. If at least one electron is located in a shell further away from the nucleus, the atom or ion is considered to be excited and has a larger energy than in the ground state. These excited states have a finite lifetime as the ion strives to return into the energetically more favorable ground state. When the excited electron decays back into a lower lying level, the excess energy may be emitted in the form of a photon, which can then be observed. The energy it takes to excite an electron to a continuum level, where it is no longer bound to the ion, is equal to the ionization potential of that electron.

The electrons around an atomic nucleus are characterized by four principle quantum

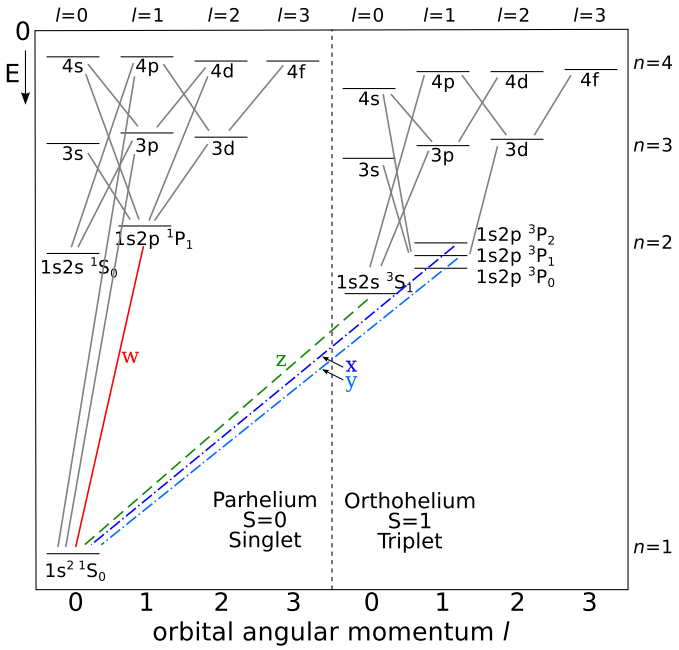

Figure 2.1: Grotrian diagram of a He-like ion, showing levels up to $n = 4$. The transitions labeled w, x, y, and z are using the designation by Gabriel (1972).

numbers $nlsm_j$: the principle quantum number n denoting the shell occupied by the electron, the orbital angular momentum l denoting its subshell, the electron spin s, and the magnetic quantum number m_j of the electron's total angular momentum j. Following Siegbahn, the principle quantum number is often denoted by letters with $n =$ K, L, M, ... corresponding to $n = 1, 2, 3, \ldots$. Transitions into the $n = 1$ shell are therefore called K-shell transitions, with Kα lines corresponding to $n = 2 \rightarrow 1$ transitions, Kβ to $n = 3 \rightarrow 1$ transitions, etc (Fig. 2.2). The orbital angular momentum l takes integer values $l = 0, 1, \ldots, n-1$ labeled with $l =$ s, p, d, f, ... (continued alphabetically). The spin can take values of $s = \pm 1/2$. The total angular momentum of the electron is the vector combination of the orbital angular momentum and the spin ranging from $j = |l - s|, \ldots, |l + s|$ in steps of 1. The subshell occupied by an electron is then described as nl_j, e.g., $2p_{3/2}$. The magnetic quantum number corresponding to the total angular momentum spans values of $m_j = -j, -j+1, \ldots, j-1, +j$. The Pauli exclusion principle, which states that no two identical electrons can occupy the same space (Pauli, 1925), therefore allows only two electrons in the $n = 1$ shell with subshell $1s_{1/2}$ ($m_j = \pm 1/2$) and opposing spins, while the $n = 2$ shell can hold up to 8 electrons, two each in $2s_{1/2}$ and $2p_{1/2}$ and four in $2p_{3/2}$ ($m_j = \pm 1/2, \pm 3/2$).

The distribution of multiple electrons in the same ion is called an electron configuration, e.g., $1s^2\, 2s_{1/2}$ for the ground state of Li-like ions, which has two electrons in the $1s_{1/2}$ subshell and one electron in $2s_{1/2}$. The electron configuration together with how these electrons couple with each other determines the energy level of the ion. There are two major coupling schemes that can be used to describe the energy levels: LS or Russell-Saunders coupling (Russell & Saunders, 1925) and jj-coupling. LS-coupling applies to low-Z ions, where the electrostatic interaction between electrons is stronger than the interaction between the electron spin and its orbit (Cowan, 1981). Thus, the orbital angular momenta l_i of the electrons couple to form the total orbital angular momentum

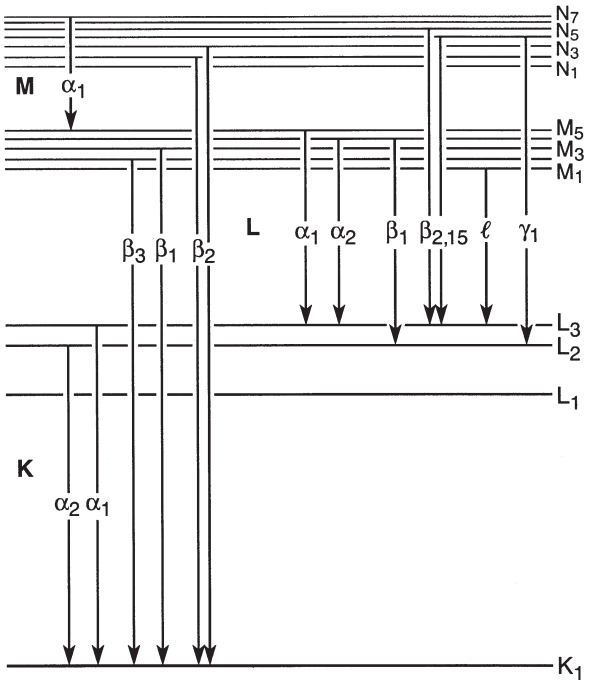

Figure 2.2: Siegbahn notation (Siegbahn, 1924) for transitions into the $n = 1$ K-shell, the $n = 2$ L-shell, and the $n = 3$ M-shell. K_1 corresponds to the $1s_{1/2}$ subshell, L_1 to $2s_{1/2}$, L_2 to $2p_{1/2}$, and L_3 to $2p_{3/2}$. Transitions from the next higher shell are labeled α and β from two shells higher. In the hydrogen atom, these series are in general called the Rydberg series (Rydberg, 1889), and specifically, in order, Lyman series ($n = 1$, Lyα, Lyβ, ...; Lyman, 1906), Balmer series ($n = 2$, Hα, Hβ, ...; Balmer, 1885), Paschen series ($n = 3$), Brackett series ($n = 4$), Pfund series ($n = 5$), and Humphreys series ($n = 6$). (From Thompson et al., 2009, Fig. 1-1).

$L = \sum_i l_i$ and the electron spins s_i add to the total spin $S = \sum_i s_i$. Both sums again are vector sums. L and S then couple to the total angular momentum $J = |L-S|, \ldots, |L+S|$. The energy level is then denoted by the term symbol ${}^{(2S+1)}L_J$. Different combinations of configurations can form the same term. To uniquely identify and distinguish these different levels, the full configuration and parental terms (${}^{(2S+1)}L$) of electrons coupling certain subshells are sometimes written down in front of the final term symbol (see, e.g., the energy level lists in Palmeri et al., 2008a). For high-Z ions (jj-coupling), the bound electrons are more relativistic such that the spin-orbit interaction becomes stronger than the Coulomb interactions between electrons and the orbital angular momentum l_i of each electron first couples with the electron spin s_i to the electron total angular momentum j_i. The j_i then couple to the total angular momentum of the system $J = \sum_i j_i$ (vector sum). Again, including the configuration and parental terms is necessary to uniquely identify energy levels. Both the LS- and the jj-coupling schemes are mere descriptions of a physical system. While these descriptions have been tested and found to be largely adequate as tools, there are systems that do not comply fully with either one of these descriptions, for example, when the spin-orbit and the Coulomb interaction have comparable strengths. These cases are often still described through LS- or jj-coupling, but other coupling schemes are available.

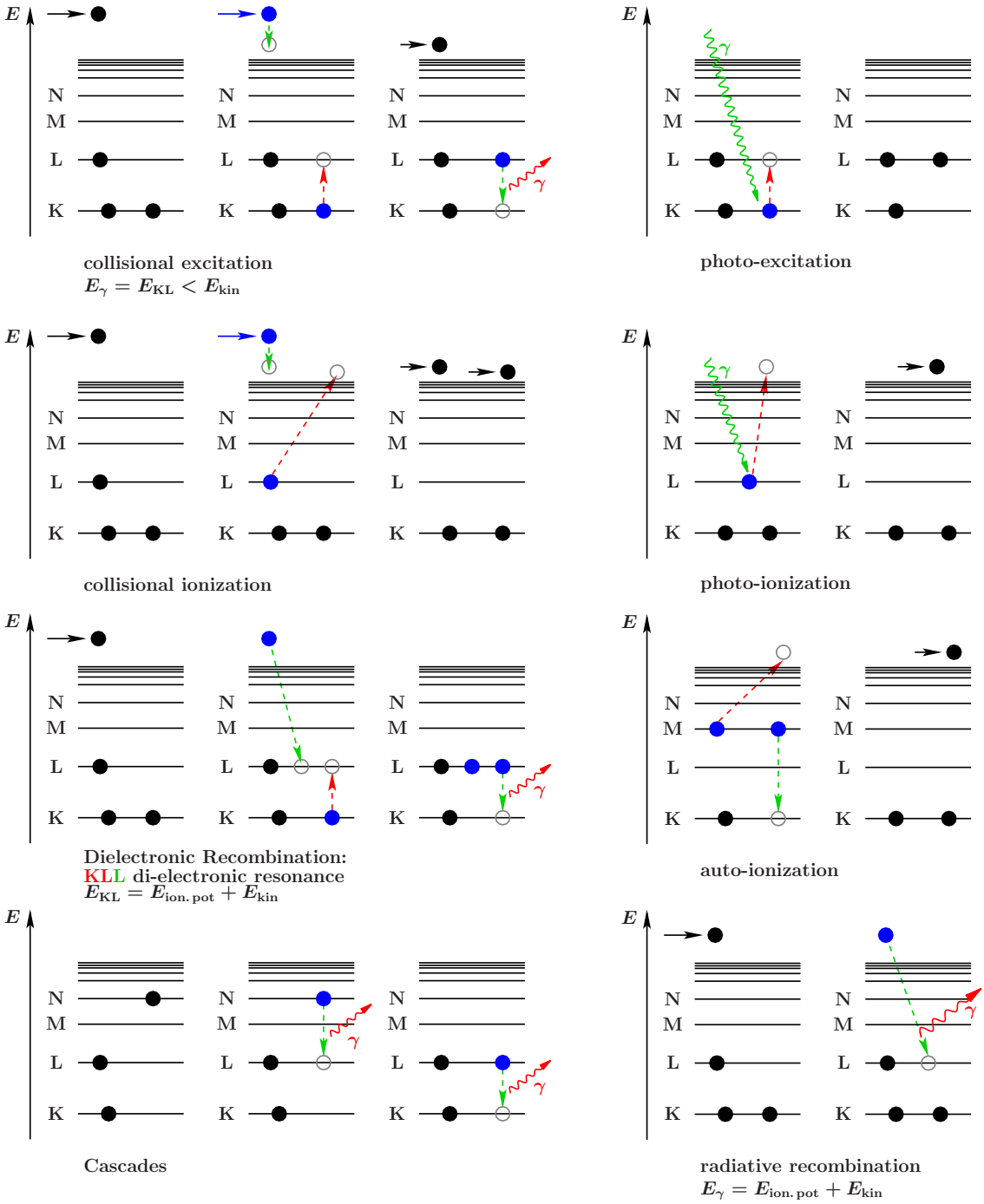

Figure 2.3: Sketches of excitation, ionization, and recombination processes.

There are a variety of processes that ultimately lead to spectral line formation (Fig. 2.3). An excited ion can decay to a lower lying energy level either spontaneously or stimulated, e.g., by collisions, releasing the energy difference as a photon to form an emission line. Collisions with electrons (or other ions) can excite an electron from a subshell in one

configuration to a different subshell of a higher-energetic level configuration while at the same time reducing the kinetic energy of the continuum electron by the corresponding energy difference between the initial and final level. In radiative recombination, a continuum electron is captured by the ion, reducing the charge by one and releasing the kinetic energy of the electron and the binding energy of the recombined ion as a photon. If the released energy matches exactly the energy difference between the recombining ion and an excited state of the recombined ion, the energy, instead of being emitted as a photon, is used to excite an electron in the resonant process of dielectronic recombination. The doubly excited recombined ion then either decays radiatively in cascades to the ground state, or in the reverse process of autoionization, one of the two excited electrons decays to a lower level while the other excited electron is ionized back into the continuum. Absorption of a photon of matching energy leads to photo-excitation, which is a resonant process. With sufficiently large collision or photon energies, excitation and ionization of inner-shell electrons is possible. Figure 2.3 shows sketches of these processes.

Ions that have the same number of electrons are generally found in the same same electron configurations. Ions along such an iso-electronic sequence, therefore, have similar level structures. The energy splitting of these levels typically scales with powers of the nuclear charge Z. For example, the structure of hydrogenic ions (ignoring fine structure) scales from the energy levels of the hydrogen atom as Z^2 in the Rydberg energy and Z^{-1} in the Bohr radius[1] (Friedrich, 1990). For multi-electron ions, however, the scaling along iso-electronic sequences is not as simple as for the hydrogenic one-electron system, because only the electron-nucleus part of the potential energy scales with Z, while the electron-electron interaction is independent (Friedrich, 1990). Because of the similarities along the iso-electronic sequence, in atomic physics ions are often referred to by their electronic structure, e.g., He-like for ions with two bound electrons. In astrophysics literature, on the other hand, roman numerals are traditionally assigned to indicate the charge state, starting with I for neutral atoms. This follows the lead of early spectroscopists who denoted the spectrum emitted from neutral atoms of an element as the "first spectrum", the one from singly ionized atoms as the "second spectrum", etc., (Cowan, 1981). Thus, Li-like Si XII denotes a Si ion with three electrons left.

2.2 Atomic Structure

To calculate the transition energies, we need to know the level structure of the ions and how this structure is affected by the interactions between the nucleus and the many electrons. The energy levels of the ion correspond to the solutions of the non-relativistic Schrödinger equation (Schrödinger, 1926a,b) or the equivalent relativistic Dirac equation (Dirac, 1928). The simplest atom is the hydrogen atom, consisting of only the nucleus (in the most abundant form of H this is just a proton) and a single electron (Thomson, 1906), with hydrogenic ions being similarly simple. Since the electron mass is much smaller than the proton mass, the hydrogen atom can be reduced to the one-body problem in

[1] The Bohr radius is the radius of the inner-most shell, i.e., approximate distance of the inner-most electron to the nucleus.

an attractive Coulomb potential (Friedrich, 1990), i.e., for these, the Schrödinger/Dirac equation can be solved analytically and many textbooks therefore use it as an example for solving the atomic structure (e.g., Condon & Shortley, 1935; Rybicki & Lightman, 1979; Condon & Odabasi, 1980; Cowan, 1981; Friedrich, 1990; Bransden & Joachain, 2003; Pradhan & Nahar, 2011). For many-electron systems the Schrödinger/Dirac equation cannot be solved analytically in general because of the two-body interaction between the bound electrons. Its solution is therefore derived by applying variational and perturbation approximations. Kallman & Palmeri (2007) give a concise overview over the various methods and their names, which we summarize in the following.

The Schrödinger/Dirac equation for multi-electron ions, according to Kallman & Palmeri (2007), has the general form

$$\left\{\sum_i h_i + \sum_{ij} V_{ij}^{\mathrm{e-e}}\right\}\Psi = E\Psi. \tag{2.1}$$

Here, h_i are the single-particle non-relativistic Schrödinger or fully-relativistic Dirac Hamiltonians describing the kinetic energy of the nucleus and electrons and the interaction of each electron with the electrostatic Coulomb potential of the nucleus (Coulomb, 1785b); $V_{ij}^{\mathrm{e-e}}$ are the potentials of the electron-electron interactions, including, e.g., the Coulomb potential for the repulsion between charges of the same sign (Coulomb, 1785a); and Ψ is the wave function of the atomic state, which has four components in the fully relativistic case. For the non-relativistic Schrödinger equation, $V_{ij}^{\mathrm{e-e}}$ only includes electrostatic Coulomb interaction (Kallman & Palmeri, 2007). In case of the fully relativistic Dirac equation, in addition to the direct electrostatic interaction $V_{ij}^{\mathrm{e-e}}$ includes the positional correlation of parallel-spin electrons according to the Pauli principle (called the exchange part of the electrostatic interaction) and the two-body magnetic (Breit) interaction (Kallman & Palmeri, 2007).

In the weakly relativistic case, where the particle energy is very close to its rest energy, components from the Dirac equation up to orders of v^2/c^2 can be added as relativistic approximations to the Schrödinger equation and treated perturbatively (Friedrich, 1990). In the relativistic approximation, the Hamiltonians h_i thus include mass-correlation[2], Darwin[3], and spin-orbit[4] terms, while spin-other-orbit[4], spin-spin, orbit-orbit, spin-contact, and two-body Darwin terms are added to $V_{ij}^{\mathrm{e-e}}$. Higher-order relativistic interactions such as those from quantum electrodynamics have to be included for heavy highly-charged ions as well. In the non-relativistic treatment, level energies in the ion are $2n^2$-fold degenerate (n is the principle quantum number), but this degeneracy is broken partially in the relativistic approximation and fully relativistic treatment, which gives rise to *fine*

[2] The mass-correlation term is also known as the mass polarization term, which is a momentum-dependent correction to the two-body interaction due to the fact that the center of mass is offset from the position of the nucleus (Friedrich, 1990).

[3] The Darwin term is a relativistic correction to the potential, which only acts on $l = 0$ (Bransden & Joachain, 2003).

[4] In the rest frame of the electron, the nucleus and other electrons constitute a moving charge that creates a magnetic field, which in turn interacts with the electron's own magnetic moment (its spin; Rybicki & Lightman, 1979).

structure splitting that splits each shell into n different levels with $j = 1/2, 3/2, \ldots, n-1/2$ (Bransden & Joachain, 2003). The remaining degeneracy in l is removed by the Lamb shift[5] (Lamb & Retherford, 1947) due to small quantum electrodynamic effects (Bransden & Joachain, 2003). For hydrogenic ions, the terms of the relativistic corrections to the kinetic energy, the spin-orbit interaction, and Darwin have the same order of magnitude, but for many-electron ions the spin-orbit term makes the strongest contribution to the fine structure splitting (Bransden & Joachain, 2003).

While the solution to the angular part of the Schrödinger equation is known exactly, the radial part does not have an exact solution because of the electron-electron interactions. Its solution therefore has to be approximated. The simplest approximation is the *central-field approximation* (Kallman & Palmeri, 2007; Friedrich, 1990; Bransden & Joachain, 2003). If there was no two-body interaction between the electrons, the Hamiltonians in the Schrödinger equation would just be the sum of N single-particle Hamiltonians (Friedrich, 1990) with the eigenfunctions of the hydrogenic ion. To maintain this independence of the electrons, the electron-electron interaction is approximated by a mean single-particle potential (mean field), where the electrostatic repulsion of a given electron by all the other electrons in the system is described by a screening potential modifying the electrostatic attraction of the nucleus (Friedrich, 1990). It can be written as (Kallman & Palmeri, 2007)

$$\sum_{j \neq i} V_{ij}^{\mathrm{e-e}} \sim V_i(r). \tag{2.2}$$

Then the atomic state function Ψ is simply the product of the atomic orbitals ϕ_i of the N electrons, which are eigenstates of the single-particle Schrödinger equations

$$\{h_i + V_i(r)\}\, \phi_i = \epsilon_i \phi_i. \tag{2.3}$$

The exact form of $V_i(r)$ can vary between calculations using different theories (Kallman & Palmeri, 2007; Cowan, 1981; Friedrich, 1990; Bransden & Joachain, 2003).

Variational principles such as the *Hartree-Fock approximation* (Dirac-Fock in the relativistic case) lead to slightly better solutions of the Schrödinger (Dirac) equation. Define a trial atomic state function (Kallman & Palmeri, 2007)

$$\Psi = (N!)^{-1/2} \det \phi_i(x_j), \tag{2.4}$$

called the Slater determinant, where x_j includes the spatial and spin coordinate. The slater determinant ensures that the state function is totally antisymmetric and independent of the ordering of the electron labels i, and it therefore ensures that the Pauli principle is obeyed[6]. For the Slater determinant that "best" describes the system the energy expectation value $E[\Psi]$ remains stationary under small (radial) variations to the atomic

[5] Vacuum fluctuations of the electromagnetic field act on the electron, causing it to oscillate rapidly, which effectively smears out the charge from a point to a small sphere. In a non-uniform electric field like that in the atom, the electron therefore experiences an effective electric potential that slightly differs from the potential in its mean position (Bransden & Joachain, 2003).

[6] The determinant vanishes for linearly dependent wave functions ϕ_i, i.e., no two electrons can occupy the same single-particle state (Friedrich, 1990).

state function (Friedrich, 1990), i.e., (Kallman & Palmeri, 2007)

$$\langle \delta\Psi | \sum_i h_i + \sum_{i<j} V_{ij}^{\mathrm{e-e}} | \Psi \rangle = 0. \tag{2.5}$$

This variation leads to the Hartree-Fock equations, a system of nonhomogeneous coupled integro-differential equations that can be solved iteratively (Kallman & Palmeri, 2007). Electron correlations within an electron configuration are essentially taken into account by the Hartree-Fock method.

The *configuration interaction* (CI) approximation makes even further improvements to solving the atomic structure (Kallman & Palmeri, 2007), as it treats effects of the interaction between configurations. Here, the trial atomic state function Ψ is taken as the superposition of multiple configurations and thus written as an expansion of the configuration state functions Φ (Kallman & Palmeri, 2007)

$$\Psi = \sum_k c_k \Phi_k \tag{2.6}$$

where Φ_k again are Slater determinants (Eq. 2.4) and c_k are the mixing coefficients. In principle, this summation can be extended to large k in order to achieve arbitrarily accurate results (Kallman & Palmeri, 2007). However, the amount of configurations allowed to interact is usually limited by computer power. In the *multiconfiguration Hartree-Fock* (MCHF) and *multiconfiguration Dirac-Fock* (MCDF) methods, the variation in Ψ is applied to both c_k and ϕ_i. If c_k is obtained from diagonalizing the multielectronic Hamiltonian matrix, after ϕ_i are derived from the Hartree-Fock equations and the monoelectronic Hamiltonian (Eq. 2.3), the method is called *superposition of configurations approach* (Kallman & Palmeri, 2007).

In a different, perturbative approach, the *many-body perturbation theory* (MBPT), the central field potential $V_i(r)$ is added to the multielectronic Hamiltonian H_0 and the remaining part of the electron-electron interaction in $V_{ij}^{\mathrm{e-e}}$ is treated as a perturbation term H_{pert} such that $H\Psi = E\Psi$ with

$$H = H_0 + H_{\mathrm{pert}} \quad \text{with} \quad H_0 = \sum_i \{h_i + V_i(r)\} \quad \text{and} \quad H_{\mathrm{pert}} = \sum_{i<j} V_{ij}^{\mathrm{e-e}} - \sum_i V_i(r). \tag{2.7}$$

To treat processes that include free electrons from the continuum such as collisional excitation or ionization and recombination, new methods are necessary. The continuum atomic state function $\Psi(\epsilon)$ for the $(N+1)$-electron system has to include the free electron of energy ϵ as

$$\Psi(\epsilon) = \sum_\alpha \chi_\alpha \phi_\alpha(\epsilon) \tag{2.8}$$

where ϕ_α are the free-electron orbitals and χ_α the atomic state functions of the N bound electrons (Kallman & Palmeri, 2007). The free-electron orbitals are described by the Schrödinger equation

$$\{h_\alpha^{\mathrm{K}} + \epsilon\}\phi_\alpha = \sum_{\alpha'} U_{\alpha\alpha'}\phi_{\alpha'}, \tag{2.9}$$

with the kinetic one-electron Hamiltonian h_α^{K} and the matrix potential $U_{\alpha\alpha'}$ of the atom or ion acting on the free electron, defined as

$$U_{\alpha\alpha'} = \int \mathrm{d}x_1 \cdots \mathrm{d}x_N \, \chi_\alpha(x_1 \cdots x_N) U(x_1 \cdots x_N x_{N+1}) \, \chi_{\alpha'}(x_1 \cdots x_N) \tag{2.10}$$

where U is the sum of the nuclear and electron-electron interaction potentials (Kallman & Palmeri, 2007).

The simplest approximation to solve these equations is the *Born approximation*, where the free-electron orbitals are considered to be plane waves, such that effectively $U_{\alpha\alpha} \sim 0$. It is most accurate for electron energies far above threshold and for collisions with neutral atoms. Since the infinite energy limit for scattering off a positive ion is exactly the Born cross section, which only varies slowly with energy, for positive ions this approximation provides good background cross sections over wide energy ranges (Kallman & Palmeri, 2007).

A more widely used approximation is the *distorted wave* (DW) approximation. It neglects the coupling between different channels and the interaction between continuum states, i.e., $U_{\alpha\alpha'} = 0$ for $\alpha \neq \alpha'$ by using the central-field approximation (Eq. 2.3) (Kallman & Palmeri, 2007). The DW approximation gives good results for background as well as resonance contributions, but resonances are often excluded from DW excitation rate calculations. At large free-electron energies ϵ, the DW orbitals are very similar to Coulomb orbitals with $U_{\alpha\alpha} \sim -(Z-N)/r$, called the *Coulomb-Born* approximation. If the exchange part of the electrostatic interaction is included, the methods are called *Coulomb-Born-Oppenheimer* or *Coulomb-Born-exchange* approximation.

All of the above approximations are only valid for free-electron energies much larger than the binding energy of the targeted bound electron. For low electron-impact energies and negative ions, the *R-matrix* method is a more suitable approximation, as it makes less-restricted assumptions about the wave functions of the continuum electron. It also includes resonance contributions to the cross sections. In this method, space is divided into internal regions, where interactions between the free and the target electrons is strong, and external regions. For the external region, the previous atomic state functions $\Psi(\epsilon)$ are used with a long-range matrix potential of the form $U_{\alpha\alpha'}(r) = \sum_\lambda C_{\alpha\alpha'}^{(\lambda)}/r^{\lambda+1}$ (Kallman & Palmeri, 2007). For the internal region, $\Psi(\epsilon)$ is expanded in terms of target eigenfunctions χ as

$$\Psi(\epsilon) = \mathscr{A} \sum_\alpha \bar{\chi}_\alpha \frac{u_{\epsilon,\alpha}(r)}{r} + \sum_i c_i \Phi_i. \tag{2.11}$$

Here, the antisymmetrization operator $\mathscr{A}$ implements the Pauli exclusion principle, $\bar{\chi}$ includes coupling of the bound states with the angular and spin parts of the free electron, $u_\epsilon(r)/r$ is the radial part of $\phi(\epsilon)$ and Φ_i are the bound states of the atom or ion, which are constructed with the target orbitals for completeness and short-range correlations. Applying a variational principle to the radial part of the free-electron state functions and to the mixing coefficients c_i produces coupled integro-differential equations, which are solved using a real, symmetric matrix. Resonances are automatically included in the atomic state function for the inner region (Eq. 2.11).

2.3 The Flexible Atomic Code

There are a variety of atomic physics codes available to calculate ion structure, radiative rates, excitation and ionization processes, and their reverse processes. They range from non-relativistic to semi-relativistic to fully relativistic treatment of the Schrödinger or Dirac equation. Most codes use different combinations of the approximations outlined above to help solve the equations and have different descriptions of the central-field potential. For nine of these code packages and their variations, Kallman & Palmeri (2007) summarize which effects are included and which approximations are employed by each code as pointed out in the last section.

With the exception of Section 6.3.1, atomic data calculations conducted specifically for use in this work are done with the Flexible Atomic Code FAC (Gu, 2003, 2004b, 2008). FAC is a fully relativistic code using the Dirac Coulomb Hamiltonian and a modified Dirac-Fock-Slater central potential (Gu, 2004a). For exchange photons higher order QED effects are treated through Breit interaction in the zero energy limit, self-energy and vacuum polarization effects through hydrogenic approximations, and continuum processes through the distorted-wave method (Gu, 2004a). The exact theoretical framework and computational methods are explained in a series of unpublished papers distributed along with the FAC package.

FAC provides routines to calculate not only the atomic structure, but also bound-bound (oscillator strengths, radiative rates, collisional (de-)excitation) and bound-free processes (collisional and photon ionization, dielectronic and radiative recombination). The accuracy of FAC, determined from comparisons between FAC and experiments, is a few eV or 10–30 mÅ at ∼10Å for energy levels (other than H-like) and 10–20 % for radiative transition rates and cross sections (Gu, 2004a). The FAC package also includes a collisional radiative model that solves the rate equations for collisional ionization equilibrium based on the previously computed atomic data and outputs a synthetic spectrum. It allows one to specify the electron distribution either as a Maxwellian or as a mono-energetic beam. A photon distribution for photoexcitation and -ionization can also be specified. Both allow table models for non-standard distributions. Each bound-bound and free-free process can be excluded from the collisional radiative model. A similar module is available that solves the population of the magnetic sublevels to determine the polarization of spectral lines of bound-bound transitions, including effects of cascades. An asymmetry function provides polarization for radiative recombination into *nl* orbitals observed at 90° to the electron beam.

2.4 Doppler Broadening

The temperature in a plasma is due to the randomly distributed kinetic energies of its constituents. This thermal motion of radiation emitting ions causes a broadening of the observed line profile, called Doppler broadening. If radiation of frequency f_0 is emitted from a source that has a velocity component v along the line of sight, the observed

frequency f of the radiation is shifted according to the Doppler effect (Doppler, 1842) as

$$f = f_0\left(1 + \frac{v}{c}\right) \tag{2.12}$$

where c is the speed of light. Statistically, many of the ions in the plasma will have a velocity component along the line of sight to the observer. Radiation of these ions is, therefore, observed Doppler shifted. Since these velocities are randomly distributed among the ions with random orientation in space, however, photons emitted by these ions show a Doppler shift that is different for each photon. Therefore, these Doppler shifts in sum do not cause a net shift in the measured line emission from transitions in these ions, but instead only lead to a broadening of the line, resulting in a Gaussian line profile.

The ion velocities in a thermal plasma follow the Maxwell-Boltzmann distribution (Maxwell, 1867; Boltzmann, 1872), i.e., the probability $P_v(v)\mathrm{d}v$ for an ion to have a velocity in the interval $[v, v + \mathrm{d}v]$ is

$$P_v(v)\mathrm{d}v = \sqrt{\frac{m}{2\pi kT}}\exp\left(-\frac{mv^2}{2kT}\right)\mathrm{d}v \tag{2.13}$$

where m is the mass of the emitting particle, T the temperature of the ensemble, and k the Boltzmann constant. To find the Doppler broadening for spectral lines, we need to find the probability distribution $P_f(f)\mathrm{d}f$ for photons emitted at f_0 to be observed at a frequency f in the interval $[f, f + \mathrm{d}f]$. It relates to the velocity distribution as

$$P_f(f)\mathrm{d}f = P_v(v_f)\frac{\mathrm{d}v}{\mathrm{d}f}\mathrm{d}f = \frac{c}{f_0}P_v\left(c\left(\frac{f}{f_0} - 1\right)\right)\mathrm{d}f \tag{2.14}$$

where v_f is the velocity that corresponds to a Doppler shift from f_0 to f (Eq. 2.12). Substituting the Maxwellian velocity distribution (Eq. 2.13) into this equation leads to a frequency distribution of

$$P_f(f)\mathrm{d}f = \sqrt{\frac{mc^2}{2\pi kTf_0^2}}\exp\left(-\frac{mc^2(f - f_0)^2}{2kTf_0^2}\right)\mathrm{d}f \tag{2.15}$$

which is a Gaussian profile (Gauß, 1809) with standard deviation $\sigma_f = \sqrt{kT/mc^2}f_0$ and full width half maximum of $\Delta f_{\mathrm{FWHM}} = \sqrt{8\ln 2}\cdot\sigma_f$. The plasma temperature T_i of ion species i can therefore be derived from the measured line width as

$$T_\mathrm{i} = \frac{m_\mathrm{i}c^2}{8\ln 2}\left(\frac{\Delta f_{\mathrm{FWHM}}}{f_0}\right)^2 = \frac{m_\mathrm{i}c^2}{8\ln 2}\left(\frac{\Delta E}{E}\right)^2 \tag{2.16}$$

where $E = hf_0$ is the photon energy of the emitted photon.

Other line broadening mechanisms can result in similar Gaussian line profiles, for example from turbulent motion. Averaging over directional velocity distributions that are not spatially resolved in the observation, e.g., the receding and the approaching edge of a rotating distant object such as stars or accretion disks, also lead to an apparently broadened line. High particle number density causes Stark broadening, but the density regime of EBIT and most astrophysical plasmas are too low for this effect. In an EBIT the dominant line broadening is due to the ion temperature.

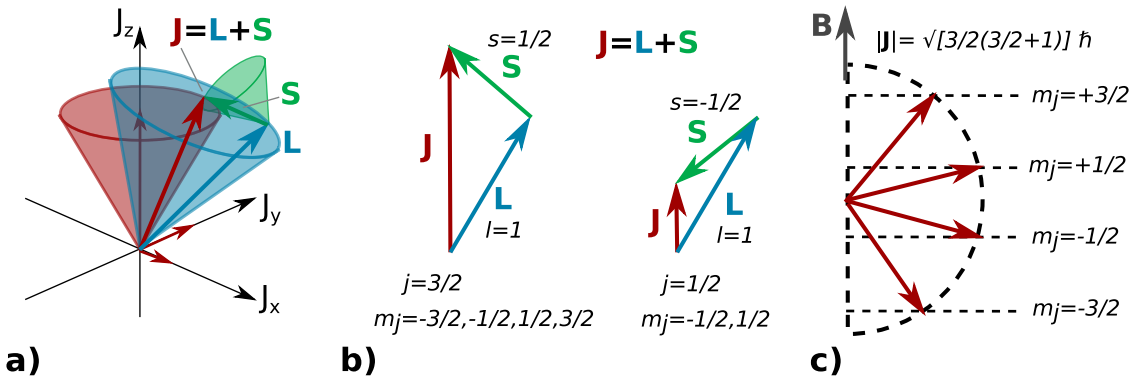

Figure 2.4: Vector representation of angular momenta (a and b) and splitting of magnetic sublevels of an $np_{3/2}$ state in a weak magnetic field (c).

2.5 Polarization

Because of the directionality of the electron beam, radiation produced in an EBIT is linearly polarized. The ions in an EBIT are excited through collisions with the electrons of the beam. Electrons in the ion occupy certain orbitals $nljm_j$ where $m_j = -j, -j+1, \ldots, j-1, j$ is the magnetic sublevel. The specific fractional population $g(m)$ of these magnetic sublevels (with $\sum_m g(m) = 1$) depends on the excitation process: for collisions with randomly oriented electrons the populations has a statistical distribution according to the statistical weights of the levels, which in turn leads to isotropic, unpolarized radiation upon decay of the excited levels. With a directed electron beam, however, the population is unevenly distributed among the sublevels, causing anisotropy and polarized radiation (Vogel, 1992). The reason is that the electron beam populates the magnetic sublevels such that dipole oscillations between $-m_j$ and $+m_j$ are aligned with the beam. Since the vectors of, e.g., $|m_j| = 1/2$ and $|m_j| = 3/2$ have a slightly different orientation (Fig. 2.4), they are populated differently by collisions of the ion with a beam electron.

Measurements at EBIT are done at 90° to the electron beam direction. In order to infer the emitted photon flux correctly from the observed radiation, correction factors for the anisotropy and polarization are needed. Alder & Steffen (1975) and Steffen & Alder (1975) treat the problem of directional distributions of γ-rays in general. Based on these publications, Vogel (1992) explain the simpler case for a cylindrical symmetry and predominant single multipole operator applicable to radiation from excited atoms in an EBIT. This section summarizes the core equations from Vogel (1992) and final results (Section 2.5.1) for the correction terms needed for the analysis of excitation cross section measurements (Chapter 8). For more details, see Vogel (1992) and references therein.

In order to find the polarization of a level with the well defined total angular momentum J_i, the population distribution among sublevels with component m along the beam axis has to be found. Here, J_i is the initial angular momentum of a collisionally excited ion that radiatively decays into a final state J_f. The statistical ensemble of these excited states emits radiation with a continuous intensity distribution $W(\theta, \phi)$. If the emitted radiation

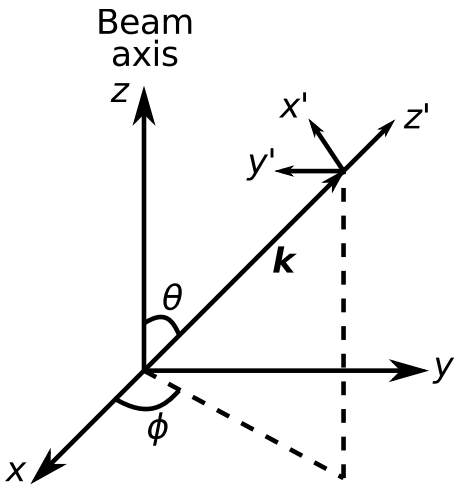

Figure 2.5: Emission geometry of radiation at EBIT. The electron beam is on the z axis. Photons are emitted into the directions $\mathbf{k}$ with meridional and azimuthal angles θ and ϕ. The polarization components $W_{x'}(\theta)$ and $W_{y'}(\theta)$ have electric field vectors along the x' and y'-axis, respectively, where the x'-axis is in the plane defined by the beam axis z and the direction of the photon $\mathbf{k}$. After Vogel (1992).

is polarized, the degree of polarization varies with the meridional and azimuthal angles θ and ϕ of the emitted photon (Fig. 2.5). For the cylindrically symmetric electron and ion distributions in EBIT, the intensity distribution only varies as $W(\theta)$, i.e, in planes parallel to the beam axis. This intensity distribution is the non-coherent sum of its polarization components $W_{x'}(\theta)$ and $W_{y'}(\theta)$ (Fig. 2.5), since collisions with electrons from an unpolarized electron beam give rise to linearly polarized photons (Inal & Dubau, 1987). The degree of linear polarization is then defined as

$$P(\theta) = \frac{W_{x'}(\theta) - W_{y'}(\theta)}{W_{x'}(\theta) + W_{y'}(\theta)} = \frac{W_{x'}(\theta) - W_{y'}(\theta)}{W(\theta)}, \tag{2.17}$$

where the denominator $W(\theta)$ represents the non-polarized intensity distribution that is seen by instruments insensitive to polarization (Vogel, 1992). For dipole X-ray lines, the maximum polarization occurs at 90° to the electron beam axis and $I_{\parallel} = 4\pi W_{x'}(90°)$ and $I_{\perp} = 4\pi W_{y'}(90°)$ such that

$$P = P(90°) = \frac{I_{\parallel} - I_{\perp}}{I_{\parallel} + I_{\perp}} = \frac{1 - I_{\perp}/I_{\parallel}}{1 + I_{\perp}/I_{\parallel}}. \tag{2.18}$$

Expanding the electromagnetic interaction operator H_{int} in a set of electromagnetic multipoles and tracing the initial state density matrix to the final state, leads to expressions for the statistical ensemble (see Vogel, 1992, for details). For a cylindrically symmetric source, the polarization components then are

$$W_{x'}(\theta) = \frac{\mathrm{d}\Omega}{8\pi} \sum_{\lambda=\mathrm{even}} B_{\lambda}(J_{\mathrm{i}}) [A_{\lambda}(\gamma) P_{\lambda}(\cos\theta) + A^{\perp}_{\lambda 2} P_{\lambda 2}(\cos\theta)], \tag{2.19}$$

$$W_{y'}(\theta) = \frac{\mathrm{d}\Omega}{8\pi} \sum_{\lambda=\mathrm{even}} B_{\lambda}(J_{\mathrm{i}}) [A_{\lambda}(\gamma) P_{\lambda}(\cos\theta) - A^{\perp}_{\lambda 2} P_{\lambda 2}(\cos\theta)], \tag{2.20}$$

where $P_{\lambda}(\cos\theta)$ are Legendre polynomials, $P_{\lambda 2}(\cos\theta)$ are associated Legendre polynomials, and B_{λ} is called the orientation parameter, A_{λ} the angular distribution coefficient, and $A^{\perp}_{\lambda 2}$ the linear polarization parameter. For linear polarization, the summation is only

over even λ, for circular polarization the sum would be over even and odd λ. The orientation parameter B_λ describes the initial state of the system and therefore only depends on J_i, m, and $g(m)$. The angular distribution coefficient A_λ and polarization parameter $A_{\lambda 2}^{\perp}$, on the other hand, describe the electromagnetic decay. In the sum of the polarization components (Eq. 2.19 and 2.20)

$$W(\theta) = W_{x'}(\theta) + W_{y'}(\theta) = \frac{\mathrm{d}\Omega}{4\pi} \sum_{\lambda=\mathrm{even}} B_\lambda(J_\mathrm{i}) A_\lambda(\gamma) P_\lambda(\cos\theta) \tag{2.21}$$

$A_{\lambda 2}^{\perp}$ vanishes. Since $W(\theta)$ is by definition unpolarized, all polarization dependence is thus contained in this polarization parameter. The angular dependence of the unpolarized emission $W(\theta)$ is then solely due to the angular distribution coefficient A_λ. Since $A_0 = B_0 = 1$ for all initial states J_i and transitions and since $P_0(\cos\theta) = 1$ for all θ, the zeroth order term describes isotropic emission.

The orientation parameter in cylindrical symmetry is described by

$$B_\lambda(J_\mathrm{i}) = \sum_m = (-1)^{J_\mathrm{i}+m} \left[(2\lambda+1)(2J_\mathrm{i}+1)\right]^{1/2} \begin{pmatrix} J_\mathrm{i} & J_\mathrm{i} & \lambda \\ -m & m & 0 \end{pmatrix} g(m) \tag{2.22}$$

where the large parenthesis denote the Wigner 3-j symbol that sums over angular momenta and is proportional to the Clebsch-Gordan coefficients. The Wigner 3-j symbol satisfies triangular relations such that $B_\lambda(J_\mathrm{i}) = 0$ for $\lambda > 2J_\mathrm{i}$. As a consequence, $B_\lambda = 0$ for $J = 1/2$ always, i.e., photons emitted from excited states with $J_\mathrm{i} = 1/2$ such as Lyα_2 are never polarized (the emission in this case is only due to the constant zeroth order term described above). The isotropy for $J_\mathrm{i} = 1/2$ is completely independent of the final state J_f, type of transition, and even of the sublevel population of the initial level, e.g., also if $g(-1/2) \neq g(1/2)$.

Since A_λ and $A_{\lambda 2}^{\perp}$ describe the electromagnetic decay of the ion, they depend on both the initial and final angular momenta, J_i and J_f, and on the multipole operator involved characterizing the transition. The full expression for these two parameters (see Vogel, 1992, Eq. 10.8 and 10.9) can be simplified for atomic decays, since the transition probability for higher-order multipoles decreases so fast that they can be neglected. Then A_λ and $A_{\lambda 2}^{\perp}$ only depend on a single multipole transition and can be described by the overlap between initial orientation state with J_i and random final state with J_f

$$F_\lambda(LL'J_\mathrm{f}J_\mathrm{i}) = (-1)^{J_\mathrm{f}+J_\mathrm{i}-1} \left[(2\lambda+1)(2L+1)(2L'+1)(2J_\mathrm{i}+1)\right]^{1/2} \times \begin{pmatrix} L & L' & \lambda \\ 1 & -1 & 0 \end{pmatrix} \begin{Bmatrix} L & L' & \lambda \\ J_\mathrm{i} & J_\mathrm{i} & J_\mathrm{f} \end{Bmatrix} \tag{2.23}$$

which vanishes for $\lambda > 2L$. Here, L denotes the order of the multipole, e.g., $L = 1$ for dipole transitions, and the large curly braces stand for the Wigner 6-j symbol used to add three angular momenta. For a pure decay then

$$A_\lambda = F_\lambda(LL'J_\mathrm{f}J_\mathrm{i}) \tag{2.24}$$

$$A_{\lambda 2}^{\perp} = -\Lambda(\kappa) \left[\frac{(\lambda-2)!}{\lambda+2)!}\right]^{1/2} \frac{\begin{pmatrix} L & L' & \lambda \\ 1 & 1 & -2 \end{pmatrix}}{\begin{pmatrix} L & L' & \lambda \\ 1 & -1 & 0 \end{pmatrix}} F_\lambda(LL'J_\mathrm{f}J_\mathrm{i}) = \Lambda(\kappa) f_\lambda(L) A_\lambda \tag{2.25}$$

where $\Lambda(\kappa)$ is a sign factor for the multipole type κ with $\Lambda(\mathrm{E}) = 1$ for electric multipoles and $\Lambda(\mathrm{M}) = -1$ for magnetic multipoles. In this approximation, the description of the polarization components simplifies to

$$W_{x'}(\theta) = \frac{\mathrm{d}\Omega}{8\pi} \sum_{\lambda=\text{even}} B_\lambda(J_\mathrm{i}) A_\lambda \left[P_\lambda(\cos\theta) + \Lambda(\kappa) f_\lambda P_{\lambda 2}(\cos\theta)\right], \tag{2.26}$$

$$W_{y'}(\theta) = \frac{\mathrm{d}\Omega}{8\pi} \sum_{\lambda=\text{even}} B_\lambda(J_\mathrm{i}) A_\lambda \left[P_\lambda(\cos\theta) - \Lambda(\kappa) f_\lambda P_{\lambda 2}(\cos\theta)\right], \tag{2.27}$$

where the only difference between electric and magnetic multipoles of the same order is the sign factor $\Lambda(\kappa)$ such that the polarization correction for a magnetic dipole (M1) has the same functional form as for an electric dipole (E1) transition, but with the polarization components being reversed between them. Calculating $W(\theta)$ and P from these polarization components then leads to the correction factor and degree of polarization for any transition. For very common transitions, the respective formulae are listed in the next subsection.

2.5.1 Degree of Polarization for Specific Transitions

E1 transitions

For an E1 transition such as w and y in He-like ions or q in Li-like ions, A_4 and higher orders are zero, and $f_2(L = 1) = -1/2$, thus

$$W_{x'}(\theta) = \frac{1}{8\pi}[1 + A_2 B_2(3\cos^2\theta - 2)] \tag{2.28}$$

$$W_{y'}(\theta) = \frac{1}{8\pi}[1 + A_2 B_2], \tag{2.29}$$

where $W_{x'}$ is perpendicular to the beam for $\theta = 0$ and parallel for $\theta = 90°$, while $W_{y'}$ is always perpendicular to the beam. Inserting these into Eq. 2.17 and using $W(90°) = W_{x'}(90°) + W_{y'}(90°)$ gives

$$P = \frac{-3A_2B_2}{2 - A_2B_2} \qquad \text{and} \qquad W(90°) = \frac{1}{8\pi}(2 - A_2B_2). \tag{2.30}$$

Finally, combining these two equations to express $W(90°)$ as a function of degree of linear polarization P results in the *polarization correction factor* for observations at 90° to the beam that is valid for all E1 transitions:

$$4\pi W(90°) = \frac{3}{3 - P}. \tag{2.31}$$

To obtain the linear polarization P for E1 transitions with specific combinations of J_i and J_f, evaluate the expressions for A_λ (Eq. 2.24) and B_λ (Eq. 2.22) and insert into the first equation in Eq. 2.30. For example, He-like line w and y have $J_\mathrm{i} = 1$ and $J_\mathrm{f} = 0$ such that

$A_2 = 1/\sqrt{2}$ and $B_2 = 1/\sqrt{2}[g(-1) - 2g(0) + g(1)]$ and consequently (using the identity $\sum_m g(m) = 1$) the *degree of polarization for lines w and y* is

$$P_{\mathrm{w,y}} = \frac{-(g(-1) - 2g(0) + g(1))}{g(-1) + 2g(0) + g(1)} = \frac{g(0) - g(1)}{g(0) + g(1)}. \tag{2.32}$$

The last step makes use of the state populations $g(-m) = g(m)$ being symmetric in the magnetic quantum number m. The expression for line q, which has half-integer angular momenta, differs from line w and y with the polarization for $J_\mathrm{i} = 3/2$ and $J_\mathrm{f} = 1/2$

$$P_\mathrm{q} = \frac{-3(g(-3/2) - g(-1/2) - g(1/2) + g(3/2))}{3g(-3/2) + 5g(1/2) + 5g(1/2) + 3g(3/2)} = \frac{-3(g(3/2) - g(1/2))}{3g(3/2) + 5g(1/2)}. \tag{2.33}$$

M1 transitions

For M1 transitions only the sign factor changes as $\Lambda(\mathrm{M}) = -1 = \Lambda(\mathrm{E})$ such that the *polarization correction factor for M1* transitions becomes, in analogy to Eq. 2.31,

$$4\pi W(90^\circ) = \frac{3}{3 + P} \tag{2.34}$$

and the *degree of polarization for line z* ($J_\mathrm{i} = 1$, $J_\mathrm{f} = 0$) is

$$P_\mathrm{z} = \frac{g(-1) - 2g(0) + g(1)}{g(-1) + 2g(0) + g(1)} = \frac{g(1) - g(0)}{g(0) + g(1)} = -P_{\mathrm{w,y}}. \tag{2.35}$$

E2 and M2 transitions

For quadrupole transitions, only A_6 and higher are zero such that the degree of polarization P and the unpolarized distribution $W(90^\circ)$ include additional terms A_4B_4 and cannot trivially be expressed as a function of each other. With $f_2(2) = \pm 1/2$ and $f_4(2) = \mp 1/12$, the degree of polarization is (Vogel, 1992; Gu et al., 1999b)

$$P = \frac{\pm(12A_2B_2 + 5A_4B_4)}{8 - 4A_2B_2 + 3A_4B_4} \tag{2.36}$$

where the top (bottom) sign corresponds to E2 (M2) transitions. If $A_4B_4 \ll A_2B_2$, the polarization and angular distribution of E2 (M2) simplify to the expression for M1 (E1) transitions (Gu et al., 1999a).

For an M2 transition with $J_\mathrm{i} = 2$, $J_\mathrm{f} = 0$

$$A_2 = -\sqrt{5/14}B_2 = \sqrt{5/14}[2g(-2) - g(-1) - 2g(0) - g(1) + 2g(2)] \tag{2.37}$$

$$A_4 = -4/\sqrt{14}B_4 = \sqrt{1/14}[g(-2) - 4g(-1) + 6g(0) - 4g(1) + g(2)] \tag{2.38}$$

$$\tag{2.39}$$

and therefore the *degree of polarization for line x* ($J_\mathrm{i} = 2$, $J_\mathrm{f} = 0$) is

$$P_\mathrm{x} = \frac{g(-2) - g(-1) - g(1) + g(2)}{g(-2) + g(-1) + g(1) + g(2)} = \frac{g(2) - g(1)}{g(2) + g(1)}. \tag{2.40}$$

2.5.2 Influence on Polarization

For excitation through a single electron impact excitation channel, the sublevel population needed to calculate the polarization is characterized by the magnetic sublevel excitation cross sections $\sigma(m)$ such that $g(m)$ above can be substituted by $\sigma(m)$ (Hakel et al., 2007). If the excited levels of an ion are not solely populated from a single lower level by collisions with beam electrons, i.e., in the presence of other feeding channels, the degree of polarization of the photon emitted during the decay differs from the expressions shown above. The additional channels can lead to a randomization of the magnetic sublevel population and thus have a depolarizing effect on the emitted radiation. Such feeding channels include, for example, cascades from higher levels, radiative recombination, charge exchange, inner-shell ionization, and collisional excitation from multiple lower levels. These feeding channels have to be taken into account when calculating the linear polarization of the observed photons. These contributions can be described analytically (e.g., Beiersdorfer et al., 1996b) or with a full atomic kinetic model such as, e.g., the FAC polarization module, to find the magnetic sublevel population. The influence of these additional channels have on polarization was explored by, e.g., Inal & Dubau (1993), Beiersdorfer et al. (1996b), Beiersdorfer & Slater (2001), Hakel et al. (2007), and Chen et al. (2015).

The expressions for polarization in the previous subsection assume a completely unidirectional beam. However, the beam electrons have a small energy component $E_\perp$ perpendicular to the beam direction, which is related to the radial position on the electron gun where the electron was born, the electrons spiraling around the magnetic field lines of EBIT's superconducting magnet, and a thermal velocity component of the electron beam (Beiersdorfer et al., 1996b, 1999a; Beiersdorfer & Slater, 2001). The magnitude of this transverse beam energy is on the order of 100-250 eV (Savin et al., 1998; Beiersdorfer et al., 1999a; Gu et al., 1999b; Beiersdorfer & Slater, 2001; Chen & Beiersdorfer, 2008). For electric dipole transitions line w and y, and for the magnetic quadrupole transition x (its set of orientation parameters resembles that of electric dipole transitions; Beiersdorfer et al., 1996b, 1999a), the polarization P_0 with $E_\perp = 0$ is related to the measured polarization P with $E_\perp \neq 0$ as (Savin et al., 1998; Beiersdorfer et al., 1999a)

$$P_0 = \frac{2P}{2 - E_\perp(3-P)/E_{\text{beam}}} \tag{2.41}$$

and for the magnetic dipole transition z as

$$P_0 = \frac{2P}{2 - E_\perp(3+P)/E_{\text{beam}}}. \tag{2.42}$$

As shown by Beiersdorfer et al. (1999a), this correction is small and well within the uncertainties of the polarization measurements. Gu et al. (1999a) derive the full formalism for polarization due to collisions with spiraling electrons.

Had it not gone well, many of the spectroscopic measurements of the last 20 years would not have been possible.

Ross Marrs (2008)

3 Electron Beam Ion Trap

The electron beam ion trap (EBIT) was developed at Lawrence Livermore National Laboratory from the electron beam ion source (EBIS). The goal of its development was to make it possible to spectroscopically study cold[1] highly charged ions at rest (Marrs et al., 1988; Levine et al., 1988, 1989). At that time, crossed or merged beam experiments (e.g., Dittner et al., 1987; Gregory et al., 1979) were limited to spectroscopic observations of charge states $q \leq +6$. Beam-foil experiments and tokamaks only allowed the study of hot ions (Levine et al., 1988). Donets (1985) demonstrated EBIS's potential as a spectroscopic device on Xe^{52+} ions, however the machine exhibited some disadvantages precluding its success: achieving high charge states was prevented by charge exchange from high levels of background gas at room temperature (Marrs, 2008) and ion heating from Coulomb collisions and plasma instabilities in the electron beam limited the degree of ionization the ions could reach (Levine et al., 1988, 1989). Additionally, EBIS lacked easy access ports for X-ray spectrometers as it was originally designed as an ion injector for accelerators (Briand et al., 1984; Marrs, 2008). The design of EBIT was geared towards addressing these issues. As a result, the first trap, EBIT-I, turned out to be an excellent device for spectroscopy and for testing fundamental atomic physics, as evidenced by the large number of measurements done (Beiersdorfer, 2008b, 2007). Its main advantages are the ability to select charge states and even excitation processes by carefully choosing the energy of the mononergetic electron beam (Decaux & Beiersdorfer, 1993). EBIT spectroscopy soon became a pillar for laboratory astrophysics in the EUV as well as the X-ray spectral ranges (Beiersdorfer, 2003). Additionally, the LLNL EBITs provide reference data for laser-produced plasmas (Schneider et al., 2008) and serve as a calibration facility for line profiles, transmission and reflection efficiencies, and the quantum efficiency of grating and crystal spectrometers and solid state detectors (Brown et al., 2010). Comprehensive overviews can be found in a number of papers (e.g., Marrs et al., 1988; Levine et al., 1988, 1989; Marrs et al., 1994; Beiersdorfer, 2003;

[1] Typical ion temperatures in EBIT range from as low as 70 eV (Beiersdorfer et al., 1995b) to about 1 keV (Beiersdorfer et al., 1996a), depending on Z and EBIT conditions. See discussions in this chapter and in Section 5.5.2.

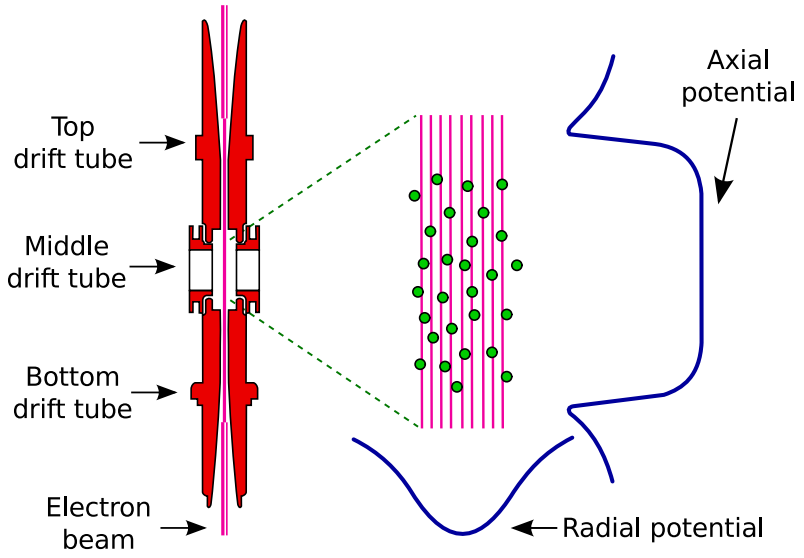

Figure 3.1: Schematic of the EBIT trapping mechanism (After `https://ebit.llnl.gov/`).

Beiersdorfer et al., 2003a; Beiersdorfer, 2008a; Marrs, 2008) and and in the many dissertations done at EBIT (e.g., Vogel, 1992; Wong, 1992; Widmann, 1999; Brown, 2000; Gu, 2000; Thorn, 2008).

3.1 EBIT

In brief, an EBIT is an electron beam coupled with an electromagnetic trap. The electron beam is guided from the electron gun through a set of three cylindrical electrodes, called drift tubes, to a collector, where it is absorbed. The electron beam collisionally ionizes and excites atoms or ions injected into the trap region. To ensure high electron current densities for these electron-ion interactions, the strong magnetic field provided by a pair of superconducting Helmholtz coils compresses the electron beam in the trap region to a diameter of 60–70 μm. Radial trapping is provided by the space charge potential of the electron beam. The axial trap is a potential well provided by setting the middle drift tube to a lower potential than the bottom and top drift tubes (Fig. 3.1). Six slots cut into the middle drift tube allow access to the trap for ion injection and observation with spectrometers, i.e., radiation from electron-ion interactions is observed at 90° to the electron beam.

A sketch of the main components of EBIT is shown in Fig. 3.2. The electron beam is born by a Pierce-type (Pierce & Millburn, 1952) electron gun. The cathode of the gun comprises a conically shaped tungsten filament covered with barium oxide as electron emissive coating. The filament is heated to high temperatures ($\approx$ 1030–1160 °C) to overcome the work function of the material and boil off electrons (thermionic emission). The conical shape gives an initial directionality to the beam. A pair of bucking coils around the electron gun counteracts the magnetic field from the trap locally to ensure that the electrons are born in a field-free environment. A focusing electrode close to the cathode is followed by the anode biased to high potential, which accelerates the electrons. When

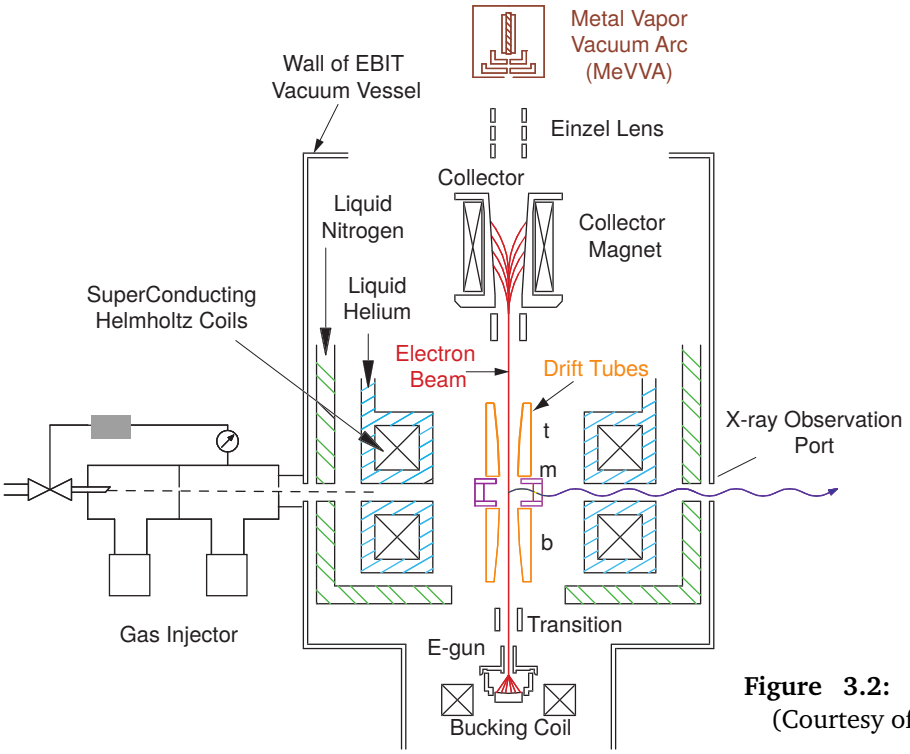

Figure 3.2: Sketch of EBIT-I (Courtesy of Klaus Widmann).

the electrons emerge through a hole in the anode, a steering electrode, dubbed the transition, guides their path to the drift tubes. The three drift tubes are biased to a common base potential (referred to as the drift tube voltage), which further accelerates the electrons to the desired beam energy. The smaller additional voltages (bottom, middle, and top drift tube voltages) for the potential well of the axial trap are added relative to this base potential for each of the individual drift tubes. After the electron beam has passed through the trap, it is disposed of in a collector electrode. To avoid damage, a magnet on the collector electrode defocuses and radially expands the electron beam before it hits the collector. The collector is cryogenically cooled with liquid nitrogen to dissipate the large amounts of deposited power, $P = IV$, where I is the beam current and V the collector potential. The collector voltage is generally set such that the power is $\lesssim 300$ watts.

Both the ionization rate and the X-ray emission rate are proportional to the current density $j_e = n_e v$ (Marrs et al., 1994). To maximize the j_e in EBIT, a pair of superconducting Helmholtz coils mounted around the trap region provides a 3 T magnetic field parallel to the beam direction that magnetically compresses the beam electrons. Measurements of the beam profile by X-ray imaging show that the electron beam has a diameter on the order of 60–70 μm (containing 80 % of the electrons), for both low and high beam energies (Levine et al., 1989; Marrs et al., 1995). At a beam current of over 200 mA, this corresponds to a current density of around 5000 A cm^{-2} (Levine et al., 1988; Marrs et al., 1995). Typical electron densities range from $2 \cdot 10^{10}$ to $5 \cdot 10^{12}$ cm^{-3}, i.e., EBIT operates in the coronal density limit (Beiersdorfer, 2003).

The trapped material is ionized by successive collisions with beam electrons, whose energies are greater than the ionization potential. Since the ions are nearly at rest, the

electron beam energy limits the highest achievable charge states. The beam energy is determined by the sum of the base drift tube voltage, the middle drift tube voltage, and the negative space charge potential of the electron beam itself, and also by the positive space charge of the trapped ions. While the exact space charge potential of the electrons is usually unknown, a good estimate can be derived from Gauss's law to (Brown, 2000)

$$V_{\mathrm{SC}}\,[\mathrm{Volts}] = -5.4\frac{I\,[\mathrm{mA}]}{\sqrt{E_{\mathrm{kin}}\,[\mathrm{keV}]}} \tag{3.1}$$

where I is the beam current and E_{kin} the beam energy. The charge of the positive ions reduces the effect of the electron space charge, typically by about half (Brown, 2000). Using this estimate, it is usually possible to set the electron beam energy to within 10s of eV of the target energy (Section 8.4.2). The beam energy can be derived from the X-ray energy of radiative recombination lines or estimated from the relative strength of dielectronic recombination resonances (Levine et al., 1989). The electron beam is quasi-monoenergetic; it has a narrow electron energy distribution with a roughly Gaussian shape with a FWHM of around 25–50 eV (Levine et al., 1989) that can be attributed to fluctuations in the space-charge potential in the trap and ripple in the drift tube high-voltage power supply (Marrs, 2008). The energy spread of the beam can be derived from the spectral width of radiative recombination lines, provided that they are observed with a spectrometer of sufficient resolution, or from the width of the intensity variation of dielectronic resonances with beam energy (Beiersdorfer et al., 1992b).

EBIT-I can reach beam energies up to 18 keV. A high-energy variant, called SuperEBIT (Fig. 3.3), can reach over 200 keV, sufficient to produce bare U^{92+} (Marrs et al., 1994). While in EBIT-mode both the electron gun and the collector are biased to ground potential, for SuperEBIT gun and collector are biased to a large negative potential. The potential difference of the electron gun to the positive drift tube potential in the trap determines the large beam energy.

How strongly the ions are trapped is determined by the product of the ion charge, q, and the trapping potential, V_{trap}. Therefore, more highly charged ions are trapped more easily than lower charge states. The trapped ions have a temperature due to Brownian motion. Ions in the high-energy tail of the corresponding Maxwellian distribution may have kinetic energies larger than the boiling temperature of the trap and escape its potential well (Levine et al., 1988). Deeper traps tend to retain higher ion temperatures, since the kinetic energy required to overcome the potential barrier is higher and fewer "hot" ions can escape.

Due to their temperature, the ions typically have a velocity component perpendicular to the beam and, consequently, do not spend all of their time inside the beam. If the ion cloud is hot compared to the radial trapping potential, it will have a much larger radius than the electron beam and the ions can spend as little as a third of their time inside the beam (Levine et al., 1988). Although the ion cloud radius is typically larger than the electron beam, due to the short life time of most excited states, the excited ions typically emit photons while still in the electron beam. The beam-ion overlap is, therefore, an important factor for excitation cross-section measurements.

The achievable degree of ionization is affected by several factors. First the amount of time

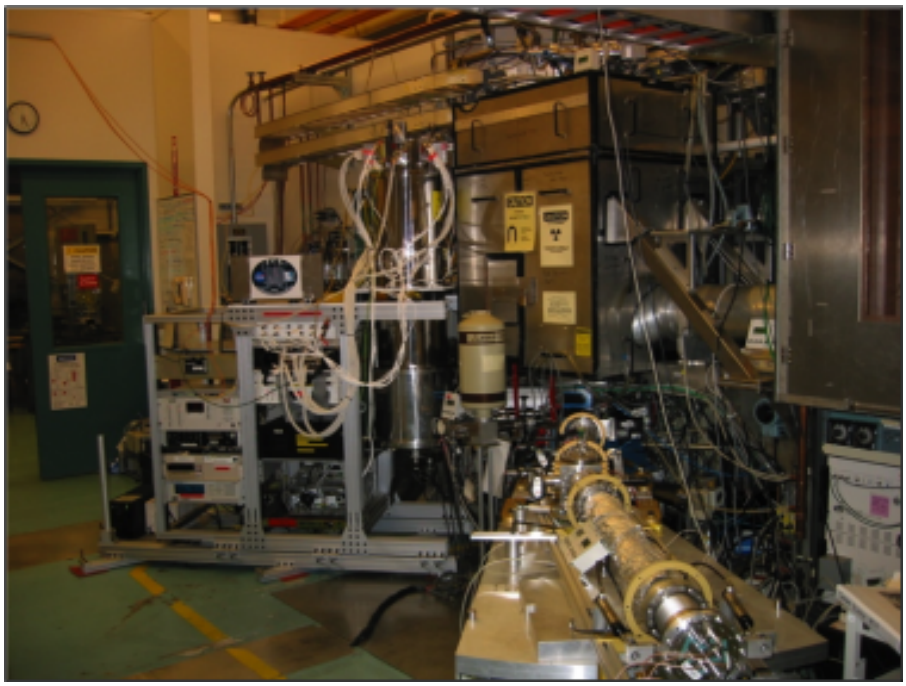

Figure 3.3: Picture of SuperEBIT at LLNL with the ECS microcalorimeter (left) and the GFFS grating spectrometer(right; Courtsey G.V. Brown).

the ions spend inside the beam is limited, as mentioned above, by the ion's perpendicular velocity component. This reduces the collision rate with beam electrons. Additionally, the charge balance is reduced by charge exchange recombination from neutral background gas, which has a large interaction cross section and occurs while the ions are outside the electron beam. This effect is kept at a minimum by operating EBIT in high vacuum, typically on the order of $\sim 10^{-11}$ Torr. The presence of background ions in the beam produced from neutral background gas in EBIT also reduces the effective collision rate between beam electrons and the ions being studied. This effect is, as in the case of charge exchange, mitigated by operating at high vacuum.

One of the largest challenges that had to be overcome in order to trap and study truly highly charged ions, such as H-like and bare uranium, is the heating of the ions by the electron beam. This problem was addressed by a serendipitous discovery (Marrs, 2008). The laws of momentum conservation dictate that in a collision between a low-mass and a more massive body, such as collisions involving a low-Z and a high-Z ion, the lighter constituent will carry away the higher velocity. The hotter (faster) ions are more likely to leave the trap, and when they do, they take energy with them, effectively lowering the average temperature in the trap. This process is referred to as evaporative cooling and can be encouraged by injecting small quantities of low-Z material along with the higher-Z material to be studied (Levine et al., 1988; Schneider et al., 1989). As a result of evaporative cooling, ions remain in the beam longer and in turn can become more ionized. For example, Au ions stayed in the trap for over 4 h after a single injection (Schneider et al., 1989).

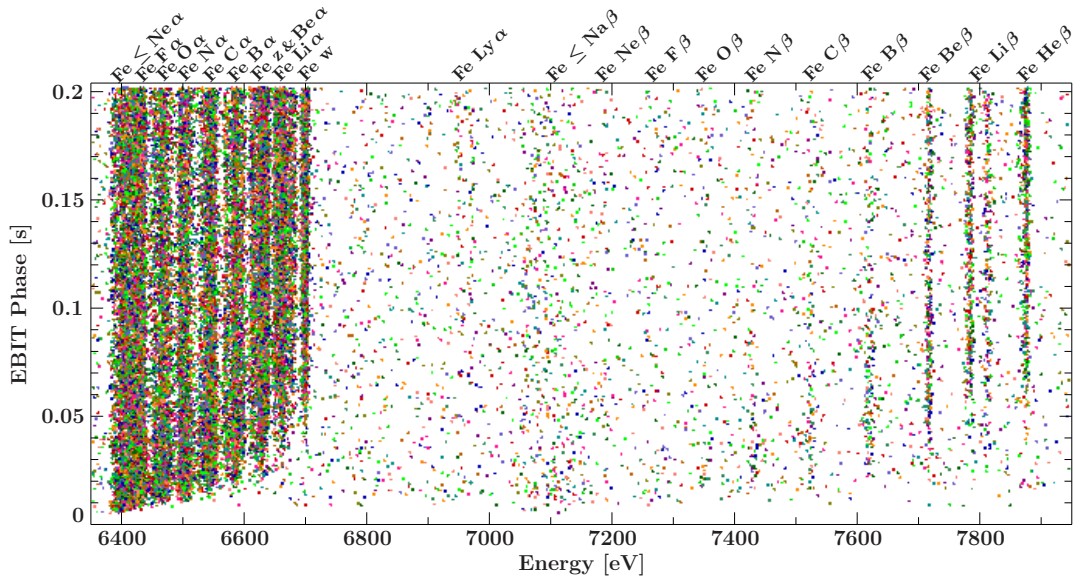

Figure 3.4: Charge state evolution with EBIT phase.

While long trapping times can be achieved through evaporative cooling, they have an unwanted side effect. Barium ($Z = 56$, Ba) and Tungsten ($Z = 74$, W) ions evaporating from the electron gun can migrate into the trap. Since these are fairly high-Z elements compared to the astrophysically relevant lower-Z elements studied here, over time they dominate the trap population. As a result, Ba has been the first element to be observed spectroscopically with EBIT (Levine et al., 1988; Marrs et al., 1988), when it was first turned on without ion injection. To avoid accumulation of these contaminants, the trap is periodically emptied: by lowering the top drift tube below the potential of the middle drift tube, all trapped ions are dumped. The time between two dumps is called the EBIT phase or EBIT cycle time. Figure 3.4 is a scatter plot of measured X-ray energy as a function of EBIT phase for K-shell transitions in Fe. Very low charge states dominate the spectrum in the first few milliseconds, but quickly ionize to higher charge states. By time tagging each detected photon with its EBIT phase, one can analyze the portion of the spectrum only at equilibrium.

EBIT is operated in one of two modes: the electron trapping mode and the magnetic trapping mode. In electron trapping mode, the electron beam is on and traps the ions radially. The electron beam can be held at a constant, mono-energetic energy or can be "swept" either linearly between different energies or in a function defined by the user[2]. In magnetic trapping mode, the beam is turned off during part of the EBIT phase and ions are trapped radially by the 3 T magnetic field, i.e., together with the electric potential of the drift tubes, EBIT acts like a Penning trap in this mode. All the measurements presented in this thesis were completed using the electron trapping mode at constant, mono-energetic beam energies.

[2]Using an arbitrary function generator attached to the drift tube and anode power supplies, the electron beam energy and beam current have been swept to create a quasi-Maxwell-Boltzmann electron distribution (truncating the very low- and high-energy tails of the distribution) for several temperatures (Savin et al., 2000)

3.2 Injection Methods

Of the first 98 elements of the periodic table, 75 have been injected into the Livermore EBITs. With its mono-energetic beam and narrow charge state distribution, EBIT is eminently suited to unravel cross sections and transition wavelengths of X-ray emission due to separate atomic physics processes (Marrs et al., 1988). To keep this advantage and in order not to add any new degeneracy from line blends of different ion species, it is important to be able to study, and therefore inject, individual elements separately.

There are several methods available to inject material into EBIT. The currently most commonly used injection method is a ballistic gas injector. Using a differential pumping scheme, the gas injector introduces a collimated stream of neutral gas directly into the trap region (Vogel, 1992). To avoid accumulation of neutral background, the gas stream is aligned such that it crosses the electron beam, where the atoms are directly ionized and captured. The injection pressure, and therefore the amount of injected material, is regulated with a thermal valve and can be finely tuned to a constant pressure. It is typically in the range of 10^{-8} to 10^{-6} Torr, i.e., 10^4 to 10^5 times as high as the EBIT base pressure. In addition to actual gases, liquids with a very high vapor pressure at room temperature, relative to the gas injector's base pressure of 10^{-7} Torr, can also be installed on the gas injector.

Solids with high vapor pressure ($\geq 10^{-7}$ Torr at ≤ 200°C; e.g., certain metalocenes or metals with low melting points), however, are instead injected with a sublimation injector. While the vapor from the sublimator is collimated and also aligned to intercept the electron beam, unlike the gas injector, it does not produce a finely directed atomic stream and has an adjustable yet not as well-defined and reproducible gas pressure. Metal ions can be injected with a Metal Vapor Vacuum Arc (MeVVA; Brown et al., 1986), where a triggered high-voltage breakdown liberates ions from the cathode. Other methods include wire probes plated with small amounts of source material and placed near the electron beam (Elliott & Marrs, 1995), which are especially useful for highly radioactive material that would otherwise contaminate the hole injector; organometallic injection (Ullrich et al., 1998), e.g., $W(CO)_6$; laser ablation where atomic vapor is produced by a high-intensity laser (Niles et al., 2006); a Knudsen cell (Yamada et al., 2007), which is essentially a high-temperature oven for metallic compounds (≤ 1900°C); and a neutral metal injector for rare earth metals with high vapor pressures like Eu ($\geq 10^{-7}$ Torr at ≤ 1000°C; Magee et al., 2014).

Not all of these different injectors can be mounted on one of the 90° ports. Due to the strong magnetic field, only neutral material can be injected into the trap through the side ports perpendicular to the field. Charged particles such as the 1–3 times ionized material produced by the MeVVA can only enter the trap from the top, i.e., parallel to the magnetic field lines. Moreover, the employed injection method depends strongly on the material to be injected and partially on the application, which defines whether pulsed or continuous injection is more desirable. For targeted and calibration measurements discussed in this work, we only used the ballistic gas injector (F, Ne, Mg, Al, Si, S, Cl, Ar, V, Fe) and the sublimator (Mn, Ni, Os).

3.3 Spectrometers

The photons produced at EBIT are observed with a number of EUV and X-ray spectrometers, including various types of solid state, grating, and crystal spectrometers, and a microcalorimeter. Overall, instrumentation at EBIT spans the electromagnetic spectrum from the visible to the X-ray region (about 1–7000 Å, Beiersdorfer, 2003). The choice of spectrometer or combination of spectrometers depends on the scope of the experiment. This section gives a brief overview of some of the X-ray spectrometers available at EBIT. Typical spectral ranges and resolving powers of these spectrometers are shown in Fig. 3.5. For a detailed description of the two spectrometers used for the measurements presented in this work, refer to Chapters 4 and 5.

Diffractive Spectrometers

Diffractive or wavelength dispersive spectrometers use a diffracting medium – gratings or a crystal – to spatially separate the photons with different wavelengths, which are then observed with a position sensitive detector, e.g., a charged coupled device (CCD) or a position sensitive proportional counter (PSPC). These spectrometers typically achieve higher resolving powers and are preferentially used for highly accurate wavelength measurements. Due to their geometry, however, wavelength dispersive spectrometers tend to cover only a rather limited wavelength region at a single setting and have relatively small throughput. For variably spaced flat field gratings, for example, the limiting factor is often the size of the detector (CCDs commonly have 1 inch chip sizes) and could, in principle, be alleviated by using multiple detectors in the image plane (see, e.g., the High-Energy Transmission Gratings on-board the *Chandra* X-ray Observatory; Canizares et al., 2005). For crystal spectrometers, the prevailing issue limiting the spectral region is the finite length of the crystal.

Crystals can only diffract photons with wavelengths about an order of magnitude below and up to their $2d$ lattice spacings (see Section 5.1), which naturally limits their overall useful wavelength region (varying as a function of the specific crystal cut) to 0.14 to 25 Å (Thompson et al., 2009), corresponding to an energy range of 0.5–88 keV. Gratings follow a similar diffraction rule with respect to their groove size, where smaller groove size diffracts shorter wavelengths. Limits in manufacturing make it inefficient to diffract higher energy photons, i.e., photons with energies greater than $\sim$ 1–2 keV. Additionally, the grating efficiency falls off rapidly at higher photon energies (Galeazzi et al., 2000). Therefore, their main application is in the extreme ultraviolet and soft X-ray region (below 10–400 Å or below about 2 keV).

Examples of grating spectrometers at the Livermore EBIT facility are the X-ray and Extreme Ultraviolet Spectrometer (XEUS; Utter et al., 1999b; Beiersdorfer et al., 2006, 2008), the Long Wavelength Extreme Ultraviolet Spectrometer (LoWEUS; Beiersdorfer et al., 1999b), the Gold Flat Field Spectrometer (GFFS; Beiersdorfer et al., 2004b), and the High-resolution Grazing incidence Grating Spectrometer (HIGGS; Beiersdorfer et al., 2014c). LoWEUS covers a wavelength range of about 200 Å with a resolving power of

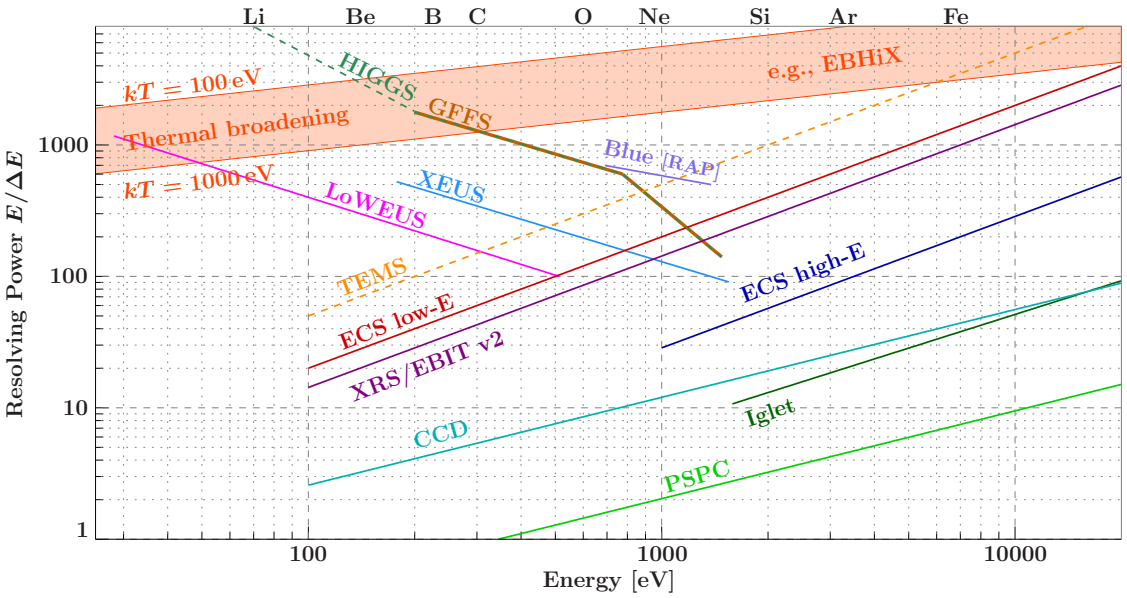

Figure 3.5: Approximate resolving power for a selection of spectrometers at the LLNL EBITs as a function of photon energy. The lines only cover the approximate energy region accessible with the respective spectrometer.
Spectrometers displayed include: EBIT Calorimeter Spectrometer (ECS) low-energy and high-energy pixels, its predecessor XRS/EBIT v2, and its successor the Transition Edge Microcalorimeter Spectrometer (TEMS) arriving in the near future (Porter et al., 2009b); the EG&G Iglet high-purity Ge detector; Charged Coupled Devices (CCDs), which at EBIT are only used as position sensitive detectors in conjunction with gratings or crystals; position sensitive proportional counters (PSPCs), again only used with crystal spectrometers; the Gold Flat Field grating Spectrometer (GFFS; Beiersdorfer et al., 2004b); the High-resolution Grazing incidence Grating Spectrometer (HIGGS; Beiersdorfer et al., 2014c); the X-ray and Extreme Ultraviolet grating Spectrometer (XEUS; Utter et al., 1999b; Beiersdorfer et al., 2006); the Long Wavelength Extreme Ultraviolet grating Spectrometer (LoWEUS; Beiersdorfer et al., 1999b); and the Blue flat crystal spectrometer using a RAP crystal (Brown et al., 1999).
Some of the crystal spectrometers like EBHiX (Beiersdorfer et al., 2016c) or the spectrometer described by Beiersdorfer (1997) have such high resolving powers that the resolution of the spectrometer is limited by the thermal or Doppler broadening of the trapped ions. Since the resolving power due to thermal broadening depends on the nuclear mass of the observed ions, the region for the thermal broadening marked in the graph is scaled to the specific ion whose K-shell transitions falls into this energy region, e.g., Si around 1.9 keV and Fe around 6.7 keV. For example, Fe lines observed around 100 eV (100 Å) have the same Doppler-limited $E/\Delta E$ as Fe lines at 6.7 keV, deviant from the broadening marked at 100 eV.

about 400. GFFS and HIGGS, in contrast, while having a large accessible wavelength range (GFFS: below 10 Å up to 50 Å; HIGGS: below 10 Å to above 300 Å), can only observe a small window of this range at a time (GFFS: 6 Å at around 16 Å or 10 Å at 38 Å; HIGGS: 14 Å at 100 Å or 21 Å at 200 Å), but with a much larger resolving power (GFFS: 600 at 16 Å up to 1200 at 38 Å; HIGGS: 4800 at 100 Å). In fact, the resolving power of the HIGGS is so high that it is limited by the ion temperature of the trapped ions.

Two general types of crystal spectrometers are in use at EBIT (Beiersdorfer, 2003), flat

crystal spectrometers in the 4–25 Å (0.5–3 keV) region (e.g., Brown et al., 1999) and bent crystal spectrometers below about 5 Å (above 3 keV). Bent crystal spectrometers are designed to increase the observed X-ray flux through their focusing properties. For examples of cylindrically bent crystals, see, e.g., Beiersdorfer (1990). For a discussion of the most recent spherically bent crystal spectrometer OHREX (Beiersdorfer et al., 2016b) see Chapter 5. Wavelength range and resolution depend strongly on the employed crystal and Bragg angle (Beiersdorfer et al., 1997a); see the X-ray data booklet (Thompson et al., 2009) for a table of crystal cuts.

For gratings and for those crystal spectrometers using a flat crystal or the von Hámos geometry the diffraction geometry dictates that the source cannot be extended in the dispersion direction. Since the main contribution to the radiation observed from EBIT comes from ions within the electron beam, EBIT is a line source and effectively acts like a slit for diffractive spectrometers (Beiersdorfer et al., 1990a; Crespo López-Urrutia et al., 2002). Therefore, traditionally grating (e.g., Beiersdorfer et al., 1999b, 2004b, 2014c; Utter et al., 1999b,a; Lapierre et al., 2007) and crystal (e.g., Beiersdorfer et al., 1990a; Beiersdorfer & Wargelin, 1994; Beiersdorfer et al., 2004a; Brown et al., 1999; Nakamura, 2000; Thorn & Beiersdorfer, 2004; Kubiček et al., 2012) spectrometers are mounted with the dispersion plane perpendicular to the electron beam direction.

Non-diffractive Spectrometers

Non-diffractive or energy dispersive spectrometers on the other hand aim to reconstruct the photon energy deposited into an absorbing medium. In traditional non-diffractive spectrometer types, the photon energy is proportional to the pulse height of an electrical signal induced by the absorbed photon, e.g., the size of the electron avalanche in a gas proportional counter or the number of electrons lifted from the valence band to the conductance band in a semi-conductor (CCDs, high-purity Ge detectors). These spectrometers cover a broad energy range (CCD: up to ~ 10 keV; HpGe: up to ~ 100 keV) and have a large effective area. But the energy resolution is limited by the random exchange of electrons into the conductance band gap and even more by statistical fluctuations of the fraction of photon energy converted into the detection channel[3], e.g., electron-hole pairs in semiconductors or free charge in ionization detectors (McCammon, 2005b; Galeazzi et al., 2000). These fluctuations affect the resolution more severely in proportional counters than in semiconductors: the energy needed to ionize the gas in the proportional counter is up to an order of magnitude larger than the energy needed to cross the band gap in a semiconductor. A photon of energy E_γ, therefore, produces fewer charge carriers in the proportional counter than in the semiconductor and fluctuations in the fraction of energy converted thus result in larger relative variations, i.e., lower resolution, for the proportional counter. At EBIT, the main application of these spectrometers has been the observation of weak signals such as radiative recombination photons, observation of photons with high energies (~ 10 keV), or observations where fast feedback is required.

[3] A channel is any form the internal energy of the detector can take (McCammon, 2005b). The detection channel is the channel that is read-out and monitored for a signal in response to a photon event.

More recently, micro-calorimeters, which measure the temperature change of an absorber due to the energy deposited by the incident photon, have been developed for X-ray spectroscopy and employed at EBIT (Porter et al., 2008b). Unlike ionization detectors, calorimeters are equilibrium detectors where all channels are in equilibrium, i.e., the photon energy is completely converted into a single detection channel, in this case heat. Calorimeters can, at least theoretically, achieve unlimited energy resolution (McCammon, 2005b). Their operating principle and use at EBIT is discussed in Chapter 4. They fill the gap for high-resolution broad-band spectrometers and open up new regimes for observations especially of extended sources[4]. For example, the first and second generation of calorimeters at EBIT-I added high-resolution measurements of X-ray emission following charge exchange recombination and measurements of absolute impact excitation cross sections for Fe L transitions to the suit of measurement capabilities at EBIT (Porter et al., 2005). The third generation extended the excitation cross section measurements further to K-shell transitions of L-shell ions for elements in the Fe group (Chapter 8).

[4]Spherical crystal spectrometers have imaging properties (see Chapter 5) and can be used with extended sources, but have small energy coverage, small effective area, and are unsuitable for space-born X-ray observatories.

The first four experiments prove, that there are rays coming from the sun, which are less refrangible than any of those that affect the sight. They are invested with a high power of heating bodies, but with none of illuminating objects; and this explains the reason why they have hitherto escaped unnoticed.

Sir William Herschel (1800a) about infrared radiation

4 ECS – The EBIT Calorimeter Spectrometer

HISTORICALLY, calorimeters were used to measure the heat capacity of materials or the heat produced in chemical reactions or in physical changes. In 1800, when Sir William Herschel discovered infrared radiation ("calorific rays") by holding a thermometer just behind the red edge of the visible light diffracted by a prism and observed a temperature change (Herschel, 1800a,b), a thermal measurement was used for the first time to detect invisible radiation (Enss, 2005). After Franz Eugen Simon found in 1935 that low temperatures significantly increase the sensitivity of calorimeters for radiation (Simon, 1935), calorimeter-type detectors have commonly been used as bolometers for infrared radiation (Low, 1961; Moseley et al., 1984). In 1984, Moseley et al. proposed to adapt these thermal detectors for the X-ray regime, recognizing their potential to fill the gap between low-throughput high-resolution wavelength-dispersive detectors and high-throughput low-resolution solid state detectors. Within only a few years, these spectrometers overcame the resolving power of conventional ionization detectors by almost an order of magnitude (Enss, 2001). Cryogenic X-ray calorimeters have been a thriving field of research since then and have made further leaps in resolution (Porter et al., 2005; Porter, 2013; Bandler et al., 2016). This chapter describes their operating principle and the specific parameters of the ECS currently in use at the LLNL EBIT facility.

4.1 Operating Principle

Basically, an X-ray microcalorimeter consists of an absorber – used to absorb the incident photon and thermalize its energy –, a thermometer – used to measure the resulting temperature change –, and a heat bath – used to dump the absorbed energy and bring the detector back to its base temperature.

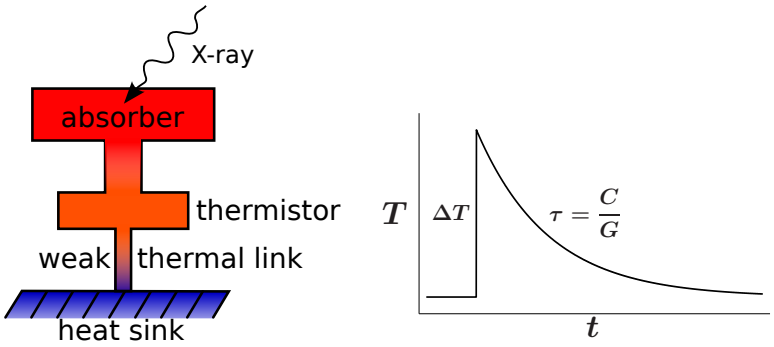

Figure 4.1: Sketch of the calorimeter operating principle.

When the X-ray is absorbed, it produces a photo-electron that is "hot", i.e., has high energy compared to the rest of the absorbing body due to the excess energy not needed in the ionization process. Collisions with other electrons in the absorber decrease the average energy of the involved electrons. Once the average energy becomes low enough (on the order of a few eV; Twerenbold, 1996), the electrons start to couple with the phonons and the absorber heats up. This process is called thermalization. In the case of the ECS, the corresponding temperature change is monitored by a thermometer sensitive to small changes at low temperatures. The microcalorimeter detector in the ECS uses doped Si semi-conductors[1] as resistive thermistors. The measured signal from the thermistor is proportional to the photon energy, E_γ, of the incident X-ray (Galeazzi et al., 2000). Through a weak thermal link, the absorber/thermistor assembly is connected to a heat sink where the excess heat from the absorbed X-ray is dumped after detection and the detector returns to its reference temperature.

Absorber

To ensure high resolution and high count rate, the absorber material needs to fulfill certain thermal requirements. The absorber must be sensitive to small amounts of absorbed heat and it must cool to its base temperature quickly. These requirements necessitate absorbers with low heat capacity, C. The heat capacity determines the amplitude of the temperature change in the absorber as a result of an absorbed photon, $\Delta T \sim E_\gamma / C$. The return to the reference temperature depends on the heat capacity of the absorber and the heat conductance, G, of the weak thermal link via

$$T(t) = E_\gamma / C \cdot \exp(-t/\tau_0) \tag{4.1}$$

where $\tau_0 = C/G$ is the time constant of the thermal decay (Fig. 4.1; Moseley et al., 1984; McCammon, 2005b). To achieve high resolution, large signal amplitudes are desirable, and thus small heat capacities. Small heat capacities also dictate fast thermal decay rates, and in turn the ability of the system to handle high photon count rates. In order for the observed amplitude ΔT of temperature change to be a good measure of the photon energy, the energy of the photon must be well thermalized before the heat in the absorber is dissipated into the heat sink, i.e., thermalization must be fast – on time scales of $t <$

[1] Other thermometer types are possible (McCammon, 2005b; Bandler et al., 2016).

τ_0 (Enss, 2001). Long decay times τ_0 lead to long dead times. The heat capacity at low (cryogenic) temperatures scales as T^3 (Debye, 1912, model), in case of crystalline insulators. For semimetals, which have a small amount of free carriers, $aT^3 + bT$ is a better model for the heat capacity. Calorimeters are therefore operated at very low temperatures, typically at $T < 0.1\,\mathrm{K}$. Different absorber materials have been tested (see, e.g., Galeazzi et al., 2000, and Smith et al., 2014b, for a discussion of advantages and disadvantages of different types of material) and the material chosen for the ECS is the semimetal HgTe, a narrow-gap semiconductor (Enss, 2001), for its fast thermalization properties and small heat capacity (Kelley et al., 1999).

The absorber mass also plays a role in the heat capacity. Therefore, the absorber is designed with a small volume (Galeazzi et al., 2000). The thickness of the absorber determines the stopping power for energetic photons and needs to be adapted for the energy range of interest (Section 4.4.2), in a compromise between detection efficiency and resolution. To maintain a large detector area for better counting statistics when observing spectra, multiple of these small calorimeters are assembled as pixels in a detector array.

Readout

For semi-conductor thermistors, the resistance change of the thermometer is measured by applying a bias voltage and monitoring the voltage drop across the thermistor at constant readout current (McCammon, 2005b). The voltage bias is accomplished with a load resistor whose resistance is so large (120 MΩ for the ECS) compared to the thermistor that it dominates the factors determining the readout current. Junction gate field effect transistors (JFETs) are used as pre-amplifiers to match the thermistor impedance to the impedance of the calorimeter analog processor (CAP) that amplifies the signal and prepares it for digitization (Thorn, 2008). A digital processor (see below) analyzes the signal for pulse height, arrival time, and additional information. JFETs have to be operated above $\sim 100\,\mathrm{K}$ to prevent charge carriers from "freezing out" (Kelley et al., 1999). For the ECS a JFET operating temperature of 130 K is chosen to minimize their noise contribution to the read-out signal. Beyond the JFETs, signal processing happens at room temperature. Each pixel in the ECS has its own individual readout chain. For more details on readout, see, e.g., McCammon (2005b), Irwin & Hilton (2005), and Porter et al. (2005).

Noise sources

There are a number of different noise sources that can influence the detector performance and degrade the detector resolution (Mather, 1982; Moseley et al., 1984; Stahle et al., 1999; McCammon, 2005b,a). A major noise source is thermodynamic fluctuation noise (phonon noise) caused by the random exchange of energy between the absorber and heat sink via the thermal link. This phonon noise is associated with the thermal impedance of the detector. The derivatives of the partition function of the system show that the spontaneous energy fluctuation of the detector ΔE relates to the temperature T and heat capacity C of the system as $\langle \Delta E^2 \rangle = k_\mathrm{B} T^2 C$, i.e., the phonon noise scales as $\sqrt{C} \sim \sqrt{T^3}$

and is independent of the thermal link heat conductivity G (Moseley et al., 1984). The phonon noise is therefore lower for detectors with smaller heat capacities and low operating temperatures. Another major noise term is the Johnson or Nyquist noise of the thermometer, i.e., thermodynamic fluctuations associated with the electrical resistance of the thermometer (Irwin & Hilton, 2005). This noise is approximately white. Electrical noise from JFETs and amplifiers also add to the thermal noise. Additional noise sources are fluctuations in the temperature of the heat bath, microphonics in the electrical leads, Johnson noise in the leads, shot noise (white noise) from stray photons, and poor coupling of the heat capacity of the absorber to the thermometer (Irwin & Hilton, 2005). These noise sources can be suppressed by proper detector design. Further excess noise can be caused by external noise sources such as pickup at harmonic frequencies of the 60 Hz power grid and other vibrations such as nearby turbo pumps. These noise sources appear as discrete noise tones in the frequency spectrum.

Pulse shape

As with all detectors, the event pulse has to be detected and filtered out from the background of noise sources. Compared to thermodynamic fluctuations, an X-ray photon event causes a larger increase in temperature and can easily be detected in the derivative of the signal. This distinct sharp rise, however, can be masked by the other noise sources such as the Johnson noise from electrothermal feedback, making signal identification harder. While a simple comparison of the pulse height over the baseline already yields better resolution than non-thermal solid-state detectors, with additional information it is possible to reach even higher resolution.

This additional information can be obtained by analyzing the pulse shape in frequency space rather than as a function of time: The power spectrum[2] of the exponential pulse of the photon event and the noise power spectrum of the thermodynamic fluctuations have the same shape (Fig. 4.2; McCammon, 2005b) – constant at low frequencies and a roll-off to $1/f$ at a frequency of $f_c = G/(2\pi C)$ – but different amplitudes. Therefore, the signal-to-noise ratio is the same in each frequency bin. With the noise being uncorrelated between different frequency bins as long as the noise properties do not change during the pulse – which is only true in the small signal limit –, each bin gives an independent estimate of the signal amplitude and the accuracy of the averaged amplitudes improves with the square root of used frequency bins.

Theoretically, using this method the pulse height could be determined to an arbitrarily high accuracy, simply by averaging over a large frequency bandwidth. However, the other sources of noise can change the $1/f$ fall-off of the noise spectrum and, therefore, limit the useful frequency range. For example, the finite rise time of the pulse and imperfect thermal coupling between absorber and thermometer introduce another roll-off at high frequency after which the noise spectrum falls faster with $1/f^2$. Frequency-independent or shot noise, caused by thermal radiation and visible light and by the read-out electronics and Johnson noise of the thermometer, lead to a flattened total noise spectrum once

[2] Transformation of the pulse shape as a function of time into the frequency domain.

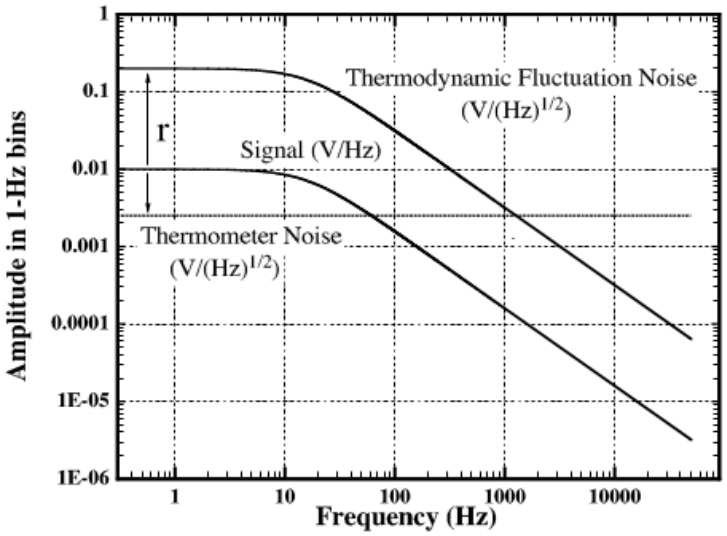

Figure 4.2: Power spectra of the noise and signal pulse in a microcalorimeter. The dimensions for the signal spectrum are different than for the noise spectra. If f_c is the roll-off point of the thermodynamical fluctuation noise (TFN), the upper limit of the useful bandwidth is rf_c, where r is the ratio of the low-frequency TFN and the Johnson noise (thermometer noise). — From McCammon (2005b, Fig. 3).

the thermodynamic fluctuation noise reaches the level of the shot noise (Fig. 4.2; McCammon, 2005b). To maximize the energy resolution, which is equivalent to maximizing the useful frequency range, the detector needs to be optimized to keep the shot noise low and to push any further roll-off frequencies beyond the frequency where the thermodynamic fluctuations reach the shot noise level. For details on how to accomplish this, see McCammon (2005b).

4.2 Optimal Filtering

Fourier transforming signals into the frequency domain is computationally expensive and not economical for real-time analysis of the pulse height for each event. To still take advantage of the improved amplitude determination of averaging the amplitude estimates over multiple samples, a technique called optimal filtering is employed. In this technique, which is described by Szymkowiak et al. (1993), templates for typical pulse shapes including noise contributions are constructed in the time domain, which then can be scaled to match the pulses of incoming events.

4.2.1 Templates

The method of template fitting (Szymkowiak et al., 1993) assumes that all pulses have the same shape $S(t)$, only differing by the amplitude A, corresponding to the pulse height, i.e., $A \cdot S(t)$. This assumption is true to a high degree, but small variations in shape as a function of photon energy can occur. To find the best estimate H for the pulse height, we use the average pulse shape as a model and find the best fit to the data, $D(t)$. Since the noise in the data is correlated between time bins, but not between frequency bins, the χ^2

minimization is done in the frequency domain, with

$$\chi^2 = \sum \frac{[D(f) - H \cdot S(f)]^2}{N^2(f)} \tag{4.2}$$

where, due to the Fourier transform, $\Delta = D(f) - H \cdot S(f)$ is now a complex quantity with magnitude $[\Delta]^2 = \Delta \cdot \Delta^*$. Setting $\mathrm{d}\chi^2/\mathrm{d}H = 0$ and transforming the result back into the time domain follows

$$H = k \cdot \sum \frac{[D(f) \cdot S^*(f)]}{N^2(f)} = k' \cdot \sum D(t) \cdot F(t) \tag{4.3}$$

where k and k' are normalization constants and $F(t) = \mathscr{F}^{-1}\left(S^*(f)/N^2(f)\right)$ is the optimal filtering template. The template, therefore, depends only on the Fourier transforms of the average pulse shape $S(t)$ and on the noise spectrum $N(f)$.

Templates are created for each detector pixel individually. To ensure sufficient time between pulses, measurements with small event rates are used. The average pulse shape $S(t)$ is calculated by averaging over multiple pulses generated by mono-energetic X-rays. In the absence of a mono-energetic X-ray source, narrow software cuts can be set in the risetime-pulseheight phase space and only events falling into that window are used to determine the pulse shape. Similarly, several noise spectra are recorded and averaged to obtain $N(f)$.

That the average pulse shape is constant over a large energy band is an incorrect assumption and a large source for non-linearities in the pulse height estimate (Boyce et al., 1999). The better the template matches the incoming pulses, the better the energy resolution of the instrument will be. Therefore templates should ideally be generated from X-ray events in the energy region of interest for the experiment, in case there is a small variation in shape depending on photon energy. Figure 4.3 shows example average pulse shapes for a low- and a high-energy pixel created from Fe Kα X-ray photons at a detector temperature of 60 mK. It can be seen nicely that the thicker high-energy pixels have a larger time constant $\tau_0 = C/G$ for the exponential decay. This is a result of their large heat capacity C.

As discussed before, a larger number of frequency bins entering the amplitude estimate increases its accuracy. One way to increase the number of bins (samples) and extend the frequency band width to larger frequencies, is to choose a high sampling frequency for the output signal of the detector. For the ECS this sampling frequency typically is $f_\mathrm{s} = 12.5\,\mathrm{kHz}$. For the low-energy pixels 2048 samples are typically used, just as for the XRS, its predecessor, while the sample length for the *Hitomi*-SXS has been reduced to 1024 (Eckart et al., 2016). For the longer decay time of the ECS high-energy pixels (Fig. 4.3) a sample length of 4096 can be more suitable, but when using them together with the low-energy pixels as, e.g., in the excitation cross section measurements (Chapter 8), we used 2048 samples for both ECS subarrays.

If the noise spectrum contains distinct peaks (noise tones), which are hard to avoid especially in a laboratory environment, at these frequencies, the signal-to-noise ratio is decreased and the template has a lower weight in these bins to account for the increased

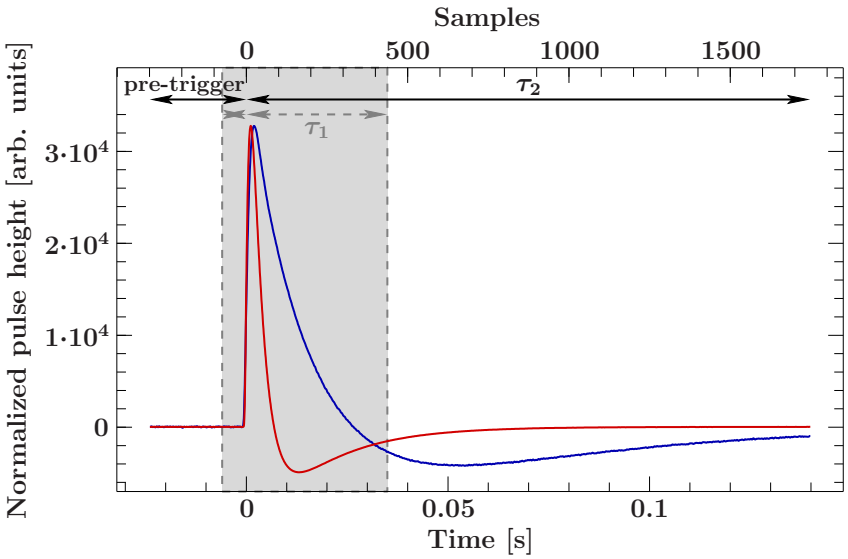

Figure 4.3: Average pulse shape of the thin low-energy pixels (red) and the thick high-energy pixels of the ECS, derived from He-like Fe Kα photons of $E_\gamma \approx 6.7\,\mathrm{keV}$. The shaded region indicates the length of the short template (see section 4.2.3).

noise. It is therefore important to keep the number of these peaks at a minimum and have a "clean" noise spectrum by shielding against environmental noise and vibrations. Otherwise, they may degrade the detector resolution.

Optimal filtering templates typically show a region with negative weights just before the pulse (Szymkowiak et al., 1993; Boyce et al., 1999). This region accounts for the baseline and effectively subtracts it from the region under the pulse. To collect this information, templates need to cover a small region before the pulse, the length of which is set by the number of pre-trigger samples (Fig. 4.3).

4.2.2 Pulse Detection

Since X-ray events in the detector cause a sharp rise in temperature, a pulse detection is triggered when the low-pass filtered derivative of the detector output signal crosses a pre-defined threshold (Boyce et al., 1999). Once an event has been detected, pulse height analysis using the optimal filtering template is applied to the event. Additionally, the shape of the pulse derivative is compared to a stored copy of the average derivative. This average derivative is scaled to the pulse height of the primary pulse and subtracted from the data. After this subtraction, the standard pulse detection algorithm searches for another event within the sample length that crosses the detection threshold for secondary pulses. If such a secondary pulse is detected, it is analyzed as well, with the appropriate measures for pulse height analysis (see Section 4.2.3).

Since the sampling bins have finite width in time, the reconstructed arrival time and amplitude of a pulse can depend on the phase of the pulse relative to the samples, i.e., how well the signal pulse lines up with the template. To account for this possible shift,

the best fit pulse height estimate H is determined for several template positions around the sample that triggered the pulse detection. These shifted estimates are called lags. The center of a quadratic fit to these lags is then taken as the final pulse height and arrival time value. This way, event arrival times can be determined to a fraction of the sample width (about 1/16 of the sample width; Szymkowiak et al., 1993).

Using templates that are not matched well to the signal of incident photons can cause problems. Reasons for mismatched templates include changes in the noise environment and changes in the average pulse shape. Changes in the noise environment negatively affect the accuracy of pulse height reconstruction through optimal filtering and can lead to reduced resolution and small gain shifts. Mismatched average pulse shapes are more detrimental. These can especially occur in the analysis of large pulses, where the pulse shape deviates from the pre-determined average pulse shape as a result of detector non-linearities. Mismatched average pulse shapes can create phantom residual deviations in the pulse shape derivative used for pulse detection that mimic the signal of a very low energy photon in the tail of the higher energy incident photon. Especially for high-energy photons (for example in the Fe K region above 7 keV), these residuals are large enough to cross the threshold and thus trigger a false detection. Since the relative timing of successive pulses determines the pulse height analysis method (see next section), these false double-triggers can unduly prevent the use of the optimal filtering template, thus creating unnecessary low resolution events and artificially degrading the resolution.

Problems with double triggers in large pulses can be avoided in multiple ways. Increasing the detector temperature increases the heat capacity and thus decreases the pulse height such that even high photon energies move into the small signal limit. A disadvantage of this method is a decreased energy resolution that goes along with the higher temperature, but the decrease is relatively small. Alternatively, the threshold for secondary pulse detection can be increased above the size of the residuals caused by mismatched average pulse shapes. However, for significant mismatches between the average pulse shape and the signal pulse the perceived pulse heights of the phantom secondary pulses can be fairly large, such that this method can miss the detection of real secondary low-energy photons. Ideally, the raw data should be analyzed using energy-dependent templates (Irwin & Hilton, 2005). Fixsen et al. (2002) and Fixsen et al. (2004) discuss possible implementations for pulse height dependent templates for transition-edge sensor (TES) devices and Peille et al. (2016) compare the performance of these.

4.2.3 Event Grades

Pulse height analysis via optimal filtering clearly works best if there is only a single pulse within the time window of the template. However, by chance or because of high count rates it is possible for two photons to hit the same pixel in shorter succession than a template length. Depending on how close together these pulses are, there are two ways to handle their analysis. To some extent the template length is arbitrary; in principle, as the pulse is over long before the end of the template for the used ECS template length (Fig. 4.3), it would be sufficient to use templates with fewer sampling bins, albeit with a possible decrease in resolution. These so-called short templates are typically a quarter

Table 4.1: Definition of event grades (Boyce et al., 1999; Seta et al., 2012)

	$\Delta t_\mathrm{p} \leq \tau_1$	$\tau_1 < \Delta t_\mathrm{p} \leq \tau_2$	$\tau_2 \leq \Delta t_\mathrm{p}$
$\Delta t_\mathrm{n} \leq \tau_1$	Ls	Ls	Lp
$\tau_1 < \Delta t_\mathrm{n} \leq \tau_2$	Ls	Ms	Mp
$\tau_2 \leq \Delta t_\mathrm{n}$	Ls	Ms	Hp

Notes: H: High-res; M: mid-res; L: low-res; p: primary; s: secondary; $\Delta t_{\mathrm{p/n}}$: time difference to the preceding or next pulse; $\tau_1 = 34.96\,\mathrm{ms}$: length of the short template (512 samples minus 75 pre-trigger samples) at a sampling frequency of $f_\mathrm{s} = 12.5\,\mathrm{kHz}$; $\tau_2 = 139.84\,\mathrm{ms}$: length of the full template (2048 samples total length minus 300 pre-trigger samples); see also Fig. 4.3 for definitions of τ_1 and τ_2, and Fig. 4.4 for a visualization of event grade timing.

of the length of a full template[3] and computed at the same time and from the same data as full template generation. If the pulses are too close together even for the use of the short template, simply the maximum of the pulse over the baseline (estimated from a few samples before the pulse) is taken as the pulse height estimate, although, as mentioned previously, with much lower resolution.

As the method of pulse height analysis greatly affects the spectral resolution of the measured spectrum, each event is assigned an event grade indicating the applied analysis method and, therefore, the quality of the data. An overview of event grade definitions is given by Boyce et al. (1999) and Seta et al. (2012). There are two types of grades. The first type specifies the used pulse height determination: *high-res* events are reconstructed with the full template, *mid-res* events with the short template, and *low-res* events without any templates. The second grade type indicates whether the event was a *primary* event, where the preceding pulse occurred at least a full template length (minus the pre-trigger length) prior, or a *secondary* event that rides on the tail of the previous pulse, i.e., the baseline is shifted compared to primary events. Secondary events are, at best, analyzed with the short (mid-res) templates, never as high-res. Table 4.1 translates all possible combinations of the relative time between the current pulse and the previous and following pulses, respectively, to their corresponding event grades. Some of these are also visualized in Fig. 4.4.

In an ideal noise environment (no noise tones), the high-res primary and mid-res primary events should have very similar resolution (Boyce et al., 1999). As long as the pulse is over before the end of the used template (short or full template), the additional samples do not add much accuracy to the pulse height estimate. Since the pre-trigger period is much shorter for the mid-res events than for the high-res events, the baseline determination has a larger uncertainty for mid-res events, consequently reducing their energy resolution slightly compared to high-res events. In the laboratory, noise tones (peaks at single frequencies) in the noise spectrum can additionally degrade the mid-res resolution, as these noise tones are more easily rejected by the long templates (Boyce et al., 1999).

[3] Other choices of short template lengths are, of course, possible, including, in principle, the use of multiple short templates.

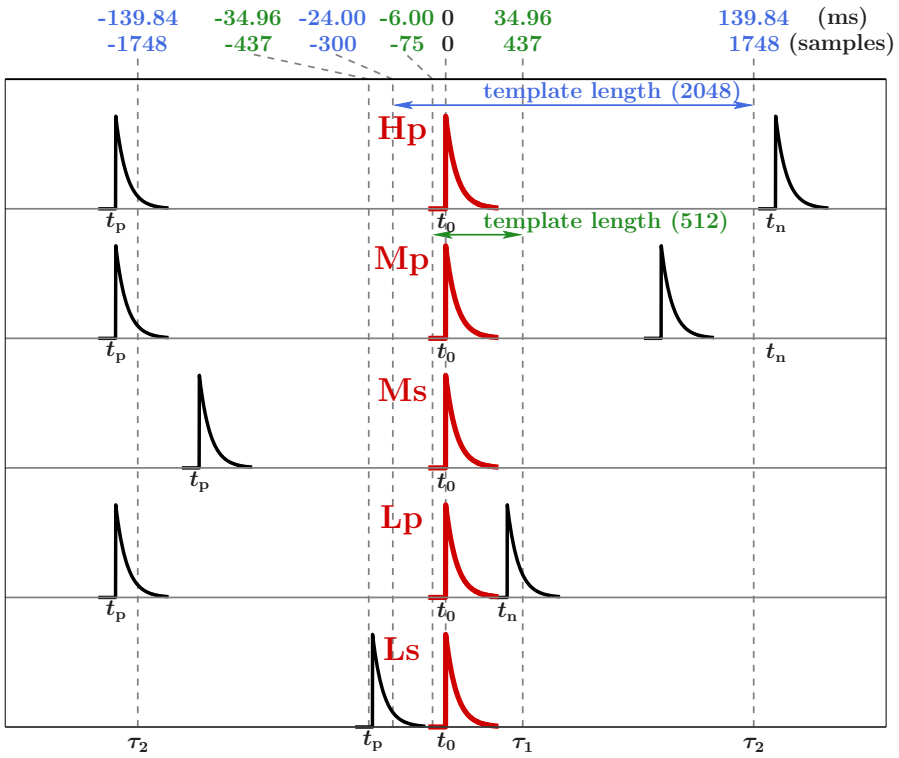

Figure 4.4: Graphical explanation of event grade definitions (after Seta et al., 2012).

Secondary mid-res events can suffer further degradation in resolution compared to primary mid-res events, because the responsitivity of the detector is suppressed as these events ride on the tails of previous pulses, where the detector temperature has not yet been restored to the bath temperature. Figure 4.5 shows the spectral resolution as a function of event grade for the low-energy pixels.

Small differences in the pulse height reconstruction of the different methods can appear as slight shifts in gain (Fig. 4.5) between the spectra of the different event grades. These apparent shifts can easily be accounted for by calibrating each event grade independently. Between primary high-res and mid-res events the effect is usually negligible. Secondary events can have a slightly smaller amplitude, since the absorber still has a somewhat higher temperature from the previous pulse than the normal reference temperature, leading to a larger heat capacity (Boyce et al., 1999). While a normalization factor is applied to the low-res pulse height to bring them to the same scale as the template reconstructed ones, low-res events, especially secondary ones, tend to require individual calibration. The branching ratio of event grades as a function of event rate can be predicted from Poisson statistics (see Appendix B). For the ECS low-energy pixels with a full template length of 2048 samples, a count rate of about one count per second per pixel is often a good compromise to maintain a large fraction of high- and mid-res events, but even lower count rates may be necessary to allow one to neglect low-res events in absolute flux measurements.

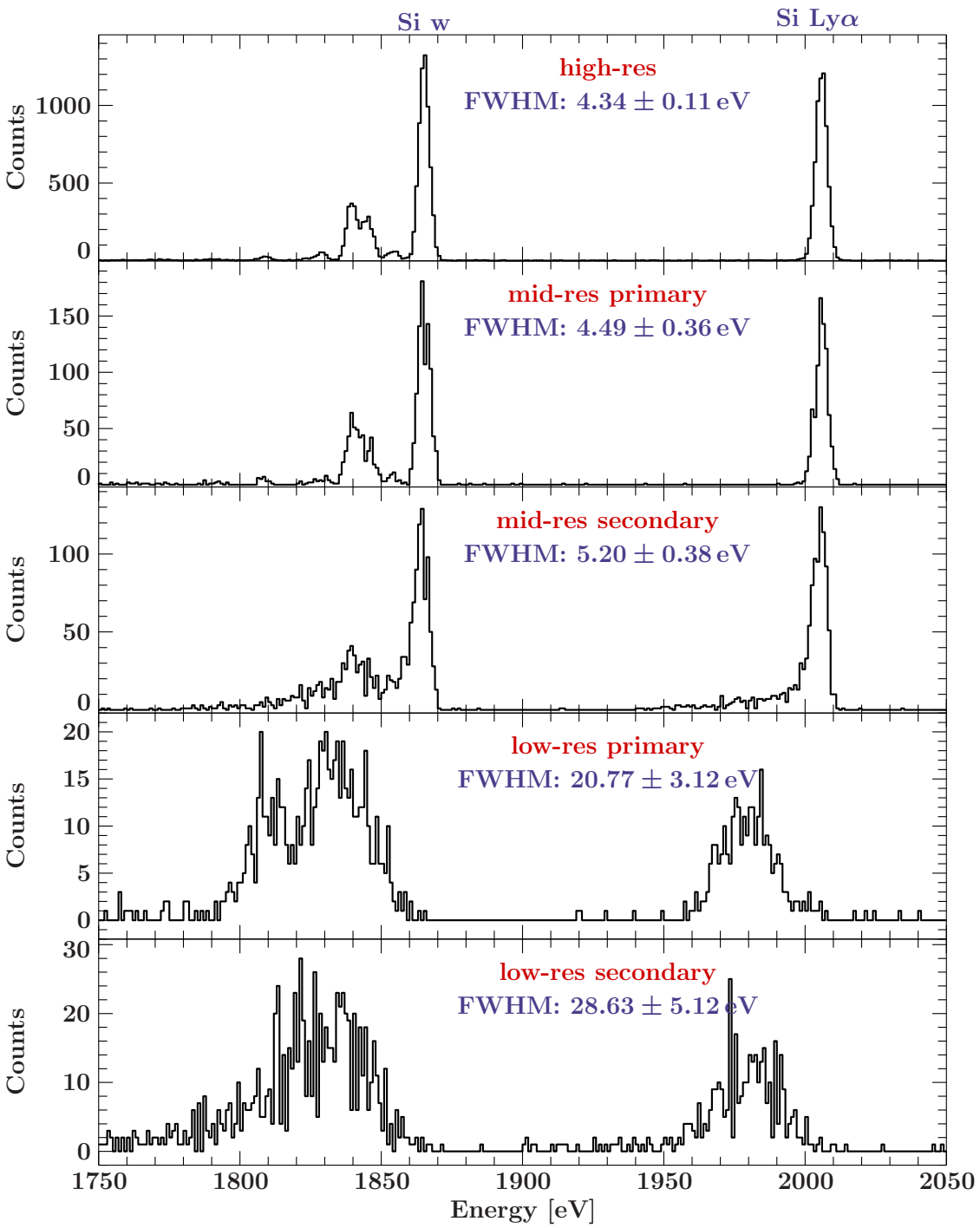

Figure 4.5: Spectral resolution of the ECS at 51 mK operating temperature for a single pixel as a function of event grade demonstrated on K-shell transitions in Si. The shown spectra for each of the event grades use the same calibration (determined from high-res events). High-res events have the highest resolution, mid-res events are comparable to high-res, and low-res events have significantly lower resolution. Note, however, that the true resolution of the low res events is not well represented here as the the high-res gain scale was used. Additionally, the energy scale of low-res events appears shifted compared to the high-res events. This shift can be removed if the low-res events are calibrated independently.

4.3 ECS

The development of X-ray calorimeters has primarily been driven by astrophysics needs. Space observations started with the X-ray Quantum Calorimeter (XQC) flown on a sounding rocket beginning in 1995 (Porter et al., 2005). There have been three attempts to launch a microcalorimeter into orbit as part of an X-ray observatory, which unfortunately have failed so far: *Astro-E* never reached orbit due to a rocket failure shortly after launch in the year 2000; in 2005, the re-flight mission *Astro-E2* (*Suzaku*) lost all coolant during the first few weeks in orbit such that the calorimeter never made an observation of a celestial source[4]; and in 2016, *Astro-H* (*Hitomi*) took a few stunning spectra (Hitomi Collaboration et al., 2016), before errors in spacecraft control caused the satellite to spin up rapidly and break apart after only a few weeks in orbit. Some proposed or planned future X-ray satellite missions incorporate the design of a microcalorimeter on board, such as the X-ray Integral Field Unit (X-IFU) onboard the *Athena* X-ray observatory (Barret et al., 2016). The recent *Hitomi* spectra reinforce this path.

Calorimeters have also been established as "work horses" for ground-based laboratory astrophysics experiments. At the LLNL EBIT facility, there have been three generations of micro-calorimeters in use for laboratory astrophysics, with a fourth generation currently in development (Porter et al., 2004, 2005, 2008a,b,c, 2009a,b). These calorimeters were designed, built, and serviced by the calorimeter group at NASA's Goddard Space Flight Center[5]. The first generation, the XRS/EBIT v1, arrived in 2000 and was essentially assembled from the *Astro-E* engineering detector model and spare parts for the cryogenic housing from laboratory testing of the detector. In 2003, this instrument was upgraded to XRS/EBIT v2 with improvements developed for the *Astro-E2* mission. These improvements almost doubled the instrument resolution from ~ 11 eV to ~ 6 eV at 6 keV (Porter et al., 2009b). Unlike the XRS/EBIT, the EBIT Calorimeter Spectrometer (ECS) delivered in 2007 was specifically designed as a permanent installation at the EBIT laboratory (Porter et al., 2008b,c). The ECS array was produced in the same fabrication run as the XRS/*Suzaku* (Porter et al., 2005). Small changes in the electronics design brought a slight improvement in resolution over the XRS/EBIT v2, while large changes in the cryogenic housing design made big improvements in its userfriendliness by making operation and cooling low maintenance (Porter et al., 2008b). The next generation calorimeter, dubbed Transition Edge Microcalorimeter Spectrometer (TEMS), will use transition edge sensors instead of the semi-conductor thermistor design and make a large leap in pixel number, spectral resolution, and count rates manageable before event grade degradation (Porter et al., 2009b). For all calorimeters in use at EBIT, the digitized raw data are forwarded from a server to the Software Calorimeter Digital Processor (SCDP) handling the real-time data analysis of triggering and pulse height reconstruction through optimal filtering as described above (Boyce et al., 1999; Adams et al., 2009). The processed events are then recorded with a custom extension of IgorPro, where the data acquisition can be

[4] At least the spacecraft survived and great science has been done with the remaining instruments, though no high-resolution spectroscopy.

[5] A single-pixel calorimeter by Le Gros et al. (1996) has been tested at the LLNL EBITs, but not used for further measurements (Beiersdorfer, 2005).

observed and analyzed live during an experiment.

The ECS array nominally includes 36 pixels, but only 32 readout channels are available. Each of the 32 wired pixels is basically a standalone detector and can be powered on and off individually. The ECS array is split into two sub-arrays: 18 low-energy pixels using 8 μm thick HgTe absorbers with an area of $625 \times 625\,\mu\text{m}^2$, spanning the energy range of 0.1–10 keV, and 14 high-energy pixels using $\sim 100\,\mu$m thick HgTe absorbers with an area of $625 \times 500\,\mu\text{m}^2$ spanning an energy range of 0.5 to over 100 keV. The actual thickness of the high-energy pixels has been estimated to $114 \pm 9\,\mu$m by weighing them and dividing the measured weight by their pixel area and number of pixels, assuming a density of $\rho_{\text{HgTe}} = 8.17\,\text{g}\,\text{cm}^{-1}$ (Thorn, 2008). Some pixels exhibit degraded resolution due to excess noise accompanied by an extra heat load that shortens the cycle duration at 51 mK. Therefore, currently only 14 low-energy pixels and 10 high-energy pixels are in use.

The instrumental response has been verified to be almost purely Gaussian with a small low-energy tail for both, the XRS (Porter et al., 2004; Cottam et al., 2005) and the ECS (Porter et al., 2009a). The low-energy tail of the XRS contains 2–4% of the total events (Cottam et al., 2005). Other small deviations in the wings could be due to nonstationary environmental noise in the building (Porter et al., 2004) and a weak low-energy continuum is attributed to photon and photoelectron escape in the absorber (Cottam et al., 2005; Porter et al., 2004, 1997). For *Hitomi*-SXS, while the core of this line spread function is found to be Gaussian at all energies, at energies above a few keV the shape is Gaussian to at least three orders of magnitude (Eckart et al., 2016).

With 4.5–5.0 eV resolution at 6 keV photon energy and 51 mK operating temperature, the resolution of the ECS low-energy pixels is comparable to the Soft X-ray spectrometer (SXS) system (Mitsuda et al., 2010) aboard the *Astro-H/Hitomi* X-ray observatory (Takahashi et al., 2010). The ECS high-energy pixels have a 34 eV FWHM resolution at 60 keV as derived from the ^{241}Am nuclear line (Porter et al., 2008c, 2009a). The ECS has a rms temperature stability of better than 200 nK at 50 mK (Porter et al., 2008b, 2009a). Typically, the ECS is operated at a heat sink temperature of 51 mK, but for the Fe K cross section measurements (Chapter 8) we increased the temperature to 60 mK to ensure the pulse heights stay in the small signal limit and to avoid the double-trigger problem. Increasing the operating temperature to 60 mK can significantly increase the FWHM, since the limiting phonon noise scales with $\sqrt{C}$, while the heat capacity in turn scales as $C \sim T^3$ with the temperature (Porter et al., 2004; Moseley et al., 1984). See Section 4.5 for a discussion of changes of gain and resolution due to the increased temperature.

To reach and maintain the ECS operating temperature of < 0.1 K, the detector array is housed in a cryostat with a 3-stage refrigeration system (Porter et al., 2008a,c). The detector assembly is cooled down to 4.2 K base temperature by an unpumped liquid helium reservoir that is shielded from room temperature with a liquid nitrogen dewar. A commercial closed cycle He^3/He^4 sorption cooler from Chase Cryogenics is used to cool the detector assembly and internal housing to 350 mK. An adiabatic demagnetization refrigerator (ADR; consisting of a paramagnetic salt pill and a superconducting magnet) is then used to cool the detector further to the desired operating temperature and keep the heat

sink stable at this temperature. Once the cooling power of the He^3 stage or of the ADR runs out, the detector warms back up to its 4.2 K base temperature and the refrigeration package has to be recycled to recharge the sorption cooler and the ADR. The recharge cycle is completely software controlled. The ECS can maintain its operating temperature for up to ~ 70 h, before a ~ 3 h long recharge cycle is necessary.

While the XRS/EBIT has added absolute excitation cross section of Fe L transitions and emission from charge exchange to the laboratory measurement capabilities at EBIT (Porter et al., 2005), the ECS adds transition energy measurements of high-Z elements (Thorn, 2008) and absolute cross sections of K-shell transitions in ions of Fe-group elements.

4.4 Effective Area

As mentioned before, spectrometers and detectors typically do not have 100 % efficiency in observing every single photon in their line of sight. Additionally, the observed flux depends on the solid angle covered by the spectrometer. The effective area of an instrument correlates this measured X-ray flux to the actual source flux as a function of photon energy. To measure absolute emission cross sections or line ratios or to compare the spectra measured with different instruments without introducing systematic errors due to detector effects, it is, therefore, important to know the effective area of the used spectrometers.

Parameters determining the effective area include transmission by optical blocking filters, the quantum efficiency of the absorbing medium, as well as the detector size. The source distance determines the solid angle. For space telescopes, properties of the telescope mirrors like the reflectivity are important factors to the effective area as well.

4.4.1 Optical Blocking Filters

Thermal radiation (infrared light) and visible or UV light can introduce high levels of shot noise to the detector and consequently degrade the energy resolution of the measured spectra, as discussed in Section 4.2.1. Additionally, the colder thermal stages of the cryostat have to be shielded from the thermal load of the "hotter" thermal stages up to room temperature, while still allowing the source signal, e.g., from EBIT, to reach the detector array. Since the ECS is a spectrometer for X-rays at much higher photon energies than the visible spectrum, this type of background can easily be avoided by employing optical blocking filters, i.e., thin foils transparent for X-rays but not optical light nor thermal radiation. There are four such aluminized polyimide films installed in front of the detector array as ports in the various layers of thermal shielding of the detector housing. These filters total 1470 Å of aluminum and 2386 Å of polyimide. Additionally, there is a thin 525 Å polyimide window installed between the ECS and EBIT to keep the lower ECS vacuum separated from the higher EBIT vacuum in order to avoid adding neutral background gas to the trap.

To maintain high event grades for high-quality measurements, the ECS cannot be oper-

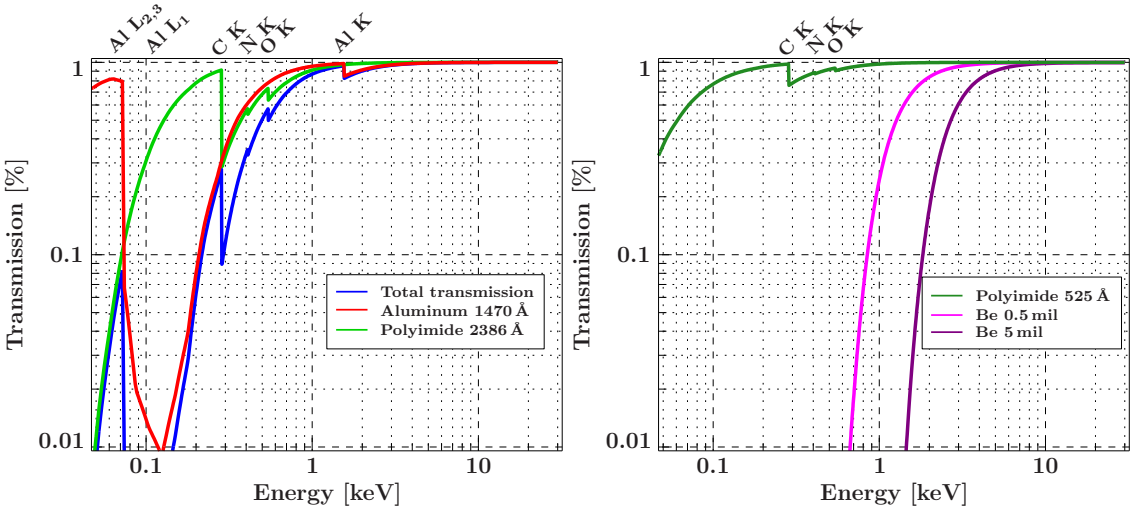

Figure 4.6: Transmission of optical blocking filters internal to the ECS (*left*) and optional additional windows in the line of sight (*right*) as a function of photon energy. Values are taken from Henke et al. (1993). The absorption edges of the material are labeled with their origin, e.g., Al K for photo-ionization of a K-shell electron in Al (Al K-edge).

ated at high count rates (Section 4.2.3). The L-shell transitions of low- to mid-Z ions have transition energies below 1–2 keV and have higher emission cross sections than K-shell transitions of the same ion, i.e., their contribution to the observed flux can dominate the ECS count rate even in cases where K-shell transitions are in the focus of interest. If other spectrometers, especially those with low throughput, are used simultaneously to the ECS, a high source flux may even be preferential. So instead of limiting the brightness of EBIT to accommodate the requirements of the ECS, it can be desirable to reduce the observed flux by other means. Therefore, additional 0.5 mil and 5 mil Be windows[6] can be inserted into the line of sight to decrease the count rate due to soft X-rays.

Figure 4.6 shows the transmission of the described filters as a function of photon energy. The transmission values are obtained from the Henke et al. (1993) tables[7]. Since these are based on photoabsorption, overall their accuracy is considered to be good to 3% (Saloman et al., 1988), but for filter transmission near unity the uncertainty can be considered much smaller. The sharp dips in the transmission are due to neutral absorption edges of the filter material. These absorption edges occur at photon energies that match the ionization potential of an inner-shell electron of the filter material. Photons with energies above and close to this energy have an increased probability of getting absorbed by photo-ionizing the corresponding inner-shell electron. While the absorption edges typically exhibit a complex fine structure, the Henke data averages over these features.

[6] The 5 mil Be window doubles as a gate valve for the ECS.
[7] `http://henke.lbl.gov/optical_constants/filter2.html`

4.4.2 Quantum Efficiency

The quantum efficiency of the absorber describes the fraction of photons of an incident photon beam that are absorbed by the material. The transmission of photons depends on the thickness and density of the material and on the interaction cross section of the photons with the atoms of the absorber, and follows the exponential attenuation law. The quantum efficiency Q can therefore be written as

$$Q = 1 - \frac{I}{I_0} = 1 - \exp\left(-\frac{\mu}{\rho} \cdot \rho d\right) \tag{4.4}$$

where I is the transmitted photon flux, I_0 the incident photon flux, μ the attenuation coefficient, and ρd the mass thickness, i.e., the mass per unit area of a material of density ρ and thickness d. The attenuation coefficient μ is often calculated or measured normalized to the density of the absorber and dubbed mass attenuation coefficient (MAC) μ/ρ in units of $\mathrm{cm^2\,g^{-1}}$ to reflect its nature of photon interaction cross section per unit mass[8], which, unlike the absorption per unit volume, is characteristic for the absorbing medium (Compton & Allison, 1935). For example, excluding solid state modifications of the cross section, 1 g of mercury absorbs the same amount of X-rays whether it is solid, liquid, or gaseous (Compton & Allison, 1935).

The photon interaction cross sections contributing to the mass attenuation include the atomic photo-effect, the coherent (Rayleigh) and incoherent (Compton) scattering, and the pair and triplet production of electrons and positrons in the fields of the atomic nucleus and electrons (Hubbell & Seltzer, 2004). Due to their complex nature, photonuclear absorption and other types of nuclear scattering tend to be neglected in the calculation of the MAC, although they can contribute up to 10 % to the total cross section, even in the soft X-rays (Hubbell & Seltzer, 2004).

Sources for Mass Absorption Coefficients

Since MAC is a measure for the loss of photons from the incident photon beam, the possibility of fluorescence photons escaping the absorber is also not accounted for in MAC. The mass energy-absorption coefficient (MEAC) μ_{en}/ρ measuring the incident energy absorbed by the material, on the other hand, includes energy lost to escaping fluorescence photons (Allison, 1961). However, for calculations of MEAC only the cross section to produce a fluorescent photon is taken into account. Thus, it is implicitly assumed that all fluorescence photons are able to leave the absorber, which is unlikely especially for large absorption coefficients or thick detectors. For our thermal detector, however, it is ultimately important how much energy is deposited in the detector by each photon. Consequently, using MAC overestimates the quantum efficiency, while MEAC underestimates it. For accurate representations of the quantum efficiency, secondary effects like reabsorbed fluorescence photons have to be taken into account, e.g., by employing Monte Carlo photon transfer codes that follow each photon to its ultimate fate.

[8] Cross sections are usually given per particle.

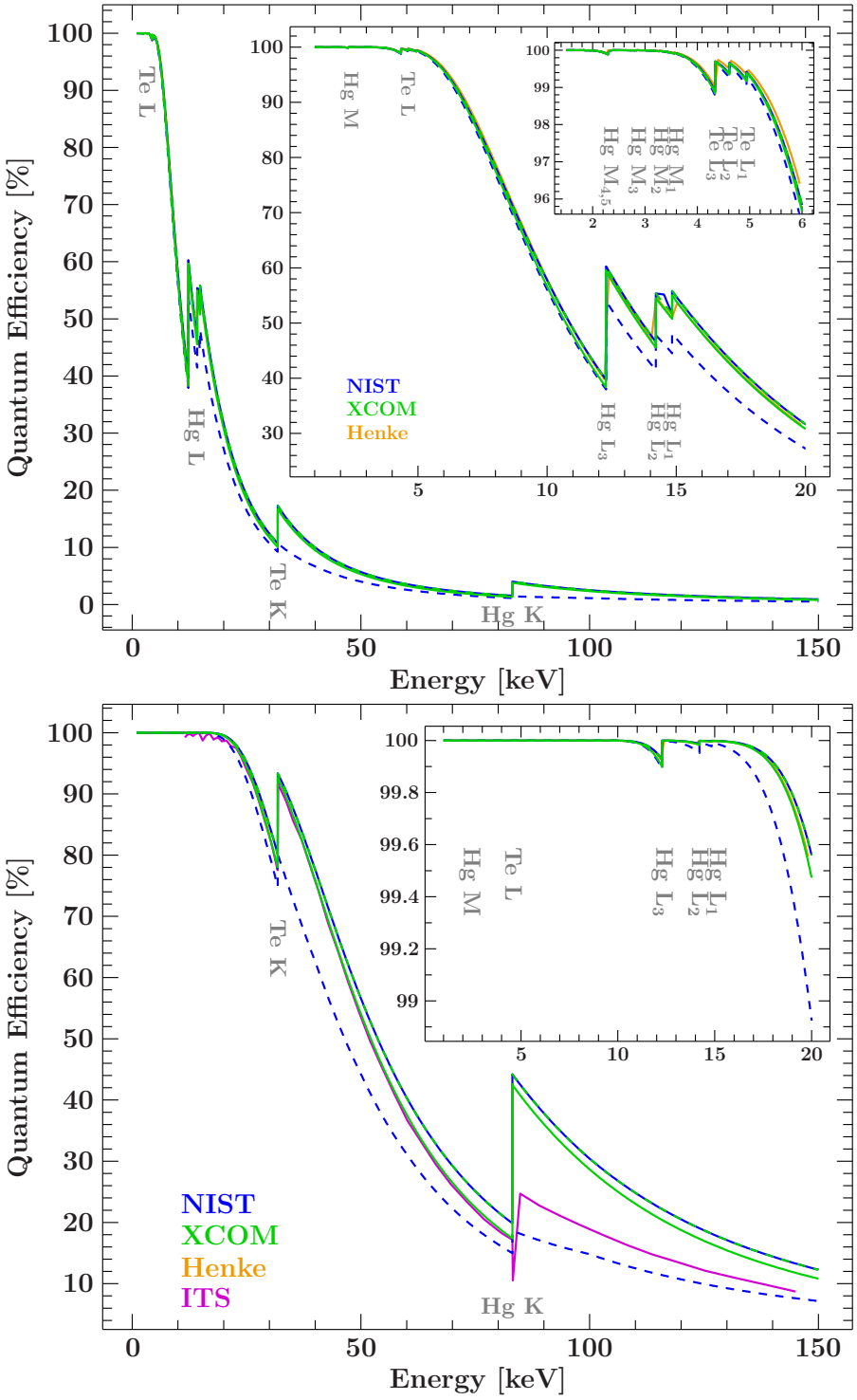

Figure 4.7: Quantum efficiency for the low-energy pixels (*top*) and the thicker high-energy pixels (*bottom*) from various sources. Absorption edges are marked. In contrast to transmission (Fig. 4.6), in absorption the edges appear as peaks rather than dips.

The MAC values for mixtures and compounds follow a simple additivity law

$$\frac{\mu}{\rho} = \sum_i w_i \left(\frac{\mu}{\rho}\right)_i \tag{4.5}$$

where $w_i = A_i / \sum_j A_j$ are the fractional weights of the mixture's constituents (Hubbell & Seltzer, 2004). Since MEAC includes secondary emission produced by charged particles traveling through the absorber, which can re-introduce dependencies on the phase of the medium, the additivity rule does not apply to MEAC. However, these effects can be small especially at our low photon energies far below 20 MeV such that the additivity rule can be used with small errors in the absence of more accurate data for compounds (Hubbell & Seltzer, 2004).

Figure 4.7 shows a comparison of the quantum efficiency derived from various sources for the low-energy pixels assuming an 8 μm thick slab of HgTe as well as for the high-energy pixels with a thickness of 114 μm: MAC and MEAC derived with the sum rule from the NIST table of X-ray MAC and MEAC[9] (Hubbell & Seltzer, 2004); the total attenuation with and without coherent scattering (taken as MAC and MEAC, respectively) listed for the compound by XCOM[10]; MAC derived from the attenuation length, i.e., the depth along the surface normal where the intensity drops to $1/e$, obtained from Henke et al. (1993), which only reaches up to photon energies of 30 keV; and the rescaled results from a Monte Carlo simulation for a thickness of 100 μm using the ITS code (Halbleib et al., 1992) taken from Thorn (2008).

The difference between MAC and MEAC can clearly be seen, especially at larger photon energies and close to absorption edges. For the thin low-energy pixels, the quantum efficiencies derived from the different sources agree to well within 1 % with each other in the region below 10 keV, which is important for the cross section measurement of the Fe K-shell transitions described later. For the thick high-energy pixels there is good agreement for most traces below about 20 keV, i.e., where we aim to measure the flux of the radiative recombination features, and the quantum efficiency in this region is essentially unity. While the quantum efficiency from the Monte Carlo simulation is expected to be most accurate, the calculation only starts at 10 keV, clearly suffers from numerical artifacts up to 20 keV, and generally does not scale well down to the much thinner low-energy pixels. For our measurements we therefore use the quantum efficiency derived from XCOM without coherent scattering as a reference, which traces the accurate ITS value closely up to the Hg K edge at 83.1 keV.

Rapid changes in quantum efficiency due to absorption edges can interfere with the line shape and flux measurements of X-rays with photon energies close to the edge energy. While there are edges in the region of our radiative recombination measurement between 12 and 15 keV, for the high-energy pixels they cause a flux change of less than 0.2 % and are therefore beyond our detection limit. In the thinner low-energy pixels these edges are more significant (Fig. 4.7) and have to be treated carefully during the data analysis.

Since there is some uncertainty in the actual thickness of the high-energy pixels, Figure 4.8 explores the effect of this thickness variation to the assumed quantum efficiency

[9] `http://www.nist.gov/pml/data/xraycoef/index.cfm`
[10] `http://physics.nist.gov/PhysRefData/Xcom/html/xcom1.html`

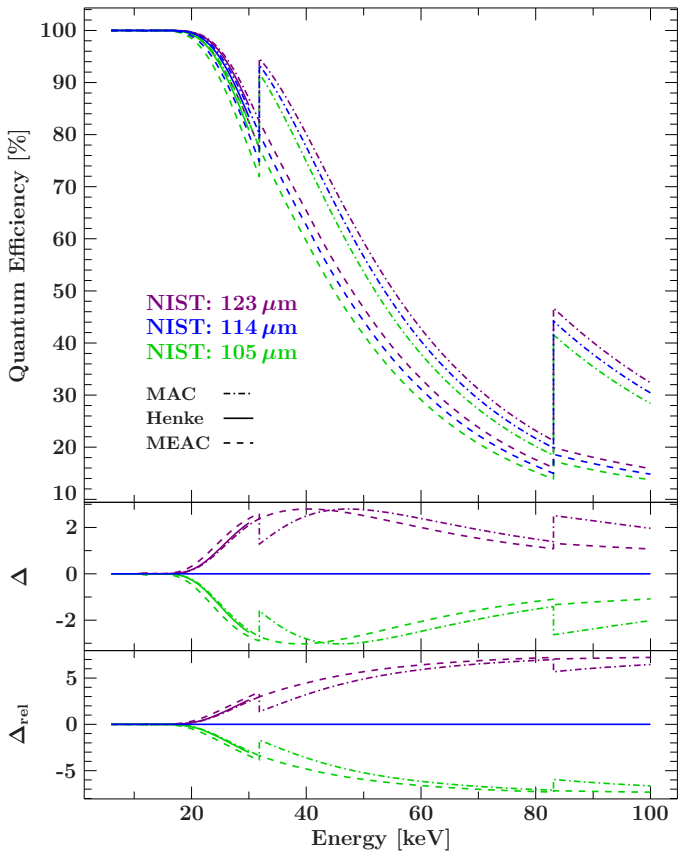

Figure 4.8: Uncertainty in the quantum efficiency of the high-energy pixels due to the uncertainty in the absorber thickness. *Top:* Quantum efficiencies for thicknesses of 114±9 μm; *Middle:* absolute difference between quantum efficiency of different thickness within the same model; *Bottom:* difference relative to the quantum efficiency at 114 μm.

on the example of the NIST values, which encompass the wide spread. Below 20 keV the exact absorber thickness has no significant influence on the quantum efficiency. At higher photon energies, the difference in quantum efficiency quickly grows to up to ±3 % or up to 7 % relative uncertainty.

The coefficients have a near power law dependence on photon energy. In the literature they are tabulated on a logarithmic energy grid with additional data points just below and above the absorption edges. Values for the quantum efficiency between the tabulated values are obtained by linear interpolation of $\log(\mu/\rho)$ versus $\log E_\gamma$.

Thicker absorbers are more likely to stop photons (Eq. 4.4), especially for larger photon energies (Fig. 4.7). However, due to the higher mass of the thick absorbers, their heat capacity is larger. Therefore, the overall temperature increase $\Delta T \sim E_\gamma/C$ compared to the control temperature T_0 due to an incident photon with energy E_γ and the corresponding pulse height is smaller for the thick absorber of the high-energy pixels than for the thin absorber of the low-energy pixels (Fig. 4.9). While the thick absorbers have a higher quantum efficiency for high-energy photons, the dynamic range of the digitizer also covers a larger energy range due to the smaller pulse height. High-energy photons would saturate the digitizer of the low energy pixels, where the pulse height would be much larger, and the peak of the pulse would appear clipped, prohibiting good pulse height estimates. With the larger heat capacity, also the time constant $\tau = C/G$ of the temperature decay (Fig. 4.1) after the thermalization of the event increases and the absorber takes more

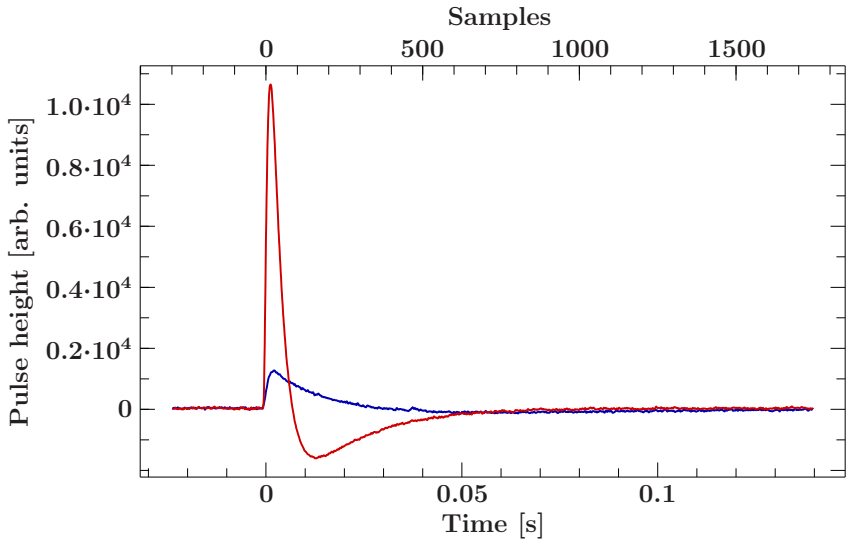

Figure 4.9: Comparison of the pulse heights of a ∼ 7 keV photon absorbed by the thin low-energy pixels (red) or the thick high-energy pixels (blue).

time to return to the control temperature. The optimal template length and the optimal time distance between two consecutive events are therefore longer for the high-energy pixels. As a compromise, for the excitation cross section measurements we choose to use a template length of 2048 samples for both pixel types. For the measurements presented in this work, only photon energies below about 20 keV are relevant, which only cover a portion of the lower end of the dynamic scale of the high-energy pixels. As Fig. 4.9 shows for the example of a 7 keV photon event, these lower energy pulses return to equilibrium faster than indicated by the full-scale average pulse (Fig. 4.3), making the effect of the shorter 2048 full template negligible.

4.4.3 Solid Angle

The low- and high-energy pixel sub-arrays of the ECS in some ways can be viewed as two different detectors and in terms of quantum efficiency certainly have to be handled as such. However, the ECS still has the advantage that both sets of pixels are parts of the same detector array in the same detector assembly and consequently have the same distance to EBIT. The difference in solid angle covered by each of the sub-arrays, therefore, reduces to the difference in detector surface – or pixel number times pixel area. Assuming that the whole array is illuminated evenly by the radiation from EBIT, i.e., there is no vignetting, the geometric correction factor for the flux ratio of direct excitation (DE) and radiative recombination (RR) photons due to solid angle is

$$\frac{A_{\mathrm{RR}}}{A_{\mathrm{DE}}} = \frac{A_{\mathrm{high-energy}}}{A_{\mathrm{low-energy}}} = \frac{10 \cdot 625 \times 500\,\mu\mathrm{m}^2}{14 \cdot 625 \times 625\,\mu\mathrm{m}^2} = 0.57. \tag{4.6}$$

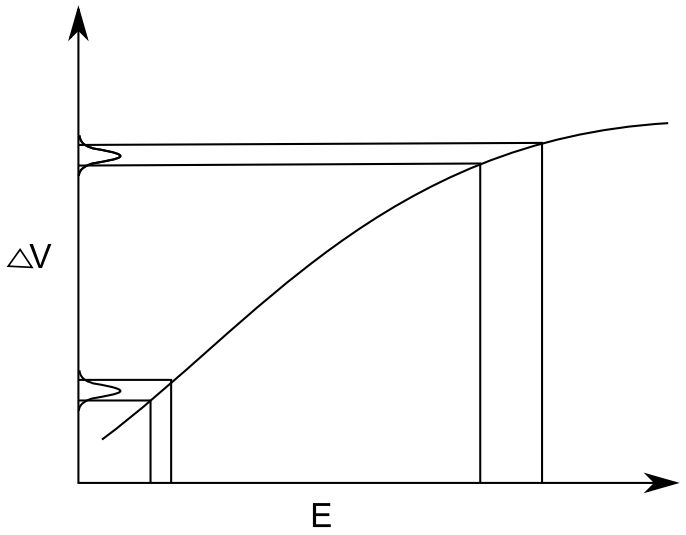

Figure 4.10: Sketch of the general ECS energy scale. The V-axis represents the reconstructed pulse height from the voltage output of the detector, the energy axis the corresponding photon energy of the incident photon.

4.5 Gain and Resolution

The output signal of the ECS is the voltage drop over the thermistor. Due to choices of normalization for the signal, the unit of the reconstructed pulse heights is an *arbitrary detector unit*, but historically the unit is sometimes still referred to as *volts*. Figure 4.10 shows the general shape of the dependence of the signal pulse height on the energy of the absorbed photons. For small signals this detector gain is close to linear. Due to the nonlinearity effects in pulse heights discussed earlier, at larger photon energies the detector gain forms a "knee" and the gain flattens (Stahle et al., 1999). The exact shape of the energy scale depends on instrument design parameters, the pulse detection algorithm, and the operating conditions, including the thermal environment and incident photon flux (Cottam et al., 2005).

The uncertainty in the measured pulse height ΔV in detector units is nearly independent of the pulse height or photon energy. Because of the gain flattening at higher photon energies, however, this signal-independent uncertainty in volts space translates to slowly decreasing resolution in energy (Fig. 4.10). For example, tests of the *Astro-E*-XRS detector arrays, using optimal filtering, found energy resolutions of 8–9 eV FWHM at the baseline, 9–10 eV at 3.3 keV (Ar K region), and 11–12 keV at 5.9 keV (Mn K region) for this device (Stahle et al., 1999). For the *Hitomi*-SXS detector, which is closer in performance to the ECS than the XRS, the FWHM detector resolution was found to scale as a quadratic function in energy with widths of order 4.5 eV at 6 keV and 5 eV at 8 keV in a laboratory environment during ground testing (Eckart et al., 2016) and slightly broadened in orbit (Leutenegger et al., 2016).

While analytic models of the calorimeter gain are investigated, the gain is generally modeled empirically with a polynomial (Cottam et al., 2005) of fourth order ($E = \mathtt{poly}(V)$). The constant (x^0) coefficient of the polynomial is set to zero, i.e., the polynomial goes through the origin, because the energy scale has to go through the origin by definition of the optimal filter. The gain polynomial is determined from fits to the measured line center

in detector units (V) vs. the known reference energy (eV) from well known transitions like the Rydberg series in He- and H-like ions. This approach is used for both the low- and the high-energy pixels. New energy scales for the ECS are determined periodically and, especially for wavelength measurements, close in time around the planned experiment.

4.5.1 Calibration of Low-Energy Pixels

Measurements of both transition energies and cross sections benefit from high-resolution that allows to disentangle the photon flux from closely spaced and otherwise blended spectral lines. Of the two ECS subarrays, the low-energy pixels with their high resolution are therefore the primary spectrometer for ECS measurements of astrophysically relevant transitions. Due to the low heat capacity of the thin low-energy pixels, photon energies well below 10 keV can be large enough to result in pulse heights that are outside of the small signal limit or even larger than the dynamic range of the digitizer. Since the ECS uses energy-independent templates for pulse height analysis and pulse detection, false double-triggers are more likely to occur towards the upper end of the dynamic range, where non-linearities are more prevalent, causing unnecessary low-res pulse height determination. Especially for flux measurements, it is important to take into account and analyze all detected photons. Due to the different resolutions and gain scales of the various event grades, the total flux of a spectral line is most easily determined with smaller systematic uncertainties if the spectrum has the highest achievable fraction of high-res events. Additionally, for these large pulses far beyond the knee it can be difficult to obtain a good fit to the broadband gain. While for experiments simply concerned with flux measurements high accuracy of the energy scale is not a primary concern, it is still necessary to obtain good alignment between the scales for each pixel. Good alignment is more easily accomplished with more accurate scales.

By changing the heat sink and detector temperature, the dynamic range can be adjusted to ensure that no parts of the energy range relevant to an experiment are clipped and that the pulse detection is well-behaved. Higher detector temperatures, however, can lower the spectral resolution of the calorimeter. For the emission cross section measurement of Fe K lines (Chapter 8), we therefore explore the behavior of the low-energy pixels at operating temperatures of 51 mK and 60 mK.

Accuracy of the Energy Scale

For the analysis of transition energy measurements, the energy scale is calibrated in a narrow energy band around the transitions of interest. During data acquisition and for ECS monitoring of EBIT conditions for other experiments (e.g., with the crystal spectrometer, Chapter 7), on the other hand, broadband calibration is more important.

The fourth order polynomial is only an approximation to the true gain function, but generally found to fit well (Leutenegger et al., 2016). Nevertheless, broadband calibration of the full energy range results in slightly larger systematic uncertainties of the energy scale than calibrating only locally around the energy range of interest for the experiment,

since outside of the knee locally the gain is close to linear. For example, the 200–300 eV wide energy range of K-shell transitions in Si and S, respectively, could be calibrated to better than 0.3 eV (at 51 mK; Section 6.1.3).

Calibrating the energy scale in the Fe region from He-like Mn Kα (6.2 keV) up to H-like Ni Lyα (8.1 keV) with w, Lyα_1 and Lyα_2 of Mn, Fe, and Ni yields an accuracy of better than 0.9 eV rms[11] at an operating temperature of 60 mK. This uncertainty is somewhat larger than in the Si/S region, but the covered energy range is larger and in a less linear part of the gain curve. The broadband calibration up to Ni K around 8.1 keV used the Rydberg series of O, Ne, S, and Ar, and $n = 3 \rightarrow 2$ transitions in Ne-like Kr in addition to the Mn, Fe and Ni lines. The resulting rms uncertainty is ~ 1.5 eV.

At 51 mK, the 6.2–8.1 keV region is also on the order of 1 eV for those pixels that show no or only very little sign of double-trigger problems. It is thus comparable to the 60 mK result. The broadband calibration, however, on the order of a few eV is much worse than at 60 mK, with most of the uncertainty coming from the lines above 6 keV.

Position of the ‘‘knee”

For wavelength measurements, it is preferable to operate outside of the knee where the scale is more linear and therefore easier to model. Mathematically, the knee is the location in the gain function where the energy scale changes the most, i.e., the knee is the location of the highest curvature of the function. In curve sketching, the curvature of a graph is given by the second derivative of the function. Extrema of the curvature are therefore roots of the third derivative. For a fourth order polynomial, the position of the knee thus is $-0.25 a_3/a_4$ in detector units, where a_n is the coefficient corresponding to order x^n. The position of the knee in energy then follows from applying the gain polynomial to this value.

Figure 4.11 compares the position of the knee for each pixel at 51 mK and 60 mK for three different calibration ranges each (subsets of the same calibration data): broadband (0.5–8.1 keV), Ar through Ni (3.1–8.1 keV), and Mn through Ni (6.1–8.1 keV). At 51 mK, the location of the knee appears to be around 3 keV according to the broadband calibration, which closely traces the full gain scale. For calibration starting with Ar lines, the knee of the calibration curve is shifted slightly towards higher energy, while for calibration above Mn it moves up to 6 keV. The reason for the perceived shift to higher energies is that the polynomial used for each of these curves has no constant term, regardless of how far away the calibrated energy region is from the origin. Therefore, the curves for non-broadband calibration turn over towards zero right below the reference line lowest in energy. For the calibration using only lines above Mn, this point is just below He-like Mn line w at 6.18 keV. Since He-like Ar line w at 3.14 keV is close to “true” position of the knee as indicated by the broadband calibration, the maximum curvature of the calibration polynomial for the calibration range from Ar through Ni experiences only a

[11] Root mean square (rms) of differences between the literature energy values of the reference calibration lines and their line centers as determined in detector units and converted to energy using the derived gain polynomial. The rms was calculated using all reference lines and all pixels.

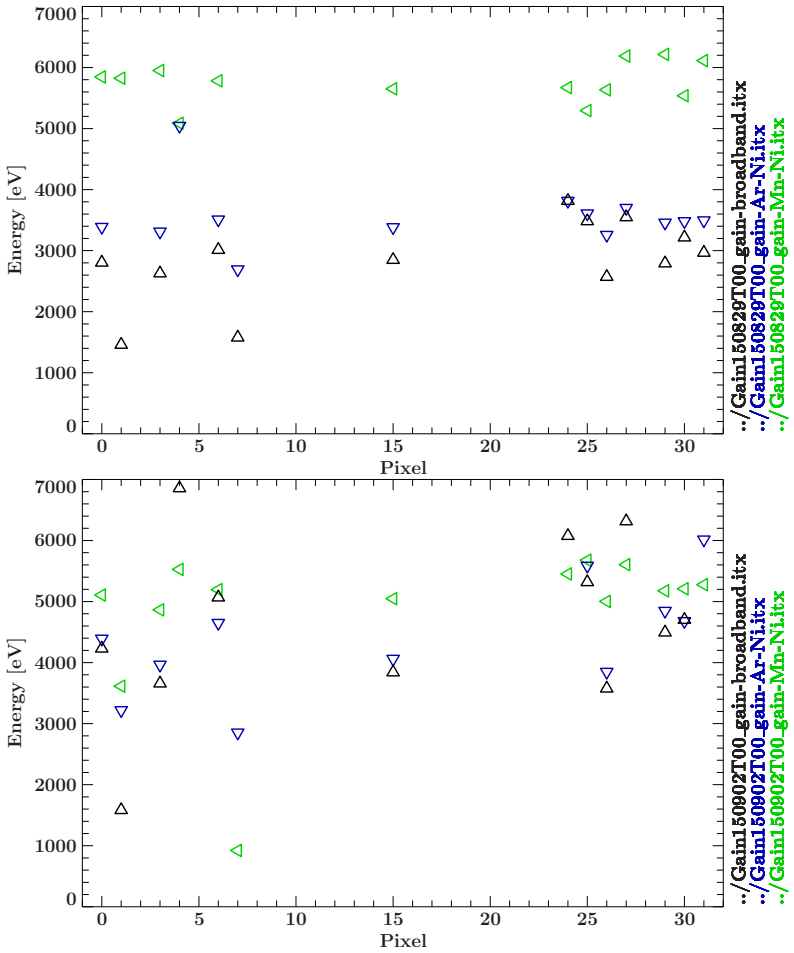

Figure 4.11: Position of the strongest curvature derived from the third derivative of the calibrated gain polynomial for each pixel at 51 mK (top) and 60 mK (bottom). The black up-triangles correspond to the broadband calibration using reference lines between O K and Ni K. The blue down-triangles only use the subset of lines covering the energy region between Ar and Ni K. The green left-triangles only cover the Mn through Ni energy region. See text for discussion.

small shift away from the actual position of the knee. At 60 mK the heat capacity of the detector is larger such that the measured pulse heights for the same set of reference lines become smaller. This means that the knee then moves to higher photon energies. Since it is closer to the Mn lines, the positions derived from the three calibration curves are closer together. Overall, at 60 mK the knee appears to be around 4–5 keV, i.e., far enough away from the energies of the Fe K transitions. For cross section measurements of K-shell transitions in Cr or V ions, it would probably be better to stay at a lower temperature.

Detector Resolution

Good detector resolution is important to resolve line blends and to measure transition energies to high accuracy. Since the resolution can degrade with increasing temperature,

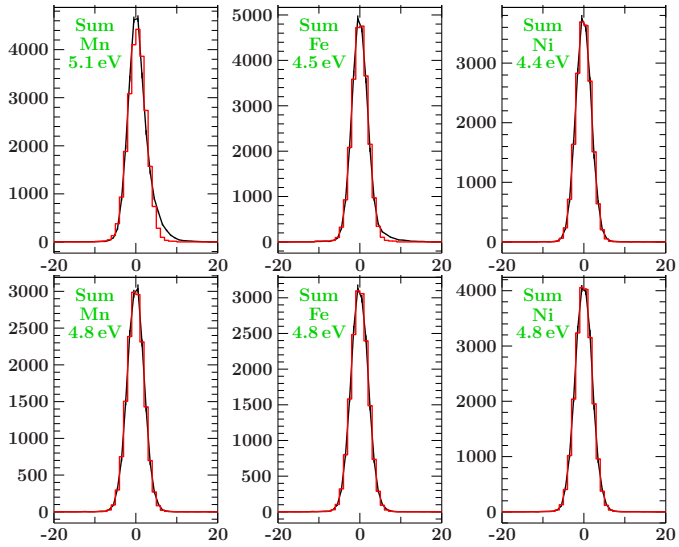

Figure 4.12: Baseline pulses at 51mK (top) and 60mK (bottom) summed for all 14 low-energy pixels. The baseline is analyzed in three different datasets, i.e., those for the Mn, Fe, and Ni calibration lines, using the gain scale from the broadband calibration. While the resolution at 60 mK is < 0.5 eV lower than at 50 mK.

here the resolution of high-res events in the Fe region is compared for 51 mK and 60 mK operating temperature. Leutenegger et al. (2016) find that the energy resolution R for a given event grade and pixel can be viewed as the baseline[12] energy resolution R_b and an energy-dependent excess broadening term $R_\mathrm{e}(E)$, which are added in quadrature

$$R(E) = \sqrt{R_\mathrm{b}^2 + R_\mathrm{e}^2(E)}. \tag{4.7}$$

Figure 4.12 shows the baseline events summed over all pixels for the three datasets of Mn, Fe, and Ni calibration for both operating temperatures. Since of the three calibration curves the broadband calibration is most accurate at low photon energies, the width of the baseline events is determined on this scale. At 60 mK the baseline resolution is 0.3–0.4 eV lower than at 51 mK. For the resolution of the spectral lines w and Lyα of Mn, Fe, and Ni as calibrated with only this set of lines, the difference in FWHM between the two heat sink temperatures (Fig. 4.13) is about the same as for the baseline events, indicating that the increased temperature did not cause additional excess noise. Since we compare the resolution of the summed spectra rather than for individual pixels, the FWHM strongly also depends on the quality of the calibration and alignment between the pixels. But since for the measurement the summed spectra are analyzed, the primary concern here is the effect of temperature on the resolution of the summed spectra.

[12] Baseline events are strings of the output signal without an X-ray signal that are analyzed with the optimal filtering template as if there was a pulse. Baseline events thus quantify the effect of baseline noise in the detector system (Leutenegger et al., 2016).

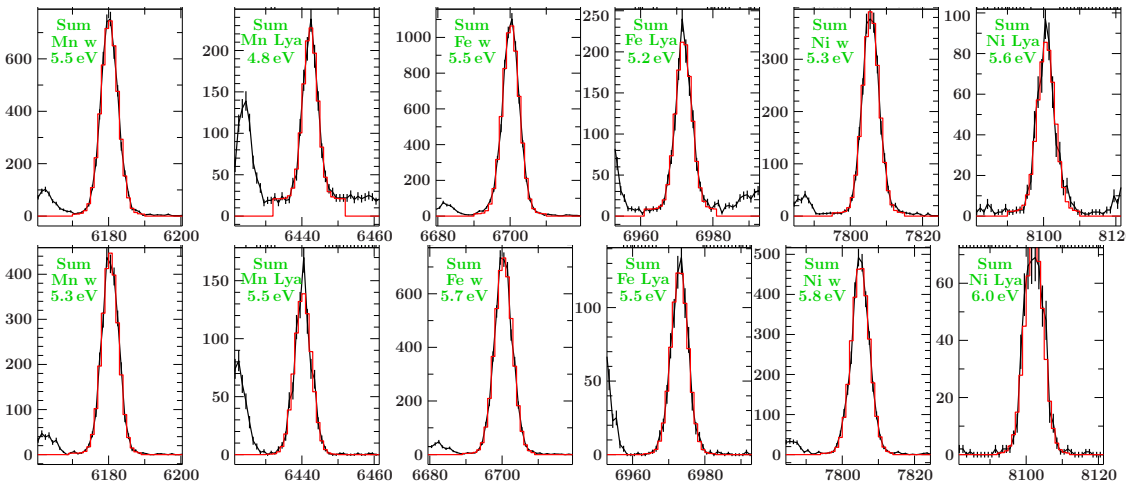

Figure 4.13: FWHM of the calibration lines Mn w, Mn Lyα_1, Fe w, Fe Lyα_1, Ni w, and Ni Lyα_1 for the calibration using only these and Lyα_2 of Mn, Fe, and Ni; top: 51 mK, bottom: 60 mK. The spectra are the sum of all 14 pixels. For the final summed spectra the detector resolution degrades by less than 10% for the 60 mK spectra compared to the 51 mK spectra.

Long-term Stability

The gain and therefore calibration of the calorimeter depends on the temperature of the detector. Small local changes in the thermal environment such as differential thermal loads between the ECS sensors and the ADR control thermometer can cause the gain to drift over time (Leutenegger et al., 2016). For slow measurements with very long exposure times it is beneficial if the gain is stable over long time-periods so that the line spread function remains well described by a Gaussian shape, the resolution does not degrade, and the energy scale and pixel alignment stay accurate in the summed spectra. While Porter et al. (2008b) see a 3 eV day/night oscillation over 36 h, Porter et al. (2009a) find the gain to be stable, i.e., a drift correction on the gain is usually unnecessary.

For the Fe cross section measurements (Chapter 8), long exposures of several days were required to collect sufficient amounts of data. Using the strongest line in the spectrum, He-like Fe w, we therefore check the long-term stability over the course of each experimental day at an operating temperature of 60 mK. Figure 4.14 shows two scatter plots of the measured pulse heights of Fe w over the course of a day for a single pixel. The top figure represents the drift on most days, while the bottom figure corresponds to a measurement started right after the ECS was recycled and reached tight temperature control at 60 mK. A linear regression to these scatter plots indicates that on an average day the total drift is less than 0.5 eV over a half day (0.3 eV over 50 ks in this example). However, directly after recycling the ADR and He7 sorption cooler of the ECS, it takes a few hours for the detector to completely reach thermal equilibrium. During this time, the gain is less stable and prone to drifts of up to a few eV until the detector settled thermally (Fig. 4.14 *bottom*).

We also calculated a pulse height average on 5 ks intervals and fitted a straight line to the trend. Overall, the slope of this fit agrees with the slope of the linear regression. Some of the curves show relatively large scatter even on short time scales between successive

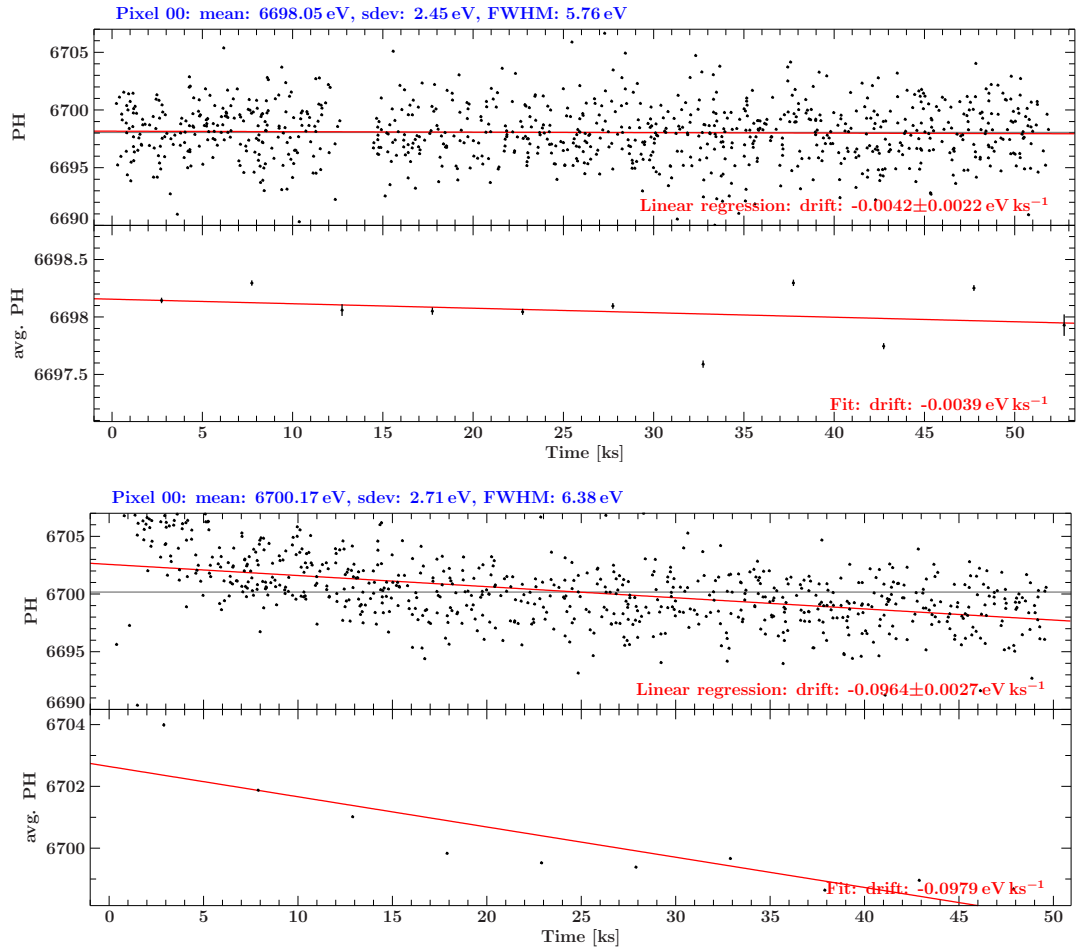

Figure 4.14: Measured pulse height (PH) distribution of He-like Fe line w photons as a function of time (in ks) since the beginning of the exposure for a single pixel (top panels). The upper figure corresponds to an average day, the lower figure to a day that started with an ECS autocycle. After the control thermometer reached the operating temperature, the detector takes a few more hours to reach thermal equilibrium. The red line indicates a linear regression to the scatter plot, the gray line is the average pulse height of the full day. The bottom panels show the pulse height averaged over 5 ks intervals and a fit to estimate the drift. Large scatter in the average pulse heights is due to small-number statistics.

5 ks intervals. Simulating such a curve by drawing random pulse heights from a Gaussian distribution with appropriate center and width and matching these pulse heights with time stamps from an even distribution with the same number of counts and exposure time shows that this scatter is completely explained by low-number statistics, i.e., it is not sensitive to variations on short time scales.

It is better to do this test on stronger line sources for higher accuracy on the drift and higher sensitivity to changes on short time scales. However, the trace of Fe w as a function of time indicates for the long exposures that a drift correction is not strictly necessary over the course of a day as long as the measurement is taken sufficiently long after the detector has been recycled to operating temperature.

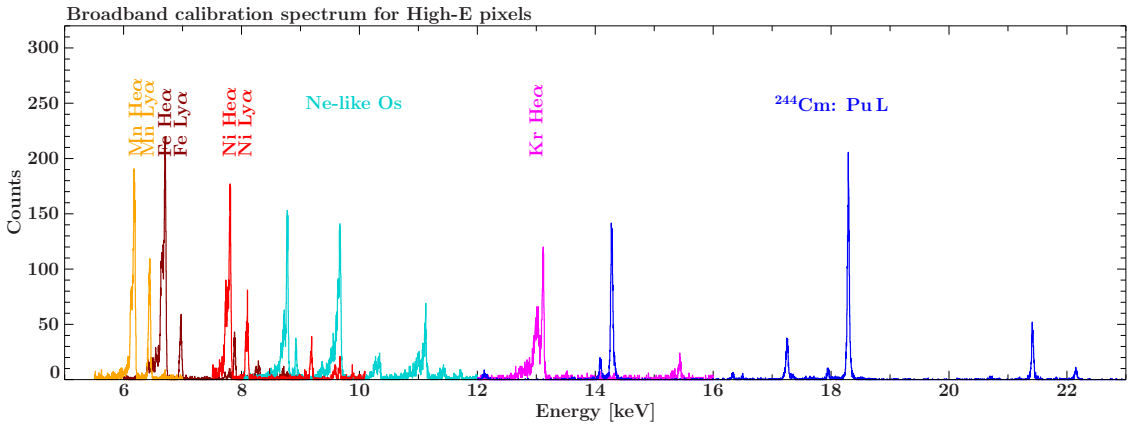

Figure 4.15: Calibration spectra for high-energy pixels.

4.5.2 Calibration of the High-Energy Pixels

The high-energy pixels are used to record the radiative recombination features during the emission cross section measurement. These features are at relatively high photon energies such that for the beam energies used in this experiment, the energy scale needs to be calibrated up to about 22 keV. Above 13 keV, K-shell transitions of He- and H-like ions are less accessible with EBIT-I. Additionally, the beam energy on EBIT-I is limited to about 30 keV by the power supply. However, instabilities in the electron beam and drift tube voltages during these experiments produced an upper limit of ~ 17 keV, precluding excitation of lines above this threshold. Therefore, the high-energy range is calibrated with radioactive sources. Specifically, in the 14–22 keV region we use neutral Pu L-shell transitions emitted by a ^{244}Cm source (reference energies from Bearden, 1967, and Indelicato et al., 1998). Radioactive sources have the additional advantage that they can calibrate the ECS over night without running EBIT. Figure 4.15 shows the broad range calibration spectrum for the high-energy pixels, including He- and H-like Mn, Fe, and Ni, Ne-like Os, He-like Kr, and Pu L.

Because of the lower resolution of these pixels, the He-like Kα triplets are not fully resolved, introducing larger uncertainties into the final energy scale than for the low-energy pixels. Additionally, the reference energies for transitions in neutrals as seen in radioactive sources are often only accurately known to about 1 eV (Indelicato et al., 1998). However, due to the lower resolution, typical bin sizes for the high-energy spectra are 3–5 eV (compared to 0.5–1 eV for the low-energy pixels). The RR features are additionally broadened from the spread in beam energy. While we derive the beam energy from the RR photon energy, good alignment between the pixels to preserve the spectral shape of the RR features is more important than getting the absolute energy scale accurate to better than on the order of 1 eV. The energy resolution at 60 mK as derived from the baseline events is ~ 30 eV and as derived from the Pu L line at 18.3 keV is ~ 31 eV[13].

[13] Note that the natural widths of the L-shell levels in Pu are already ~ 10 eV (Krause & Oliver, 1979). The width of this line due to the detector resolution is therefore derived from the Gaussian width of a Voigt profile.

We shall assume simply that X-ray phenomena are a branch of optics.

Charles G. Darwin (1914)

5 High-resolution Imaging Crystal Spectrometer

While the ECS makes a good compromise of resolving power versus quantum efficiency in a broad energy band compared to CCD and solid state detectors, in some cases it is desirable to aim for even higher resolution. For example, in order to take advantage of X-ray diagnostics of plasma temperature or density to high accuracy, it is often necessary to determine the exact line profile of an X-ray feature, while avoiding complication from instrumental line width. In addition, blending of lines in mid to low resolution spectrometers may render a diagnostic unusable. For these purposes, wavelength dispersive instruments such as grating and crystal spectrometers may deliver the best results. However, since wavelength dispersive instruments depend on geometry effects, they usually have a small bandpass and low throughput.

To re-gain some throughput, focusing geometries can be employed. Here, we discuss a high-resolution imaging spherical crystal spectrometer, dubbed the OHREX Orion High Resolution X-ray spectrometer, designed for a laser produced plasma experiment, and tested and calibrated at the LLNL EBIT (Beiersdorfer et al., 2016b). The Orion laser is a laser facility at the UK's atomic weapons establishment (Hopps et al., 2015). The operating principle and design of this spherical crystal spectrometer can most easily be understood by breaking it down into the four underlying geometries: Bragg's law as used for flat crystals; reflection of spherical mirrors; cylindrically bent crystals in the focusing von Hámos (1933) type configuration, where the crystal is bent perpendicular to the plane of dispersion; and the Johann (1931) geometry employing the Rowland (1882, 1883) circle, where the cylindrical crystal is bent parallel to the dispersion plane. General design parameters of the spherically bent crystal spectrometer are constrained by the superposition of these effects, whereas specific parameter values are dictated by consideration of the specific experimental setup at the facility where the instrument is to be employed. In the following, each of these aspects of the OHREX are highlighted, and testing and calibration at EBIT as well as some modifications creating the sister spectrometer, dubbed EBHiX, specific to EBIT applications are discussed.

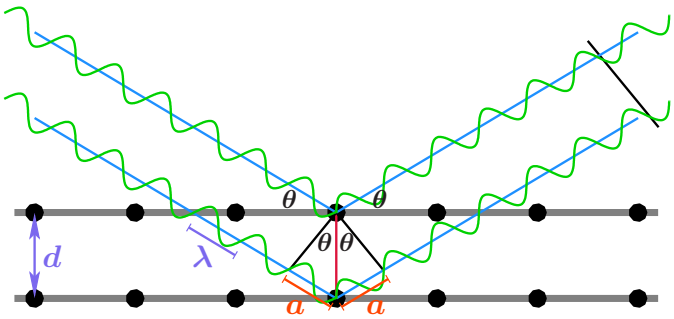

Figure 5.1: Sketch of Bragg reflection off of the atoms in a crystal lattice. For reflection to occur, rays of the same wavelength λ and phase that are reflected form the first and second plane have to interfere constructively, i.e., $2a = n\lambda$.

5.1 Bragg's Law

The lattice structure of crystals had already been proposed by Bravais around 1850 (Bravais, 1850). Once there were strong hints that X-radiation has extremely short wavelengths (Chapter 1, although it was not entirely clear yet whether X-rays are waves or particles), Laue, who had estimated the lattice constant from the crystal density, proposed that it should be possible to study the crystal lattice by X-ray diffraction (Laue et al., 1912). He had his coworkers Friedrich and Knipping successfully test his theory using unprecedentedly long exposure times for their experiments. These findings revived the field of crystallography and led to the development of the first crystal spectrometer by Bragg & Bragg (1913) and Bragg's law.

5.1.1 General Law

To study the reflections of X-rays from crystals, Bragg & Bragg (1913) built a simple apparatus: a flat crystal mounted with its face sitting on the axis of a rotatable table, and a shielded X-ray tube with a slit and a tubular ionization chamber, also equipped with a slit, mounted facing the crystal, acting as source and detector, respectively. Both X-ray tube and ionization chamber were rotatable about the crystal in the table center. Aiming the collimated X-ray beam at an angle θ to the crystal surface and recording the maximum ionization current of the ionization chamber at a reflection angle of $\sim 2\theta$, Bragg & Bragg (1913) found "peculiar and considerable variations in the intensity of the reflection at different angles", when the ionization chamber and X-ray beam were simultaneously rotated about the crystal. Specifically, they observed three peaks corresponding to the characteristic lines of the X-ray tube's target material, in this case platinum. Since the relative magnitudes and spacing of these lines as well as their absorption characteristics remained the same in higher diffraction orders, i.e., the spectrum repeated at larger angles, and for different crystal cuts, Bragg & Bragg (1913) were able to correctly identify the origin of these spectra.

Using relatively simple geometric arguments, Bragg & Bragg (1913) were able to derive

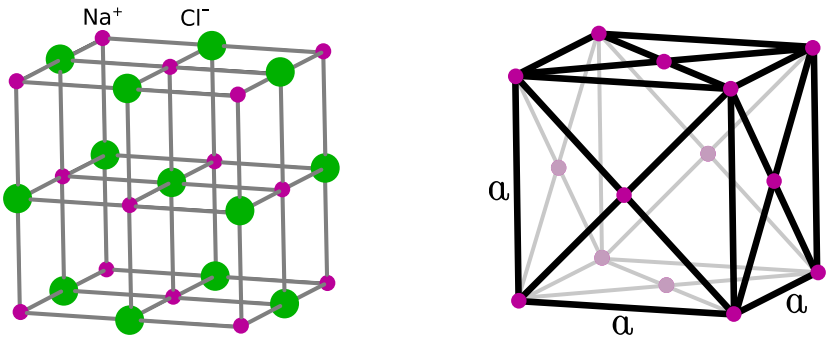

Figure 5.2: Crystal lattice of rock salt (NaCl). a) 2D plane, b) unit cell (fcc: face-centered cubic). The 100 planes are parallel to one of the sides of the unit cell; the 110 cut is defined by the planes cutting diagonally through the unit cell, i.e., cutting the cube in half; the 111 cut is the plane defined through three corners of the unit cell, i.e., the plane cutting off a corner of the cube.

the relationship between the wavelength of the diffracted X-rays and the lattice spacing of the crystal to set a wavelength scale to their measured spectra. Figure 5.1 shows a schematic representation of a crystal. Mono-chromatic X-rays of wavelength λ incident onto the crystal surface under an angle θ can be reflected off of different planes inside the crystal. In order for reflection to occur, all reflected rays have to interfere constructively, i.e., the path difference the light travels if reflected from the second plane or the first plane has to be a multiple integer of the wavelength, leading to Bragg's law

$$n\lambda = 2d \sin\theta \tag{5.1}$$

where n is the order of diffraction, d is the lattice spacing, and θ is the angle of incidence measured from the crystal plane. Here, the lattice spacing d is the distance between two successive identical planes, not just neighboring planes. Take, for example rock salt (NaCl), which contains an equal number of sodium and chlorine atoms, arranged in an alternating pattern (Fig. 5.2). In rock salt 100, i.e., the cut with crystal planes parallel to a side of the cube, directly neighboring planes appear shifted by one row as Cl and Na alternate, while the next neighbor is identical, i.e., in this 100 cut the lattice spacing is the distance between two Na atoms or, equivalently, between two Cl atoms, as shown by the unit cell (Fig. 5.2). Bragg & Bragg (1913) were able to confirm this definition of the lattice spacing as well, since they measured the smallest reflection angles using rock salt 111, i.e., the cut of rock salt with the largest lattice spacing.

While, for any given crystal, Bragg's law relates an exact reflection angle θ_0 to each wavelength λ, there is actually a small range of angles around θ_0 that can also reflect the same wavelength λ. The reason is that refraction of the incident wave upon entering the crystal displaces the maximum reflection of a wave slightly from the reciprocal lattice points of the crystal (Als-Nielsen & McMorrow, 2011). The location of maximum reflection coincides with the reflection angle θ_1 due to index of refraction corrections to Bragg's law (see next Section). The difference $\Delta\theta = \theta_1 - \theta_2$ is on the order of arcseconds or μrad. To determine the amplitude of the radiation reflected by the crystal, one has to integrate over all reflected waves. In an extended perfect crystal, incident radiation

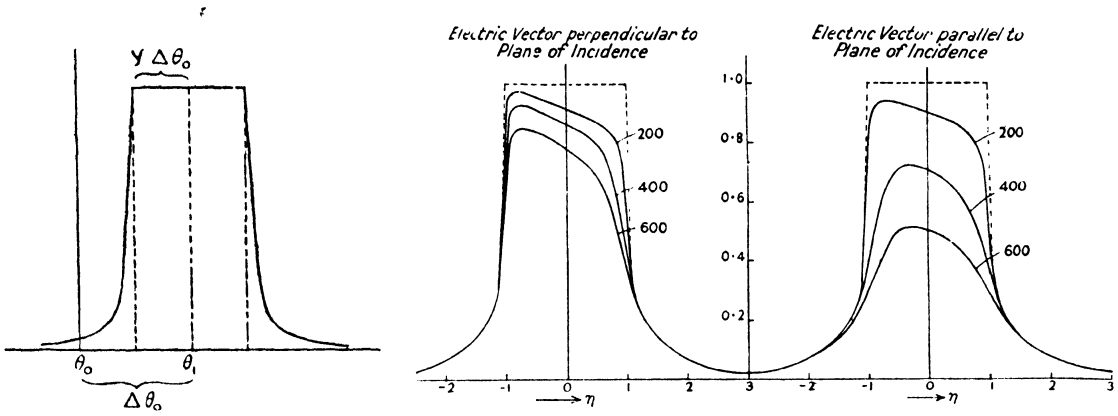

Figure 5.3: Shape of the rocking curve (reflection curve) for a perfect crystal without absorption multiple reflections (*left*) and additionally including absorption (*right*). θ_0 is the reflection angle corresponding to Bragg's law, θ_1 corresponding to the corrected Bragg's law. — From James (1962, Figs. 25 & 27.).

can pass through multiple atomic planes, loosing intensity with each passage as part of the beam is reflected by each plane. On its way to leave the crystal the reflected radiation has an additional chance to be re-scattered into the direction of the incident beam. The treatment of these multiple scattering events is called dynamical diffraction theory (Als-Nielsen & McMorrow, 2011). Each transmission or reflection event at one of these planes causes a phase shift of the resulting wave compared to the incident wave. In the sum, the reflected amplitude around the Bragg angle θ_0 then has the shape as shown in Fig. 5.3, *left*, where the flat part in the middle corresponds to total reflection. This reflection curve is called the *Darwin curve* after the treatment of imperfect crystals by Darwin (1922) or the *rocking curve*. If in addition to transmission and reflection also absorption by the crystal is taken into account (first treated by Prins, 1930), the rocking curve becomes asymmetric, the center of gravity of the curve is shifted to slightly smaller angles than θ_1, and the flat part for total reflection disappears (James, 1962). Since the absorption of radiation in a crystal depends on the polarization of the incident radiation (Section 5.6), the rocking curve differs for radiation polarized parallel or perpendicular to the crystal planes, with the perpendicular polarization suffering from stronger absorption (Fig. 5.3, *right*). The total reflectivity of a crystal for each wavelength is determined by the integral over the rocking curve. Thus, crystals with wider rocking curves tend to have higher reflectivity, however, a large rocking curve width also corresponds to lower spectral resolution. For detailed discussions of the derivation of the rocking curve see, e.g., James (1962) and Als-Nielsen & McMorrow (2011).

For extended sources, radiation emitted from different regions of the source will fulfill Bragg's law at different locations on the crystal for the same wavelength. Thus, on the detector plane, spectra originating from different regions of the extended source will appear shifted from one another, effectively "washing out" the spectral resolution created by the dispersive element. To achieve high spectral resolution, it is therefore important that the projection of the source onto the crystal is small compared to the width of the rocking curve, at least in the dispersion direction. This requirement can be satisfied by

implementing a slit or pinhole in the core of extended sources Hence, at EBIT, no slit is required if, in the case of flat crystal spectrometers, the 50 μm wide electron beam is viewed with the dispersion direction perpendicular to the beam.

5.1.2 Higher-order Corrections due to Index of Refraction Effects

Bragg's method laid the cornerstone for X-ray spectroscopy and provided the first means to study X-ray wavelengths. By refining the setup and substituting the ionization chamber with photographic plates, Moseley (1913) were able to systematically measure the wavelengths of characteristic X-rays of elements excited by cathode ray tubes[1]. While Bragg's law is a good start for the accuracy of these early experiments, Darwin (1914) predicted that the measured position, i.e., the observed Bragg angle, of the X-ray line is slightly shifted due to refraction. Accordingly, using a perfect crystal, close examination shows the maximum of the diffraction pattern indeed at an angle $\theta > \theta_0$, where θ_0 corresponds to the correct wavelength in air through Bragg's law (Eq. 5.1; Compton & Allison, 1935). Following the book of Compton & Allison (1935), this section shows the derivation of an approximate correction to Bragg's law.

The index of refraction $\mu = v/v'$ is defined as the ratio of the phase velocities[2] in air (v) and the crystal (v'). Since the frequency of the light $\nu = v/\lambda$ remains the same in air and the medium, $\mu = \lambda/\lambda'$. Because of Snell's law of refraction[3], also $\mu = \cos\theta/\cos\theta'$. For X-rays the deviation of the refractive index from unity is so small that we can write $\mu = 1-\delta$, where δ is called the unit decrement. Therefore,

$$\mu = \frac{v}{v'} = \frac{\lambda}{\lambda'} = \frac{\cos\theta}{\cos\theta'} \equiv 1-\delta < 1, \tag{5.2}$$

where λ is the wavelength in air and θ the observed glancing angle (*cf.* Fig. 5.4). Since the reflections occur inside the crystal after the ray has been bent at the entrance, Bragg's law applies to the wavelength λ' and the angle θ' *inside* the crystal (not to λ and θ outside)

$$n\lambda' = 2d\,\sin\theta'. \tag{5.3}$$

Combining equations 5.2 and 5.3 and eliminating the primed quantities[4], we find

$$n\lambda = 2d\left(1-\frac{2\delta-\delta^2}{\sin^2\theta}\right)^{1/2}\sin\theta \approx 2d\left(1-\frac{\delta}{\sin^2\theta}\right)\sin\theta, \tag{5.4}$$

[1] This study led directly to a scaling law for Kα transitions as a function of Z (Moseley, 1913, 1914), as well as further insights into the atomic structure.

[2] The phase velocity in vacuum is the speed of light c. The "absolute" refractive index between vacuum and a medium is often denoted as $n_\mathrm{r} = c/v$.

[3] Snell's law relates the angles of incidence and refraction (measured to the normal of the transition between the media, i.e., $\phi = 90^\circ - \theta$) to the absolute refractive indices as $n_{\mathrm{r},1}\sin\phi_1 = n_{\mathrm{r},2}\sin\phi_2$.

[4] Start with $\lambda/\lambda' = (1-\delta)$ and substitute λ' through Eq. 5.3, then square the resulting equation:

$$\left(\frac{n\lambda}{2d}\right)^2 = (1-\delta^2)\sin^2\theta' = (1-\delta^2)(1-\cos^2\theta') = (1-\delta^2)\left(1-\frac{\cos^2\theta'}{\cos^2\theta}\cos^2\theta\right) = (1-\delta^2)\left(1-\frac{1}{(1-\delta)^2}\cos^2\theta\right)$$

where in the last step again Eq. 5.2 is used. Expanding the last expression, converting back to $\sin^2\theta$, and taking the square root then leads to Eq. 5.4.

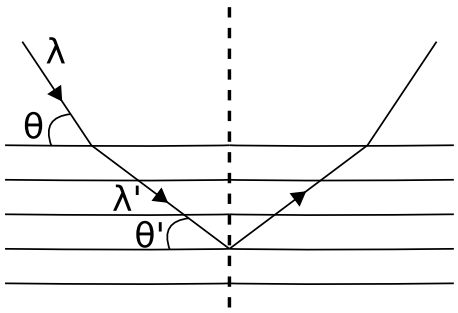

Figure 5.4: Sketch to explain the refractive index μ, after Compton & Allison (1935). The phase velocity of the wave (wavelength λ) in air v is larger than in the crystal (v'), resulting in a shift to longer wavelengths in the medium (λ'). Therefore, the frequency of the light remains the same ($\nu = \nu'$). Due to Snell's law, the angle of incidence θ to the crystal surface decreases to θ'.

where the latter comes from expanding the radical and neglecting higher powers of δ (Compton & Allison, 1935, p. 674). Since the refractive index μ, and therefore the unit decrement δ, depend on wavelength (Eq. 5.2) and since the Bragg angle θ depends on the order of refraction n, the correction to Bragg's law also depends on n. Defining an order dependent equivalent to the lattice spacing,

$$d_n = d\left(1 - \left[\frac{\delta}{\sin^2\theta}\right]_n\right) \tag{5.5}$$

shows that the uncorrected Bragg's law can be used as long as wavelength determinations are made only in one order (Compton & Allison, 1935, p. 681). Combining multiple diffraction orders necessitates the use of the corrected version of Bragg's law (Eq. 5.4).

To be able to apply the correction, the value of the unit decrement δ and its wavelength dependence still have to be found. For this, consider the reason behind the change of phase velocity between air and the crystal medium (Compton & Allison, 1935, p. 274*ff.*). The incident wave acts on the electrons of the medium, causing them to oscillate. After a small period of time, these oscillations take on the frequency of the incident wave and a wave of the same frequency is scattered by the electron. The differential equation describing forced, damped oscillations of an electron has to be solved for this displacement of the electron from its rest position. The polarization of the medium, defined as the electric moment per unit volume, is proportional to this displacement, and in turn enters the dielectric constant κ of the medium. The dielectric constant is a complex quantity, since it depends linearly on the solution of the differential equation. Now, according to Maxwell, the phase velocity of a wave in a medium is related to the dielectric constant via

$$v = \frac{c}{\sqrt{\kappa}} \tag{5.6}$$

and, thus, is complex as well. Substituting this relation into the general equation of a wave moving through a medium shows that the imaginary part of the complex dielectric constant introduces an absorption coefficient into the wave equation, reducing the wave amplitude during passage through the medium, whereas only the real part influences the phase velocity.

From Eq. 5.6 also follows that the index of refraction $\mu = \sqrt{\kappa}$. Writing the dielectric constant as $\kappa = 1 - 2\delta - 2i\beta$, where δ and β can be shown to be small, and expanding the root, gives (Compton & Allison, 1935, p. 277)

$$\mu = 1 - \delta - i\beta \quad \text{with} \quad \delta = \sum_q \delta_q = -\frac{2\pi n_q e^2 m_e c^2 (k_q^2 - k^2)}{m_e^2 c^4 (k_q^2 - k^2)^2 + 4e^4 k^6/9}. \tag{5.7}$$

Here, k is the wave number of the incident light and n_q is the number of electrons per unit volume of the characteristic, or natural, frequency $\nu_q = k_q c/2\pi$ and δ is the sum over all of these frequencies. The natural frequency of an atom corresponds to the K, L, M, etc., excitation limits that give rise to absorption edges.

The second term of the denominator, $4e^4k^6/9$, is due to electromagnetic damping. For light close to the frequency ν_q this term is needed to keep δ finite, but it is negligible as long as the frequency ν of the incident photon is far away from any natural frequency of the medium, reducing

$$\delta_q = -\frac{2\pi n_q e^2}{m_e c^2 (k_q^2 - k2)} = \frac{n_q e^2}{2\pi m_e (\nu^2 - \nu_q^2)} \tag{5.8}$$

and for frequencies $\nu^2 \gg \nu_q^2$ much greater than any critical absorption of the medium (Compton & Allison, 1935, p. 280; James, 1962, p. 54)

$$\delta = \frac{n_e e^2}{2\pi m_e \nu^2} = \frac{n_e e^2 \lambda^2}{2\pi m_e c^2} = \frac{e^2}{2\pi m_e c^2} \frac{1}{m_H} \frac{Z}{A} \rho \lambda^2 \tag{5.9}$$

where n_e is the total number of electrons per cubic centimeter, which can be expressed as $n_e = Z/(m_H A \rho)$, where ρ is the density of the medium, m_H is the mass of the hydrogen atom, A the atomic weight (or the sum of the atomic weights in a molecule), and Z the total number of electrons in the atom (molecule).

Inserting the solution for the unit decrement δ (Eq. 5.9) back into the order dependent set of lattice spacings d_n (Eq. 5.5) and approximating the relation of wavelength λ and observed glancing angle θ with the uncorrected Bragg equation (Eq. 5.1) eliminates the wavelength dependence, while emphasizing the dependence on order:

$$d_n = d\left(1 - \frac{(2d)^2}{n^2} \frac{\delta}{\lambda^2}\right) = d\left(1 - \frac{(2d)^2}{n^2} \frac{e^2}{2\pi m_e c^2} \frac{1}{m_H} \frac{Z}{A} \rho\right) \tag{5.10}$$

where $d_\infty \approx d$, the lattice spacing derived, e.g., via density considerations. Tabulated values can be found in Thompson et al. (2009). Note that these formulae are in cgs units, i.e., the value of the elementary charge is expressed in statcoulomb (statC), also known as the electrostatic unit of charge (esu).

Using Mohr et al. (2015) as reference values for $c = 2.997\,924\,58 \cdot 10^{10}\,\mathrm{cm\,s^{-1}}$, $e = 1.602\,176\,6208(98) \cdot 10^{-19}\,\mathrm{C} \equiv 4.803\,204\,673 \cdot 10^{-10}\,\mathrm{esu}$, $m_H = 1\,\mathrm{a.u.} = 1.660\,539\,040(20) \cdot 10^{-24}\,\mathrm{g}$, and $m_e = 9.109\,383\,56(11) \cdot 10^{-28}\,\mathrm{g}$, and Haynes (2015) values for the molecular mass $A_{SiO_2} = 60.085\,\mathrm{a.u.}$ and density $\rho_{SiO_2} = 2.648\,\mathrm{g\,cm^{-3}}$ of quartz (SiO_2), the correction term for quartz is

$$\frac{\delta}{\lambda^2}(SiO_2) = 3.57 \cdot 10^{-6} \frac{1}{\mathring{A}^2}. \tag{5.11}$$

Substituting this correction term into d_n (Eq. 5.10) and, using $d \approx d_\infty$, gives the corrected Bragg's law for quartz crystals

$$n\lambda = 2d_\infty \left(1 - \frac{3.57 \cdot 10^{-6}}{\text{Å}^2} \cdot \frac{(2d_\infty)^2}{n^2}\right) \sin\theta, \tag{5.12}$$

which is applied for the wavelength calibration of crystal spectra in Section 5.5.2 and Chapter 7 for which reference lines where observed in both first and second order for the same spectral range.

These formulae are only valid in wavelength regions far away from absorption edges of the crystal because of the approximations made during their derivation and due to the neglect of absorption in the medium. However, the order of magnitude of the correction ($\sim 10^{-6}$ Å) is already smaller than the accuracy of the lattice constants for most crystals. The corrections to these corrections due to a more stringent derivation are even smaller. For our purposes, these formulae following the Lorentz dispersion theory (Lorentz, 1923) developed for the index of refraction in the optical regime with modifications to include absorption theory for X-rays by Compton (1922) are sufficient. A more thorough treatment is given by the Kramers-Kallmann-Mark theory of the refractive index, applying the dispersion theory by Kramers (1924a,b) to the X-ray wavelength dependent index of refraction by Kallmann & Mark (1926, 1927) and by Kronig (1926), which match the Lorentz theory in the limit of wavelengths far away from the absorption edges (Compton & Allison, 1935, p. 265).

5.2 Spherical Mirrors

Crystal spectrometers tend to have a small effective area because of the relatively low reflectivity of the crystals. A way to increase the intensity of the measured spectrum is to try to focus more of the reflected light onto the detector. To carry out any focusing during reflection, the reflecting surface has to be curved. Employing geometrical optics, we can determine the relative source and image positions as a function of focus or radius of curvature. Optics, especially geometrical optics, is usually done with light in the visible spectral range in mind. In the visible case, most ray tracing can be described in the paraxial approximation, where the light rays hit the elements of the optical setup in near normal incidence. Due to their short wavelengths, however, total reflection of X-rays only happens at very shallow incidence angles on the order of $\sim 1\,^\circ$. While partial reflection, e.g., off crystals, also occurs at fairly large incidence angles, these angles typically still do not approach $90\,^\circ$ where the paraxial approximation holds. This regime of glancing angles is often described in form of defects to the image due to off-center effects of optical elements. The image due to rays reflected off a spherical mirror under a large angle suffers from astigmatism, i.e., the focal length in the sagittal and meridional directions differ from another. Accordingly, here first the relationship between source, image, and focal distances for a spherical (concave) mirror in the paraxial approximation is derived, followed by a treatment of deviations from this formula due to off-axis source positions.

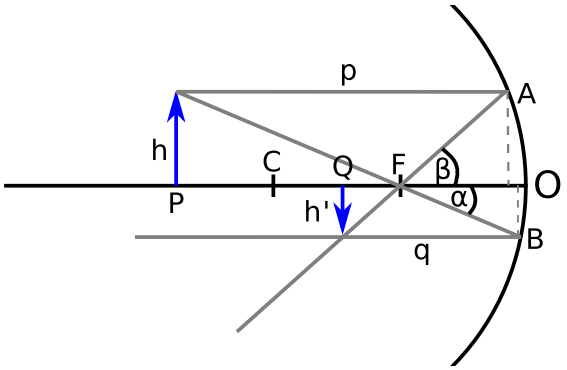

Figure 5.5: Schematic of rays reflected by a concave spherical mirror (center C, focus F with $f = R/2$) in the paraxial approximation.

5.2.1 Paraxial Geometry

In the paraxial geometry, the height of incidence is so small that for all practical purposes the incident rays can be considered close to the optical axis. This also means that all relevant angles are small enough to use small angle approximation, i.e., $\sin\alpha \approx \alpha \approx \tan\alpha$. Consider a spherical concave mirror with a radius of curvature R, where C denotes the center of the sphere (Fig. 5.5) and F the position of the focus. Generally, the focal length is half of the radius of curvature, i.e., $f = R/2$. Now consider a point source at a distance h from the optical axis and a distance $p = \overline{\mathrm{PO}}$ from the apex O of the mirror. Rays emitted parallel to the axis are reflected by the mirror through the focal point F, while rays going through the focus are reflected parallel to the axis. The location where these two reflected beams intersect denotes the position of the image of the point sources. The image has a distance h' from the axis and $q = \overline{\mathrm{QO}}$ from the mirror apex. Within the paraxial approximation, the curvature between the apex and the two reflection points A and B is negligible such that, using trigonometry,

$$\tan\alpha = \frac{h'+h}{p} = \frac{h'}{f} \quad \text{and} \quad \tan\beta = \frac{h'+h}{q} = \frac{h}{f}.$$

Eliminating h and h', the simple relation, dubbed mirror equation, between source distance p, image distance q and focal length f follows as

$$\frac{1}{p} + \frac{1}{q} = \frac{1}{f} = \frac{2}{R}. \tag{5.13}$$

5.2.2 Reflection at glancing angles – Astigmatism

Before going into the detailed geometrical derivation of reflection under larger angles, a more qualitative approach is given first. The mirror equation (Eq. 5.13) is derived in a projection, i.e., an infinitesimal slab in the paper plane with the optical axis being normal to the mirror surface. Imagine instead the source location hovering above the paper plane, but still close to the axis in the z-direction. This situation resembles the case where the

spherical mirror stays frozen in place, but the slab that contains the source position and the mirror apex is rotated around the apex out of the paper plane. The slab no longer cuts the sphere through the center but instead cuts off a segment. Then the circle representing the sphere in the two dimensional consideration of the previous section effectively does not have radius R any more, but is the smaller circle of radius $R_\mathrm{m} = R\sin\theta$, where $90° - \theta$ is the angle by which the source plane was rotated, i.e., θ here is measured from the mirror surface like the Bragg angle is from the crystal surface. In other words, we are using the circle where the rotated optical axis appears to be normal to the circle apex. The focus is then at $f_\mathrm{m} = R_\mathrm{m}/2 = (R\sin\theta)/2$ and is called the meridional focus.

Due to the large offset of the source from the axis, the geometry is no longer symmetrical and the sagittal focus has to be considered separately through the plane perpendicular to the paper that contains source and apex. To reconcile this case with the paraxial approximation, again the radius of curvature for the circle normal to the optical axis in this orientation is wanted. Here, the great circle of our sphere R appears to be a segment of a larger sphere with radius $R_\mathrm{s} = R/\sin\theta$, making the sagittal focus $f_\mathrm{s} = R_\mathrm{s}/2 = R/(2\sin\theta)$. The sagittal and meridional foci only coincide for $\theta = 90°$. This difference explains why off-axis source locations are commonly treated under defects of the mirror.

Following the more detailed geometrical derivation of Longhurst (1967)[5] for an off-axis source location P, the same conclusion is reached, but additionally the two foci f_m and f_s are shown to actually be line foci. Figure 5.6 (after Fig. 16-17 of Longhurst, 1967) shows a spherical concave mirror $\mathrm{M_1M_2}$ with radius R, center C, and apex O. P denotes the location of the off-axis point source. Since the source itself never exhibits astigmatism, the source "foci"[6] are the same in both the sagittal and the meridional directions and equal the distance of the source to the apex, i.e., $p_\mathrm{s} = p_\mathrm{m} \equiv p = \overline{\mathrm{PO}}$. T and S mark the tangential (meridional) and sagittal foci with distances $q_\mathrm{m} = \overline{\mathrm{OT}}$ and $q_\mathrm{s} = \overline{\mathrm{OS}}$, respectively, from O. The line PC may be taken as an axis of the extended spherical surface through point A. While S is the sagittal focus of the primary ray reflected in O, rays reflected in $\mathrm{M_1}$ or $\mathrm{M_2}$ exhibit a small aberration and focus in $\mathrm{S_1}$ and $\mathrm{S_2}$, respectively, on the axis ACP. When rotating the diagram around this axis ACP, the rays $\mathrm{PM_1}$ and $\mathrm{PM_2}$ build a sagittal fan of rays, while S, $\mathrm{S_1}$, and $\mathrm{S_2}$ remain stationary in space, defining the sagittal focal line $\mathrm{S_1S_2}$. On the other hand, the tangential fan of rays described by $\mathrm{PM_1M_2}$ traces a tangential (meridional) focal line through T (perpendicular to the plane of the diagram) during the same rotation around ACP (Longhurst, 1967).

Quantitatively, first consider the sagittal focus at S. In the figure (Fig. 5.6) the triangle $\triangle$POS consists of two sub-triangles $\triangle$POC and $\triangle$COS. Equating their areas

$$\triangle\mathrm{POS} = \frac{1}{2}p_\mathrm{s}q_\mathrm{s}\sin 2I_\mathrm{pr} = \frac{1}{2}p_\mathrm{s}R\sin I_\mathrm{pr} + \frac{1}{2}Rq_\mathrm{s}\sin I_\mathrm{pr} = \triangle\mathrm{POC} + \triangle\mathrm{COS},$$

using the identity $\sin 2x = 2\sin x\cos x$, and dividing by $p_\mathrm{s}Rq_\mathrm{s}\sin I_\mathrm{pr}$ leads to the optical

[5] see Michette (1986) for an alternative approach

[6] The sagittal and meridional distances, p_s and p_m, of the source to the mirror are not truly foci, but describe the position where the source is *in focus*. To simplify the language, p_s and p_m, and in analogy q_s and q_m, here are referred to as "foci". See also Section 5.5.1.

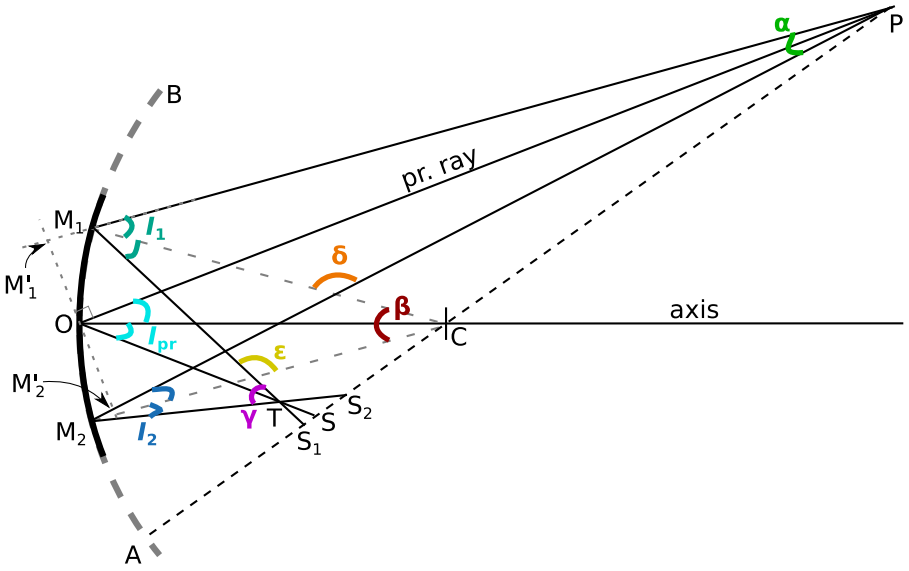

Figure 5.6: Astigmatism of a spherical mirror. — After Longhurst (1967, Fig. 16-17).

equation for the *sagittal* focus, S,

$$\frac{1}{p_s} + \frac{1}{q_s} = \frac{2\cos I_{\mathrm{pr}}}{R} = \frac{2\sin\theta}{R} \tag{5.14}$$

where $\theta = 90° - I_{\mathrm{pr}}$ is the glancing angle relative to the tangent as commonly used for Bragg's law.

For the derivation of the tangential or meridional focus, take I_1 and I_2 as the angles of incidence at M_1 and M_2, and the angles α, β, γ, δ, and ϵ as in the figure: α, β, and γ are the opening angle of the mirror segment $\mathrm{M}_1\mathrm{M}_2$ at the source position P, the center of the sphere C, and the image (focal) point T, respectively; δ is the obtuse angle between $\mathrm{M}_1\mathrm{C}$ and $\mathrm{M}_2\mathrm{P}$, while ϵ is between $\mathrm{M}_2\mathrm{C}$ and $\mathrm{M}_1\mathrm{T}$. From simple triangular considerations, it follows:

$$\left.\begin{array}{ll} 90° - \delta = I_1 + \alpha = I_2 + \beta & \Rightarrow I_1 - I_2 = \beta - \alpha \\ 90° - \epsilon = I_1 + \beta = I_2 + \gamma & \Rightarrow I_1 - I_2 = \gamma - \beta \end{array}\right\} \Rightarrow \alpha + \gamma = 2\beta.$$

Expressing the angles through the distances at hand leads to the focal relation. The opening angle β at the center C of the sphere has the same proportion to a full circle with 2π as the arc length $\overline{\mathrm{M}_1\mathrm{M}_2}$ has to the circumference $2\pi R$. Therefore,

$$\beta = \frac{\overline{\mathrm{M}_1\mathrm{M}_2}}{R}.$$

If the mirror surface $\mathrm{M}'_1\mathrm{M}'_2$ were perpendicular to the principle ray, parallax would tell us that $\tan\alpha = \mathrm{M}'_1\mathrm{M}'_2/p_{\mathrm{m}}$. The real mirror surface, however, is at an angle, projecting $\mathrm{M}'_1\mathrm{M}'_2 = \mathrm{M}_1\mathrm{M}_2\cos I_{\mathrm{pr}}$. Additionally, the mirror $\mathrm{M}_1\mathrm{M}_2$ is small compared to the source distance p_{m}, allowing for small angle approximation. It follows

$$\alpha = \frac{\mathrm{M}_1\mathrm{M}_2\cos I_{\mathrm{pr}}}{p_{\mathrm{m}}} \quad \text{and similarly for the image} \quad \gamma = \frac{\mathrm{M}_1\mathrm{M}_2\cos I_{\mathrm{pr}}}{q_{\mathrm{m}}}.$$

Combining these angles gives the optical equation for the tangential or *meridional* focus, T, as

$$\frac{1}{p_\mathrm{m}} + \frac{1}{q_\mathrm{m}} = \frac{2}{R\cos I_\mathrm{pr}} = \frac{2}{R\sin\theta}. \tag{5.15}$$

5.3 von Hámos Geometry

In order to increase the intensity falling onto the detector, it is desirable to attempt to focus the reflected X-rays into a small image. Focusing is generally achieved through reflection from curved surfaces and, in principle, there are two directions in which curvature can be added to flat crystals: perpendicular or parallel to the dispersion direction. Aside from imaging errors, cylindrical crystals with the curvature perpendicular to the dispersion direction act like flat crystals in regards to X-ray diffraction. Therefore, these shall be discussed first.

While bent crystal spectrometers have been proposed and used earlier (see, e.g., Cauchois, 1932, for an overview), von Hámos & Stschwerbina (1933) were the first to employ this particular geometry. The von Hámos geometry was first proposed by Gouy (1916) and is explained mathematically in von Hámos (1933). Isotropic radiation propagating from a point source keeps its divergence when reflected by a flat crystal (Fig. 5.7). The idea of the von Hámos geometry is to bend the crystal cylindrically around an axis through the source positions and parallel to the crystal surface to focus the diverging rays back down into an image point (Fig. 5.8). Rays of the same wavelength λ from an on-axis point source clearly still follow Bragg's law and are focused into the same point. The only requirements for the crystal are that the planes of the lattice stay parallel to the tangential plane of the cylinder in each point when bending the crystal, and the dimensions of the mosaic elements of the lattice are small compared to the radius of curvature (von Hámos, 1933).

As the imaging happens perpendicular to the dispersion direction, the spectrometer also works for line sources, such as EBIT or a slit in front of an extended source, as long as they are oriented perpendicular to the dispersion accordingly. To describe the properties of the image in terms of location, shape, dispersion, and image defects affecting the spectral resolution, we follow the geometrical considerations of von Hámos (1933). An alternative approach to derive the relations is taken by van den Berg & Brinkman (1955).

To set up the geometry, assume a monochromatic source, where λ matches the reflection angle θ through Bragg's law, and place it on the diameter of a half-cylinder (Fig. 5.9). For convenience, the coordinate system has its center (denoted as O) on the cylinder axis, the cylinder axis aligns with the x-axis, and the line source coincides with the y-axis. Choose an arbitrary point on the line source with the coordinates P ($x = 0$; $y = y_0$; $z = 0$). Radiation emitted from this point P under an azimuth angle ϕ (direction in the zy-plane) is reflected in F at a glancing angle θ in the radial plane (fulfilling Bragg's law; note that the use of ϕ and θ to denote the azimuthal and Bragg angle, respectively are exchanged compared to von Hámos (1933) in order to associate the Bragg angle consistently with θ throughout this chapter) to form an image in Q. To describe the spectroscopic properties

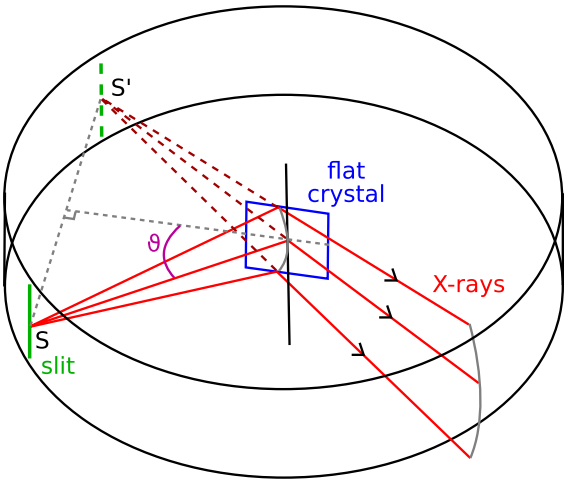

Figure 5.7: Reflection of a point source off a flat crystal. The direction of the rays changes but their spread does not. The reflected rays can be perceived as coming from a virtual point behind the crystal. — After van den Berg & Brinkman (1955).

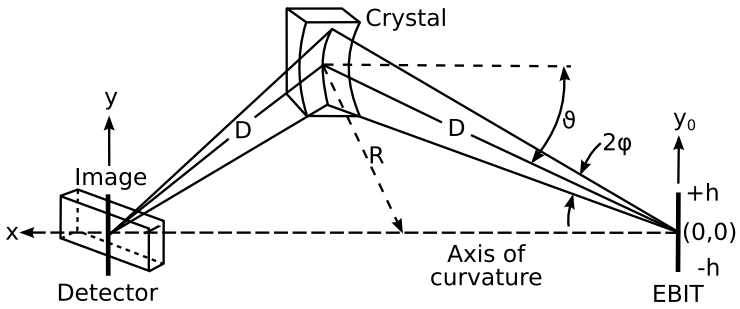

Figure 5.8: Sketch of the von Hámos geometry. The isotropic radiation (mono-chromatic wavelength λ) of a point source is imaged back into a point by the curvature of the crystal. — After Beiersdorfer et al. (1990a).

of the crystal, we need to know this image location in the source plane, i.e., Q ($x = x_1$; $y = y_1$; $z = 0$), as a function of the parameters of the line source and the crystal dimensions (lattice spacing $2d$, radius of curvature R). Figure 5.9 displays these points on the half-cylinder of the crystal and their respective projections onto the zy-plane in $x = 0$ and the zx-plane in $y = 0$. Points in the zy-projection are denoted with primed versions of their letter representation in the three-dimensional view, while those in the zx-projection are denoted with double-primed letters.

First, we derive y_1, as this can be done entirely in the zy-plane, while x_1 requires both planes. The projection of F in the zy-plane is the point m′ ($x = 0$; $y = R\sin\phi$; $z = R\cos\phi$). Draw a line through m′O, and drop a perpendicular from Q′ onto this line (intersecting it in point H) and from P′ (intersecting in G). Then Q′H and P′G both have angle ϕ to the y-axis. During reflection, incident and reflection angle are equal. In the zy-projection, therefore, $\measuredangle$Q′m′O = $\measuredangle$Om′P′. With three identical angles, triangles $\triangle$Q′Hm′ and $\triangle$P′Gm′

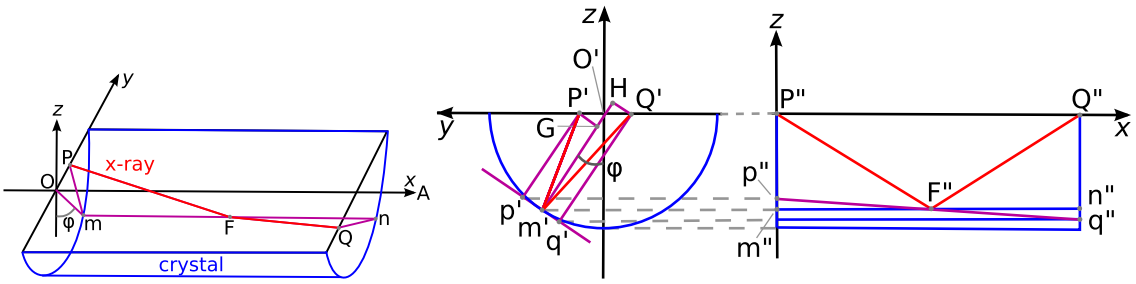

Figure 5.9: Von Hámos geometry. Left: three-dimensional view of the cylindrical crystal (blue) and a reflected X-ray beam (read); Right: projections of the reflection into the zy- and the zx-plane. Note that ϕ and θ are swapped compared to the paper in order to keep θ associated with the Bragg angle. — After von Hámos (1933).

are similar and thus the ratios of the triangle edges are the same in both triangles:

$$\frac{\overline{\mathrm{P'G}}}{\overline{\mathrm{m'G}}} = \frac{\overline{\mathrm{Q'H}}}{\overline{\mathrm{m'H}}} \quad \Rightarrow \quad \frac{y_0 \cos\phi}{R - y_0 \sin\phi} = \frac{-y_1 \cos\phi}{R - y_1 \sin\phi}$$

where the last part follows from trigonometry. Note that y_1 is negative such that the minus sign is necessary to get the absolute value for the length $\overline{\mathrm{OQ'}}$. Solving for y_1 gives us the y-coordinate of the image Q as

$$y_1 = \frac{-y_0 R}{R - 2y_0 \sin\phi}. \tag{5.16}$$

To derive x_1, first consider the zx-plane where $\overline{\mathrm{P''Q''}} = \overline{\mathrm{m''n''}} = \overline{\mathrm{m''F''}} + \overline{\mathrm{F''n''}}$, as the length of the cylinder is constant. For $\overline{\mathrm{m''F''}}$ Pythagoras theorem determines the length from the triangle $\triangle$pFm, but note that this triangle is not in the xz plane such that both the y- and z-component of p need to be taken into account. From the triangle $\triangle$pPF follows

$$\overline{\mathrm{pF}} = \overline{\mathrm{Pp}} \cdot \cot\theta = (R - y_0 \sin\phi)\cot\theta.$$

The length $\overline{\mathrm{pm}}$ equals $\overline{\mathrm{P'G}} = y_0 \cos\phi$. Combined we get

$$\overline{\mathrm{m''F''}} = \sqrt{\overline{\mathrm{pF}}^2 - \overline{\mathrm{pm}}^2} = \sqrt{(R - y_0 \sin\phi)^2 \cot\phi - y_0^2 \cos^2\phi}.$$

The projection into the zy-plane at $x = x_1$ looks exactly the saem as in $x = 0$, thus $\overline{\mathrm{n''F''}}$ is analogue to $\overline{\mathrm{m''F''}}$ by substituting y_1 for y_0 and inserting Eq. 5.16

$$\overline{\mathrm{n''F''}} = \sqrt{(R - y_1 \sin\phi)^2 \cot\theta - y_1^2 \cos^2\phi} = \frac{R}{R - 2y_0 \sin\phi} \cdot \overline{\mathrm{m''F''}}.$$

Finally, with $x_1 = \overline{\mathrm{P''Q''}}$, we find

$$x_1 = \frac{2(R - y_0 \sin\phi)}{R - 2y_0 \sin\phi} \sqrt{(R - y_0 \sin\phi)^2 \cot^2\theta - y_0 \cos^2\phi}. \tag{5.17}$$

Generally, the radius of curvature R is chosen much larger than the length of the slit. With a power series expansion (Taylor) in $y_0/R \ll 1$ up to (excluding) the quadratic term, the formulae for x_1 and y_1 simplify to (Beiersdorfer et al., 1990a)

$$\begin{aligned} x_1 &= 2R\cot\theta\left\{1+\left[\left(1+\frac{1}{2\cot^2\theta}\right)\sin^2\phi-\frac{1}{2\cot^2\theta}\right]\frac{y_0^2}{R^2}\right\} \xrightarrow{\phi=0} 2R\cot\theta\left[1-\frac{1}{2\cot^2\theta}\frac{y_0^2}{R^2}\right] \\ y_1 &= -y_0-2\frac{y_0^2}{R}\sin\phi. \end{aligned} \tag{5.18}$$

For a small range of azimuthal angles around $\phi = 0$, the image of a slit on the y-axis has the form of a parabola. For points further away from the cylinder axis, the shape of the image parabola changes slightly, causing astigmatism that broadens the composite image (Beiersdorfer et al., 1990a). All of these parabolas, however, have the common point $x = 2R\cot\theta$ on the x-axis ($y_0 = 0$) for monochromatic light. The imaging error due to astigmatism is determined by the azimuth ϕ dependent portion of the image location (von Hámos, 1933), i.e.,

$$\Delta x_1 = 2R\cot\theta\left(1+\frac{1}{2\cot^2\theta}\right)\sin^2\phi\,\frac{y_0^2}{R^2} \tag{5.19}$$

$$\Delta y_1 = -2\sin\phi\,\frac{y_0^2}{R}. \tag{5.20}$$

The opening angle $2\phi_{\max}$ of the crystal limits the range of possible azimuthal angles $\phi_{\max}$ and is one way to control the magnitude of the image error. Reducing the opening angle of the crystal comes with a loss in the number of reflected rays and reduces the image intensity due to the reduced solid angle. A larger contributing factor to the image error is the length y_0 of the slit relative to the cylinder radius R. For a perfect point source, the positional uncertainty of the image vanishes, but again a longer slit increases the total reflected photon flux. Since x is the dispersion direction, the error Δx_1 limits the resolving power $\lambda/\Delta\lambda$. The targeted resolving power is, therefore, a good defining factor for a compromise between intensity and the product ($\sin\phi\, y_0/R$) of opening angle and slit length.

For the relationship between Δx_1 and $\Delta\lambda$, we first need to find the dispersion. All parabolas for a given wavelength have the common apex point $x_1 = 2R\cot\theta$, where θ has to fulfill Bragg's law $\sin\theta = n\lambda/2d$. With the identity $\cot(\arcsin(x)) = \sqrt{1-x^2}/x$, the λ dependent version of x_1 simplifies to

$$x_1 = 2R\sqrt{\left(\frac{2d}{n\lambda}\right)^2-1}. \tag{5.21}$$

The dispersion then is

$$\frac{\mathrm{d}\lambda}{\mathrm{d}x_1} = \left(\frac{\mathrm{d}x_1}{\mathrm{d}\lambda}\right)^{-1} = \frac{\lambda^2}{2R}\,\frac{n}{2d}\sqrt{1-\left(\frac{n\lambda}{2d}\right)^2} = \frac{\lambda}{2R}\cos\theta\sin\theta. \tag{5.22}$$

Approximating the dispersion as $\Delta\lambda/\Delta x_1$ and using Eq. 5.19 in its wavelength dependent form (substituting $\cot\theta$ by $\sqrt{(2d/n\lambda)^2-1}$ as in Eq. 5.21) leads to the spectrometer parameters as a function of resolving power

$$\sin^2\phi\,\frac{y_0^2}{R^2} = \frac{\Delta\lambda}{\lambda}\,\frac{1}{\left[1-\frac{1}{2}\left(\frac{n\lambda}{2d}\right)^2\right]}. \tag{5.23}$$

In other words, the length of the slit gives a resolving power of $\Delta\lambda \gtrsim R^2/y_0^2$ (Beiersdorfer et al., 1990a). The width of the source Δx_0 superimposes shifted versions of the same image at x_1. The effect on the resolving power similarly follows from the dispersion (Eq. 5.22) by $\Delta\lambda/\Delta x_0$ to

$$\frac{\lambda}{\Delta\lambda} = \frac{2R}{\Delta x_0}\left(\frac{n\lambda}{2d}\sqrt{1-\left(\frac{n\lambda}{2d}\right)^2}\right)^{-1} = \frac{2R}{\Delta x_0}\,\frac{1}{\cos\theta\sin\theta}. \tag{5.24}$$

The final limiting factor to the resolving power is the spatial resolution Δs of the detector. Since on the cylinder axis the distance D between source and image is $x = 2R\cot\theta$, the distance between crystal and detector (respectively between crystal and source) follows from trigonometry ($D = x/2/\cos\theta$) to $D = R/\sin\theta$. At the center of the detector, the resolving power is then limited by (Beiersdorfer et al., 1990a)

$$\frac{\lambda}{\Delta\lambda} = \frac{2R}{\Delta s\cos\theta} \tag{5.25}$$

and drops further by $\sin(\theta-\alpha)/\sin\theta$ at the edge of the detector where $\alpha \approx \ell\sin\theta/(2R)$ with detector length ℓ, in case the detector is mounted perpendicular to the line of sight. Because the detector distance is $D = R/\sin\theta$, the resolving power of the von Hámos spectrometer does not drop at small Bragg angles, contrary to the Johann geometry. Instead of loosing resolving power, the loss at small angles is in collected photon flux (Beiersdorfer et al., 1990a).

5.4 Johann Geometry

Although previous studies had not been very successful in designing cylindrically bent crystal spectrometers and one author even showed that a geometrically exact solution is not possible, Johann (1931) successfully proposed a geometry with the crystal curvature in the plane of dispersion. Johann (1931)'s achievement was to realize that an exact solution is not necessary as long as the aberrations are small enough. He adapted the Rowland circle geometry, originally designed for concave gratings (Rowland, 1882, 1883), to cylindrically bent crystals. In short, the Rowland circle is a circle of radius $r = R/2$, where R is the crystal radius of curvature. It is an image circle and touches the crystal in its apex B (Fig. 5.10*a*). X-rays of a certain wavelength λ are reflected only if they fulfill the Bragg condition, where, in this cylindrical geometry, the Bragg angle θ is measured towards the tangent of the crystal in the point of reflection. Then, $\phi = 90° - \theta$

is the angle of the X-ray to the radius of the crystal. An X-ray coming from point K on the Rowland circle is reflected in the crystal apex B to intersect the Rowland circle in point L (Fig. 5.10*b*). The inscribed angle theorem postulates that any point A on the Rowland circle sees the arc KM (M being the center of the crystal circle) under the very same angle $\measuredangle\mathrm{KAM} = \phi$ (Fig. 5.10*c*). A ray reflected in A then also intersects the Rowland circle in L, since the arcs KM and ML have equal length. The reflecting crystal surface, however, is displaced a short distance behind the Rowland circle. The path of the rays is therefore translated in parallel along the chord AM to be reflected in A′ on the crystal surface (Fig. 5.10*d*). The rays now intersect the Rowland circle in K′ (source side) and L′ (image side). This shows that an exact solution does not exist for this spectrometer setup, but as long as the distances KK′ and LL′ are small, it will still work for spectroscopy. Clearly, the positional uncertainty depends on the length of the crystal. With simple geometry, the corresponding limit to the resolving power can be derived (Johann, 1931).

Reflection of a crystal segment C′ on the other side of the apex B has a similar effect in shifting the image point on the Rowland circle (Fig. 5.10*e*). This shift actually has the same direction as the shift caused by reflection in A′ such that reflection in the apex B produces a sharp, well-defined edge of light in L (Fig. 5.10*e*, purple line).

Due to the inscribed angle theorem discussed above, in first approximation, the entire crystal surface reflects light simultaneously only depending on wavelength, i.e., Bragg angle, and focuses the divergent rays originating on a single point of the Rowland circle back into a single, though slightly broadened towards longer wavelength, point on the circle. With small enough opening angles, the Johann geometry therefore brings an increase in observed intensity without sacrificing much resolution. An added benefit is that this spectrometer geometry does not require a slit in front of the source (Johann, 1931). In fact, because of the inscribed angles, each point on the Rowland circle (on one side of the symmetry line MB) corresponds to a different Bragg angle on the crystal. Therefore, extended sources are required to extend the observable wavelength range. Otherwise the accessible wavelength range at a single setting is limited by the size of the focal spot on the Rowland circle.

The dispersion relation of the Johann geometry is defined by the sharp long wavelength edge of the reflected rays, i.e., by the chord LB. The chord LB defines an isosceles triangle with the center O of the Rowland circle, with the acute angles $\phi = 90° - \theta$ (Fig. 5.10*f*). Therefore, the central angle $\measuredangle\mathrm{BOL} = 2\theta$ such that the dispersion retains a simple sine dependence along the Rowland circle (Johann, 1931).

The expected maximum line width is determined by the distance $a = \overline{\mathrm{SP}}$ (Fig. 5.10*g*) between the crystal and the Rowland circle at the edges of the crystal (Johann, 1931). For fixed crystal radii, this distance gets larger with longer crystals, i.e., this distance needs to be determined as a function of opening angle. Let $\alpha/2$ be the opening angle of the half crystal arc PB as seen at the center of the crystal circle (Fig. 5.10*g*). Then, because of the inscribed angle theorem, the crystal arc projected onto the Rowland circle as arc SB spans the angle α at the center of the Rowland circle. In trigonometry, the distance between a unit circle and its tangent is described by the function $\mathrm{exsec}(x) = \sec(x) - 1$.

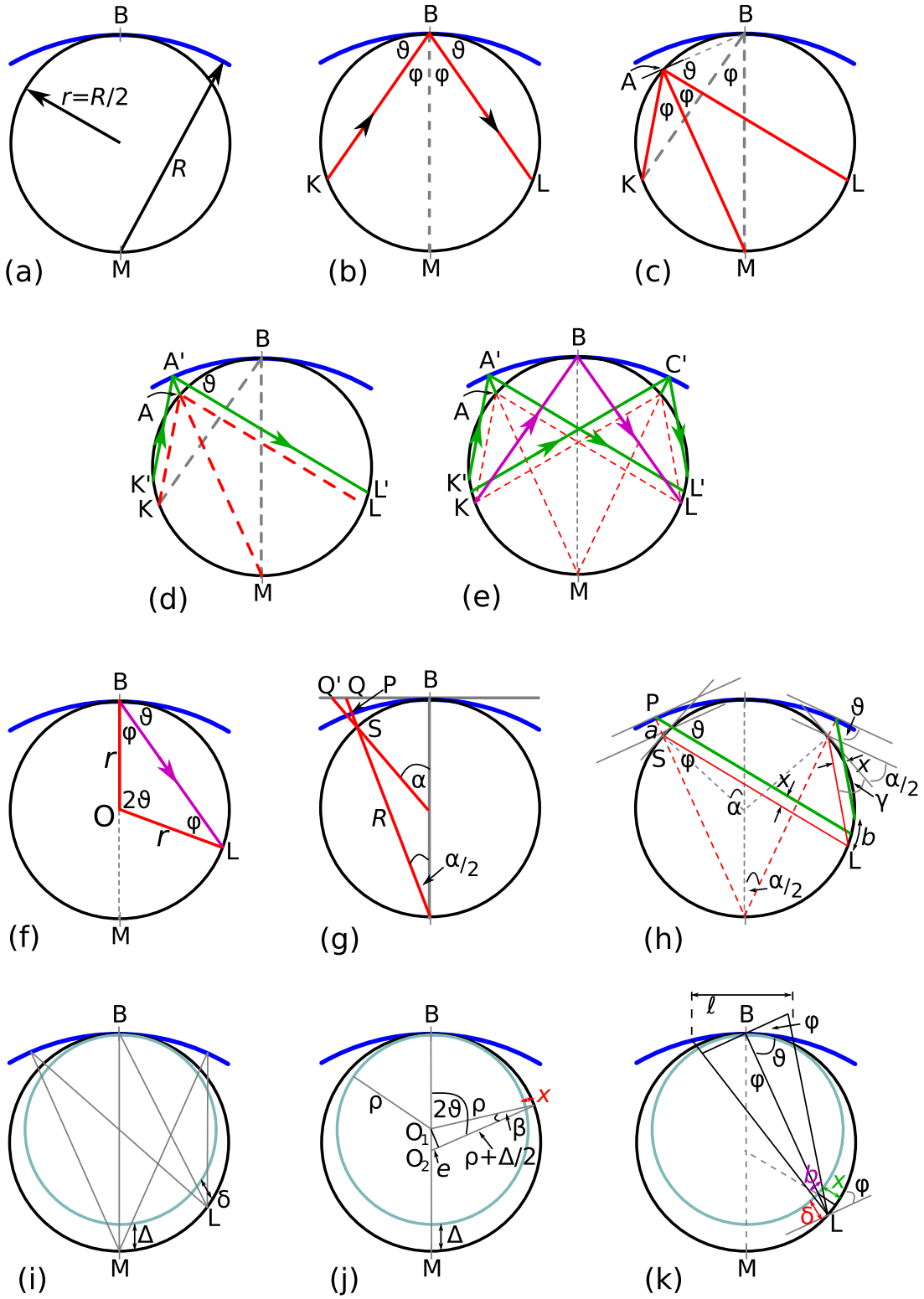

Figure 5.10: Johann geometry after sketches from Johann (1931). The blue arc through B represents the crystal bent to a radius R (center M). The black circle corresponds to the Rowland circle of radius $r = R/2$. — Drawings after Johann (1931).

Therefore (Johann, 1931),

$$\overline{\mathrm{QP}} = R\cdot(\sec(\alpha/2)-1) = 2r\cdot\left(\frac{1}{\cos(\alpha/2)}-1\right) \tag{5.26}$$

$$\sim 2r\cdot\left(\left(1-\frac{\alpha^2}{2^2\cdot 2!}\right)^{-1}-1\right) = 2r\left(1+\frac{\alpha^2}{8}-1\right) \sim \frac{1}{4}r\alpha^2 \tag{5.27}$$

where the first approximation uses the series expansion of cosine up to the quadratic term and the second approximation uses the series expansion of $1/(1-x^2)$ around $x=0$ up to the second term, i.e., it is assumed that the opening angle α of the crystal is small. This is a valid assumption since typically large crystal radii R are used (e.g., Section 5.5). Similarly,

$$\overline{\mathrm{Q'S}} = r(\sec\alpha-1) \sim 1/2\cdot r\alpha^2 = 2\cdot\overline{\mathrm{QP}}. \tag{5.28}$$

Since for small angles $\overline{\mathrm{Q'S}} \to \overline{\mathrm{QS}}$, the distance between crystal and Rowland circle follows as

$$a = \overline{\mathrm{SP}} = \overline{\mathrm{QS}} - \overline{\mathrm{QP}} = 2\cdot\overline{\mathrm{QP}} - \overline{\mathrm{QP}} = \overline{\mathrm{QP}} = \frac{1}{4}r\alpha^2. \tag{5.29}$$

Additionally, the line width, represented by the arc b depends on the angle under which the reflected rays strike the X-ray detector (Fig. 5.10*h*): Let x be the parallel shift of the reflected ray. This shift is identical for reflection on both edges of the crystal, as we assume a symmetrical geometry. Nevertheless, as seen from the sketch, this distance x is projected into arcs of different lengths when coming from the source (b_s) or image (b_i) side of the crystal. To express the shift x in terms of known values, we can take a as the hypotenuse of a right triangle such that $x = a\sin\phi = a\cos\theta$. Next we need to find the projection angles of x onto the Rowland circle. The point S on the Rowland circle together with the centers of the crystal and image circles defines an isosceles triangle, i.e., the radii of the image and crystal circles span an angle of $\alpha/2$ at the reflection point on the Rowland circle. Therefore, the tangent onto the image circle and the tangent onto the crystal along the chord MC also span an angle of $\alpha/2$ between them, such that the angle of the rays striking the detector are at most $\alpha/2$ different from the Bragg reflection angle (Johann, 1931). It follows that on the image side, the angle γ_i of the reflected ray relative to the tangent of the Rowland circle is $\gamma_\mathrm{i} = \theta - \alpha/2$. Similarly, on the source side the corresponding angle is $\gamma_\mathrm{s} = \theta + \alpha/2$. For small arcs b, the circle segment is close to a straight line of the same length. Therefore, again using right-angled triangles, $x = b_\mathrm{i}\sin(\theta-\alpha/2)$ and $x = b_\mathrm{s}\sin(\theta+\alpha/2)$. On average, for small opening angles, thus, $x \approx b\sin\theta$. Substituting x and expressing the opening angle $\alpha = \ell/R = \ell/(2r)$ in terms of the crystal length ℓ then leads to the line broadening b due to the distance between the crystal and the Rowland circle as (Johann, 1931)

$$b = a\cot\theta = \frac{1}{4}r\alpha^2\cot\theta = \frac{1}{16}\frac{\ell^2}{r}\cot\theta = \frac{1}{8}\frac{\ell^2}{R}\cot\theta. \tag{5.30}$$

This error is small at large Bragg angles θ but at small Bragg angles needs to be reduced by employing shorter crystals. In either case $\ell \ll R$, since small angle approximation for α was used in the derivation.

The line width b corresponds to the image error due to reflection off a crystal element at a distance $1/2\ell$ from the crystal center. Increasing the crystal length does not increase the intensity of points on the Rowland circle closer to L, but rather the increased observed intensity is due to the additional line width. This information can be used to derive the expected line shape of the reflection. It scales as $1/\sqrt{x}$, where x is the distance on the Rowland circle from the principal ray in L (Johann, 1931).

Further line broadening can be caused by alignment issues. The derivation of b assumed that the crystal touches the Rowland circle in B and that the detector follows the curvature of the circle (Johann, 1931). If either the crystal or the detector is shifted parallel to the Rowland circle by a distance a, then the lines shift by $d = a\cot\theta$ (in analogy to the derivation of b). Furthermore, it is possible that the crystal focus differs from the image circle of the detector such that there is a difference $\Delta = 2\rho - R$ between the crystal radius R and the detector circle diameter 2ρ (Fig. 5.10*i*). This difference results in a symmetric line broadening b. For the limit of $\theta = 90°$, this broadening has, from the intercept theorem (assuming a small opening angle to neglect the curvature), the size $b = \ell/R \cdot \Delta$ (Johann, 1931). For smaller Bragg angles θ the same concept applies, but we need to know how $\mathrm{BM} = R \to \mathrm{BL}$ and $\Delta \to \delta$ scale as a function of θ. The chord BL changes as $\mathrm{BL} = 2\rho\cos\phi = 2\rho\sin\theta \sim R\sin\theta$, assuming that $\Delta \ll R$. To derive δ, first we find the distance x between the two circles in the radial direction of the smaller detector circle (Fig. 5.10*j*). From the triangle we find

$$(\rho + x)\cos\beta = (\rho + \Delta/2) - e \quad \text{and} \quad e = \overline{\mathrm{O_1O_2}}\cos(2\theta) = \frac{\Delta}{2}\cos(2\theta). \tag{5.31}$$

Again, assuming only a small difference between the circles, i.e., small Δ, means $\cos\beta \to 1$. Therefore, from these two equations follows (Johann, 1931)

$$x = \frac{\Delta}{2}(1 - \cos(2\theta)). \tag{5.32}$$

Since the reflected ray intersects the Rowland circle under the angle θ in L (Fig. 5.10*k*), δ relates to x as $\delta = x/\sin\theta$. Inserting both BL and δ into b derived from the intercept theorem results in the line broadening due to focusing differences (Johann, 1931)

$$b = \frac{\ell\delta}{\mathrm{BL}} = \frac{\ell}{R}\frac{x}{\sin^2\theta} = \frac{\ell}{R}\frac{\Delta}{2}\frac{1-\cos(2\theta)}{\sin^2\theta} = \frac{\ell\Delta}{R} \tag{5.33}$$

where the latter uses the identities $\cos(2\theta) = \cos^2\theta - \sin^2\theta$ and $\cos^2\theta + \sin^2\theta = 1$. Note that this error is independent of the Bragg angle θ and therefore no correction is necessary for relative wavelength measurements. For absolute wavelength measurements it should be noted that the lattice constant decreases a little upon bending the crystal (Johann, 1931).

The uncertainties as derived above are in units of length. To determine the resolving power, $\lambda/\Delta\lambda = \tan\theta/\Delta\theta$, it is more convenient to translate these into uncertainties on the observed Bragg angle. Beiersdorfer (1988) lists these as

$$\Delta\theta_0 = 2\arctan\left(\frac{d/2}{R\sin\theta}\right) \tag{5.34}$$

due to the detector channel size d for the detector channel that touches the Rowland circle;

$$\Delta\theta_1 = \frac{\ell^2}{8R^2 \tan\theta} \tag{5.35}$$

due to focusing errors originating from the length ℓ of the crystal (related to Eq. 5.30);

$$\Delta\theta_2 = \frac{h^2}{8R^2 \sin\theta \cos\theta} \tag{5.36}$$

due to height h of the crystal (Schnopper & Kalata, 1969);

$$\Delta\theta_3 = \frac{\ell \ell_\mathrm{d}^2}{8R^3 \sin^2\theta} \tag{5.37}$$

due to a flat X-ray detector of length ℓ_d being tangent to the Rowland circle; and

$$\Delta\theta_4 = \frac{\Delta d \cdot \ell}{R^2 \sin\theta} \tag{5.38}$$

due to the detector being displaced from the Rowland circle by Δd.

In the cylindrically bent version of the Johann geometry, the reflected rays from a point source on the Rowland circle are still diverging out of the plane of the Rowland circle, similar to the diverging reflection of a flat crystal spectrometer (see Fig. 5.7).

5.5 OHREX & EBHiX Spherical Crystal Spectrometers

Beiersdorfer et al. (2016b) designed an imaging, high-resolution, spherical crystal spectrometer, dubbed the Orion high-resolution X-ray (OHREX) spectrometer, for diagnostics of high-density plasmas at the Orion laser facility (Hopps et al., 2015). X-ray spectroscopy is the traditional tool for plasma diagnostics of laser-produced plasmas (Nagel et al., 1974), where, generally speaking, the electron density is derived from the observed line profile due to Stark broadening and the electron temperature from the relative intensity of resonance lines to their dielectronic recombination satellites (Hammel et al., 1992, 1993; Mancini et al., 2013). In addition to high resolving powers in order to resolve these features, OHREX requires large effective area, since the high-powered short-pulse laser produces very small plasmas that radiate only for a few picoseconds, and time resolution is desired. With minor modifications, the spectrometer was developed for use at EBIT and dubbed the EBIT high-resolution X-ray (EBHiX) spectrometer (Beiersdorfer et al., 2016c), which also is a relatively weak source. Calibration and testing of OHREX has been done by Beiersdorfer et al. (2016c), Brown et al. (2016), and Hell et al. (2016a).

5.5.1 Design Considerations

General

The general design of the OHREX spectrometer (Beiersdorfer et al., 2016b) derives from designs for spectrometers used at tokamaks for imaging of their large plasmas (Bitter

et al., 1999, 2004; Hill et al., 2008) and at the Titan laser facility (Chen et al., 2014). It is also similar to the design of a proposed spectrometer for ITER (Beiersdorfer et al., 2010). In order to collect as much flux as possible, the basic idea for the spectrometer design is to combine the spatial focusing of the cylindrical von Hámos geometry with the spectral focusing of the cylindrical Johann geometry into a spherical crystal. For a spherical crystal the focusing properties of the spherical mirror also apply for those rays that fulfill the Bragg condition (Eq. 5.1). In this case, the meridional focus (Eq. 5.15) is associated with the spectral focus and the sagittal focus (Eq. 5.14) with the spatial focus.

In their design description, Beiersdorfer et al. (2016b) assume that a spherically bent crystal has four foci, two each for the location of the image (q_m, q_s) and the location of the source (p_m, p_s); or, in a different pairing, two each for the meridional/horizontal focusing associated with spectral focusing (p_m, q_m) and for the sagittal/vertical focusing associated with spatial focusing (p_s, q_s). This is an attempt in simplifying the language. More traditionally, spherical crystals are described having two foci, the meridional focus $f_\mathrm{m} = 1/2R\sin\theta$ on the right hand side of Eq. 5.15 and the sagittal focus $f_\mathrm{s} = R/(2\sin\theta)$ on the right hand side of Eq. 5.14, while p_m and p_s would be the location where the source is *in focus* and q_m and q_s the location where the image is *in focus*, in the meridional and sagittal plane, respectively (*cf.* Section 5.2).

Maximizing the observed intensity requires that the the meridional image location q_m coincides with the spectral focus of the Johann geometry, i.e., falls onto the Rowland circle at

$$q_\mathrm{m} = R\sin\theta. \tag{5.39}$$

At the same time, the signal-to-noise ratio of the image is maximized if the image covers only a small area on the detector, i.e., the spatial (sagittal) image q_s should coincide with the spectral image location, again on the Rowland circle, with

$$q_\mathrm{s} = q_\mathrm{m} = R\sin\theta. \tag{5.40}$$

For the image to be in focus on the Rowland circle, the spherical mirror equations directly requires the source position to be

$$p_\mathrm{m} = R\sin\theta \tag{5.41}$$

$$p_\mathrm{s} = -\frac{R\sin\theta}{\cos(2\theta)} = -\frac{p_\mathrm{m}}{\cos(2\theta)}. \tag{5.42}$$

By design, the image (q_m, q_s) is focused into a point. Therefore, the source foci have to be line foci (Fig. 5.11), in a reversal of the propagation direction in the derivation of the focus equations for a spherical mirror (Fig. 5.6, Section 5.2). From these equations it is also clear that the sagittal source location is only real, if $\theta > 45°$; for $\theta = 45°$ the rays are parallel and for $\theta < 45°$ the rays diverge, making a virtual image with $p_\mathrm{s} < 0$. OHREX, therefore, operates at a Bragg angle $\theta > 45°$ (Beiersdorfer et al., 2016b).

Also, the source locations (p_m, p_s) in the meridional and sagittal planes do not generally coincide at any Bragg angles of practical use. However, this is actually advantageous: as illustrated again in Fig. 5.12, in the Johann geometry (Section 5.4) each point on the

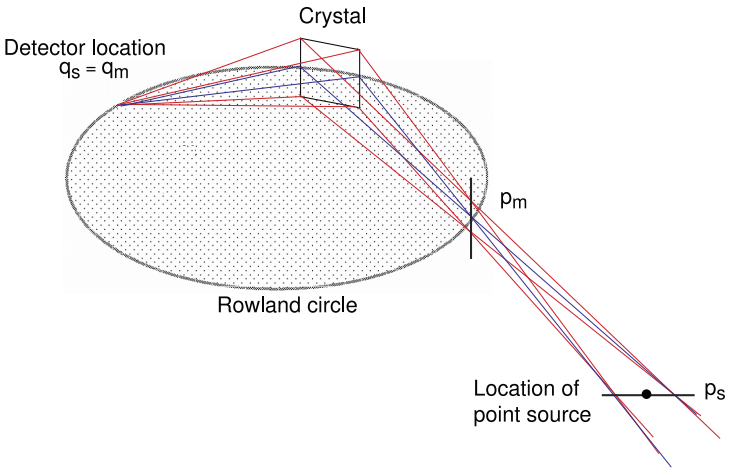

Figure 5.11: Focusing of OHREX. From — Beiersdorfer et al. (2016b, Fig. 1).

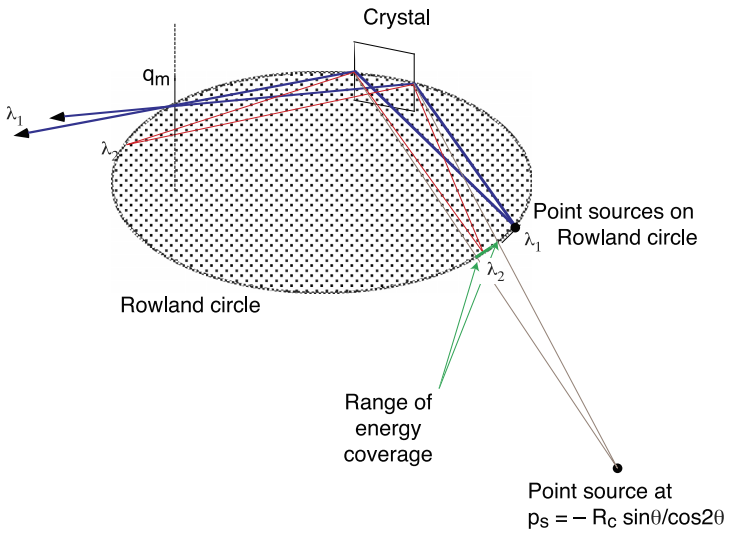

Figure 5.12: Energy range. — From Beiersdorfer et al. (2016b, Fig. 2).

Rowland circle sees the crystal at a different Bragg angle, corresponding to a specific X-ray wavelength. Effectively, therefore, for each wavelength a point on the Rowland circle makes the point source that results in the focused meridional image (q_m), automatically fulfilling the condition for p_m. Thus, having the source focused on the Rowland circle in p_m would result in a monochromatic image. On the other hand, placing the source at the sagittal source position p_s illuminates a segment of the Rowland circle, allowing for a range of wavelengths to be observed simultaneously, where the wavelength range is determined by the length of the crystal. Placing the source at p_s also maintains the spatial focusing at q_s and allows X-rays reflected from the full crystal height h to be collected in a small area on the detector, such that a taller crystal increases the collected flux as in the von Hámos geometry (Section 5.3).

The collection area in the meridional direction is determined by the source size. For a point source, only the width of the rocking curve of the crystal contributes to the meridional reflection of X-rays and the crystal length only determines the wavelength range. For extended sources, this effective crystal length l_{eff} increases until for very large sources the true length of the crystal limits the reflected flux. The largest limiting factor for the spectral resolution is the Johann error

$$\Delta\theta = \frac{(l_{\mathrm{eff}})^2}{8R^2 \tan\theta}. \tag{5.43}$$

For a point source such as Orion or the beam width of EBIT, $l_{\mathrm{eff}} \ll R$ such that the resolving power of the spectrometer is only limited by the intrinsic resolution of the crystal and possible defects from bending the crystal. For point sources, the spectral resolution is therefore insensitive to small deviations from the exact image and source positions, i.e., careful focusing is unnecessary for fixed Bragg angles.

Orion-specific: OHREX

The above design conditions can be fulfilled by various combinations of nominal Bragg angles, crystal radius, and source and image positions. The specific values for these parameters are defined by the setup at the Orion laser facility. The Orion laser has a very low shot rate. OHREX should therefore be easy to set up, preferentially be able to be aligned and tested offline, without the necessity for tedious realignment of crystals if new crystals are installed, and easy to service for crystal and image plate changes (Beiersdorfer et al., 2016b).

Since the image and source positions depend on the nominal Bragg angle of the instrument, any significant change in angle would require not only changing the angle of the detector arm, but also a change in source and detector distances from the crystal. To avoid this issue, OHREX operates at a fixed Bragg angle of 51.3°. Different wavelength ranges are accessible through the use of different crystal cuts with appropriate lattice spacing $2d$. Quartz crystals typically have high resolving power (Burek, 1976) and uniform focusing quality (Hill et al., 2014; Pereira et al., 2015) and are, thus, ideally suited for the OHREX. Additionally, various cuts of quartz cover the desired wavelength bands with a common Bragg angle of $\theta = 51.3°$ (Beiersdorfer et al., 2016b).

OHREX uses image plates as X-ray detector, which have to be replaced after every shot, breaking the vacuum of the spectrometer. To allow easy access to the image plates and for switching the crystals, OHREX is mounted on the outside of the Orion chamber, separated by a gate valve (Beiersdorfer et al., 2016b). With a chamber radius of 2 m and some extra space for flanges and the valve, this determines the sagittal source distance to $p_{\mathrm{s}} = 240\,\mathrm{cm}$. From Eq. 5.42, the required crystal radius is $R = 67.2\,\mathrm{cm}$. The distance between crystal and detector then follows as $q_{\mathrm{m}} = 52.4\,\mathrm{cm}$, leading to a demagnification of the source by a factor 0.22 or roughly a 5:1 ratio.

To double either the wavelength coverage or the collected signal, OHREX can house two crystals simultaneously. The crystals have a surface area of $40 \times 60\,\mathrm{mm}$. The crystal holders are mounted directly on the removable side plates of the spectrometer body

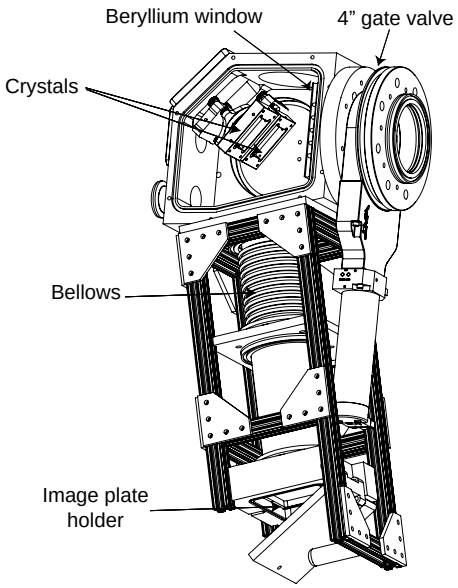

Figure 5.13: OHREX drawing (Beiersdorfer et al., 2016b).

(Fig. 5.13). Crystals can therefore easily be exchanged by taking the side plate off and replacing it with another side plate with a pre-mounted crystal. This way, no *in situ* alignment is necessary: crystals can be set up and their alignment tested on a duplicate spectrometer, even at a different facility (Section 5.5.2), without loosing their alignment (Beiersdorfer et al., 2016b,c). The crystal holders are equipped with micrometer screws for small adjustments to the crystal angle and for moving the image across the detector face. The latter ensures that there is no spatial overlap of the images from the two crystals on the detector. Bellows on the detector arm allow for small adjustments to the focus.

EBIT-specific Modifications: EBHiX

For use at EBIT in form of the EBHiX spectrometer, the image plate holder is substituted by a liquid nitrogen cooled, open-nose CCD camera with a 1300×1340 pixel array and $20\,\mu\text{m} \times 20\,\mu\text{m}$ pixel size (Beiersdorfer et al., 2016c). The area of the CCD chip is smaller than the area of the image plates. With its total width of 26.8 cm, it cuts off about one third of the spectral coverage of the crystal (Beiersdorfer et al., 2016c; Hell et al., 2016a). The spatial resolution of the CCD is almost a factor of four better than the resolution of the image plate (Beiersdorfer et al., 2016b,c). To preserve the source distance of 240 cm, a vacuum tube is mounted between the 4" gate valve of the EBHiX chamber (Fig. 5.13) and the EBIT gate valve. A $50\,\mu$m Be window installed at the EBIT port flange keeps the EBHiX's low vacuum of 10^{-6}–10^{-9} torr separated from EBIT's high vacuum of $\leq 10^{-10}$ torr and acts as a block for stray visible light from the trap (Beiersdorfer et al., 2016c). Due to the fixed Bragg angle design, crystals can easily be swapped between OHREX and EBHiX without loosing their alignment. Figure 5.14 shows photographs of EBHiX installed at EBIT-I.

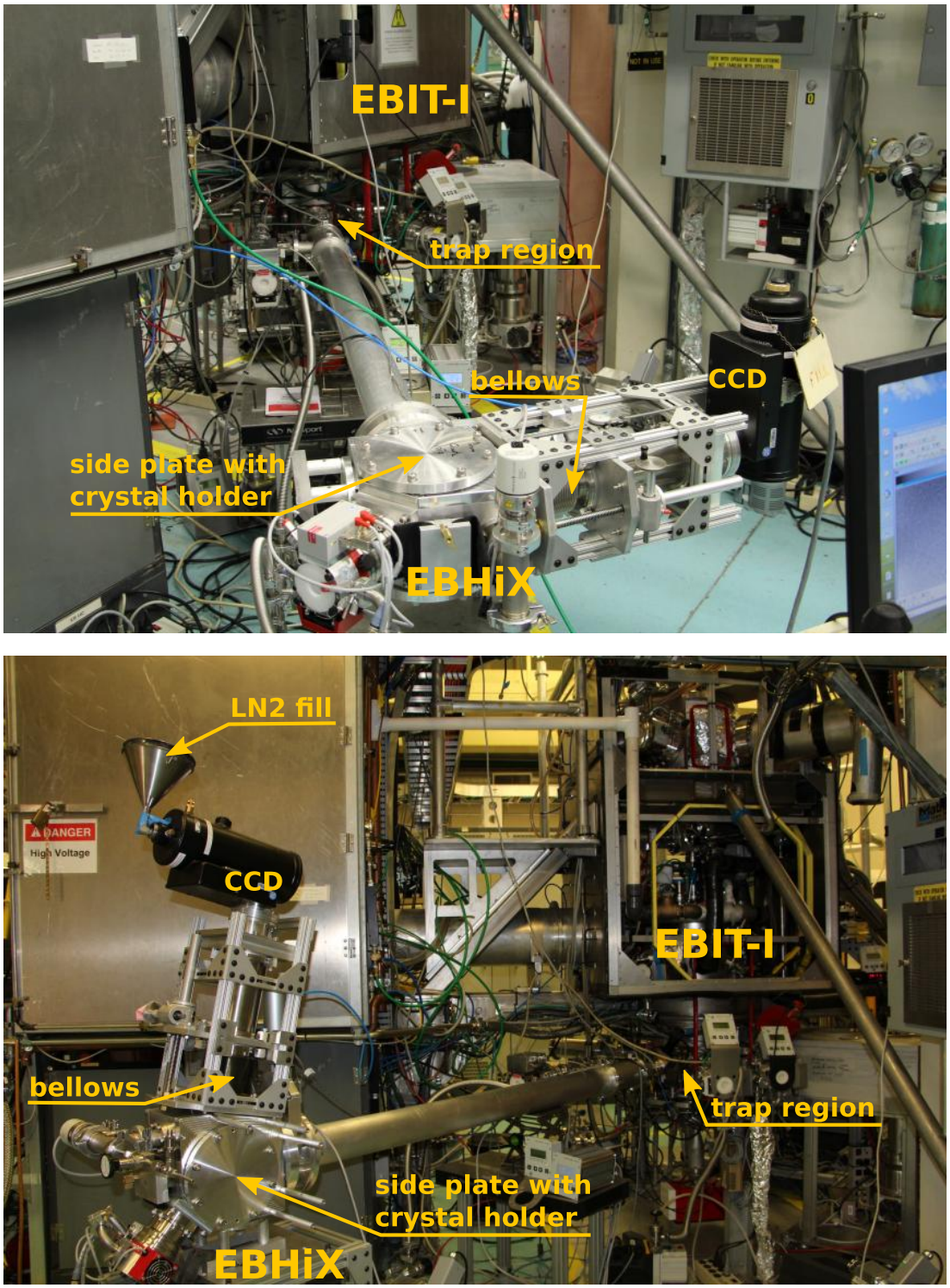

Figure 5.14: EBHiX at EBIT. *Top*: horizontal, *bottom*: vertical.

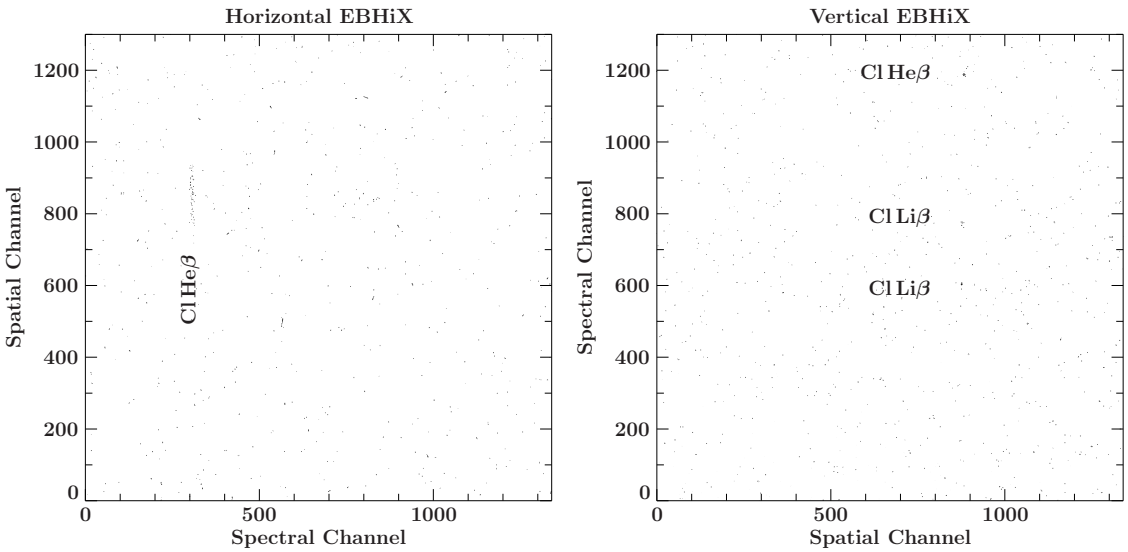

Figure 5.15: CCD image in perpendicular and parallel orientation.

Since EBHiX is an imaging spectrometer employing a spherically bent crystal, it can be operated either with the dispersion plane perpendicular (horizontal EBHiX, Fig. 5.14 *top*) or parallel (vertical EBHiX, Fig. 5.14 *bottom*) to the electron beam. It is therefore well suited for polarization measurements (see Section 5.6 for a proof of concept). For the vertical EBHiX, the CCD camera is tilted by 12.2° from the horizontal (Beiersdorfer et al., 2016c), but due to its bottle neck the camera's dewar can hold enough liquid nitrogen to keep the CCD at its operating temperature for about 12 h before a refill is required.

In the horizontal position, the 50 μm beam diameter is focused in the spectral direction, acting like a point source for the Johann geometry with negligible l_{eff} (Eq. 5.43), while the 2 cm trap length is focused in the spatial (cross-dispersion) direction into a $\sim$ 200 pixel (4 mm) wide image. In the vertical orientation, the small beam width is imaged in spatial direction (see Section 5.5.2 and Brown et al., 2016), while the trap length has to be focused in the spectral direction. In this case, l_{eff} is significantly larger and can be a limiting factor for the spectral resolution. Unlike the horizontally mounted EBHiX, the vertical EBHiX is therefore sensitive to small deviations of the detector position from the focused image location and careful focusing is important for maximum resolving power. See Figure 5.15 for example CCD images.

5.5.2 Performance at EBIT

The performance of both the OHREX spectrometer in operation at the ORION laser facility and the EBHiX have been tested at EBIT (Beiersdorfer et al., 2016b,c; Brown et al., 2016; Hell et al., 2016a). The following is an overview of the performance of the EBHiX, much of which has been taken in verbatim from Hell et al. (2016a).

The spectral and spatial resolution of several crystals have been tested at EBIT (see below). All these crystals, even in a spherical focussing geometry, have small reflectivity.

Coupled to the somewhat low flux of EBIT, the count rate of the EBHiX may be low, i.e., on the order of 1–2 counts per line per hour (Mn Lyα in second order) to $\sim$ 40 counts per line per hour (Si w in first order)[7]. To ensure that the maximum number of photons are detected from each image, a detection and filtering algorithm was developed. The filtering technique detects individual photon events based on a pulse height analysis of the spectral image (Hell et al., 2016b). The filter algorithm assumes that every X-ray event is the result of a single incident photon, i.e., no double photon events occur in any detector channel. This is a valid assumption because of the low efficiency of the spectrometer and the relatively short single-image exposure times. Pulse heights are filtered for a narrow range corresponding to observed photons to discriminate against cosmic rays. The extracted spectra, therefore, have very low background. Figure 5.16 shows the extracted spectra of Si and S, each made of 24 one-hour images.

As discussed by Brown et al. (2016) and (Hell et al., 2016a), the high spatial resolution of the CCD detector allows us to assess the spatial focusing of the spectrometer using the width of the electron beam. To do this, we rotated the EBHiX such that the plane of dispersion is parallel to the electron beam. In this orientation, with the spectrometer's spatial demagnification factor of 5:1 (Beiersdorfer et al., 2016b), it should theoretically be possible to focus the image of the $\sim$ 50 μm beam width down to a single pixel in the spatial direction. However, of all the crystals tested the best focus we could achieve adjusting the distance to the detector, while the source distance remains fixed, resulted in an image spanning about 9 pixels, i.e., about 180 μm. This was from focussing Cl Kβ on the quartz $11\bar{2}0$ crystal in this work and from focussing the Ne-like Mo lines 3G and M2 on quartz $10\bar{1}1$ and Ge 111 crystals by Brown et al. (2016). In both cased the widths are limited by effects of crystal bending (Brown et al., 2016).

For very weak spectra the smaller spatial focus helps to identify the position of the image on the chip. Additionally, in cases such as, e.g., H-like Mn Lyα observed in second order on a quartz $11\bar{2}0$ crystal, where the photon energy and cosmic rays yield a similar detector response, the smaller image region to be extracted with the parallel setup can greatly reduce the background from cosmic rays (see also Chapter 7). But note that here, due to the long trap, i.e., source size, already small deviations of the detector position from the spectral focal length can deteriorate the spectral resolution of the spectrometer.

Using the EBHiX setup at SuperEBIT and EBIT-I, we (Hell et al., 2016a) tested a number of different quartz crystals at the nominal 51.3 ° Bragg angle. Table 5.1 lists the examined quartz cuts, the measured reference, the diffraction order of the observed lines, and the orientation of EBHiX relative to the beam. The quartz $10\bar{1}1$ crystal covers the energy range around H-like Si Lyβ, which is surrounded by the Rydberg series of He-like Si and close to the He-like S line z. Of all the crystals tested, the quartz $10\bar{1}1$ crystal shows the largest number of possible calibration lines, which are spread evenly across the entire observed spectral range. The relatively long exposure times coupled with the large number of known X-ray lines in this region made it possible to actually determine the shape

[7] The exact flux strongly depends on the observed ions ($n = 3 \rightarrow 2$ transitions in Ne-like Mo are much stronger than Kα transitions in lower-Z elements like Si and Ar, which in turn are stronger than Kα transitions in Fe group elements), on the EBIT conditions, and on the thickness and material of the filter used to separate the EBHiX vacuum from the EBIT vacuum.

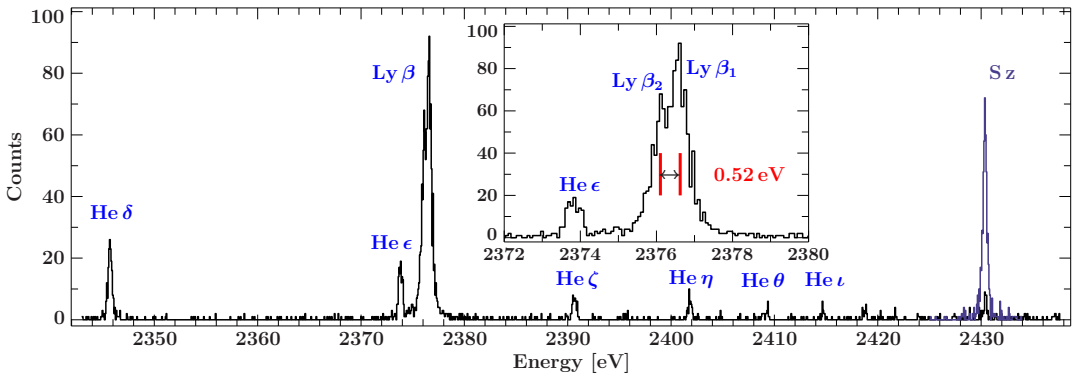

Figure 5.16: Calibration spectrum of He- and H-like Si recorded with horizontal EBHiX using a quartz $10\bar{1}1$ crystal at SuperEBIT. The He-like S line z is shown as well. The Si and S spectra are summed over 24 one-hour exposures each. — From Hell et al. (2016a, Fig. 1).

of the dispersion curve. This calibration spectrum is also used to determine the energy scale for the high-resolution measurement of K-shell transitions of lower charge states of S done with this crystal (Section 6.2). Figure 5.16 shows the recorded calibration spectra with clear line features of He-like Si transitions up to $n = 8 \rightarrow 1$ (He-η) and indications of even higher order members of the series. As the inset shows, Si Ly β_1 and Ly β_2 are marginally resolved, determining the spectral resolution to slightly better than 0.52 eV (Garcia & Mack, 1965). This is comparable to the 0.6 eV resolution measured for Ne-like Mo lines using the same crystal (Beiersdorfer et al., 2016c). It corresponds to a resolving power of about 4600, much lower than the intrinsic resolution of the quartz crystal.

The observed line shape is best described by a Voigt profile (Hell et al., 2016a). The spectral range is determined by fitting a polynomial to the Bragg angles θ of the reference lines as a function of their line centers in detector channels. The angles are derived using Eq. 5.12, i.e., through Bragg's law that is corrected for index of refraction effects (Eq. 5.4), using Eq. 5.11 for the wavelength independent correction term for quartz. While we only use the strong lines S z and Si He δ, He ϵ, Lyβ_1 and Lyβ_2 for calibration, the resulting line centers of the weak features Si He ζ and He η can be used to test its accuracy. We find that the dispersion is best described by a polynomial of 2$^{\text{nd}}$ order. A 3$^{\text{rd}}$ order polynomial fitted to the five strong lines adds too much curvature between Si Lyβ and S z (Fig. 5.17), but closely traces the shape of the 2$^{\text{nd}}$ order polynomial if fitted to all seven lines. The 2$^{\text{nd}}$ order polynomial, therefore, leads to a more reliable energy scale when the reference lines are unevenly spaced across the spectral range and, consequently, is used to model the dispersion of all examined crystals.

In EBIT, line broadening due to the temperature of the trapped ions, i.e., Doppler broadening (Section 2.4), occurs (Beiersdorfer et al., 1995a,b, 1996a). Since the intrinsic resolving power $\lambda/\Delta\lambda$ of quartz crystals typically exceeds 10 000 (Burek, 1976) and the chosen crystals have very uniform focussing quality (Hill et al., 2014; Pereira et al., 2015), EBHiX has very high nominal resolving power and the spectral line widths measured at EBIT are dominated by the Doppler broadening. Table 5.1 therefore also lists the full width at half maximum (FWHM) of just the Gaussian component ΔE_{G} of the fitted

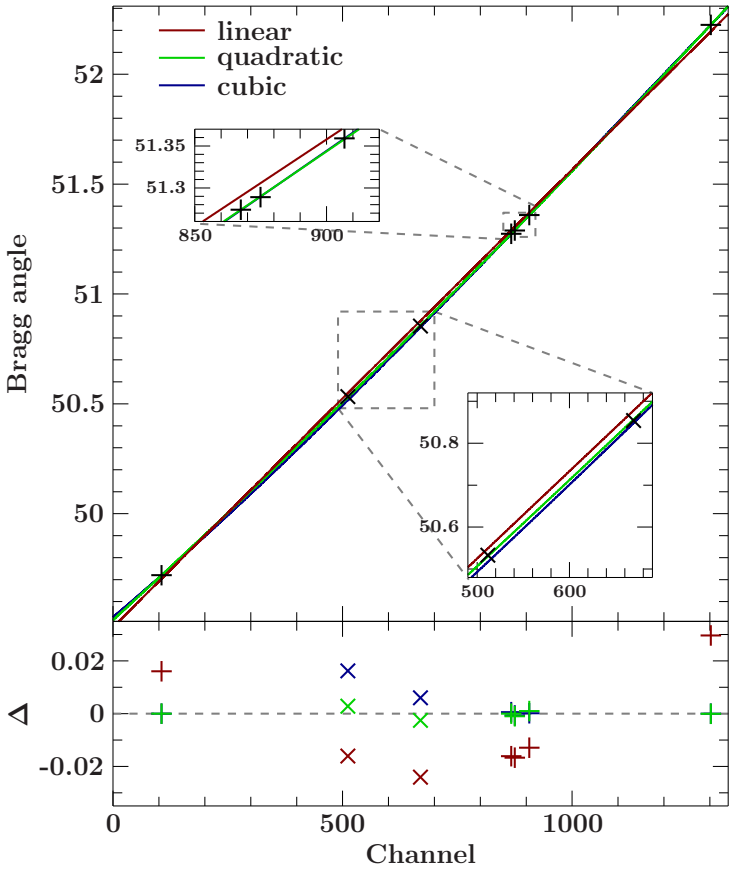

Figure 5.17: Comparison of the linear (red), quadratic (green), and cubic (blue) fit to the five calibration lines (pluses). The lower panel shows the residuals between the respective calibration polynomials applied to the fitted line center and the reference Bragg angles used for calibration. The crosses represents the positions of the weak features Si He ζ and He η (crosses) that have not been included in the polynomial fits. The linear polynomial is not a good description of the gain. The 2nd and 3rd order polynomial only differ in the two weak feature, with the 3rd order underestimating the line position. If the 3rd order polynomial is fit to all 7 lines, it is virtually indistinguishable from the 2nd order polynomial.

Voigt profiles as well as the FWHM ΔE_V of the whole Voigt profile, and the respective translation into ion temperature for each of the calibration lines. The Gaussian widths constitute only a lower limit for the ion temperature, since both the natural line width and the spectrometer response have only very minor contributions to these lines (Hell et al., 2016a).

Overall, the measured temperatures are typical for EBIT (Beiersdorfer et al., 1995a,b, 1996a, 1997a) and the temperatures derived from different lines of the same ion within one measurement are consistent with each other within the uncertainties. However, there are two caveats, as discussed by Hell et al. (2016a). Firstly, in case of the quartz $10\bar{1}0$ cut, the Si K edge of the crystal at 1839 eV falls into the energy range covered by EBHiX in first order, strongly changing the crystal reflectivity in that region. While the Li-like line q at 1845 eV thus appears to be suppressed, the Si line z at 1839.45 eV is still visible in the spectrum, albeit with an impact to its line shape: if fitted with a Gaussian line profile, the

Table 5.1: List of calibration lines (transition energy E_{ref}, observed in diffraction order n) for various quartz crystals mounted with the plane of dispersion perpendicular ($\perp$) or parallel ($\parallel$) to the electron beam. The calibrated spectra are fit with Voigt profiles and the ion temperature T_{ion} in EBIT is derived from the FWHM of just the Gaussian component ΔE_{G} and the full Voigt profile ΔE_{V}, respectively. All energies and temperatures are in units of eV. — From Hell et al. (2016a, Table 1).

Line	n	E_{ref}	ΔE_{G}	T_{ion}	ΔE_{V}	T_{ion}
Quartz $10\bar{1}1$ ($\perp$)						
Si He δ	1	2345.709[a]	0.35(12)	107(73)	0.44(09)	167(65)
Si He ϵ	1	2373.786[a]	0.35(07)	101(41)	0.41(07)	138(48)
Si Lyβ_1	1	2376.104[b]	0.28(09)	67(44)	0.51(06)	220(47)
Si Lyβ_2	1	2376.624[b]	0.28(09)	67(44)	0.51(06)	220(47)
S z	1	2430.347[c]	0.28(09)	64(42)	0.45(07)	159(46)
Quartz $10\bar{1}0$ ($\perp$)						
Si w	1	1865.000[c]	0.38(28)	$196(^{+342}_{-182})$	0.66(18)	587(328)
Si z	1	1839.448[c]	0.45(12)	278(146)	0.47(10)	303(127)
Ar He β	2	3683.854[d]	1.06(24)	553(251)	1.07(25)	567(265)
Quartz $11\bar{2}0$ ($\perp$)						
Cl He β	1	3271.543[d]	0.92(12)	467(120)	1.02(08)	574(93)
Mn Lyα_2	2	6423.561[e]	1.25(28)	347(157)	1.57(23)	551(156)
Mn Lyα_1	2	6441.665[e]	0.87(28)	168(110)	1.20(22)	321(114)
Quartz $11\bar{2}0$ ($\parallel$)						
Cl He β	1	3271.543[d]	0.92(19)	475(194)	1.09(15)	661(182)
Mn Lyα_2	2	6423.562[e]	1.53(43)	524(290)	1.67(26)	624(193)
Mn Lyα_1	2	6441.665[e]	2.12(26)	999(245)	2.12(23)	999(227)
Quartz $21\bar{3}1$ ($\parallel$)						
V w	1	5205.330[f]	1.29(28)	526(229)	1.32(18)	550(148)
V x	1	5188.861[f]	–	–	–	–
V y	1	5180.297[f]	–	–	–	–
V z	1	5153.897[f]	1.03(22)	342(146)	1.05(15)	355(103)
V q	1	5172.474[f]	1.1(4)	387(282)	1.12(21)	402(151)

Notes: [a]Verner et al. (1996b); [b]Garcia & Mack (1965); [c]Drake (1988); [d]Vainshtein & Safronova (1985) corrected for ground state of Drake (1988); [e]Johnson & Soff (1985); [f] Beiersdorfer et al. (1991).

FWHM of Si z is half as large as for Si w. With the Voigt profile, the Gaussian widths are comparable between the two lines and the differences of the crystal response are picked up by the Lorentzian profile instead, where the Lorentzian width of Si w is significantly larger than for Si z. We therefore do not recommend to use the quartz $10\bar{1}0$ crystal in first order for plasma diagnostics with EBHiX unless the lines of interest are below and far from the edge.

Secondly, the quartz $11\bar{2}0$ crystal was used both with the dispersion plane of EBHiX set up perpendicular to the electron beam and in the parallel configuration during a separate measurement. These calibration measurements are used to determine the energy scale

Table 5.2: Observable energy range of the OHREX spectrometer, mounted with a CCD at EBIT or with a larger image plate at Orion, for various crystals (lattice spacing $2d$; Thompson et al., 2009) in 1st and 2nd diffraction order around the photon energy at a nominal Bragg angle of 51.3°. — From Hell et al. (2016a, Table 2).

Crystal	$2d$ [Å]	diff. order	$E(51.3°)$ [eV]	Range [eV]	
				EBIT	Orion[a]
Quartz $10\bar{1}1$	6.687	1	2376	95	150
		2	4752	189	300
Quartz $10\bar{1}0$	8.512	1	1867	65	110
		2	3733	130	260
Quartz $11\bar{2}0$	4.912	1	3234	127	190
		2	6469	255	380
Quartz $21\bar{3}1$	3.082	1	5155	208	320
		2	10309	417	640

[a] Beiersdorfer et al. (2016b)

for measurements of K-shell transitions in M-shell ions of Fe (Chapter 7). As seen from Table 5.1, the measured widths of the Mn lines in the parallel setup are larger than in the perpendicular setup despite similar EBIT conditions during the two measurements. This indicates that the Mn lines were not optimally focused in the spectral direction during this measurement in the parallel setup, which, because of the macroscopic trap length, is much more sensitive to the focal quality than the perpendicular setup, such that the line width was not solely due to the ion temperature. The likely reason is that the focusing was done on the stronger Cl He β line, whose Bragg angle is about 1° different from the Mn lines, and the focal length $q = R_c \sin\theta$ changes by a few mm over this spectral range. Since the laser-produced plasmas at Orion are point sources, not line sources, the orientation of OHREX is irrelevant and focusing issues do not affect its plasma diagnostic capabilities at Orion.

Note that the somewhat large uncertainties on the measured line widths are not attributed to the spectrometer setup (Hell et al., 2016a), but solely due to counting statistics (Fig. 5.18). The primary objectives for the studies at EBIT were to check the crystal alignment and to gauge the spectral ranges for the crystals to be used at Orion. Both tasks can be accomplished with fairly weak spectra. Therefore, the total exposure times at EBIT were kept relatively short for those spectra that are not used as calibration for a subsequent EBIT measurement (Section 6.2, Chapter 7). For the Mn lines in second order, the statistics are limited due to the extremely low count rate of, at best, a few photons per hour. Yet, in most cases the line centroids could be determined to within about one pixel.

Table 5.2 summarizes the spectral energy ranges covered by the spectrometer for use at EBIT and Orion (Hell et al., 2016a). The constant factor between these two setups is attributed to the larger area of the image plate, while the 1-inch CCD camera does not cover the full range of the crystal (Section 5.5.1). We (Hell et al., 2016a) emphasize again that the Quartz $10\bar{1}0$ crystal has the Si K edge in this energy range, impacting line profile measurements due to the sudden changes in reflectivity close to the edge. This crystal should, therefore, not be used in first order at the Bragg angles employed here.

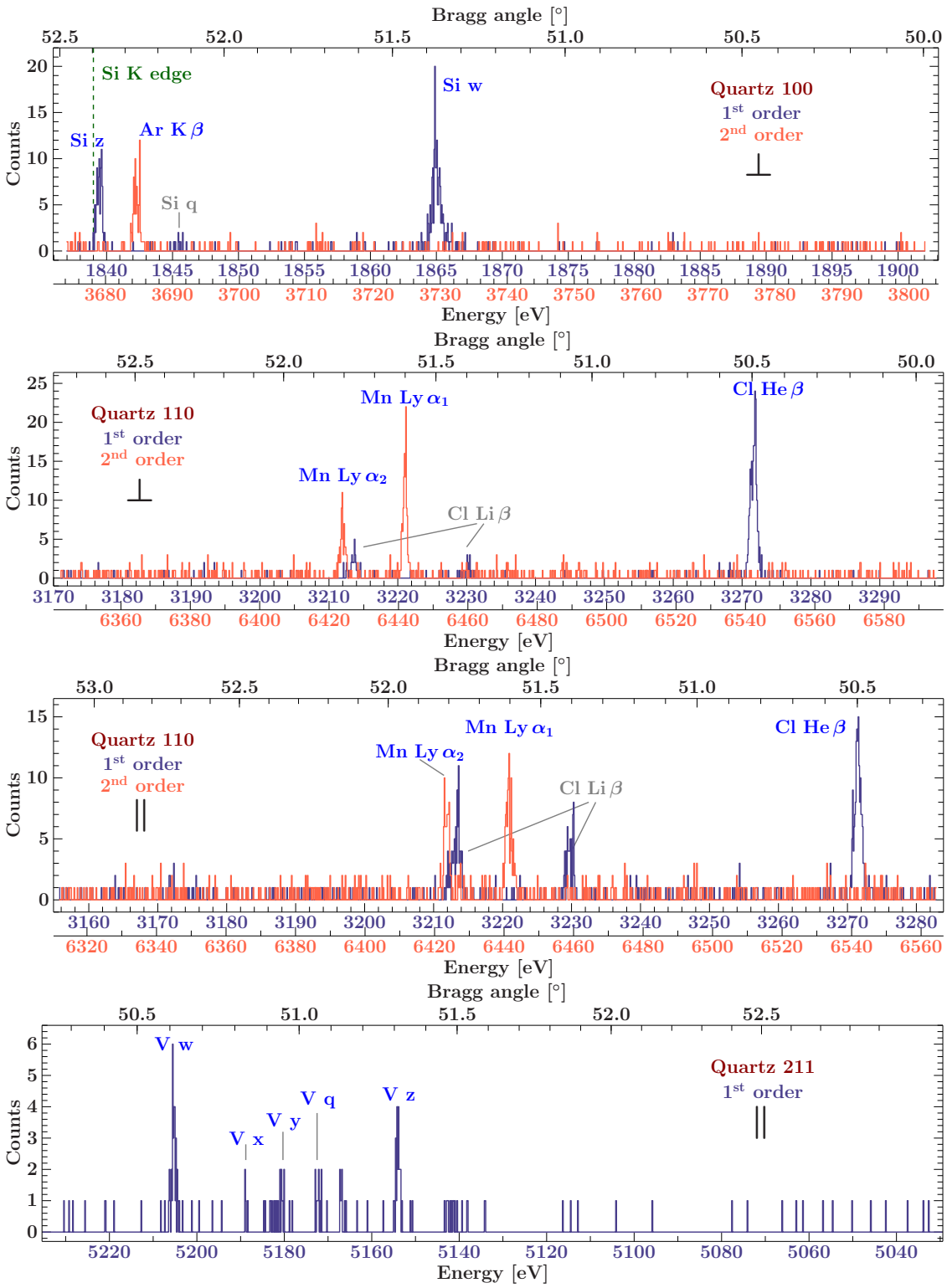

Figure 5.18: EBHiX calibration spectra in first (blue) and second (red) order for various quartz crystals with EBHiX in the vertical (||) or horizontal (⊥) orientation. Even small signal as for the quartz 211 is sufficient to verify the crystal alignment and energy coverage, allowing for quick setup verification.

5.6 Polarization of H-like Mn

The radiation emitted by EBIT is linearly polarized (Section 2.5), splitting the total emitted flux $I^{\mathrm{em}} = I_{\parallel} + I_{\perp}$ into a component polarized parallel ($I_{\parallel}$) and one polarized perpendicular ($I_{\perp}$) to the beam axis, with the degree of polarization defined as

$$P = \frac{I_{\parallel} - I_{\perp}}{I_{\parallel} + I_{\perp}} = \frac{1 - I_{\perp}/I_{\parallel}}{1 + I_{\perp}/I_{\parallel}}. \tag{5.44}$$

While grazing incidence grating spectrometers reflect both of these polarization components equally well (Utter et al., 1999b; Beiersdorfer et al., 2004b), crystal spectrometers act as polarizers. Radiation that is polarized parallel to the crystal surface (perpendicular to the plane of dispersion) is easily reflected by the crystal. But for radiation polarized parallel to the plane of dispersion, in order to preserve the polarization relative to the propagation direction, the polarization vector has to change its angle by $180° - 2\theta$ upon Bragg reflection, along with the change of propagation direction. This polarization component is, therefore, suppressed, as it has a large probability to be absorbed by the crystal. How strongly suppressed this component is, is a function of Bragg angle and peaks around the Brewster angle at $\theta = 45°$ (Burek, 1976), i.e., near the Brewster angle at 45° crystals reflect only the polarization component parallel to the crystal surface, while away from this angle the admixture of the perpendicular component increases (Henke et al., 1993; Beiersdorfer et al., 1996b, 1997b; Shlyaptseva et al., 1997). If $R_{\perp}$ and $R_{\parallel}$ denote the crystal reflectivity for the perpendicular and parallel polarization components, respectively, then their ratio $R = R_{\perp}/R_{\parallel}$ varies as $R = |\cos(2\theta)|$ for perfect crystals and as $R = \cos^2(2\theta)$ for mosaic crystals (Burek, 1976; Henke et al., 1993). Real crystals are usually between these two limits.

Operating a crystal spectrometer with the plane of dispersion parallel to the electron beam, i.e., rotated by 90° to the traditional setup, – as is possible with the EBHiX (Section 5.5) – can therefore be interesting for polarization measurements. There are multiple experimental setups suitable for polarization measurements that involve the polarization selective effects of a crystal spectrometer. In the first technique (Nakamura et al., 2001; Robbins et al., 2006), it is assumed that, at least for very simple systems, the total effective excitation cross sections for the transition of interest are sufficiently well predicted by theoretical calculations. Then only a single crystal spectrometer is used to measure the emission line and the degree of polarization is determined from the deviation of the measured flux from the theoretically expected total flux. In the second technique (Henderson et al., 1990; Robbins et al., 2004, 2006), the crystal spectrometer is paired with a spectrometer that is insensitive to the polarization of the radiation, e.g., a micro-calorimeter or a grating spectrometer. Here, the flux of the crystal spectrometer is compared to the measured total flux instead of comparing to theory. In a third approach (Beiersdorfer et al., 1996b), the line flux is measured with two different crystals installed in the same crystal spectrometer. Here, the used crystals need to have sufficiently different lattice spacing $2d$ such that the different Bragg angles of the same line change the reflectivity ratio $R(\theta)$ enough to derive the polarization from the changes in measured flux.

All of these techniques have in common that at least one of the crystal spectrometers should operate close to a 45° Bragg angle to maximize the difference between the measured polarized flux and the (unpolarized) reference flux. The first method has the disadvantage that it relies on calculations of the emission cross section, which can have large relative uncertainties, especially for more complex ions (Chapter 1). For the second and third method the effective area of the respective spectrometers have to be normalized to each other. To some degree this can be mitigated by normalizing the line of interest to the flux of a close-by unpolarized reference line, but certain parameters like the total crystal reflectivity are a function of photon energy and differ between the two employed spectrometers. Especially the third method depends on well known values for the crystal reflectivity. It uses a second order effect for the polarization measurement, increasing the uncertainty of the measurement.

As mentioned in Section 5.5.1, the fact that EBHiX can be mounted at EBIT parallel or perpendicular to the electron beam makes it a perfect instrument for polarization studies. Since both the horizontal and the vertical spectrometer use the same crystal cut, they observe the lines of interest at the same Bragg angles. Then the polarization measurement does not depend on the total crystal reflectivity $R_{\mathrm{tot}} = R_{\parallel} + R_{\perp}$, but only on the relative reflectivity R of the polarization components. This is a big advantage over the other available methods described above and makes this technique the most direct measurement of polarization. Using an unpolarized transition as a reference line for flux normalization between the two spectrometer orientations takes care of possible differences in effective area, e.g., due to the larger l_{eff} of the vertical setup (Section 5.5). All other energy-dependent components of the effective area, such as filter transmission and quantum efficiency, are identical between the two spectrometer orientations and, therefore, do not affect the ratio of $I_{\parallel}$ and $I_{\perp}$ of the same spectral line.

By orienting the crystal spectrometer with the dispersion either perpendicular or parallel to the beam, the perpendicular ($I_{\perp}$) or parallel ($I_{\parallel}$) polarization component are suppressed, respectively[8]. Comparing the measured reflected intensity of a transition between the two orientations then leads to the polarization fraction P. However, since the polarization components are only completely separated at Bragg angles of $\theta = 45°$, while EBHiX operates around 51.3°, the observed flux $I^{\mathrm{obs}} = R_{\parallel} I_{\parallel} + R_{\perp} I_{\perp}$ is a mixture of the polarization components weighted by their crystal reflectivity. The flux measured by each orientation of EBHiX then is

$$I^{\mathrm{H}} = R^{\mathrm{H}}_{\parallel} I_{\parallel} + R^{\mathrm{H}}_{\perp} I_{\perp} = R_{\parallel} I_{\parallel} + R_{\perp} I_{\perp} \tag{5.45}$$

$$I^{\mathrm{V}} = R^{\mathrm{V}}_{\parallel} I_{\parallel} + R^{\mathrm{V}}_{\perp} I_{\perp} = R_{\perp} I_{\parallel} + R_{\parallel} I_{\perp}. \tag{5.46}$$

Here, R^{H}_{X} and R^{V}_{X} are the orientation dependent reflectivity with $\perp$ and $\parallel$ relative to the crystal. Since the plane of dispersion of the vertical EBHiX is rotated by 90° relative to the horizontal EBHiX and the beam direction (using the same crystal), the parallel and perpendicular reflectivity of the vertical setup are swapped compared to the horizontal

[8] Note that for EBHiX mounted in the horizontal position, i.e., with the spectrometer perpendicular to the electron beam, X-rays polarized parallel to the beam are preferentially reflected. The vertical (parallel) EBHiX measures the perpendicular polarization.

setup, i.e., $R_{\parallel}^{\mathrm{V}} = R_{\perp}^{\mathrm{H}} \equiv R_{\perp}$ and $R_{\perp}^{\mathrm{V}} = R_{\parallel}^{\mathrm{H}} \equiv R_{\parallel}$. Solving the system of linear equations (Eq. 5.45 & 5.46) for $I_{\parallel}$ and $I_{\perp}$ gives

$$I_{\parallel} = \frac{R_{\parallel} I^{\mathrm{H}} - R_{\perp} I^{\mathrm{V}}}{R_{\parallel}^2 - R_{\perp}^2} \quad and \quad I_{\perp} = \frac{R_{\parallel} I^{\mathrm{V}} - R_{\perp} I^{\mathrm{H}}}{R_{\parallel}^2 - R_{\perp}^2}. \tag{5.47}$$

Substituting these into Eq. 5.44 results in the degree of polarization as a function of the observables I^{H} and I^{V}:

$$P = \frac{1+R}{1-R} \cdot \frac{I^{\mathrm{H}} - I^{\mathrm{V}}}{I^{\mathrm{H}} + I^{\mathrm{V}}} \tag{5.48}$$

where $R = R_{\perp}/R_{\parallel}$. At $\theta = 45°$, where $R(45°) = 0$, this equation reduces back to the uncorrected version of Eq. 5.44 with I^{H} purely resembling the parallel polarization component $I_{\parallel}$ and I^{V} measuring only the perpendicular component $I_{\perp}$.

For an unpolarized emission line (such as Lyα_2 with upper level total angular momentum $j = 1/2$), the total flux splits equally into both polarization components, i.e., $I_{\parallel}^{\mathrm{unpol}} = I_{\perp}^{\mathrm{unpol}}$. Combining this with Eq. 5.47 shows that then also $I_{\mathrm{unpol}}^{\mathrm{V}} = I_{\mathrm{unpol}}^{\mathrm{H}}$, which proves the applicability of unpolarized transitions as flux normalization between the two spectrometer orientations.

If the polarization measurement is done with a single spectrometer changing orientation in successive runs rather than two identical spectrometers simultaneously, EBIT's flux needs to be normalized between the measurements to ensure the same total flux and the same underlying EBIT conditions. Since the degree of polarization is a function of electron impact energy, the EBIT conditions, specifically beam energy and current, have to be repeated between the two runs. The unpolarized reference line used to account for possible differences in effective area simultaneously accounts for changes in source flux between the two consecutive runs, as it is not necessary to distinguish between the two effects. Additionally, a second independent spectrometer, whose settings do not change between the two runs, can be employed to monitor EBIT (Brown et al., 2010). A flux normalization constant between the two runs is determined by flux changes observed with this spectrometer. This can for example be done by using a second independent This second spectrometer does not have to be oblivious to polarized radiation, since its orientation relative to EBIT remains the same between the two runs.

Since the H-like Mn Lyα lines for the EBHiX calibration of the quartz $11\bar{2}0$ crystal have been observed both with the horizontal and the vertical setup (Fig. 5.18, see also Chapter 7), these measurements lend themselves to a proof of concept for the EBHiX as a spectrometer for polarization measurements. Figure 5.18 already shows nicely how the intensity ratio of the polarized line Mn Lyα_1 to the unpolarized Mn Lyα_2 is significantly reduced for the vertical orientation suppressing the stronger parallel polarization component[9]. To facilitate this polarization measurements, the same beam energy ($E_{\mathrm{beam}} = 17\,\mathrm{keV}$) and beam current ($I_{\mathrm{beam}} \sim 155\,\mathrm{mA}$) were employed for both calibration runs. From the horizontal (perpendicular) EBHiX measurement, we obtain $I^{\mathrm{H}} = I_{\mathrm{Ly}\alpha_1}/I_{\mathrm{Ly}\alpha_2} = 136/72 = 1.889 \pm 0.275$, while the vertical (parallel) EBHiX setting

[9] Note that the increased ratio of Cl Liβ to Cl Heβ in the vertical EBHiX shown in the same figure is due to an intentional change in charge balance towards Li-like Cl.

gives $I^{\mathrm{V}} = I_{\mathrm{Ly}\alpha_1}/I_{\mathrm{Ly}\alpha_2} = 98/76 = 1.289 \pm 0.197$. This yields a ratio $I^{\mathrm{V}}/I^{\mathrm{H}} = 0.682 \pm 0.144$. The Mn Ly$\alpha_1$ line is observed at a Bragg angle of $\theta = 51.60°$ and quartz crystals are very close to being perfect crystals, i.e., here $R = |\cos(2\theta)| = 0.228$ giving a correction factor for the polarization of 1.59. The measured degree of polarization is therefore $P = 0.30 \pm 0.16$.

More dedicated polarization measurements with better statistics have previously been done at EBITs, especially for Ne-, Li-, and He-like systems (Henderson et al., 1990; Takács et al., 1996; Beiersdorfer et al., 1996b, 1997b, 1999a; Robbins et al., 2004). In fact, polarization for Ne-like Ba has been shown in the very early days of EBIT spectroscopy (Beiersdorfer et al., 1990b). Nakamura et al. (2001) measured the polarization of H-like Ti Lyα at three different energies, employing the "one-crystal technique", where one polarization component is measured relative to the unpolarized Lyα_2 line and the polarization then inferred from a comparison to arguably good calculations of the total emission cross section. Unlike previous measurements in other charge states, the measured polarization of the H-like transition Lyα_1 was systematically lower than predicted by theory. To investigate this discrepancy, Robbins et al. (2006) made similar measurements for H-like Ar and Fe at the LLNL SuperEBIT, also extending the studied collision energy range up to 25 times threshold. For both ions, they used the "two-spectrometer technique", combining a crystal spectrometer with the XRS/EBIT calorimeter. To gauge possible systematics compared to Nakamura et al. (2001), Robbins et al. (2006) repeated the Fe measurement with the "one-crystal" method for comparison. They found that, if the electron impact energy (beam energy) is expressed in units of excitation threshold for the Lyα_1 transition, the polarization as a function of collision energy is virtually independent of Z, as postulated by Itikawa et al. (1991). Their measurements agreed well with Nakamura et al. (2001), but still had an offset compared to distorted-wave calculations.

Both groups did extensive error analysis and were able to exclude various possible systematic shifts as explanations for the discrepancy. The $2s_{1/2} \rightarrow 1s_{1/2}$ M1 transition has a very small branching ratio and corrections due to it's contributing flux to Lyα_2 have little influence on P. The beam electrons have a small velocity component $v_\perp$ perpendicular to the beam direction, which would have a depolarizing effect on the line emission, if this velocity component was a significant fraction of the velocity in the main electron direction. For SuperEBIT, however, this component has a negligible effect. Similarly, cascades following charge exchange with the randomly distributed neutral background gas would act depolarizing. But corresponding tests in magnetic trapping mode showed that CX contributes less than 2 % to the total flux (Robbins et al., 2006). Calculations of the integrated crystal reflectivity (taken from Henke et al., 1993) entering the polarization computation in both setups have been shown in other experiments to be very accurate. Furthermore, the theoretical total emission cross section ratio needed as normalization in the one-crystal technique would have to be far outside any probable calculation uncertainty (Nakamura et al., 2001).

In the meantime, Bostock et al. (2009) were able to show that the Breit interaction makes an important contribution to the polarization of H-like mid-Z ions. They used a relativistic convergent close-coupling (RCCC) method to calculate the magnetic sublevel

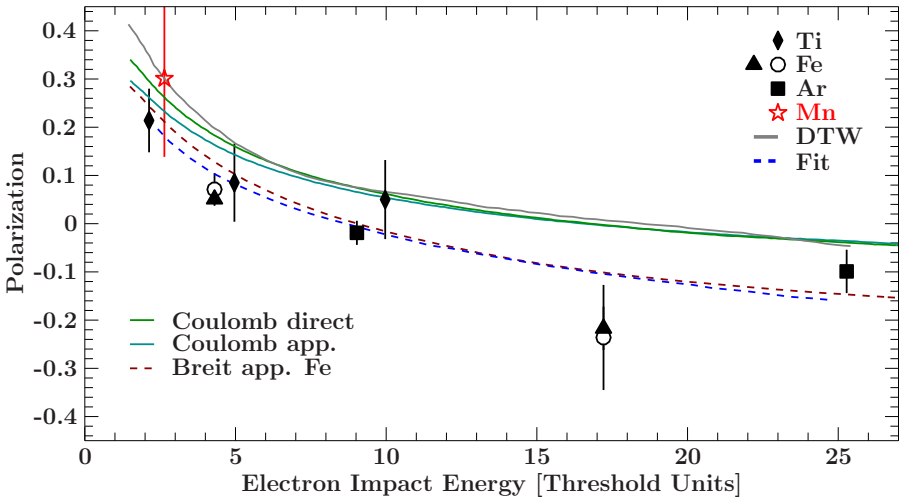

Figure 5.19: Mn Polarization. The red star shows polarization resulting from the new Mn measurement. The Ti data points are from Nakamura et al. (2001), Ar and Fe from (Robbins et al., 2006). The filled black points are from the one-crystal method, the empty ones from the two-spectrometer technique. The gray line is a distorted-wave (DTW) calculation, the dashed blue line a fit to the Ti, Ar, and Fe data points by Robbins et al. (2006). The dark green line and the slightly lower dark cyan line are Coulomb interaction calculations from (Bostock et al., 2009), direct excitation only and the apparent polarization including cascades, respectively. The red dashed line adds relativistic corrections in form of the Breit interaction (with cascades), clearly showing that relativistic effects have an important contribution to these highly charged ions.

resolved cross sections for the Coulomb potential alone, and including Breit[10] or Møller[11] interactions. The Breit interaction has a somewhat larger effect on the $m = 1/2$ sublevel than on the $m = 3/2$ sublevels, but in opposite directions. Therefore, it barely changes the total cross section of the $2p_{3/2}$ level, while the effect on polarization is significant. The Møller interaction is only important for very high-Z ions like H-like U. Cascades affect all magnetic sublevels almost equally and therefore have only minor contribution to the polarization. Again, the RCCC calculations show only small Z-dependence in threshold units.

As seen in Fig. 5.19, our Mn data point agrees with the previous measurements to within the error bars. The large relative uncertainty is attributed to the extremely low counting statistics. The discussions of systematic offsets by Nakamura et al. (2001) and Robbins et al. (2006) can be extrapolated to the current measurement, strengthening its agreement with previous results, despite the low counting statistics. Additionally, by using the same spectrometer in two orientations relative to the electron beam, our measurement does not need to rely on either calculations for the crystal reflectivity (the value for the

[10] Breit interaction uses classical arguments to add relativistic effects to the Coulomb potential (Bostock et al., 2009).

[11] Møller derives the relativistic Coulomb interaction for electron-electron scattering processes using QED, including Coulomb and Breit interaction along with any other relativistic corrections. The Møller interaction depends on the energy transferred in the collision and, in the limit of low-energy transfer, reduces to Coulomb and Breit interaction (Bostock et al., 2009).

relative reflectivity R is well know), the total flux calibration of a second, different spectrometer, or the calculation of the total emission cross section. One advantage is, for example, that the M1 line blending with Lyα_2 does not contaminate the measurement, since it is unpolarized as well and no theory is entering the calculation of the polarization. This method is the most direct measurement method available for polarization measurements and can be employed for further polarization measurements in the future. In future, more dedicated polarization measurements, two EBHiX's, one in each orientation, will be used simultaneously instead of doing subsequent runs as in the present measurement.

This numerical agreement between the experimental values and those calculated from a theory designed to explain the ordinary hydrogen spectrum is remarkable, as the wave lengths dealt with in the two cases differ by a factor of about 2000.

Henry G.J. Moseley

6 K-shell Transitions in L-shell Ions

As discussed in Section 1.4.1, K-shell transitions in L-shell ions have been observed in the spectra of a variety of celestial sources and are expected to be found in even more objects and from more elements in the future. Reference wavelengths for these transitions in sulfur (Cyg X-1) and silicon (Cyg X-1, Vela X-1, and others) ions are the most pressing need, since the lack of these already prohibits the utilization of the full potential of existing observations. While we have a campaign to measure these transitions in all astrophysically relevant ions (Hell et al., 2015, see also Section 6.3.3), Si and S were the first to be measured due to their direct application to wind diagnostics in Vela X-1 and Cyg X-1. First measurements of these ions were presented by Hell (2012) along with preliminary results for Doppler shifts in Cyg X-1. Hell et al. (2016b) re-examined this first data set, added a second experimental run as a control measurement, expanded the FAC model used for line identification, discussed the line shape more thoroughly, provided reference line centers for the line blend of each ionization state, and demonstrated the power of these new reference wavelengths by re-examining previously published Doppler shifts of Vela X-1 observations. Section 6.1 summarizes these updated results with an additional discussion on Cyg X-1, Section 6.2 features higher-resolution crystal measurements of the N- through Li-like S ions and their comparison to the ECS results in Section 6.1, and Section 6.3 gives an outlook on the next steps of this project, including new wavelength calculations by Beiersdorfer et al. (2016a), measurements of Kβ transitions in the S ions, and an extension of this campaign to other astrophysically relevant elements.

6.1 ECS Measurements of Kα Transitions in Si and S

This section is taken largely in verbatim from Hell et al. (2016b), with Section 6.1.7 extended by the application of the measurements to Cyg X-1 spectra in addition to the discussion of Vela X-1 by Hell et al. (2016b).

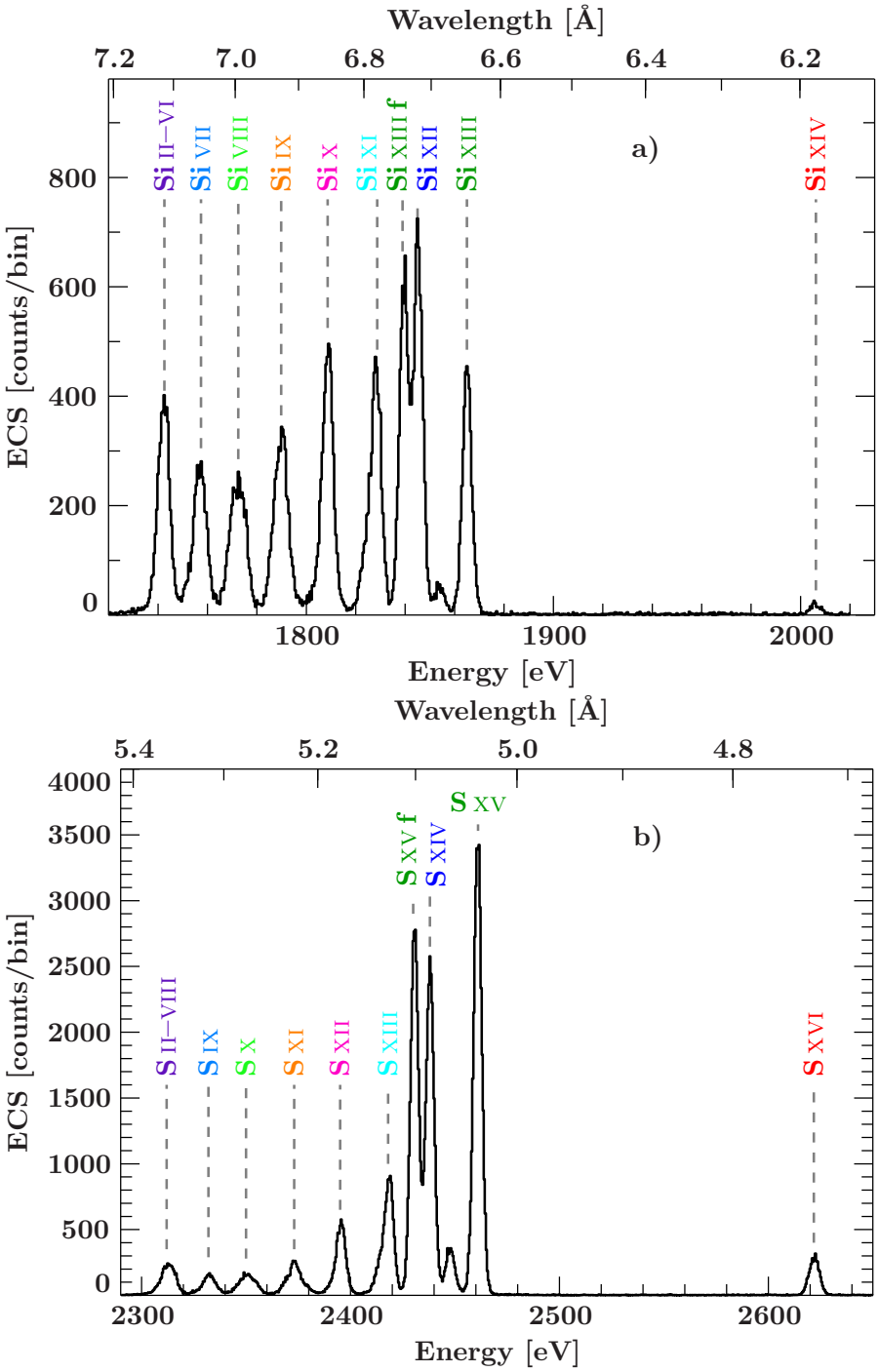

Figure 6.1: Calibrated and summed *a)* silicon and *b)* sulfur spectra from all 16 low-energy ECS pixels (Run-I). The color code of the ion labels is used whenever we specifically distinguish between isoelectronic sequences throughout this section. — From Hell et al. (2016b, Fig. 1).

6.1.1 Experimental Setup

The measurements presented here (Hell et al., 2016b) were carried out using both the LLNL EBIT-I (Run I)[1] and SuperEBIT (Run II) traps. For the details of their operation see Chapter 3 and references therein. During this experiment, neutral sulfur and silicon were injected into the EBIT's trap region as gaseous sulfur hexafluoride, SF_6, and decamethyltetrasiloxane, $C_{10}H_{30}O_3Si_4$, respectively, using a well collimated ballistic gas injector. Once the neutral material intersects the electron beam, the molecules are broken apart and resulting atoms are collisionally ionized and trapped.

The electron impact excitation energies of the K-shell transitions in the silicon and sulfur ions are $\gtrsim$1.73 keV, while the ionization energies for the L-shell ions range from 166.8 eV for Ne-like Si V to 707.2 eV for Li-like S XIV (Cowan, 1981). Hence, in order to excite the Kα lines the electron beam energy must be $\sim$ 3–10 times the ionization threshold. Under typical operating conditions at these energies, the charge state distribution would be dominated by lithium- and helium-like ions. In order to produce a significant amount of lower charge states at the high electron impact energies required for inner-shell excitation, several methods have been developed (Decaux & Beiersdorfer, 1993; Schmidt et al., 2004). In the present experiment, the neutral gas injection pressure is set to values several orders of magnitude larger than EBIT's base pressure of $\lesssim 10^{-10}$ Torr, short EBIT cycle times and relatively low electron beam currents were employed. Together, these operating parameters yield a significant fraction of low charge states at high electron impact energy. The spectral signature of significant amounts of several L-shell ions can easily be seen in the X-ray spectra (see Fig. 6.1). Note that the electron beam energies employed at these measurements were well away from any dielectronic recombination resonances of the respective measured elements, i.e., the emission lines originate entirely from electron impact excitation and inner-shell ionization, contrary to the laser experiments reported by Faenov et al. (1994).

The spectrum of the X-ray radiation from the trapped ions is recorded with 16 low-energy pixels of the ECS (Chapter 4.3). The energy resolution of the ECS for these measurements was 4.5–5.0 eV, typical for the ECS. The spectra shown here (Hell et al., 2016b) are similar in quality to a spectrum (Hitomi Collaboration et al., 2016) measured with the Soft X-ray Spectrometer (SXS) system (Mitsuda et al., 2010) aboard the *Astro-H/Hitomi* X-ray observatory (Takahashi et al., 2010; Takahashi et al., 2016) or in the planned X-IFU instrument on *Athena* (Nandra et al., 2014; Ravera et al., 2014). To assess the systematic errors in our measurement in Hell (2012), we conducted a second experimental run using SuperEBIT (Run-II). SuperEBIT was used for Run-II because of beam time availability (Hell et al., 2016b).

6.1.2 Calibration

Because of slight variations in performance, each pixel in the ECS array is calibrated separately. The energy scale for each pixel is determined by fitting 4$^{\text{th}}$ order polynomial

[1] The Run I data have previously been presented in Hell (2012).

Table 6.1: Calibration results (Hell et al., 2016b, Table 1).

Z	line	FWHM (eV)	line energy (eV)			ΔE_{ref}	ΔE_{FAC}
			fit	reference	FAC		
Si	w	$4.36^{+0.08}_{-0.12}/4.92 \pm 0.12$	1864.84 ± 0.05	1864.9995	1864.812	−0.16	0.03
Si	Ly α	—	$2005.59^{+0.17}_{-0.20}$	2005.494[a]	2005.516[a]	0.10	0.07
S	w	$4.55 \pm 0.04/4.98 \pm 0.14$	2460.609 ± 0.018	2460.6255	2460.417	−0.017	0.191
S	Ly α_1	—	$2622.97^{+0.18}_{-0.26}$	2622.700	2622.730	0.27	0.24
S	Ly α_2	—	$2620.00^{+0.21}_{-0.34}$	2619.701	2619.731	0.30	0.27

[a] Mean value of Ly α_1 and Ly α_2 weighted by their statistical weights.

Notes: Comparison between the fitted line centers (fit) of the He-like $1s\,2p \rightarrow 1s^2$ line w with the reference value (reference) of Drake (1988) and of the H-like $2p \rightarrow 1s$ Ly α lines of Si and S with the values of Garcia & Mack (1965), which were used for calibration. The full width half maximum (FWHM) determined from line w (used as detector resolution throughout the fits) is listed for Run-I / Run-II. ΔE_i gives the difference between the fit and the respective theoretical values. Listed uncertainties are purely statistical.

functions to the measured pulse heights in volts space of known reference emission lines (Porter et al., 1997; Cottam et al., 2005); here, the X-ray line emission from K-shell transitions in He-like ions (Kα / line w: $1s\,2p\,{}^1P_1 \rightarrow 1s^2\,{}^1S_0$; K$\beta$: $1s\,3p \rightarrow 1s^2$; Kγ: $1s\,4p \rightarrow 1s^2$) and H-like ions (Ly α: $2p \rightarrow 1s$; Ly β: $3p \rightarrow 1s$). Specifically, for the Run-I measurement (Hell, 2012), the 1.7 to 1.9 keV band containing the lower charge states of silicon was calibrated with Kα, Ly α, Kβ, and Ly β lines of neon and silicon. For the 2.3 to 2.5 keV band containing the lower charge states of sulfur, Kα, Ly α, and Kβ of sulfur and Kα–Kγ of fluorine were used. For Run-II (Hell et al., 2016b), Ne and S Kα, Ly α, and Kβ, and Si Kα–Kγ and Ly α were used to calibrate the silicon spectra, and Ne Kα, Ly α, and Kβ, Si and S Kα and Ly α, and Ar Kα were used to calibrate the sulfur spectra.

In both Hell (2012) and Hell et al. (2016b), the reference wavelengths of the He-like systems used for calibration originate from Drake (1988) in case of the $1s\,2p \rightarrow 1s^2$ resonance line labeled "w" in the notation of Gabriel (1972). The wavelengths for $1s\,3p \rightarrow 1s^2$ Kβ and $1s\,4p \rightarrow 1s^2$ Kγ Rydberg states were taken from Vainshtein & Safronova (1985), but corrected for the ground state of Drake (1988) according to Beiersdorfer et al. (1989) such that the reference energy used for calibration is

$$E(\mathrm{K}\beta) = E_{\mathrm{V}}(\mathrm{K}\beta) - E_{\mathrm{V}}(\mathrm{K}\alpha) + E_{\mathrm{D}}(\mathrm{K}\alpha) \tag{6.1}$$

where E_{V} are the transition energies from Vainshtein & Safronova (1985) and E_{D} the values from Drake (1988). Values for the Lyman series in the H-like systems are from Garcia & Mack (1965). The wavelengths were converted to energy using $E = hc\lambda^{-1}$ where $hc = 12398.42\,\mathrm{eV\,Å}$ (with values for h, c and e from CODATA 2014, Mohr et al., 2015; see also Appendix A).

6.1.3 Quality of the Calibration

After calibration, the ECS events were binned to an energy grid of 0.5 eV. Figure 6.1 shows the summed Si and S spectra of all 16 low-energy ECS pixels for Run-I (Hell et al., 2016b).

To gauge the accuracy of the energy scale, the location of the H-like Ly α lines and the He-like line w of Si and S are determined from a simultaneous fit of the calibrated Run-I and Run-II spectra. Similar to the approach in Hell (2012), the fitted values are then compared to the initial reference values (Hell et al., 2016b). Table 6.1 shows the value from the comparison as well as from our FAC calculation, which is used as a guide for line identification (see below, Section 6.1.5). For silicon line w, the calibrated values are 0.16 eV lower than the reference values, for sulfur line w, they are 0.017 eV lower. For the S Ly α lines, the difference between theory and experiment is slightly larger, but still well below 0.5 eV (Table 6.1). Combining the uncertainties of the Ly α and w lines amounts to 0.13 eV for silicon and 0.23 eV for sulfur, which are taken as the systematic uncertainties. FAC results agree with Drake (1988) to within 0.2 eV in case of the transition energies in He-like ions, and within 0.03 eV for the transition energies in H-like ions.

The fitted widths of the He-like lines of about 4.5–5.0 eV are consistent with the expected energy resolution of the ECS in this energy region. With the more careful re-calibration of the Run I data by (Hell et al., 2016b), the resolution improved slightly compared to Hell (2012) due to a better alignment of the individual pixels.

6.1.4 Spectral Analysis – Fit Method

In order to determine the transition energies of as many individual lines as the data allow, the spectra from Run-I and Run-II were fitted simultaneously for each element (Hell et al., 2016b), using the Interactive Spectral Interpretation System ISIS (Houck & Denicola, 2000; Houck, 2002; Noble & Nowak, 2008). The modeled energy range spans 1720–1880 eV for the Si spectra and 2290–2480 eV for the S spectra. The models for Run-I and Run-II consist of a sum of individual Gaussian lines, where the centers of these lines are tied between Run-I and Run-II, their widths are fixed to the respective resolution (Table 6.1), and their normalizations are left to vary freely. Fixing the line widths is valid because the natural line widths and the Doppler widths are small compared to the resolution of the calorimeter, no other line broadening mechanism is present in these experiments, and the energy resolution of the calorimeter is constant over these small energy ranges. In order to account for the flux above background found between the main peaks of the spectra, e.g., Fig. 6.2, the models include a single second order polynomial for each data set (Hell et al., 2016b), as was done in Hell (2012). A possible explanation for the presence of this continuum are weak unresolved lines (see Fig. 6.5 in Section 6.1.6), low-energy spectral redistribution due to photon and electron escape events (Cottam et al., 2005), or some combination of both.

In order to determine the number of Gaussian components required to describe the data, we test the statistical significance of each line (Hell et al., 2016b). Similar to the technique used in Hell (2012), a Monte Carlo type simulation (see `mc_sig` of the Remeis ISISscripts), generates 10^3 realizations of fake spectra based on the existing best fit model: for each energy bin of the fake spectrum, it draws a random number from a Poisson distribution with the mean equal to the modeled value. These fake spectra are fitted with the model used to create them (model A) and with a model containing an additional Gaussian line (model B). Because of the increased number of degrees of freedom, the χ^2-value

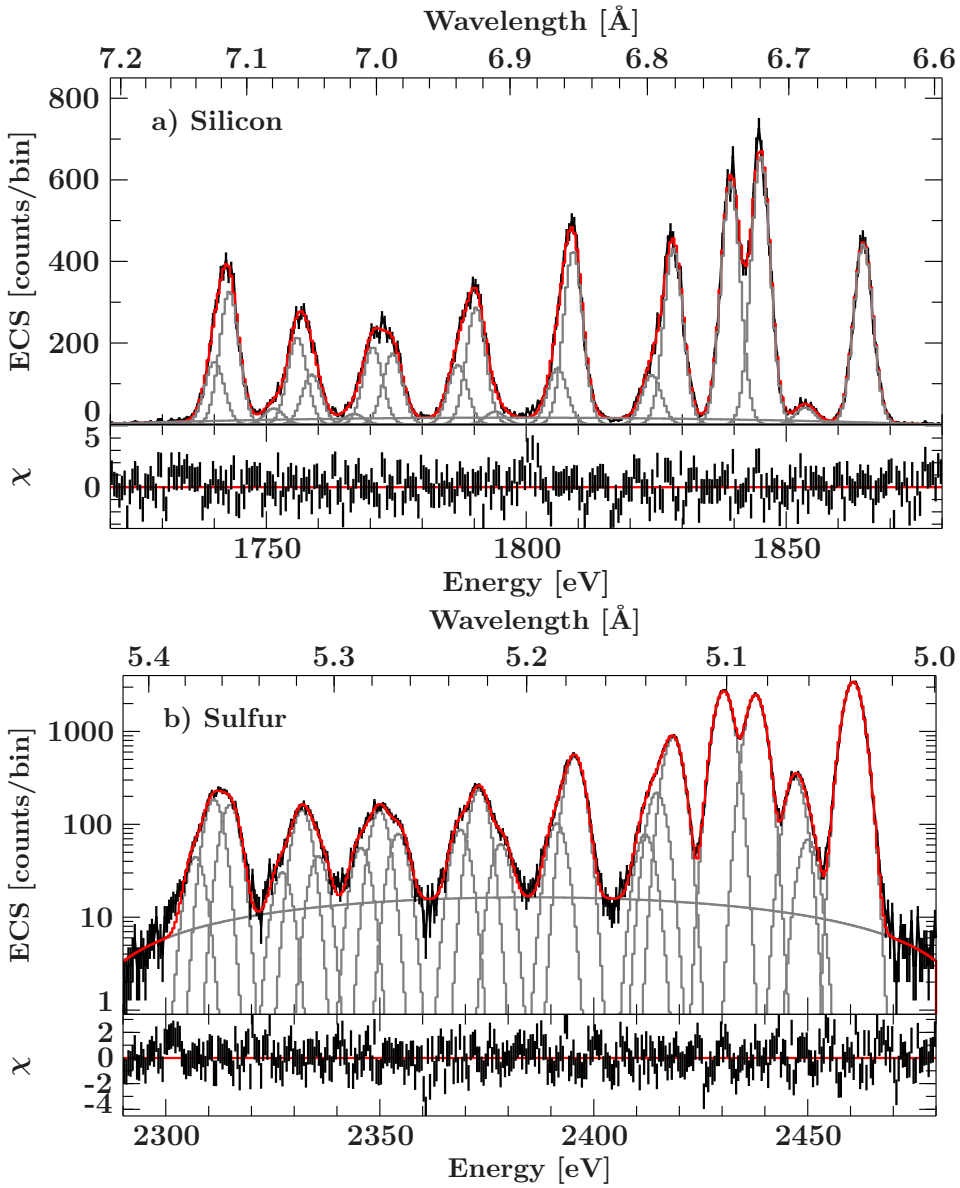

Figure 6.2: Overview of the components fitted to the Si (top) and S (bottom) spectra. The data are shown in black, the red line shows the total model, model components are gray. — From Hell et al. (2016b, Fig. 2).

for model B will be at least slightly better than the χ^2 for model A. The additional line in model B is only accepted if the improvements, $\Delta\chi^2_{\mathrm{fake},i} = \chi^2_{\mathrm{B},i} - \chi^2_{\mathrm{A},i}$, of 99% of the simulated cases are smaller than the improvement in the real spectrum. Figure 6.2 shows the final distribution of the single Gaussian components for silicon and for sulfur. Tables 6.4 and 6.5 list the resulting line centers with their statistical 90% confidence limits.

As an additional consistency check for the accuracy of our results, in a second approach we allow for a constant shift of the Run-II data compared to the Run-I data (Hell et al., 2016b). The derived constants of $0.13^{+0.06}_{-0.05}$ eV for Si and -0.12 ± 0.05 eV for S are consistent with our estimate of the systematic uncertainty of our calibration (Section 6.1.3).

6.1.5 Line Identification with FAC

To identify the lines associated with our measured spectra, we use FAC (Section 2.3; Gu, 2004b, 2008) to calculate the wavelengths of transitions in the involved ions and model the measured spectra (Hell et al., 2016b). Our FAC calculations take into account radiative (de-)excitation, collisional (de-)excitation and ionization, autoionization, dielectronic recombination, and radiative recombination. Since at EBIT densities the coronal limit applies, electron impact collisional excitation, inner-shell ionization, and subsequent radiative cascades are the main processes to populate upper states. At the electron beam energies used here, no emission from dielectronic recombination exists for the ions of interest and no X-rays from radiative recombination fall into our energy band. Although the main application for our results is photoionized plasmas (Section 1.4.1), the collisional nature of EBIT does not compromise this task.

Our calculations (Hell et al., 2016b) include emission from all the $n \rightarrow 1$ transitions in Na-like to H-like silicon and sulfur, where $2 \leq n \leq 5$, allowing interactions between all levels, including $\Delta n = 0$ transitions[2]. For these limits, the calculation could be completed in a reasonable time. The contribution to the line strength from higher n transitions is negligible. Since the charge state distribution in EBIT depends on ionization and recombination processes, the level populations are estimated for all ions in a single calculation. The other plasma code parameters are the electron beam energy, which we assume to follow a Gaussian distribution with an energy spread of $\sim 40\,\mathrm{eV}$ (Beiersdorfer et al., 1992b; Gu et al., 1999a), and an electron density of $10^{12}\,\mathrm{cm}^{-3}$, which we estimate from beam current and energy. The relative abundances of the trapped ions are set to be 1. The simulation of the spectrum produced in the trap is therefore not self-consistent.

Figure 6.3 illustrates the resulting FAC simulations for silicon and sulfur, considering the presence of H- through Na-like ions. The line centers of transitions calculated by FAC are convolved with a Gaussian line with a FWHM of 4.6 eV, i.e., the resolution of the calorimeter (see Section 6.1.3).

While the strongest K-shell line features from each charge state are easily resolved (Figs. 6.1 and 6.3), identifying the transitions that contribute to each feature is accomplished by comparison to the FAC calculation as follows (Hell et al., 2016b, following the approach of Hell, 2012). For each feature we plot the data and individual model components and overlay them with the transitions obtained from FAC (Figs. 6.10 and 6.11). Then we assume that for every Gaussian fit component the main contribution comes from the strongest FAC lines at this energy and identify the model component with these lines. The results are listed in Tables 6.4 (Si) and 6.5 (S). In each row the FAC lines are followed by the corresponding transitions as calculated by Palmeri et al. (2008a, see Section 6.1.6 for details) and CHIANTI, if available. For most measured peaks, the distribution of the FAC lines agrees well enough with the measurements to allow a reliable identification. Both the Si and S spectra behave very similarly, so our description of the spectra (Hell et al., 2016b) here focuses on the contributions by iso-electronic sequence, for the most part not distinguishing in Z except in the rare cases where significant differences occur between the Si and S spectra.

[2] This is an expansion of the model used in Hell (2012), both in terms of ion range and principle quantum number n included.

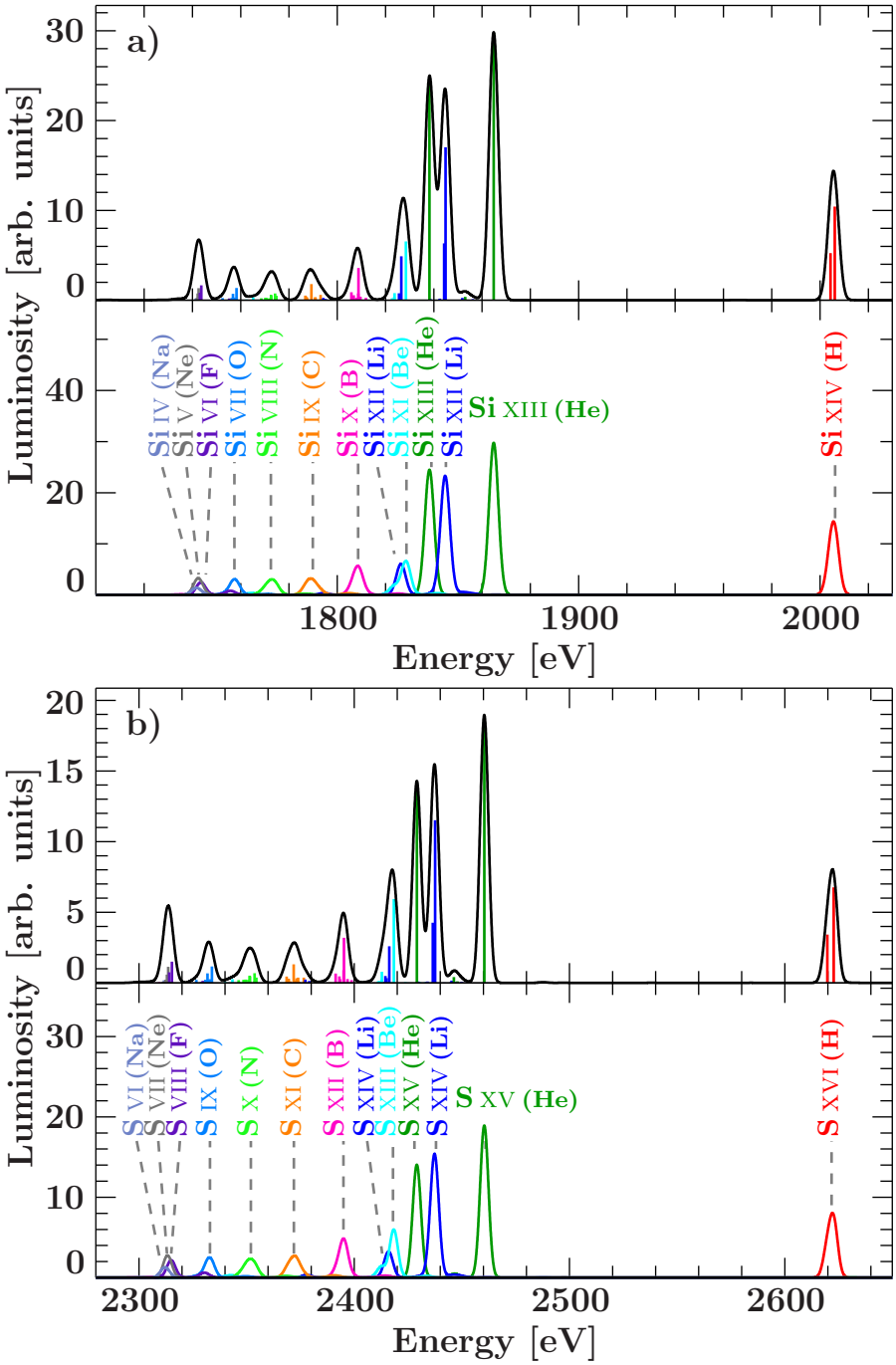

Figure 6.3: FAC simulation of the *a)* Si and *b)* S Kα spectra. For each subfigure the top panel shows the transition energies with their predicted luminosity and the total spectrum (black line) resulting from a convolution with Gaussians at the resolution of the ECS. The bottom panels show the convoluted spectra individually for each ionization state, which sum to the black line of the top panel. The impact of line blends can be seen quite clearly. Labels include the corresponding iso-electronic sequence in parentheses. — From Hell et al. (2016b, Fig. 3).

As described by Hell et al. (2016b), the main Li-like, Be-like, and B-like features are each dominated by a single strong transition that is easily reproduced by the Gaussian components fitted to the spectra (see features labeled Li-2, Be-1, B-1 in Figs. 6.10 and 6.11 panels e-g). Although there are a few weaker transitions surrounding these strong lines, they do not strongly affect the fitted line centers. Both the Be- and B-like features have a low-energy shoulder caused by weaker transitions that have a just large enough separation from the strong transition to be resolved. According to our FAC calculations, the Li-like ion also has a relatively strong transition that sits right between the Be-like lines. Although in the synthetic Si spectrum the Li-like line appears to have similar strength as the strong Be-like line, a comparison of Fig. 6.3 to the measured Si spectrum shows that due to the incorrect assumption of charge balance entering our simulation, the synthetic spectra overestimate the Li-like features relative to the Be-like ones. Accordingly, despite this Li-like transition being unresolved in Si, it does not seem to affect the fitted line centers of the Be-like transitions Be-1 and Be-2 much (Fig. 6.10, panel f). For S on the other hand (Fig. 6.11, panel f), the Li-like transitions are attributed to their own Gaussian component (Be-2) while the weak Be-like line is assigned to a separate component (Be-3). As discussed based on more recent high-resolution crystal spectra of these transitions (Section 6.2), the separation of components Be-2 and Be-3 in this data set not be as significant as suggested by the Monte Carlo simulation.

The transition rich spectra of the lower charge states (C-like, O-like, and N-like) are more complex as they have many transitions of similar strength rather than a distinct strong transition among a few weak ones (Figs. 6.10 and 6.11, panels b-d). However, some of these transitions tend to cluster into groups. The separation of these groups is larger for the higher-Z element S, making it easier for them to be partially resolved. As discussed for iron by Decaux et al. (1997), starting around C-like ions the Kα line emission of the lower charge states probably has strong contributions from states excited through inner-shell ionization in addition to the collisionally excited states (Hell et al., 2016b).

In the C-like ions (Figs. 6.10 and 6.11, panel d), the strongest fitted component, C-2, is made up of the strongest calculated transitions at slightly lower energies than the component's center and a few weaker transitions at and slightly above the fitted energy. The C-like feature also has a strong low-energy shoulder (C-3) from transitions similar in strength to the ones from the C-2 cluster, and a weaker high-energy shoulder (C-1) consisting of a C-like and two weak Li-like transitions (Hell et al., 2016b).

The N-like transitions split into four main groups (Figs. 6.10 and 6.11, panel c). They are accompanied by a Be-like transition in the low-energy tail of their spectral feature. Again, the larger spacing in S is beneficial, although in both Si and S this feature is modeled by three components. While N-1 coincides well with the first group of calculated transitions on the high-energy side for both components, the second group containing the other two of the strongest four transitions falls right between N-1 and N-2 in Si, but is clearly attributed to N-2 in S. N-2 also encompasses the third group of transitions, while N-3 contains the last group of N-like transitions and the mentioned Be-like transition.

The O-like peak is also described by three Gaussians (Figs. 6.10 and 6.11, panel b). The strongest line calculated with FAC makes up the weaker component at high energies (O-

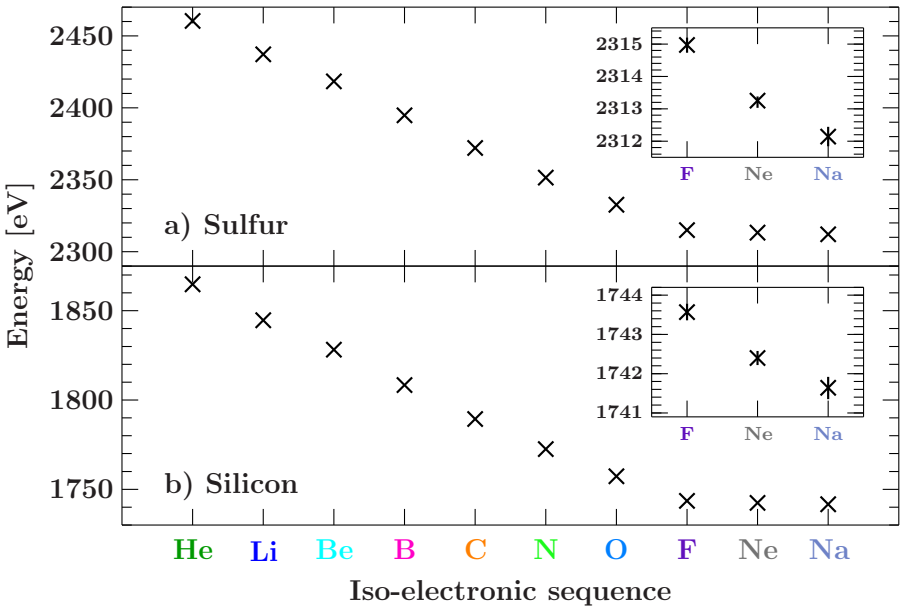

Figure 6.4: Energies of the line centers for different ionization stages of sulfur (a) and silicon (b), derived from FAC calculations. Lines for ions with more than 9 electrons (F-like) blend strongly with a predicted energy spacing of ~ 1 eV between charge states. — From Hell et al. (2016b, Fig. 4).

1), while the main component (O-2) consists of a number of weaker transitions. A single O-like transition accounts for the low-energy shoulder (O-3).

The lowest energy peak (Figs. 6.10 and 6.11, panel a) consists of a blend of K-shell transitions in F-like ions as well as emission from lower charge states (Fig. 6.4; Hell et al., 2016b). This is a result of the fact that, for charge states other than F-like, emission is dominated by inner-shell ionization followed by radiative decay in these cases and the effect of additional spectator electrons in $n \geq 3$ shell on these transition energies is relatively small. Additionally, owing to the open $n = 3$ shell, the M-shell ions have a more complex energy level structure – and, therefore, a multitude of transitions – in each of these charge states. The energy ranges covered by these transitions overlap severely (Fig. 6.5). Specifically, the Kα transition energies from these charge states fall within a 3 eV energy band and are therefore unresolved (Fig. 6.4). Consequently, although the F-like ion only has two distinct transitions, we cannot resolve this charge state individually from the transitions in M-shell ions in these low-Z elements (Hell et al., 2016b). Even for higher-Z elements such as Fe, the rich spectra of the M-shell ions are very hard to resolve, although they span a much wider energy range (Chapter 7). This last peak is modeled by two (Si) and three (S) Gaussian components, respectively (Hell et al., 2016b). In both cases, we attribute the first, i.e., high-energy, component (F-1) to a mixture of transitions in F-like and Ne-like ions. In case of the Si XX-1 line at 1740.04 eV, however, there are no lines of considerable strength in our calculations that could be used for identification. We tentatively identify this line as a blend of Kα emission from very low charge states with more than 10 electrons. Similarly, although Table 6.5 lists weak transitions in Na-like

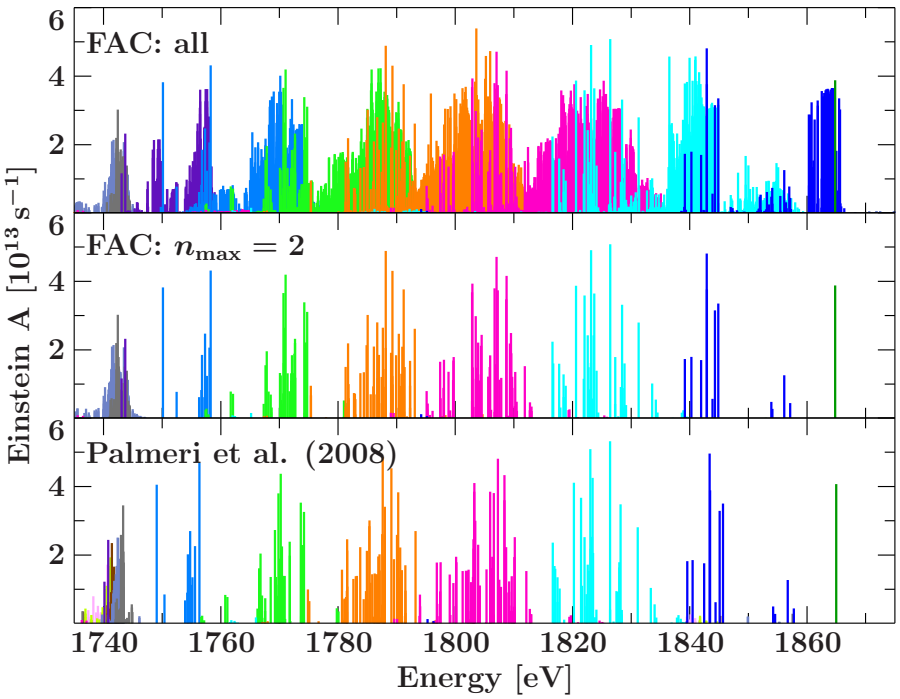

Figure 6.5: Comparison between the atomic data of Si presented by P08 (*bottom*) and the calculation with FAC (*middle*: only $2\ell \rightarrow 1s$ transitions as in P08; *top*: all calculated transitions in this shown energy range, including satellites with an electron in up to the $n_{max} = 5$ shell) for He- through Ne-like ions. Different colors represent different ionization states (see Fig. 6.1). — From Hell et al. (2016b, Fig. 5).

S VI and B-like S XII for the lines F-2 and F-3, these lines probably also have a significant contribution from weak lines from near-neutral ions, as discussed for the case of silicon.

Also notable is that for both Si and S, line z as calculated with FAC (Si: 1838.20 eV, S: 2429.075 eV) has a large offset (>1 eV) compared to the measured line center (Si: 1839.33 eV, S: 2430.380 eV). This offset has not improved with our revised FAC model compared to Hell (2012). Our measurement is, however, again consistent with the reference values reported by Drake (1988, Si: 1839.448 eV; S: 2430.347 eV).

6.1.6 Comparison with Palmeri et al. (2008a)

For completeness and to provide a test for the accuracy of the Kα line energies employed by XSTAR, we (Hell et al., 2016b) compare our measurements and our FAC calculations to those of Palmeri et al. (2008a), denoted as P08 in the following. Note that the calculated transition wavelengths listed by P08 have been empirically shifted by P08 for ions with $3 \leq N \leq 9$, where N is the number of electrons. A qualitative comparison between the results obtained with FAC and the lines published by P08 is displayed in Fig. 6.5 for silicon. Since the P08 data do not provide line fluxes, the line distributions are shown via their radiative transition rates (Einstein A). P08 only list $2\ell \rightarrow 1s$ transitions. We therefore also filter for these lines calculated with FAC. The transitions with a spectator electron

in a higher n shell blend strongly with Kα transitions of the next ionization state, but according to the FAC calculations, their contribution to the Kα line strength is negligible (Fig. 6.3).

As expected, the positions of the He-like lines agree very well. For lower ionization states Hell et al. (2016b) find that the general distribution of the lines is still similar, but the predicted energy separation of some line features does not agree. For example, there are two O-like Si VII lines around 1750 eV (Fig. 6.5), specifically the transitions $1s^2 2s 2p^5\ {}^1P_1^o \rightarrow 1s 2s 2p^6\ {}^1S_0$ and $1s^2 2s^2 2p^4\ {}^1S_0 \rightarrow 1s 2s^2 2p^5\ {}^1P_1^o$ (P08) respectively $(1s^2\, 2s_{1/2}\, 2p_{1/2}^2 (2p_{3/2}^3)_{3/2})_1 \rightarrow (1s_{1/2}\, 2s_{1/2}\, 2p_{1/2}^2\, 2p_{3/2}^4)_0$ and $1s^2\, 2s^2\, 2p_{1/2}^2 (2p_{3/2}^2)_0 \rightarrow (1s_{1/2}\, 2s^2\, 2p_{1/2}^2 (2p_{3/2}^3)_{3/2})_1$ (FAC), for which the ratio of the transition probabilities is approximately the same in both calculations (P08: 0.21; FAC: 0.20). The separation of their line energies, however, is almost twice as large in FAC (2.32 eV) as in P08 (1.33 eV). The most outstanding difference is that in the P08 calculations the two F-like spectral lines at $\sim$ 1741 eV have distinctly lower energies than the Ne-like lines, although the Ne-like iso-electronic sequence has an electron more than the F-like ions. This behavior is in contrast to the FAC calculations where the F-like lines have higher energies.

Comparing FAC (jj-coupling) and P08 (LS-coupling) is not trivial since the two calculations are based on different coupling schemes (Hell et al., 2016b). It is therefore necessary to translate one scheme into the other. The calculations are in sufficient agreement such that most lines can be identified through a comparison of the line lists instead of resorting to a complicated formal mapping between both schemes (see, e.g., Calvert & Tuttle, 1979; Dyall, 1986). Following the method of Hell (2012), we (Hell et al., 2016b) do this comparison by first sorting the levels of both calculations according to energy and then matching the levels in order of increasing energy. The match is cross-checked via the total angular momentum J, which is the only good quantum number common between the two coupling schemes and therefore should be identical between them. In cases where J does not match between two assigned levels, LS-coupling multiplets can be rearranged for their Js to fit the jj-coupling partners. This is possible because within these multiplets the differences between the calculated level energies are smaller than the estimated uncertainty of the calculations and, in most cases, smaller than the energy differences between P08 and FAC results. See Hell (2012) or Hell et al. (2016b) for an example of this approach. The comparison demonstrates the point made in Section 1.3.1 that the uncertainty in calculated values of closely spaced energy levels can cause an inversion of the order of these levels (Smith & Brickhouse, 2014).

6.1.7 Center of Line Blends

In most experimental cases, the spectral resolution is not adequate to distinguish between single features of the given lines. This is especially true for satellite based instrumentation. Therefore, the ability to determine the energy for each identified line is precluded. In order to provide the means to derive Doppler shifts also for these cases, in a second approach we (Hell et al., 2016b) fit the spectra with a single Gaussian for each of the readily distinguishable line blends, leaving the line widths free to vary. The obtained line

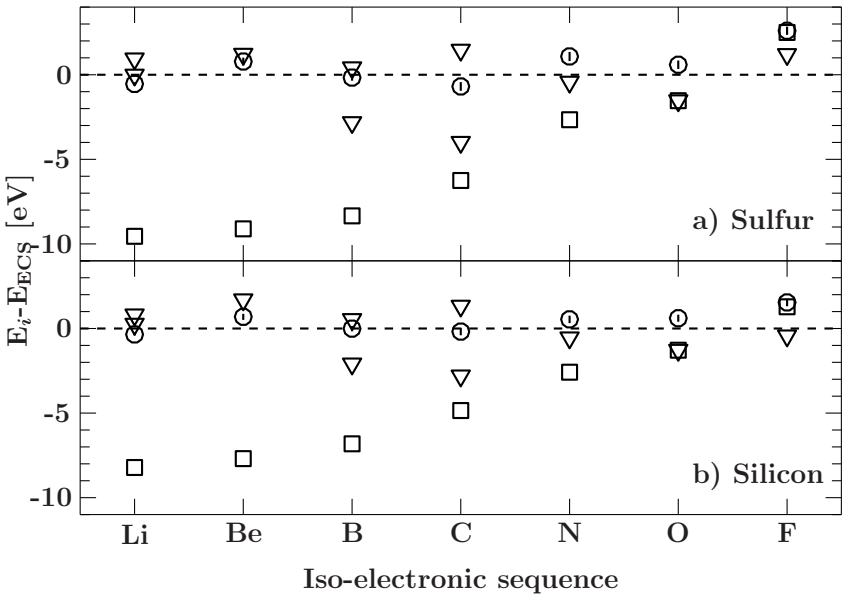

Figure 6.6: Deviation of the theoretical line centers in Table 6.2 from the centers measured with the ECS, as a function of iso-electronic sequence. While the lines derived from FAC (○) and taken from Behar & Netzer (2002, ▽) agree fairly well with our measurement, the deviation of the House (1969, □) values become significant for higher charge states. — From Hell et al. (From 2016b, Fig. 7)

centers, which are listed in Table 6.2 and displayed in Fig. 6.6, are sufficient as reference energies to derive Doppler shifts for collision dominated or photoionized plasmas where 1s–2p transitions are dominant, as demonstrated below. This is a generally more user friendly and publicly distributable approach to derive Doppler shifts than Hell (2012)'s method of comparing the shifts of the synthetic FAC spectrum with respect to the celestial and the laboratory reference spectrum, respectively, with each other. Note that again the listed uncertainties of line centers are on the 90% confidence level and in addition to a systematic uncertainty of 0.13 eV for Si and 0.23 eV for S. For comparison, we (Hell et al., 2016b) also fitted our FAC models with Gaussians[3], and list the reference energies from Behar & Netzer (2002) and House (1969) in Table 6.2. Based on a similar argument, Behar & Netzer (2002) only list the strongest (photo-absorption) lines, i.e., lines with the largest oscillator strength, for the iso-electronic sequences He I to F I of the most common elements in astrophysics. According to their calculations, these lines account for more than 70%, and in most cases even more than 90%, of the absorption effect for the respective transitions. The good agreement of the energies of their principal lines with our measurements supports their argument. The House (1969) tables, on the other hand, deviate significantly from our results, especially for the higher charge states; this is probably a direct consequence of averaging over the fine structure.

[3]Note that the uncertainties on these values are derived from the fit and purely statistical.

Table 6.2: Center [eV] of unresolved line blends for Si and S (Hell et al., 2016b, Table 3)

Ion[a]	this work	FAC	Behar	House
Silicon				
Si XII (Li)	1845.02 ± 0.07	1844.67 ± 0.07	1845.83	1836.80
			1845.28	
Si XI (Be)	1827.51 ± 0.06[b]	1828.20 ± 0.18	1829.21	1819.82
Si X (B)	1808.39 ± 0.05	1808.38 ± 0.16	1808.93	1801.57
			1806.30	
Si IX (C)	1789.57 ± 0.07	1789.39 ± 0.22	1786.77	1784.72
			1790.90	
Si VIII (N)	1772.01 ± 0.09	1772.55 ± 0.22	1771.46	1769.43
Si VII (O)	1756.68 ± 0.08	1757.29 ± 0.21	1755.40	1755.40
Si VI (F)	1742.03 ± 0.06[c]	1743.57 ± 0.22	1741.60	1743.31
Sulfur				
S XIV (Li)	2437.761 ± 0.027	2437.22 ± 0.10	2438.71	2428.21
			2437.75	
S XIII (Be)	2417.51 ± 0.05[b]	2418.29 ± 0.23	2418.73	2408.40
S XII (B)	2394.95 ± 0.05	2394.78 ± 0.18	2395.37	2386.61
			2392.13	
S XI (C)	2372.81 ± 0.09	2372.12 ± 0.26	2368.82	2366.56
			2374.27	
S X (N)	2350.40 ± 0.12	2351.48 ± 0.27	2349.97	2347.74
S IX (O)	2332.06 ± 0.10	2332.65 ± 0.25	2330.53	2330.53
S VIII (F)	2312.37 ± 0.09[c]	2314.97 ± 0.24	2313.57	2314.87

[a] Listed is the ion and its iso-electronic sequence in parentheses
[b] blends with a Li-like transition
[c] blends with lower charge states

Notes: Listed are the statistical uncertainties, which are in addition to 0.13 eV (Si) and 0.23 eV (S) systematic uncertainty. A fit to the FAC models (given uncertainties derived from the fit), the energy of the strongest line according to Behar & Netzer (2002), and the lines by House (1969) averaging over the fine structure are listed as well. For O-like Si and S, Behar & Netzer (2002) and House (1969) list exactly the same value to three decimals in units of Å.

Application to Vela X-1

To demonstrate the impact of our measurements, we (Hell et al., 2016b) use our new reference energies (Table 6.2) to re-determine Doppler shifts for Vela X-1 from the published wavelengths. Figure 6.7 shows a comparison between our laboratory Si spectra and the ones measured with *Chandra*-HETG at orbital phase $\phi_{\rm orb} = 0.5$. Schulz et al. (2002, $\phi_{\rm orb} = 0.0$, i.e., eclipse) and Goldstein et al. (2004, $\phi_{\rm orb} = 0$ and $\phi_{\rm orb} = 0.5$) both fitted the lines originating from some of the lower charge states of Si in the *Chandra* spectra, but did not model the intermediate charge states up to Li-like. Using House (1969) as a reference for the transition wavelengths resulted in Doppler shifts that not only differ between these charge states, but also deviate significantly from the He- and H-like

Table 6.3: Doppler shifts in $\mathrm{km\,s^{-1}}$ for Vela X-1 (Hell et al., 2016b, Table 4)

Ion	$\phi = 0.0$				$\phi = 0.5$	
	S02[a]	G04[b]	S02 new[c]	G04 new[c]	G04[b]	G04 new[c]
Si IX	-432 ± 173	-570^{+271}_{-490}	383 ± 173	244^{+272}_{-491}	-1028^{+275}_{-137}	-215^{+276}_{-137}
Si VIII	43 ± 214	-119^{+389}_{-488}	479 ± 214	317^{+390}_{-489}	-396	40
Si VII	-170 ± 170	-85	48 ± 170	133	-527^{+321}_{-249}	-309^{+321}_{-249}
Si VI	0 ± 211	⋯	-9 ± 211	⋯	⋯	⋯

[a] Doppler shifts from Schulz et al. (2002)
[b] Doppler shifts from Goldstein et al. (2004)
[c] Doppler shifts from S02 and G04, respectively, adjusted for the new reference energies measured at EBIT (Table 6.2)

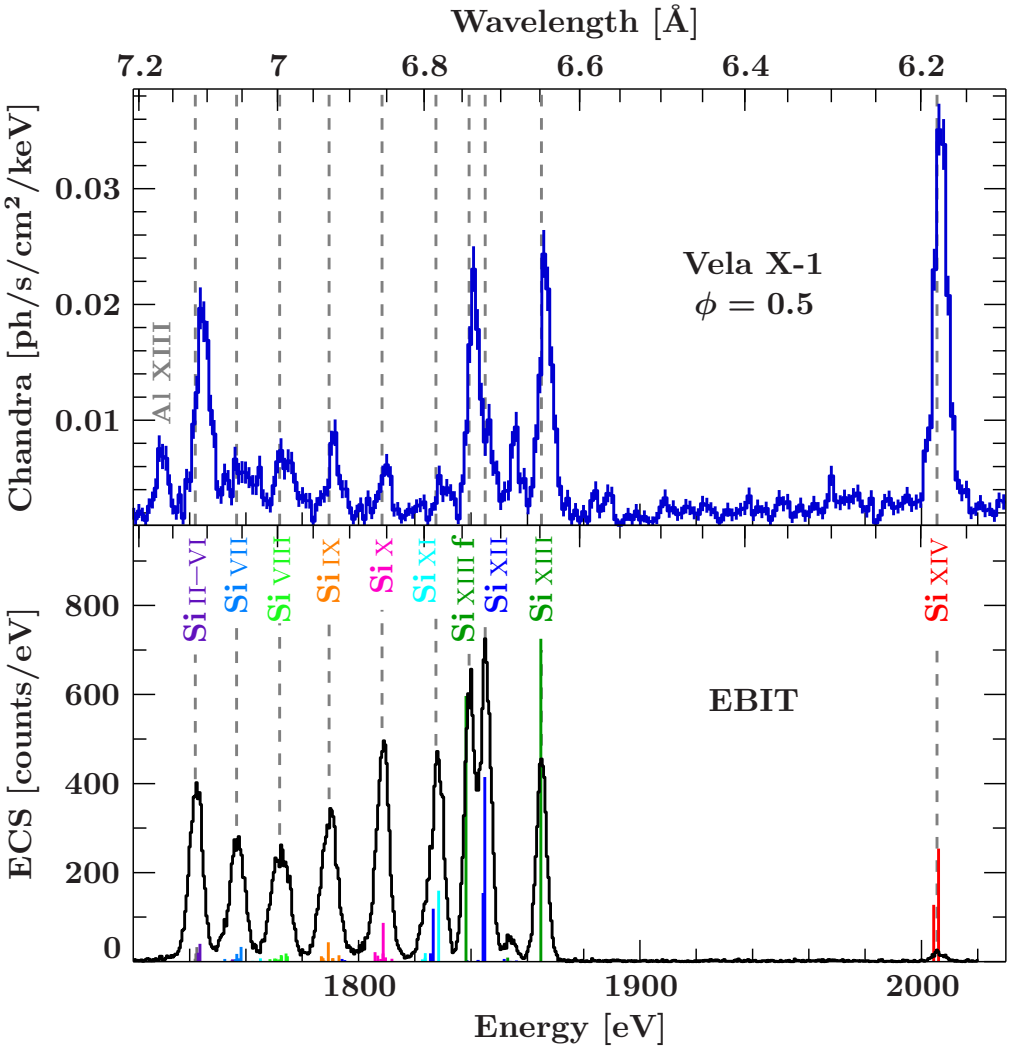

Figure 6.7: Comparison of the Vela X-1 Si spectral region observed by *Chandra*-HETG at orbital phase $\phi = 0.5$ (ObsID 1927) to the EBIT/ECS spectrum. The colored sticks are the transitions calculated with FAC. — From Hell et al. (2016b, Fig. 8).

ions in the same observation, even switching signs from blue to red-shifted (Goldstein et al., 2004). Determining the Doppler shifts based on our laboratory reference spectra (Table 6.3) results in Doppler shifts that are similar for all Si ions and now also agree with the Doppler shifts determined from the He- and H-like species, for which the rest-wavelengths are well known. This is more consistent with the picture of photons being reprocessed by clumps of material with an onion-like structure, where the outer layers shield the colder and denser core of the clump from the ionizing radiation of the compact object. Grinberg et al. (2017) discuss further implications from these results in detail.

Application to Cyg X-1

Similar results for the clump structure were also obtained for Cyg X-1 (Hell et al., 2013; Miškovičová et al., 2016; Hirsch et al., 2017), where these lines are seen in absorption. The five *Chandra*-HETG observations of Cyg X-1 in the low/hard state suitable for the study of the excess absorption from clumps were each divided into multiple spectra (Hanke, 2011; Hell, 2012; Hell et al., 2013) corresponding to different stages of dipping (Section 1.4.1). For ObsIDs 3814 and 8525 at orbital phase $\phi \approx 0$ this results in four spectra each, dubbed non-dip, weak dip, dip, and strong dip. The shorter ObsID 9847 ($\phi \approx 0.2$) was only divided into three dipping phases due to lower statistics. ObsID 11044 ($\phi \approx 0.5$) is completely free of dips and was therefore not split. ObsID 3815 ($\phi \approx 0.75$) only shows low levels of dipping and was only divided into non-dip and weak dip spectra.

Based on the ECS measurements, the Doppler shifts of the L-shell ions of Si and S were determined in each of these spectra. As Fig. 6.8 shows, the velocity derived from the Doppler shifts changes as a function of orbital phase, but within the same orbital phase is consistent between all dipping stages and ionization states. The strong dip spectrum of $\phi \approx 0$ is the only one that appears to be shifted a little compared to the other dipping stages, which is probably due to the low statistics of the heavily absorbed spectrum. This discrepancy is resolved in the re-examination of Hirsch et al. (2017). The consistency of the Doppler shifts within each orbital phase shows that the different ions travel through space together, indicating the onion-like structure as described above. The average velocities of the Si and S ions for each dipping stage agree well with the range of Doppler shifts Miškovičová et al. (2016) found for all ions in the non-dip stage (Fig. 6.9). Conclusions on the orbital modulation Miškovičová et al. (2016) draw from these ions therefore similarly apply to the L-shell ions of Si and S in the different dipping phases.

Figure 6.9 also shows the radial velocities of the black hole and the companion star and the expected wind velocities (according to the focused wind model of Gies & Bolton, 1986) projected onto the line of sight as a function of distance to the black hole. The phase shift of $\Delta\phi = 0.25$ between the black hole and the wind as predicted by the model is not seen in the observed Doppler shifts (Miškovičová et al., 2016). Nevertheless, the velocity range of the ions at $\phi \approx 0$ is consistent with a distance to the black hole of $\lesssim 0.25d$, where d is the distance between the back hole and its companion star. With $\lesssim 0.5d$ the ions at phase $\phi \sim 0.75$ appear to be further away from the black hole, but this can be expected as this is the brightest of the hard state observations, i.e., the radiation

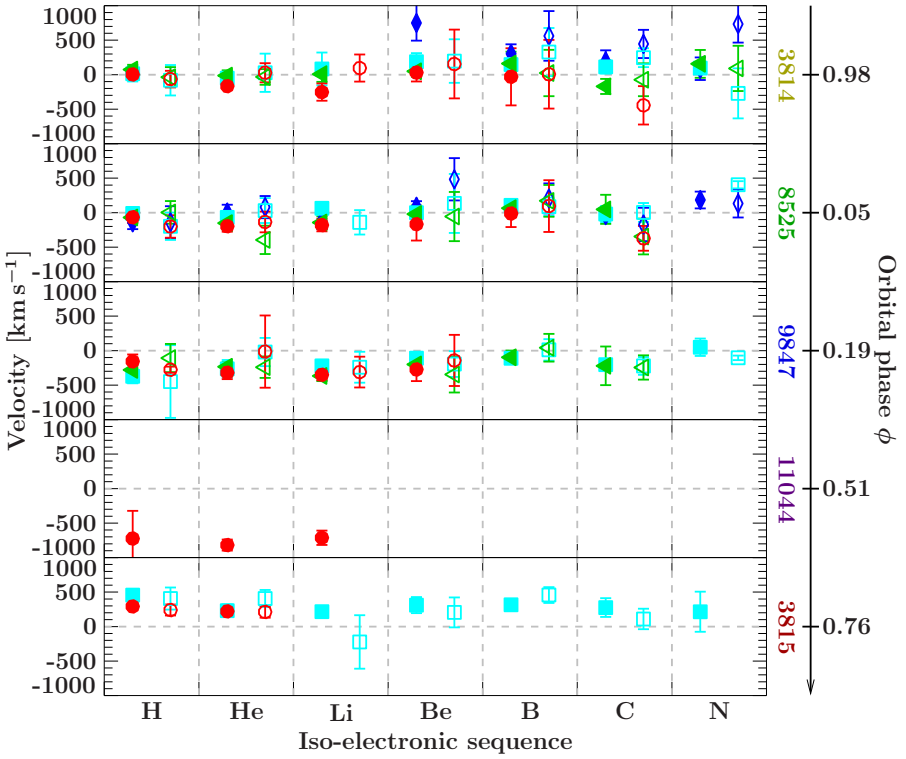

Figure 6.8: Doppler shifts of the H- through N-like Si (filled symbols) and S (empty symbols) ions in Cyg X-1 as a function of dipping stage and orbital phase (ObsIDs 3814, 8525, 9847, 11044, and 3815). The shifts are derived from the FAC spectra with energies corrected for the laboratory measurements as described in Hell (2012). The different dipping stages are non-dip (red circle), weak dip (green triangles), dip (cyan squares), and strong dip (blue diamonds).

pressure from the black hole is higher than for the other observations. The Doppler shifts of these three observations, 3814, 3815, and 8525, indicate that the absoring medium is close to the black hole and have a possible origin in the focused wind. ObsID 9847, on the other hand, shows a blue shift (negative radial velocity) that is much higher than the radial velocity of the black hole towards the observer, although at $\phi \sim 0.2$ the wind model predicts redshifts (Miškovičová et al., 2016). However, at this orbital phase the black hole is observed through a region where the stellar wind is highly disturbed, in the so-called bow shock of the black hole (Manousakis, 2011; Blondin & Woo, 1995, and references therein). These turbulences can cause a significant non-radial velocity in the wind material, which looks like a high blue shift at this phase (Miškovičová et al., 2016).

For more extensive details on the analysis of the non-dip spectra refer to Miškovičová et al. (2016). For a detailed study of the orbital modulation of the dipping phases see Hirsch et al. (2017). Hirsch et al. (2017) re-examine the HETG observations based on a slightly more physical selection of the dipping stages: instead of just basing the selection criteria on changes in the hardness ratio of the energy bands 0.5–1.5 keV and 3–10 keV, Hirsch et al. (2017) choose their selection criteria based on changes in the color-color

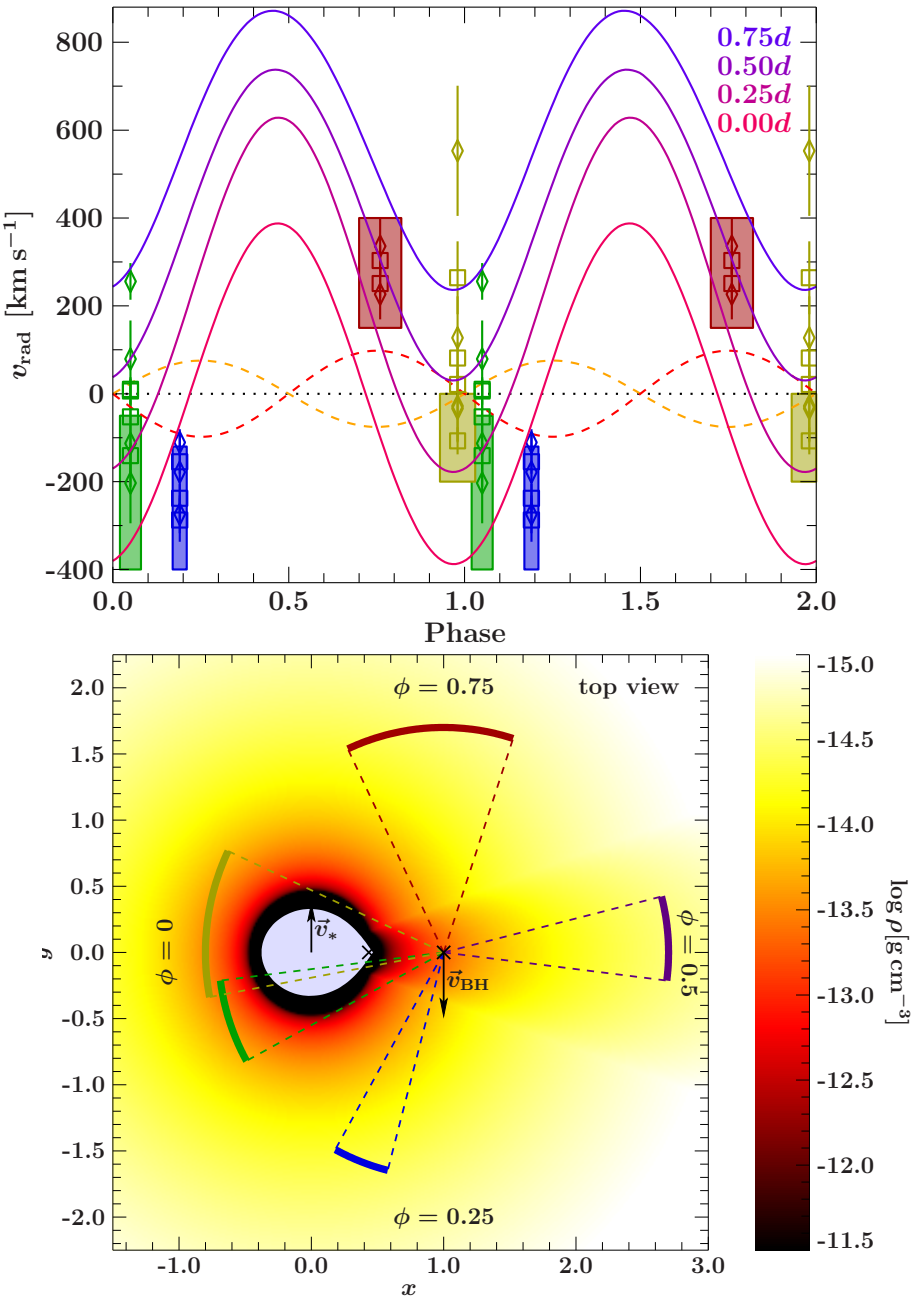

Figure 6.9: *Top:* Average Doppler shifts for each dipping stage shown in Fig. 6.8 as a function of orbital phase; repeated twice for clarity. The boxes indicate the range of Doppler shifts derived from all ions during non-dip (Miškovičová et al., 2016). Shown for comparison are the radial velocities of the black hole (red dotted line) and the companion star (orange dotted line), and the expected wind velocity projected onto the line of sight as a function of distance to the black hole ((Miškovičová et al., 2016), where d is the distance between the black hole and its companion. *Bottom:* Stellar wind density according to the focused wind model of Gies & Bolton (1986); colored arcs represent the orbital phase covered by the *Chandra*-HETG observations discussed here (from Miškovičová et al., 2016, Fig. 7).

diagram[4], which is a better tracer for the spectral changes of the continuum radiation due to increased absorbing columns. While the Doppler shifts shown in Figs. 6.8 and 6.9 were still derived with the indirect method of Hell (2012) by comparing the offset of the synthetic FAC spectra to both the HETG and the ECS spectra, Miškovičová et al. (2016) and Hirsch et al. (2017) base their Doppler shifts on the newly provided reference energies from Table 6.2 (Hell et al., 2016b). The results from both methods are consistent with each other.

6.1.8 Summary

The Kα emission line energies from Si^{4+} through Si^{12+} and S^{6+} through S^{14+} have been measured using the ECS calorimeter at the LLNL EBIT facility (Hell et al., 2016b). The results have been compared to our own FAC calculations and earlier calculations of Palmeri et al. (2008a), Behar & Netzer (2002), and House (1969). The newly available data (Table 6.2) can directly be applied to resolve astrophysical problems such as, e.g., wind diagnostics in high mass X-ray binary systems like Vela X-1 (Liedahl & Brown, 2008) and Cyg X-1 (Miškovičová et al., 2016). The 90% confidence limits of $\lesssim 0.5\,\mathrm{eV}$ on the measured line centers presented here correspond to Doppler shifts of less than $90\,\mathrm{km\,s^{-1}}$. These measurements, therefore, provide line centers with an accuracy slightly better than the uncertainty of $\sim 100\,\mathrm{km\,s^{-1}}$ on the *Chandra* HETG (Marshall et al., 2004; Canizares et al., 2005; Chandra X-ray Center, 2015). When future missions with higher effective area make high-resolution spectra of point as well as extended celestial sources more commonly available, we expect to see these lines to be resolved in a variety of sources. Our results will then be especially useful for extended sources like supernova remnants which have yet to be observed in high resolution.

6.1.9 Overview of Spectral Fits

In this section we (Hell et al., 2016b) present the full list of measured line energies obtained with EBIT for Si (Table 6.4) and S (Table 6.5). The tables contain the best-fit values from the EBIT measurement, their identification with transitions from FAC calculations in jj-coupling including the calculated line energy, and, in LS-coupling, a comparison to calculations by P08 (Palmeri et al., 2008a) and database entries of CHIANTI, where available. In addition, Figs. 6.10 and 6.11 give a detailed overview of the data, the best-fit including the individual Gaussian model components, and the location and theoretical relative line strengths of the transitions according to the FAC calculations.

[4] A color is the relative number of counts of two energy bands. The color-color diagram displays the "hard" hardness ratio (hard color: (1.5–3 keV)/(3–10 keV)) vs. the "soft" hardness ratio (soft color: (0.5–1.5 keV)(1.5–3 keV)) for many short time intervals in the observation. See Hanke (2011) and Hirsch et al. (2017) for a discussion.

Table 6.4: Identification of the fitted silicon line centers. (Hell et al., 2016b, Table 5)

			jj-coupling			LS-coupling			
Key	Fit (eV)	Ion	Lower Level	Upper Level	FAC (eV)	Lower Level	Upper Level	P08 (eV)	CHI.
Li-1	1853.67 ± 0.20	He-like Si XIII	$1s^2$	$(1s_{1/2}\,2p_{1/2})_1$	1852.98	$1s^2\ {}^1S_0$	$1s2p\ {}^3P^o_1$	1853.30	1853.75
		Li-like Si XII	$1s^2\,3s_{1/2}$	$((1s_{1/2}\,2s_{1/2})_0\,3p_{3/2})_{3/2}$	1851.80	⋯	⋯	⋯	⋯
		Li-like Si XII	$1s^2\,2p_{3/2}$	$(1s_{1/2}\,(2p^2_{3/2})_0)_{1/2}$	1856.13	$1s^22p\ {}^2P^o_{3/2}$	$1s(^2S)\,2p^2(^1S)\ {}^2S_{1/2}$	1856.78	1854.37
Li-2	1845.09 ± 0.05	Li-like Si XII	$1s^2\,2s_{1/2}$	$((1s_{1/2}\,2s_{1/2})_0\,2p_{1/2})_{1/2}$	1844.29	$1s^22s\ {}^2S_{1/2}$	$1s(^2S)\,2s2p(^3P^o)\ {}^2P^o_{1/2}$	1845.11	1843.66
		Li-like Si XII	$1s^2\,2s_{1/2}$	$((1s_{1/2}\,2s_{1/2})_0\,2p_{3/2})_{3/2}$	1844.86	$1s^22s\ {}^2S_{1/2}$	$1s(^2S)\,2s2p(^3P^o)\ {}^2P^o_{3/2}$	1845.66	1844.21
z	1839.33 ± 0.05	He-like Si XIII	$1s^2$	$(1s_{1/2}\,2s_{1/2})_1$	1838.20	$1s^2\ {}^1S_0$	$1s2s\ {}^3S_1$	⋯	1839.42
Be-1	$1828.29^{+0.07}_{-0.08}$	Be-like Si XI	$1s^2\,2s^2$	$(1s_{1/2}\,2s^2\,2p_{3/2})_1$	1828.46	$1s^22s^2\ {}^1S_0$	$1s2s^22p\ {}^1P^o_1$	1828.19	⋯
		Li-like Si XII	$1s^2\,2s_{1/2}$	$((1s_{1/2}\,2s_{1/2})_1\,2p_{3/2})_{5/2}$	1826.55	$1s^22s\ {}^2S_{1/2}$	$1s(^2S)\,2s2p(^3P^o)\ {}^4P^o_{5/2}$	⋯	1828.19
Be-2	$1824.15^{+0.18}_{-0.20}$	Be-like Si XI	$1s^2(2s_{1/2}\,2p_{3/2})_2$	$((1s_{1/2}\,2s_{1/2})_1\,(2p^2_{3/2})_2)_2$	1823.71	$1s^22s2p\ {}^3P^o_2$	$1s(^2S)\,2s2p^2(^4P)\ {}^3P_2$	1823.43	⋯
		Be-like Si XI	$1s^2(2s_{1/2}\,2p_{1/2})_0$	$(((1s_{1/2}\,2s_{1/2})_0\,2p_{1/2})_{1/2}\,2p_{3/2})_1$	1823.64	$1s^22s2p\ {}^3P^o_0$	$1s(^2S)\,2s^22p(^2D)\ {}^3D_1$	1823.32	⋯
B-1	$1809.02^{+0.10}_{-0.15}$	B-like Si X	$1s^2\,2s^2\,2p_{3/2}$	$(1s_{1/2}\,2s^2(2p^2_{3/2})_2)_{3/2}$	1808.76	$1s^22s^22p\ {}^2P^o_{3/2}$	$1s2s^22p^2\ {}^2P_{3/2}$	1808.38	⋯
		B-like Si X	$1s^2\,2s^2\,2p_{1/2}$	$((1s_{1/2}\,2s^2\,2p_{1/2})_1\,2p_{3/2})_{1/2}$	1808.71	$1s^22s^22p\ {}^2P^o_{1/2}$	$1s2s^22p^2\ {}^2P_{1/2}$	1808.38	⋯
B-2	$1806.02^{+0.29}_{-0.49}$	B-like Si X	$1s^2\,2s^2\,2p_{3/2}$	$((1s_{1/2}\,2s^2\,2p_{1/2})_1\,2p_{3/2})_{5/2}$	1805.88	$1s^22s^22p\ {}^2P^o_{3/2}$	$1s2s^22p^2\ {}^2D_{5/2}$	1805.32	⋯
		B-like Si X	$1s^2\,2s^2\,2p_{1/2}$	$((1s_{1/2}\,2s^2\,2p_{1/2})_0\,2p_{3/2})_{3/2}$	1806.83	$1s^22s^22p\ {}^2P^o_{1/2}$	$1s2s^22p^2\ {}^2D_{3/2}$	1806.11	⋯
C-1	1794.0 ± 1.0	C-like Si IX	$1s^2(2s^2\,2p_{1/2}\,2p_{3/2})_2$	$(1s_{1/2}\,2s^2(2p^3_{3/2})_{3/2})_1$	1793.10	$1s^22s^22p^2\ {}^1D_2$	$1s2s^22p^3\ {}^1P^o_1$	1793.23	⋯
		Li-like Si XII	$1s^2\,2p_{3/2}$	$1s_{1/2}\,2s^2$	1794.18	$1s^22p\ {}^2P^o_{3/2}$	$1s2s^2\ {}^2S_{1/2}$	1795.26	1794.29
		Li-like Si XII	$1s^2\,2p_{1/2}$	$1s_{1/2}\,2s^2$	1795.17	$1s^22p\ {}^2P^o_{1/2}$	$1s2s^2\ {}^2S_{1/2}$	1796.27	1795.31
C-2	$1790.34^{+0.25}_{-0.40}$	C-like Si IX	$1s^2(2s^2\,2p_{1/2}\,2p_{3/2})_2$	$((1s_{1/2}\,2s^2\,2p_{1/2})_1\,(2p^2_{3/2})_2)_2$	1789.27	$1s^22s^22p^2\ {}^1D_2$	$1s2s^22p^3\ {}^1D^o_2$	1789.09	⋯
		C-like Si IX	$1s^2\,2s^2\,(2p^2_{3/2})_2$	$((1s_{1/2}\,2s^2\,2p_{1/2})_1\,(2p^2_{3/2})_0)_1$	1790.97	$1s^22s^22p^2\ {}^3P_2$	$1s2s^22p^3\ {}^3P^o_1$	1790.59	⋯
		C-like Si IX	$1s^2\,2s^2\,(2p^2_{3/2})_2$	$(1s_{1/2}\,2s^2(2p^3_{3/2})_{3/2})_2$	1790.81	$1s^22s^22p^2\ {}^3P_2$	$1s2s^22p^3\ {}^2P^o_2$	1790.41	⋯
C-3	$1786.85^{+0.25}_{-0.35}$	C-like Si IX	$1s^2\,2s^2\,(2p^2_{3/2})_2$	$((1s_{1/2}\,2s^2\,2p_{1/2})_1\,(2p^2_{3/2})_2)_3$	1786.83	$1s^22s^22p^2\ {}^3P_2$	$1s2s^22p^3\ {}^3D^o_3$	1786.26	⋯
		C-like Si IX	$1s^2\,2s^2\,(2p^2_{3/2})_0$	$(1s_{1/2}\,2s^2(2p^3_{3/2})_{3/2})_1$	1786.98	$1s^22s^22p^2\ {}^1S_0$	$1s2s^22p^3\ {}^1P^o_1$	1786.88	⋯
		C-like Si IX	$1s^2(2s^2\,2p_{1/2}\,2p_{3/2})_1$	$((1s_{1/2}\,2s^2\,2p_{1/2})_0\,(2p^2_{3/2})_2)_2$	1787.43	$1s^22s^22p^2\ {}^3P_1$	$1s2s^22p^3\ {}^3D^o_2$	1786.67	⋯

Notes: Identification of the fitted Si lines with transitions of the FAC simulation. The first column is the key to the line labels in Fig. 6.10, the third column indicates the ionization state. For the He-like lines the key of Gabriel (1972) is used. Columns 4–6 show the identification with FAC lines, columns 7–9 the corresponding transitions from Palmeri et al. (2008a), and column 10 lists energies from CHIANTI. Note that these calculated transition wavelengths listed by P08 have been empirically shifted by P08 for ions with $3 \leq N \leq 9$, where N is the number of electrons. Statistical uncertainties are shown as 90 % confidence intervals. There is an additional systematic uncertainty of 0.13 eV on all lines.

Table 6.4: — *continued*

Key	Fit (eV)	Ion	jj-coupling		FAC (eV)	LS-coupling		P08 (eV)	CHI.
			Lower Level	Upper Level		Lower Level	Upper Level		
N-1	$1774.29^{+0.20}_{-0.19}$	N-like Si VIII	$1s^2\,2s^2\,(2p_{1/2}(2p^2_{3/2})_2)_{5/2}$	$((1s_{1/2}\,2s^2\,2p_{1/2})_1\,(2p^3_{3/2})_{3/2})_{3/2}$	1774.25	$1s^22s^22p^3\ ^2D^o_{5/2}$	$1s2s^22p^4\ ^2P_{3/2}$	1773.66	···
		N-like Si VIII	$1s^2\,2s^2\,(2p_{1/2}(2p^2_{3/2})_2)_{3/2}$	$((1s_{1/2}\,2s^2\,2p_{1/2})_1\,(2p^3_{3/2})_{3/2})_{1/2}$	1774.74	$1s^22s^22p^3\ ^2D^o_{3/2}$	$1s2s^22p^4\ ^2P_{1/2}$	1774.19	···
		N-like Si VIII	$1s^2\,2s^2\,(2p^3_{3/2})_{3/2}$	$(1s_{1/2}\,2s^2(2p^2_{3/2})_0)_{1/2}$	1774.47	$1s^22s^22p^3\ ^2P^o_{3/2}$	$1s2s^22p^4\ ^2S_{1/2}$	1773.86	···
N-2	$1770.5^{+0.5}_{-4.9}$	N-like Si VIII	$1s^2\,2s^2\,(2p^2_{3/2})_{3/2}$	$((1s_{1/2}\,2s^2\,2p_{1/2})_1\,(2p^3_{3/2})_{3/2})_{3/2}$	1770.21	$1s^22s^22p^3\ ^2P^o_{3/2}$	$1s2s^22p^4\ ^2P_{3/2}$	1769.46	···
		N-like Si VIII	$1s^2\,2s^2\,(2p_{1/2}(2p^2_{3/2})_0)_{1/2}$	$((1s_{1/2}\,2s^2\,2p_{1/2})_1\,(2p^3_{3/2})_{3/2})_{1/2}$	1770.74	$1s^22s^22p^3\ ^2P^o_{1/2}$	$1s2s^22p^4\ ^2P_{1/2}$	1770.01	···
		N-like Si VIII	$1s^2\,2s^2\,(2p_{1/2}(2p^2_{3/2})_2)_{5/2}$	$((1s_{1/2}\,2s^2\,2p_{1/2})_1\,(2p^3_{3/2})_{3/2})_{5/2}$	1772.56	$1s^22s^22p^3\ ^2D^o_{5/2}$	$1s2s^22p^4\ ^2D_{5/2}$	1771.78	···
		N-like Si VIII	$1s^2\,2s^2\,(2p_{1/2}(2p^2_{3/2})_2)_{3/2}$	$(1s_{1/2}\,2s^2\,2p^2_{1/2}\,(2p^2_{3/2})_2)_{3/2}$	1172.66	$1s^22s^22p^3\ ^2D^o_{3/2}$	$1s2s^22p^4\ ^2D_{3/2}$	1771.76	···
		N-like Si VIII	$1s^2\,2s^2\,(2p_{1/2}(2p^2_{3/2})_2)_{3/2}$	$((1s_{1/2}\,2s^2\,2p_{1/2})_0\,(2p^3_{3/2})_{3/2})_{3/2}$	1172.02	$1s^22s^22p^3\ ^4S^o_{3/2}$	$1s2s^22p^4\ ^4P_{3/2}$	1770.60	···
N-3	$1766.9^{+1.0}_{-1.3}$	N-like Si VIII	$1s^2\,2s^2\,(2p^2_{3/2})_{3/2}$	$((1s_{1/2}\,2s^2\,2p_{1/2})_1\,(2p^3_{3/2})_{3/2})_{5/2}$	1768.52	$1s^22s^22p^3\ ^2P^o_{3/2}$	$1s2s^22p^4\ ^2D_{5/2}$	1767.59	···
		Be-like Si XI	$1s^2\,(2p_{1/2}2p_{3/2})_2$	$(1s_{1/2}\,2s^2\,2p_{3/2})_1$	1765.18	$1s^22p^2\ ^1D_2$	$1s2s^22p\ ^1P^o_1$	1766.01	···
O-1	1758.7 ± 0.5	O-like Si VII	$1s^2\,2s^2\,(2p_{1/2}(2p^3_{3/2})_{3/2})_2$	$(1s_{1/2}\,2s^2\,2p^2_{1/2}\,(2p^3_{3/2})_{3/2})_1$	1758.28	$1s^22s^22p^4\ ^1D_2$	$1s2s^22p^5\ ^1P^o_1$	1756.35	···
O-2	1756.0 ± 0.4	O-like Si VII	$1s^2\,2s^2\,2p^2_{1/2}\,(2p^2_{3/2})_2$	$(1s_{1/2}\,2s^2\,2p^2_{1/2}\,(2p^3_{3/2})_{3/2})_2$	1756.79	$1s^22s^22p^4\ ^3P_2$	$1s2s^22p^5\ ^3P^o_2$	1754.39	···
		O-like Si VII	$1s^2\,2s^2\,2p^2_{1/2}\,(2p^2_{3/2})_2$	$(1s_{1/2}\,2s^2\,2p_{1/2}\,2p^4_{3/2})_1$	1757.38	$1s^22s^22p^4\ ^3P_0$	$1s2s^22p^5\ ^3P^o_1$	1754.96	···
		O-like Si VII	$1s^2\,2s^2\,(2p_{1/2}(2p^3_{3/2})_{3/2})_1$	$(1s_{1/2}\,2s^2\,2p_{1/2}\,2p^4_{3/2})_0$	1757.32	$1s^22s^22p^4\ ^3P_1$	$1s2s^22p^5\ ^3P^o_0$	1754.78	···
		O-like Si VII	$1s^2\,2s^2\,(2p_{1/2}(2p^3_{3/2})_{3/2})_1$	$(1s_{1/2}\,2s^2\,2p^2_{1/2}\,(2p^3_{3/2})_{3/2})_2$	1756.30	$1s^22s^22p^4\ ^3P_1$	$1s2s^22p^5\ ^3P^o_2$	1753.91	···
		O-like Si VII	$1s^2\,2s^2\,2p^4_{3/2}$	$(1s_{1/2}\,2s^2\,2p_{1/2}\,2p^4_{3/2})_1$	1756.70	$1s^22s^22p^4\ ^3P_0$	$1s2s^22p^5\ ^3P^o_1$	1754.29	···
O-3	1751.4 ± 0.6	O-like Si VII	$1s^2\,2s^2\,2p^2_{1/2}\,(2p^2_{3/2})_0$	$(1s_{1/2}\,2s^2\,2p^2_{1/2}\,(2p^3_{3/2})_{3/2})_1$	1752.47	$1s^22s^22p^4\ ^1S_0$	$1s2s^22p^5\ ^1P^o_1$	1750.40	···
F-1	$1742.88^{+0.15}_{-0.17}$	F-like Si VI	$1s^2\,2s^2\,2p^2_{1/2}\,(2p^3_{3/2})_{3/2}$	$1s_{1/2}\,2s^2\,2p^6$	1743.71	$1s^22s^22p^5\ ^2P^o_{3/2}$	$1s2s^22p^6\ ^2S_{1/2}$	1740.79	···
		F-like Si VI	$1s^2\,2s^2\,2p_{1/2}\,2p^4_{3/2}$	$1s_{1/2}\,2s^2\,2p^6$	1743.09	$1s^22s^22p^5\ ^2P^o_{1/2}$	$1s2s^22p^6\ ^2S_{1/2}$	1740.15	···
		Ne-like Si V	$1s^2\,2s^2\,2p^2_{1/2}\,((2p^3_{3/2})_{3/2}\,3s_{1/2})_1$	$(1s_{1/2}\,2s^2\,2p^6\,3s_{1/2})_1$	1742.23	$1s^22s^22p^53s\ ^3P^o_1$	$1s2s^22p^63s\ ^3S_1$	1743.06	···
		Ne-like Si V	$1s^2\,2s^2\,(2p_{1/2}2p^4_{3/2}\,3s_{1/2})_1$	$(1s_{1/2}\,2s^2\,2p^6\,3s_{1/2})_0$	1742.44	$1s^22s^22p^53s\ ^1P^o_1$	$1s2s^22p^63s\ ^1S_0$	1743.33	···
		Ne-like Si V	$1s^2\,2s^2\,2p^2_{1/2}\,((2p^3_{3/2})_{3/2}\,3s_{1/2})_2$	$(1s_{1/2}\,2s^2\,2p^6\,3s_{1/2})_1$	1742.56	$1s^22s^22p^53s\ ^3P^o_2$	$1s2s^22p^63s\ ^3S_1$	1743.38	···
X-1	$1740.04^{+0.27}_{-0.36}$	Na–Si-like Si I–IV	···	···	···				

Notes: Identification of the fitted Si lines with transitions of the FAC simulation. The first column is the key to the line labels in Fig. 6.10, the third column indicates the ionization state. For the He-like lines the key of Gabriel (1972) is used. Columns 4–6 show the identification with FAC lines, columns 7–9 the corresponding transitions from Palmeri et al. (2008a), and column 10 lists energies from CHIANTI. Note that these calculated transition wavelengths listed by P08 have been empirically shifted by P08 for ions with $3 \leq N \leq 9$, where N is the number of electrons. Statistical uncertainties are shown as 90 % confidence intervals. There is an additional systematic uncertainty of 0.13 eV on all lines.

Table 6.5: Identification of the fitted sulfur line centers. (Hell et al., 2016b, Table 6)

			jj-coupling			LS-coupling			
Key	Fit (eV)	Ion	Lower Level	Upper Level	FAC (eV)	Lower Level	Upper Level	P08 (eV)	CHI.
Li-1	2450 ± 1.0	Li-like S XIV	$1s^2\,2p_{3/2}$	$(1s_{1/2}\,(2p^2_{3/2})_0)_{1/2}$	2449.95	$1s^2 2p\ ^2P^o_{3/2}$	$1s(^2S)\,2p^2(^1S)\ ^2S_{1/2}$	2450.67	2449.26
		Li-like S XIV	$1s^2\,2p_{1/2}$	$(1s_{1/2}\,(2p^2_{3/2})_0)_{1/2}$	2451.78	$1s^2 2p\ ^2P^o_{1/2}$	$1s(^2S)\,2p^2(^1S)\ ^2S_{1/2}$	2452.51	2451.15
Li-2	$2447.02^{+0.19}_{-0.27}$	Li-like S XIV	$1s^2\,2s_{1/2}$	$((1s_{1/2}\,2s_{1/2})_1\,2p_{3/2})_{1/2}$	2447.65	$1s^2 2s\ ^2S_{1/2}$	$1s(^2S)\,2s2p(^1P^o)\ ^2P^o_{1/2}$	2448.01	2447.04
		He-like S XV	$1s^2$	$(1s_{1/2}\,2p_{1/2})_1$	2446.32	$1s^2\ ^1S_0$	$1s2p\ ^3P^o_1$	2446.65	2447.14
Li-3	$2437.797^{+0.023}_{-0.024}$	Li-like S XIV	$1s^2\,2s_{1/2}$	$((1s_{1/2}\,2s_{1/2})_0\,2p_{1/2})_{1/2}$	2436.55	$1s^2 2s\ ^2S_{1/2}$	$1s(^2S)\,2s2p(^3P^o)\ ^2P^o_{1/2}$	2437.52	2437.04
		Li-like S XIV	$1s^2\,2s_{1/2}$	$((1s_{1/2}\,2s_{1/2})_0\,2p_{3/2})_{3/2}$	2437.58	$1s^2 2s\ ^2S_{1/2}$	$1s(^2S)\,2s2p(^3P^o)\ ^2P^o_{3/2}$	2438.47	2437.99
z	$2430.380^{+0.024}_{-0.019}$	He-like S XV	$1s^2$	$(1s_{1/2}\,2s_{1/2})_1$	2429.08	$1s^2\ ^1S_0$	$1s2s\ ^3S_1$	⋯	2430.35
Be-1	$2418.51^{+0.10}_{-0.09}$	Be-like S XIII	$1s^2\,2s^2$	$(1s_{1/2}\,2s^2\,2p_{3/2})_1$	2418.38	$1s^2 2s^2\ ^1S_0$	$1s2s^2 2p\ ^1P^o_1$	2418.45	⋯
Be-2	$2414.7^{+1.0}_{-4.0}$	Li-like S XIV	$1s^2\,2s_{1/2}$	$((1s_{1/2}\,2s_{1/2})_1\,2p_{3/2})_{5/2}$	2416.26	$1s^2 2s\ ^2S_{1/2}$	$1s(^2S)\,2s2p(^3P^o)\ ^4P^o_{5/2}$	⋯	2416.99
		Li-like S XIV	$1s^2\,2s_{1/2}$	$((1s_{1/2}\,2s_{1/2})_1\,2p_{1/2})_{1/2}$	2414.51	$1s^2 2s\ ^2S_{1/2}$	$1s(^2S)\,2s2p(^3P^o)\ ^4P^o_{1/2}$	2414.92	2415.24
		Li-like S XIV	$1s^2\,2s_{1/2}$	$((1s_{1/2}\,2s_{1/2})_1\,2p_{1/2})_{3/2}$	2415.02	$1s^2 2s\ ^2S_{1/2}$	$1s(^2S)\,2s2p(^3P^o)\ ^4P^o_{3/2}$	2415.67	2415.76
Be-3	$2412.0^{+0.8}_{-1.4}$	Be-like S XIII	$1s^2\,(2s_{1/2}\,2p_{3/2})_2$	$((1s_{1/2}\,2s_{1/2})_1\,(2p^2_{3/2})_2)_2$	2412.83	$1s^2 2s2p\ ^3P^o_2$	$1s(^2S)\,2s2p^2(^4P)\ ^3P_2$	2412.89	⋯
		Be-like S XIII	$1s^2\,(2s_{1/2}\,2p_{1/2})_0$	$(((1s_{1/2}\,2s_{1/2})_1\,2p_{1/2})_{1/2}\,2p_{3/2})_1$	2412.82	$1s^2 2s2p\ ^3P^o_0$	$1s(^2S)\,2s2p(^2D)\ ^3D_1$	2412.75	⋯
B-1	$2395.51^{+0.06}_{-0.10}$	B-like S XII	$1s^2\,2s^2\,2p_{3/2}$	$(1s_{1/2}\,2s^2\,(2p^2_{3/2})_2)_{3/2}$	2395.25	$1s^2 2s^2 2p\ ^2P^o_{3/2}$	$1s2s^2 2p^2\ ^2P_{3/2}$	2394.90	⋯
		B-like S XII	$1s^2\,2s^2\,2p_{1/2}$	$((1s_{1/2}\,2s^2\,2p_{1/2})_1\,2p_{3/2})_{1/2}$	2395.11	$1s^2 2s^2 2p\ ^2P^o_{1/2}$	$1s2s^2 2p^2\ ^2P_{1/2}$	2394.86	⋯
		B-like S XII	$1s^2\,2s^2\,2p_{1/2}$	$((1s_{1/2}\,2s^2\,2p_{1/2})_1\,2p_{3/2})_{1/2}$	2396.87	$1s^2 2s^2 2p\ ^2P^o_{1/2}$	$1s2s^2 2p^2\ ^2P_{3/2}$	2396.52	⋯
B-2	$2391.36^{+0.20}_{-0.42}$	B-like S XII	$1s^2\,2s^2\,2p_{3/2}$	$((1s_{1/2}\,2s^2\,2p_{1/2})_1\,2p_{3/2})_{5/2}$	2391.41	$1s^2 2s^2 2p\ ^2P^o_{3/2}$	$1s2s^2 2p^2\ ^2D_{5/2}$	2390.87	⋯
		B-like S XII	$1s^2\,2s^2\,2p_{1/2}$	$((1s_{1/2}\,2s^2\,2p_{1/2})_0\,2p_{3/2})_{3/2}$	2393.07	$1s^2 2s^2 2p\ ^2P^o_{1/2}$	$1s2s^2 2p^2\ ^2D_{3/2}$	2392.27	⋯
		B-like S XII	$1s^2\,2s^2\,2p_{3/2}$	$((1s_{1/2}\,2s^2\,2p_{1/2})_1\,2p_{3/2})_{1/2}$	2393.50	$1s^2 2s^2 2p\ ^2P^o_{3/2}$	$1s2s^2 2p^2\ ^2P_{1/2}$	2393.24	⋯
C-1	$2378.26^{+0.27}_{-0.20}$	C-like S XI	$1s^2\,2s^2\,(2p_{1/2}\,2p_{3/2})_2$	$(1s_{1/2}\,2s^2\,(2p^3_{3/2})_{3/2})_1$	2376.60	$1s^2 2s^2 2p^2\ ^1D_2$	$1s2s^2 2p^3\ ^1P^o_1$	2376.59	⋯
		Li-like S XIV	$1s^2\,2p_{3/2}$	$1s_{1/2}\,2s^2$	2377.32	$1s^2 2p\ ^2P^o_{3/2}$	$1s2s^2\ ^2S_{1/2}$	2378.50	2378.32
		Li-like S XIV	$1s^2\,2p_{1/2}$	$1s_{1/2}\,2s^2$	2379.16	$1s^2 2p\ ^2P^o_{1/2}$	$1s2s^2\ ^2S_{1/2}$	2380.37	2380.19
C-2	$2373.25^{+0.14}_{-0.16}$	C-like S XI	$1s^2\,2s^2\,(2p_{1/2}\,2p_{3/2})_2$	$((1s_{1/2}\,2s^2\,2p_{1/2})_1\,(2p^2_{3/2})_2)_2$	2371.92	$1s^2 2s^2 2p^2\ ^1D_2$	$1s2s^2 2p^3\ ^1D^o_2$	2371.59	⋯
		C-like S XI	$1s^2\,2s^2\,(2p^2_{3/2})_2$	$((1s_{1/2}\,2s^2\,2p_{1/2})_1\,(2p^2_{3/2})_0)_1$	2373.92	$1s^2 2s^2 2p^2\ ^3P_2$	$1s2s^2 2p^3\ ^3P^o_1$	2373.36	⋯
		C-like S XI	$1s^2\,2s^2\,(2p_{1/2}\,2p_{3/2})_1$	$((1s_{1/2}\,2s^2\,2p_{1/2})_1\,(2p^2_{3/2})_2)_1$	2373.23	$1s^2 2s^2 2p^2\ ^3P_1$	$1s2s^2 2p^3\ ^3S^o_1$	2372.77	⋯
		C-like S XI	$1s^2\,2s^2\,(2p^2_{3/2})_2$	$(1s_{1/2}\,2s^2\,(2p^3_{3/2})_{3/2})_2$	2373.52	$1s^2 2s^2 2p^2\ ^3P_2$	$1s2s^2 2p^3\ ^3P^o_2$	2372.95	⋯
C-3	$2368.83^{+0.20}_{-0.24}$	C-like S XI	$1s^2\,2s^2\,(2p^2_{3/2})_2$	$((1s_{1/2}\,2s^2\,2p_{1/2})_1\,(2p^2_{3/2})_2)_3$	2368.58	$1s^2 2s^2 2p^2\ ^3P_2$	$1s2s^2 2p^3\ ^3D^o_3$	2367.83	⋯
		C-like S XI	$1s^2\,2s^2\,(2p_{1/2}\,2p_{3/2})_1$	$((1s_{1/2}\,2s^2\,2p_{1/2})_0\,(2p^2_{3/2})_2)_2$	2369.55	$1s^2 2s^2 2p^2\ ^3P_1$	$1s2s^2 2p^3\ ^3D^o_2$	2368.55	⋯
		C-like S XI	$1s^2\,2s^2\,(2p^2_{3/2})_0$	$(1s_{1/2}\,2s^2\,(2p^3_{3/2})_{3/2})_1$	2369.14	$1s^2 2s^2 2p^2\ ^1S_0$	$1s2s^2 2p^3\ ^1P^o_1$	2368.87	⋯

Notes: Identification of the fitted S lines with transitions of the FAC simulation. The first column is the key to the line labels in Fig. 6.10, the third column indicates the ionization state. For the He-like lines the key of Gabriel (1972) is used. Columns 4–6 show the identification with FAC lines, columns 7–9 the corresponding transitions from Palmeri et al. (2008a), and column 10 lists energies from CHIANTI. Note that these calculated transition wavelengths listed by P08 have been empirically shifted by P08 for ions with $3 \leq N \leq 9$, where N is the number of electrons. Statistical uncertainties are shown as 90 % confidence intervals. There is an additional systematic uncertainty of 0.23 eV on all lines.

Table 6.5: — *continued*

Key	Fit (eV)	Ion	jj-coupling		FAC (eV)	LS-coupling		P08 (eV)	CHI.
			Lower Level	Upper Level		Lower Level	Upper Level		
N-1	$2354.33^{+0.23}_{-0.29}$	N-like S X	$1s^2\,2s^2\,(2p_{1/2}(2p^2_{3/2})_2)_{5/2}$	$((1s_{1/2}\,2s^2\,2p_{1/2})_1(2p^3_{3/2})_{3/2})_{3/2}$	2353.74	$1s^2 2s^2 2p^3\ ^2D^o_{5/2}$	$1s 2s^2 2p^4\ ^2P_{3/2}$	2352.86	···
		N-like S X	$1s^2\,2s^2\,(2p_{1/2}(2p^2_{3/2})_2)_{3/2}$	$((1s_{1/2}\,2s^2\,2p_{1/2})_1(2p^3_{3/2})_{3/2})_{1/2}$	2354.57	$1s^2 2s^2 2p^3\ ^2D^o_{3/2}$	$1s 2s^2 2p^4\ ^2P_{1/2}$	2353.85	···
		N-like S X	$1s^2\,2s^2\,(2p^3_{3/2})_{3/2}$	$1s_{1/2}\,2s^2\,2p^4_{3/2}$	2353.80	$1s^2 2s^2 2p^3\ ^2P^o_{3/2}$	$1s 2s^2 2p^4\ ^2S_{1/2}$	2352.91	···
N-2	$2349.94^{+0.23}_{-0.32}$	N-like S X	$1s^2\,2s^2\,(2p_{1/2}(2p^2_{3/2})_2)_{5/2}$	$((1s_{1/2}\,2s^2\,2p_{1/2})_1(2p^3_{3/2})_{3/2})_{5/2}$	2351.45	$1s^2 2s^2 2p^3\ ^2D^o_{5/2}$	$1s 2s^2 2p^4\ ^2D_{5/2}$	2350.45	···
		N-like S X	$1s^2\,2s^2\,(2p_{1/2}(2p^2_{3/2})_2)_{3/2}$	$(1s_{1/2}\,2s^2\,2p^2_{1/2}(2p^2_{3/2})_2)_{3/2}$	2351.61	$1s^2 2s^2 2p^3\ ^2D^o_{3/2}$	$1s 2s^2 2p^4\ ^2D_{3/2}$	2350.37	···
		N-like S X	$1s^2\,2s^2\,(2p_{1/2}(2p^2_{3/2})_0)_{1/2}$	$((1s_{1/2}\,2s^2\,2p_{1/2})_1(2p^3_{3/2})_{3/2})_{1/2}$	2349.55	$1s^2 2s^2 2p^3\ ^2P^o_{1/2}$	$1s 2s^2 2p^4\ ^2P_{1/2}$	2348.59	···
		N-like S X	$1s^2\,2s^2\,(2p^3_{3/2})_{3/2}$	$((1s_{1/2}\,2s^2\,2p_{1/2})_1(2p^3_{3/2})_{3/2})_{3/2}$	2348.63	$1s^2 2s^2 2p^3\ ^2P^o_{3/2}$	$1s 2s^2 2p^4\ ^2P_{3/2}$	2347.61	···
		N-like S X	$1s^2\,2s^2\,(2p_{1/2}(2p^2_{3/2})_2)_{3/2}$	$((1s_{1/2}\,2s^2\,2p_{1/2})_0(2p^3_{3/2})_{3/2})_{3/2}$	2350.86	$1s^2 2s^2 2p^3\ ^4S^o_{3/2}$	$1s 2s^2 2p^4\ ^4P_{3/2}$	2349.12	···
		N-like S X	$1s^2\,2s^2\,(2p_{1/2}(2p^2_{3/2})_2)_{3/2}$	$(1s_{1/2}\,2s^2\,2p^2_{1/2}(2p^2_{3/2})_2)_{5/2}$	2349.70	$1s^2 2s^2 2p^3\ ^4S^o_{3/2}$	$1s 2s^2 2p^4\ ^4P_{5/2}$	2348.10	···
N-3	$2345.6^{+0.4}_{-0.6}$	N-like S X	$1s^2\,2s^2\,(2p^3_{3/2})_{3/2}$	$((1s_{1/2}\,2s^2\,2p_{1/2})_1(2p^3_{3/2})_{3/2})_{5/2}$	2346.34	$1s^2 2s^2 2p^3\ ^2P^o_{3/2}$	$1s 2s^2 2p^4\ ^2D_{5/2}$	2345.17	···
		Be-like S XIII	$1s^2\,(2p_{1/2}\,2p_{3/2})_2$	$(1s_{1/2}\,2s^2\,2p_{3/2})_1$	2343.42	$1s^2 2p^2\ ^1D_2$	$1s 2s^2 2p\ ^1P^o_1$	2344.54	···
O-1	$2335.6^{+0.5}_{-4.3}$	O-like S IX	$1s^2\,2s^2\,(2p_{1/2}(2p^3_{3/2})_{3/2})_2$	$(1s_{1/2}\,2s^2\,2p^2_{1/2}(2p^3_{3/2})_{3/2})_1$	2333.91	$1s^2 2s^2 2p^4\ ^1D_2$	$1s 2s^2 2p^5\ ^1P^o_1$	2331.76	···
O-2	$2331.82^{+0.27}_{-0.48}$	O-like S IX	$1s^2\,2s^2\,2p^2_{1/2}(2p^2_{3/2})_2$	$(1s_{1/2}\,2s^2\,2p^2_{1/2}(2p^3_{3/2})_{3/2})_2$	2331.82	$1s^2 2s^2 2p^4\ ^3P_2$	$1s 2s^2 2p^5\ ^3P^o_2$	2329.13	···
		O-like S IX	$1s^2\,2s^2\,2p^2_{1/2}(2p^2_{3/2})_2$	$(1s_{1/2}\,2s^2\,2p_{1/2}\,2p^4_{3/2})_1$	2332.91	$1s^2 2s^2 2p^4\ ^3P_2$	$1s 2s^2 2p^5\ ^3P^o_1$	2330.18	···
		O-like S IX	$1s^2\,2s^2\,(2p_{1/2}(2p^3_{3/2})_{3/2})_1$	$(1s_{1/2}\,2s^2\,2p_{1/2}\,2p^4_{3/2})_0$	2332.76	$1s^2 2s^2 2p^4\ ^3P_1$	$1s 2s^2 2p^5\ ^3P^o_0$	2329.83	···
		O-like S IX	$1s^2\,2s^2\,(2p_{1/2}(2p^3_{3/2})_{3/2})_1$	$(1s_{1/2}\,2s^2\,2p^2_{1/2}(2p^3_{3/2})_{3/2})_2$	2330.84	$1s^2 2s^2 2p^4\ ^3P_1$	$1s 2s^2 2p^5\ ^3P^o_2$	2328.21	···
		O-like S IX	$1s^2\,2s^2\,2p^4_{3/2}$	$(1s_{1/2}\,2s^2\,2p_{1/2}\,2p^4_{3/2})_1$	2331.61	$1s^2 2s^2 2p^4\ ^3P_0$	$1s 2s^2 2p^5\ ^3P^o_1$	2328.91	···
O-3	$2327.2^{+0.5}_{-0.7}$	O-like S IX	$1s^2\,2s^2\,2p^2_{1/2}(2p^2_{3/2})_0$	$(1s_{1/2}\,2s^2\,2p^2_{1/2}(2p^3_{3/2})_{3/2})_1$	2316.67	$1s^2 2s^2 2p^4\ ^1S_0$	$1s 2s^2 2p^5\ ^1P^o_1$	2324.33	···
F-1	$2315.00^{+0.17}_{-0.24}$	F-like S VIII	$1s^2\,2s^2\,2p^2_{1/2}(2p^3_{3/2})_{3/2}$	$1s_{1/2}\,2s^2\,2p^6$	2315.36	$1s^2 2s^2 2p^5\ ^2P^o_{3/2}$	$1s 2s^2 2p^6\ ^2S_{1/2}$	2312.40	···
		F-like S VIII	$1s^2\,2s^2\,2p_{1/2}\,2p^4_{3/2}$	$1s_{1/2}\,2s^2\,2p^6$	2314.13	$1s^2 2s^2 2p^5\ ^2P^o_{1/2}$	$1s 2s^2 2p^6\ ^2S_{1/2}$	2311.15	···
		Ne-like S VII	$1s^2\,2s^2\,2p^2_{1/2}((2p^3_{3/2})_{3/2}3s_{1/2})_2$	$(1s_{1/2}\,2s^2\,2p^2_{1/2}\,2p^4_{3/2}\,3s_{1/2})_1$	2313.58	$1s^2 2s^2 2p^5 3s\ ^3P^o_2$	$1s 2s^2 2p^6 3s\ ^3S_1$	2314.74	···
		Ne-like S VII	$1s^2\,2s^2\,2p^2_{1/2}((2p^3_{3/2})_{3/2}3s_{1/2})_1$	$(1s_{1/2}\,2s^2\,2p^2_{1/2}\,2p^4_{3/2}\,3s_{1/2})_1$	2312.99	$1s^2 2s^2 2p^5 3s\ ^3P^o_1$	$1s 2s^2 2p^6 3s\ ^3S_1$	2314.17	···
		Ne-like S VII	$1s^2\,2s^2\,(2p_{1/2}\,2p^4_{3/2}\,3s_{1/2})_1$	$(1s_{1/2}\,2s^2\,2p^2_{1/2}\,2p^4_{3/2}\,3s_{1/2})_0$	2313.35	$1s^2 2s^2 2p^5 3s\ ^1P^o_1$	$1s 2s^2 2p^6 3s\ ^1S_0$	2312.62	···
F-2	$2311.22^{+0.27}_{+0.41}$	Na-like S VI	$1s^2\,2s^2\,((2p_{1/2}\,2p^4_{3/2}\,3s_{1/2})_1\,3p_{3/2})_{5/2}$	$((1s_{1/2}\,2s^2\,2p^2_{1/2}\,2p^4_{3/2}\,3s_{1/2})_0\,3p_{3/2})_{3/2}$	2311.62	$1s^2 2s^2 2p^5 3s 3p\ ^2D_{5/2}$	$1s 2s^2 2p^6 3s 3p\ ^2P^o_{3/2}$	2312.71	···
		B-like S XII	$1s^2\,(2p_{1/2}(2p^2_{3/2})_2)_{5/2}$	$(1s_{1/2}\,2s^2\,(2p^2_{3/2})_2)_{3/2}$	2309.50	$1s^2 2p^3\ ^2D^o_{5/2}$	$1s 2s^2 2p^2\ ^2P_{3/2}$	2310.12	···
		Na–S-like S I–VI	···	···	···				
F-3	$2306.9^{+0.4}_{-0.7}$	B-like S XII	$1s^2\,(2p_{1/2}(2p^2_{3/2})_2)_{3/2}$	$((1s_{1/2}\,2s^2\,2p_{1/2})_1\,2p_{3/2})_{1/2}$	2307.79	$1s^2 2p^3\ ^2D^o_{3/2}$	$1s 2s^2 2p^2\ ^2P_{1/2}$	2308.57	···
		B-like S XII	$1s^2\,(2p_{1/2}(2p^2_{3/2})_2)_{5/2}$	$((1s_{1/2}\,2s^2\,2p_{1/2})_1\,2p_{3/2})_{5/2}$	2305.65	$1s^2 2p^3\ ^2D^o_{5/2}$	$1s 2s^2 2p^2\ ^2D_{5/2}$	2306.12	···
		B-like S XII	$1s^2\,(2p_{1/2}(2p^2_{3/2})_2)_{3/2}$	$(1s_{1/2}\,2s^2\,(2p^2_{3/2})_2)_{5/2}$	2304.74	$1s^2 2p^3\ ^4S^o_{3/2}$	$1s 2s^2 2p^2\ ^4P_{5/2}$	2303.85	···

Notes: Identification of the fitted S lines with transitions of the FAC simulation. The first column is the key to the line labels in Fig. 6.10, the third column indicates the ionization state. For the He-like lines the key of Gabriel (1972) is used. Columns 4–6 show the identification with FAC lines, columns 7–9 the corresponding transitions from Palmeri et al. (2008a), and column 10 lists energies from CHIANTI. Note that these calculated transition wavelengths listed by P08 have been empirically shifted by P08 for ions with $3 \leq N \leq 9$, where N is the number of electrons. Statistical uncertainties are shown as 90 % confidence intervals. There is an additional systematic uncertainty of 0.23 eV on all lines.

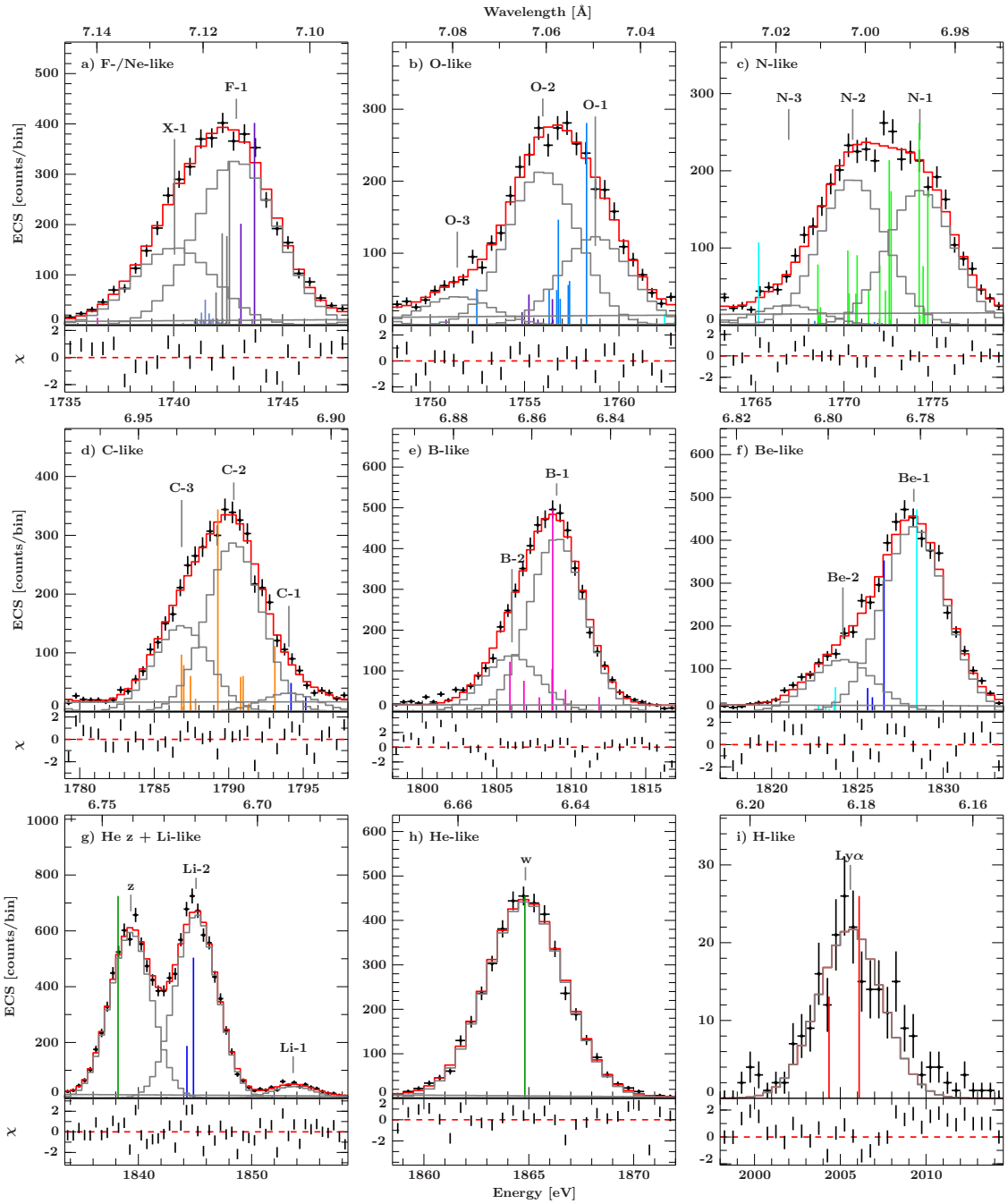

Figure 6.10: Fit of the measured Si Kα spectrum. The data are shown in black, the red line shows the model, model components are shown as gray lines. Vertical lines represent the theoretical predictions according to FAC, color-coded for charge states (see Fig. 6.1). The FAC lines are renormalized such that the strongest FAC line in each panel matches the highest peak, i.e., relative FAC line strengths are preserved within but not between panels. Line labels can be used as an identifier for the transitions listed in Table 6.4. — From Hell et al. (2016b, Fig. 9).

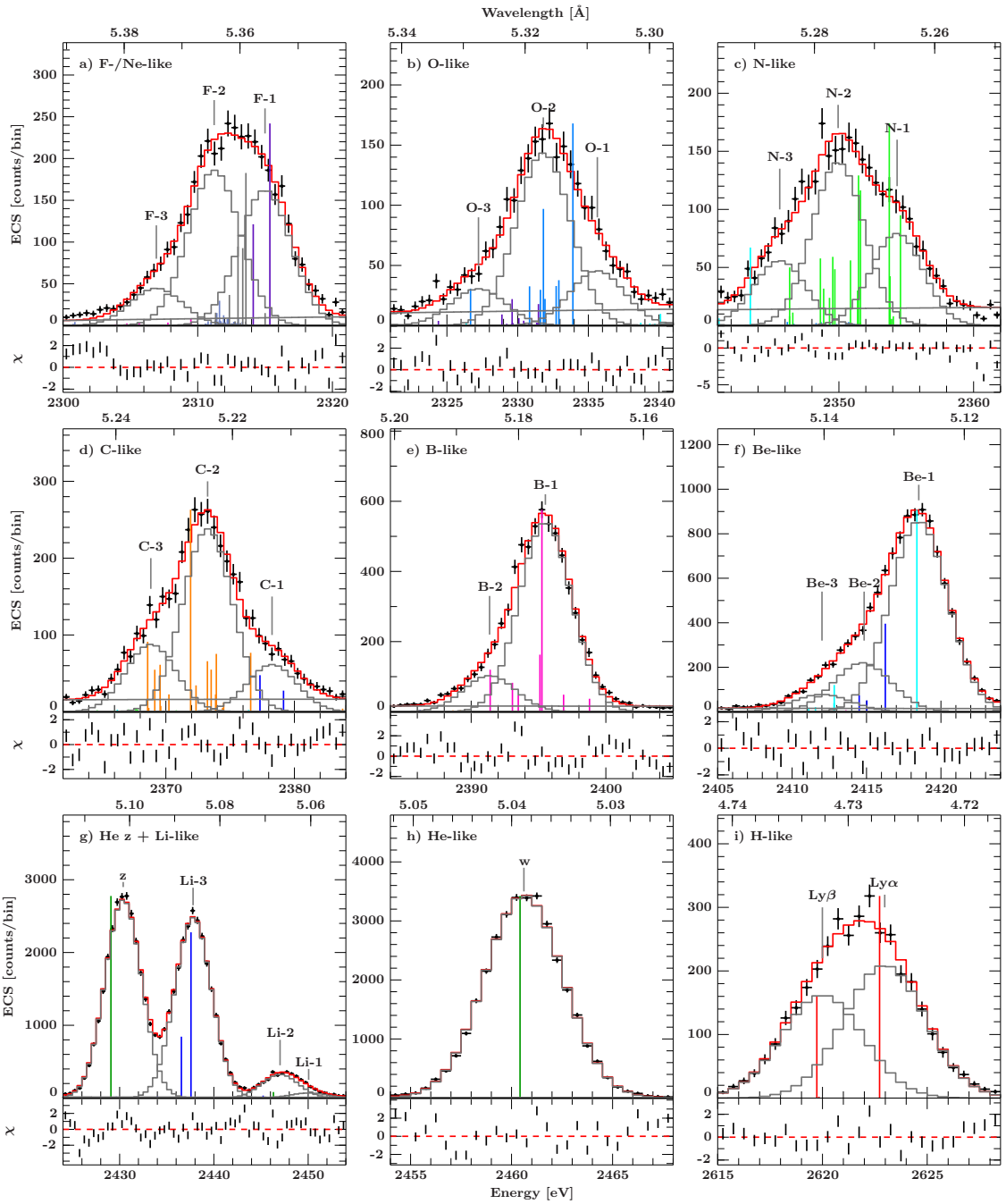

Figure 6.11: Same as Fig. 6.10 for the S spectrum. Line labels denote transitions listed in Table 6.5. — From Hell et al. (2016b, Fig. 10).

6.2 High-resolution Measurement of the S Lines

While the ECS allows us to resolve the major features of the Kα transitions in different L-shell ions, the transitions within each charge state are still heavily blended. The derived line centers of the blends are well suited as a reference for Doppler shift determination in astrophysical sources observed with similar resolution. For comparison to atomic physics calculations the situation is more complex. In cases like the Be- or B-like S ion, where the Kα line blend is dominated by a strong transition that is surrounded by a few much weaker transitions, measurements at ECS resolution can closely reproduce the energy of this strong component. Ions with multiple electrons like C-like or N-like have no distinctly strongest component, but instead are composed of many transitions with comparable line strengths. Here, the ECS can only deliver an average energy for multiple transitions. In order to better gauge the atomic physics, therefore, these remaining line blends should be further resolved.

According to the theoretical distribution of lines in, e.g., sulfur (Fig. 6.11) spectrometer resolving powers exceeding about $E/\Delta E = 2500$ are necessary to reach this goal. Such high resolution currently can only be achieved by wavelength dispersive spectrometers. Since their effective area typically is small, these measurements require long exposure times to acquire adequate signal-to-noise ratios, especially in those cases where the flux is distributed between many weak lines. Long exposures make it harder to systematically measure a large range of elements. However, in the meantime we can use such a measurement to gauge the systematics of the corresponding ECS measurement and extrapolate the conclusions to similar measurements in other elements.

6.2.1 Experimental Setup and Data Analysis

Here, we present our measurements of N- through Li-like S made with the high-resolution imaging crystal spectrometer EBHiX (Beiersdorfer et al., 2016c), mounted with the plane of dispersion perpendicular to the electron beam direction (Chapter 5), using a quartz $10\bar{1}1$ crystal. The measurement was carried out at SuperEBIT using the same technique as for the previous ECS measurements of these lines (Section 6.1.1). Figure 6.12 shows the resulting spectrum together with the previous ECS measurement and its fit model. This qualitative comparison already confirms that the ECS analysis is well suited to reproduce the position of the main contributions to the line blends. For a more detailed comparison, see Section 6.2.3.

The energy scale of the EBHiX spectrum is calibrated with the Rydberg series of He-like Si, Si Lyβ, and S line z, using a second order polynomial in Bragg angle, as discussed in Section 5.5.2. The Si and S spectra were collected by stacking 24 one-hour exposures each. The extracted EBHiX spectrum is virtually background free due to single-photon counting, which allows pulse height discrimination of the $\sim 2.4\,\mathrm{keV}$ photons to higher-energetic cosmic rays (Section 5.5.2).

From comparison of the calibration line centers after calibration to their reference values, we estimate our systematic calibration uncertainty to 0.046 eV, which corresponds to

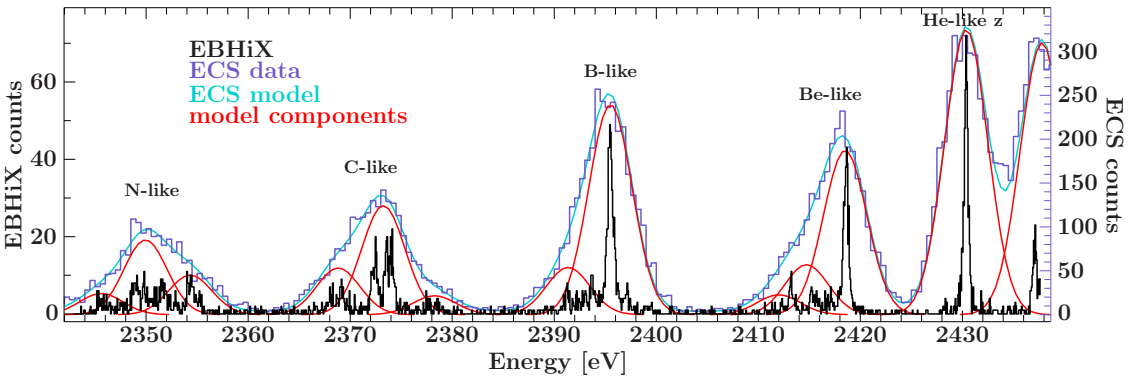

Figure 6.12: Comparison between high-resolution crystal spectra from EBHiX to ECS data and model. While the ECS is a broadband spectrometer, the spectral range of the EBHiX spectrum is limited by the geometry of the crystal spectrometer to the displayed part of the spectrum. To extend the measurement to other regions the EBHiX settings would have to be changed and the spectral range recalibrated.

about two thirds of a detector channel. Since the two components of Si Lyβ are just about resolved (Fig. 5.16), the spectral resolution is ≤ 0.52 eV. The FWHM of the Voigt profiles used to model the lines is also about 0.5 eV (Table 5.1). This corresponds to a total resolving power $E/\Delta E$ of about 4750. The observed bandwidth is limited by the spectrometer geometry. While the spectral scale has been calibrated as a function of Bragg angle, the spectral fits of the calibrated data are conducted as a function of energy for direct comparison with the ECS data.

Because of the low counting statistics of the present EBHiX spectrum – less than 20 counts per bin in many of the weak line features (Fig. 6.12) –, the data are not sufficiently close to a normal distribution to justify the use of χ^2 minimization. Instead, we find the best fitting model using Cash statistics (Cash, 1979), which more appropriately assumes that the data follow a Poission distribution. See Appendix C for the definition and a discussion of Cash statistics.

The spectral lines are modeled with a Voigt profile. At the present resolution, the observed line profile is not dominated by the detector resolution, but sensitive to the emitted line profiles, specifically Doppler broadening due to the temperature of the trapped ions (Section 5.5.2). Since all of the observed charge states in the S spectrum occupy the trap simultaneously, we can assume that they all have the same temperature, and therefore line width. Theoretically, the lower charge states are less well bound by the radial beam potential and their ion cloud might be slightly larger than the cloud of the more highly charged ions. The different sizes of the ion clouds lead to an incomplete spatial overlap of the different ions and can potentially influence the temperature equilibrium between them. But this effect has not yet been observed and is therefore unlikely to affect our line widths. Therefore, for the spectral fits, the widths of the used Voigt profiles are fixed to the width of S line z. Monte Carlo simulations (Section 6.1.4) again have been used to ascertain the significance of additional model components in possible line blends.

6.2.2 Line Identification

Figures 6.13–6.17 show a detailed overview of the spectral modeling, overplotted with the FAC model used for the ECS analysis (Section 6.1.5). The fitted line centers and intensities are listed in Table 6.6 along with their possible identification with FAC transitions. Due to the high-resolution of the data, this identification from theory is less straight forward and more ambiguous than for the ECS data (Section 6.1.5). For the ECS, model components were identified with the strongest FAC lines falling into the general energy range covered by this component. At a FWHM of ~ 4.5 eV of the model components, the uncertainty in transition energy calculations in most cases does not displace a transition outside of its corresponding modeled line blend nor does it matter if two nearby calculated lines switched places. The EBHiX data now resolves many of these line blends. If the calculated energy of a transition is even 0.5 eV off compared to its "true" measured position, it might fit the neighboring measured line perfectly and during line identification might therefore incorrectly be associated with that line instead. On the other hand, the uncertainty in calculated transition energies can vary slightly from transition to transition. It is therefore possible that a transition fits its measured line perfectly, while another transition within the same ion is shifted. This can be especially problematic in the line rich spectra of multi-electron ions with open subshells such as C-like and N-like. Relative intensities could help to resolve such ambiguities, if they are reliable. In the following we give a short reasoning behind the choice of line identification in Table 6.6. All visible transitions are listed in the table. There are many additional possible transitions that were calculated, but their line strengths according to the collisional radiative model are at least an order of magnitude smaller than those of the listed lines. Two relatively strong FAC lines are listed, although they have not been assigned to one of the measured lines. Similarly, three of the measured lines (6, 17, and 28) could not clearly be identified with a theoretical transition, as discussed below.

Energy range 2428–2438 eV

Li-like S is only partially covered by the EBHiX measurement. The strongest Li-like line q (line 1 in Fig. 6.13) is cut off by the edge off the CCD chip, leaving only part of the low-energy tail. While we fitted this line anyway to avoid its tail disturbing the line center of line 2, the derived line center for line 1 is not reliable. Line 2 is identified with the weaker of the two shown FAC transitions, indicating that the calculated transition energy is about 0.5 eV too low.

Energy range 2411–2422 eV

As in the ECS data, the Be-like lines have a strong dominating transition, i.e., line 4 (Fig. 6.14. Again the corresponding FAC transition is shifted to lower energies, but this time only by 0.2 eV. There are four more Be-like lines in the FAC model of this region. Assuming a similar shift to lower energies, the stronger FAC line at 2412.831 eV and its weak blend at 2412.817 eV are assigned to line 9 at 2413.23 eV. The predicted line ratio of

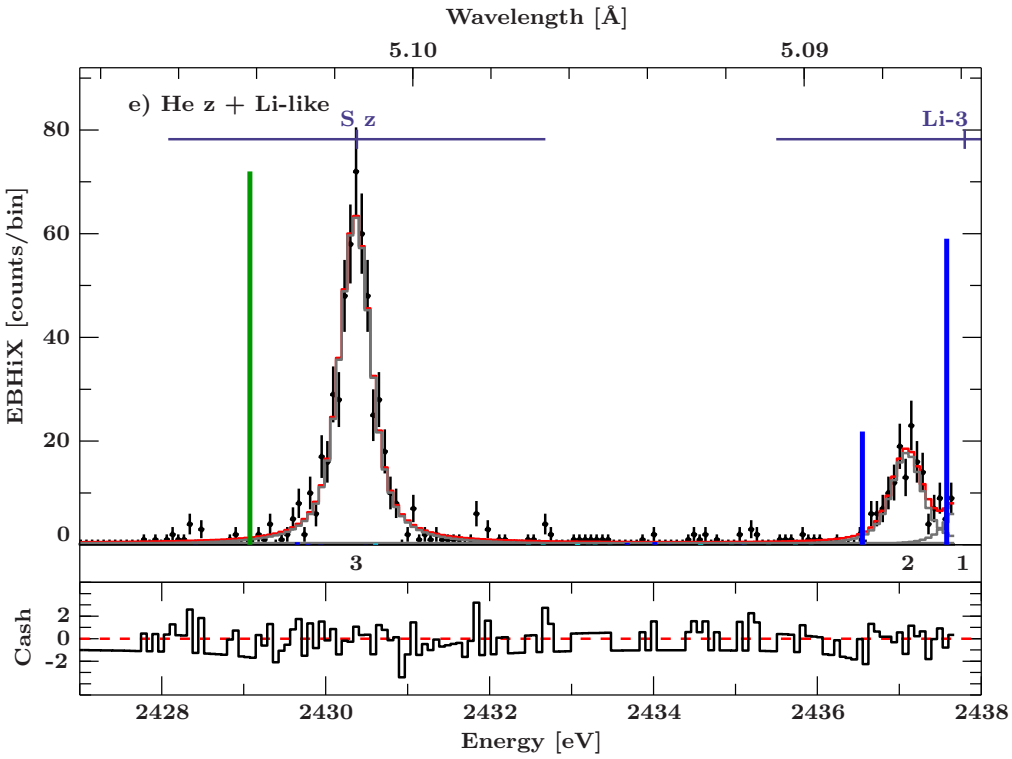

Figure 6.13: Detailed overview of the spectral fits to the EBHiX data for the Be-like S region of 2428–2438 eV. The data are shown in black, the model in red, and individual model components (keys 1–39, Table 6.6) in gray. The model components from the ECS measurement (Fig. 6.10) are marked in slate blue, indicating their line center, FWHM range, and key. As in Fig. 6.10, the vertical lines represent the color-coded (Fig. 6.1) FAC lines and relative FAC line strengths are not preserved between panels.

these two lines to the strong line is comparable to the measured line ratios of lines 4 and 9. Line 10 is identified with two weak lines at 2411.567 eV and 2411.110 eV, although they do not overlap. The shifts in the FAC calculations increase to 0.5 eV for line 9 and up to 1 eV for the weaker line 10.

The FAC model does not indicate any additional lines for Be-like S in this region, leaving lines 5–8 for the Li-like lines shown in Fig. 6.14. The stronger of the calculated Li-like lines here sits right between the measured lines. Since line 2 indicates a 0.5 eV shift towards lower energies, we assume that the Li-like lines around 2416 eV are similarly shifted. Then line 5 (the stronger of line 5 and 6) is identified with the strong transition, while the two weaker transitions at 2414.021 eV and 2414.509 eV are assigned to line 8 and 7, respectively, resulting in shifts of 0.7–1 eV for each of these lines. Note that the 2414.509 eV FAC line is closer to line 8 than to line 7 to which it is assigned, but due to the overall apparent shift we believe this identification with line 7 is justified. Line 6 remains unidentified. It is possible that it shares the identification of line 5, but according to the Monte Carlo method its presence is significant in 99.9% of simulated spectra. As discussed in Section 6.1.5, the relative line strengths of the FAC calculation

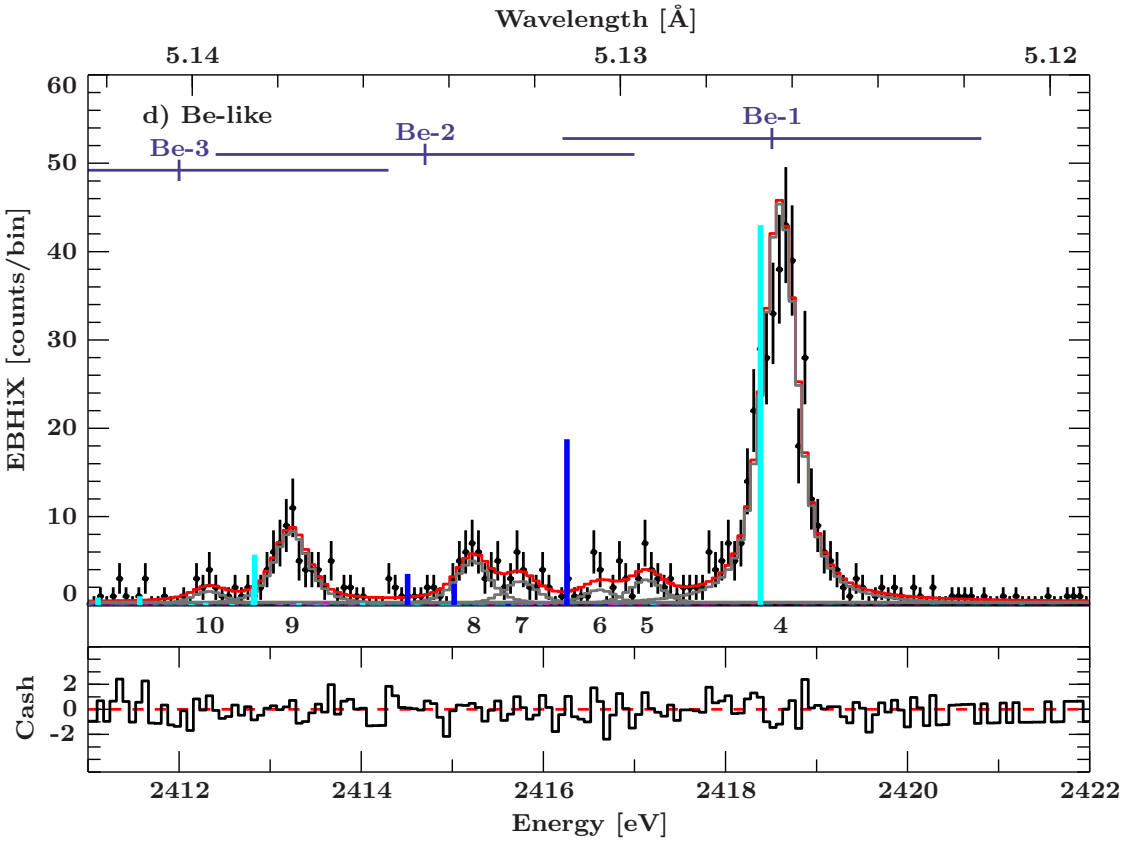

Figure 6.14: Detailed overview of the spectral fits to the EBHiX data for the Be-like S region of 2411–2422 eV. See caption of Fig. 6.13 for description.

between the Li- and Be-like lines is likely overestimating the Li-like relative to the Be-like contribution due to incorrect assumptions in the ionization balance. This flaw of the FAC model explains the overall mismatch of the Li-like line strengths to the measured lines in this region. But theory here does not match the measured ratio of lines 7 and 8 relative to line 5, either. Removing excitation through either collisional excitation or collisional ionization from the collisional radiative model suggests that the upper level of these lines is mostly populated by collisional inner-shell ionization of Be-like ions. Reducing the electron density in the calculation from $1 \cdot 10^{12}\,\mathrm{cm}^{-3}$ to $1 \cdot 10^{10}\,\mathrm{cm}^{-3}$ brings the calculated line ratios into better agreement with the measured ratio of line 5 and 8, but at the same time disrupts the good agreement of the Be-like lines with the measured ratio of line 9 to line 4.

Energy range 2388–2401 eV

The B-like complex (Fig. 6.15) again is dominated by a strong transition that is surrounded by a few weaker ones on both sides. All but one of the fitted lines (line 17) have a FAC transition falling within their line profile. Lines 11, 12, 15, 16, and 18 are simply identified with the respective FAC transition they overlap with. Then, the FAC transitions

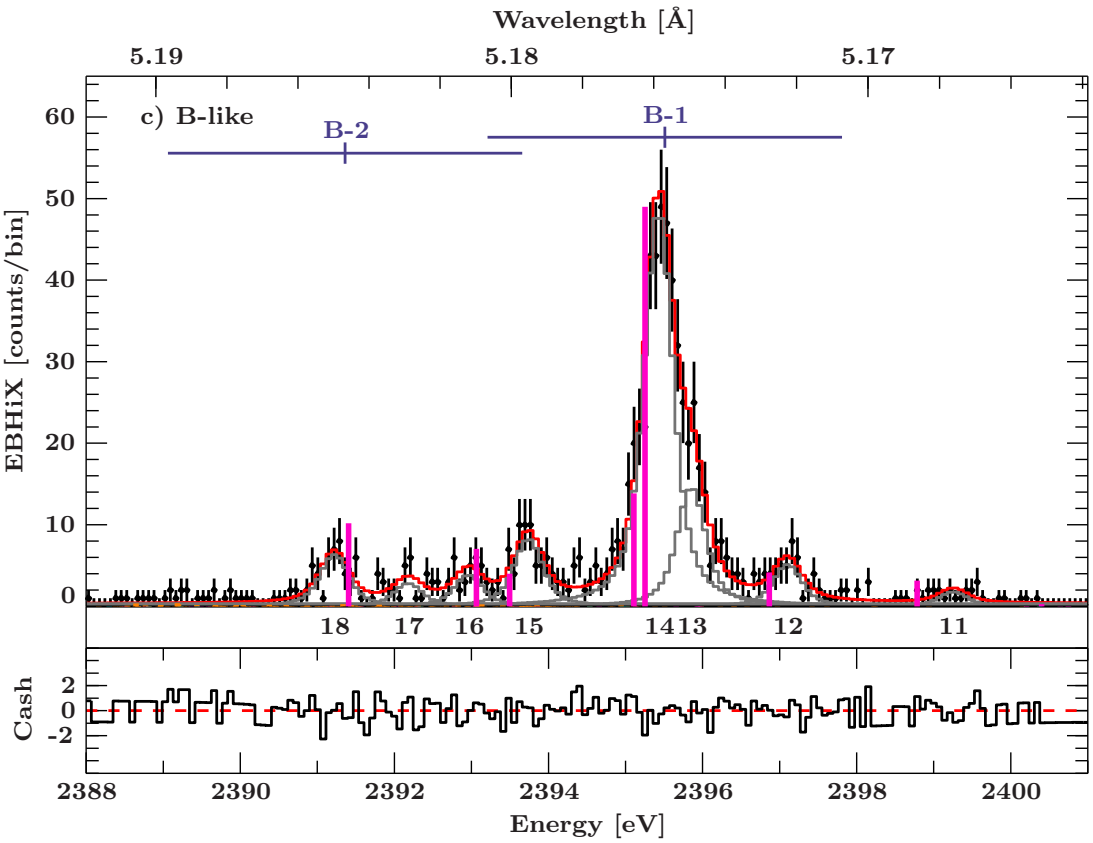

Figure 6.15: Detailed overview of the spectral fits to the EBHiX data for the B-like S region of 2388–2401 eV. See caption of Fig. 6.13 for description.

associated with lines 11, 12, and 15 appear to be shifted towards lower energies by up to 0.6 eV, while those associated with 16 and 18 are shifted towards higher energies by up to 0.2 eV. The strong line 14 has a high-energy shoulder modeled as line 13. There are two FAC transitions that fall into the range of line 14, while no strong line is directly in the range of line 13. Since the two FAC lines appear fairly close to each other and their line ratios are close to the measured ratio of lines 14 and 13, we assign the weaker of these two lines to line 13 and the stronger to line 14, effectively changing the energy ordering of these two calculated lines. Then, the calculated transition energies are offset by 0.6 eV and 0.3 eV, respectively, towards lower energies, which is in accordance with the shifts of the other B-like lines.

Overall, the calculated B-like line ratios agree with the trend in the observed relative line ratios in the B-like system. The shown calculated line ratio of line 15 and 16 is inverted compared to the measured lines. This could be due to polarization effects not included in the calculation or, alternatively, density effects could play a role; reducing the electron density from $1 \cdot 10^{12}\,\mathrm{cm}^{-3}$ to $1 \cdot 10^{10}\,\mathrm{cm}^{-3}$ inverts this ratio, but at the same time would bring the FAC identification of the two lines 13 and 14 to more comparable line strengths, contrary to the measurement. The lower energy levels of the two lines 15 and 16 are separated by 1.61 eV, while the upper levels are separated by 2.04 eV,

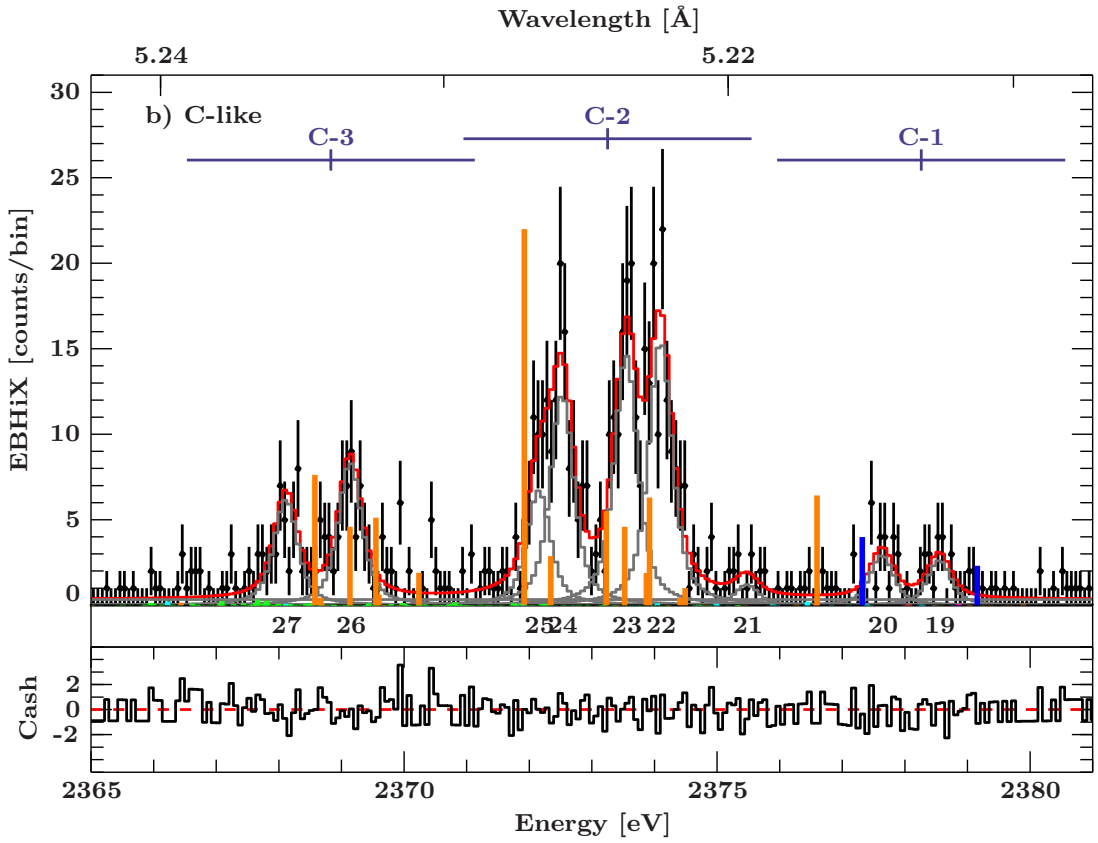

Figure 6.16: Detailed overview of the spectral fits to the EBHiX data for the C-like S region of 2365–2381 eV. See caption of Fig. 6.13 for description.

i.e., a calculation uncertainty in the level separation of the upper levels of only 0.5 eV is enough to change the energy order of these two transitions and about 1 eV error is required to swap the lines, but preserve their energy difference. Swapping the lines would change their transition energy error relative to the measured line centers of line 15 and 16 from 0.3 eV and 0.1 eV, respectively, to 0.7 eV and 0.5 eV. If collisional excitation is turned off in the collisional radiative model, the FAC lines associated with lines 13 and 15 disappear, indicating that these are only excited through collisional excitation, while the upper levels of the other B-like lines are populated by a mixture of collisional ionization and excitation.

Energy range 2365–2381 eV

The C-like (Fig. 6.16) and N-like (Fig. 6.17) line complexes include more transitions than the more highly-charged ions and both feature more evenly distributed line strengths among its members rather than an individual dominating transition. Like in the ECS measurement, the EBHiX measurement of the C-like transitions split into three groups of lines, namely lines 19–20, lines 21–25, and lines 26–27. Lines 19 and 20 are identified with two Li-like transitions. The predicted ratio of these two lines is comparable to the ob-

served one. For this reason and because its calculated transition energy is well separated from any observed lines, the FAC line $(1s_{1/2}\,2s^2\,(2p^3_{3/2})_{3/2})_1 \rightarrow ((1s^2\,2s^2\,2p_{1/2})_{1/2}\,2p_{3/2})_2$ is not assigned to any observed line. However, it might belong to either line 20 or line 21. It could also belong to an unobserved line close to this energy that could be indicated by a slightly elevated background level, but better statistics are necessary to test this. In calculations at lower electron densities, this line becomes much weaker.

Since all of the FAC transitions in the range of lines 21–25 appear to be shifted slightly towards lower energies, line 21 is identified with the two very weak transitions at 2374.5 eV. Lines 22 and 23 are associated with the two respective FAC transitions they each overlap with. Unlike lines 13 and 14 in the B-like ion, line 24 and line 25 are identified with the FAC transitions in the calculated energy ordering, although the calculated strength of the tranistion at higher energy appears to be the smaller of the two lines, in contrast to the measured transitions. At a density of $1 \cdot 10^{11}\,\mathrm{cm}^{-3}$ these two lines become more comparable in strength and at $1 \cdot 10^{10}\,\mathrm{cm}^{-3}$ the line ratio is inverted. The FAC transition $(1s_{1/2}\,2s^2\,2p^2_{1/2}\,2p_{3/2})_1 \rightarrow 1s^2\,2s^2\,2p^2_{1/2}$ again remains unassigned, but could be a high-energy shoulder to line 26. Line 26 is identified with the next two FAC transitions (and an additional weak one), while line 27 is assigned the lowest-energy FAC transition in this group along with its weak blend, although this transition according to FAC is right inbetween line 26 and 27. Overall, the transition energies in C-like S as calculated with FAC agree with the measurement to about 0.5 eV, and 1 eV in case of the weak lines ascribed to line 21. The transitions at 2372.345 eV, 2373.230 eV, and 2373.871 eV again are solely due to direct collisional excitation.

Energy range 2343–2356 eV

Finally, the crystal spectrum of the N-like transitions (Fig. 6.17) splits roughly into the four groups of lines as described in Section 6.1.5, but seems to reveal some additional lines filling in the gaps. Consequently, lines 28, 31, 37, and 29 stay without clear identification. For large enough uncertainties of the FAC calculation, at least lines 28 and 39 could be accounted for, but lines 31 and 37 remain difficult to explain. Better counting statistics could help to better resolve this issue. For the other lines, starting at the high-energy end of this energy range, line 29 is identified with the single FAC transition almost in perfect agreement with the measured line center with only a 0.05 eV difference. Line 30 is described by the four transitions with overlap of its model component. Two of these transitions are fairly weak, with the two stronger transitions being offset towards lower energy by 0.2–0.25 eV. If this group of five FAC lines is considered to be shifted by slightly larger offsets, the single transition assigned to line 29 could be associated with line 28 instead and the remaining four transitions be split between lines 29 and 30.

The identification of lines 32 and 33 is straight forward with the three (line 32) and one (line 33) FAC transition in close to their measured line centers, suggesting an uncertainty of the FAC calculation of about 0.1–0.2 eV for these transitions. There are five FAC transitions in the range of lines 34–36. Associating line 35 with the two transitions to either side of its line center, leaves the low-energy transitions of the group of five for line 36 and the two remaining transitions on the high-energy side for line 34. Alterna-

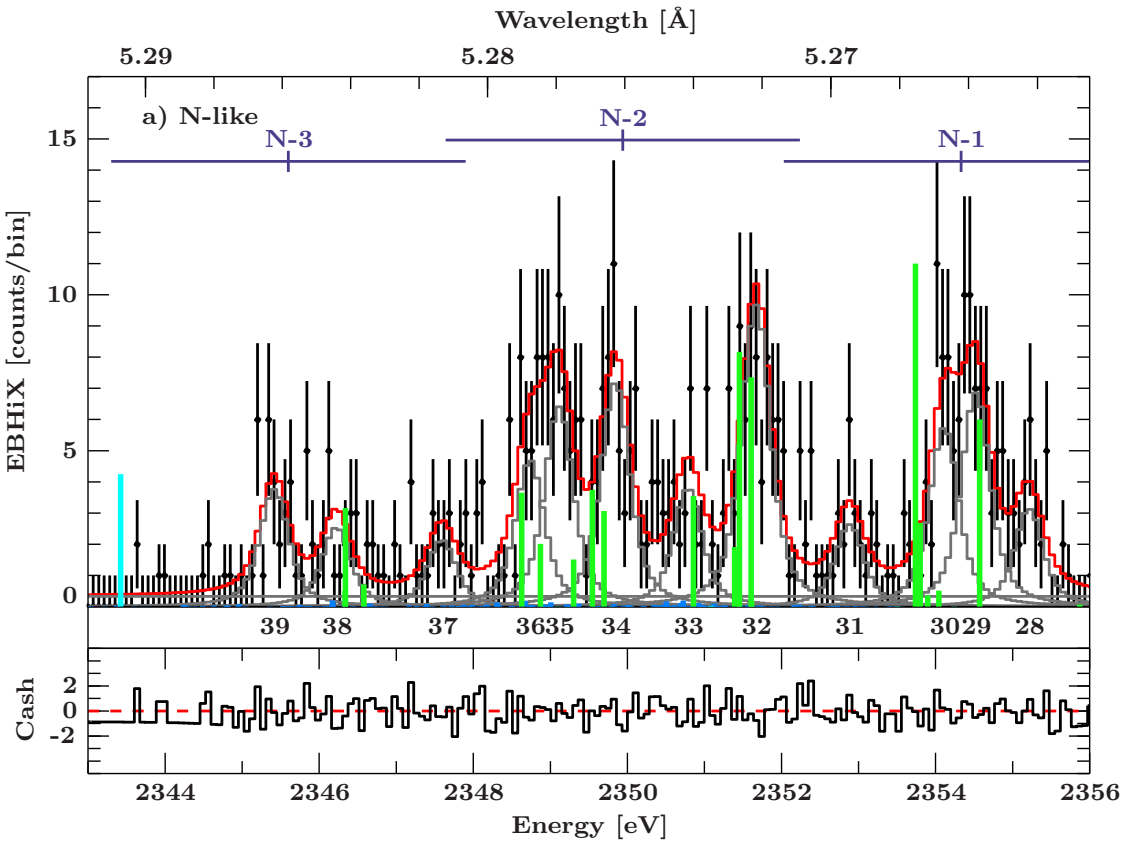

Figure 6.17: Detailed overview of the spectral fits to the EBHiX data for the N-like S region of 2343–2356 eV. See caption of Fig. 6.13 for description.

tively, one could argue that the hole FAC group is shifted to lower energies compared to the measured lines, and assign the three higher-energy transitions to line 34, leaving one transition each for line 35 and 36. In this case, the theoretical line ratio of lines 35 and 36 would appear inverted compared to the measured ratio, which remains stable when using smaller electron densities in the collisional radiative model. In both cases, the energy shift of the calculated transitions is below 0.5 eV.

An identification of line 37 with any of the marked FAC transitions would require a calculation uncertainty upwards of 1 eV. The line thus remains unidentified. The three FAC transitions around 2346.5 eV, the two lower of which are closely blending, are assigned to line 38 with energy shifts of less than 0.3 eV, leaving no considerably strong transitions to identify line 39 with. Allowing for the possibility that the calculated transition energies are up to 1 eV too large, line 39 could be identified with the two lower-ernergy transitions. Both for the measured lines 38 and 39 and for the FAC transitions, the lower-energy lines are the stronger of the two lines, which would support a possible identification with a larger shift.

The seemingly small errors in transition energy of the N-like system calculated by FAC are a little surprising considering that Palmeri et al. (2008a) applied the second largest

empirical adjustment to their calculations of N-like transitions (only exceeded by the shift applied to O-like) out of their 2–9 electron ions. The small shifts could indicate that the line identification as shown here may be inaccurate. Further investigation is needed to resolve this question.

The Be-like FAC transition around 2343.5 eV does not appear to be represented by the spectrum. It is possible that the crysal setting was such that the CCD chip was overflown by the crystal range only on one side of the chip, while the low energy cutoff of the crystal fell onto the camera right before the edge of the CCD chip, therefore not recording a possible line there. On the other hand, the inaccurate charge balance assumption entering the collisional radiative model could overrepresent this Be-like outlier compared to the N-like lines.

6.2.3 Comparison to the ECS Measurement

In addition to the overview of the spectral fits to the EBHiX data, Figures 6.13–6.17 also indicate the energies of the fitted line centers from the ECS data from Hell et al. (2016b) and the FWHM range (±2.3 eV) around them. For the ECS main components in Be- and B-like, namely Be-1 and B-1, we can directly compare the ECS results to the corresponding strongest line in the crystal data (lines 4 and 14, respectively). For the Be-like line, $E_{\mathrm{ECS}} = 2418.51^{+0.10}_{-0.09}$ compared to $E_{\mathrm{EBHiX}} = 2418.597 \pm 0.024$ agree within their statistical errorbars. The same holds true for the B-like line with $E_{\mathrm{ECS}} = 2395.51^{+0.06}_{-0.10}$ and $E_{\mathrm{EBHiX}} = 2395.43 \pm 0.04$. Therefore, in cases where the line blend is dominated by a single strong transition, the energy of this transition can still be gauged at ECS resolution.

In more complex cases with multiple transitions of similar intensities blending, the ECS can only provide mean energies for groups of lines. To assess the accuracy of this average transition energy for the ECS model, we calculate the weighted mean transition energy of the EBHiX lines falling within the FWHM around the respective ECS line centers (Fig. 6.13–6.17). The area of the EBHiX model components (Table 6.6) is used as the weight. Table 6.7 lists these mean energies and the line IDs of the components used to derive the average. Note that the EBHiX spectrometer is operating at Bragg angles close to 45°, where the polarizing effect of the crystal reflection is strongest (Section 5.6). Since the ECS is insensitive to polarization, this effect can change the line ratios measured with EBHiX relative to those seen by the ECS. No corrections for polarization have been made to the measured line intensities entering the weighted line energies, as the exact line ratios are not important for this comparison: such a correction would not change the clear dominance of strong lines such as lines 4 and 14, nor would it elevate a single line to clearly dominate forests of lines with comparable strength as found in C-like and N-like.

Table 6.7 shows that overall the line centers found in the ECS analysis agree well within their uncertainties with the averaged EBHiX line energies. Note that, unlike with the ECS, the fitted energy of S line z in the EBHiX data does not constitute an actual measurement of this transition energy, as it has been used for calibration. However, since this line is (almost) unblended in both data sets, it can be used as an indicator of the systematics between the respective energy scales. The difference between its derived line centers

Table 6.6: Fit and identification of the S lines in the EBHiX spectrum

							$n_e = 1 \cdot 10^{12}\,\mathrm{cm}^{-3}$		
ID	Fit	Norm	Ion	FAC	Lower	Upper	full	no CE	no CI
(1)	$(2437.77^{+0.47}_{-0.27})$	70^{+470}_{-50}	Li-like S	2437.577	$1s^2\,2s_{1/2}$	$((1s_{1/2}\,2s_{1/2})_0\,2p_{3/2})_{3/2}$	1.15(+1)	4.44(0)	1.03(+1)
2	2437.09 ± 0.05	155^{+27}_{-24}	Li-like S	2436.550	$1s^2\,2s_{1/2}$	$((1s_{1/2}\,2s_{1/2})_0\,2p_{1/2})_{1/2}$	4.26(0)	—	4.10(0)
3*	2430.361 ± 0.019	550^{+50}_{-40}	He-like S	2429.075	$1s^2$	$(1s_{1/2}\,2s_{1/2})_1$	1.40(+1)	1.33(+1)	7.59(−1)
4	2418.597 ± 0.024	390 ± 40	Be-like S	2418.383	$1s^2\,2s^2$	$(1s_{1/2}\,2s^2\,2p_{3/2})_1$	5.94(0)	2.04(0)	5.44(0)
5	$2417.13^{+0.15}_{-0.14}$	25^{+15}_{-13}	Li-like S	2416.260	$1s^2\,2s_{1/2}$	$((1s_{1/2}\,2s_{1/2})_1\,2p_{3/2})_{5/2}$	2.59(0)	8.74(0)	2.19(−1)
6	2416.61 ± 0.22	15^{+14}_{-11}	—	—	—	—			
7	2415.75 ± 0.16	23^{+16}_{-13}	Li-like S	2415.021	$1s^2\,2s_{1/2}$	$((1s_{1/2}\,2s_{1/2})_1\,2p_{1/2})_{3/2}$	3.33(−1)	6.92(−1)	1.44(−1)
8	$2415.23^{+0.09}_{-0.10}$	43^{+17}_{-15}	Li-like S	2414.509	$1s^2\,2s_{1/2}$	$((1s_{1/2}\,2s_{1/2})_1\,2p_{1/2})_{1/2}$	4.85(−1)	—	7.37(−2)
9	2413.23 ± 0.06	72^{+18}_{-16}	Be-like S	2412.831	$(1s^2\,2s_{1/2}\,2p_{3/2})_2$	$((1s_{1/2}\,2s_{1/2}\,(2p^2_{3/2})_2)_1$	7.87(−1)	4.29(−4)	1.30(−2)
			Be-like S	2412.817	$(1s^2\,2s_{1/2}\,2p_{1/2})_0$	$(((1s_{1/2}\,2s_{1/2})_1\,2p_{1/2})_{1/2}\,2p_{3/2})_1$	2.57(−1)	7.82(−4)	2.78(−2)
10	$2412.33^{+0.16}_{-0.15}$	13^{+10}_{-8}	Be-like S	2411.567	$(1s^2\,2s_{1/2}\,2p_{3/2})_2$	$(((1s_{1/2}\,2s_{1/2})_1\,2p_{1/2})_{3/2}\,2p_{3/2})_3$	1.37(−1)	4.26(−7)	1.30(−2)
			Be-like S	2411.110	$(1s^2\,2s_{1/2}\,2p_{3/2})_2$	$(((1s_{1/2}\,2s_{1/2})_1\,2p_{1/2})_{1/2}\,2p_{3/2})_1$	1.18(−1)	3.59(−4)	1.28(−2)
11	$2399.25^{+0.25}_{-0.29}$	15^{+10}_{-8}	B-like S	2398.785	$1s^2\,2s^2\,2p_{3/2}$	$(1s_{1/2}\,2s^2\,(2\,p_{3/2})_0)_1$	2.06(−1)	6.00(−2)	1.10(−1)
12	2397.10 ± 0.10	44^{+16}_{-14}	B-like S	2396.865	$1s^2\,2s^2\,2p_{1/2}$	$(1s_{1/2}\,2s^2\,(2p_{3/2})_2)_{3/2}$	2.71(−1)	1.25(−1)	1.49(−1)
13	2395.85 ± 0.10	130^{+70}_{-50}	B-like S	2395.109	$1s^2\,2s^2\,2p_{1/2}$	$((1s_{1/2}\,2s^2\,2p_{1/2})_1\,2p_{3/2})_{1/2}$	9.03(−1)	—	8.44(−1)
14	2395.43 ± 0.04	420^{+60}_{-70}	B-like S	2395.252	$1s^2\,2s^2\,2p_{3/2}$	$(1s_{1/2}\,2s^2\,(2p_{3/2})_2)_{3/2}$	3.19(0)	1.47(0)	1.75(0)
15	2393.74 ± 0.07	71^{+19}_{-17}	B-like S	2393.495	$1s^2\,2s^2\,2p_{3/2}$	$((1s_{1/2}\,2s^2\,2p_{1/2})_1\,2p_{3/2})_{1/2}$	2.60(−1)	—	2.43(−1)
16	$2392.96^{+0.12}_{-0.13}$	33^{+16}_{-13}	B-like S	2393.065	$1s^2\,2s^2\,2p_{1/2}$	$((1s_{1/2}\,2s^2\,2p_{1/2})_0\,2p_{3/2})_{3/2}$	4.59(−1)	3.83(−1)	2.11(−1)
17	$2392.18^{+0.13}_{-0.17}$	24^{+14}_{-11}	—	—	—	—			
18	2391.22 ± 0.08	54^{+16}_{-14}	B-like S	2391.407	$1s^2\,2s^2\,2p_{3/2}$	$((1s_{1/2}\,2s^2\,2p_{1/2})_1\,2p_{3/2})_{5/2}$	6.64(−1)	$4.99e-1$	2.20(−1)
19	$2378.55^{+0.14}_{-0.12}$	22^{+12}_{-9}	Li-like S	2379.155	$1s^2\,2p_{1/2}$	$1s_{1/2}\,2s^2$	1.37(−1)	4.53(−2)	1.26(−2)
20	2377.63 ± 0.11	25^{+12}_{-10}	Li-like S	2377.319	$1s^2\,2p_{3/2}$	$1s_{1/2}\,2s^2$	2.38(−1)	7.84(−2)	2.18(−2)

NOTES: — Line 3 (S z) is a calibration line and not an actual measurement, its fitted line center can only be used to gauge the calibration uncertainty. Line 1 is cut off by the detector edge; it is only included for completeness and cannot be trusted. There is an additional systematic uncertainty of 0.046 eV from calibration on all fitted line centers. Fitted lines are identified with the transitions listed under them. Lines 6, 17, 28, 31, 37, and 39 have no clear identification (see text). FAC transitions that have a '—' in the columns ID, Fit, and Norm are not assigned to any measured lines, but only listed for completeness.

COLUMNS: — Fit: fitted line center in eV. Norm: Fitted area of the line profile. Ion: charge state of the transition. FAC: transition energy (eV) calculated with FAC. Lower/Upper: lower and upper level of the transition. $n_e = 1 \cdot 10^{12}\,\mathrm{cm}^{-3}$: line strength calculated with FAC's collisional radiative model in photons s^{-1} for this electron density n_e, with either the full model as described in Section 6.1.5, with disabled collisional excitation (no CE), or with disabled collisional ionization (no CI); numbers in parentheses denote powers of 10, i.e., $1.15(+1) \equiv 1.15 \cdot 10^{+1}$.

Table 6.6: — *continued*

ID	Fit	Norm	Ion	FAC	lower	upper	$n_e = 1 \cdot 10^{12}\,\mathrm{cm}^{-3}$		
							full	no CE	no CI
—	—	—	C-like S	2376.597	$((1s^2\,2s^2\,2p_{1/2})_{1/2}\,2p_{3/2})_2$	$(1s_{1/2}\,2s^2\,(2p^3_{3/2})_{3/2})_1$	3.82(−1)	2.01(−1)	6.72(−2)
21	$2375.48^{+0.26}_{-0.31}$	10^{+10}_{-8}	C-like S	2374.490	$(1s^2\,2s^2\,2p_{1/2}\,2p_{3/2})_1$	$((1s_{1/2}\,2s^2\,2p_{1/2})_0\,(2p^2_{3/2})_0)_0$	6.02(−2)	5.15(−2)	1.98(−2)
			C-like S	2374.409	$(1s^2\,2s^2\,2p_{1/2}\,2p_{3/2})_1$	$(1s_{1/2}\,2s^2\,(2p^3_{3/2})_{3/2})_2$	2.49(−2)	1.56(−2)	8.25(−3)
22	2374.10 ± 0.06	132^{+28}_{-26}	C-like S	2373.921	$1s^2\,2s^2\,(2p^2_{3/2})_2$	$((1s_{1/2}\,2s^2\,2p_{1/2})_1\,(2p^2_{3/2})_0)_1$	3.75(−1)	2.19(−1)	1.84(−1)
			C-like S	2373.871	$1s^2\,2s^2\,2p^2_{1/2}$	$(1s_{1/2}\,2s^2\,2p_{1/2})_1\,(2p^2_{3/2})_2)_1$	1.13(−1)	1.34(−4)	1.43(−1)
23	2373.55 ± 0.06	125^{+29}_{-26}	C-like S	2373.524	$1s^2\,2s^2\,(2p^2_{3/2})_2$	$(1s_{1/2}\,2s^2\,(2p^3_{3/2})_{3/2})_2$	2.73(−1)	1.71(−1)	9.05(−2)
			C-like S	2373.230	$(1s^2\,2s^2\,2p_{1/2}\,2p_{3/2})_1$	$(1s_{1/2}\,2s^2\,2p_{1/2})_1\,(2p^2_{3/2})_2)_1$	3.28(−1)	3.91(−4)	4.17(−1)
24	2372.52 ± 0.08	110 ± 40	C-like S	2372.345	$1s^2\,2s^2\,(2p^2_{3/2})_2$	$(1s_{1/2}\,2s^2\,2p_{1/2})_1\,(2p^2_{3/2})_2)_1$	1.71(−1)	2.04(−4)	2.18(−1)
25	$2372.15^{+0.11}_{-0.12}$	57^{+35}_{-29}	C-like S	2371.920	$((1s^2\,2s^2\,2p_{1/2})_{1/2}\,2p_{3/2})_2$	$((1s_{1/2}\,2s^2\,2p_{1/2})_1\,(2p^2_{3/2})_2)_2$	1.31(0)	8.09(−1)	2.16(−1)
—	—	—	C-like S	2370.239	$1s^2\,2s^2\,2p^2_{1/2}$	$(1s_{1/2}\,2s^2\,2p^2_{1/2}\,2p_{3/2})_1$	1.13(−1)	1.53(−1)	3.64(−2)
26	$2369.14^{+0.07}_{-0.08}$	71^{+19}_{-16}	C-like S	2369.551	$(1s^2\,2s^2\,2p_{1/2}\,2p_{3/2})_1$	$((1s_{1/2}\,2s^2\,2p_{1/2})_0\,(2p^2_{3/2})_2)_2$	3.05(−1)	2.86(−1)	7.67(−2)
			C-like S	2369.137	$1s^2\,2s^2\,(2p^2_{3/2})_0$	$(1s_{1/2}\,2s^2\,(2p^3_{3/2})_{3/2})_1$	2.73(−1)	1.43(−1)	4.80(−2)
			C-like S	2369.598	$(1s^2\,2s^2\,2p_{1/2}\,2p_{3/2})_1$	$(1s_{1/2}\,2s^2\,2p^2_{1/2}\,2p_{3/2})_1$	3.75(−2)	5.10(−2)	1.21(−2)
27	$2368.11^{+0.09}_{-0.10}$	53^{+17}_{-14}	C-like S	2368.577	$1s^2\,2s^2\,(2p^2_{3/2})_2$	$((1s_{1/2}\,2s^2\,2p_{1/2})_1\,(2p^2_{3/2})_2)_3$	4.54(−1)	3.48(−1)	1.11(−1)
			C-like S	2368.666	$1s^2\,2s^2\,(2p^2_{3/2})_2$	$((1s_{1/2}\,2s^2\,2p_{1/2})_0\,(2p^2_{3/2})_0)_2$	2.57(−2)	3.72(−3)	6.45(−3)

Table 6.6: — *continued*

ID	Fit	Norm	Ion	FAC	lower	upper	$n_e = 1 \cdot 10^{12}\,\mathrm{cm}^{-3}$ full	no CE	no CI
28	$2355.21^{+0.12}_{-0.14}$	27^{+14}_{-12}	—	—	—	—			
29	$2354.52^{+0.14}_{-0.11}$	59 ± 25	N-like	2354.573	$(1s^2\,2s^2\,2p_{1/2}\,(2p^2_{3/2})_2)_{3/2}$	$(1s_{1/2}\,2s^2\,2p_{1/2})_1\,(2p^3_{3/2})_{3/2})_{1/2}$	3.77(−1)	3.19(−1)	7.49(−2)
30	$2354.11^{+0.12}_{-0.11}$	49^{+28}_{-22}	N-like	2353.740	$(1s^2\,2s^2\,2p_{1/2}\,(2p^2_{3/2})_2)_{5/2}$	$((1s_{1/2}\,2s^2\,2p_{1/2})_1\,(2p^3_{3/2})_{3/2})_{3/2}$	6.91(−1)	2.87(−1)	1.73(−1)
			N-like	2353.798	$1s^2\,2s^2\,(2p^3_{3/2})_{3/2}$	$1s_{1/2}\,2s^2\,2p^4_{3/2}$	1.68(−1)	1.20(−1)	2.34(−2)
			N-like	2353.898	$(1s^2\,2s^2\,2p_{1/2}\,(2p^2_{3/2})_2)_{3/2}$	$((1s_{1/2}\,2s^2\,2p_{1/2})_1\,(2p^3_{3/2})_{3/2})_{3/2}$	2.28(−2)	9.48(−3)	5.70(−3)
			N-like	2354.042	$(1s^2\,2s^2\,2p_{1/2}\,(2p^2_{3/2})_0)_{1/2}$	$1s_{1/2}\,2s^2\,2p^4_{3/2}$	3.20(−2)	2.28(−2)	4.44(−3)
31	$2352.88^{+0.13}_{-0.14}$	22^{+12}_{-10}	—	—	—	—			
32	2351.67 ± 0.07	83^{+20}_{-18}	N-like	2351.606	$(1s^2\,2s^2\,2p_{1/2}\,(2p^2_{3/2})_2)_{3/2}$	$(1s_{1/2}\,2s^2\,2p^2_{1/2}\,(2p^2_{3/2})_2)_{3/2}$	4.62(−1)	3.30(−1)	7.29(−2)
			N-like	2351.454	$(1s^2\,2s^2\,2p_{1/2}\,(2p^2_{3/2})_2)_{5/2}$	$((1s_{1/2}\,2s^2\,2p_{1/2})_1\,(2p^3_{3/2})_{3/2})_{5/2}$	5.13(−1)	4.15(−1)	6.71(−2)
			N-like	2351.391	$(1s^2\,2s^2\,2p_{1/2}\,(2p^2_{3/2})_2)_{3/2}$	$1s_{1/2}\,2s^2\,2p^4_{3/2}$	1.720(−1)	1.57(−1)	3.58(−2)
33	$2350.78^{+0.16}_{-0.18}$	33^{+15}_{-13}	N-like	2350.857	$(1s^2\,2s^2\,2p_{1/2}\,(2p^2_{3/2})_2)_{3/2}$	$((1s_{1/2}\,2s^2\,2p_{1/2})_0\,(2p^3_{3/2})_{3/2})_{3/2}$	2.23(−1)	2.73(−1)	7.17(−2)
34	2349.84 ± 0.08	62^{+19}_{-17}	N-like	2349.697	$(1s^2\,2s^2\,2p_{1/2}\,(2p^2_{3/2})_2)_{3/2}$	$(1s_{1/2}\,2s^2\,2p^2_{1/2}\,(2p^2_{3/2})_2)_{5/2}$	1.93(−1)	5.77(−2)	1.08(−1)
			N-like	2349.546	$(1s^2\,2s^2\,2p_{1/2}\,(2p^2_{3/2})_0)_{1/2}$	$(1s_{1/2}\,2s^2\,2p_{1/2})_1\,(2p^3_{3/2})_{3/2})_{1/2}$	2.35(−1)	1.99(−1)	4.67(−2)
35	$2349.11^{+0.17}_{-0.31}$	55^{+30}_{-32}	N-like	2349.302	$1s^2\,2s^2\,(2p^3_{3/2})_{3/2}$	$(1s_{1/2}\,2s^2\,2p_{1/2})_1\,(2p^3_{3/2})_{3/2})_{1/2}$	9.49(−2)	8.03(−2)	1.88(−2)
			N-like	2348.872	$(1s^2\,2s^2\,2p_{1/2}\,(2p^2_{3/2})_0)_{1/2}$	$((1s_{1/2}\,2s^2\,2p_{1/2})_1\,(2p^3_{3/2})_{3/2})_{3/2}$	1.26(−1)	5.25(−2)	3.16(−2)
36	$2348.73^{+0.54}_{-0.19}$	40^{+33}_{-27}	N-like	2348.628	$1s^2\,2s^2\,(2p^3_{3/2})_{3/2}$	$((1s_{1/2}\,2s^2\,2p_{1/2})_1\,(2p^3_{3/2})_{3/2})_{3/2}$	2.30(−1)	9.54(−2)	5.74(−2)
37	$2347.59^{+0.28}_{-0.25}$	18^{+12}_{-9}	—	—	—	—			
38	2346.22 ± 0.23	22^{+13}_{-10}	N-like	2346.579	$(1s^2\,2s^2\,2p_{1/2}\,(2p^2_{3/2})_0)_{1/2}$	$(1s_{1/2}\,2s^2\,2p^2_{1/2}\,(2p^2_{3/2})_2)_{3/2}$	4.43(−2)	3.17(−2)	6.99(−3)
			N-like	2346.341	$1s^2\,2s^2\,(2p^3_{3/2})_{3/2}$	$((1s_{1/2}\,2s^2\,2p_{1/2})_1\,(2p^3_{3/2})_{3/2})_{5/2}$	1.99(−1)	1.61(−1)	2.60(−2)
			N-like	2346.335	$1s^2\,2s^2\,(2p^3_{3/2})_{3/2}$	$(1s_{1/2}\,2s^2\,2p^2_{1/2}\,(2p^2_{3/2})_2)_{3/2}$	3.17(−2)	2.26(−2)	5.00(−3)
39	2345.42 ± 0.11	32^{+14}_{-12}	—	—	—	—			
—	—	—	Be-like	2343.422	$(1s^2\,2p_{1/2}\,2p_{3/2})_2$	$(1s_{1/2}\,2p^2_{1/2}\,2p_{3/2})_1$	2.67(−1)	9.19(−2)	2.44(−1)

Table 6.7: Comparison of ECS fitted line centers to weighted mean energy of EBHiX features.

ECS Key	ECS E_γ	EBHiX $\langle E_\gamma \rangle$	EBHiX Keys
Li-3	$2437.797^{+0.023}_{-0.024}$	—	1,2
S z	$2430.380^{+0.024}_{-0.019}$	(2430.361 ± 0.019)	3
Be-1	$2418.51^{+0.10}_{-0.09}$	2418.44	4–6
Be-2	$2414.7^{+1.0}_{-4.0}$	⟨2413.502⟩	⟨5–10⟩
Be-3	$2412.0^{+0.8}_{-1.4}$		
B-1	$2395.51^{+0.06}_{-0.10}$	2395.44	12–15
B-2	$2391.36^{+0.20}_{-0.42}$	2391.94	16–18
C-1	$2378.26^{+0.27}_{-0.20}$	2378.02	19,20
C-2	$2373.25^{+0.14}_{-0.16}$	2373.317	21–25
C-3	$2368.83^{+0.20}_{-0.24}$	2368.700	26,27
N-1	$2354.33^{+0.23}_{-0.29}$	2354.272	28–31
N-2	$2349.94^{+0.23}_{-0.32}$	2350.039	32–37
N-3	$2345.6^{+0.4}_{-0.6}$	2346.207	37–39

Notes: Li-3: an EBHiX averaged line center is not given as the presumably stronger line is cut off from the observable energy range. S z: Note that this line has been used for calibration in OHREX and is not an actual measurement of the transition energy. Be-2/Be-3: see text for discussion.

is within the statistical uncertainty of both lines, as well as covered by the systematic uncertainty of both energy scales (Sections 6.1.3 and 6.2.1).

While the average energy of the features contributing to Be-1 and B-1 differs slightly from the energy of the strongest feature alone, the average EBHiX energy still agrees equally well with the ECS line centers. Similarly, for the line-heavy C-like and N-like ions the center of grapvity for clustering groups of lines is reproduced well by the ECS analysis. The only exception are the Be-like line Be-2 and Be-3, which do not seem to match the "true" line distribution 5–10 very well. A possible explanation is the close proximity of the group of lines 5–8 to the strong transition 4 of less than half a resolution element of the ECS and their low relative intensity. For this constellation, the dominant model component Be-1 can push the weaker Be-2, and subsequently Be-3, out to lower energies. This behavior is reflected in the large and very asymmetric uncertainties of the two weak features Be-2 and Be-3. While the Monte Carlo simulation had warranted the use of an additional component Be-3 to describe the Be-like blends and there are indeed two groups of lines (5–8 and 9–10), the weighted average of these two energies fits the weighted average of the EBHiX results much better. Indeed, in an earlier analysis of only the Run-I ECS data (Hell, 2012), we had modeled the Be-like complex with only two components, Be-1 and Be-2* (Be-2* accounting for both the Be-2 and Be-3 features of the fit by Hell et al., 2016b), where the center of Be-2* at 2413.57 ± 0.19 eV matches the mean EBHiX energies of lines 5-10 well.

The line center of the Li-like line blend Li-3 agrees with the EBHiX component 1, although

this line is cut off by the detector in the EBHiX spectrum, leaving only a possible wing of the line to determine its line center. While this agreement indicates that the feature is likely real rather than an edge effect from the detector, we do not recommend to draw any reliable conclusions from this agreement, as the determined center of component 1 is an extrapolation beyond the observed spectral range.

In conclusion, although the ECS cannot resolve all line blends, careful analysis of the measured profiles of the line blends is a good proxy for the average transition energy of individual line clusters.

6.3 Outlook

6.3.1 New Wavelength Calculations

The ECS measurement of K-shell transitions in Si and S showed that there can be fairly large uncertainties between calculated and measured transition energies, especially in case of the Palmeri et al. (2008a) data. New calculations for the K-shell transition energies in these ions with higher expected accuracy become available from Beiersdorfer et al. (2016a), who use the multi-reference Møller-Plesset (MRMP) atomic physics code described by Ishikawa et al. (1991) and Ishikawa & Vilkas (2001). The code has proved to provide very accurate results for L-shell and M-shell transition energy in the past (Vilkas & Ishikawa, 2004; Ishikawa et al., 2009; Díaz et al., 2013; Beiersdorfer et al., 2012a,b, 2013, 2014a,b, 2015), with uncertainties on the order of only one part in 10 000 or 0.1–0.2 eV. But Beiersdorfer et al. (2016a) are the first to investigate the code's performance for K-shell transitions in multi-electron ions.

Beiersdorfer et al. (2016a) start their assessment by comparing their calculations to the transitions in F-like Si VI and O-like Si VII identified by Hell et al. (2016b, see Section 6.1). Table 6.8 shows their results in comparison to the HRF calculations of Palmeri et al. (2008a, P08), the FAC calculations of Hell et al. (2016b), and the ECS measurements by Hell et al. (2016b). Both FAC and MRMP are consistently larger than P08, who have shifted their transition energies by ~ 3.7 eV towards lower energy for both Si ions. P08's disagreement with the experimental uncertainties indicates that they likely overestimated the correction needed. The differences between FAC and MRMP are relatively small, with some MRMP transitions having smaller and other larger energies than the FAC transitions. While both FAC and MRMP have some overlap with the experimental values, MRMP appears to fit the measurement better (Beiersdorfer et al., 2016a). Similar to the discussion in Chapter 7, using the EBHiX for time-resolved spectroscopy could enable us to resolve the blend of Kα transitions for ions below F-like S (Fig. 6.4 and 6.5), which would help to benchmark the atomic codes for these low charge states as well.

A comparison to the full range of Si and S ions and especially to the high-resolution crystal measurements of S will demonstrate the full potential of the MRMP calculations. With its high accuracy, the MRMP calculation might even be able to resolve the issue of the potentially ambiguous identification of the EBHiX data with FAC transitions (Section 6.2.2),

Table 6.8: New MRMP calculations compared to previous Si results (Beiersdorfer et al., 2016a)

Ion	Key	Transition	P08	FAC	MRMP	ECS
F-like Si VI	F-1	$1s^2\,2s^2\,2p_{1/2}^2\,2p_{3/2}^3\ (J=3/2)$	1740.79	1743.71	1743.52	1742.88 ± 0.16
		$\rightarrow 1s_{1/2}\,2s^2\,2p_{1/2}^2\,2p_{3/2}^4\ (J=1/2)$				
		$1s^2\,2s^2\,2p_{1/2}\,2p_{3/2}^4\ (J=1/2)$	1740.15	1743.09	1742.89	
		$\rightarrow 1s_{1/2}\,2s^2\,2p_{1/2}^2\,2p_{3/2}^4\ (J=1/2)$				
O-like Si VII	O-1	$1s^2\,2s^2\,2p_{1/2}\,2p_{3/2}^3\ (J=2)$	1756.35	1758.28	1758.86	1758.7 ± 0.5
		$\rightarrow 1s_{1/2}\,2s^2\,2p_{1/2}^2\,2p_{3/2}^3\ (J=1)$				
O-like Si VII	O-2	$1s^2\,2s^2\,2p_{1/2}^2\,2p_{3/2}^2\ (J=2)$	1754.39	1756.79	1756.44	1756.0 ± 0.4
		$\rightarrow 1s_{1/2}\,2s^2\,2p_{1/2}^2\,2p_{3/2}^3\ (J=2)$				
		$1s^2\,2s^2\,2p_{1/2}^2\,2p_{3/2}^2\ (J=2)$	1754.96	1757.38	1757.03	
		$\rightarrow 1s_{1/2}\,2s^2\,2p_{1/2}\,2p_{3/2}^4\ (J=1)$				
		$1s^2\,2s^2\,2p_{1/2}\,2p_{3/2}^3\ (J=2)$	1754.78	1757.32	1756.98	
		$\rightarrow 1s_{1/2}\,2s^2\,2p_{1/2}\,2p_{3/2}^4\ (J=0)$				
		$1s^2\,2s^2\,2p_{1/2}\,2p_{3/2}^3\ (J=1)$	1753.91	1756.30	1755.95	
		$\rightarrow 1s_{1/2}\,2s^2\,2p_{1/2}^2\,2p_{3/2}^3\ (J=2)$				
		$1s^2\,2s^2\,2p_{3/2}^4\ (J=0)$	1754.29	1756.70	1756.36	
		$\rightarrow 1s_{1/2}\,2s^2\,2p_{1/2}\,2p_{3/2}^4\ (J=1)$				
O-like Si VII	O-3	$1s^2\,2s^2\,2p_{1/2}^2\,2p_{3/2}^2\ (J=2)$	1750.40	1752.47	1752.34	1751.4 ± 0.6
		$\rightarrow 1s_{1/2}\,2s^2\,2p_{1/2}^2\,2p_{3/2}^3\ (J=1)$				

Notes: Table from Beiersdorfer et al. (2016a). The key is the same as in Table 6.4 and Fig. 6.10. All transition energies are in eV. P08: Palmeri et al. (2008a). FAC: calculation by Hell et al. (2016b), see Table 6.4. MRMP: Beiersdorfer et al. (2016a). ECS: measurement by Hell et al. (2016b), see Table 6.4.

and, consequently, help to better benchmark the accuracy of the FAC calculations, which currently are more commonly available to the community (Section 6.3.3).

6.3.2 $n = 3 \rightarrow 1$ Transitions in S

K-shell transitions beyond the $n = 2 \rightarrow 1$ Kα transitions are usually not covered by the few measurements that are available for L-shell ions, although exceptions do exist (e.g., Li- and Be-like Fe measured at a tokamak Smith et al., 1993). Reasons for this neglect likely include the limited energy range of the employed crystal spectrometers and the exceedingly small line strengths of the higher members of the Rydberg series. In parallel to the long exposure times necessary to collect the crystal spectra shown in Section 6.2, the ECS was therefore used to measure these weaker transitions in S. Figure 6.18 shows the corresponding measurement in comparison to the FAC model from Section 6.1.5. As seen in Fig. 6.18, sufficient data was taken to determine the transition energies for Kβ transitions in F- through Li-like S. Additionally, $n = 4 \rightarrow 1$ Kγ transitions for Li- and Be-like S are clearly resolved around 2970 eV and 2900 eV, respectively. The FAC model indicates the energies of Kγ transitions in lower charge states, but because of the overlap of the energy range covered by the Kγ transitions with the range of the Kβ transitions, the Kγ transitions of these charge states lower than Be-like blend with the Kβ lines of higher charge states and are too weak to be resolved. Similarly, one of the two distinct

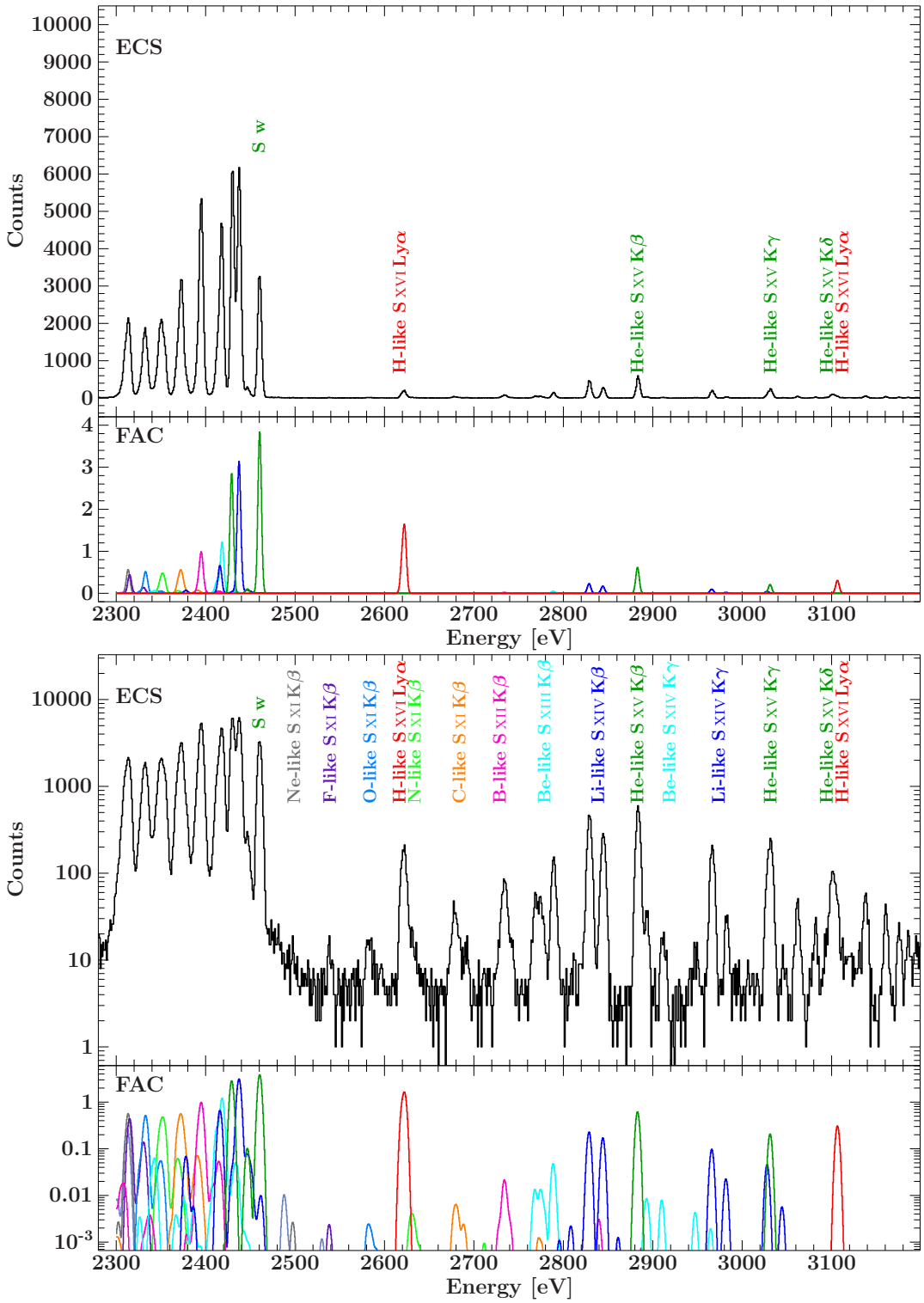

Figure 6.18: Broadband S spectrum including the higher orders of the Rydberg series, shown on both a linear (top figure) and a logarithmic (bottom figure) intensity scale to illustrate how weak the Kβ transitions are in the L-shell ions of S compare to the He-like Kβ line. The S measurement (top panels) was taken with the ECS on SuperEBIT. The FAC spectrum (bottom panels) from the model in Section 6.1.5 confirms the identification of these lines.

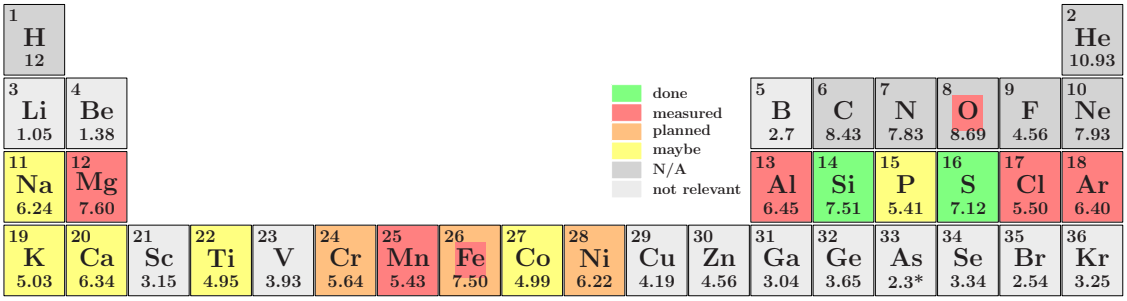

Figure 6.19: Periodic table of the elements highlighting the progress of our effort to measure K-shell transitions of astrophysically interesting L-shell ions with the ECS. The number below the elemental symbol represents the solar abundance of each element from Asplund et al. (2009). Elements with abundances below 5 are considered not relevant. Elements with $Z \leq 10$ are not included in the campaign (see text). The measurements of Si and S are published (Hell et al., 2016b). Mg, Al, Cl, Ar, and Mn have been measured and are pending careful analysis. O and Fe have previously published measurements (Gu et al., 2005; Decaux et al., 1997). Further measurements for Cr, Fe, and Ni are planned. Measurements of Na, P, K, Ca, Ti, and Co are considered less important and contingent on beam time availability.

$n = 5 \rightarrow 1$ Kδ transitions of Li-like S around 3040 eV blends with He-like Kγ, and one of the two Be-like Kδ transitions around 2950 eV blends with the Li-like Kγ line. The ECS measurement features further lines above 3050 eV that are missing a corresponding line in the FAC calculations. These lines are members of the Rydberg series of mostly He- and Li-like ions with an electron excited to $n > 5$. They are missing in the FAC model, since only electrons up to the $n = 5$ shell were included in the calculation (Section 6.1.5).

These measurements provide an important benchmark for calculations of transitions involving more highly excited levels, which can have different systematic uncertainties than the Kα transitions (Beiersdorfer et al., 1989). Due to the long exposure times necessary for the cross section measurements (Chapter 8), transition energy measurements for Kβ lines in Fe ions are also available (Fig. 8.9).

6.3.3 Measurements in Additional Elements

As discussed in Section 1.4.1, K-shell transitions in L-shell ions are expected to be observed in a number of elements beyond Si and S. In an ongoing effort, we are collecting similar ECS spectra for reference for astrophysically abundant elements between Na and Ni (Hell et al., 2015). Figure 6.19 shows a section of the periodic table of elements, listing the solar abundances for each element as determined by Asplund et al. (2009). The fields of the table are color coded according to the progress made. Elements with an abundance below about 5 are deemed non-relevant for astrophysics studies for now. Elements with $Z \leq 10$ are considered not applicable (N/A) to this project as the energy of K-shell transitions in these elements are below 1 keV, where wavelength dispersive spectrometers have far better resolution than the ECS (Section 3.3).

The remaining elements are sorted for their importance for astrophysics and beam time availability. Kα transitions in Si and S were the most pressing issue because of the Cyg

X-1 and Vela X-1 observations (Section 1.4.1). The results for these two elements are published (Hell et al., 2016b). The next key elements are the Fe group elements, especially Cr, Mn, Fe, and Ni, as these are routinely observed in celestial sources and are likely to include at least charge states down to Be-like (Fig. 1.9). Traces of K-shell transitions of lower charge states of Mg have also recently been uncovered in *Chandra*-HETG observations of Vela X-1 (Grinberg et al., 2017). Measurements of Na, P, K, Ca, Ti, and Co have a lower priority.

Wavelengths measurements at an EBIT are already available in the literature for some of the ions of interest. For example, Gu et al. (2005) reported measurements of O III–VI. Measurements of the Li-like spectra of V (Beiersdorfer et al., 1991) and Co (Smith et al., 1995) are also available. L-shell ions of Fe have previously been studied at tokamaks (Beiersdorfer et al., 1993) and EBIT-II (Decaux et al., 1997; Decaux et al., 2003), using crystal spectrometers, but their accuracy is only on the order of 1 eV (Section 7.1). Due to the typically limited spectral range of these spectrometers, transitions from electrons excited to higher principle quantum numbers n, resulting in higher orders of the Rydberg series, have not been included in these measurements. These will be determined from the cross section measurements discussed in Chapter 8.

EBIT measurements similar to the Si and S data presented in (Hell et al., 2016b) are available for some of the missing elements (Mg, Al, Cl, Ar, and Mn). Further measurements are planned for Cr, Fe, and Ni. Study of the less important elements Na, P, K, Ca, Ti, and Co is contingent on beam time availability. These measurements will be used to benchmark the transition energies available in current atomic databases for astrophysics, especially in AtomDB (Foster et al., 2012). Specifically, the EBIT measurements are used to gauge the precision of calculations with FAC, which have recently been included into AtomDB v.3 to make up for the database's previous lack of K-shell transitions in L-shell ions accross the periodic table. Conclusions drawn from the comparison to several measured elements will be beneficial also for the ions of those elements that have not been observed in the laboratory.

As will be seen later it is desirable to determine angles of incidence and reflection with great accuracy. This was not anticipated, and the circular scale was only divided into degrees, and was made too small.

Bragg & Bragg (1913) about the design of one of the first crystal spectrometers

7 High-resolution Measurements of K-shell Transitions in Fe

ACCURATE wavelengths for K-shell transitions in iron are important for all of its charge states, as motivated in Sections 1.4.2 and 1.4.3. This chapter reviews the existing high-resolution wavelength measurements of K-shell transitions in Fe and discusses recent attempts to resolve individual components of the tightly spaced K-shell transitions in M-shell ions.

7.1 Overview of Existing Wavelength Measurements

Until 1993, solar X-ray observations provided the highest resolution ($\lambda/\Delta\lambda = 1000$–$2500$) measurements of the Fe K-shell spectrum available at the time (Beiersdorfer et al., 1993, see references therein for identification and wavelength measurements of the Fe spectrum from solar flares); comparable laboratory measurements existed only for Be-like through He-like Fe XXIII–XXV. Beiersdorfer et al. (1993) then measured F- through He-like Fe XVIII–XXV at the Princeton Large Torus (PLT) tokamak, using a Johann-type crystal spectrometer equipped with a quartz $11\bar{2}0$ crystal. They measured 40 features, some of them line blends, to an accuracy of 0.1–0.4 mÅ (0.3–1.3 eV) with a resolving power of $\lambda/\Delta\lambda = 3000$, comparable to the Doppler broadening in the tokamak, and with better counting statistics than the previous solar flare observations. The larger uncertainties are ascribed to the line emission from the lower charge states, since these lines were weaker and furthest away from the calibrations line. Since the tokamak plasma has a Maxwellian electron energy distribution, these features include transitions due to dielectronic recombination.

Decaux & Beiersdorfer (1993) observed K-shell transitions in L-shell Fe ions by taking spectra as a function of EBIT phase, i.e., the spectra were measured during the relatively short ionizing portion of the EBIT phase. The measurement used a von Hámos spectrometer with a Si 220 crystal and a resolving power of $\lambda/\Delta\lambda = 1700$. Decaux &

Beiersdorfer (1993) only list the measured wavelengths for the two F-like features. Decaux et al. (1995) produced an ionizing plasma with the same method to create the first experimental simulation of a transient plasma in the laboratory and measure K-shell transitions in Cl- through F-like Fe X–XVIII. The spectra were recorded with von Hámos-type spectrometer using a LiF(200) crystal at a resolving power of $\lambda/\Delta\lambda \approx 2300$. They report an accuracy of ~ 0.5 mÅ, calibrated from the stronger of the two F-like Fe XVIII lines. Although the K-shell transitions in these ions are heavily blended even at these high spectral resolutions and when time resolved (integrating only over the first 7–14 ms), they tentatively identify two Cl-like Fe X transitions and associate two more structures in the spectral shape generally with transitions in Al-like Fe XIV and Na-like Fe XVI. Additionally, Decaux et al. (1995) discussed the number of transitions originating from inner-shell ionization versus electron impact excitation for each of these M-shell ions.

Decaux et al. (1997) concentrated again on K-shell transition in L-shell Fe ions and measured 32 features, some consisting of line blends, with an accuracy of 0.3–0.5 mÅ (1.0–1.8 eV), using a von Hámos spectrometer with $\lambda/\Delta\lambda \geq 2000$. Using the spectral model of Jacobs et al. (1989), Decaux et al. (1997) calculated the rate coefficients for inner-shell ionization and electron impact excitation populating the upper level of all of the identified transitions. Especially for F-like Fe XVIII through C-like Fe XXI both processes contribute significantly in producing the observed lines. Decaux et al. (2003) measured the L-shell Fe spectra with a von Hámos spectrometer using a LiF(200) crystal with $\lambda/\Delta\lambda \sim 2300$ at EBIT-II and make a detailed comparison to their theoretical work in order to investigate line-formation processes for these spectra. They calibrated their dispersion from the F-like Fe XVIII line F1 and the strongest C-like C XXI feature C9 with reference wavelength from earlier measurements and estimate their experimental uncertainty to be on the order of 0.5 mÅ. While they list the same experimental wavelength values for transitions in the high charge states as (Decaux et al., 1997), starting on the long-wavelength (low-energy) side of C-like Fe Decaux et al. (2003) report additional measured wavelengths compared to the previous measurement.

Rudolph et al. (2013) published the newest set of wavelength measurements for F-like Fe XVIII through He-like Fe XXV using X-ray resonant photoexcitation by coupling the portable Flash-EBIT to the PETRA III synchrotron X-ray photon source. In this setup, Flash-EBIT is used to breed and trap the Fe ions up to He-like with electron beam energies below the excitation threshold for K-shell transitions. Resonant photoexcitation is achieved by carefully aligning the photon beam with the trapped ions in the electron beam and sweeping the energy of the photon beam. Analyzing the signal intensity of a Ge detector as a function of photon beam energy gives the measured Fe spectrum. The resolution $E/\Delta E \geq 20\,000$ of this measurement is therefore determined by the energy resolution of PETRA's photon beam and the experimental uncertainty of ~ 0.07 eV is dominated by the energy calibration of the photon beam. Note that this measurement includes wavelength measurements of the He-like Fe XXV resonance lines w and y, since the photon beam is calibrated from absorption edges.

A variety of transition wavelength calculations outside of EBIT are available as well. Behar & Netzer (2002) list the one or two strongest transitions in F- through He-like Fe calculated with HULLAC, similar to their calculations of Si and S (Section 6.1.7). Palmeri

et al. (2003a) give a complete set of wavelengths for K-shell transitions in F-like Fe XVIII through He-like Fe XXV from calculations with AUTOSTRUCTURE, the Breit-Pauli *R*-matrix suite (BPRM), and HFR. They rank the accuracy of their level energies at 3 eV and of their transition wavelengths at 2 mÅ, i.e., almost an order of magnitude less accurate than the quoted uncertainties of Decaux et al. (1997). Mendoza et al. (2004) and Palmeri et al. (2003b) report the wavelengths for transitions in Cl-like Fe X through Ne-like Fe XVII and in Mn-like Fe II through Ar-like Fe IX, respectively. The configurations taken into account by Mendoza et al. (2004) for the M-shell Fe ions do not include electrons in the 3*d* shell, just as our FAC calculation for these ions (Section 7.2.3). Bautista et al. (2004) calculated the effective collision strengths for Ne-like Fe XVII through Be-like Fe XXIII with AUTOSTRUCTURE and BPRM and included tables of the corresponding level energies.

For F-like Fe XVIII through Li-like Fe XXIV, level energies for K-shell vacancies and the corresponding K-shell transitions are included in the CHIANTI database using the values from Palmeri et al. (2003a) and Bautista et al. (2004). The same references are included in the XSTAR atomic database uaDB. AtomDB v.2 (Foster et al., 2012) only includes K-shell transitions down to the Li-like Fe XXIV ion, using level energy calculations by Whiteford et al. (2002). Whiteford et al. (2002) use the same method as Whiteford et al. (2001) for He-like Fe XXV, whose upper level for line w is 11 eV too high, with similar discrepancies for other transitions. After a massive update, AtomDB v.3 now also includes K-shell transitions from L-shell ions, mostly originating from FAC calculations (A. Foster, priv. comm.).

7.2 EBHiX Measurement of M-shell Fe Ions

7.2.1 Experimental Setup

Here, we use the new EBHiX spectrometer (Beiersdorfer et al., 2016c), which has the potential to exceed the resolving powers of previous experiments (Section 5.5), at the LLNL EBIT-I to resolve previously unresolved lines in F-like Fe XVIII to Cl-like Fe X. At a Bragg angle of $\theta \sim 51.3°$, a quartz 110 crystal in second order exactly covers the energy range of these transitions, i.e., the bandwidth between 6380 and 6440 eV.

At first, EBHiX was mounted in its original horizontal position with the plane of dispersion perpendicular to the electron beam direction. As a reminder, in this orientation the small beam width is imaged in the spectral direction, making the spectrometer insensitive to the exact focussing (Section 5.5), which in turn makes it easier to achieve high resolution. However, the flux emitted by EBIT for K-shell transition in these Fe ions is very low, the spectrometer is far away from the source, and the X-rays are only reflected by the crystal in second order, i.e., at smaller crystal reflectivity, resulting in only a few observed photon events per hour in the relevant spectral range. Additionally, the cosmic rays transversing the detector deposit an amount of energy similar to the 6.4 keV photon energy of the Fe lines, resulting in a similar response (pulse height) in the CCD. The low photon flux and the decreased efficiency of filtering the signal from cosmic rays based on pulse height discrimination leads to a low signal-to-noise ratio, as seen in Figure 7.1 (*top*) especially

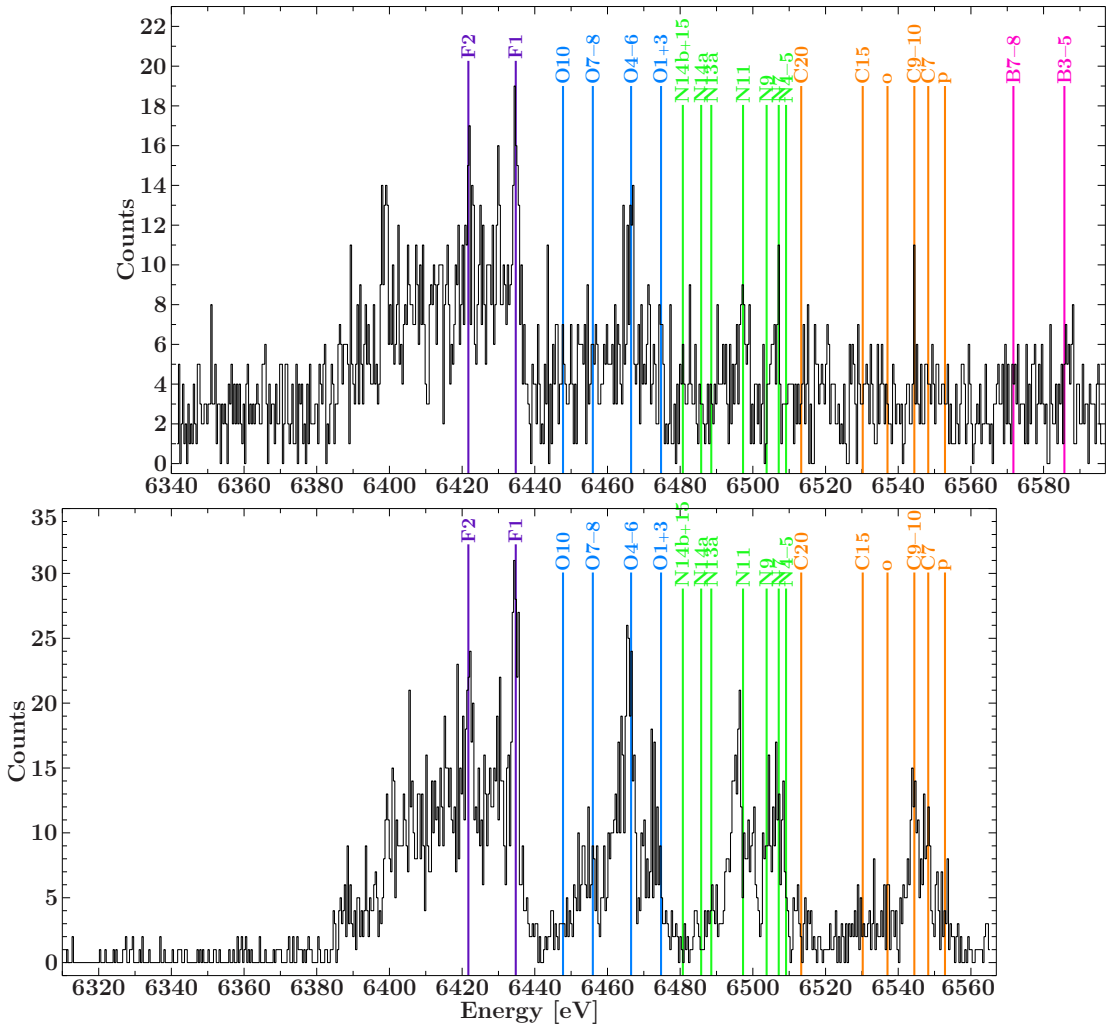

Figure 7.1: K-shell transitions of medium charge states of Fe measured with a quartz 110 crystal using EBHiX in the horizontal (*top*, sum of 139 1h-exposures) and vertical (*bottom*, sum of 159 1h-exposures) orientation, respectively. The spectra are rebinned by a factor of 2 compared to the spatial resolution of the CCD. The horizontal measurement suffers from high background. The vertical measurement has a slightly higher charge balance than the horizontal one, as indicated by the clear contribution from C-, N-, and O-like Fe. For comparison, the line centers of B- through F-like Fe as measured by Decaux et al. (1997) are marked.

below 6380 keV where no signal from Fe is expected.

In order to improve the signal to noise-ratio, we rotated the EBHiX spectrometer to be mounted in its vertical orientation, i.e., with the plane of dispersion parallel to the electron beam direction (Section 5.5.2). While this setup is much more sensitive to the correct image position and has a larger Johann error (Eq. 5.43), the spatial extend of the observed spectra in the cross-dispersion direction is reduced by about a factor of 10. Accordingly, the spectra are extracted from a smaller region of the CCD image, thus greatly reducing the influence of cosmic rays as their probability to hit the extraction region is decreased. Figure 7.1 (*bottom*) shows the successful reduction in background line-free

spectral region below 6380 keV.

The charge balance of the vertical spectrum is somewhat higher than that of the horizontal spectrum. This change in charge balance between the two measurements is attributed to changes in the EBIT parameters. Both spectra were taken at a beam energy of $E_{\mathrm{beam}} \sim 8\,\mathrm{keV}$ and with Fe being injected as $Fe(CO)_5$ via a ballistic gas injector. But the horizontal spectrum was measured at $I_{\mathrm{beam}} \approx 150\,\mathrm{mA}$ beam current and an EBIT cycle time of $t_{\mathrm{cycle}} = 12\,\mathrm{ms}$ (1 ms dump time), while the vertical measurement was using $I_{\mathrm{beam}} \approx 190\,\mathrm{mA}$ beam current, $t_{\mathrm{cycle}} = 15\,\mathrm{ms}$ (1 ms dump time) cycle time, and a doubled injection pressure. Lengthening of the EBIT phase plays the dominant role in the increased charge balance towards higher charge states, as seen in Fig. 3.4.

The spectra are calibrated with a 2^{nd} order polynomial in Bragg angle (derived from Bragg's law including the higher-order corrections, Section 5.1.2), using the He-like Cl Kβ line ($E = 3271.543\,\mathrm{eV}$) observed in first order and H-like Mn Lyα_1 ($E = 6441.665\,\mathrm{eV}$) and Ly$\alpha_2$ ($E = 6423.562\,\mathrm{eV}$) lines in second order (Section 5.5.2). From Table 5.1 we find for the horizontal setup a resolving power of $E/\Delta E \geq 4000$ for Mn and $E/\Delta E \approx 3200$ for Cl. The resolving power in the vertical setup is slightly smaller with $E/\Delta E \sim 3500$ for the Mn Lyα lines and about 3000 for the Cl Kβ line. It is limited by focussing and trapped-ion temperature. The focussing for the vertical setup was done on the brightest measured line, i.e., Cl Kβ on the far side of the CCD chip. As discussed in Section 5.5.2, the smaller resolution of the vertical setup is due to its sensitivity to the exact detector (image) distance, while the focal length changes by a few mm over the width of the CCD chip. The resolution of the Fe spectra is estimated to be of the same order of magnitude as for the calibration lines of the respective setup. This is supported by the comparison of the F-like Fe line F1, which, despite the higher background, is sharper in the horizontal spectrum than in the vertical spectrum (Fig. 7.1).

Since a second order polynomial is uniquely defined by three points, the calibrated line centers of the three calibration lines are not useful estimates of the systematic calibration uncertainty in this case. Additionally, all three calibration lines are on one side of the energy region covered by the K-shell transitions in M-shell Fe ions, i.e., their energy scale is an extrapolation. To get a rough estimate on the magnitude of the systematic uncertainty on the energy scale, we therefore compare the scale as derived from the quadratic fit to a scale derived by a linear fit to the three calibration points, since to first order the gain is linear. Figure 7.2 shows the difference between these two scales as a function of the quadratic scale. Since we do believe that the second order polynomial is a good approximation of the energy scale following the EBHiX calibration in Section 5.5.2, we take the difference of this comparison as an upper limit for the systematic uncertainty. Therefore, the estimated accuracy of the scale is better than 1 eV in the M-shell ion region (6380–6440 eV) and better than 0.4 eV for the L-shell ions (6440–6560 eV). This is slightly better than the accuracy of 0.5 mÅ ($\sim 1.7\,\mathrm{eV}$) quoted by Decaux et al. (1995) for their measurement of the M-shell Fe ions. Their scale was derived using the location of the stronger F-like Fe XVIII line (F1), which sits close to the Mn Lyα_1 lines used here, and the strong strong C-like Fe XXI line C9.

A Monte Carlo simulation of 2000 quadratic gain polynomials confirms the deviation

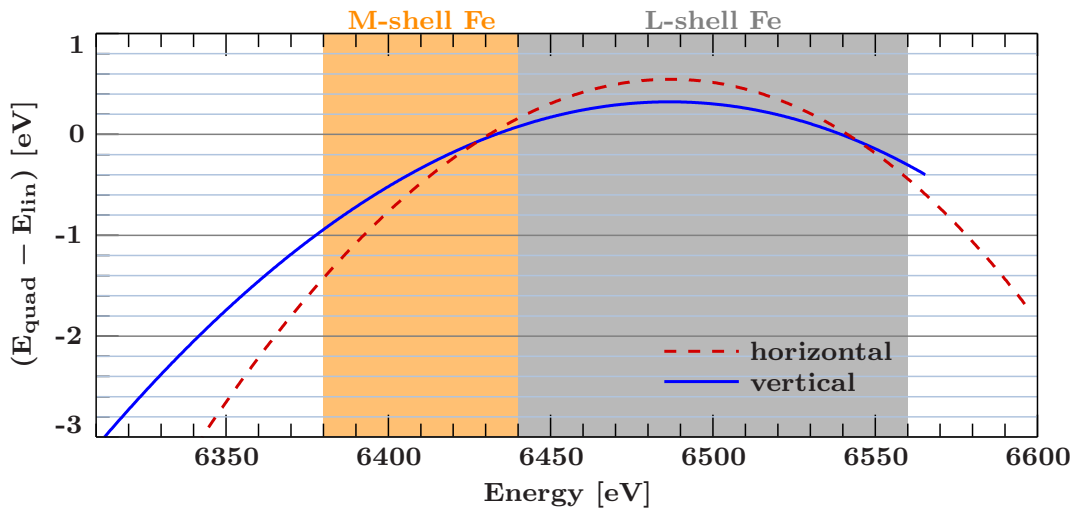

Figure 7.2: Upper limit for the uncertainty estimate of the calibrated energy scale for the horizontal (red, dashed) and vertical (blue, solid) EBHiX measurement. The x-axis is the energy scale derived from the quadratic polynomial. The y-axis shows the difference between the quadratic scale and a scale derived from a linear fit to the calibration lines. The orange shaded region marks the spectral region covered by K-shell transitions in M-shell ions, the gray shaded region marks the L-shell ions up to C-like Fe.

of a linear scale as an upper limit. In the simulation, we calculate fake quadratic gain polynomials from new, simulated sets of calibration lines. To create such a set, for each of the three original calibration lines we draw a new line center in units of detector channels from a Gaussian distribution with mean equal to the original line center and standard deviation equal to the $1\,\sigma$ confidence limits of the fitted line centers. The fake polynomials are then compared to the original gain polynomial (Fig. 7.3). For each CCD pixel mean and standard deviation for the energies determined from each of the fake gain polynomials is also shown. In both the horizontal and vertical setup, the deviation of the linear scale from the quadratic scale is in the outskirts of the energy region covered by the fake polynomials and well outside the $1\,\sigma$ region of the energy distribution. Taking this simulation as a tighter constraint for the systematic uncertainty of the energy scale slightly improves the estimated accuracy of the scale below the upper limit quoted above to better than 0.6 eV in the M-shell ion region (6380–6440 eV) and better than 0.3 eV for the L-shell ions (6440–6560 eV).

7.2.2 Discussion of the Spectra – L-shell Ions

In addition to comparing the spectra of the horizontal and vertical setup to each other, Figure 7.1 shows the line centers of K-shell transitions in the L-shell Fe ions as measured by Decaux et al. (1997) with a von Hámos crystal spectrometer at EBIT and a resolution of $\lambda/\Delta\lambda > 2000$. Overall, there is good agreement between the vertical EBHiX spectra and the values from Decaux et al. (1997), especially for the F-like and C-like features and the closely spaced lines N4–9. N11 appears to separate into two transitions in our

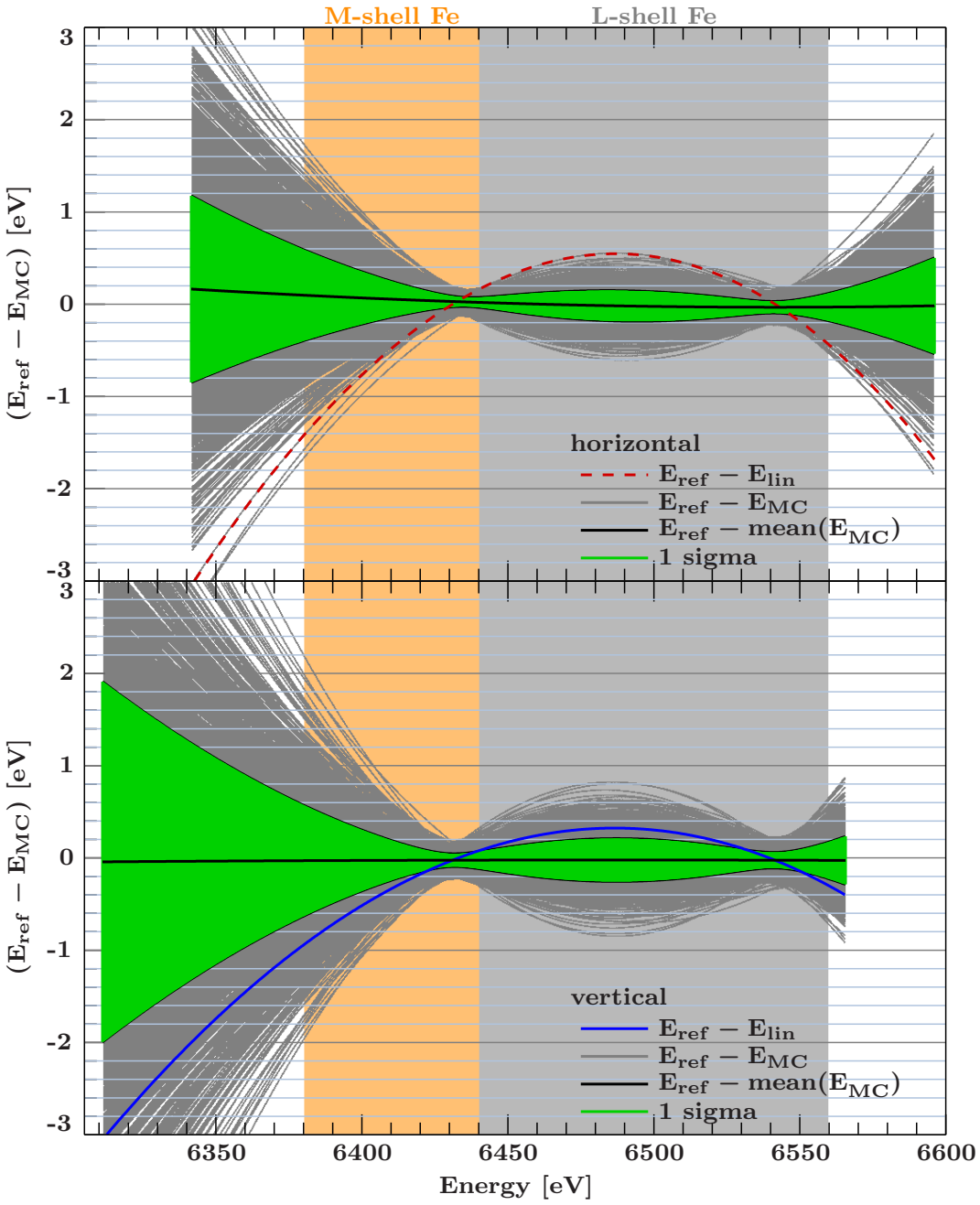

Figure 7.3: Estimate of calibration uncertainty from Monte Carlo simulations. The line centers of the three calibration lines are drawn randomly from a Gaussian distribution with standard deviation equal to the $1\,\sigma$ uncertainty of the line center fit. A new quadratic gain polynomial is then calculated for each set of these simulated reference lines. The gray lines show the energy difference of the Monte Carlo polynomials E_{MC} to the original gain polynomial E_{ref} derived from the best fit line centers. The black line corresponds to the mean of energy of the Monte Carlo polynomials in each CCD channel. The green area shows the $1\,\sigma$ range of the E_{MC} in each channel. The red and blue lines correspond to the difference to a linear fit as shown in Fig. 7.2.

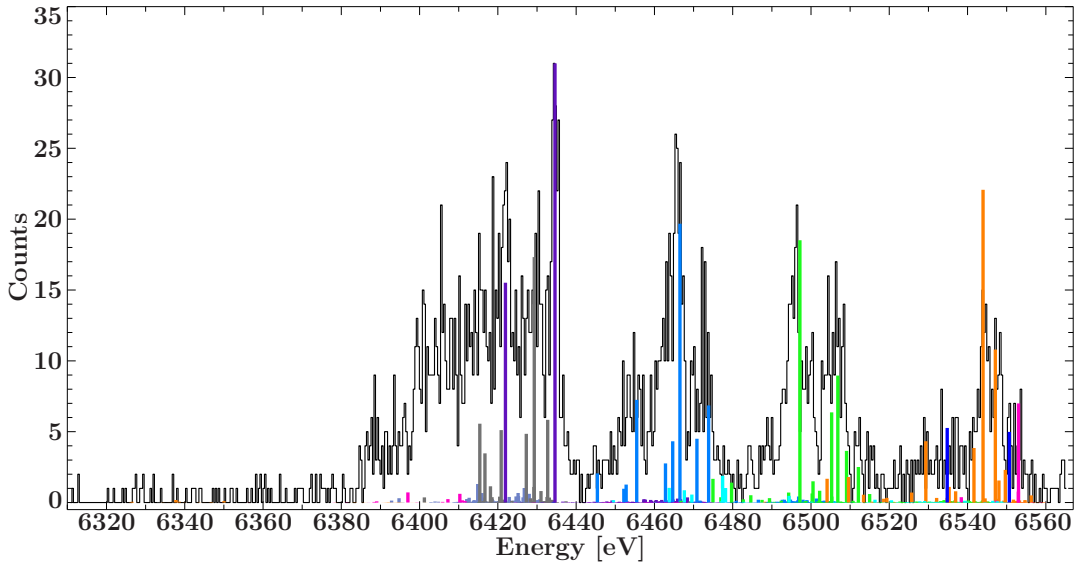

Figure 7.4: The vertical EBHiX spectrum (Fig. 7.1, *bottom*) in comparison to the FAC model. The FAC model shown here was calculated using the same method as for the Si and S models in Section 6.1.5, including transitions from H- through Na-like Fe and assuming a uniform ion distribution. The color code for the FAC transitions follows the color code in Fig 6.4.

measurement, a stronger line at the lower energy side of N11 and a weaker shoulder on its high energy side. While Decaux et al. (1997) do not list additional theoretical lines even as a line blend for this feature, our own FAC calculations using the same approach as in Section 6.1.5 indicate three weak N-like transitions that can account for this shoulder. These transitions are $(1s^2\,2s^2\,2p_{1/2}\,(2p^2_{3/2})_0)_{1/2}$ – $((1s_{1/2}\,2s^2\,2p_{1/2})_1\,(2p^3_{3/2})_{3/2})_{1/2}$ at 6500.313 eV, $(1s^2\,2s^2\,2p_{1/2}\,(2p^2_{3/2})_2)_{5/2}$ – $(1s_{1/2}\,2s^2\,2p^2_{1/2}\,(2p^2_{3/2})_2)_{3/2}$ at 6500.519 eV, and $(1s^2\,2s^2\,2p_{1/2}\,(2p^2_{3/2})_0)_{1/2}$ – $((1s_{1/2}\,2s^2\,2p_{1/2})_1\,(2p^3_{3/2})_{3/2})_{3/2}$ at 6502.209 eV according to the FAC transition energies, which are slightly too high in energy compared to the measured features.

Similarly, the O-like lines are better resolved than the previous measurement. The feature O1+3 splits into two lines O1 and O3 (Fig. 7.1) as predicted by the identification of Decaux et al. (1997) and confirmed by our FAC calculation (Fig. 7.4), whose configurations for these two lines agree with Decaux et al. (1997), but the EBHiX data indicate a slightly lower energy for the line blend than in the previous measurement. This is consistent with the theoretical model of Decaux et al. (1997), which predicts the higher energy component O1 to clearly dominate this line blend, while the line strengths are more comparable between the two lines in the FAC calculation. The three contributions to the blend O4–6 also agree with our FAC calculation and the two weaker components manifest as a clear shoulder in the line profile of this blend in the EBHiX spectrum. The feature O7-8 are identified with two transitions by Decaux et al. (1997), where the FAC model predicts a sizable contribution by three transitions. The missing line is the transition $1s^2\,2s^2\,2p^4_{3/2}$ – $(1s_{1/2}\,2s^2\,2p_{1/2}\,2p^4_{3/2})_1$ and according to FAC has the lowest energy of these three components. Finally, the weaker low-energy component of the line blend C9-10 also has an

indication of a shoulder to the strong component in the higher resolution EBHiX data.

For the spectrum measured with the horizontal EBHiX the flux level around the transitions in M-shell ions (6380–6440 eV) is clearly elevated relative to the line-free background levels below 6380 eV. The flux in the region of the N- and O-like transitions appears also increased, indicating that at least some emission from these ions has been observed. Above these energies, the flux is much the same as in the background region with no perceivable photon contributions. Comparison to the Decaux et al. (1997) results shows that some of the stronger features, e.g., O4–6 and F1, can reliably be identified as spectral lines. Others like the N-like transitions seem to have features at the correct energies, but compared to the vertical spectrum, this coincidence could very well be by chance.

7.2.3 Discussion of the Spectra – M-shell Ions

The primary goal of this experiment was to use the high resolution of the EBHiX spectrometer for a renewed attempt at resolving the main spectral components for some of the M-shell ions contributing to this highly blended spectral region. Figure 7.5 shows the blown up spectra of the horizontal (*top*) and vertical (*middle*) EBHiX run containing the emission from the M-shell ions in comparison to a simple FAC model (*bottom*). The F-like lines, which have been measured before by Decaux & Beiersdorfer (1993) and Decaux et al. (1995), stand out clearly, but other lines could not be resolved further despite the higher resolving power of this measurement.

The FAC spectrum is the result of a collisional radiative model, assuming equal ion densities for all included Fe ions, similar to the method in Section 6.1.5. The model includes radiative transitions, collisional excitation and ionization, autoionization, radiative recombination, and dielectronic recombination. Although dielectronic recombination does not play a role at the electron beam energy employed during the experiment, it is included in the model setup for cases where the model is calculated at different beam energies. For up to the Na-like Fe XVI ion the atomic physics calculations from the previous Section 7.2.2 have been used again. For Mg-like Fe XV to Cl-like Fe X new calculations have been made. While up to Na-like Fe XVI levels with an electron excited up to the $n = 5$ shell were included in the calculation, for Mg-like Fe XV and Al-like Fe XIV the calculation was limited to the $n = 3$ shell. The $\sim$ 5000 energy levels in the Al-like ion jump to $\sim$ 13000 levels in Si-like Fe XIII. The large number of energy levels allows for an even larger number of transitions between any two of these levels, making the calculation very computationally expensive. Therefore, for Si- through Cl-like Fe XIII– X no configurations with electrons in the $3d$ subshell were included in the calculation. The line intensities resulting from the collisional radiative model are convolved with a Gaussian of 2 eV full-width half-maximum and added, to simulate a resolving power of $\sim$ 3200, i.e., comparable to the resolution of the vertical EBHiX measurement.

The spectrum of each ion appears roughly double-peaked, with the two major components being spaced about 10–15 eV apart and the higher energy component being stronger. But only F-like Fe XVIII and Cl-like Fe X, which have closed (sub-)shells in the up-

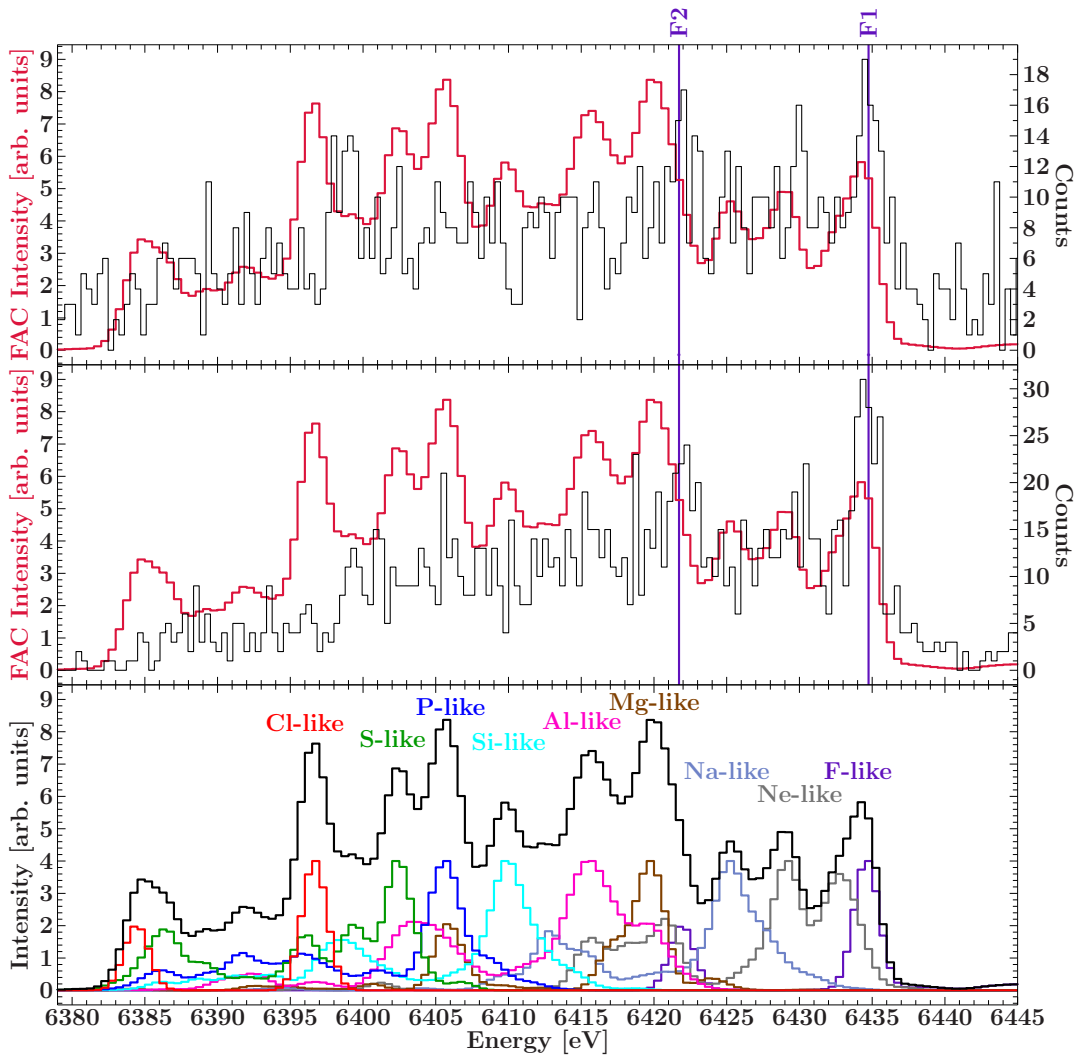

Figure 7.5: Zoom into the M-shell ion region from Fig. 7.1 for the horizontal (*top*) and vertical (*middle*) EBHiX spectrum (black histogram) in comparison to a simple FAC model for these ions (crimson histogram). The contribution from each ion to the FAC spectrum is broken down in the *bottom* panel. The position of the two F-like Fe XVIII transitions F1 and F2 from Decaux et al. (1997) are marked for orientation.

per level, truly consist of only two transitions. Although there are two clearly dominating transitions in Na-like Fe XVI due to its closed 3*s* subshell, a large number of weak transitions broaden their line profile. The other ions have a plethora of lines of varying relative intensities, up to the point where two main peaks can each split into several sub-peaks. Figure 7.6 shows this line distribution for each of the ions.

Especially the low energy tails of these wide-spread transitions overlap heavily with the next lower charge states. Nevertheless, the synthetic spectrum, assuming a uniform charge balance, indicates that at least the strongest peak in each of the M-shell ions should be resolvable at a 2 eV resolution. Yet, the measured spectra show, at best, little

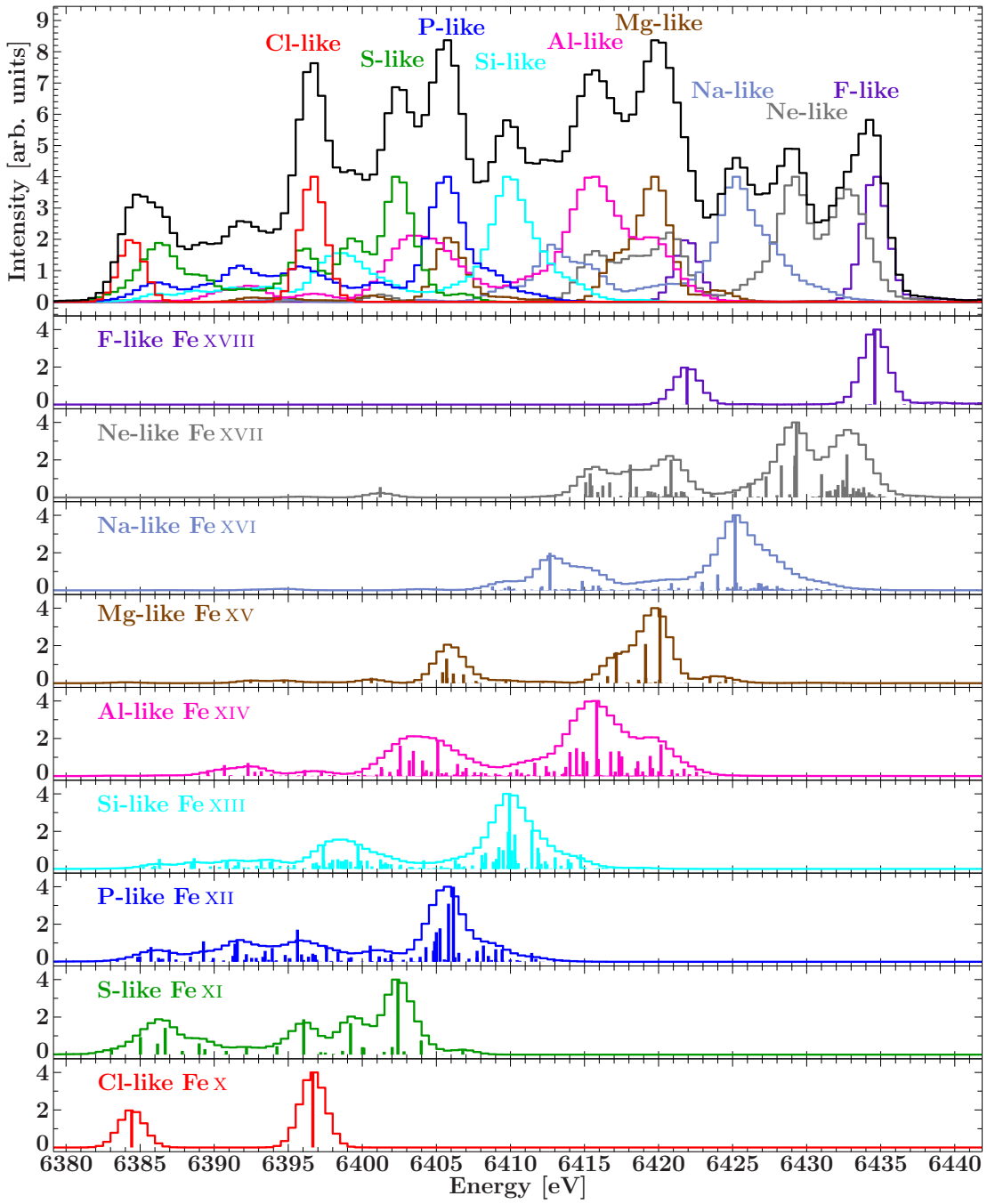

Figure 7.6: Overview of the transitions contributing to the emission of each of the M-shell Fe ions contributing to the total flux in the 6380–6440 eV spectral region. The top panel is the same FAC spectrum as shown in Fig. 7.5, the other panels decompose the summed spectrum of each charge state between Cl-like Fe X and F-like Fe XVIII into the individual transitions from the FAC calculation. As described in the text, for the calculation no electrons were allowed to enter the 3*d* subshell in Cl- through Si-like charge states of Fe (Fe X– XIII).

indication of structure beyond the F-like lines.

For example, the Ne-like Fe XVII shoulder to the F1 line appears to be present. While the overall FAC model appears to be shifted towards lower energies compared to the data (Fig. 7.5, *top* and *middle*), the two F-like Fe XVIII transition energies according to FAC are 6421.925 eV (F2) and 6434.600 eV (F1), respectively, which is close to the 1.93046 Å (6422.52 eV) and 1.92670 Å (6434.75 eV) measured by Decaux & Beiersdorfer (1993). The apparent shift at the high energy flank of the spectrum disappears if the F-like line strength is scaled up to better reflect the measured charge balance.

Decaux et al. (1995) tentatively identify small features at 1.9388 ± 0.0005 mÅ (6394.9 ± 1.6 eV) and 1.9413 ± 0.0005 mÅ (6386.7 ± 1.6 eV) as the two Cl-like Fe X transitions, compared to their HULLAC calculation at 1.9379 Å (6397.864 eV) and 1.9415 Å (6386.001 eV), respectively. Our FAC calculation produces these at 6396.657 eV and 6384.429 eV, respectively, i.e., shifted towards lower energy compared to the HULLAC values. There might be a hint of the lower energy line around 6387 eV in both data sets but the statistics are not sufficient for it to clearly stand out. Features at 6399 eV (vertical EBHiX spectrum) and at 6398 eV (horizontal EBHiX spectrum) look like distinct lines, but do not agree well with the predicted position of the stronger Cl-like line. Better counting statistics are necessary to see if these features are real. The charge balance in both our measurement is probably too high for the Cl-like lines to stand out, as Decaux et al. (1995) observed these features in the integrated 0–7 ms spectrum, but not in the 7–14 ms spectrum, while the EBHiX spectra are integrated over the first 14 and 11 ms of EBIT phase, respectively.

There are multiple arguments that could explain why the increased resolution compared to earlier measurements was not sufficient to resolve any new features in the spectrum of the M-shell ions. First and foremost, much higher detected flux rates are needed to collect sufficient statistics for small variations in the spectral shape to be significant. Higher count rates can be accomplished by any combination of higher spectrometer sensitivity and higher source flux. The spectrometer effective area could be increased by re-designing the instrument with a shorter source distance. As the EBIT phase diagram of Fe (Fig. 3.4) shows, there is a short period of 20–30 ms at the beginning of the cycle (right after the trap was dumped) with an increased event density before the lower charge states start to burn out, which indicates that is takes some time to fill up the trap with fresh ions. Filling the trap more efficiently after dumps could therefore increase the source flux. Using a MeVVA instead of the gas injector might help with this task.

Transitions with spectator electrons in the $3d$ shell that have been excluded from the FAC model could be responsible for filling in the gaps between the peaks that according to the current version of the model should be resolved. Additionally, emission from even lower charge states from Ar-like Fe IX down to neutral Fe I overlap with the emission from the M-shell ions. As discussed by Decaux et al. (1995), the neutral Kα lines are at higher energies than some of the M-shell ions, since the partially filled $3d$ shell screens the $2p$ electron much better than the $1s$ electron. Particularly, Fe I Kα_1 has wavelength (energy) of 1.936042 Å (6404.004 eV) and Kα_2 is at 1.939980 Å (6391.004 eV) (Bearden, 1967, see Hölzer et al., 1997, for measurements of the fine structure). These near-neutral charge states, however, are expected to ionize through within the first 1 ms and, therefore,

should not have a large contribution to the observed flux (Decaux et al., 1995).

With a more realistic non-uniform charge balance, where the relative ion density decreases for lower charge states, the stronger high-energy component in each of the ions does not stand out above the low-energy tails of the next higher charge states. As a consequence, the shape of the summed spectrum smears out. In this case, the only chance to resolve any of these lines is to resolve them in time, i.e., by studying the changes to the spectral shape on much shorter time scales of, e.g., ~ 1 ms, instead of integrating a spectrum over the first ~ 10 ms of the EBIT phase. To do this, a spectrometer with higher sensitivity is needed and an event based detector that is capable of reading out each photon event individually and tag it with a time stamp to make an event list that allows for cuts in EBIT phase after the measurement.

It doesn't matter how beautiful your theory is, it doesn't matter how smart you are. If it doesn't agree with experiment, it's wrong.

Richard P. Feynman

8 Effective Emission Cross Sections

As motivated in general in Chapter 1 and in particular in Section 1.4.3, it is important for plasma diagnostics of collisional plasmas to know the cross sections for collisional excitation through electron impact. This chapter discusses the theory of cross sections, available reference data, and the measurements at EBIT for K-shell transitions in Fe ions. These measurements result in absolute electron impact excitation cross sections for lines such as, e.g., He-like Fe w and H-like Fe Lyα, but they only result in effective emission cross sections in cases where the contribution to the population of the excited level from multiple excitation mechanisms, e.g., collisional excitation and inner-shell ionization, cannot be disentangled as is often the case in K-shell transitions of L-shell ions.

8.1 Theory

If a particle, or a beam of particles, of type A passes through a medium of discrete particles of type B, there is a probability of particles A to interact with a particle B (Fig. 8.1) such that they are absorbed or scattered out of the beam direction. In the simplest setup, a beam of point particles passes through a set of spherical objects (radius r) and the interaction probability is basically determined by the effective area occupied by the medium B (Fig. 8.1). The interaction probability per particle B, i.e., the effective interaction area of particle B, is therefore called a *cross section* (Rybicki & Lightman, 1979). In the classical analogue of the description of this simple scenario, the cross section is the area $\sigma = \pi r^2$ around particle B that particle A has to cross in order to interact (Fig. 8.1*a*). Following the interaction, particle A is no longer traveling within the beam. For point particles A, $r = r_\mathrm{B}$, but for extended particles A, the effective interaction area depends on the radii of both particles as $r = r_\mathrm{A} + r_\mathrm{B}$ (Fig. 8.1*b*; Demtröder, 2008). The fraction dN of particles A interacting with the medium depends on the flux density $\dot{N} = n_\mathrm{A} v \mathrm{A}$ (density n, velocity v) of particles A per unit time and area crossing dx-thick slab of particles B of density n_B in

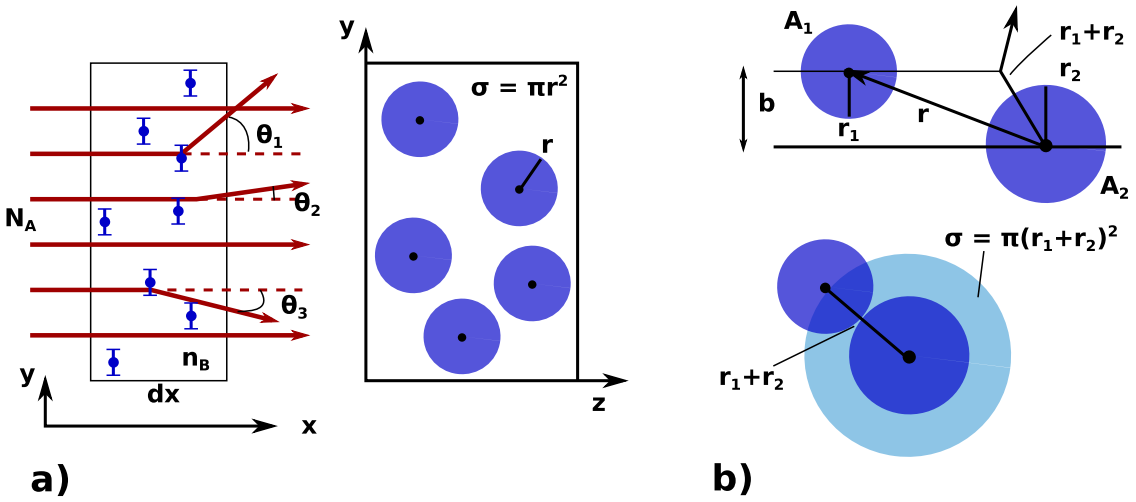

Figure 8.1: Sketch of the classical representation for the interaction cross section a) for point particles A (after Demtröder, 2005, Fig. 2.77) and b) for extended particles A where b is the impact parameter (after Demtröder, 2008, Fig. 7.15).

the x-direction (Demtröder, 2005). For small enough areal density $n_\mathrm{B}\mathrm{d}x$ of the medium, each particle A interacts with a particle B at most once. Then the flux density of beam A changes as (Demtröder, 2005)

$$\mathrm{d}\dot{N} = -\dot{N}\sigma n_\mathrm{B}\mathrm{d}x. \tag{8.1}$$

Dividing by $\dot{N}$ and integrating along the path direction then gives the remaining particle density of the beam after crossing depth x of the medium

$$\dot{N} = \dot{N}_0 \exp(-n_\mathrm{B}\sigma x) \quad \text{with} \quad \dot{N}_0 = \dot{N}(x=0). \tag{8.2}$$

This integrated cross section σ is related to the mean free path $\lambda = 1/(n_\mathrm{B}\sigma)$ (Demtröder, 2005) and the mean time between two interactions is $\tau = \lambda/\langle v\rangle$, where $\langle v\rangle$ is the mean relative velocity between particles A and B (Demtröder, 2008).

More precisely, and taking quantum mechanical effects into account, the cross section depends on the interaction potential $V(r)$ between A and B, on the distance r between A and B, on the masses m_A and m_b, and on the relative velocity $v_\mathrm{A}-v_\mathrm{B}$ (Demtröder, 2005). It is therefore characteristic for the medium and type of interaction, e.g., photo-absorption, electron capture (i.e., recombination processes), or the scattering of electrons leaving particle B in an ionized or excited state (i.e., electron impact ionization and excitation). While the integrated (total) cross section is related to the total probability of an event, the differential cross section $\mathrm{d}\sigma/\mathrm{d}\Omega$, i.e., the cross section as a function of solid angle Ω, singles out the probability that a scattering happens in which the scattering partner is scattered into a direction Ω, e.g., a photon emitted by the decay of a state excited by electron impact being emitted at a certain angle.

The simplest non-relativistic collision problem, involving the scattering of a spinless particle in a real potential $V(\mathbf{r})$, can be solved (Bransden & Joachain, 2003, p. 575*ff.*) by

solving the time-dependent Schrödinger equation

$$\mathrm{i}\hbar\frac{\partial}{\partial t}\Psi(\mathbf{r},t) = H\Psi(\mathbf{r},t) = \left[-\frac{\hbar}{2m}\nabla^2 + V(\mathbf{r})\right]\Psi(\mathbf{r},t). \tag{8.3}$$

If the particle beam is switched on longer than a beam particle takes to cross the interaction region, the problem is reduced to a stationary one with $\Psi(\mathbf{r},r) = \psi(\mathbf{r})\exp(-\mathrm{i}Et/\hbar)$ and $\psi(\mathbf{r})$ a solution of the time-independent Schrödinger equation $H\psi(\mathbf{r}) = E\psi(\mathbf{r})$, where E is the kinetic energy of the particle. For a potential that goes to zero faster than $1/r$, for large r the scattering wave function has to solve the free-particle Schrödinger equation

$$\left[E - \frac{\hbar}{2m}\nabla^2\right]\psi(\mathbf{r}) = 0 \tag{8.4}$$

such that

$$\psi(\mathbf{r}) \underset{r\to\infty}{=} \psi_{\mathrm{inc}}(\mathbf{r}) + \psi_{\mathrm{sc}}(\mathbf{r}) \tag{8.5}$$

where ψ_{inc} describes the incident beams and ψ_{sc} the scattered particles (Bransden & Joachain, 2003). Taking the monoenergetic particle beam as oriented along the z-axis, the incident particles can be described by a plane wave

$$\psi_{\mathrm{inc}} = A\exp(\mathrm{i}kz). \tag{8.6}$$

Here, A is related to the number of particles per unit volume as $|\psi_{\mathrm{inc}}|^2 = A^2$ and the particles have velocity $v = \hbar k/m$ with magnitude $k = |\mathbf{k}_{\mathrm{i}}| = |\mathbf{k}_{\mathrm{f}}|$ of the incident (i) and scattered (f) wave vectors. At large $\mathbf{r}$ the scattered particles then are represented by an outward flow in form of a spherical wave

$$\psi_{\mathrm{sc}} = Af(k,\theta,\phi)\frac{\exp(\mathrm{i}kr)}{r}. \tag{8.7}$$

with an amplitude $f(k,\theta,\phi)$ that depends on the direction $\mathbf{r}$ and the energy $E(k)$ (Bransden & Joachain, 2003). This amplitude is known as the *scattering amplitude*. Following the definition of the differential cross section above, one can show

$$\frac{\mathrm{d}\sigma}{\mathrm{d}\Omega} = |f(k,\theta,\phi)|^2. \tag{8.8}$$

Integration then leads to the total cross section

$$\sigma_{\mathrm{tot}} = \int\frac{\mathrm{d}\sigma}{\mathrm{d}\Omega}\mathrm{d}\Omega = \int_0^{2\pi}\mathrm{d}\phi\int_0^{\pi}\mathrm{d}\theta\sin\theta|f(k,\theta,\phi)|^2 \tag{8.9}$$

by integrating over all scattering angles (Bransden & Joachain, 2003).

8.1.1 Electron Impact Excitation Cross Sections

Of interest for this chapter are scattering processes where the particle beam A is EBIT's electron beam passing through an ion cloud (particles B). The corresponding cross sections are the electron impact excitation cross sections. Electron impact excitation (EIE) is in this chapter also referred to as direct excitation (DE).

In order to calculate EIE cross sections, the scattering amplitude has to be calculated for the wave functions including all bound and the free electron (Eq. 2.8) that solve the Schrödinger/Dirac equation with free electron orbitals (Eq. 2.9). Different approaches to find the solution are summarized in Section 2.2. Since the total wave function Ψ of the system includes multiple single-particle wave functions for the $(N+1)$-electron system, the scattering amplitude assumes matrix form. Following the work of Rose (1961), Carse & Walker (1973), and Walker (1974), Zhang et al. (1990) define a relativistic scattering amplitude $B^{m_{s_i}}_{m_{s_f}}$ for transitions between magnetic sublevels as

$$B^{m_{s_i}}_{m_{s_f}} = \frac{2\pi}{k_i} \sum_{\substack{l_i,m_{l_i},j_i,m_i \\ l_f,m_{l_f},j_f,m_f}} (\mathrm{i})^{l_i-l_f+1} \exp\left[\mathrm{i}(\delta_{\kappa i}+\delta_{\kappa f})\right] Y^{m_{l_i}*}_{l_i}(\hat{\mathbf{k}}_i) Y^{m_{l_f}}_{l_f}(\hat{\mathbf{k}}_f) \times \tag{8.10}$$
$$\times C\left(l_i \frac{1}{2} m_{l_i} m_{s_i}; j_i m_i\right) C\left(l_f \frac{1}{2} m_{l_f} m_{s_f}; j_f m_f\right) T(\alpha_i, \alpha_f).$$

Here, the scattering electron has initial spin m_{s_i}, wave number k_i, and direction $\hat{\mathbf{k}}_i$ which turn into final m_{s_i}, k_i, and $\hat{\mathbf{k}}_i$. The state of the target ion changes from $\beta_i J_i M_i$ to $\beta_f J_f M_f$, where J and M are the total angular momentum and its magnetic quantum number and β stands for all remaining quantum numbers required to define the state of the ion. Y^l_m are spherical harmonics, C are Clebsch-Gordan coefficients, δ_κ are phase shifts, and T is the T-matrix for $\alpha = klj m \beta J M$. The κ are the relativistic quantum number defined as

$$\kappa = -l-1 \quad \text{for } j = l+1/2 \tag{8.11}$$
$$\kappa = l \quad \text{for } j = l-1/2. \tag{8.12}$$

If the scattering electrons are unpolarized, one can average over the initial spins and sum over final spins (Zhang et al., 1990). The differential EIE cross sections for excitation from one magnetic sublevel $\beta_i J_i M_i$ to another $\beta_f J_f M_f$ are then obtained from the squared magnitude of the scattering matrix elements $B^{m_{s_i}}_{m_{s_f}}$ and the total cross section by integrating, giving

$$\frac{\mathrm{d}\sigma}{\mathrm{d}\hat{k}_f} = \frac{1}{2} \sum_{m_{s_i},m_{s_f}} |B^{m_{s_i}}_{m_{s_f}}|^2 \qquad \text{and} \qquad \sigma(\beta_i J_i M_i \to \beta_f J_f M_f) = \frac{1}{2} \sum_{m_{s_i},m_{s_f}} \int |B^{m_{s_i}}_{m_{s_f}}|^2 \,\mathrm{d}\hat{\mathbf{k}}_f, \tag{8.13}$$

respectively. For randomly oriented targets, e.g., thermal ions, the population of the initial magnetic sublevels is statistically distributed and one can average over the initial magnetic sublevels

$$\sigma(\beta_i J_i \to \beta_f J_f M_f) = \frac{1}{2J_i} \sum_{M_i} \sigma(\beta_i J_i M_i \to \beta_f J_f M_f). \tag{8.14}$$

For the total EIE cross section into level $\beta_f J_f$ sum over all final magnetic sublevels M_f (Zhang et al., 1990).

It is customary (Kallman & Palmeri, 2007) to use the collision strength Ω (Hebb & Menzel, 1940, note that the collision strength Ω has nothing to do with the solid angle used earlier

in this chapter) instead of the cross section σ as it is designed to be symmetric, i.e., $\Omega_{ij} = \Omega_{ji}$, through the inclusion of the statistical weight and dimensionless with

$$\sigma_{ij} = \frac{\pi a_0^2}{g_i k_i^2} \Omega_{ij} \tag{8.15}$$

where a_0 is the Bohr radius, g_i the statistical weight of the initial (lower) level, and

$$k_i^2 = \frac{a_0^2 p_i^2}{\hbar^2} = E_i[\mathrm{Ry}] \left(1 + \frac{\alpha^2}{4} E_i[\mathrm{Ry}] \right) \tag{8.16}$$

the square of the relativistic wave number k_i as a function of the kinetic energy E_i of the impact electron in units of Rydberg and α the fine structure constant (Zhang et al., 1990). In astrophysical literature, where thermal plasmas are prevalent, often the Maxwellian averaged effective collision strength Υ_{ij} can be found. According to (Burgess & Tully, 1992), it was first introduced by Seaton (1953) as

$$\Upsilon_{ij} = \int_o^\infty \Omega_{ij} \exp\left(-\frac{E_j}{kT} \right) \mathrm{d}\left(\frac{E_j}{kT} \right). \tag{8.17}$$

Similarly, averaging the differential excitation cross section $\mathrm{d}\sigma_{ij}/\mathrm{d}\Omega$ over a single-electron velocity distribution $f_\mathrm{e}(\mathbf{v}_\mathrm{e})$ and integrating over the solid angle gives the rate coefficient (Jacobs & Beiersdorfer, 2008, after Oxenius, 1986)

$$C(z, i, E_i \rightarrow j) = \iint \mathrm{d}\mathbf{v}_e \mathrm{d}\Omega \ |\mathbf{v}_e| f_\mathrm{e}(\mathbf{v}_e) \ \frac{\mathrm{d}\sigma(z, i, E_i \rightarrow j; \mathbf{v}_e, \Omega)}{\mathrm{d}\Omega}. \tag{8.18}$$

Since such a convolution is not invertible, the effective collision strengths and rate coefficients cannot directly be benchmarked by the measurements at individual impact electron energies as presented in this work. The quasi-Maxwellian sweep experiments at EBIT (e.g., Savin et al., 1999, 2000; May et al., 2003; Wong et al., 2003; Savin et al., 2008; Gu et al., 2012) can be compared directly to effective collision strengths and rate coefficients as a function of electron temperature. However, the first step is to test the more fundamental "raw" cross sections as a function of energy.

8.1.2 Radiative Recombination Cross Sections

In radiative recombination (RR) an electron from the incident beam is captured by one of the target ions, releasing a photon with the excess energy. In other words, during the collision with the ion, the electron looses so much energy that it remains in one of the discrete bound states around the nucleus rather than being able to leave the ion again (Kramers, 1923). While the incident electron can recombine into any empty level of the target ion, recombination into those levels with the lowest principle quantum number n has the largest cross sections (Kramers, 1923; Kim & Pratt, 1983), as shells with lower n have the larger energy difference to the continuum and electrons in lower n shells are bound to the nucleus more strongly. The energy of the emitted photon, $E_\gamma = E_\mathrm{e} + I_\mathrm{pot}$,

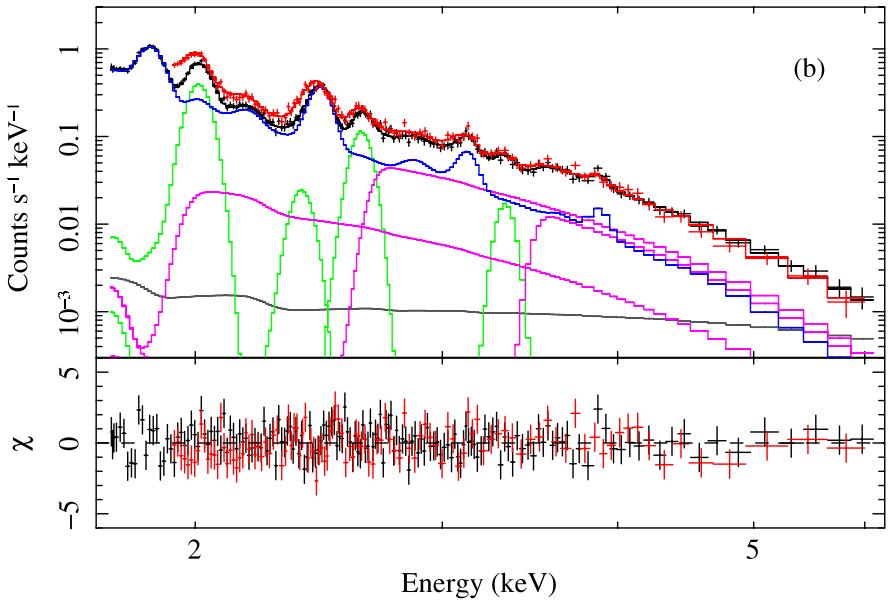

Figure 8.2: *Suzaku* XIS (CCD) spectrum of the supernova remnant IC 443. The magenta lines show the modeled radiative recombination continuum (RRC) for recombination into H-like Mg, Si, and S. The RRC components are above the ionization potentials for the He-like ions of 1.96 keV (Mg), 2.67 keV (Si) and 3.49 keV (S; Cowan, 1981). The sharp edges on the low-energy side of the RRC here are washed out from the CCD resolution of the observed spectrum. — From Yamaguchi et al. (2009, Fig. 3).

equals the kinetic energy E_e of the recombining electron plus the ionization potential (binding energy) I_{pot} of the recombined electron. Because of the E_γ's dependence on the kinetic energy of the incoming electron, in a thermal plasma the RR features build a radiative recombination continuum (RRC) with sharp edges at the binding energy of the recombining level (Fig. 8.2). With a mono-energetic electron beam or a very narrow energy distribution, RR forms distinct, resolved features. At EBIT these are well described with a Gaussian line shape for RR into individual fine-structure levels. When recombination is into a single level or clearly spread levels, the shape of the RR feature represents the energy distribution of beam electrons. Since the binding energies of neighboring orbitals within an n shell are closely spaced, typically with energy differences smaller than the energy spread of the beam electrons, the Gaussian lines within a charge state and principle quantum number n add to a RR complex with distinct and electron energy dependent line shape (Fig. 8.3 and Section 8.5.2).

RR cross sections are typically calculated from the cross sections of the inverse process, photoionization (PI), via detailed balance or the Milne (1924) relation. Since no electron-electron correlations are involved, radiative recombination is the simplest atomic-scattering process and can be calculated very accurately (Chantrenne et al., 1992; Chen & Beiersdorfer, 2008). Photoionization is essentially an extension of photoexcitation into the regime where the absorbed photon energy is greater than the ionization potential such that a bound electron makes a transition into a continuum state rather than an excited bound state (Cowan, 1981; Bransden & Joachain, 2003).

The Milne relation is derived from detailed balance. The principle of detailed balance was formulated by Boltzmann (1872) and states that in equilibrium the transition probability from state a to state b is the same as the reverse probability from state b to state a for any given two states a and b (Bransden & Joachain, 2003). The Milne relation, thus, is

$$g_\mathrm{f} p_\gamma^2 \sigma_\mathrm{PI} = g_\mathrm{i} p_\mathrm{e}^2 \sigma_\mathrm{RR} \tag{8.19}$$

where g_i is the statistical weight of the recombining ion (for RR the initial ion), g_f the statistical weight of the recombined ion (for RR the final ion), $p_\gamma = hf/c$ the momentum of the photon with frequency f and energy $E_\gamma = hf$, and p_e the momentum of the recombining (RR) or photo-electron (PI). The exact form of the Milne relation (Eq. 8.19) then depends on the choice of electron momentum. Possible choices include the simple non-relativistic momentum $p_\mathrm{e}^2 = 2m_\mathrm{e}E_\mathrm{e}$ as used by Pradhan & Nahar (2011), which is equivalent to $p_\mathrm{e}^2 = (4/\alpha^2c^2)E_\mathrm{e}$ with E_e in units of Rydberg[1] (Cowan, 1981), or the relativistic momentum from Eq. 8.16.

Dielectronic recombination (DR) is the resonant version of RR, where the emitted photon energy is directly absorbed to excite another bound electron. If the calculation of photoionization includes resonances, the recombination cross section obtained through the Milne relation therefore constitutes the combined cross sections for RR and DR (Pradhan & Nahar, 2011). To calculate the RR cross section separately, the "background" photoionization is needed, i.e., excluding resonances. These can be calculated, for example, with the central-field approximation. It should be noted that these background cross sections also neglect resonant enhancement that can cause underestimation of the total rate (Pradhan & Nahar, 2011).

Similar to the EIE cross sections, RR cross sections are often averaged over an electron energy distribution, $f_\mathrm{e}(\mathbf{v}_\mathrm{e})$, typically a Maxwellian distribution for thermal electrons, to give the rate coefficient for radiative recombination

$$\alpha_\mathrm{RR} = \langle \sigma_\mathrm{RR} v \rangle = \int \mathrm{d}\mathbf{v}_\mathrm{e} \, |\mathbf{v}_\mathrm{e}| f_\mathrm{e}(\mathbf{v}_\mathrm{e}) \, \sigma_\mathrm{RR}. \tag{8.20}$$

8.2 Measurement Approach

EBIT is well suited to fundamentally study collisional excitation cross sections. Due to EBIT's nearly mono-energetic beam, the excitation cross sections can be measured directly as a function of electron impact energy rather than measuring effective cross sections folded with a complex electron energy distribution as, e.g., in devices creating

[1] To convert between the momentum with electron energy in Ry, eV, or J, do

$$p_\mathrm{e}^2 = \frac{4E_\mathrm{e}[\mathrm{Ry}]}{\alpha^2c^2} = \frac{4E_\mathrm{e}[\mathrm{eV}]\cdot 1\,\mathrm{Ry}}{\alpha^2c^2} = E_\mathrm{e}[\mathrm{eV}]\frac{4}{c^2}\left(\frac{4\pi\epsilon_0\hbar c}{e^2}\right)^2 \frac{m_\mathrm{e}e^4}{8\epsilon_0^2h^2} = E_\mathrm{e}[\mathrm{eV}]\cdot 2m_\mathrm{e}e^2 = E_\mathrm{e}[\mathrm{J}]\cdot 2m_\mathrm{e} = p_\mathrm{e}^2$$

where the Rydberg depends on the Rydberg constant R_∞ as $1\,\mathrm{Ry} = hcR_\infty = (m_\mathrm{e}e^4)/(8\epsilon_0^2h^2) \approx 13.6\,\mathrm{eV}$ and the fine structure constant is defined as $\alpha = e^2/(4\pi\epsilon_0^2\hbar c) = \hbar/(m_\mathrm{e}ca_0)$ with the vacuum permittivity or electric constant ϵ_0. Similarly, $E_\mathrm{e}[\mathrm{Ry}] = E_\mathrm{e}[\mathrm{eV}]\cdot\hbar^2/(2m_\mathrm{e}a_0^2)$.

thermal plasmas. Since EBIT operates in the coronal limit, where the radiative decay is much faster than the collisional excitation rates, overall the observed photon emission rate equals the excitation rate (Vogel, 1992). This is true for excited levels with a branching ratio $\beta_{ij} \approx 1$, i.e., that have only one main decay channel, as, for example, the resonance line w in He-like ions. If the excited level can decay through multiple channels, including both autoionization channels and radiative decay to various lower levels, the measured flux has to be corrected for the branching ratio for the observed transition. Additionally, at EBIT, as mentioned before, due to the directional beam the radiation is polarized such that for dipole transitions the emission is boosted perpendicular to the electron beam. This effect has to be corrected for when deriving the total cross sections from the measurements.

Since in EBIT's coronal plasma the trapped ions are in the ground state, the excited level is generally populated directly only from a single lower level and branching ratios of excitation are of no concern. However, in some ions the levels of the ground configuration are closely spaced in energy such that a small percentage of the ground state population is distributed to these levels (Decaux et al., 2003), which opens additional channels for excitation to the upper level of an observed transition. It is also in principle possible for other excitation mechanisms to contribute to the level population of the excited level in question. For example, inner-shell ionization is the main population channel for the upper level of the forbidden line z in He-like ions and can have significant impact in lower charge states like L-shell ions (Jacobs et al., 1997; Decaux et al., 1997; Decaux et al., 2003). Cascades from higher levels can also add to the upper level population of an observed transition. Dielectronic recombination creates doubly excited configurations, but since dielectronic recombination is a resonant process, it is negligible for electron beam energies outside of these resonances. If the contributions of these different excitation mechanisms cannot be disentangled or if the line blends cannot be resolved, the EBIT measurements for these lines results "only" in effective emission cross sections rather than the more fundamental electron impact excitation cross sections. If the measured DE cross sections include cascade contributions from higher levels, they are often referred to as effective DE cross sections (Chen & Beiersdorfer, 2008; Chen et al., 2002; Wong et al., 1995). In these cases, the agreement between measurement and theory depends on a more complex plasma model including cross sections and decay rates for multiple transitions rather than benchmarking the fundamental excitation cross section of just a single transition.

The observed flux from EBIT, at 90° to the beam axis, for a transition from upper level j to lower level i is

$$C_{ji}^{\mathrm{obs}} = \eta(\lambda_{ji}) \cdot I_{ji}^{\mathrm{EIE}} \tag{8.21}$$

where I_{ji}^{EIE} is the emitted flux and $\eta(\lambda_{ji})$ represents the wavelength dependent spectrometer response, including collection area (solid angle) and quantum efficiency of the detector, filter transmission, and, for crystal spectrometers, the crystal reflectivity including corrections for the line polarization.

The flux emitted by EBIT at 90° to the beam following electron impact excitation from

lower level i to upper level j is then (Brown, 2000; Gu, 2000; Chen & Beiersdorfer, 2008)

$$I_{ji}^{\mathrm{EIE}} = \frac{1}{4\pi} \cdot P_{ij} \cdot \beta_{ji} \cdot \langle v_{\mathrm{e}} \sigma_{ij} \rangle \cdot \int n_{\mathrm{e}} n_q \, \mathrm{d}^3 r. \tag{8.22}$$

Here, β_{ji} is the branching ratio for upper level j to radiatively decay into level i. P_{ij} is the polarization of the transition due to excitation with directional electrons. The total electron impact excitation σ_{ij} is averaged over the electron velocity v_{e}, since the electron beam is not truly monoenergetic but has a small spread of approximately 50 eV FWHM. The density integral depends on the electron density n_{e}, the beam-ion overlap, and the charge balance (Gu, 2000). The beam-ion overlap, in turn, depends on the electrostatic and magnetic potentials that define the beam radius and the ion trap, but also on the charge q and charge-to-mass ratio q/m of the ions that determine together with the trap potential how well the ions are confined in the trap (Vogel, 1992).

To measure absolute excitation cross sections to a high degree of accuracy – better than 10-15% (Chapter 1) –, the beam-ion overlap would have to be known to an accuracy that cannot easily be attained. This overlap is independent of transitions such that it cancels in flux ratios of two transitions within the same ionic species. Therefore, relative excitation cross sections of two transitions can easily be determined. If the cross section for at least one transition in each ion is known very well, the flux of all other measured transitions in the same ion can be normalized relative to the flux of this reference line, bringing their emission cross sections to an absolute scale. Photon emission from radiative recombination are a suitable choice for such reference lines. Their cross sections can be calculated much more accurately than those for direct excitation (Section 8.3.4), since only one electron and a photon have to be taken into account. Cross sections normalized to these RR features are therefore absolute cross sections (Chen & Beiersdorfer, 2008), given that RR cross sections are the most accurate reference available.

Normalizing to RR lines imposes constraints onto the instrumental requirements for the measurement of absolute electron impact excitation cross sections (Chen & Beiersdorfer, 2008). The ionization potentials for L-shell ions of Fe range from 1.2 keV to 2.0 keV and it takes 8.8 keV and 9.3 keV to create H-like and bare Fe, respectively (Cowan, 1981). Since $E_\gamma^{\mathrm{RR}} = E_{\mathrm{kin}} + I_{\mathrm{pot}}$ and it takes $E_{\mathrm{kin}} > 6\,\mathrm{keV}$ to be able to excite K-shell transitions in Fe ions, the employed spectrometers need to cover a broad range of photon energies. Additionally, the ionization potentials for neighboring charge states of L-shell Fe ions are about 0.1 keV apart (Fig. 8.3), with fine structure closing the gap further. Therefore, high spectral resolution is required at high photon energies in order to resolve the RR into the $n = 2$ shell for L-shell Fe ions. The spectral resolving power in the spectral region of the DE lines needs to be sufficient to resolve line blends as well. To avoid that the uncertainty of the measured cross sections is dominated by counting statistics, sufficiently large instrumental throughput is required for both sets of lines, DE and RR. Since $\sigma_{\mathrm{RR}} \ll \sigma_{\mathrm{DE}}$ (Fig. 8.4), a large effective area is especially important for the RR features, i.e., at high photon energies.

A convenient feature, but not a requirement, would be to combine the above requirements in a single spectrometer such that the solid angle, which depends on detector size and distance to the source, cancels in the line ratios and can be neglected. Such an

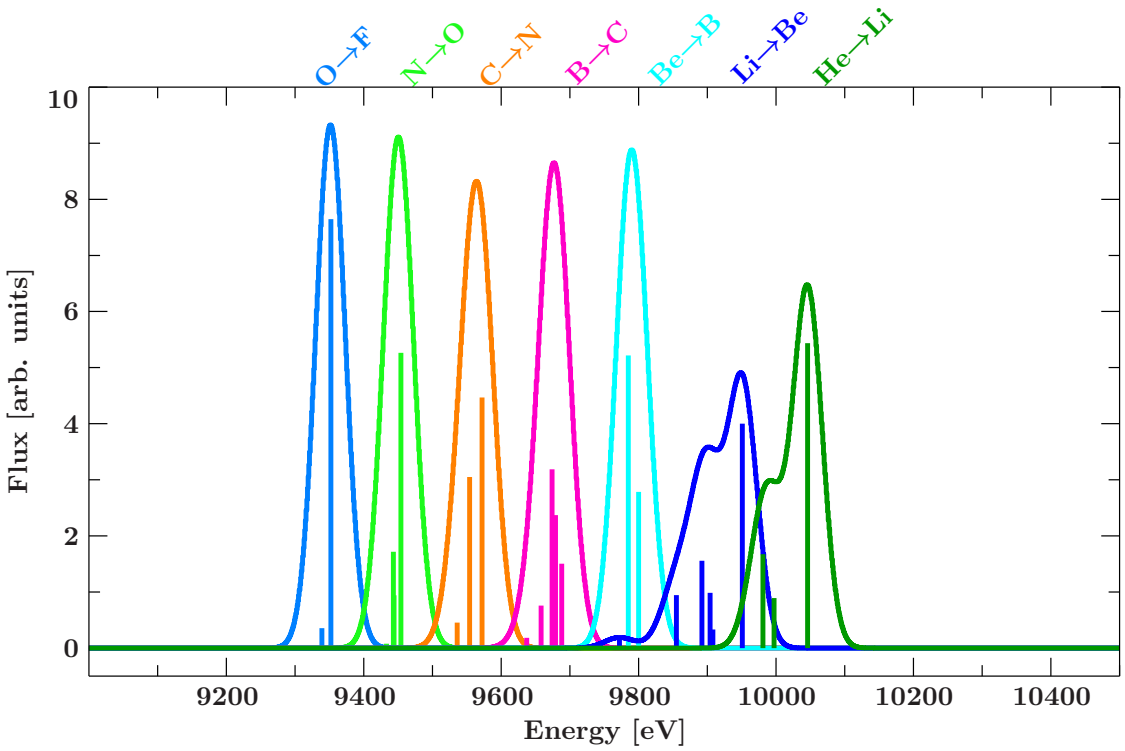

Figure 8.3: Model spectrum of the fine-structure resolved radiative recombination into the $n = 2$ shell for an electron beam energy of $E_{\mathrm{beam}} = 8\,\mathrm{keV}$ and a FWHM of 50 eV. The calculation uses the RR cross sections from Chen et al. (2005) and assumes a total of 500 counts for each charge state.

approach has been demonstrated with the XRS microcalorimeter on L-shell transitions of L-shell Fe ions at low electron energies (Chen et al., 2005). In previous experiments for K-shell transitions in Fe group elements, the direct excitation of He- and Li-like ions has been measured with a crystal spectrometer, while the radiative recombination was observed with a solid-state Ge detector by Wong et al. (1995), who therefore estimate the ionization balance from the resonance line of each charge state. The ECS fulfills almost all instrumental requirements as stated above. The high-energy pixel array covers a smaller solid angle than the Ge detector, but is capable to resolve the RR features. The low-energy pixel array has lower spectral resolution than an adequate crystal spectrometer, but is still sufficient to resolve the strong K-shell transitions in highly charged Fe ions and has a much larger effective area than the crystal spectrometer. While the low- and high-energy pixels are not exactly a single detector covering the full required bandwidth, they are housed in the same instrument, greatly simplifying their geometry compared to normalizing between a crystal and a Ge detector. The ECS is, therefore, currently the best instrument available at EBIT to do these measurements.

For the ECS, the detector response $\eta(\lambda_{ji}) = Q(\lambda_{ji}) \cdot T(\lambda_{ji}) \cdot A$ in Eq. 8.21 only depends on the quantum efficiency, the transmission of the optical blocking filters, and the solid angle. Combining Eq. 8.21 with the formula for the emitted flux (Eq. 8.22), taking the ratio of the direct excitation line flux I_{DE} to the radiative recombination flux I_{RR}, and

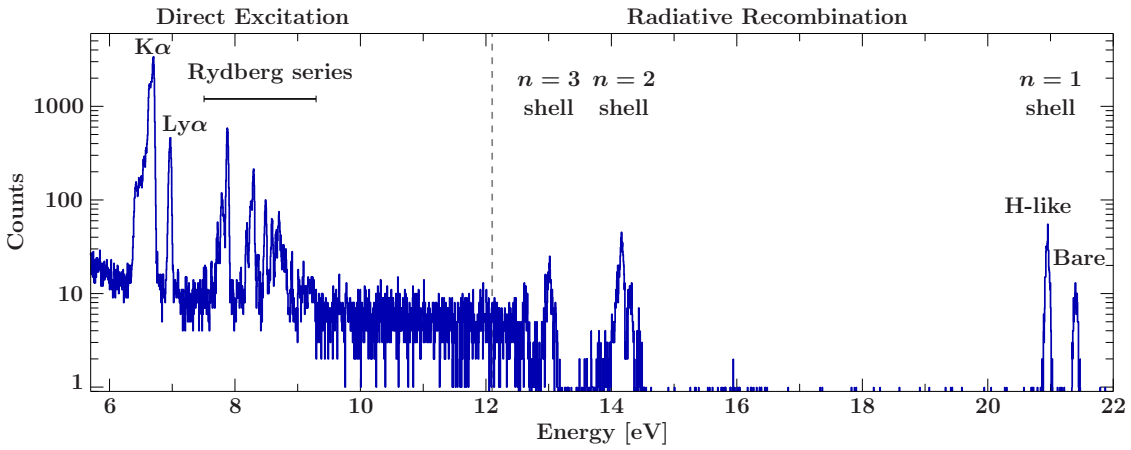

Figure 8.4: Broadband spectrum of Fe measured with the high-energy pixels of the ECS. Line emission below $\sim$ 9.3 keV is due to direct excitation of Fe ions. The weak features are from radiative recombination into the $n = 3$ (13 keV), $n = 2$ (14.2 keV) and $n = 1$ shell (into H-like Fe at 21 keV, and into bare at 21.5 keV). The contribution from bare through F-like Fe ions to the $n = 2$ feature is resolved (Section 8.4). The vertical dashed line marks the beam energy of 12.1 keV, beyond which no direct excitation or bremsstrahlung continuum can occur (the edge is washed out because of the tails of the narrow Gaussian beam energy distribution).

solving for the excitation cross section gives

$$\sigma_{\mathrm{DE}} = 4\pi \frac{1}{P_{\mathrm{DE}}} \frac{1}{\beta_{\mathrm{DE}}} \cdot \sigma^{90}_{\mathrm{DE}} = 4\pi \frac{1}{P_{\mathrm{DE}}} \frac{1}{\beta_{\mathrm{DE}}} \frac{C_{\mathrm{DE}}}{Q_{\mathrm{DE}} T_{\mathrm{DE}}} \frac{Q_{\mathrm{RR}} T_{\mathrm{RR}}}{C_{\mathrm{RR}}} \frac{A_{\mathrm{RR}}}{A_{\mathrm{DE}}} \cdot \sigma^{90}_{\mathrm{RR}} \tag{8.23}$$

where P_{DE} is the polarization of the emission line, $\sigma^{90}_{\mathrm{DE}}$ and $\sigma^{90}_{\mathrm{RR}} = P_{\mathrm{RR}}\sigma_{\mathrm{RR}}/(4\pi)$ the differential collisional excitation and radiative recombination cross sections at 90° to the beam direction (including polarization effects), C_X is the number of collected photons of the respective DE or RR feature from the ECS measurement, Q_X is the quantum efficiency of the detector at the DE and RR line photon energies, T_X is the transmission of the optical blocking filters at the respective photon energies, and A_X are the solid angles subtended by the detectors observing the DE and RR photons. For the optical blocking filters and quantum efficiency of the ECS see Sections 4.4.1 and 4.4.2, for the expected ratio of solid angles see Section 4.4.3.

This measurement technique in general has been introduced successfully by Marrs et al. (1988) and employed by, e.g., Wong et al. (1995) using crystal spectrometers in combination with solid state detectors. The XRS / ECS approach has been used for Ne-like Fe before with beam energies far below 6 keV, using only the low-energy pixels (e.g. Chen et al., 2005; Brown et al., 2006).

8.3 Available Calculations

To determine the absolute cross sections from the measured line fluxes, reference values are needed for radiative recombination cross sections including polarization, for the de-

gree of polarization for direct excitation, and for branching ratios. Since the scope of the experiment is to benchmark available calculations for excitation cross sections, references for these are needed as well. This section summarizes the data available in the literature. The list may not be exhaustive.

8.3.1 Collisional Excitation Cross Sections

Electron impact excitation cross sections in the literature are often convolved into effective collision strengths Υ_{ij} or rate coefficients, especially if they were provided for the astrophysics community where thermal electron energy distributions are the most common electron distributions. In this work, the cross sections are only measured at a few distinct electron energies. A few energy points are not sufficient to convolve the measured cross sections with a Maxwellian energy distribution to directly compare them to the effective collision strengths. Unfortunately, in many cases because of storage space limitations the underlying cross section calculations are not retained after the collision strengths have been published (A. Foster, priv. comm.).

Table 8.1 lists references providing electron impact excitation calculations for K-shell transitions in Fe ions, including the available transitions, the electron energy or temperature range of the calculations, and a short description of the used calculation method. The list is dominated by references for He- and H-like Fe and a few Li-like ions. Similar to transition energies of K-shell transitions in L-shell ions (Section 1.4.1), other atomic data for inner-shell excitation are scarce as well. For this reason AtomDB v.3 filled in the missing atomic data for these transitions with their own FAC calculations where necessary (Foster et al., 2016). They compare their calculations for L-shell Fe ions to the only other relevant calculation they could find, i.e., Bautista et al. (2004) using AUTOSTRUCTURE. Generally, the FAC calculations by Foster et al. (2016) agree within 20% with the Bautista et al. (2004) results, some of the data even have an agreement of better than 10%. The largest differences are for C-like Fe XXI, which consistently shows lower values in FAC than in Bautista et al. (2004), and B-like Fe XXII, which is consistently larger in FAC. For He-like Fe, AtomDB uses calculations from Whiteford using the ICFT code.

The CHIANTI atomic database uses the calculations from Ballance et al. (2002) for H-like Fe and Whiteford et al. (2001) for He-like Fe. Note that the energy levels listed by Whiteford et al. (2001) differ by several eV compared to generally accepted values. CHIANTI lists Whiteford et al. (2001) also as a reference for Li-like Fe, but the paper itself does not include Li-like. For K-shell transitions in F- through Be-like Fe, CHIANTI refers to Bautista et al. (2004). Starting at Ne-like Fe, CHIANTI does not include K-shell holes in their database.

8.3.2 Polarization

The polarization can be calculated from the level populations of the magnetic sublevels, which are proportional to the excitation cross sections of these levels, using the formulae discussed in Section 2.5. See Table 8.1 for calculations that include the cross sections

Table 8.1: Excerpt of available calculations for electron impact excitation cross sections.

Reference	Ions	Transitions	Msub	E / T range	Comments
Walker (1974)	H-like, $Z = 25$, 50, 100	Lyα	no	$E = 0.8E_\mathrm{i}$, E_i, $4E_\mathrm{i}$	relativistic and non-relativistic Coulomb-Born approximation using Dirac wavefunctions
Walker (1975)	H-like, $Z = 25$, 50, 100	Lyα	no	$E = 0.8E_\mathrm{i}$, E_i, $4E_\mathrm{i}$	add Breit and Møller interactions to previous calc.
Moores & Pindzola (1992)	H-like, $Z = 26$, 42, 54, 67, 79, 92	Lyα	no	$E = 1.025E_\mathrm{e} - 6E_\mathrm{e}$	fully relativistic DW
Fontes et al. (1993)	H-like, $Z = 26$, 54, 92	Lyα, Lyβ	no	$E_\mathrm{scat.}(Z) = 0.07$, 0.3, 2 keV	DW with a Dirac-Fock-Slater potential, including Breit interaction
	He-like, $Z = 26$, 54, 92	Kα	no	$E_\mathrm{scat.}(Z) = 0.07$, 0.3, 1 keV	
	Li-like, $Z = 26$, 54, 92	Kα	no	$E_\mathrm{scat.}(Z) = 0.07$, 0.3, 1 keV	
Kisielius et al. (1996)	H-like He, Fe	Lyα–γ	no	$\log T_\mathrm{Fe}(K) = 6.0$, 6.5, 7.0, 7.5	Dirax R-Matrix
Ballance et al. (2002)	H-like Fe	Lyα–γ	no	$\log T(K) = 6.0$–8.0	Breit-Pauli R-Matrix
Malespin et al. (2011)	H-like, Cr, Mn, Fe, Co, Ni	Lyα–δ	no	$\log T(K) = 5.8$–8.5	comparison of Dirac R-Matrix, intermediate coupling R-Matrix, semi-relativ. DW, and fully relativ. DW
Aggarwal & Kingston (1993)	H-like Fe	Lyα–δ (*)	no	$\log T(K) = 4.8$–7.2	LS-coupling, R-Matrix
Aggarwal et al. (2008)	H-like Fe	Lyα–δ	no	$E = 700$–1500 Ry $\log T(K) = 5.6$–7.7	R-Matrix (DARC), FAC
Whiteford et al. (2001)	He-like, Ar, Fe	Kα–γ(Ar)/δ(Fe)	no	$T = 10^6$–10^9 K (Fe)	R-Matrix
Whiteford et al. (2002)	Li-like Ar, Fe	Kα, Kβ	no	$T = 10^5$–10^9 K (Fe)	R-Matrix
Bautista et al. (2004)	Ne- – Be-like Fe	Kα	no	$\log T(K) = 4.8$–7.2	Breit-Pauli R-Matrix
Bautista et al. (2003)	Li-like Fe	Kα	no	$\log T(K) = 5$–8	Breit-Pauli R-Matrix
Zhang et al. (1990)	He-/Li-like Fe, Ne-like Fe, Mo	Kα	yes	$E = 550$–2000 Ry	fully relativ. DW with Dirac-Fock-Slater potential
Inal & Dubau (1987)	He-/Li-like Fe	Kα	yes	$E = 550$–2000 Ry, $E < 20E_\mathrm{e}$	DW
Inal & Dubau (1993)	He-like Fe	Kα, Kβ	yes	$E = 550$–2000 Ry	DW, cascades
Fontes et al. (1999)	He-like Fe, Xe	w, x, y, z	yes	$E = 550$–2000 Ry	Coulomb, Coulomb-Breit
Aggarwal & Keenan (2013)	He-like Fe, Co, Ni, Cu, Zn	Kα–δ	no	$E_\mathrm{Fe} = 700$–1300 Ry	R-Matrix (DARC), FAC
Chen et al. (2015)	He-like Fe	w, y	yes	$E = 6.8$, 8 keV	fully relativ. DW

Notes: Msub: cross sections resolved for magnetic sublevels (needed for polarization). E / T range: electron energy range (points) for calculated collision strengths Ω or temperature range for effective collision strengths Υ. E_i: energy of ground state. E_e: threshold energy for excitation. E_scat: final scattering energy. (*) fine structure (j) not resolved. For some collections, the available electron energy/temperature range depends on the element; in this case the range for Fe is listed.

to the magnetic sublevels. In order to take depolarizing effects such as transverse beam energy and radiative cascades into account, a collisional radiative model for the sublevel has to be invoked, e.g., the polarization module provided by FAC.

Measurements by Henderson et al. (1990), Beiersdorfer et al. (1996b), Beiersdorfer et al. (1997b), and Beiersdorfer et al. (1999a) verified the DW calculations for He-like and Li-like Fe from Inal & Dubau (1987) and Zhang et al. (1990). The measurements by Beiersdorfer et al. (1996b), however, show significant disagreement with the Coulomb-Born approximation without exchange by Shlyaptseva et al. (1981) and Vinogradov et al. (1992). Measurements for H-like Ar, Ti, and Fe Lyα_1 (Nakamura et al., 2001; Robbins et al., 2006) disagreed with DW calculations. Bostock et al. (2009) find that the Breit interaction is important for mid-Z elements, while Møller interaction becomes relevant for high-Z elements such as uranium. The Breit interaction affects the $m_j = 1/2$ magnetic sublevel more than the $m_j = 3/2$ sublevel, but since the effect has opposite signs the effect of Breit interaction on the total cross section is small (Bostock et al., 2009).

Itikawa et al. (1991) suggested based on calculations for H- and He-like low-Z ions ($Z \leq 8$) and in the high-Z limit ($Z = \infty$) that the polarization is almost independent of Z if the electron impact energy is expressed in threshold units. Reed & Chen (1993) confirmed this result for the non-relativistic limit, but found Z dependence in fully relativistic polarization calculations. The Z dependence and the difference between relativistic and non-relativistic results are small for ions up to the Fe group elements and impact energies below about three times threshold. Bostock et al. (2009) also find only minor variations (using threshold units) in the polarization for H-like ions in this Z range. In lieu of other sources, scaling the polarization between Fe group elements (Reed & Chen, 1993, calculated Ti) for He- and H-like ions (lines w, x, and Lyα) introduces only small uncertainties. Line y has a strong Z-dependence, as confirmed by measurements (Beiersdorfer et al., 1999a), because relativity mixes the triplet and singlet levels. The polarization of line z has a weaker Z-dependence due to changes in the radiative branching ratio (Beiersdorfer et al., 1999a), but is strongly affected by cascades (Beiersdorfer et al., 1996b).

Zhang et al. (1990) and Inal & Dubau (1987) provide magnetic sublevel calculations for some Kα transitions in He- and Li-like Fe. Smith et al. (2000) quote the polarization for He-like Fe Kβ_1 and Kβ_2 at two electron energies (~ 8.0 and ~ 9.9 keV). Inal & Dubau (1993) provide the polarization for lines w, x, and y with and without cascades and for the He-like Kβ transitions in the energy range of 500–2000 Ry (6.8–27 keV). The polarization for H-like Fe Lyα_1 can be taken from Bostock et al. (2009). Lyα_2 is unpolarized. For all other transitions, calculations with FAC's polarization module are taken, taking into account cascades and autoionization.

Polarization calculations in general are accurate to within 20%, which affects the accuracy of EIE cross section measurements by only a few percent (Chen & Beiersdorfer, 2008). Chen et al. (2015) compare polarization calculations for He-like Fe lines w and y at 6.8 and 8.0 keV beam energy to available EBIT measurements by Beiersdorfer et al. (1996b) and are consistent within the measurement uncertainties. The depolarizing effect of the transverse beam energy ($E_\perp = 100$–250 eV Savin et al., 1998; Beiersdorfer et al., 1999a; Gu et al., 1999b; Beiersdorfer & Slater, 2001; Chen & Beiersdorfer, 2008)

was taken into account for EIE cross section measurements after 1999 (Chen & Beiersdorfer, 2008). The effect of polarization is estimated (Chen, 2002) to have an effect of up to 60% on cross sections infered from measurements, if not taken into account (Chen & Beiersdorfer, 2008). Chen et al. (2005) use polarization calculations from FAC, which they claim to be in very good agreement with calculations using the code of Zhang et al. (1990).

8.3.3 Branching Ratios

Excited levels can have multiple (spontaneous) decay paths to different levels, including autoionizing channels[2] that do not emit a photon. In order to derive the level population of the excited level, the observed photon flux of a transition has to be normalized to its branching ratio[3], i.e., the probability A^{r}_{ji} of the excited level to radiatively decay through this observed path

$$\beta_{ji} = \frac{A^{\mathrm{r}}_{ji}}{\sum_k A^{\mathrm{r}}_{jk} + \sum_l A^{\mathrm{a}}_{jl}} \tag{8.24}$$

where the sums are over the spontaneous radiative decay rates (Einstein A coefficient) A^{r}_{jk} from upper level j to any level k and the autoionization rates A^{a}_{jl} from level j to levels l. This assumes the plasma to be in the coronal density limit, where only spontaneous decay channels exist. For some resonance transitions such as, e.g., He-like line w or H-like Lyα, the branching ratio is essentially unity. For others it has to be computed from Eq. 8.24.

Lists of radiative decay rates (Einstein A-values) and Auger rates are found easily in the literature, e.g., Palmeri et al. (2003a) for Kα transitions in Fe XVIII–Fe XXV. These can be used to calculate the branching ratios from Eq. 8.24 by hand. Readily computed branching ratios are less commonly available. Branching ratios for He-like Fe Kβ_1 and Kβ_2 are quoted in Smith et al. (2000). Wong (1992) derived their branching ratios for He-like Fe from the radiative rates provided by Lin et al. (1977) and for Li- and Be-like Fe by Chen (1985). Smith et al. (1993) list branching ratios for Kβ satellite transitions in Li- and Be-like Fe. Chen & Crasemann (1988) calculated branching ratios for Kα transitions in select B-like ions with $Z = 6$–54 using MCDF calculations including Breit interaction and QED corrections. Chen et al. (1997) did the same for select C-like ions.

The collisional radiative model of FAC lists the radiative decay rate of transitions and the total decay rate of their upper levels along with the calculated luminosity of the line. Since the listed total decay rate includes both radiative and Auger contributions, its value can be taken as the denominator of Eq. 8.24. The ratio of these two decay rates therefore gives the branching ratio. For example, for the $1s_{1/2}3p_{3/2}\ ^1\!1_1 \rightarrow 1s^2\ ^1\!0_0$ (Kβ_1) transition, FAC gets a branching ratio of 0.937 compared to the 0.934 ratio from MCDF theory used

[2] Autoionization is mostly relevant for doubly-excited states.

[3] Some authors, e.g., Chen & Crasemann (1988) call this ratio "line fluorescence yield", for other authors, e.g., Kallman et al. (2004), the fluorescence yield is the net radiative rate out of the upper level divided by the net rate into the level. While the former definition of the branching ratio gives a constant in coronal plasmas, i.e., where no induced decay occurs, the latter definition of the fluorescence yield depends on the plasma conditions, specifically the processes populating the upper level.

by Smith et al. (2000) and for the $1s_{1/2}3p_{1/2}\ ^3 1_1 \rightarrow 1s^2\ ^1 0_0$ ($K\beta_2$) transition, FAC gets a branching ratio of 0.574 compared to the 0.595 ratio used by Smith et al. (2000).

Smith et al. (2000) show that HULLAC consistently produces a smaller radiative branching ratio for the He-like $K\beta_2$ line than the MCDF calculations, with the discrepancy being much larger at small Z ($Z \sim 12$: 1.4% vs. 4%) than for mid-Z ($Z \sim 26$). More elaborate relativistic configuration-interaction (RCI) calculations such as Chen & Cheng (1997) fall between the HULLAC and MCDF calculations and are deemed to be accurate on the 1% level (Smith et al., 2000). According to Chen & Cheng (1997), transition rates for strong lines are accurate to within 10%, while weaker lines can be off by up to a factor of 2. Similarly, for values $> 10^{13}\,s^{-1}$, Palmeri et al. (2003a) find their A-values and partial Auger rates to be accurate to the 20% level.

8.3.4 Radiative Recombination Cross Sections

Radiative recombination cross sections are arguably the most important theoretical ingredient to inferring the EIE cross sections from the measurements, as the RR cross sections are used to bring the measurements to an absolute scale. Photoionization measurements compared to theory indicate uncertainties on the 3–5% level (Saloman et al., 1988), as quoted by many previous EIE cross section experiments (e.g., Chantrenne et al., 1992; Gu et al., 1999a; Widmann et al., 2000; Chen et al., 2002, 2005, 2006; Brown et al., 2006). While these photoionization measurements have been conducted on neutral atoms, measurements of radiative recombination for highly charged heavy ions by Stöhlker et al. (1997) and Stöhlker et al. (1999) also agree with theory to better than 5% (Widmann et al., 2000).

Similar to EIE cross sections, literature often provides radiative recombination cross sections only as a function of temperature, after convolution with a Maxwellian energy distribution, rather than more fundamentally as a function of energy (e.g., Badnell, 2006). Photoionization cross sections are typically listed as a function of the absorbed photon energy. The continuum spectra of the nearby celestial sources providing the photons for the ionization vary so much between sources that an effective photoionization cross section convolved with a photon distribution is not practical. Since the RR cross sections are connected to the photoionization cross sections through the Milne relation (Eq. 8.19), photoionization cross sections can be an alternative source for the needed reference values. The Opacity Project and the related IRON Project provide photoionization cross sections for many of the ions relevant to our EBIT measurements. Verner et al. (1996a) provide analytic fits to these calculations, interpolating and smoothing over resonances near ionization thresholds. Unfortunately, these calculations exclude any fine structure from their tables. The XSTAR code subsequently circumvents this issue by splitting cross sections into fine structure according to the statistical weight of the energy levels (Bautista & Kallman, 2001). This approach is not suitable as a reference for the EIE cross section measurements.

For the experiment at EBIT, in addition to the fine-structure resolved RR cross sections as a function of electron energy, it is important to know the polarization effects on the RR

emission. These data are even harder to find in the available literature. Scofield (1989) calculate the angular and polarization correlations for radiative recombination for He-like Ni and Ne-like Ba. While Scofield (1989) provides the theoretical framework to calculate these corrections, there are no accessible databases containing these calculations.

An exception is Chen et al. (2005), who included a table with parameterized RR cross sections for recombination into the $n = 2$ shell of He- through O-like Fe ions (calculations by Scofield). Their listed RR cross sections include the polarization correction for radiation observed perpendicular to the beam axis, but are not divided by 4π. The RR cross sections provided by Chen et al. (2005) are only valid in the impact-electron energy range 0.5–10 keV, which is lower than most electron energies chosen for the EIE cross section measurements presented in this chapter. Therefore, these reference values are used to benchmark new FAC calculations aimed at providing the needed reference differential RR cross sections perpendicular to the electron beam.

FAC[4] calculates the total RR cross sections for each configuration, but also provides a function to calculate the asymmetry of the RR emission based on Scofield (1989). The theory by Scofield (1989) only provides corrections for individual target orbitals, not fine structure levels. The reason is that anisotropy only depends on the orbital the continuum electron recombines into, regardless of the final fine structure level (configuration) of the recombined ion. For example, the anisotropy corrections for an electron recombining into the $2s_{1/2}$ orbital of a H-like ion in the ground state is the same whether the newly created He-like ion has the configuration $1s_{1/2}2s_{1/2}\ ^1S_0$ or $1s_{1/2}2s_{1/2}\ ^3S_1$. Applying this correction to the RR cross section is only straight forward if it is obvious into which subshell the electron recombined. Configurations where this is not obvious are usually doubly excited, i.e., in addition to the recombining electron another electron in the recombining ion moved during the process. These recombination channels exist only through level mixing and have cross sections so small that they are negligible compared to the main channels.

While FAC can calculate RR for any multipole, electric dipole (E1) transitions have by far the strongest contribution to the RR cross sections (Scofield, 1989). Other multipole types are therefore ignored in this calculation. Since the RR is an electric dipole transition, the degree of polarization P converts to the same correction factor as for a directly excited E1 transition. The differential RR cross section then is

$$\sigma_{\mathrm{RR}}^{90} = \frac{1}{4\pi}\,\frac{3}{3-P}\sigma_{\mathrm{RR}}. \tag{8.25}$$

If instead of the degree of polarization, only the ratio $p = \sigma_\perp/\sigma_\parallel$ of cross sections perpendicular and parallel are given, as, e.g., the FAC asymmetry function provides, then the degree of polarization (using Eq. 5.44) is

$$P = \frac{1-p}{1+p}\text{ , resulting in }\quad \sigma_{\mathrm{RR}}^{90} = \frac{1}{4\pi}\,\frac{3(1+p)}{2+4p}\sigma_{\mathrm{RR}}. \tag{8.26}$$

[4]Note that `fac.RRTable` produces RR cross sections whose magnitude matches cross sections by Scofield within the uncertainties, but the corresponding PI cross sections in the same `fac.RRTable` are smaller than Scofield's numbers by a factor g_f (statistical weight of the recombined ion). Similarly, the PI cross sections produced by the `fac.Asymmetry` function match the values from `fac.RRTable`, but the RR cross sections from `fac.Asymmetry` are smaller by a factor g_f than both the values from `fac.RRTable` and Scofield. The reason is that `fac.Asymmetry` is only for individual orbitals (M. F. Gu, priv. comm).

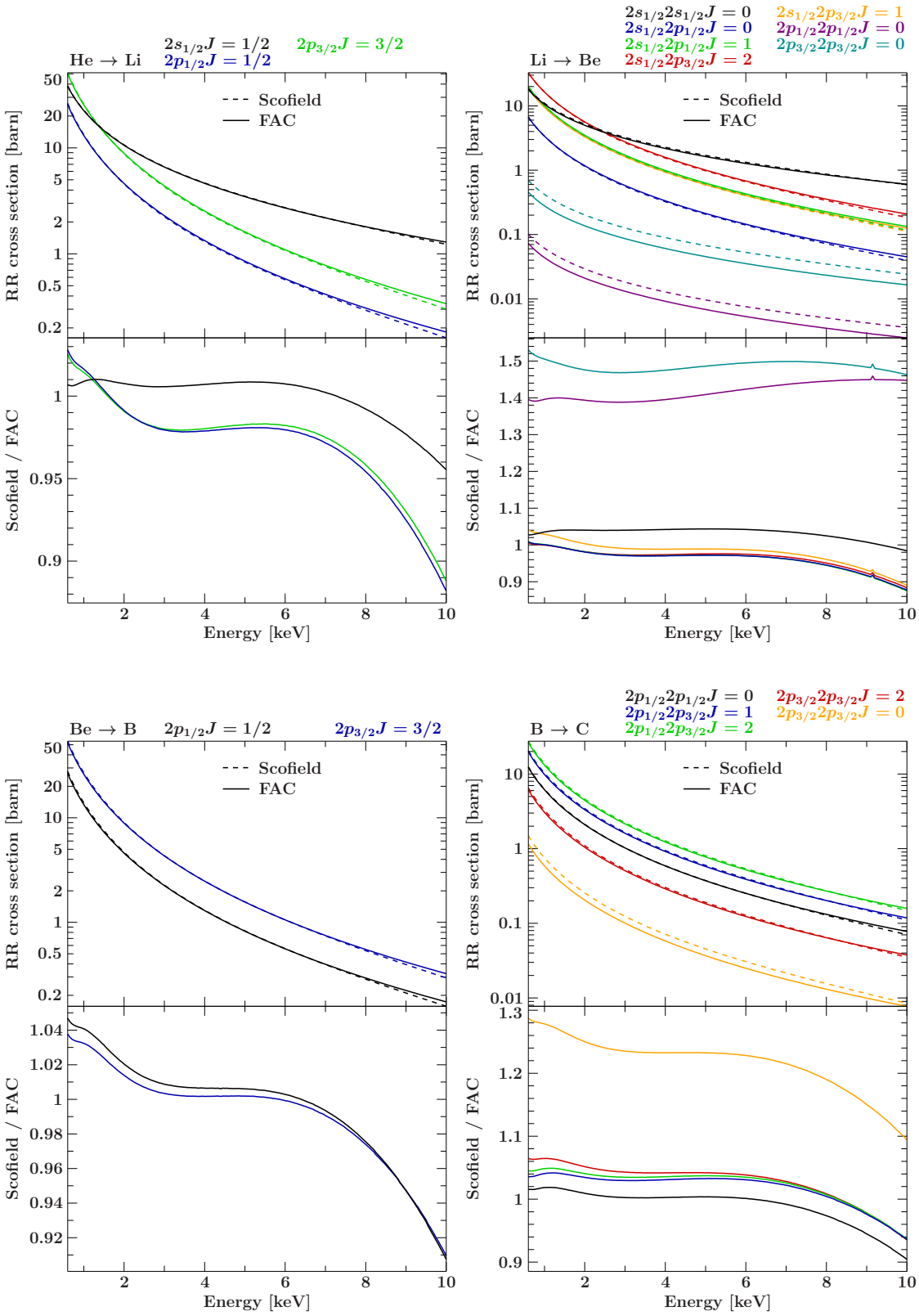

Figure 8.5: Comparison of differential RR cross sections $4\pi\sigma_{\mathrm{RR}}^{90}$ calculated with FAC (solid) and calculated by Scofield (dashed; Chen et al., 2005) for RR into the $n = 2$ shell of He-, Li-, Be-, and B-like Fe. Level notation is from Chen et al. (2005). The lower panels show the ratio of the FAC to the Scofield cross sections.

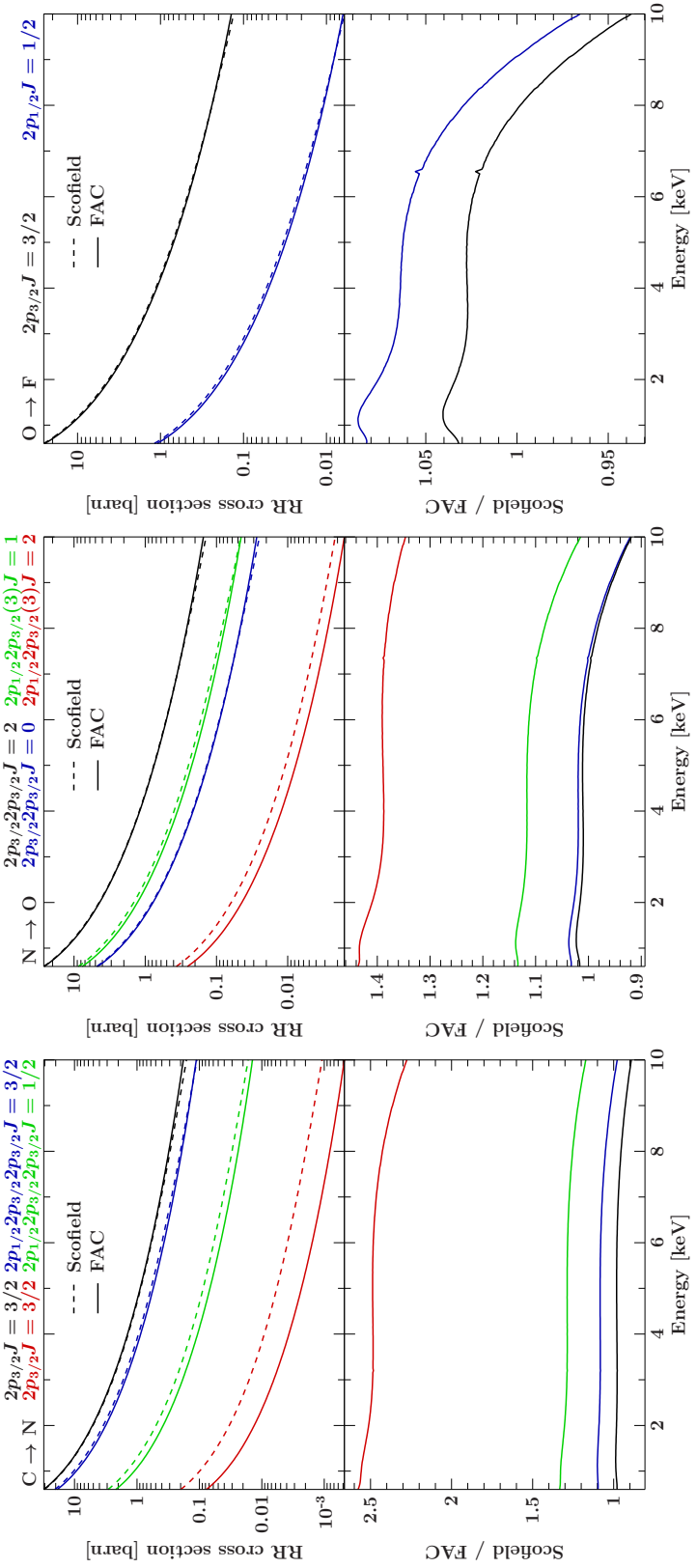

Figure 8.6: Same as Fig. 8.5 for RR into $n = 2$ of C-, N-, and O-like Fe.

The trend of RR cross sections as a function of energy and including polarization corrections for emission at 90° to the beam used by Chen et al. (2005) have been fitted with the formula

$$\sigma = a\left(\frac{1}{E}\right)^0 + b\left(\frac{1}{E}\right)^1 + c\left(\frac{1}{E}\right)^2 + d\left(\frac{1}{E}\right)^3 + e\left(\frac{1}{E}\right)^4 + f\left(\frac{1}{E}\right)^5 \tag{8.27}$$

where a through f are the fit parameters and E the electron impact energy in keV. The same formula is used to fit the RR cross sections calculated with FAC on a 50 eV grid to provide a continuous function that is suitable for the spectral model for the measured RR features (Section 8.5.2).

Figure 8.5 (upper left) shows a comparison between the differential RR cross section (multiplied by 4π) of Scofield (Chen et al., 2005) and of the new FAC calculation for He-like Fe recombining into Li-like Fe. Overall, the agreement between the two theories is acceptable and within the 3% expected uncertainty. Above 8 keV FAC and Scofield deviate by up to 10%. Without the individual RR and anisotropy components and original data from Scofield the cause for this deviation cannot well be investigated. Reasons for the deviation could be, e.g., edge effects from the parameterized model fit to the Scofield data; uncertainties in the polarization correction; atomic physics in the high energy limit; and others. Figure 8.5 (upper right) shows the comparison of the two theories for Li-like recombining into Be-like Fe. It shows a $\sim$ 50% difference for the weak RR cross sections of the more highly excited levels, which could indicate effects of the central potential (M. F. Gu, priv. comm.). Because of their relative weakness, the uncertainty in these two features makes only $\sim$ 2% of the total cross section of RR into $n = 2$. The other levels again agree within about 5% below 8 keV. Figures 8.5 (bottom) and 8.6 show the comparison for the remaining L-shell ions of Fe, which confirm the somewhat large discrepancy for weak RR features. Based on this comparison, a 5% uncertainty is assumed for the total differential RR cross sections for any n shell.

8.4 Overview of the Data

Spectra for the EIE cross section measurements have been collected at various EBIT conditions, varying the beam energy and current, and the charge balance of the trapped ions. This section gives a quick overview of the available data, how the spectral shape changes depending on EBIT conditions, and the employed calibration lines for the ECS spectra.

8.4.1 Calibration

For this experiment, the ECS was operated at 60 mK detector temperature. New optimal filtering templates were created for each pixel at the beginning of the experiment. The energy scale of the low energy pixels was calibrated in the region 3.2–8.1 keV, using the Rydberg series of Ar, Mn, Fe, and Ni as reference lines, specifically, He–like Ar Kα–Kδ, H-like Ar Lyα–Lyγ, line w of He-like Mn, Fe, and Ni, and Lyα_1 and Lyα_2 of H-like Mn, Fe, and Ni. The energy scale of the high-energy pixels was calibrated using line w of

He-like Mn, Fe, and Ni, Lyα of H-like Mn, Fe, and Ni, He-like Kr line w, and L-shell transitions in neutral Pu, namely Lℓ (L_3M_1), Lα_2 (L_3M_4), Lα_1 (L_3M_5), Lβ_2 (L_3N_5), Lβ_1 (L_2M_4), Lγ_1 (L_2N_4), and Lγ_6 (L_2O_4). Additionally, $n = 3 \rightarrow 2$ transitions in Ne-like osmium ($Z = 76$) were measured to ensure the alignment in the gap between the Ni and Kr lines. The Os lines (9–11 keV), Kr (13 keV), and Pu L (12–22 keV) calibrate the spectral range containing the RR emission for the various employed beam energies. While Ar, Mn, Fe, Ni, Os, and Kr lines were produced with EBIT, the Pu L lines stem from radioactive decay of a sealed ^{244}Cm source. In order to illuminate the ECS pixel array with the ^{244}Cm source without breaking the vacuum to EBIT, the source was installed behind a quartz window on the EBIT port opposite the port for the ECS, i.e., the radiation passed through EBIT (while EBIT was off) before detection with the ECS. The somewhat large source distance has the additional advantage to keep the count rate low enough to operate in the regime of incident power below ~ 9 keV/s/pixel where the detector gain is not affected from the heat load despite the high photon energies.

Transition energies for the He-like Kα lines are taken from Drake (1988). Ar Kβ–Kδ are from Vainshtein & Safronova (1985) and corrected for the ground state of Drake (1988) according to Beiersdorfer et al. (1989). The H-like Ar Rydberg series is taken from Garcia & Mack (1965). The H-like Lyα reference for Mn, Fe, and Ni is from Johnson & Soff (1985). Values for Pu L are from Bearden (1967), and Indelicato et al. (1998). The only available reference energies for Ne-like Os are from a table for $n = 3 \rightarrow 2$ transitions in Ne-like ions provided by Scofield (priv. comm.).

Both sets of pixels were each calibrated by first aligning all pixels of the respective set to the same arbitrary scale, i.e., the scales of pixels 0 and 8 for low-energy and high-energy, respectively) by shifting and stretching with a linear function, resulting in an individual alignment polynomial for each pixel. Then the aligned pixels are added up and a single 4th order gain polynomial is determined for the reference pixel scale. Thus, applying the final calibration to the data of any given day is a two step process: apply the linear alignment polynomial to the pulse height in pixel units, then apply the 4th order gain polynomial to the result.

For a discussion of the long-term stability of the ECS gain see Section 4.5.1 – in short, the stability is very good. Nevertheless, it is good to monitor and correct for minor gain shifts. The Fe K spectra in both the low- and high-energy pixels are “self-calibrating”, i.e., their count rate is strong enough to allow one to use these lines for ensuring that there is no differential drift between the pixels or absolute drift in the energy scale. The data rate for the RR features, on the other hand, is too low for this purpose. Additionally, their X-ray energy, specifically the contribution of the electron beam energy, is one of the parameters that need to be measured and, therefore, cannot serve as reference for energy calibration. To monitor possible drifts in the 12–21 keV energy range that hosts the RR lines, the ^{244}Cm source was installed in front of the ECS over night every night the EBIT was not running for EIE cross section measurements during the campaign.

Table 8.2: Overview of EBIT conditions

DT [kV]	I_{beam} [mA]	t_{cycle} [ms]	p_{inj} [10^{-9} Torr]	c.b.	t_{exp} [h]	E_{beam} [keV]	FWHM [eV]	ΔE [eV]
11.0	190	15 000	1.9	hc	23.5	10.952 ± 0.006	88^{+11}_{-9}	82
11.0	190	86	7.1	mc	27.3	10.961 ± 0.012	103^{+20}_{-12}	98
11.0	190	10	68	lc	26.4	(10.92)	–	–
11.0	154	9 000	1.9	hc	41.5	11.015 ± 0.003	55^{+5}_{-4}	45
12.1	152	6 000	1.3	hc	42.2	12.123 ± 0.003	57^{+5}_{-4}	48
12.1	152	204	32	mc	104.6	12.108 ± 0.002	59 ± 3	50
8.05	150	204	49	mc	78.2	8.032 ± 0.002	58 ± 2	49

Notes: DT: drift tube voltage, predicted beam energy (additional middle DT voltage set such that it cancels with estimated space charge potential); I_{beam}: beam current; t_{EP}: EBIT phase period; p_{inj}: injection pressure; c.b.: charge balance ([hc] high charge balance, mostly H-, He-, and Li-like Fe; [mc] medium charge balance, Ne- through He-like Fe; [lc] low charge balance, below B-like Fe); E_{beam}: beam energy determined from fit ($n = 2$); FWHM: width of the measured RR features ($n = 2$); $\Delta E = (\text{FWHM}^2 - 31^2)^{1/2}$: beam energy spread, i.e., FWHM corrected for 31 eV detector resolution.

8.4.2 Spectral Shape as a Function of EBIT Conditions

Table 8.2 lists the combination of beam energies and charge balances employed to measure excitation cross sections. The beam energy and spread as derived from the resulting RR spectra are included as well.

The Fe K spectra for the EIE cross section measurements have been collected at beam energies of $\sim$ 8, 11, and 12 keV. The 8 keV data point was chosen to be close to the excitation threshold of He-like line w (6.7 keV), while still being high enough to excite the He-like Kβ lines (7.9 keV). Since the ionization potential of He-like to H-like Fe is 8.83 keV (Cowan, 1981), this beam energy also prohibits the production of H-like Fe. The data points at 11 keV and 12 keV were chosen such that the photon energy of the features for RR into $n = 2$ are close to the energy of the He-like Kr and Pu Lα_1 calibration lines, respectively. The vicinity to the calibration lines strengthens the confidence in the pixel alignment – and thus the confidence in the measured line shapes of the RR features –, which can be helpful to identify issues early on during the setup phase of the experiment.

Data were also taken at two different beam currents. The first set of measurements at 11 keV beam energy (Table 8.2) were taken at 190 mA beam current to maximize the photon flux from EBIT. As Fig. 8.7 shows, the RR features at these high beam currents have a relatively low resolution of 80–100 eV, while the spread of the electron energies was expected to be on the order of or better than about 50 eV. Repeating the high-charge-balance 11 keV measurement at a much lower beam current of 150 mA leads to a large improvement in the beam energy spread (Fig 8.8). At high beam currents, the repulsion by the Coulomb force between the many electrons increases and the beam physically spreads out to a larger beam radius, which also increases the spread in electron energy.

Although the lower beam current reduces the count rate of the experiment, the higher resolution is very beneficial in resolving the shapes of the RR features, especially in a broad ion charge distribution like the medium charge balance measurements. For exam-

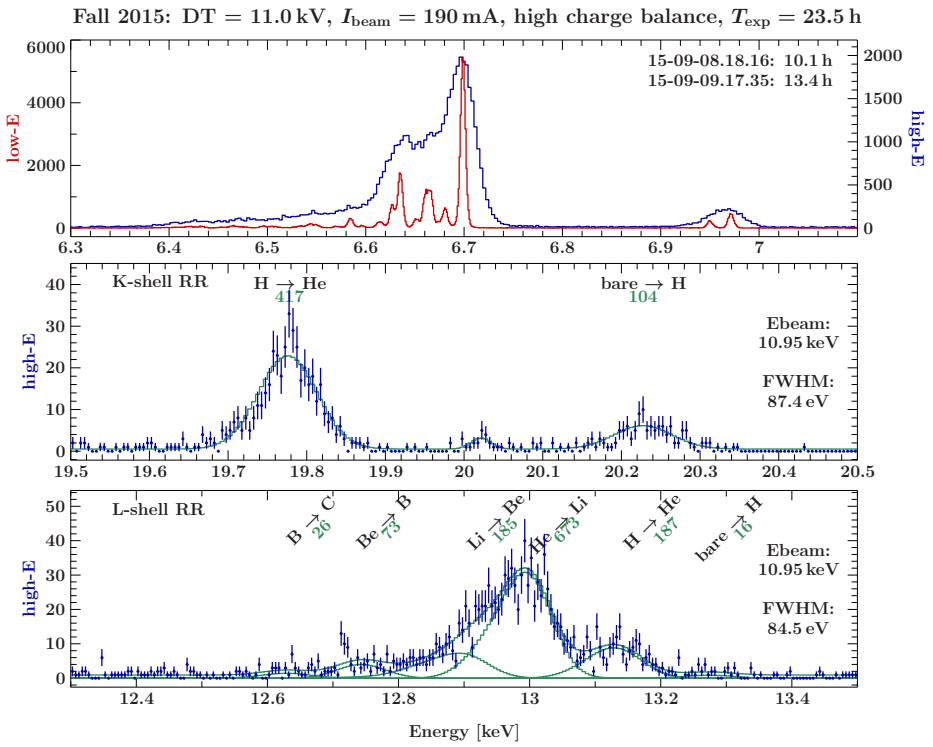

Figure 8.7: ECS spectra (red: low-energy pixels, blue: high-energy pixels) of the $E_{beam} \sim 11$ keV high charge balance data at high beam current. Top: DE spectrum; Middle: RR into $n = 1$; bottom: RR into $n = 2$. The green line shows the fitted model components of the RR features of each charge state, with the green numbers indicating their fitted number of counts.

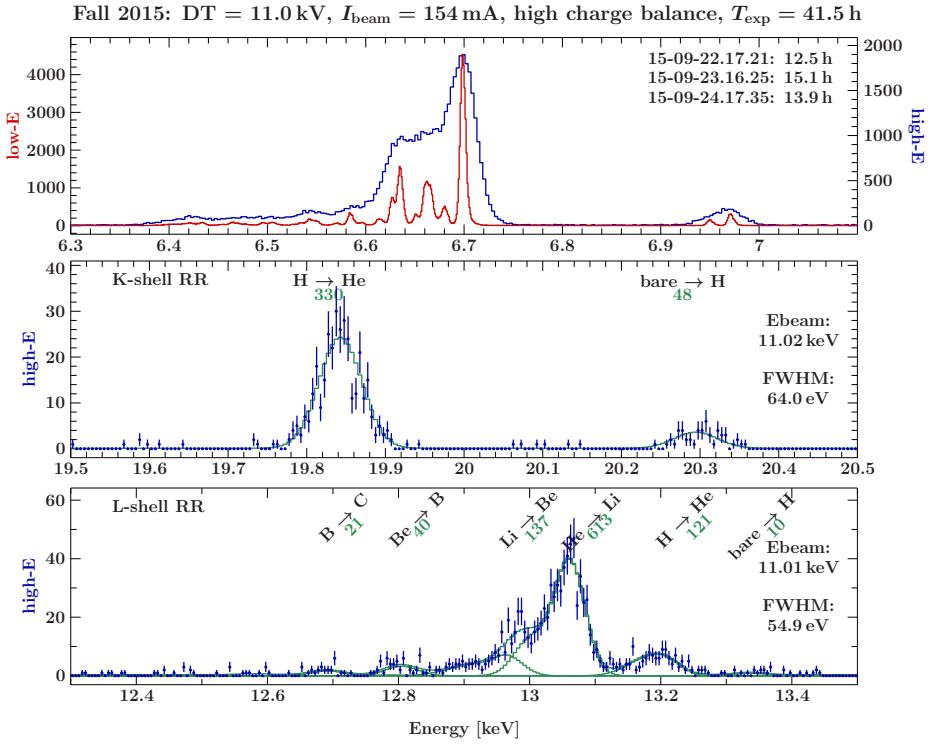

Figure 8.8: ECS spectra at $E_{beam} \sim 11$ keV high charge balance data at lower beam current. The DE spectrum looks essentially the same as in Fig. 8.7, but the RR spectrum has much better resolution due to the smaller beam current.

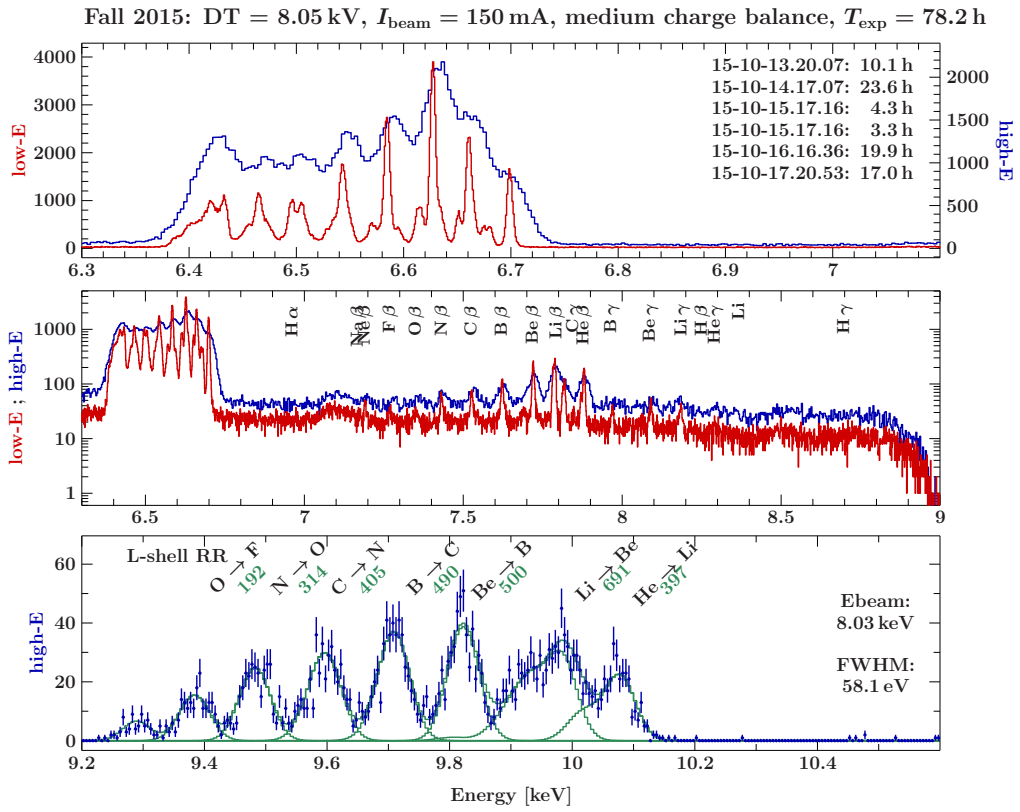

Figure 8.9: ECS spectra of the $E_{beam} \sim 8$ keV medium charge balance measurement. The middle panel shows the extended range of the DE spectrum on a logarithmic flux scale, to emphasize the presence of $n = 3 \rightarrow 1$ Kβ transitions of L-shell ions of Fe. The bottom panel demonstrates that the RR into $n = 2$ RR features of all L-shell ions are fully resolved by the ECS high-energy pixels. Although the ion population is fairly evenly distributed between O- and B-like Fe (Fig. 8.13), the flux (number of counts, green) in the RR feature for O-like Fe recombining into F-like Fe is much lower than the B-like Fe recombining into C-like Fe.

ple, the confidence interval for the area of the He-like RR feature in the medium charge balance 11 keV measurement is twice as large as the same feature with similar number of counts in the better resolved measurements at lower beam currents. Therefore, the remaining data points were measured at the lower beam current of 150 mA.

Fe was injected into the trap as ironpentacarbonyl, $Fe(CO)_5$. By varying the EBIT cycle time and the injection pressure, the charge balance of the trapped Fe ions can be modified. Long trap times and low injection pressures lead to a high charge balance, dominated by He-like Fe – since the electron beam energy is below 1.5 times ionization threshold necessary to make H-like Fe, the H-like Fe production is not yet very efficient. Transitions in He-like and H-like Fe are the main targets for these high charge balance measurements. Despite the high charge balance, traces of K-shell transitions in lower charge states are still detected. A medium charge balance, which leads to comparable line strengths for K-shell transitions in Ne- through He-like Fe ions (Section 8.5.2), is achieved through a slightly higher injection pressure and shorter EBIT cycles (Table 8.2). The medium charge

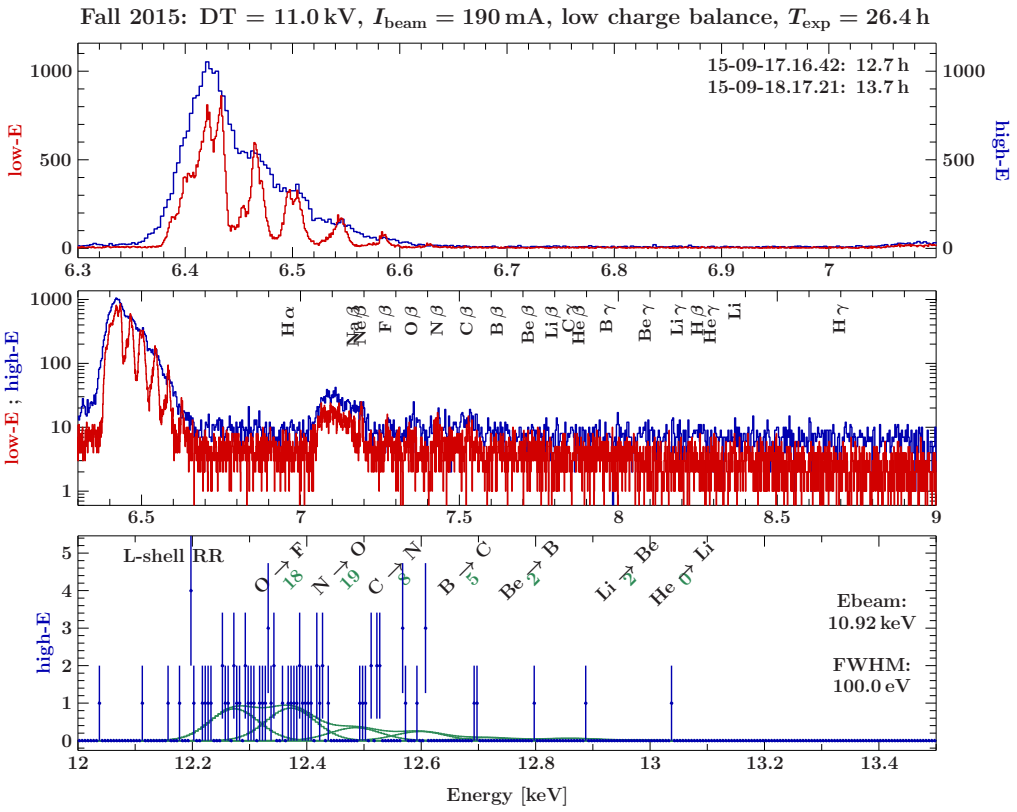

Figure 8.10: ECS spectra of the low charge balance data taken at a beam energy of 11 keV. The total RR cross sections decrease with decreasing ion charge (Fig. 8.11), making the count rate for the RR features in these low charge states much smaller than for the higher charge states.

balance measurements are conducted to derive the EIE cross sections also for transitions in L-shell ions. See Fig. 8.9 for the resulting spectrum of the $E_{beam} \sim 8$ keV measurement; the RR into $n = 2$ for the L-shell ions of Fe are resolved this beautifully for the first time at these high electron energies. Additionally, the changed charge balance provides a test of sensitivity for the cross sections for the He- and possibly the Li-like transitions, obtained from the high-charge-balance data, to charge balance conditions. These medium charge balance data (with the exception of the 8 keV beam energy which is below the ionization threshold for creating H-like Fe) still show small traces of H-like Fe that can be used to derive excitation cross sections, albeit with correspondingly larger uncertainties. With very short EBIT cycles, the reachable charge states can be limited to about C-like Fe (Fig. 8.10). This charge balance was tested during the 11 keV beam energy runs in hopes to improve the signal rate for the low charge states, for which at least effective emission cross sections should be obtained. Since the RR cross sections into $n = 2$ decrease with decreasing ion charge, the signal rate remains weak and the efforts to measure cross sections for the very low charge states are beyond the scope of this thesis.

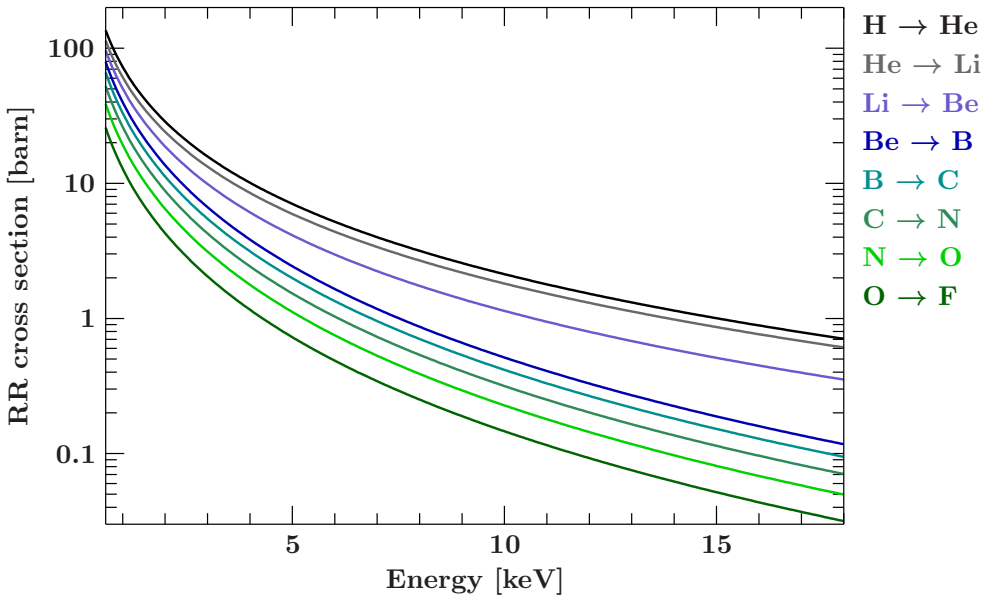

Figure 8.11: Total differential radiative recombination cross sections $4\pi\sigma_R^{90}R$ for RR into the $n = 2$ shell from FAC calculations. The magnitude of the RR cross sections decreases with decreasing ion charge.

8.5 EIE Cross Sections – Fe, High Charge States

8.5.1 Direct Excitation Spectrum

The spectrum of the directly excited K-shell transitions are first analyzed using the data recorded with the ECS's low energy pixels to determine the flux of each line. The model consists of a constant to account for background and a Gaussian for each resolved transition. Since high-resolution wavelength measurements with EBIT exist for the K-shell spectra of L-shell ions (Decaux et al., 1997), these are used as a reference to determine the number of Gaussian components in the model. The previously measured wavelengths from Decaux et al. (1997) are used as start values for the line centers, but are allowed to vary during the final fit to make it possible to compensate for uncertainties in the measured wavelengths of Decaux et al. (1997) and uncertainties in the photon energy calibration of the ECS low-energy pixels. As seen in Fig. 8.12 for the example of the 11 keV medium charge balance data, the line centers as measured by Decaux et al. (1997) agree well with the line shapes of the ECS data.

The widths of the Gaussian components for Kα transitions in the He-like Fe ion and lower charge states are tied to the width of He-like Fe line w. The widths for H-like Fe Lyα and the higher order Rydberg series of all charge states are left free to vary, because these lines are distributed over a wider energy range where the energy resolution of the calorimeter may change. The area of the Gaussian lines is taken as the measured flux of the line. Since the spectral model is folded with the instrument response due to the quantum efficiency of the pixels, this fitted line flux already includes the correction terms

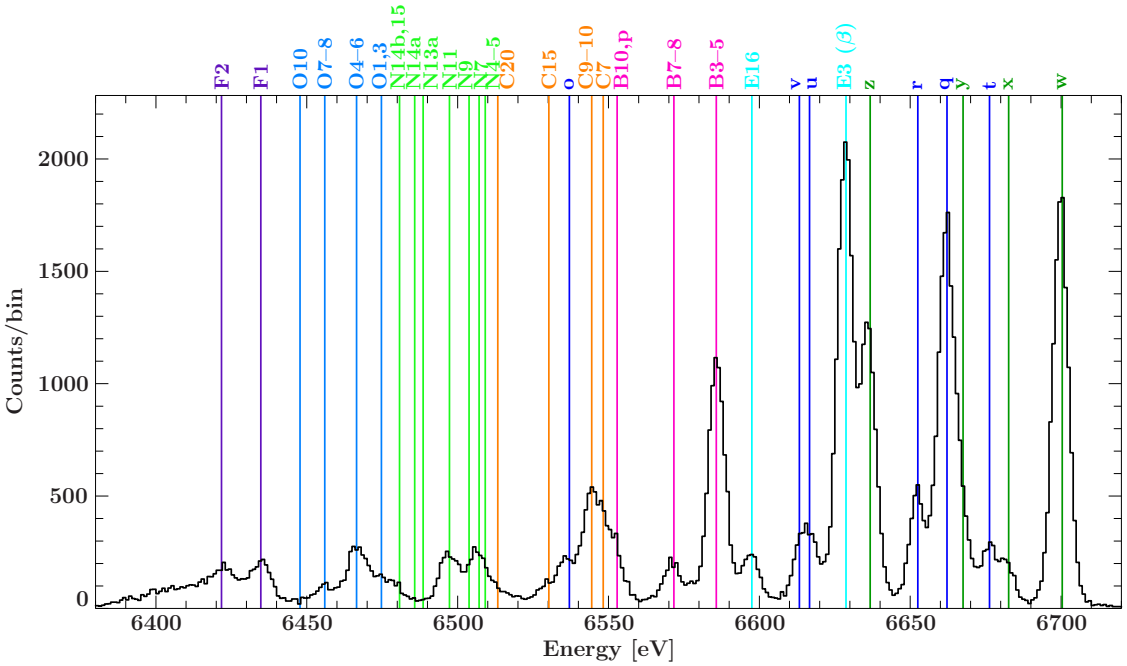

Figure 8.12: The 11 keV medium charge balance ECS data in comparison to transition energies previously measured with a high-resolution crystal spectrometer at EBIT by Decaux et al. (1997).

for the quantum efficiency.

Since the RR spectrum is only measured with the ECS's high-energy pixels, the true geometric factor for the flux correction between the low- and high-energy pixels due to differences in solid angle is of interest. To determine this factor, a slightly modified version of the spectral model fit to the low-energy pixel data is applied to the K-shell spectra as measured with the high-energy pixels: The normalizations (area) and the line centers of the Gaussian components are fixed to the previous values, while the line widths are adjusted to the lower resolution of the high-energy pixels. To account for cross-calibration uncertainties of the energy scales for the two pixel types, the spectral model as determined from the low-energy pixels is allowed to shift as a whole by a constant amount in energy when fit to the high-energy pixel data. Then a constant scaling parameter, i.e., the parameter for the geometric factor, is multiplied to the spectral model. The geometric factor as estimated from the pixel geometry and number in Section 4.4.3 is used as a start value for this scaling parameter, but the parameter is allowed to vary during the fit. A constant background model is again added to the model spectrum and the whole model is folded with the quantum efficiency of the thicker high-energy pixels. The fitted geometric factor is within 2% of the value derived in Section 4.4.3.

Unlike the quantum efficiency, the optical blocking filter transmission does not affect the fit of the geometric factor, as the filter transmission is the same for both the low-energy and high-energy pixel spectra. The correction for absorption from the filters is therefore applied to the fitted line flux after the fit.

8.5.2 Radiative Recombination Spectrum

While Wong et al. (1995) had to derive the charge balance from the resonance lines in He-like (w) and Li-like (q) Fe, the ECS now for the first time resolves the RR into the $n = 2$ shell at electron beam energies sufficient to excite the K-shell transitions in Fe ions, i.e., above 6 keV. The resolved RR not only serves as a normalization to bring the DE cross sections onto an absolute scale, but also allows us to directly infer the charge balance.

Since the RR spectra have distinct line shapes due to the fine-structure levels of the ions (Fig. 8.3), the measured RR spectra are fit with a physical model. The model includes a single component

$$R_{Z,N,n}(E) = \frac{A}{\sum_i \sigma_i^{\mathrm{RR}}(E_{\mathrm{beam}})} \sum_i \frac{\sigma_i^{\mathrm{RR}}(E_{\mathrm{beam}})}{\sqrt{2\pi}\,\Delta E_{\mathrm{res}}} \exp\left(-\frac{(E - E_{\mathrm{beam}} - E_i^{\mathrm{ipot}})^2}{2\Delta E_{\mathrm{res}}}\right) \tag{8.28}$$

for each charge state (element Z, N number of electrons) and principle quantum number ($n = 2$ or $n = 1$) determining the line shape. The line shape of the model component is produced by centering a Gaussian around the ionization potential E_i^{ipot} for each of the available RR channels i in shell n of this ion, relative to the beam energy E_{beam}. The relative strength of the Gaussians for each channel is defined by the relative value of the corresponding cross sections σ_i^{RR}. Here, σ_i^{RR} are the differential RR cross sections for emission at 90° to the beam direction, taking polarization into account, and are taken from the literature[5] (Section 8.3.4). Each Gaussian in the RR feature has the same width ΔE_{res}, which is determined by the energy spread of the beam and the detector resolution (Table 8.2). The RR model components are normalized such that the fitted area A directly represents the number of photons measured in this feature. The fit parameters for each model component are thus the area A of the RR feature, the beam energy E_{beam}, and the width of the lines.

The spectra for RR into the $n = 1$ and $n = 2$ shell are fitted separately. In both cases the total model consists of a constant background and the sum of the RR line complexes $R_{Z,N,n}(E)$ for each charge state q present. The model is then again folded with the quantum efficiency of the detector before fitting. The beam energy E_{beam} and the line width FWHM parameters are tied between the RR components, i.e., there are only up to two[6] estimates for E_{beam} and FWHM per data set, one from the $n = 1$ and one from the $n = 2$ recombination (see Figs. 8.7–8.9 for plots of the fitted RR model components). While the width of the lines is dominated by spread in beam energy, the magnitude of the detector resolution of 31 eV for the high energy pixels (Section 4.5.2) is a significant fraction of the beam spread, making the fitted width of the RR a quadratic sum of the beam energy spread and the detector resolution. Table 8.2 lists the resulting values for E_{beam} and FWHM obtained from the fits to the $n = 2$ spectra. The fits of the RR spectra are done using Cash statistics (Appendix C) because of the low signal.

[5] Since the theoretical differential RR cross sections as a function of energy were described with a parameterized function (Eq. 8.27), the value of the cross section can easily be obtained at any electron beam energy in the applicable energy range during the fit of the measured RR spectrum.

[6] the medium charge balance data do not have sufficient ion fractions in H-like and bare to allow a reasonable fit

Radiative recombination can also happen into the $n = 3$ shell. For the lower charge states with $N_e > 10$, where the $n = 2$ shell is completely filled in the ground state, the $n = 3$ shell as the lowest lying open shell provides the main recombination channels. The energy levels with the $n = 3$ shell are very close together and the ionization potentials for this shell do not vary much as a function of charge state ($\Delta E_{ipot} \sim 30$–40 eV between ions below Ne-like Fe; Cowan, 1981). RR into the various orbitals of the $n = 3$ shell of Ne-like Fe spans an energy range of ~ 80 eV (Brown et al., 2006). Therefore, the energy spacing between charge states is not only smaller than the achievable energy resolution that is limited by the ~ 50 eV spread in energy of the beam electrons, it is also smaller than the energy spanned by RR within M-shell Fe ions. Additionally, because of the low ionization potentials of these low charge states, the RR features for these ions are close to the high-energy cut off of the bremsstrahlung continuum that is determined by the beam energy (Fig. 8.4).

From the flux in the RR feature of each charge state q relative to the actual RR cross section, the charge balance in the trap is infered as

$$n_q = \frac{I_q^{RR}/\sigma_q^{RR}}{\sum_q I_q^{RR}/\sigma_q^{RR}} \tag{8.29}$$

where the flux $I_q^{RR} = C_q^{RR}/(Q_q^{RR} T_q^{RR})$ again is the measured number of counts C_q^{RR} corrected for quantum efficiency Q_q^{RR} and filter transmission T_q^{RR}. Figure 8.13 shows the resulting charge balance for the medium and high charge balance data sets (Table 8.2). To determine the charge balance, RR into $n = 1$ has been used for recombination into the bare and H-like ions. For He-like through O-like Fe, the RR into $n = 2$ is used. The high charge balance data are clearly dominated by the population of He-like ions of 40–50%. Wong et al. (1995) had a cleaner and higher charge balance with 95% He-like and 5% Li-like Fe at an electron beam energy of 6.8 keV. This is likely due to differences in injection method. Wong et al. (1995) used a MeVVA with injection once at the beginning of each EBIT cycle, while neutral Fe was added to the trap continuously during the current experiment. The H-like Fe abundance is low because overall the charge balance is relatively low, as evidenced by the presence of small populations of Li- through N-like Fe, and because the electron impact ionization cross sections for ionizing He-like Fe peaks at 2–2.5 times ionization threshold (Lotz, 1968; Vogel, 1992), i.e., while H-like Fe is created at beam energies of 11 and 12 keV, its production is not yet very efficient.

The medium charge balance data show a relatively flat distribution of the ion populations for Be- through O-like Fe. Generally, the ion population of a charge state should not be smaller than the population of both of its neighboring charge states. Extreme outliers can indicate a problem with the assumed RR cross sections used to derive the population. The estimated populations of the C-like Fe ions in the medium charge balance measurement at 11 and 12.1 keV beam energy are smaller than their neighbors. However, the distribution at 12.1 keV is flat within the uncertainties, and outlier at 11 keV is not significant due to the low counting statistics (~ 30 counts) at the low resolution of this RR spectrum.

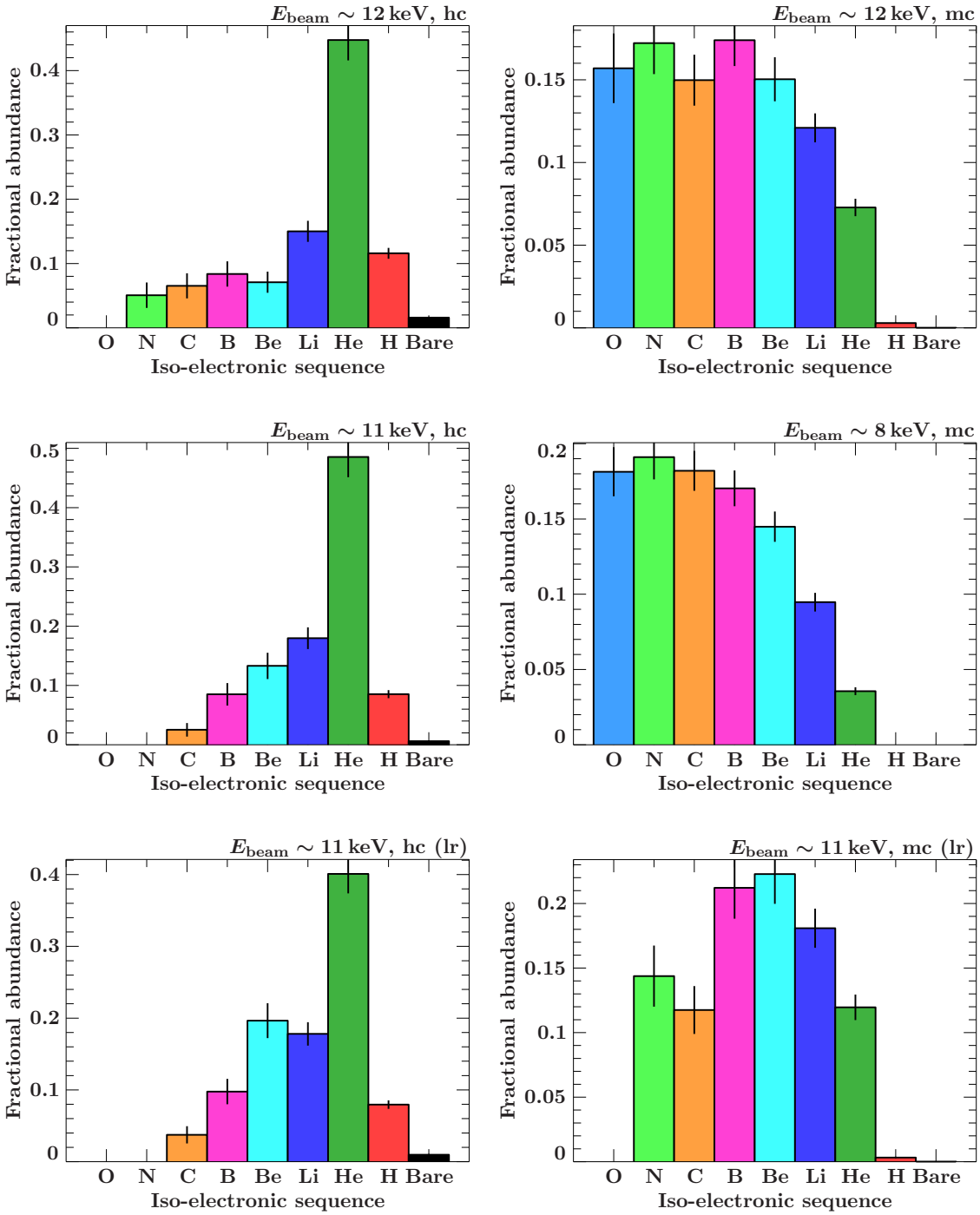

Figure 8.13: Relative ion abundance derived from the RR lines for the different data sets (beam energy, hc/mc: high/medium charge balance, lr: lower resolution of the RR features due to larger energy spread of the electron beam). The error bars are a combination of Poisson statistics of the fitted number of counts of the respective RR feature ($n = 1$ for bare and H-like, $n = 2$ for the others) and an estimated 5% uncertainty on the RR cross sections. Ions below oxygen recombining into fluorine are not included.

8.5.3 EIE Cross Section Results

The fit method as described in the last two sections provides the values for $C_{\mathrm{DE}}/Q_{\mathrm{DE}}$ and $C_{\mathrm{RR}}/Q_{\mathrm{RR}}$ for Eq. 8.23. Inserting also the filter transmission, geometric factor, polarization correction for direct excitation, branching ratio, and differential RR cross section then gives the results for the absolute electron impact excitation cross section measurements. Since the calibration and fits of the data are not quite finalized yet, this section presents first results for the transitions w in He-like Fe and Lyα_1 and Lyα_2 in H-like Fe.

Sources of Uncertainties, Error Propagation

The excitation cross sections are not a direct result from the model fit to the data, but rather have to be derived from directly measured parameters, i.e., the observed flux, with a complex function (Eq. 8.23). It is therefore necessary to carefully assess the uncertainties Δf_i contributing to the uncertainty $\Delta\sigma$ on the end result for the excitation cross sections σ. The combined uncertainties Δf_i of all contributing factors f_i are taken into account through error propagation

$$\Delta\sigma^2 = \sum_i \left(\frac{\partial\sigma}{\partial f_i}\right)\Delta f_i^2. \tag{8.30}$$

For functions of sums, products, and ratios, error propagation simplifies to a quadratic sum

$$\delta\sigma^2 = \left(\frac{\Delta\sigma}{\sigma}\right)^2 = \sum_i \delta f_i^2 \tag{8.31}$$

of the contributing uncertainties, if the relative uncertainties $\delta f_i = \Delta f_i/f_i$ are used.

Table 8.3 lists the contributing factors for the cross sections for He-like Fe line w and H-like Fe lines Lyα_1 and Lyα_2. The uncertainties for the counting statistics of the DE and RR lines represent the 68%-confidence level derived from the fitted area. For these the table shows the full range of relative uncertainties covered by the six analyzed data sets (Table 8.2) for medium to high charge balance for the different electron beam energies. The larger uncertainties belong to the measurements with lower counting statistics. For example, the number of observed photons for line w ranges from 12 000 for the medium charge balance measurements to 40 000 for the high charge balance measurements.

H-like Fe Lyα_2, i.e., the weaker of the two Lyα lines, ranges from 60 and 230 counts at medium charge balance (corresponding to 13% and 7% uncertainty) to 1100–2200 counts at the high charge balance (corresponding to uncertainties $\leq$ 3%). The counting statistics for the RR features behave similarly. The RR into $n = 2$ of He-like Fe ranges from 300–700 counts, corresponding to $\leq$ 6% uncertainty. The quoted upper limit of 10.6% uncertainty corresponds to the 11 keV medium charge balance measurement, where the resolution of the RR features was poor because of the high beam current employed (Section 8.4) such that together with the large Li-like fraction the fit is less well constrained. For the normalization of the H-like cross section, the uncertainties for RR into $n = 1$ are listed. Again, in the high charge balance data, the number of counts in this feature ranges

Table 8.3: Relative uncertainties (%) contributing to the uncertainty of the cross section measurements (1σ confidence level [68%])

Source	w	Lyα_1	Lyα_2
Counting statistics (DE)	**0.51–0.90**	**1.5**–8.8	**2.2**–13
Counting statistics (RR)	**4.6**–10.6	**4.7**–20	**4.7**–20
Filter transmission (DE)	1	1	1
Filter transmission (RR)	0.5	0.5	0.5
Quantum efficiency (DE)	3.6	3.6	3.6
Quantum efficiency (RR)	1.5	3.5	3.5
Geometric factor	2	2	2
Polarization correction ($\frac{3}{3-P}$)	5	2.2	–
Branching Ratio	–	–	–
Radiative recombination (incl. pol.)	5	5	5
Total uncertainty	**9.6**–13.6	**9.2**–23.2	**9.1**–25.0

Notes: A range of uncertainties is given for the counting statistics of both DE and RR that reflects the range covered by all data sets listed in Table 8.2. The bold values are the more typical uncertainties. For example, the high-charge balance measurements (bold) are specifically intended for cross section measurements of the H-like Fe Lyα lines, while the large upper limits listed for both DE and RR for these lines are from the medium charge balance measurements that have only a very small H-like ion fraction. The He-like lines, however, are prominently present in both medium and high charge balance sets. For these the upper limit for the RR counting statistics is from the measurements that had a large electron energy spread during the measurement. See text for details.

from 300–500 counts, which also corresponds to $\leq 6\%$ uncertainty, since RR into $n = 1$ of H-like Fe does not blend with any other features. For the medium charge balance data, there are only 25–60 counts in these lines, corresponding to 13–20% uncertainty.

For the E1 transitions line w and Lyα_1 the correction term for polarization is $P_{\mathrm{DE}} = 3/(3-P)$, where P is the degree of linear polarization for the respective transition. The relative uncertainty $\delta f_{\mathrm{pol.corr.}}$ of the polarization correction then relates to the relative uncertainty δf_P of the degree of polarization as

$$\delta f_{\mathrm{pol.corr.}} = \frac{\Delta f_{\mathrm{pol.corr.}}}{P_{\mathrm{DE}}} = \frac{1}{P_{\mathrm{DE}}} \cdot \left| \frac{\partial P_{\mathrm{DE}}}{\partial P} \right| \cdot \Delta f_P = \frac{3-P}{3} \cdot \frac{3}{(3-P)^2} \cdot P \delta f_P = \delta f_P \cdot \frac{P}{3-P}. \quad (8.32)$$

Assuming a relative uncertainty on P of 20% (Section 8.3.2) then results in $\delta f_{\mathrm{pol.corr.}} \approx 2.2\%$ for H-like Fe Lyα_1 ($P \approx 0.29$ at 11 keV and $P \approx 0.28$ at 12 keV; linear interpolation from Bostock et al., 2009) and in $\delta f_{\mathrm{pol.corr.}} \approx 5\%$ for He-like Fe line w ($P \approx 0.60$ at 8 keV, $P \approx 0.57$ at 11 keV, and $P \approx 0.56$ at 12 keV; linear interpolation from Zhang et al., 1990).

The uncertainties for the other contributing factors have already been discussed in other parts of the this work and are listed in this table. The branching ratio is listed as a contributing factor, since, in general, it has to be taken into account. However, for the shown transitions listed in the table, the upper level has no other decay channel available, fixing the branching ratio at 1. The total uncertainties of the dedicated measurements (Table 8.3, bold values) are on the order of 10%. Even the measurement of line w at

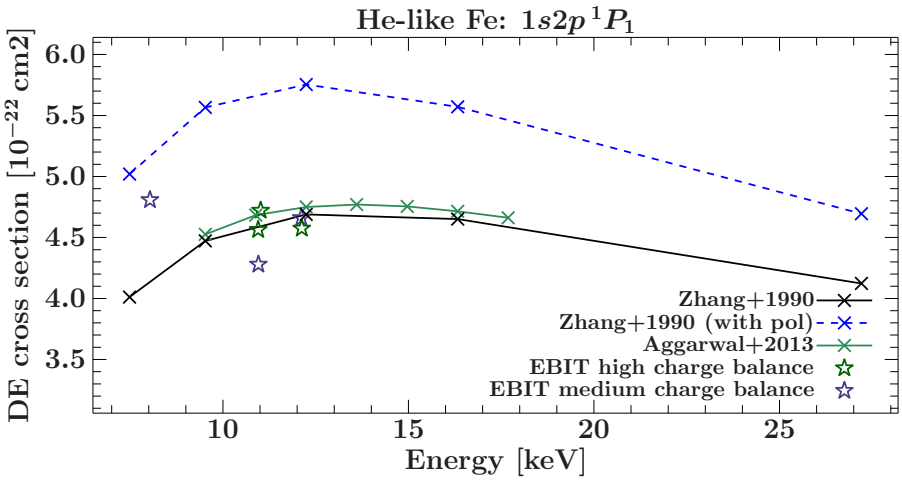

Figure 8.14: Absolute electron impact excitation measurements (green stars: high charge balance; purple stars: medium charge balance). The black line are the total electron impact excitation cross sections by Zhang et al. (1990), the green are from Aggarwal & Keenan (2013). The blue dashed line are the cross sections from Zhang et al. (1990) multiplied by the polarization correction derived from their sublevel cross sections to demonstrate the magnitude of the polarization effect has on the cross sections if it is not accounted for.

low spectral resolution due to high beam currents is accurate to better than 15%, and the cross sections derived from the weak signatures of the H-like Fe Lyα lines in the medium charge balance data is within 25%. The largest contributions to the uncertainty are due to the polarization correction and the normalization to RR, i.e., those parameters that rely on theoretical calculations for reference.

Comparison to Theory

Figure 8.14 shows the absolute excitation cross sections for He-like Fe line w derived from the measurements in comparison to theoretical cross sections by Zhang et al. (1990) and Aggarwal & Keenan (2013). The measured values are corrected for polarization derived from the magnetic sublevel cross sections by Zhang et al. (1990), i.e., they represent $\sigma_{\rm DE} = 4\pi\sigma^{90}_{\rm DE}/P_{\rm DE}$. To show the significance of the polarization contribution to line w, the blue dashed line represents the absolute theoretical cross sections $4\pi\sigma^{90}_{\rm DE,theo}$ from Zhang et al. (1990) multiplied by the polarization corrections derived also from their magnetic sublevel cross sections. The absolute (unpolarized) cross sections by Aggarwal & Keenan (2013) closely trace the earlier calculations by Zhang et al. (1990). While Wong et al. (1995) measured the excitation cross section of line w at a beam energy of 6.8 keV (close to excitation threshold) with a slightly smaller magnitude than the the theory by Zhang et al. (1990), the results for the current measurement at 8 keV appears to be somewhat larger than the theoretical cross sections. The cross sections at 11 and 12 keV are close to the theoretical predictions. As expected, the measured cross sections for line w are, within the uncertainties, independent of the charge balance.

Figure 8.15 shows the absolute excitation cross sections for H-like Fe Lyα_1 and Lyα_2. Lyα_1

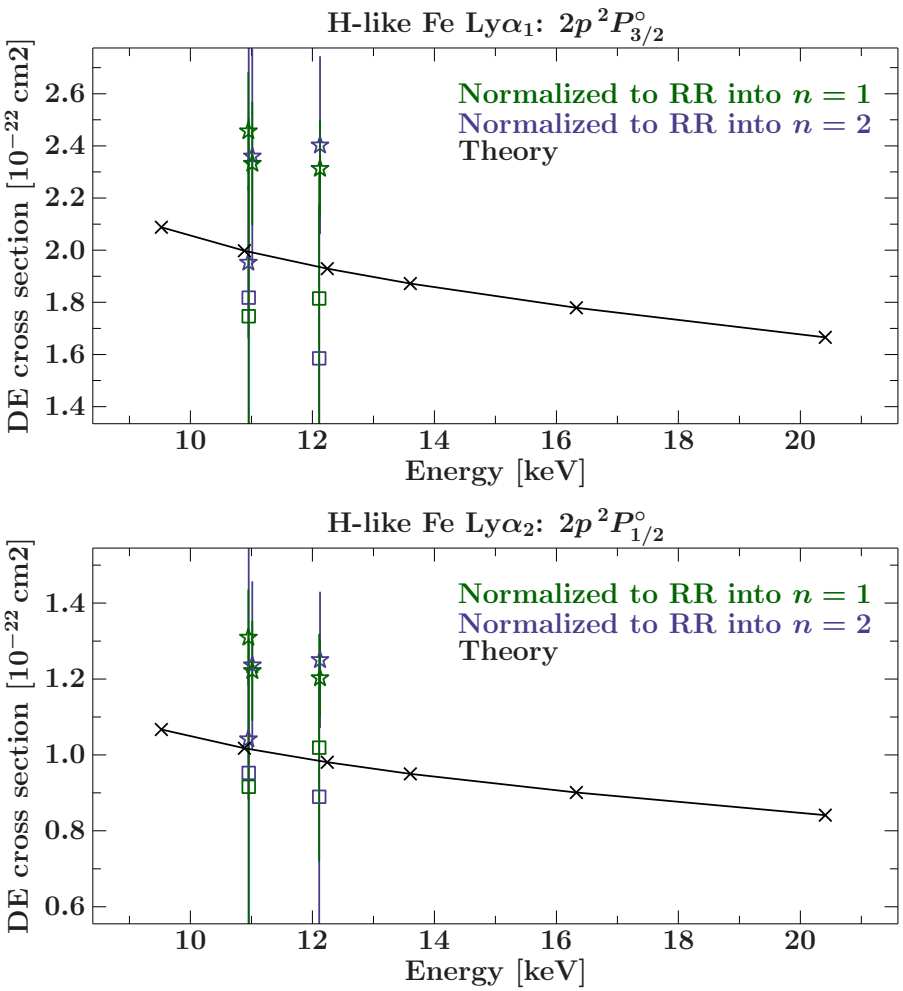

Figure 8.15: Electron impact excitation measurements for H-like Fe Lyα_1 (top) and Lyα_2 (bottom). The EBIT measurement is normalized to RR into the $n = 1$ shell (green) and the $n = 2$ shell (blue), respectively. The stars are the dedicated high charge balance measurements, the squares are ratios from the medium charge balance measurements with low counting statistics in the H-like lines. The cross sections for Lyα_1 are corrected for polarization using Bostock et al. (2009), Lyα_2 is intrinsically unpolarized. The black line shows the theory by Aggarwal et al. (2008).

is corrected for polarization effects using the degree of polarization from Bostock et al. (2009), Lyα_2 has a $j = 1/2$ upper level and is therefore intrinsically unpolarized. Since the ECS high-energy pixels resolve the $n = 2$ RR complex, for each data set there are two estimates for the excitation cross section, one normalized to RR into $n = 1$ and one for RR into $n = 2$. The latter has larger uncertainties due to the lower $n = 2$ RR cross section and the corresponding lower photon flux in this feature. The excitation cross sections derived from the dedicated high charge balance measurements are the more reliable results. These results slightly exceed the predicted cross sections from Aggarwal et al. (2008). The excitation cross sections derived from the medium charge balance data (squares) consistently lie below the theory and the high charge balance results, but also have much higher uncertainties because of the low counting statistics.

8.6 Outlook

The analysis presented in this chapter is a proof of concept that shows that the current setup for the excitation cross section measurements at EBIT employing the high-energy pixels of the ECS deliver results with the 10-15% level of accuracy required by astrophysics. Future missions, such as *Athena*, or any SXS-type instrument will provide accuracies of < 10%, hence improvements in atomic data must be made. In terms of the data set presented here, there are several sources of improvement. The first of these is to finalize the calibration of the energy scales for both the low- and high-energy pixels. The better the calibration and alignment are, the easier it is to correctly describe the number of observed photons with the model fit, especially in the wings between the large peaks, which is important in flux measurements. Using the best calibration, also the transition energies can be measured, which is expected to bring a slight improvement to the relatively large uncertainties of the wavelengths measured by Decaux et al. (1997, see Section 7.1). Transition energy measurements for the $n = 3$–1 Kβ transitions for the lower charge states of Fe similar to Section 6.3.2 will be provided for the first time. Then, after finalizing the calibration, updated cross sections for the presented transitions w, Lyα_1 and Lyα_2 and new cross sections for the remaining transitions in Li-like and He-like Fe, i.e., besides line w, will be provided.

EIE cross sections for L-shell Fe ions

For the lower charge states, inner-shell ionization (with thresholds between 7.1 keV for neutral Fe I and 8.7 keV for Li-like Fe XXIV) has cross sections comparable to the collisional excitation cross sections, making inner-shell ionization an important line formation process (Decaux et al., 1997). Especially in F-like Fe XVIII through C-like Fe XXI inner-shell ionization competes with collisional excitation to populate the upper levels of the same transitions, leaving no obvious markers for either process (Decaux et al., 1997; Jacobs et al., 1997, see also Section 6.2.2 for a discussion of a similar situation in sulfur). Decaux et al. (2003) explored the model for the intensity contributions from collisional excitation and inner-shell ionization in more detail and as a function of electron densities. They based their calculations on the model of Jacobs et al. (1997), an updated version of Jacobs et al. (1989). Comparing the models to data taken at EBIT-II, Decaux et al. (2003) found that an intermediate density model ($n_e \sim 10^{13}\,\mathrm{cm}^{-3}$) describes the experimental data best. While EBIT is usually assumed to operate in the coronal limit ($n_e < 10^{12}\,\mathrm{cm}^{-3}$), where all ions are considered to be in the ground state, the intermediate density model allows that a fraction of the trapped ions in EBIT to occupy low-lying energy levels above the ground state (Decaux et al., 2003). Because the relative contribution of inner-shell ionization and collisional excitation to the population of the upper levels in $n = 2$–1 transitions in these L-shell Fe cannot readily be disentangled, the EBIT measurement only provides absolute effective emission cross sections for these transitions rather than absolute excitation cross sections. The Kβ lines in these L-shell ions (up to F-like), however, do not suffer from the same degeneracy, since their upper level cannot be populated by inner-shell ionization of an ion whose $n = 3$ shell is empty in the ground state configuration.

EIE cross sections of Kβ transitions

The presented data allow excitation cross section measurements for higher-order Rydberg series such as $n = 3$–1 Kβ and $n = 4$–1 Kγ transitions. In order to be able to measure resonance scattering from the He-like resonance line w, the abundance of He-like ions in the plasma has to be known. The He-like Kβ lines are a better reference for the abundance of He-like Fe than line z, since they have the same excitation mechanism as line w, while the line formation process of line z is complicated. The excitation cross sections of the He-like Kβ lines are therefore an important reference for astrophysics. Smith et al. (2000) have measured the ratio of the intercombination line Kβ_2 to the resonance line Kβ_1 in various He-like ions between Mg and Fe with electron beam energies close to the excitation threshold of these lines, thus avoiding cascade contributions to these transitions. They find a Z-dependent difference between the measured and predicted Kβ_2/Kβ_1 ratio – with theory significantly underpredicting the ratio – following similar results from tokamaks (Smith et al., 1993; Beiersdorfer et al., 1995c). With the new measurements, this ratio can be explored for a range of electron impact energies.

Sweeping the electron beam energy

The analysis as described in this Chapter is suitable to benchmark the overall, smoothed trend of the collisional excitation cross sections as a function of electron impact energy. At electron energies close to the excitation threshold, peaks of increased cross sections appear due to resonant excitation processes. Chantrenne et al. (1992) measured these at EBIT in He-like Ti for many discrete electron energies. In order to search for these resonances experimentally, it is possible to sweep the electron beam energy of EBIT by driving the drift tube power supply with a programmable function generator (e.g., Brown et al., 2006, for Ne-like Fe L). This way the Fe K spectra can be measured as a (almost) continuous function of electron energy rather than sampling individual electron energy points, although, naturally, the data have to be binned to energy bins of finite widths to ensure enough counting statistics for each energy point. After having established the experimental setup for the steady-state measurement, sweeping the electron beam energy to search for and measure the strengths of resonances is the next step in benchmarking the K-shell transitions in highly-charged Fe ions.

Fe peak elements

Similar excitation cross section measurements are planned for Fe peak elements, especially Mn and Cr, but also Ni, as K-shell transitions of their ions are detected in an increasing number of celestial sources. For example, the Mn to Cr mass ratio in supernova remnants is a tracer for the metallicity of the progenitor star of type Ia supernovae (Badenes et al., 2008). To derive the mass ratio from the measured line fluxes in the observed spectra, the flux ratio has to be normalized to the specific emissivities of the corresponding ions. Collisional excitation cross sections are an important contribution to these emissivities in the collisional plasmas of supernova remnants.

But though the professed aim of all scientific work is to unravel the secrets of nature, it has another effect, not less valuable, on the mind of the worker. It leaves him in possession of methods which nothing but scientific work could have led him to invent.

James Clerk Maxwell

9 Summary

CHAPTER 1 has discussed general atomic data needs for X-ray astrophysics and the need for benchmarking the available theoretical calculations to high accuracy. It also outlined specific examples of astrophysical objects that can directly benefit from improved atomic physics databases. The remainder of this thesis has demonstrated that measurements at the LLNL EBIT with state of the art instrumentation are capable of fulfilling these needs.

Specifically, we used the ECS microcalorimeter with a $\sim$ 4.6 eV spectral resolution to measure the Kα transition energies for L-shell ions of Si and S (Section 6.1; Hell et al., 2016b). The measurement accuracy of better than $\sim$ 0.5 eV for the strong transitions corresponds to Doppler shifts of less than 90 km s^{-1} and is therefore slightly better than the wavelength scale calibration of *Chandra*-HETG of $\sim$ 100 km s^{-1} (Marshall et al., 2004; Canizares et al., 2005; Chandra X-ray Center, 2015). The new reference data were directly applied to X-ray spectra of the high-mass X-ray binaries Vela X-1 and Cyg X-1, where the improved Doppler shifts give a better handle on studying the clumpy winds of the supermassive companion stars and how the interaction with the compact object influences the wind structure. Additionally, the Kα spectra of N- through Li-like S have been measured with the imaging, spherically bent crystal spectrometer EBHiX at the very high resolution of $\sim$ 0.5 eV (Section 6.2). The EBHiX measurements resolve more transitions and confirm the results for the line centers of blended lines as derived from the ECS measurements. The accuracy of the line centers derived from the EBHiX data is better than 0.2 eV in most cases and better than 0.1 eV for the strong transitions. This corresponds to Doppler shifts of better than $\sim$ 30 km s^{-1}, i.e., within the requirements of the planned *Athena* X-ray observatory (Nandra et al., 2013). These results will enter the AtomDB database (Foster et al., 2012).

Comparison of these new reference data to calculations with FAC suggest that the FAC transition energies of Kα transitions in Si and S are good to about 1 eV or 4–6 parts per 10 000 (Chapter 6). New MRMP calculations by Beiersdorfer et al. (2016a) are expected to be good to 1 part in 10 000 and, in a first comparison, match the ECS results for O-

and F-like Si better than FAC. Similar measurements for transition energies in L-shell ions of other astrophysically abundant elements between Na and Ni and an expansion to Kβ transitions of the same ions are under way (Section 6.3).

The high resolving power of the EBHiX crystal spectrometer was also used to to try to resolve line complexes from individual M-shell ions of Fe (Chapter 7), which are heavily blended. These charge states are important as they can contribute to the "neutral Fe line" at $\sim$ 6.4 keV often seen in CCD spectra of celestial objects (Section 1.4.2). For this experiment we used the EBHiX with a quartz 110 crystal in second order, whose resolution was about 2 eV in the vertical spectrometer mounting, i.e., with the plane of dispersion perpendicular to the electron beam direction. A simple FAC model – excluding the $3d$ subshell in Cl- through Si-like charge states of Fe due to computational limitations – suggested that a 2 eV resolution should be sufficient to resolve the main peaks of different ions. However, the data did not support new line identification beyond the two known F-like Fe Kα lines, although the spectral resolution of this measurement with EBHiX slightly superseded the resolution of previous measurements. Small modifications to the spectrometer to further increase the observed line flux and switching to a detector capable of detecting and time tagging individual photons in event mode might allow us to resolve the radiation emitted from different M-shell Fe ions as a function of EBIT phase.

In another experimental campaign, we demonstrated that the ECS with its high- and low-energy pixel arrays is ideally suited to measure absolute electron impact excitation (EIE) cross sections for Fe group elements to an accuracy of about 10% (Chapter 8). The EIE cross sections are brought to an absolute scale by normalizing the flux from collisionally excited transitions to the flux observed from the radiative recombination (RR) features of the same ion. With the ECS high-energy pixels, the RR into $n = 2$ of L-shell Fe ions was for the first time resolved at collision energies high enough to excite K-shell transitions in these ions. The high-energy pixels have a much better resolving power than solid state detectors and have the additional advantage that they are house in the same instrument as the low-energy pixels, thus greatly simplifying the cross calibration between the EIE and the RR spectra. Multiple data sets were recorded at three different electron beam energies ($\sim$ 8, 11, and 12 keV) and with different charge balances. The high charge balance measurements focus on transitions in H-like and He-like Fe, while the medium charge balance measurements allow for cross section measurements for transitions in O- through He-like Fe. Due to the large bandwidth of the ECS, it is possible to also derive EIE cross sections for the $n = 3 \rightarrow 1$ Kβ transitions from these data. Presented here are the EIE cross section results for the transitions line w in He-like Fe and Lyα_1 and Lyα_2 in H-like Fe. They are compared to theoretical calculations by Zhang et al. (1990) and Aggarwal & Keenan (2013) in case of He-like Fe and to calculations from Aggarwal et al. (2008) for H-like Fe. The presented capability of benchmarking EIE cross section measurements to an accuracy of 10% again fulfills the goals for data needs defined by the astrophysics community (Chapter 1). These measurements at EBIT thus help to take full advantage of observations with future space-borne X-ray observatories with calorimeters, such as those on *Hitomi* and *Athena*, which provide high-resolution spectroscopy for astrophysical objects on a new level. Improvements to the analysis of the presented data and cross sections for lower charge states and Kβ transitions will follow as well as new

measurements at additional electron impact energies (Section 8.6).

Since the approach for measuring the EIE cross sections on an absolute scale relies on the normalization to well known RR cross sections, reliable sources for calculated fine-structure resolved RR cross sections are very important, including polarization corrections for observation perpendicular to an electron beam. In the past, EIE cross section measurements at the LLNL EBITs (e.g., Chen et al., 2005) have often relied on calculations by J. Scofield (based on, e.g., Scofield, 1989). As these calculations exist only for a limited number of ions, we explored FAC as an alternative resource (Section 8.3.4). For this effort, cross sections for RR into $n = 2$ of L-shell ions of Fe, including polarization corrections, were calculated with FAC and compared to calculations by Scofield as published by Chen et al. (2005). Overall the two codes agree within the 3–5% uncertainties usually quoted for this type of calculation. While RR cross sections for the more excited configurations in the $n = 2$ to shell can have larger discrepancies, but since the cross sections for these levels are fairly weak compared to those of the lower lying levels, their contribution to the total RR cross section and the overall line shape is small. Thus, FAC was identified as a potential new source for RR cross section calculations as normalization for EIE cross section measurements at EBIT. Further research into the origin of observed discrepancies of the weak RR cross sections are planned.

In addition to the experiments and measurements related to astrophysics as described above, the performance of the new EBHiX crystal spectrometer as designed by Beiersdorfer et al. (2016b) was assessed at EBIT (Section 5.5.2). Multiple quartz crystals were set up and calibrated using X-ray lines diffracted in first and second order. These measurements were then used as a temperature diagnostic for the trapped ions in EBIT by deriving the Doppler broadening due to the ion motion from the observed line widths. Since EBHiX is an imaging spectrometer, it is possible to use it with the plane of dispersion either parallel or perpendicular to the electron beam direction, thus making it an ideal instrument for measurements of the linear polarization of X-ray transitions. This capability was demonstrated using the H-like Mn lines Lyα_1 and Lyα_2 (Section 5.6). Further polarization measurements are planned. Since the EIE cross section measurements depend on polarization corrections, these measurements can greatly benefit from polarization measurements with EBHiX.

A Physical Constants

In the X-ray regime, the spectral position of transitions is interchangeably quoted in terms of the transition energy in units of, e.g., electron volts (eV), Rydberg (Ry), or atomic units (a.u. = 2 Ry), in terms of the transition wavelength usually in units of Ångstrom (Å = 10^{-10} m), or in terms of the wavenumber (inverse wavelength) in units of cm^{-1} (Kayser), but sometimes also in more "user-friendly" units. Theoretical calculations, especially of level energies, are often reported in Ry, a.u., or Kayser. For experiments, however, the choice of units is often dictated by the natural unit of the employed spectrometer: eV (or keV) for energy dispersive instruments such as microcalorimeters and solid state detectors; Å for wavelength dispersive instruments like grating and crystal spectrometers.

The energy E of a photon and its wavelength λ are connected through the identity $E = hc/\lambda$, where h is Planck's constant and c the speed of light. The fundamental value of h is in units of J s, i.e., computation of the constant to convert between transition energies in eV and wavelengths in Å involves the elementary charge e as well:

$$E[\mathrm{eV}]\,\lambda[\text{Å}] = \frac{h[\mathrm{J\,s}]\,c[\text{Å}\,\mathrm{s}^{-1}]}{e[\mathrm{C}]} = 12398.42\,\mathrm{eV\,Å}. \tag{A.1}$$

While the speed of light is a constant with a defined value (set to the value of Cohen & Taylor, 1973, as confirmed by the Conférence Générale des Poids et Mesures 1975, through the new definition of the meter as distance traveled by light in vacuum in 1 s time in 1983; Giacomo, 1984), other constants are derived quantities whose values have to be measured. With advances in science and technology, the exact values can vary somewhat with time. For high-precision high-resolution spectroscopy, it is therefore not only important to know these constants to a high degree of accuracy, but also to know exactly which value is underlying the quoted transitions in a particular measurement or calculation.

The National Institute for Standards and Technology (NIST) has a Committee on Data for Science and Technology (CODATA) who publish revised versions of physical constants starting in 1973, revised in 1986, and since 1998 every 4 years. These reference values

Table A.1: Evolution of derived values for physical constants with time.

$h[10^{-34}\,\mathrm{J\,s}]$	$e[10^{-19}\,\mathrm{C}]$	$hc/e[\mathrm{eV\,Å}]$	source
6.626 176(36)	1.602 189 2(46)	12398.521	CODATA 1973[a]
6.626 075 5(40)	1.602 177 33(49)	12398.4245	CODATA 1986[b]
6.626 068 76(52)	1.602 176 462(63)	12398.41857	CODATA 1998[c] / ISIS
6.626 068 96(33)	1.602 176 87(40)	12398.41579	XDB 2009[d] with typo
6.626 069 3(11)	1.602 176 53(14)	12398.41903	CODATA 2002[e]
6.626 068 96(33)	1.602 176 487(40)	12398.41875	CODATA 2006[f] / XDB 2009[d] typo corr.
6.626 069 57(29)	1.602 176 565(35)	12398.41929	CODATA 2010[g]
6.626 070 040(81)	1.602 176 6208(98)	12398.41974	CODATA 2014[h]

[a] CODATA 1973: Cohen & Taylor (1973); Cohen (1976)
[b] CODATA 1986: Cohen & Taylor (1987)
[c] CODATA 1998: Mohr & Taylor (2000)
[d] XDB 2009 (X-ray Data Booklet; Thompson et al., 2009) references CODATA 1998, but the quoted values match the numbers from CODATA 2006, with one exception: a digit of e has been omitted. This has the consequence that the conversion constant derived from h, c, and e does not yield the same number as the quoted value of $\hbar c$[MeV fm].
[e] CODATA 2002: Mohr & Taylor (2005)
[f] CODATA 2006: Mohr et al. (2008)
[g] CODATA 2010: Mohr et al. (2012)
[h] CODATA 2014: Mohr et al. (2015)

Notes: The speed of light in vacuum is exact at $c = 299\,792\,458\,\mathrm{m\,s^{-1}}$ (after 1973)

are assessed carefully from all, including the most current and state of the art, available measurements and insights. Their values can be accessed dating back to 1998 through the official CODATA web page at `http://www.nist.gov/pml/div684/fcdc/codata.cfm`.

As can be seen from Table A.1, the value of the conversion constant has changed rather significantly from the values commonly used in the 1980s, but since then has stabilized to a precision of 7 significant digits. This corresponds to energy values being good to the meV level – if converted from higher precision wavelengths. Since reference energies or wavelengths used for calibration of wavelength measurements should always have at least 1-2 digits higher precision than the desired experimental outcome (within the capabilities of the spectrometer), the accuracy of this conversion constant will increasingly matter as better instruments for high-resolution spectroscopy become available.

B Event Grade Distribution

The relative abundance of the event rates in the pulse height analysis of the microcalorimeter data depends on the event rate: the higher the event rate, the more likely it becomes that multiple events occur within the time window needed for the use of the long, or even the short, template. The probability of k events occurring in a certain time interval Δt can be described by Poisson statistics as $P(k) = (\lambda^k/k!) \cdot \exp(-\lambda)$, where λ is the average number of counts per interval and can be written in terms of the average count rate ν as $\lambda = \nu \cdot \Delta t$. To determine the probability of a certain event grade for an event at t_0, we need to know how likely the previous event at Δt_p and the next event Δt_n fall into a specific time interval before or after the current event. There are three possible intervals Δt: $\Delta t \leq \tau_1$, $\tau_1 < \Delta t \leq \tau_2$, and $\tau_2 < \Delta t$, where τ_1 and τ_2 are the length of the short and full templates minus their respective pre-trigger points. If the distance between two events is shorter than τ_1, i.e., $\Delta t \leq \tau_1$, both become low-res events independently of whether they are Δt_p and t_0 or t_0 and Δt_n. If both events are at least τ_1 apart, but either Δt_p or Δt_n is closer than τ_2, i.e., $\tau_1 < \Delta t \leq \tau_2$, the short templates are used for both events. Only for $\Delta t > \tau_2$ before and after t_0 allows for the full template to be used.

The probability that no event occurs within Δt is $P(k = 0) = \exp(-\nu \Delta t)$. This makes the probability for Δt between two events fo fall in either of these three intervals $P(\tau_2 < \Delta t) = \exp(-\nu\tau_2)$, $P(\tau_1 < \Delta t \leq \tau_2) = \exp(-\nu\tau_1) - \exp(-\nu\tau_2)$, $P(\Delta t \leq \tau_1) = (1 - \exp(-\nu\tau_1))$. Let P_p and P_n be the probability of the previous and next event. Then the probability for each event grade is the sum of $P_\mathrm{p} \cdot P_\mathrm{n}$ over all combinations of Δt_p and Δt_n that lead to this event grade. From Table B.1 we get

$$\mathrm{Hp} = \mathrm{e}^{-2\nu\tau_2} \tag{B.1}$$

$$\mathrm{Mp} = \mathrm{e}^{-\nu\tau_2}\left(\mathrm{e}^{-\nu\tau_1} - \mathrm{e}^{-\nu\tau_2}\right) \tag{B.2}$$

$$\mathrm{Ms} = \left(\mathrm{e}^{-\nu\tau_1} - \mathrm{e}^{-\nu\tau_2}\right)\mathrm{e}^{-\nu\tau_1} \tag{B.3}$$

$$\mathrm{Lp} = \mathrm{e}^{-\nu\tau_2}\left(1 - \mathrm{e}^{-\nu\tau_1}\right) \tag{B.4}$$

$$\mathrm{Ls} = \left(1 - \mathrm{e}^{-\nu\tau_1}\right) \cdot \left(1 + \mathrm{e}^{-\nu\tau_1} - \mathrm{e}^{-\nu\tau_2}\right) \tag{B.5}$$

where H, M, and L stand for high-, mid-, and low-res event grades and p and s denote

primary and secondary events respectively. It is interesting to note that Hp + Mp + Ms + Lp + Ls = 1, i.e., the sum of these rates is unity.

Figure B.1 shows the resulting event grade distribution (branching ratios) for a sampling rate of 12.5 kHz, full template length of 2048 samples (300 samples pre-trigger) and short template length of 512 samples (75 pre-trigger), corresponding to $\tau_1 = 34.96$ ms and $\tau_2 = 139.84$ ms.

Table B.1: Definition of event grades and their probabilities (Seta et al., 2012)

$P_p \cdot P_n$	$\Delta t_p \leq \tau_1$	$\tau_1 < \Delta t_p \leq \tau_2$	$\tau_2 \leq \Delta t_p$
$\Delta t_n \leq \tau_1$	Ls $(1-e^{-\nu\tau_1}) \cdot (1-e^{-\nu\tau_1})$	Ls $(e^{-\nu\tau_1}-e^{-\nu\tau_2}) \cdot (1-e^{-\nu\tau_1})$	Lp $e^{-\nu\tau_2} \cdot (1-e^{-\nu\tau_1})$
$\tau_1 < \Delta t_n \leq \tau_2$	Ls $(1-e^{-\nu\tau_1}) \cdot (e^{-\nu\tau_1}-e^{-\nu\tau_2})$	Ms $(e^{-\nu\tau_1}-e^{-\nu\tau_2}) \cdot (e^{-\nu\tau_1}-e^{-\nu\tau_2})$	Mp $e^{-\nu\tau_2} \cdot (e^{-\nu\tau_1}-e^{-\nu\tau_2})$
$\tau_2 \leq \Delta t_n$	Ls $(1-e^{-\nu\tau_1}) \cdot e^{-2\nu\tau_2}$	Ms $(e^{-\nu\tau_1}-e^{-\nu\tau_2}) \cdot e^{-\nu\tau_2}$	Hp $e^{-\nu\tau_2} \cdot e^{-\nu\tau_2}$

Notes: H: High-res; M: mid-res; L: low-res; p: primary; s: secondary; $\Delta t_{p/n}$: time difference to the preceding or next pulse; $\tau_1 = 34.96$ ms: length of the short template (512 samples minus 75 pre-trigger samples) at a sampling frequency of $f_s = 12.5$ kHz; $\tau_2 = 139.84$ ms: length of the full template (2048 samples total length minus 300 pre-trigger samples); see also Fig. 4.4 and B.1.

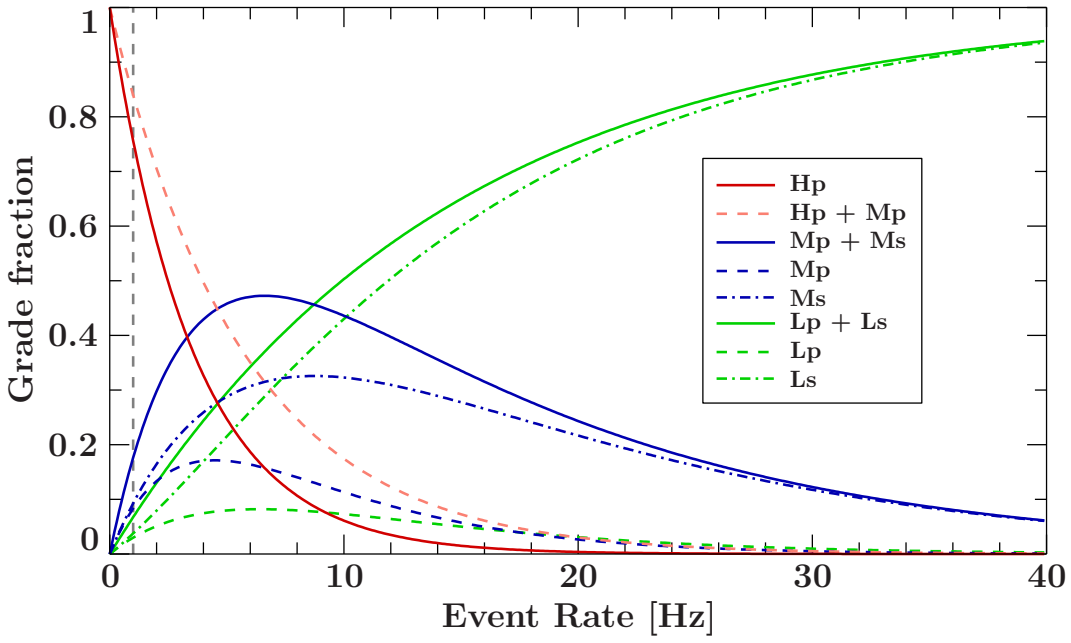

Figure B.1: Fractions of event grades depending on event rate for template lengths of 2048 and 512 (short). The vertical dashed line marks the 1 count per second per pixel rate that is optimal for the ECS low-energy pixels. — After (Seta et al., 2012).

C Statistics for Model Fitting

Measured data often are grouped into histograms with bins of finite width. This binning can be a direct consequence of features of the experimental setup like finite widths of detector channels (e.g., CCD pixels). For continuous numeric data like lists of photon energies, where it is unlikely that two events have the exact same value, binning is an attempt at rendering the data comprehensible (Barlow, 1989). To find a good, often empirical description of the data, a parameterized model is adjusted to fit the data using statistical methods. While the statistical methods described below are valid in general, for their implementation and use in X-ray astrophysics see, e.g., Lampton et al. (1976), Avni (1976), Cash (1979), Gehrels (1986), Nousek & Shue (1989), Mittaz et al. (1999) and (Arnaud et al., 2015).

The likelihood L is the product of the probabilities in each data bin that the observed number of counts results from the assumed model, given that the data are uncorrelated between bins and that the model is correct. As such, the likelihood measures the difference between the data and the model (Nousek & Shue, 1989). The maximum likelihood gives the set of parameters for the assumed model that match the data best. However, this does not suggest that the estimate corresponds to the most likely value, but rather that this estimate makes the data most likely (Barlow, 1989).

A common expression for the probabilities used in the likelihood function is based on a Gaussian distribution, giving the likelihood as

$$L = \prod_{i=1}^{N} P_i(C_i, M_i) = \prod_{i=1}^{N} \frac{1}{\sigma_i \sqrt{2\pi}} \exp\left(-\frac{(C_i - M_i)^2}{2\sigma_i}\right), \tag{C.1}$$

i.e., the probability P_i to observe a certain number of counts C_i in a bin is its Gaussian probability centered around the model predicted value M_i for that bin (Nousek & Shue, 1989). Taking the natural logarithm[1] and multiplying by a factor[2] of -2 leads to the

[1] As the logarithm varies much more slowly with the parameters of the model (Sivia & Skilling, 2006) and the logarithm converts the product into a sum, which is easier to optimize (Barlow, 1989).

[2] Optimization algorithms for minimization are more readily available than for maximization (Barlow,

χ^2-statistic

$$\chi^2 = \sum_i \frac{(C_i - M_i)^2}{\sigma_i^2}. \tag{C.2}$$

Minimizing this expression with respect to each model parameter is known as the method of least squares and leads to the set of parameters, i.e., the best fit, corresponding to the maximum likelihood. Because of its form, this method is also known as the principle of least squares (Barlow, 1989). Here, the sum is over each bin in the spectrum, C_i the measured number of counts in bin i, M_i the number of counts in bin i as predicted by the model, and σ_i is a measure for the uncertainty such that bins with a larger uncertainty contribute to χ^2 with a smaller weight. The uncertainty σ_i represents the unknown standard deviation of the Poisson distribution from which C_i is sampled. It is often approximated by the statistical uncertainty of the data $\sigma_i = \sqrt{C_i}$, but other definitions are possible (Siemiginowska, 2009).

Confidence intervals for the fitted parameters are derived by finding the parameter value that corresponds to an increase of χ^2 by a certain $\Delta\chi^2$ whose value depends on the desired confidence level, e.g., $\Delta\chi^2 = 2.71$ for a single of the p model parameters and a 90% confidence level (Avni, 1976). The reduced χ^2, $\chi^2_{\mathrm{red}} = \chi^2/n$ where $n = N - p$ is the number of degrees of freedom for N bins and p free parameters, can be used as an indicator for goodness of fit. Since the χ^2-distribution has mean n, for a good fit $\chi^2_{\mathrm{red}} \approx 1$ is expected (Barlow, 1989), i.e., on average the C_i should scatter within σ_i around M_i. Values of $\chi^2_{\mathrm{red}} \ll 1$ indicate that either the error bars assigned to the data are too large, that χ^2_{red} is not sampled from the χ^2-distribution, or that the data have been manipulated (Siemiginowska, 2009).

The residuals of the fit, i.e., the deviation between model and data in each individual bin i, indicate how well the model matches the data over the full data range and can help to find possible features that are not included in the model yet. These residuals can be calculated as $\chi^2 = (C_i - M_i)^2/\sigma_i^2$ (but preserving the sign of $(C_i - M_i)$), i.e., the expression in the sum of Eq. C.2, as $\chi = (C_i - M_i)/\sigma_i$, or as ratio $= C_i/M_i$, where each of these options emphasizes different deviations. For example, the use of χ^2 residuals particularly highlights the bins with large deviations. For a good fit, i.e., when no features have been missed or overestimated by the assumed model, the residuals should scatter statistically around 0 (χ^2, χ) or 1 (ratio). In this work the residuals of the fit are shown as χ.

As described above, the method of χ^2-minimization requires the underlying data in each bin to follow a Gaussian (or normal) distribution (Gauß, 1809). However, if events occur independently at a constant rate (source intensity), the observed number of counts in each energy bin of a measured photon spectrum follows a Poisson distribution (Poisson, 1837) $P(k) = (\lambda^k/k!) \cdot \exp(-\lambda)$, where $P(k)$ is the probability to observe k photons out of an expected number of λ photons in that energy bin. But in the limit of large numbers $\lambda \to \infty$, the Poisson distribution converges to a Gaussian distribution with mean λ and standard deviation $\sqrt{\lambda}$. Even for smaller numbers of events the Poisson distribution can be well approximated by a Gaussian distribution (Fig. C.1). Generally, with 20 counts per bin the data are considered to be sufficiently close to a normal distribution to justify the

1989).

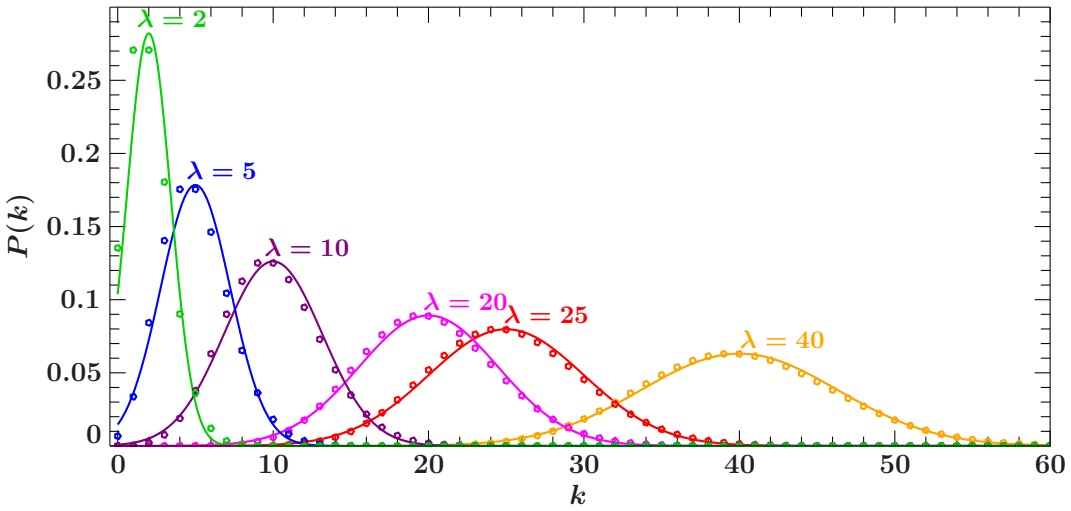

Figure C.1: Comparison between shapes of Poisson (circles) and Gaussian (lines) distribution for for various mean values λ and standard deviation $\sqrt{\lambda}$. For larger λ the Poisson distribution converges to a Gaussian distribution.

use of χ^2-minimization (Berry & Burnell, 2005; Cash, 1979), but some authors set the limit as low as 10 counts (Barlow, 1989; Gehrels, 1986).

For data sets with lower counting statistics, the data either need to be rebinned to reach the Gaussian limit or the χ^2-statistic has to be substituted by a statistic that assumes a Poisson distribution of the data, e.g., the Cash statistic (Cash, 1979). Cash (1979) used Bayesian statistics to show that, besides the Gaussian in Eq. C.1, almost any probability distribution can be used to construct the log likelihood $-2\ln L$. In the limit of large numbers of counts, the quantity $-2\ln L$ then always has a χ^2-distribution. Deriving the log likelihood based on Poisson-distributed data and adjusting model-independent terms, which do not influence the best-fit parameters, gives the Cash statistic (in astrophysical data analysis software also referred to as "C-statistic" or "cstat") as implemented in the spectral analysis packages XSPEC and ISIS for X-ray astrophysics (Arnaud et al., 2015)

$$\mathscr{C} \equiv 2\sum_i (M_i - C_i) + C_i \ln\left(\frac{C_i}{M_i}\right) \tag{C.3}$$

which is the expression to minimize with respect to all parameters instead of using χ^2. Note that this expression is independent of the statistical uncertainty of the data. Cash statistics was designed such that it converges to the χ^2 results where use of χ^2 is valid (Arnaud et al., 2015). In the extreme, Cash statistics can even be used on unbinned data or data on a very fine mesh where each bin has either zero or one observed count (Cash, 1979). Nousek & Shue (1989) compare results of using χ^2 and $\mathscr{C}$ statistics for the low and high-count regimes and find that the $\mathscr{C}$-statistic minimization (in combination with the Powell minimization algorithm[3]) produces much more accurate fits in the low-count regime than using the χ^2-statistic. Because of the low counting statistics of the

[3]Nousek & Shue (1989) also find that, for χ^2-statistics in the low-count regime, Powell's minimization method produces smaller errors in the results than Marquardt's algorithm.

present EBHiX spectrum (Section 6.2), this spectrum is therefore analyzed using the more appropriate Cash statistics to utilize the full high-resolution.

Since $\Delta\mathscr{C}$ follows the χ^2-distribution, confidence intervals for parameters are still well-defined for the Poisson-based Cash statistics, albeit with different values for $\Delta\mathscr{C}$ than for $\Delta\chi^2$ for the same confidence levels (Gehrels, 1986; Mittaz et al., 1999). While Cash statistics do not have a goodness of fit criterion (Siemiginowska, 2009) or a rule of thumb like $\chi^2_{\mathrm{red}} \approx 1$ for χ^2-statistics, the residuals again show parts of the data that are not well described by the model. Similar to the χ residual, the residuals for each bin are computed from the square root of the expression in the sum in $\mathscr{C}$ (Eq C.3) while preserving its sign. These residuals shown in figures in this thesis are denoted by "Cash" with $\texttt{Cash} = \mathscr{C}/\sqrt{|\mathscr{C}|}$.

All of physics is either impossible or trivial. It is impossible until you understand it, and then it becomes trivial.

Ernest Rutherford

References

Adams J.S., Bandler S.R., Brown L.E., et al., 2009 1185, 274

Aggarwal K.M., Hamada K., Igarashi A., et al., 2008, A&A 484, 879

Aggarwal K.M., Keenan F.P., 2013, Phys. Scr. 87, 055302

Aggarwal K.M., Kingston A.E., 1993, ApJS 85, 187

Alder K., Steffen R.M., 1975, Emission and absorption of electromagnetic radiation. In: Hamilton W.D. (ed.) The Electromagnetic Interaction in Nuclear Spectroscopy, Vol. Chapter 1. North-Holland / American Elsevier, p. 1

Alfvén H., 1941, Arkiv för Matematik, Astronomi och Fysik 27A, 1

Allen S.W., Evrard A.E., Mantz A.B., 2011, ARA&A 49, 409

Allison J.W., 1961, Aust. J. Phys. 14, 443

Als-Nielsen J., McMorrow D., 2011, Elements of Modern X-ray Physics, John Wiley & Sons, Ltd Publication, 2nd edition

Arnaud K., Dorman B., Gordon C., 2015, Xspec – An X-ray Spectral Fitting Package: User's Guide for version 12.9.0, available online at `heasarc.nasa.gov/xanadu/xspec/XspecManual.pdf`

Asplund M., Grevesse N., Sauval A.J., Scott P., 2009, ARA&A 47, 481

Avni Y., 1976, ApJ 210, 642

Badenes C., Bravo E., Hughes J.P., 2008, Astrophys. J., Lett. 680, L33

Badnell N.R., 2006, ApJS 167, 334

Ballance C.P., Badnell N.R., Berrington K.A., 2002, J. Phys. B 35, 1095

Balmer J.J., 1885, Wiedemann's Annalen 25

Bandler S.R., Adams J.S., Chervenak J.A., et al., 2016, In: den Herder J.W.A., Takahashi T., Bautz M. (eds.) Space Telescopes and Instrumentation 2016: Ultraviolet to Gamma Ray, Vol. 9905., p.99050Q

Barkla C.G., 1911, Phil. Mag. (6) 22, 396

Barlow R., 1989, Statistics. A guide to the use of statistical methods in the physical sciences, The Manchester Physics Series, Wiley, New York

Barret D., Lam Trong T., den Herder J.W., et al., 2016, In: den Herder J.W.A., Takahashi T., Bautz M. (eds.) Space Telescopes and Instrumentation 2016: Ultraviolet to Gamma Ray, Vol. 9905., p. 99052F

Bautista M.A., Kallman T.R., 2001, ApJS 134, 139

Bautista M.A., Mendoza C., Kallman T.R., Palmeri P., 2003, A&A 403, 339

Bautista M.A., Mendoza C., Kallman T.R., Palmeri P., 2004, A&A 418, 1171

Bearden J.A., 1967, Rev. Mod. Phys. 39, 78

Behar E., Netzer H., 2002, ApJ 570, 165

Beiersdorfer P., 1988, Ph.D. thesis, Department of Astriphysical Sciences, Princeton University, New Jersey, USA

Beiersdorfer P., 1990, In: X-ray and inner-shell processes, Vol. 215. AIP Conf. Proc., p.648

Beiersdorfer P., 1997, In: American Institute of Physics Conference Series, Vol. 389. American Institute of Physics Conference Series, p.121

Beiersdorfer P., 2003, ARA&A 41, 343

Beiersdorfer P., 2005, In: Smith R. (ed.) X-ray Diagnostics of Astrophysical Plasmas: Theory, Experiment, and Observation, Vol. 774. American Institute of Physics Conference Series, p.83

Beiersdorfer P., (ed.) 2007, Twenty Years of Spectroscopy with the Livermore Electron Beam Ion Traps: EBIT-I, EBIT-II, SuperEBIT – Selected Publications Vol. I–VI, University of California, Berkeley

Beiersdorfer P., 2008a, Can. J. Phys. 86, 1

Beiersdorfer P., (ed.) 2008b, Proceedings of the

workshop on Twenty years of spectroscopy with EBIT, Vol. 86(1)

Beiersdorfer P., 2009, Can. J. Phys. 87, 9

Beiersdorfer P., Behar E., Boyce K.R., et al., 2003a, Nucl. Instrum. Methods Phys. Res., Sect. B 205, 173

Beiersdorfer P., Bitter M., May M.J., Roquemore L., 2003b, Rev. Sci. Instrum. 74, 1974

Beiersdorfer P., Bitter M., Roquemore L., et al., 2006, Rev. Sci. Instrum. 77, 10F306

Beiersdorfer P., Bitter M., von Goeler S., Hill K.W., 1989, Phys. Rev. A 40, 150

Beiersdorfer P., Bode M.P., Ishikawa Y., Diaz F., 2014a, ApJ 793, 99

Beiersdorfer P., Brown G., Utter S., et al., 1999a, Phys. Rev. A 60, 4156

Beiersdorfer P., Brown G.V., 2015, Phys. Rev. A 91, 032514

Beiersdorfer P., Brown G.V., Goddard R., Wargelin B.J., 2004a, Rev. Sci. Instrum. 75, 3720

Beiersdorfer P., Brown G.V., Hell N., Santana J.A., 2016a, In: Banaś D., Pachuki K., Pajek M. (eds.) 18th International Conference on the Physics of Highly Charged Ions (HCI 2016). Nucl. Instrum. Methods Phys. Res., Sect. B, p. *submitted*

Beiersdorfer P., Cauble R., Chantrenne S., et al., 1992a, In: MacGillivray W.R., McCarthy I.E., Standage M.C. (eds.) Electron and Atomic Collisions – XVII. ICPEAC, Brisbane 1991., p.313

Beiersdorfer P., Chen M.H., Marrs R.E., et al., 1991, Phys. Rev. A 44, 396

Beiersdorfer P., Clementson J., Dunn J., et al., 2010, J. Phys. B 43, 144008

Beiersdorfer P., Crespo López-Urrutia J.R., Förster E., et al., 1997a, Rev. Sci. Instrum. 68, 1077

Beiersdorfer P., Decaux V., Elliott S.R., et al., 1995a, Rev. Sci. Instrum. 66, 303

Beiersdorfer P., Decaux V., Widmann K., 1995b, Nucl. Instrum. Methods Phys. Res., Sect. B 98, 566

Beiersdorfer P., Diaz F., Ishikawa Y., 2012a, ApJ 745, 167

Beiersdorfer P., Hell N., Lepson J.K., et al., 2015, ApJ 815, 3

Beiersdorfer P., Lepson J.K., Bitter M., et al., 2008, Rev. Sci. Instrum. 79, 10E318

Beiersdorfer P., Lepson J.K., Desai P., et al., 2014b, ApJS 210, 16

Beiersdorfer P., Lepson J.K., Díaz F., et al., 2013, Phys. Scr. T156, 014007

Beiersdorfer P., Lepson J.K., Schneider M.B., Bode M.P., 2012b, Phys. Rev. A 86, 012509

Beiersdorfer P., López-Urrutia J.C., Decaux V., et al., 1997b, Rev. Sci. Instrum. 68, 1073

Beiersdorfer P., López-Urrutia J.R.C., Springer P., et al., 1999b, Rev. Sci. Instrum. 70, 276

Beiersdorfer P., Magee E., Brown G., et al., 2014c, Rev. Sci. Instrum. 85, 11E422

Beiersdorfer P., Magee E.W., Brown G.V., et al., 2016b, Rev. Sci. Instrum. 87, 063501

Beiersdorfer P., Magee E.W., Hell N., Brown G.V., 2016c, Rev. Sci. Instrum. 87, 11E339

Beiersdorfer P., Magee E.W., Träbert E., et al., 2004b, Rev. Sci. Instrum. 75, 3723

Beiersdorfer P., Marrs R.E., Henderson J.R., et al., 1990a, Rev. Sci. Instrum. 61, 2338

Beiersdorfer P., Osterheld A.L., Chen M.H., et al., 1990b, Phys. Rev. Lett. 65, 1995

Beiersdorfer P., Osterheld A.L., Decaux V., Widmann K., 1996a, Phys. Rev. Lett. 77, 5353

Beiersdorfer P., Osterheld A.L., Phillips T.W., et al., 1995c, Phys. Rev. E 52, 1980

Beiersdorfer P., Phillips T., Jacobs V.L., et al., 1993, ApJ 409, 846

Beiersdorfer P., Phillips T.W., Wong K.L., et al., 1992b, Phys. Rev. A 46, 3812

Beiersdorfer P., Slater M., 2001, Phys. Rev. E 64, 066408

Beiersdorfer P., Vogel D.A., Reed K.J., et al., 1996b, Phys. Rev. A 53, 3974

Beiersdorfer P., Wargelin B.J., 1994, Rev. Sci. Instrum. 65, 13

Bernitt S., Brown G.V., Rudolph J.K., et al., 2012, Nat 492, 225

Berry R., Burnell J., 2005, The handbook of astronomical image processing, Willmann-Bell, Inc., 2nd edition

Bitter M., Hill K.W., Roquemore A.L., et al., 1999, Rev. Sci. Instrum. 70, 292

Bitter M., Hill K.W., Stratton B., et al., 2004, Rev. Sci. Instrum. 75, 3660

Blondin J.M., Woo J.W., 1995, ApJ 445, 889

Boehringer H., Voges W., Fabian A.C., et al., 1993, MNRAS 264, L25

Bohr N., 1913a, Phil. Mag. 26, 1

Bohr N., 1913b, Phil. Mag. 26, 476

Bohr N., 1913c, Phil. Mag. 26, 857

Boiko V.A., Chugunov A.Y., Ivanova T.G., et al., 1978, MNRAS 185, 305

Boltzmann L., 1872, Wien. Ber. 66, 275

Boroson B., Vrtilek S.D., Kallman T., Corcoran M., 2003, ApJ 592, 516

Bostock C.J., Fursa D.V., Bray I., 2009, Phys. Rev. A 80, 052708

Boyce K.R., Audley M.D., Baker R.G., et al., 1999, In: Siegmund O.H., Flanagan K.A. (eds.) EUV, X-Ray, and Gamma-Ray Instrumentation for Astronomy X, Vol. 3765. Proceedings of SPIE, p.741

Bragg W.H., Bragg W.L., 1913, Proceedings of the Royal Society of London A: Mathematical, Physical and Engineering Sciences 88, 428

Bransden B.H., Joachain C.J., 2003, Physics of Atoms and Molecules, Prentice Hall, Inc.

Bravais A., 1850, Journal de l'Ecole Polytechnique 19, 1

Briand J.P., Charles P., Arianer J., et al., 1984, Phys. Rev. Lett. 52, 617

Brickhouse N., Federman S., Kwong V.H.S., et al., 2006, Laboratory Astrophysics White Paper (based on the 2006 NASA Laboratory Astrophysics Workshop at the University of Nevada, Las Vegas, 14-16 February, 2006), White Paper of the 2006 NASA Laboratory Astrophysics Workshop `http://www.physics.unlv.edu/labastro/`

Brickhouse N.S., Dupree A.K., Edgar R.J., et al., 2000, ApJ 530, 387

Brinkman A.C., van Rooijen J.J., Bleeker J.A.M., et al., 1987, Astrophysical Letters and Communications 26, 73

Brocksopp C., Tarasov A.E., Lyuty V.M., Roche P., 1999, A&A 343, 861

Brown G.V., 2000, Ph.D. thesis, Auburun University, Auburn, Alabama

Brown G.V., Beiersdorfer P., Chen H., et al., 2001, Astrophys. J., Lett. 557, L75

Brown G.V., Beiersdorfer P., Chen H., et al., 2006, Phys. Rev. Lett. 96, 253201

Brown G.V., Beiersdorfer P., Clementson J., et al., 2010, In: Space Telescopes and Instrumentation 2010: Ultraviolet to Gamma Ray, Vol. 7732. Proceedings of SPIE, p. 77324Q

Brown G.V., Beiersdorfer P., Hell, N.and Magee E.W., 2016, Rev. Sci. Instrum. 87, 11D620

Brown G.V., Beiersdorfer P., Liedahl D.A., et al., 1998, ApJ 502, 1015

Brown G.V., Beiersdorfer P., Widmann K., 1999, Rev. Sci. Instrum. 70, 280

Brown I.G., Galvin J.E., MacGill R.A., Wright R.T., 1986, Appl. Phys. Lett. 49, 1019

Brucato R.J., Kristian J., 1972, Astrophys. J., Lett. 173, L105

Burek A., 1976, Space Sci. Instrum. 2, 53

Burgess A., Tully J.A., 1992, A&A 254, 436

Burnight T.R., 1949, Phys. Rev. 76, 165

Busquet M., Bar-Shalom A., Klapisch M., Oreg J., 2006, J. Phys. IV 133, 973

Calvert J., Tuttle E., 1979, Il Nuovo Cimento B 54, 413 10.1007/BF02904024

Canizares C.R., Bradt H.V.D., Clark G.W., et al., 1987, Astrophysical Letters and Communications 26, 87

Canizares C.R., Davis J.E., Dewey D., et al., 2005, PASP 117, 1144

Carse G.D., Walker D.W., 1973, J. Phys. B 6, 2529

Cash W., 1979, ApJ 228, 939

Castor J.I., Abbott D.C., Klein R.I., 1975, ApJ 195, 157

Cauchois Y., 1932, J. Phys. Radium 3, 320

Chandra X-ray Center 2015, The Chandra Proposers' Observatory Guide, version 18, available online at `http://cxc.harvard.edu/proposer/POG/html/index.html`

Chang C., Cui W., 2007, ApJ 663, 1207

Chantrenne S., Beiersdorfer P., Cauble R., Schneider M.B., 1992, Phys. Rev. Lett. 69, 265

Chen H., 2002, In: Beiersdorfer P., Fujimoto T. (eds.) Proceedings of the 3rd US-Japan Work-

shop on Plasma Polarization Spectroscopy, 18-21 June 2001, Vol. UCRL-ID-146907., p. 319

Chen H., Beiersdorfer P., 2008, Can. J. Phys. 86, 55

Chen H., Beiersdorfer P., Scofield J.H., et al., 2005, ApJ 618, 1086

Chen H., Beiersdorfer P., Scofield J.H., et al., 2002, Astrophys. J., Lett. 567, L169

Chen H., Bitter M., Hill K.W., et al., 2014, Rev. Sci. Instrum. 85, 11E606

Chen H., Gu M.F., Beiersdorfer P., et al., 2006, ApJ 646, 653

Chen M.H., 1985, Phys. Rev. A 31, 1449

Chen M.H., Cheng K.T., 1997, Phys. Rev. A 55, 166

Chen M.H., Crasemann B., 1988, Atomic Data Nucl. Data Tables 38, 381

Chen M.H., Reed K.J., M. M.D., et al., 1997, Atomic Data Nucl. Data Tables 65, 289

Chen Z.B., Dong C.Z., Jiang J., 2015, Phys. Scr. 90, 054007

Churazov E., Forman W., Jones C., et al., 2004, MNRAS 347, 29

Cohen E.R., 1976, Atomic Data Nucl. Data Tables 18, 587

Cohen E.R., Taylor B.N., 1973, J. Phys. Chem. Ref. Data 2, 663

Cohen E.R., Taylor B.N., 1987, Rev. Mod. Phys. 59, 1121

Compton A.H., 1922, Bull. Natl. Res. Counc. US 4, Pt. 2, 1

Compton A.H., 1923, Phys. Rev. 21

Compton A.H., Allison S.K., 1935, X-rays in Theory and Experiment, D. van Nostrand Company, Inc., 2nd edition

Condon E.U., Odabasi H., 1980, Atomic structure, Cambridge University Press

Condon E.U., Shortley G.H., 1935, The Theory of Atomic Spectra, Cambridge University Press

Cottam J., Boyce K.R., Brown G.V., et al., 2005, In: Smith R. (ed.) X-ray Diagnostics of Astrophysical Plasmas: Theory, Experiment, and Observation, Vol. 774. AIP Conf. Proc., p.379

Coulomb C.A.d., 1785a, Histoire de l'Académie Royale des Sciences 569–577

Coulomb C.A.d., 1785b, Histoire de l'Académie Royale des Sciences 578–611

Cowan R.D., 1981, The Theory of Atomic Structure and Spectra, University of California Press Berkeley Los Angelos London

Crespo López-Urrutia J.R., Beiersdorfer P., Widmann K., Decaux V., 2002, Can. J. Phys. 80, 1687

Darwin C., 1922, Phil. Mag. 43, 800

Darwin C.G., 1914, Phil. Mag. 27, 315

Davidson K., 1972, ApJ 171, 213

De Pontieu B., McIntosh S.W., Carlsson M., et al., 2011, Science 331, 55

Debye P., 1912, Ann. d. Phys. 344, 789

Decaux V., Beiersdorfer P., 1993, Phys. Scr. T47, 80

Decaux V., Beiersdorfer P., Kahn S.M., Jacobs V.L., 1997, ApJ 482, 1076

Decaux V., Beiersdorfer P., Osterheld A., et al., 1995, ApJ 443, 464

Decaux V., Jacobs V.L., Beiersdorfer P., et al., 2003, Phys. Rev. A 68, 012509

Demtröder W., 2005, Experimentalphysik 3: Atome, Moleküle und Festkörper, Springer-Verlag Berlin Heidelberg, 3rd edition

Demtröder W., 2008, Experimentalphysik 1: Mechanik und Wärme, Springer-Verlag Berlin Heidelberg, 5th edition

den Herder J.W., Brinkman A.C., Kahn S.M., et al., 2001, A&A 365, L7

Dere K.P., Landi E., Mason H.E., et al., 1997, A&AS 125, 149

Dessart L., Owocki S.P., 2003, A&A 406, L1

Díaz F., Vilkas M.J., Ishikawa Y., Beiersdorfer P., 2013, ApJS 207, 11

Dirac P.A.M., 1928, Proc. R. Soc. Lond. A 117, 610

Dittner P.F., Datz S., Miller P.D., et al., 1987, Phys. Rev. A 35, 3668

Donets E.D., 1985, Nucl. Instrum. Methods Phys. Res., Sect. B 9, 522

Doppler C., 1842, Abh. d. königl. böhm. Ges. d. Wiss. 5, 465

Drake G.W., 1988, Can. J. Phys. 66, 586

Dupree A.K., Gursky H., Black J.H., et al., 1980, ApJ 238, 969

Dyall K., 1986, Comput. Phys. Commun. 39, 141

Eckart M.E., Adams J.S., Boyce K.R., et al., 2016, In: den Herder J.W.A., Takahashi T., Bautz M. (eds.) Space Telescopes and Instrumentation 2016: Ultraviolet to Gamma Ray, Vol. 9905., p. 99053W

Edlén B., 1943, Z. Astrophys. 22, 30

Einstein A., 1905, Annalen der Physik 322, 132

Elliott S.R., Marrs R.E., 1995, Nucl. Instrum. Methods Phys. Res., Sect. B 100, 529

Enss C., 2001, J. Low Temp. Phys. 124, 353 10.1023/A:1017502724149

Enss C., 2005, Cryogenic particle detection, Vol. 99 of *Topics in Applied Physics*, Topics in Applied Physics, Springer

Epp S.W., Crespo López-Urrutia J.R., Simon M.C., et al., 2010, J. Phys. B 43, 194008

Epp S.W., López-Urrutia J.R.C., Brenner G., et al., 2007, Phys. Rev. Lett. 98, 183001

Eversberg T., Lépine S., Moffat A.F.J., 1998, ApJ 494, 799

Fabian A.C., Arnaud K.A., Bautz M.W., Tawara Y., 1994, Astrophys. J., Lett. 436, L63

Fabian A.C., Hu E.M., Cowie L.L., Grindlay J., 1981, ApJ 248, 47

Fabian A.C., Sanders J.S., Ettori S., et al., 2000, MNRAS 318, L65

Faenov A.Y., Pikuz S.A., Shlyaptseva A.S., 1994, Phys. Scr. 49, 41

Feldmeier A., Puls J., Pauldrach A.W.A., 1997, A&A 322, 878

Ferland G.J., Porter R.L., van Hoof P.A.M., et al., 2013, Rev. Mex. Astron. Astrophys. 49, 137

Fixsen D.J., Moseley S.H., Cabrera B., Figueroa-Feliciano E., 2002, AIP Conf. Proc. 605, 339

Fixsen D.J., Moseley S.H., Cabrera B., Figueroa-Feliciano E., 2004, Nucl. Instrum. Methods Phys. Res., Sect. A 520, 555

Fontes C.J., Sampson D.H., Zhang H.L., 1993, Phys. Rev. A 47, 1009

Fontes C.J., Zhang H.L., Sampson D.H., 1999, Phys. Rev. A 59, 295

Forman W., Jones C., Cominsky L., et al., 1978, ApJS 38, 357

Forman W., Jones C., Tananbaum H., et al., 1973, Astrophys. J., Lett. 182, L103

Forman W., Kellogg E., Gursky H., et al., 1972, ApJ 178, 309

Foster A.R., Ji L., Smith R.K., Brickhouse N.S., 2012, ApJ 756, 128

Foster A.R., Smith R.K., Brickhouse N.S., 2016, ApJ in prep.

Friedman H., Lichtman S.W., Byram E.T., 1951, Phys. Rev. 83, 1025

Friedrich H., 1990, Theoretical Atomic Physics, Springer-Verlag Berlin Heidelberg New York, 1st edition

Friedrich W., Knipping P., Laue M., 1913, Ann. d. Phys. 346, 971

Fritz G., Kreplin R.W., Meekins J.F., et al., 1967, Astrophys. J., Lett. 148, L133

Fürst F., 2011, Ph.D. thesis, Dr. Karl Remeis-Sternwarte, Astronomisches Institut der Universität Erlangen-Nürnberg, Sternwartstr. 7, 96049 Bamberg, Germany

Fürst F., Suchy S., Kreykenbohm I., et al., 2011, A&A 535, A9

Gabriel A.H., 1972, MNRAS 160, 99

Gabriel A.H., Jordan C., 1969, MNRAS 145, 241

Galeazzi M., McCammon D., Sanders W.T., 2000, In: X-ray and inner shell processes: 18th International Conference, Vol. 506. American Institute of Physics Conference Ser., p.638

Garcia J.D., Mack J.E., 1965, Journal of the Optical Society of America 55, 654

Garmire G.P., Bautz M.W., Ford P.G., et al., 2003, In: J. E. Truemper & H. D. Tananbaum (ed.) X-Ray and Gamma-Ray Telescopes and Instruments for Astronomy. Proc. SPIE 4851, p.28

Gauß C.F., 1809, Theoria motus corporum coelestium in sectionibus conicis solem ambientium, Perthes et Besser, Hamburg

Gehrels N., 1986, ApJ 303, 336

Giacconi R., Branduardi G., Briel U., et al., 1979, ApJ 230, 540

Giacconi R., Gursky H., Paolini F.R., Rossi B.B.,

1962, Phys. Rev. Lett. 9, 439

Giacconi R., Kellogg E., Gorenstein P., et al., 1971, Astrophys. J., Lett. 165, L27

Giacomo P., 1984, Metrologia 20, 25

Gies D.R., Bolton C.T., 1986, ApJ 304, 371

Gies D.R., Bolton C.T., Thomson J.R., et al., 2003, ApJ 583, 424

Girish V., Rana V.R., Singh K.P., 2007, ApJ 658, 525

Goldstein G., Huenemoerder D.P., Blank D., 2004, Astron. J. 127, 2310

Gouy G., 1916, Ann. de Phys. Ser. 9 5, 241

Greenwood J.B., Williams I.D., Smith S.J., Chutjian A., 2000, Astrophys. J., Lett. 533, L175

Gregory D., Dunn G.H., Phaneuf R.A., Crandall D.H., 1979, Phys. Rev. A 20, 410

Grinberg V., Hell N., Neilsen J., et al., 2017, in prep.

Grinberg V., Hell N., Pottschmidt K., et al., 2013, A&A 554, A88

Grinberg V., Leutenegger M.A., Hell N., et al., 2015, A&A 576, A117

Grotrian W., 1928, Graphische Darstellung der Spektren von Atomen und Ionen mit ein, zwei und drei Valenzelektronen, 2 Teile

Grotrian W., 1931, Z. Astrophys. 3, 199

Gu M., Beiersdorfer P., Brown G., et al., 2012, Can. J. Phys. 90, 351

Gu M.F., 2000, Ph.D. thesis, Columbia University

Gu M.F., 2003, ApJ 582, 1241

Gu M.F., 2004a, FAC 1.1.1 Manual

Gu M.F., 2004b, In: Cohen J.S., Kilcrease D.P., Mazavet S. (eds.) Atomic Processes in Plasmas, Vol. 730. AIP Conf. Proc., p.127

Gu M.F., 2008, Can. J. Phys. 86, 675

Gu M.F., Kahn S.M., Savin D.W., et al., 2001, ApJ 563, 462

Gu M.F., Kahn S.M., Savin D.W., et al., 1999a, ApJ 518, 1002

Gu M.F., Savin D.W., Beiersdorfer P., 1999b, J. Phys. B 32, 5371

Gu M.F., Schmidt M., Beiersdorfer P., et al., 2005, ApJ 627, 1066

Gursky H., Kellogg E.M., Leong C., et al., 1971, Astrophys. J., Lett. 165, L43

Haga H., Wind C.H., 1899, Ann. d. Phys. 304, 884

Haga H., Wind C.H., 1903, Ann. d. Phys. 315, 305

Hakel P., Mancini R.C., Harris C., et al., 2007, Phys. Rev. A 76, 012716

Halbleib J.A., Kensek R.P., Valdez G.D., et al., 1992, IEEE Trans. Nucl. Sci. 39, 1025

Hammel B.A., Keane C.J., Cable M.D., et al., 1993, Phys. Rev. Lett. 70, 1263

Hammel B.A., Keane C.J., Kania D.R., et al., 1992, Rev. Sci. Instrum. 63, 5017

Hanke M., 2011, Ph.D. thesis, Dr. Karl Remeis-Sternwarte, Astronomisches Institut der Universität Erlangen-Nürnberg, Sternwartstr. 7, 96049 Bamberg, Germany

Hanke M., Wilms J., Nowak M.A., et al., 2009, ApJ 690, 330

Hanke M., Wilms J., Nowak M.A., et al., 2008, In: Microquasars and Beyond.

Harrison F.A., Craig W.W., Christensen F.E., et al., 2013, ApJ 770, 103

Haynes W.M., 2015, CRC Handbook of chemistry and physics: a ready-reference book of chemical and physical data, CRC Press, 96th edition

Hebb M.H., Menzel D.H., 1940, ApJ 92, 408

Hell N., 2012, *Master's thesis*, Dr. Karl Remeis-Sternwarte, Universität Erlangen-Nürnberg

Hell N., Beiersdorfer P., Magee E.W., Brown G.V., 2016a, Rev. Sci. Instrum. 87, 11D604

Hell N., Brown G.V., Wilms J., et al., 2015, In: XXIX IAU General Assembly, Vol. 1. Astronomy in Focus, p. in press

Hell N., Brown G.V., Wilms J., et al., 2016b, ApJ 830, 26

Hell N., Miškovičová I., Brown G.V., et al., 2013, Phys. Scr. T156, 014008

Henderson J.R., Beiersdorfer P., Bennett C.L., et al., 1990, Phys. Rev. Lett. 65, 705

Henke B.L., Gullikson E.M., Davis J.C., 1993, Atomic Data and Nuclear Data Tables 54, 181

Herrero A., Kudritzki R.P., Gabler R., et al., 1995, A&A 297, 556

Herschel F.W., 1800a, Phil. Trans. R. Soc. Lond. 90, 284

Herschel F.W., 1800b, Phil. Trans. R. Soc. Lond. 90, 255

Hill K.W., Bitter M., Delgado-Aparacio L., et al., 2014, Rev. Sci. Instrum. 85, 11D612

Hill K.W., Bitter M.L., Scott S.D., et al., 2008, Rev. Sci. Instrum. 79, 10E320

Hiltner W.A., Werner J., Osmer P., 1972, Astrophys. J., Lett. 175, L19

Hirsch M., Hell N., Grinberg V., et al., 2017, in prep.

Hitomi CollaborationAharonian F., Akamatsu H., et al., 2016, Nat 535, 117

Holczer T., Behar E., 2012, ApJ 747, 71

Holczer T., Behar E., Kaspi S., 2007, ApJ 663, 799

Hölzer G., Fritsch M., Deutsch M., et al., 1997, Phys. Rev. A 56, 4554

Hopps N., Oades K., Andrew J., et al., 2015, Plasma Phys. Controlled Fusion 57, 064002

Houck J.C., 2002, In: G. Branduardi-Raymont (ed.) High Resolution X-ray Spectroscopy with XMM-Newton and Chandra., published electronically

Houck J.C., Denicola L.A., 2000, In: N. Manset, C. Veillet, & D. Crabtree (ed.) Astronomical Data Analysis Software and Systems IX, Vol. 216. Astron. Soc. Pacific, Conf. Ser., p. 591

House L.L., 1969, ApJS 18, 21

Hubbell J.H., Seltzer S.M., 2004, Tables of X-ray Mass Attenuation Coefficients and Mass Energy-Absorption Coefficients (version 1.4), [online] `http://physics.nist.gov/xaamdi` Originally published as NISTIR 5632, National Institute of Standards and Technology, Gaithersburg, MD (1995).

Huenemoerder D.P., Phillips K.J.H., Sylwester J., Sylwester B., 2013, ApJ 768, 135

Hughes J.P., Safi-Harb S., Bamba A., et al., 2014, ArXiv e-prints

Hulburt E.O., 1938, Phys. Rev. 53, 344

Hutchings J.B., 1976, ApJ 203, 438

Hwang U., Petre R., Hughes J.P., 2000, ApJ 532, 970

Inal M.K., Dubau J., 1987, J. Phys. B 20, 4221

Inal M.K., Dubau J., 1993, Phys. Rev. A 47, 4794

Indelicato P., Boucard S., Lindroth E., 1998, Eur. Phys. J. D 3, 29

Irwin K., Hilton G.C., 2005, Transition-Edge Sensors. In: Enss C. (ed.) Cryogenic Particle Detection. Topics Appl. Phys., Vol. 99 Springer-Verlag Berlin Heidelberg, p.63

Ishikawa Y., Encarnación J.M.L., Träbert E., 2009, Phys. Scr. 79, 025301

Ishikawa Y., Quiney H.M., Malli G.L., 1991, Phys. Rev. A 43, 3270

Ishikawa Y., Vilkas M.J., 2001, Phys. Rev. A 63, 042506

Itikawa Y., Srivastava R., Sakimoto K., 1991, Phys. Rev. A 44, 7195

Jacobs V.L., Beiersdorfer P., 2008, Can. J. Phys. 86, 217

Jacobs V.L., Decaux V., Beiersdorfer P., 1997, J. Quant. Spectrosc. Radiat. Transfer 58, 645

Jacobs V.L., Doschek G.A., Seely J.F., Cowan R.D., 1989, Phys. Rev. A 39, 2411

James R., 1962, The optical principles of the diffraction of X-rays, G. Bell and Sons Ltd

Jansen F., Lumb D., Altieri B., et al., 2001, A&A 365, L1

Johann H.H., 1931, Z. Physik 69, 185

Johnson W.R., Soff G., 1985, Atomic Data Nucl. Data Tables 33, 405

Kaastra J.S., Mewe R., Nieuwenhuijzen H., 1996, In: Yamashita K., Watanabe T. (eds.) 11th Colloquium on UV and X-ray Spectroscopy of Astrophysical and Laboratory Plasmas., p.411

Kahn S.M., Gu M.F., Savin D.W., et al., 1998, In: Proc. Lab. Space Sci. Workshop, Cambridge, MA.

Kallman T.R., Bautista M.A., Goriely S., et al., 2009, ApJ 701, 865

Kallman T.R., McCray R., 1982, ApJS 50, 263

Kallman T.R., Palmeri P., 2007, Rev. Mod. Phys. 79, 79

Kallman T.R., Palmeri P., Bautista M.A., et al., 2004, ApJS 155, 675

Kallman T.R., White N.E., 1982, Astrophys. J., Lett. 261, L35

Kallmann H., Mark H., 1926, Naturwissenschaften 14, 648

Kallmann H., Mark H., 1927, Ann. d. Phys. 387, 585

Kaspi S., Brandt W.N., George I.M., et al., 2002, ApJ 574, 643

Kastner J.H., Huenemoerder D.P., Schulz N.S., et al., 2002, ApJ 567, 434

Kelley R.L., Audley M.D., Boyce K.R., et al., 1999, In: Siegmund O.H., Flanagan K.A. (eds.) EUV, X-Ray, and Gamma-Ray Instrumentation for Astronomy X, Vol. 3765. Proceedings of SPIE, p.114

Kelley R.L., Mitsuda K., Allen C.A., et al., 2007, PASJ 59, 77

Kim Y.S., Pratt R.H., 1983, Phys. Rev. A 27, 2913

Kinkhabwala A., Sako M., Behar E., et al., 2002, ApJ 575, 732

Kisielius R., Berrington K.A., Norrington P.H., 1996, A&AS 118, 157

Klapisch M., 1971, Comput. Phys. Commun. 2, 239

Koch P.P., 1912, Ann. d. Phys. 343, 507

Koyama K., Tsunemi H., Dotani T., et al., 2007, PASJ 59, 23

Kramers H.A., 1923, Phil. Mag. 46, 836

Kramers H.A., 1924a, Nat 113, 673

Kramers H.A., 1924b, Nat 114, 310

Kramida A., Ralchenko Y., Reader J., NIST ASD Team 2016, NIST Atomic Spectra Database (version 5.0), [Online]. Available: `http://physics.nist.gov/asd`

Krause M.O., Oliver J.H., 1979, J. Phys. Chem. Ref. Data 8, 329

Kreykenbohm I., Wilms J., Kretschmar P., et al., 2008, A&A 492, 511

Krolik J.H., McKee C.F., Tarter C.B., 1981, ApJ 249, 422

Kronig R.D.L., 1926, J. Opt. Soc. Am. 12, 547

Kubiček K., Braun J., Bruhns H., et al., 2012, Rev. Sci. Instrum. 83, 013102

Lamb W.E., Retherford R.C., 1947, Phys. Rev. 72, 241

Lampton M., Margon B., Bowyer S., 1976, ApJ 208, 177

Landi E., Young P.R., Dere K.P., et al., 2013, ApJ 763, 86

Lapierre A., Crespo López-Urrutia J.R., Baumann T.M., et al., 2007, Rev. Sci. Instrum. 78, 123105

Laue M.v., Friedrich W., Knipping P., 1912, Sitz. Math. Phys. Klasse Bayer. Akad. Wiss.

Le Gros M., Silver E., Beiersdorfer P., et al., 1996, The First on-line EBIT Plasma Measurement with a Microcalorimeter, University of California Lawrence Livermore National Laboratory Report UCRL-ID-124429 p. 22, Electron Beam Ion Trap Annual Report 1995

Lee J.C., Ogle P.M., Canizares C.R., et al., 2001, Astrophys. J., Lett. 554, L13

Leutenegger M.A., 2006, Ph.D. thesis, Columbia University

Leutenegger M.A., Audard M., Boyce K.R., et al., 2016, In: den Herder J.W.A., Takahashi T., Bautz M. (eds.) Space Telescopes and Instrumentation 2016: Ultraviolet to Gamma Ray, Vol. 9905., p.99053U

Levine A.M., Lang F.L., Lewin W.H.G., et al., 1984, ApJS 54, 581

Levine M.A., Marrs R.E., Bardsley J.N., et al., 1989, Nucl. Instrum. Methods Phys. Res., Sect. B 43, 431

Levine M.A., Marrs R.E., Henderson J.R., et al., 1988, Physica Scripta Volume T 22, 157

Liedahl D., Sako M., Kahn S., et al., 2002, April Meet. Am. Phys. Soc. Abstr.X11.003

Liedahl D.A., Brown G.V., 2008, Can. J. Phys. 86, 183

Lin C.D., Johnson W.R., Dalgarno A., 1977, Phys. Rev. A 15, 154

Longhurst R., 1967, Geometrical and physical optics, Longmans

Lorentz H., 1923, The theory of electrons, G.E. Stechert, NY

Lotz W., 1968, Z. Physik 216, 241

Low F.J., 1961, J. Opt. Soc. Am. 51, 1300

Lucy L.B., Solomon P.M., 1970, ApJ 159, 879

Lyman T., 1906, ApJ 23, 181

Madsen K.K., Beardmore A.P., Forster K., et al., 2017, AJ 153, 2

Magee E., Beiersdorfer P., Brown G., Hell N.,

2014, Rev. Sci. Instrum. 85, 11E820

Malespin C., Ballance C.P., Pindzola M.S., et al., 2011, A&A 526, A115

Mancini R.C., Iglesias C.A., Ferri S., et al., 2013, High Energy Density Physics 9, 731

Manousakis A., 2011, Thèse de doctorat, Université de Genève, Geneva

Markert T.H., Canizares C.R., Dewey D., et al., 1994, In: Siegmund O.H., Vallerga J.V. (eds.) EUV, X-Ray, and Gamma-Ray Instrumentation for Astronomy V, Vol. 2280. Proceedings of SPIE, p.168

Markova N., Puls J., Scuderi S., Markov H., 2005, A&A 440, 1133

Marrs R.E., 2008, Can. J. Phys. 86, 11

Marrs R.E., Beiersdorfer P., Elliott S.R., et al., 1995, Physica Scripta Volume T 59, 183

Marrs R.E., Beiersdorfer P., Schneider D., 1994, Phys. Today 47, 27

Marrs R.E., Elliott S.R., Knapp D.A., 1994, Phys. Rev. Lett. 72, 4082

Marrs R.E., Levine M.A., Knapp D.A., Henderson J.R., 1988, Phys. Rev. Lett. 60, 1715

Marshall H.L., Dewey D., Ishibashi K., 2004, In: Flanagan K., Siegmund O. (eds.) X-ray and Gamma-Ray Instrumentation for Astronomy XIII, Vol. 5165. Proceedings of SPIE, p.457

Mather J.C., 1982, Appl. Opt. 21, 1125

Maxwell J.C., 1867, Phil. Trans. Soc. Lond. 157, 49

May M.J., Beiersdorfer P., Jordan N., et al., 2005, Nucl. Instrum. Methods Phys. Res., Sect. B 235, 231

May M.J., Fournier K.B., Beiersdorfer P., et al., 2003, Phys. Rev. E 68, 036402

McCammon D., 2005a, Semiconductor Thermistors. In: Enss C. (ed.) Cryogenic Particle Detection. Topics Appl. Phys., Vol. 99 Springer-Verlag Berlin Heidelberg, p.35

McCammon D., 2005b, Thermal Equilibrium Calorimeters - An Introduction. In: Enss C. (ed.) Cryogenic Particle Detection. Topics Appl. Phys., Vol. 99 Springer-Verlag Berlin Heidelberg, p.1

McClintock J.E., Rappaport S., Joss P.C., et al., 1976, Astrophys. J., Lett. 206, L99

McNamara B.R., O'Connell R.W., Sarazin C.L., 1996, AJ 112, 91

Mendoza C., Kallman T.R., Bautista M.A., Palmeri P., 2004, A&A 414, 377

Mewe R., 1999, In: van Paradijs J., Bleeker J.A.M. (eds.) X-Ray Spectroscopy in Astrophysics, Vol. 520. Lecture Notes in Physics, Berlin Springer Verlag, p. 109

Mewe R., Schrijver J., 1978a, A&A 65, 99

Mewe R., Schrijver J., 1978b, A&A 65, 115

Miceli M., Decourchelle A., Ballet J., et al., 2006, A&A 453, 567

Michette A.G., 1986, Optical systems for soft X-rays, Plenum Press NY

Miller J.M., Pooley G.G., Fabian A.C., et al., 2012, ApJ 757, 11

Miller J.M., Wojdowski P., Schulz N.S., et al., 2005, ApJ 620, 398

Millikan R.A., 1914, Phys. Rep. 4, 73

Milne E., 1924, Phil. Mag. 47, 209

Mitsuda K., Bautz M., Inoue H., et al., 2007, PASJ 59, 1

Mitsuda K., Kelley R.L., Boyce K.R., et al., 2010, In: Space Telescopes and Instrumentation 2010: Ultraviolet to Gamma Ray, Vol. 7732. Proceedings of SPIE

Mittaz J.P.D., Carrera F.J., Romero-Colmenero E., et al., 1999, MNRAS 308, 233

Miškovičová I., Hanke M., Wilms J., et al., 2010, In: poster at the 7th Integral/BART Workshop, IBWS2010, 14-18 Apr 2010.

Miškovičová I., Hell N., Hanke M., et al., 2016, A&A 590, A114

Mohr P.J., Newell D.B., Taylor B.N., 2015, ArXiv e-prints

Mohr P.J., Taylor B.N., 2000, Rev. Mod. Phys. 72, 351

Mohr P.J., Taylor B.N., 2005, Rev. Mod. Phys. 77, 1

Mohr P.J., Taylor B.N., Newell D.B., 2008, Rev. Mod. Phys. 80, 633

Mohr P.J., Taylor B.N., Newell D.B., 2012, Rev. Mod. Phys. 84, 1527

Moores D.L., Pindzola M.S., 1992, J. Phys. B 25, 4581

Moseley H.G.J., 1913, Phil. Mag. 26, 1024

Moseley H.G.J., 1914, Phil. Mag. 27, 703

Moseley S.H., Mather J.C., McCammon D., 1984, J. Appl. Phys. 56, 1257

Nagel D.J., Burkhalter P.G., Dozier C.M., et al., 1974, Phys. Rev. Lett. 33, 743

Nakamura N., 2000, Rev. Sci. Instrum. 71, 4065

Nakamura N., Kato D., Miura N., et al., 2001, Phys. Rev. A 63, 024501

Nandra K., Barret D., Barcons X., et al., 2014, ATHENA: The Advanced Telescope for High ENergy Astrophysics, Mission proposal addressing *The Hot and Energetic Universe* science theme

Nandra K., Barret D., Barcons X., et al., 2013, ArXiv e-prints

Neupert W.M., 1971, Sol. Phys. 18, 474

Niles A.M., Magee E.W., Thorn D.B., et al., 2006, Rev. Sci. Instrum. 77, 10F106

Noble M.S., Nowak M.A., 2008, PASP 120, 821

Nobukawa M., Koyama K., Tsuru T.G., et al., 2010, PASJ 62, 423

Nousek J.A., Shue D.R., 1989, ApJ 342, 1207

Nowak M.A., Wilms J., Hanke M., et al., 2012, Mem. Soc. Astron. Ital. 83, 202

Nugent J.J., Jensen K.A., Nousek J.A., et al., 1983, ApJS 51, 1

Orosz J.A., McClintock J.E., Aufdenberg J.P., et al., 2011, ApJ 742, 84

Oskinova L.M., Feldmeier A., Hamann W.R., 2006, MNRAS 372, 313

Oskinova L.M., Feldmeier A., Kretschmar P., 2012, MNRAS 421, 2820

Owocki S.P., Rybicki G.B., 1984, ApJ 284, 337

Oxenius J., 1986, Kinetic theory of particles and photons. Theoretical foundations of Non-LTE plasma spectroscopy, Springer Series in Electrophysics, Springer Berlin

Paerels F., Cottam J., Sako M., et al., 2000, Astrophys. J., Lett. 533, L135

Paerels F.B.S., Kahn S.M., 2003, ARA&A 41, 291

Palmeri P., Mendoza C., Kallman T.R., Bautista M.A., 2003a, A&A 403, 1175

Palmeri P., Mendoza C., Kallman T.R., et al., 2003b, A&A 410, 359

Palmeri P., Quinet P., Mendoza C., et al., 2008a, ApJS 177, 408

Palmeri P., Quinet P., Mendoza C., et al., 2008b, ApJS 179, 542

Palmeri P., Quinet P., Mendoza C., et al., 2011, A&A 525, A59

Palmeri P., Quinet P., Mendoza C., et al., 2012, A&A 543, A44

Park S., Badenes C., Mori K., et al., 2013, Astrophys. J., Lett. 767, L10

Park T., Kashyap V.L., Siemiginowska A., et al., 2006, ApJ 652, 610

Pauli W., 1925, Z. Physik 31, 765 10.1007/BF02980631

Peille P., Ceballos M.T., Cobo B., et al., 2016, In: den Herder J.W.A., Takahashi T., Bautz M. (eds.) Space Telescopes and Instrumentation 2016: Ultraviolet to Gamma Ray, Vol. 9905., p. 99055W

Pereira N.R., Macrander A.T., Hill K.W., et al., 2015, Rev. Sci. Instrum. 86, 103704

Peter H., Dwivedi B.N., 2014, Frontiers in Astronomy and Space Sciences 1, 2

Pierce J.R., Millburn N.J., 1952, Electron Gun, Patent US 2585582

Planck M., 1900a, Verhandl. der Deutschen Physikalischen Gesellsch. 2 13, 202

Planck M., 1900b, Verhandl. der Deutschen Physikalischen Gesellsch. 2 17, 237

Poisson S.D., 1837, Probabilité des jugements en matière criminelle et en matière civile, précédées des règles générales du calcu des probabilitiés, Bachelier, Paris

Porquet D., Dubau J., 2000, A&AS 143, 495

Porquet D., Mewe R., Dubau J., et al., 2001a, A&A 376, 1113

Porquet D., Mewe R., Raassen A.J.J., et al., 2001b, In: Giacconi R., Serio S., Stella L. (eds.) X-ray Astronomy 2000, Vol. 234. Astron. Soc. Pacific, Conf. Ser., p. 121

Porter F., Deiker S., Kelley R., et al., 1997, In: Cooper S. (ed.) Proc. 7th International Workshop on Low Temperature Detectors., p. 113

Porter F.S., 2013, X-ray Calorimeters. In: Huber M.C.E., Pauluhn A., Culhane J.L., Timothy J.G., Wilhelm K., Zehnder A. (eds.) Observing Photons in Space: A Guide to Exper-

imental Space Astronomy. ISSI Scientific Report Series 9 Springer New York, 2 edition, Ch. 28, p.497

Porter F.S., Adams J.S., Beiersdorfer P., et al., 2009a, In: Young B., Cabrera B., Miller A. (eds.) 13th International Workshop on Low Temperature Detectors. AIP Conf. Proc., p.454

Porter F.S., Beck B.R., Beiersdorfer P., et al., 2008a, Can. J. Phys. 86, 231

Porter F.S., Beiersdorfer P., Brown G.V., et al., 2008b, Journal of Low Temperature Physics 151, 1061

Porter F.S., Beiersdorfer P., Brown G.V., et al., 2009b, J. Phys. Conf. Series 163, 012105

Porter F.S., Brown G.V., Boyce K.R., et al., 2004, Rev. Sci. Instrum. 75, 3772

Porter F.S., Brown G.V., Cottam J., 2005, X-ray Astronomy and Astrophysics. In: Enss C. (ed.) Cryogenic Particle Detection. Topics Appl. Phys., 99 Springer-Verlag Berlin Heidelberg, p.359

Porter F.S., Gygax J., Kelley R.L., et al., 2008c, Rev. Sci. Instrum. 79, 307

Pradhan A.K., Nahar S.N., 2011, Atomic Astrophysics and Spectroscopy, Cambridge University Press, New York, 1st edition

Prins J.A., 1930, Z. Physik 63, 477

Ravera L., Barret D., den Herder J.W., et al., 2014, In: Takahashi T., den Herder J.W.A., Baut M. (eds.) Space Telescopes and Instrumentation 2014: Ultraviolet to Gamma Ray, Vol. 9144. Proceedings of SPIE

Reed K.J., Chen M.H., 1993, Phys. Rev. A 48, 3644

Reeves J.N., Porquet D., Braito V., et al., 2013, ApJ 776, 99

Reid M.J., McClintock J.E., Narayan R., et al., 2011, ApJ 742, 83

Robbins D.L., Beiersdorfer P., Faenov A.Y., et al., 2006, Phys. Rev. A 74, 022713

Robbins D.L., Faenov A.Y., Pikuz T.A., et al., 2004, Phys. Rev. A 70, 022715

Röntgen W.C., 1895, Sitzungsber. der Würzburger Physik.-Medic. Gesellsch. 9, 132

Rose M.E., 1961, Relativistic Electron Theory, Wiley, New York

Rowland H.A., 1882, Phil. Mag. 13, 469

Rowland H.A., 1883, Phil. Mag. Series 5 16, 197

Rudolph J.K., Bernitt S., Epp S.W., et al., 2013, Phys. Rev. Lett. 111, 103002

Russell H.N., Saunders F.A., 1925, ApJ 61, 38

Rybicki G.B., Lightman A.P., 1979, Radiative Processes in Astrophysics, John Wiley and Sons, Inc.

Rydberg J.R., 1889, Kungliga Svenska Vetenskapsakademien Handlingar 23

Sadakane K., Hirata R., Jugaku J., et al., 1985, ApJ 288, 284

Sako M., Kahn S.M., Paerels F., et al., 2002, In: G. Branduardi-Raymont (ed.) High Resolution X-ray Spectroscopy with XMM-Newton and Chandra.

Salama F., Leckrone D., Mathis J., et al., 2002, Laboratory Astrophysics White Paper (based on the 200w NASA Laboratory Astrophysics Workshop at the NASA Ames Research Center, 1–3 May, 2002), White Paper of the 2002 NASA Laboratory Astrophysics Workshop `http://www.astrochemistry.org/nasalaw.html`

Saloman E.B., Hubbell J.H., Scofield J.H., 1988, Atomic Data Nucl. Data Tables 38, 1

Sanford P., Mason K.O., Ives J., 1975, MNRAS 173, 9P

Sato N., Hayakawa S., Nagase F., et al., 1986, PASJ 38, 731

Savin D.W., Allamandola L., Federman S., et al., 2010, Laboratory Astrophysics White Paper (based on the 2010 NASA Laboratory Astrophysics Workshop in Gatlinberg, Tennessee, 25-28 October 2010), White Paper of the 2010 NASA Laboratory Astrophysics Workshop `http://www-cfadc.phy.ornl.gov/nasa_law/`

Savin D.W., Badnell N.R., Beiersdorfer P., et al., 2008, Can. J. Phys. 86, 209

Savin D.W., Bartsch T., Chen M.H., et al., 1997, Astrophys. J., Lett. 489, L115

Savin D.W., Beck B., Beiersdorfer P., et al., 1999, Phys. Scr. T80, 312

Savin D.W., Beiersdorfer P., Kahn S.M., et al.,

2000, Rev. Sci. Instrum. 71, 3362

Savin D.W., Brickhouse N.S., Cowan J.J., et al., 2012, Rep. Prog. Phys. 75, 036901

Savin D.W., Gu M.F., Beiersdorfer P., 1998, In: Fujimoto T., Beiersdorfer P. (eds.) Proceedings of the US-Japan Workshop on Plasma Polarization Spectroscopy, 26-29 January 1998, Vol. 37., p.90

Schmidt M., Beiersdorfer P., Chen H., et al., 2004, ApJ 604, 562

Schneider M.B., Levine M.A., Bennett C.L., et al., 1989, In: Hershcovitch A. (ed.) International symposium on electron beam ion sources and their applications, Vol. 188. Am. Inst. Phys., Conf. Ser., p.158

Schneider M.B., Mancini R., Widmann K., et al., 2008, Can. J. Phys. 86, 259

Schnopper H.W., Kalata K., 1969, Appl. Phys. Lett. 15, 134

Schrödinger E., 1926a, Phys. Rev. 28, 1049

Schrödinger E., 1926b, Ann. d. Phys. 79, 361

Schulz N.S., Canizares C.R., Lee J.C., Sako M., 2002, Astrophys. J., Lett. 564, L21

Scofield J.H., 1989, Phys. Rev. A 40, 3054

Seaton M.J., 1953, Proc. R. Soc. London, Ser. A 218, 400

Serlemitsos P.J., Boldt E.A., Holt S.S., et al., 1975, Astrophys. J., Lett. 201, L9

Seta H., Tashiro M.S., Ishisaki Y., et al., 2012, IEEE Trans. Nucl. Sci. 59, 366

Shlyaptseva A.S., Mancini R.C., Neill P., Beiersdorfer P., 1997, Rev. Sci. Instrum. 68, 1095

Shlyaptseva A.S., Urnov A.M., Vinogradov P.N., 1981, Lebedev Physical Institute of the USSR Academy of Sciences Report No. 194, (unpublished)

Siegbahn K.M., 1924, Spektroskopie der Röntgenstrahlen, Springer Berlin

Siemiginowska A., 2009, Statistics, 1st School on Multiwavelength Astronomy `http://pulsar.sternwarte.uni-erlangen.de/black-hole/1stschool/coursematerial/statistics_paris2009.pdf`

Simionescu A., Werner N., Urban O., et al., 2012, ApJ 757, 182

Simon F., 1935, Nat 135, 763

Sivia D.S., Skilling J., 2006, Data Analysis – A Bayesian Tutorial, Oxford University Press, 2nd edition

Smith A.J., Beiersdorfer P., Decaux V., et al., 1995, Phys. Rev. A 51, 2808

Smith A.J., Beiersdorfer P., Reed K.J., et al., 2000, Phys. Rev. A 62, 012704

Smith A.J., Bitter M., Hsuan H., et al., 1993, Phys. Rev. A 47, 3073

Smith R.K., Brickhouse N.S., 2014, Chapter Four - Atomic Data Needs for Understanding X-ray Astrophysical Plasmas. In: Arimondo E., Berman P.R., Lin C.C. (eds.) , Vol. 63. Advances In Atomic, Molecular, and Optical Physics Academic Press, p.271

Smith R.K., Odaka H., Audard M., et al., 2014a, ArXiv e-prints

Smith S.J., Adams J.S., Bandler S.R., et al., 2014b, J. Low Temp. Phys. 176, 356

Sommerfeld A., 1912, Ann. d. Phys. 343, 473

Stahle C.K., Brekosky R.P., Dutta S.B., et al., 1999, Nucl. Instrum. Methods Phys. Res., Sect. A 436, 218

Stark J., 1907, Physik. Zeitschrift 8, 881

Steffen R.M., Alder K., 1975, Angular distribution and correlation of gamma rays. In: Hamilton W.D. (ed.) The Electromagnetic Interaction in Nuclear Spectroscopy, Vol. Chapter 12. North-Holland / American Elsevier, p. 505

Stöhlker T., Ludziejewski T., Bosch F., et al., 1999, Phys. Rev. Lett. 82, 3232

Stöhlker T., Mokler P.H., Kozhuharov C., Warczak A., 1997, Comments on Atomic and Molecular Physics 33, 271

Strüder L., Briel U., Dennerl K., et al., 2001, A&A 365, L18

Sundqvist J.O., Owocki S.P., 2013, MNRAS 428, 1837

Szymkowiak A.E., Kelley R.L., Moseley S.H., Stahle C.K., 1993, J. Low Temp. Phys. 93, 281

Takács E., Meyer E.S., Gillaspy J.D., et al., 1996, Phys. Rev. A 54, 1342

Takahashi T., Abe K., Endo M., et al., 2007, PASJ 59, 35

Takahashi T., Kokubun M., Mitsuda K., et al., 2016, In: den Herder J.W.A., Takahashi T., Bautz M. (eds.) Space Telescopes and Instrumentation 2016: Ultraviolet to Gamma Ray, Vol. 9905., p. 99050U

Takahashi T., Mitsuda K., Kelley R., et al. 2010, In: Arnaud M., Murray S.S., Takahashi T. (eds.) Space Telescopes and Instrumentation 2010: Ultraviolet to Gamma Ray, Vol. 7732. Proceedings of SPIE

Tamagawa T., 2010, In: I. Tanihara, H. J. Ong, A. Tamii, T. Kishimoto, T. Kajino, S. Kubono, & T. Shima (ed.) The 10th International Symposium on Srigin of Matter and Evolution of Galaxies, Vol. 1269. American Institute of Physics Conference Series, p.137

Tamagawa T., Hayato A., Nakamura S., et al., 2009, PASJ 61, 167

Tamura T., Maeda Y., Mitsuda K., et al., 2009, Astrophys. J., Lett. 705, L62

Tamura T., Yamasaki N.Y., Iizuka R., et al., 2014, ApJ 782, 38

Tanaka Y., Inoue H., Holt S.S., 1994, PASJ 46, L37

Tarter C.B., Tucker W.H., Salpeter E.E., 1969, ApJ 156, 943

Thompson A., Attwood D., Gullikson E., et al., 2009, X-ray Data Booklet, Lawrence Berkeley National Laboratory, University of California, 3rd edition

Thomson J.J., 1897, Philosophical Magazine Series 5 44, 293

Thomson J.J., 1906, Phil. Mag. Ser. 6 11, 769

Thorn D., Beiersdorfer P., 2004, Rev. Sci. Instrum. 75, 3937

Thorn D.B., 2008, Ph.D. thesis, University of California Davis, 1 Shields Ave, Davis, CA 95616, USA

Tousey R., Watanabe K., Purcell J.D., 1951, Phys. Rev. 83, 792

Trümper J., 1982, Advances in Space Research 2, 241

Trümper J., Hasinger G., Aschenbach B., et al., 1991, Nat 349, 579

Turner M.J.L., Abbey A., Arnaud M., et al., 2001, A&A 365, L27

Twerenbold D., 1996, Rep. Prog. Phys. 59, 349

Ullrich A., Grübling P., Zschornack G., 1998, Rev. Sci. Instrum. 69, 813

Underwood J.H., Milligan J.E., Deloach A.C., Hoover R.B., 1977, Appl. Opt. 16, 858

Utter S.B., Beiersdorfer P., López-Urrutia J.R.C., Träbert E., 1999a, Rev. Sci. Instrum. 70, 288

Utter S.B., Brown G.V., Beiersdorfer P., et al., 1999b, Rev. Sci. Instrum. 70, 284

Vaiana G.S., van Speybroeck L., Zombeck M.V., et al., 1977, Space Sci. Instrum. 3, 19

Vainshtein L.A., Safronova U.I., 1985, Phys. Scr. 31, 519

van den Berg C.B., Brinkman H., 1955, Physica 21, 85

Vegard L., 1938, Geof. Publ. 12, 3

Verner D.A., Ferland G.J., Korista K.T., Yakovlev D.G., 1996a, ApJ 465, 487

Verner D.A., Verner E.M., Ferland G.J., 1996b, Atomic Data and Nuclear Data Tables 64, 1

Vilkas M.J., Ishikawa Y., 2004, Phys. Rev. A 69, 062503

Vinogradov A.V., Urnov A.M., Shlyaptseva A.S., 1992, In: Sobelman I.I. (ed.) Atomic and Ionic Spectra and Elementary Processes in Plasma, Vol. 192., Nova Science, Commack, NY, p. 93

Vogel D.A., 1992, Ph.D. thesis, Georgia Institute of Technology, Georiga, USA

Voges W., Aschenbach B., Boller T., et al., 1999, A&A 349, 389

von Hámos L., Stschwerbina W., 1933, Nachr. Ges. Wiss. Göttingen, Math.-physik. KI. 232–34

von Hámos L., 1933, Ann. d. Phys. 409, 716 5. Folge, Band 17

Walborn N.R., 1973, Astrophys. J., Lett. 179, L123+

Walker D.W., 1974, J. Phys. B 7, 97

Walker D.W., 1975, J. Phys. B 8, 760

Walter B., Pohl R., 1908, Ann. d. Phys. 330, 715

Walter B., Pohl R., 1909, Ann. d. Phys. 334, 331

Watanabe S., Sako M., Ishida M., et al., 2006, ApJ 651, 421

Webster B.L., Murdin P., 1972, Nat 235, 37

Weisskopf M.C., Brinkman B., Canizares C.,

et al., 2002, PASP 114, 1

Whiteford A.D., Badnell N.R., Ballance C.P., et al., 2002, J. Phys. B 35, 3729

Whiteford A.D., Badnell N.R., Ballance C.P., et al., 2001, J. Phys. B 34, 3179

Widmann K., 1999, Ph.D. thesis, Technische Universität Graz, Austria

Widmann K., Beiersdorfer P., Brown G.V., et al., 2000, In: X-ray and inner-shell processes: 18th International Conference, Vol. 506. AIP Conf. Proc., p.444

Wien W., 1907, Nachr. Göttinger Ges. d. Wissensch. 598–601

Wong K.L., 1992, Ph.D. thesis, University of California Davis, Davis, California, USA

Wong K.L., Beiersdorfer P., Reed K.J., Vogel D.A., 1995, Phys. Rev. A 51, 1214

Wong K.L., May M.J., Beiersdorfer P., et al., 2003, Phys. Rev. Lett. 90, 235001

Wood K.S., Meekins J.F., Yentis D.J., et al., 1984, ApJS 56, 507

Xiang J., Lee J.C., Nowak M.A., Wilms J., 2011, ApJ 738, 78

Yamada C., Nagata K., Nakamura N., et al., 2007, J. Phys. Conf. Series 58, 403

Yamaguchi H., Eriksen K.A., Badenes C., et al., 2014, ApJ 780, 136

Yamaguchi H., Koyama K., 2010, Mem. Soc. Astron. Ital. 81, 382

Yamaguchi H., Ozawa M., Koyama K., et al., 2009, Astrophys. J., Lett. 705, L6

Yang X.J., Tsunemi H., Lu F.J., Chen L., 2009, ApJ 692, 894

Yang X.J., Tsunemi H., Lu F.J., et al., 2013, ApJ 766, 44

Zhang H.L., Sampson D.H., Clark R.E.H., 1990, Phys. Rev. A 41, 198

It takes a thousand men to invent a telegraph, or a steam engine, or a phonograph, or a photograph, or a telephone or any other important thing—and the last man gets the credit and we forget the others. He added his little mite — that is all he did. These object lessons should teach us that ninety-nine parts of all things that proceed from the intellect are plagiarisms, pure and simple; and the lesson ought to make us modest. But nothing can do that.

Mark Twain

Acknowledgments

Personal

First and foremost I would like to thank both of my advisors, Jörn Wilms and Greg Brown. Their efforts and patience made it possible for me to split my time between the Remeis Observatory, Germany, and LLNL, California, which allowed me to see the best of both worlds. Their involvement goes far beyond teaching and sharing all their knowledge and excitement about physics. You know how to keep science fun.

It takes a village and many institutions to raise a student. I would like to thank all my collaborators and friends who were involved in making this a fun and successful experience on a scientific and a personal level. This includes people at the Remeis Observatory and LLNL, who make these places home; at the MIT Kavli Institute for Astrophysics and Space Research, the Harvard Smithsonian Center for Astrophysics, NASA's Goddard Space Flight Center, the Max-Planck-Institut für Kernphysik, the LCLS at the Stanford Linear Accelerator Center (SLAC), DESY, BESSY, NSLS at the Brookhaven National Laboratory, and the Canadian Light Source (CLS) for their hospitality; and the German Academic Exchange Service (DAAD) for introducing me to Greg.

In particular I would like to thank: Peter Beiersdorfer – for your contagious enthusiasm about everything, especially physics. Ed Magee – for being EBIT doctor, nurse, shaman, and whisperer in one person, for the peaches, and the company at EBIT. David Layne – for getting up early so I don't have to, for keeping everything running, and for your entertainment. F. Scott Porter – for your support in everything calorimeter, including taking the time to proofread the ECS chapter. Maurice Leutenegger – for interesting discussions, physics or not. José Crespo – for inviting me to participate in your experiments with the Flash-EBIT at X-ray light sources. Victoria Grinberg – for never giving up trying to teach me not to think logically, for feeding and walking me when we lived in the same city, and overall for taking my crap and dishing it right back. Maria Hirsch – for keeping me company almost every day despite the distance, being my moral support hotline, and for reading my mind. Mina Gräfe – for epic road trips and surrendering your couch indefinitely. Susanne Raab – I managed to finish despite all your best efforts to keep me distracted. Alex Markowitz – for your visits to the Bay Area and your calming influence.

Katja Pottschmidt – for welcoming stray students into your home. Tom Lockard – for providing the exact right amount of the exactly right kind of distraction during the writing phase of this thesis; our joint time at EBIT will be epic. Lia Corrales and Javier García – for great atomic physics discussions and all the fun times in Boston/Cambridge and at conferences. Randall Smith, Adam Foster, and the AtomDB telecon – for sharing their insights to atomic phsysics applications and plasma models in X-ray astrophysics. Julia Vogel and Maurice Leutenegger – for their help taking the M-shell Fe data, allowing me to sleep and spend time in my office. Jörn – for enjoying being a tour guide everywhere we travel. Greg and his family – for sharing their cats with me. And, of course, my parents – for their great support, for giving my stuff a home, reading my mail, and generally making living between two countries so much easier; I promise I will keep coming home.

Software

All data analysis of this work used the Interactive Spectral Interpretation System (ISIS; Houck & Denicola, 2000; Houck, 2002; Noble & Nowak, 2008). This research has made use of the Remeis ISISscripts, a collection of ISIS functions provided by ECAP/Remeis observatory and MIT (`http://www.sternwarte.uni-erlangen.de/isis/`). Thanks to John E. Davis for providing the `slxfig` module used for creating the presented plots and some of the shown figures. ECS data acquisition and the real-time analysis is done through custom software, including the Software Calorimeter Digital Processor (SCDP) and an IgorPro extension, the XRSGSE, provided by the GSFC calorimeter team. Thanks to Kevin Boyce for answering questions about IgorPro and the GSE. Spectral calibration of the ECS data in this work heavily relies on software (CXRS) written by M. F. Gu in ISIS with a Python user interface. New calculations of atomic data presented here were done with the Flexible Atomic Code.

Financial

Work at LLNL was performed under the auspices of the US DOE under Contract DE-AC52-07NA27344 and supported by NASA grants to LLNL and GSFC. Work for the Friedrich-Alexander Universität Erlangen-Nürnberg was supported by the Bundesministerium für Wirtschaft und Technologie under Deutsches Zentrum für Luft- und Raumfahrt grant number DLR 50 OR 1113 and by the European Space Agency under contract number 4000114313/15/NL/CB. Thank you for paying me to work on fun things.